Transactions of the ASME®

Transactions of the ASME, Journal of Heat Transfer (ISSN 0022-1481) is published bi-monthly (Feb., Apr., June, Aug., Oct., Dec.) by The American Society of Mechanical Engineers, Three Park Avenue, New York, NY 10016. Periodicals postage paid at New York, NY and additional mailing offices. POSTMASTER: Send address changes to Transactions of the ASME, Journal of Heat Transfer, c/o THE AMERICAN SOCIETY OF MECHANICAL ENGINEERS, 22 Law Drive, Box 2300, Fairfield, NJ 07007-2300.
CHANGES OF ADDRESS must be received at Society headquarters seven weeks before they are to be effective. Please send old label and new address.
STATEMENT from By-Laws. The Society shall not be responsible for statements or opinions advanced in papers or ... printed in its publications (B7.1, Para. 3), **COPYRIGHT** © **2003** by The American Society of Mechanical Engineers. For authorization to photocopy material for internal or personal use under those circumstances not falling within the fair use provisions of the Copyright Act, contact the Copyright Clearance Center (CCC), 222 Rosewood Drive, Danvers, MA 01923, tel: 978-750-8400, *www.copyright.com*. Request for special permission or bulk copying should be addressed to Reprints/Permission Department. **INDEXED** by Applied Mechanics Reviews and Engineering Information, Inc. Canadian Goods & Services Tax Registration #126148048.

Journal of Heat Transfer

Published Bimonthly by The American Society of Mechanical Engineers

VOLUME 125 • NUMBER 2 • APRIL 2003

TECHNICAL PAPERS

(Contents continued on inside back cover)

This journal is printed on acid-free paper, which exceeds the ANSI Z39.48-1992 specification for permanence of paper and library materials. ♾™
♻ 85% recycled content, including 10% post-consumer fibers.

Journal of Heat Transfer Volume 125, Number 2 APRIL 2003

ANNOUNCEMENT

The ASME Journal of Heat Transfer is abstracted and indexed in the following:

Applied Science and Technology Index, AMR Abstracts Database, Chemical Abstracts, Chemical Engineering and Biotechnology Abstracts (Electronic equivalent of Process and Chemical Engineering), Civil Engineering Abstracts, Compendex (The electronic equivalent of Engineering Index), Corrosion Abstracts, Current Contents, E & P Health, Safety, and Environment, Ei EncompassLit, Engineered Materials Abstracts, Engineering Index, Enviroline (The electronic equivalent of Environment Abstracts), Environment Abstracts, Environmental Engineering Abstracts, Environmental Science and Pollution Management, Fluidex, Fuel and Energy Abstracts, Index to Scientific Reviews, INSPEC, International Building Services Abstracts, Mechanical & Transportation Engineering Abstracts, Mechanical Engineering Abstracts, METADEX (The electronic equivalent of Metals Abstracts and Alloys Index), Petroleum Abstracts, Process and Chemical Engineering, Referativnyi Zhurnal, Science Citation Index, SciSearch (The electronic equivalent of Science Citation Index), Theoretical Chemical Engineering

Estimation of Surface Temperature and Heat Flux Using Inverse Solution for One-Dimensional Heat Conduction

Masanori Monde
e-mail: monde@me.saga-u.ac.jp

Hirofumi Arima

Yuhichi Mitsutake

Department of Mechanical Engineering,
Saga University,
Saga 840-8502, Japan

An analytical method has been developed for the inverse heat conduction problem using the Laplace transform technique when the temperatures are known at two positions within a finite body. On the basis of these known temperatures, a closed form to the inverse solution can be obtained to predict surface conditions. The method first approximates the measured temperatures with a half polynomial power series of time as well as a time lag, which takes for a monitor to sense the temperature change at the point. The expressions for the surface temperature and the surface heat flux are explicitly obtained in the form of the power series of time. The surface temperature and heat flux calculated for some representative problems show agreement with the known values. The method can be applied to the case where an initial temperature distribution exists.
[DOI: 10.1115/1.1560147]

Keywords: Analytical, Computational, Conduction, Heat Transfer, Inverse

1 Introduction

The inverse heat conduction problem (IHCP) has been extensively investigated to estimate surface conditions under a severe environmental condition. In an unsteady state, direct measurement of surface temperature and heat flux is usually difficult. For the case of re-entry of a space vehicle and heat transfer from the surface of a nuclear reactor at loss of coolant event, it is necessary to estimate surface conditions such as temperature and heat flux accurately. However, one may encounter difficulties in directly measuring surface temperature and heat flux. A clue to solve this problem is to use IHCP [1,2]. Most of the studies have been approached to the IHCP by using numerical methods [3–7] for the following reasons: 1) development of computer architecture and increase in computer capacities and 2) mathematically nonconvergency of the exact solution of IHCP when $\tau \rightarrow 0$ [1]. In spite of development of numerical methods, the analytical approaches [8–12] for the IHCP in one-dimension and simple configuration in 2 or 3 dimensions still have merits in being easy to obtain the surface temperature and heat flux distributions since solutions can be explicitly obtained.

Recently, Monde [13] and Monde et al. [14] succeeded in determining the analytical solution for one-dimensional heat conduction using the Laplace transformation and demonstrated that the surface temperature or the surface heat flux could be calculated accurately. It may be worth mentioning finally that Monde and Mitsutake [15] proposed a new method based on these explicit solutions, which made it possible to measure thermal diffusivity and thermal conductivity more accurately and easier than a direct solution.

We briefly review the analytical methods [8–14] for the IHCP using the Laplace transform, which reached the same Laplace transformed solutions expressed by Eqs. (9) and (11), later. Sparrow et al. [9] and Imber and Khan [10] expanded the hyperbolic function in a series of exponential function of the Laplace parameter, s, to express a convolution of initial temperature and exponential functions. Usage of a table for Laplace Transforms as listed in a textbook [16], gave the inverse solutions in a form of a series of convolution functions. They did not take into account of time lag for a sensor. A special function [9] to express a measured temperature was introduced to avoid the divergence in their calculation. Imber and Khan [10] also introduced a trial function to approximate the measured temperature using a polynomial series of time. Shoji [12] first expanded the Laplace transformed solution in a series of s around $s=0$, and then expressed the measured temperature as a derivative with respect to time to calculate the inverse solution numerically using a finite difference method. The Monde method [13] was different from the other author's methods and had merit in the following respects: (1) the Laplace transformed solution was expanded in a series of s around $s=0$; (2) a trial function to approximate the measured temperature was a half polynomial series of time, which constitutes a general solution for one-dimensional heat conduction as shown by $T=f(\xi/\sqrt{\tau})$; (3) the time lag, which takes to sense temperature change, was taken into account; (4) a final function of the Laplace transformed solution was performed correctly by inverse Laplace transform, resulting into the explicit inverse solutions; and (5) the CPU time is short due to the explicit solutions. Monde [13] shows that his method is superior to the Imber and Khan [10], and Shoji [12] methods in some respects of estimate accuracy, predictive time in which the inverse solutions become available and robust against a disturbance included in the temperature change. However, mathematical manipulation in his method is slightly complicated compared with their methods and then the software also becomes complicated.

The objective of this paper is not only to expand Monde's method in rectangular coordinates to cylindrical and spherical coordinates but also to propose a new idea in order to alleviate the difficulty associated with the estimation of the surface condition upon rapid changes. It is found that this method can be applied to the case where an initial temperature distribution in a body exists, whereas in the previous works [13,14], an influence of the initial temperature distribution on the inverse solution had not been discussed yet.

Contributed by the Heat Transfer Division for publication in the JOURNAL OF HEAT TRANSFER. Manuscript received by the Heat Transfer Division October 21, 2001; revision received October 25, 2002. Associate Editor: G. S. Dulikravich.

2 Analysis of One-Dimensional Heat Conduction

Figures 1(*a*) and (*b*) show two points in different coordinates in which the temperatures are measured. The one-dimensional heat conduction equation with constant physical properties and no internal heat generation in a solid can be written in non-dimensional form as:

$$\frac{\partial\theta}{\partial\tau}=\frac{1}{\xi^{\kappa}}\left(\frac{\partial}{\partial\xi}\xi^{\kappa}\frac{\partial\theta}{\partial\xi}\right)\quad 0<\xi<1 \tag{1}$$

where $\kappa=0$ corresponds to rectangular coordinates, $\kappa=1$ to cylindrical, and $\kappa=2$ to spherical coordinates. For an initial condition of $\theta=\theta_0(\xi)$, Laplace transformation of Eq. (1) becomes:

$$\frac{1}{\xi^{\kappa}}\frac{d}{d\xi}\left(\xi^{\kappa}\frac{d\overline{\theta}}{d\xi}\right)-p^2\overline{\theta}=-\theta_0 \tag{2}$$

where $\overline{\theta}$ is temperature in Laplace transformed form and $p^2=s$, s is Laplace's parameter.

2.1 Initial Temperature Distribution and General Solution. The temperature in a solid is considered constant where $\partial\theta/\partial\tau=0$, before a transient heat conduction starts. Therefore, the initial temperature distribution in a solid with heat generation q can be given for the three different coordinates by the following equation:

$$\frac{1}{\xi^{\kappa}}\left(\frac{\partial}{\partial\xi}\xi^{\kappa}\frac{\partial\theta}{\partial\xi}\right)=q(\xi) \tag{3}$$

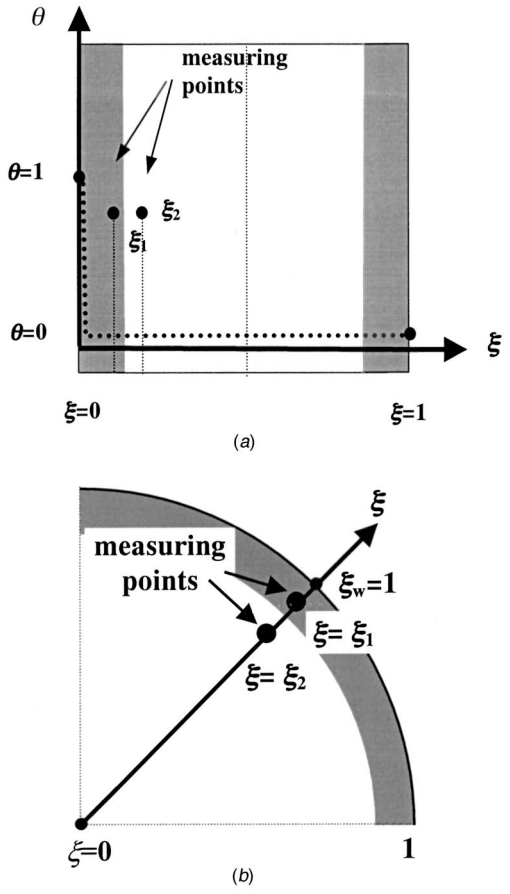

Fig. 1 (*a*) Sketch illustrating two measuring points for rectangular coordinates; and (*b*) Sketch illustrating two measuring points for cylindrical and spherical coordinates

For $\kappa=0$ and $q(\xi)=\Sigma_{n=0}q_n\xi^n$ approximating the heat generation, the initial temperature distribution can be determined from Eq. (3) as:

$$\theta_0(\xi)=\int_{\xi}\int q(\xi)d\xi=a_0+a_1\xi+\sum_{n=0}\frac{q_n}{(n+2)!}\xi^{n+2} \tag{4-1}$$

and for a special case of constant heat generation

$$\theta_0(\xi)=a_0+a_1\xi+(q_0/2)\xi^2 \tag{4-2}$$

where two constants, a_0 and a_1 can be determined from a given steady boundary condition.

It is necessary to mention that without the heat generation, the initial temperature distribution becomes either constant or linear. For the constant distribution, one can set $\theta_0=0$ without loss of generality and then we will consider the case for the constant heat generation, for simplest one, which may be encountered in engineering applications.

The general solution of Eq. (2) with initial temperature distribution, $\theta_0(\xi)$, for $\kappa=0$ can be easily given as:

$$\overline{\theta}(\xi,s)=\mathrm{Ae}^{-p\xi}+\mathrm{Be}^{p\xi}+\frac{1}{s}\theta_0(\xi)+\frac{q_0}{s^2} \tag{5}$$

where A, B are constants of integration to be determined using the boundary conditions.

2.2 Solution for Finite Body. In the case of IHCP for a finite plane, two known temperatures in the plate are necessary at least to close Eq. (2). Therefore, let the two temperatures at two different points of $\xi=\xi_1$, $\xi_2(\xi_1<\xi_2)$ be as:

$$\overline{\theta}(\xi_n,s)=\overline{f}_n(s),\quad n=1,2 \tag{6}$$

Substitution of Eq. (6) in Eq. (5) gives

$$\overline{f}_n(s)=\mathrm{Ae}^{-p\xi_n}+\mathrm{Be}^{p\xi_n}+\frac{1}{s}\theta_0(\xi_n)+\frac{q_0}{s^2},\quad n=1,2 \tag{7}$$

After determining the constants, A and B in Eq. (7), and then substituting the values of A and B into Eq. (5), we obtain the temperature distribution in the body as follows:

$$\begin{aligned}\overline{\theta}(\xi,s)=&\frac{\overline{f}_1(s)\sinh\{p(\xi_2-\xi)\}-\overline{f}_2(s)\sinh\{p(\xi_1-\xi)\}}{\sinh\{p(\xi_2-\xi_1)\}}\\&-\frac{(\theta_0(\xi_1)/s+q_0/s^2)\sinh\{p(\xi_2-\xi)\}}{\sinh\{p(\xi_2-\xi_1)\}}\\&+\frac{(\theta_0(\xi_2)/s+q_0/s^2)\sinh\{p(\xi_1-\xi)\}}{\sinh\{p(\xi_2-\xi_1)\}}+\frac{1}{s}\theta_0(\xi)+\frac{1}{s^2}q_0\end{aligned} \tag{8}$$

and the surface temperature can be easily obtained by setting $\xi=0$ as:

$$\begin{aligned}\overline{\theta}_w(s)=&\frac{\overline{f}_1(s)\sinh\{p(\xi_2)-\overline{f}_2(s)\sinh(p\xi_1)}{\sinh\{p(\xi_2-\xi_1)\}}\\&-\frac{(\theta_0(\xi_1)/s+q_0/s^2)\sinh(p\xi_2)}{\sinh\{p(\xi_2-\xi_1)\}}\\&+\frac{(\theta_0(\xi_2)/s+q_0/s^2)\sinh(p\xi_1)}{\sinh\{p(\xi_2-\xi_1)\}}+F(A_0,B_0,s)\end{aligned} \tag{9}$$

where $F(A_0,B_0,s)$ is a function related only to the initial temperature distributions and independent of the ξ coordinate, namely, constant values for the fixed points of ξ_1 and ξ_2 except for functions of the parameter, s.

Likewise, the solution for the heat flux can also be obtained as:

$$\overline{\Phi}(\xi,s)=p\frac{\overline{f}_1(s)\cosh\{p(\xi_2-\xi)\}-\overline{f}_2(s)\cosh\{p(\xi_1-\xi)\}}{\sinh\{p(\xi_2-\xi_1)\}}$$
$$-p\frac{(\theta_0(\xi_1)/s+q_0/s^2)\cosh\{p(\xi_2-\xi)\}}{\sinh\{p(\xi_2-\xi_1)\}}$$
$$+p\frac{(\theta_0(\xi_2)/s+q_0/s^2)\cosh\{p(\xi_1-\xi)\}}{\sinh\{p(\xi_2-\xi_1)\}}-\frac{1}{s}\frac{d\theta_0(\xi)}{d\xi} \tag{10}$$

where, $\overline{\Phi}(\xi,s)=-\overline{\theta}(\xi,s)/\partial\xi$

The surface heat flux becomes at $\xi=0$,

$$\overline{\Phi}_w(s)=\frac{p\overline{f}_1(s)\cosh(p\xi_2)-p\overline{f}_2(s)\cosh(p\xi_1)}{\sinh\{p(\xi_2-\xi_1)\}}$$
$$-\frac{(\theta_0(\xi_1)/s+q_0/s^2)p\cosh(p\xi_2)}{\sinh\{p(\xi_2-\xi_1)\}}$$
$$+\frac{(\theta_0(\xi_2)/s+q_0/s^2)p\cosh(p\xi_1)}{\sinh\{p(\xi_2-\xi_1)\}}+G(C_0,D_0,s) \tag{11}$$

where $G(C_0,D_0,s)$ is also a function related only to the initial temperature distributions and independent of the ξ coordinate, namely constant values for the fixed points of ξ_1 and ξ_2 except for functions of the parameter, s. In addition to these, the values of $(\theta_0(\xi_1)/s+q_0)/s^2)$ and $(\theta_0(\xi_2)/s+q_0/s^2)$ in Eqs. (9) and (11) are also constant and have the same characteristics as $F(A_0,B_0,s)$ and $G(C_0,D_0,s)$.

2.3 Approximate Equation for Temperatures at a Measuring Point. In order to perform inverse Laplace transformation of Eqs. (9) and (11), we first have to give the known functions, $\overline{f}_n(s)$, $n=1,2$ included in $\overline{\theta}_w(s)$ and $\Phi_w(s)$ explicitly. In addition, $f_n(s)$, $n=1,2$ is the Laplace transformed function of $f_n(\tau)$ which is already determined so as to approximate the measured temperatures at points of $\xi=\xi_1$, $\xi_2(\xi_1<\xi_2)$.

Any function $f_n(\tau)$ is available in approximating the temperature change. Therefore, Monde [13] tried some different kinds of functions and recommended half polynomial series of time with a time lag, as given by Eq. (12), since it gives the best estimation among them

$$f_n(\tau)=\sum_{k=0}^{N}\frac{b_{k,n}}{\Gamma(k/2+1)}(\tau-\tau_n^*)^{k/2},\quad n=1,2 \tag{12}$$

where coefficients $b_{k,n}$ can be determined by using, for example, the least mean square method from the measured temperature and N gives the number of terms of the polynomial series. This time lag τ_n^* can be determined from $\mathrm{erfc}(\xi_n/2\sqrt{\tau_n})=\min(\theta)$. The reason why polynomial series of time is recommended is that a general solution for one dimensional heat conduction is provided in the functional form of $\theta=f(\xi/\sqrt{\tau})$.

The Laplace transformed form of Eq. (12) is easily obtained as:

$$\overline{f}_n(s)=e^{-s\tau_n^*}\sum_{k=0}^{N}b_{k,n}/s^{(k/2+1)}\quad n=1,2 \tag{13}$$

After substituting Eq. (13) into Eqs. (9) and (11), one performs inverse Laplace transformation to give the surface temperature and heat flux. However, even if one performs this inverse transformation exactly, we can only know the estimated solution of surface temperature and heat flux for $\tau>\tau_{\min}$, because the solution always diverges as $\tau\to0$ [1].

Therefore, in order to follow another way rather than direct inverse Laplace transformation of Eqs. (9) and (11), we first expand Eqs. (9) and (11), hyperbolic function in a series around $s=0$, and then perform inverse Laplace transformation to obtain the approximate solutions [13].

2.4 Approximate Equation of Inverse Problem Solution in Rectangular Coordinates With Constant Heat Generation. The approximate equations for surface temperature and heat flux can be obtained by performing an inverse Laplace transformation of Eqs. (9) and (11) as:

$$\theta_w(\tau)=\sum_{j=-1}^{N}C_{j,12}(\tau-\tau_1^*)^{j/2}/\Gamma\left(\frac{j}{2}+1\right)$$
$$-\sum_{j=-1}^{N}C_{j,21}(\tau-\tau_2^*)^{j/2}/\Gamma\left(\frac{j}{2}+1\right)+W(q_0) \tag{14}$$

$$\Phi_w(\tau)=\sum_{j=-1}^{N}D_{j,12}(\tau-\tau_1^*)^{j/2}/\Gamma\left(\frac{j}{2}+1\right)$$
$$-\sum_{j=-1}^{N}D_{j,21}(\tau-\tau_2^*)^{j/2}/\Gamma\left(\frac{j}{2}+1\right)+Y(q_0) \tag{15}$$

The details in the derivation of $C_{j,12}$, $C_{j,21}$, $D_{j,12}$, and $D_{j,21}$ in Eqs. (14) and (15) are explained and summarized in the Appendix. Then, $W(q_0)$ and $Y(q_0)$ in Eqs. (14) and (15) become $W=-q_0(c_{1,2}-c_{1,1})-q_0(c_{0,2}\xi_1^2-c_{0,1}\xi_2^2)/2$ and $Y=-q_0(d_{1,2}-d_{1,1})-q_0(d_{0,2}\xi_1^2-d_{0,1}\xi_2^2)/2$, respectively, and the constants of $c_{0,1}$, $c_{0,2}$, $c_{1,1}$ and $c_{1,2}$, and $d_{0,1}$, $d_{0,2}$, $d_{1,1}$ and $d_{1,2}$ are also listed in the Appendix (see Table A5). When we set $q_0=0$, all coefficients in $W(q_0)$ and $Y(q_0)$ become 0. Then, Eqs. (14) and (15) become the approximate ones for the initial temperature distribution θ_0 being constant (or 0). In other words, the approximate equations for the initial temperature with linear temperature distribution are the same as those with constant temperature distribution.

It should be noted that in any finite plane, a steady state temperature distribution exists as the initial one, whereas in the semi-infinite body, any temperature distribution except for a constant temperature never exist. Therefore, it is not necessary to consider any initial temperature distribution except for the constant.

2.5 Solution Procedure in Cylindrical and Spherical Coordinates. How to obtain the inverse solutions in cylindrical and spherical coordinates are explained here briefly, since they are identical to the method for the rectangular case.

The initial temperature distributions at a steady state with the constant heat generation of $q=q_0$ can be expressed in cylindrical and spherical coordinates as:

$$\theta_0(\xi)=a_0+a_1\ln\xi+q_0/4 \tag{16}$$

$$\theta_0(\xi)=a_0+a_1/\xi+q_0/6 \tag{17}$$

It may be necessary to mention that the two constants, a_0 and a_1 are determined from a given initial boundary condition and one can set $a_1=0$ due to the symmetric condition, provided that the point of $\xi=0$ is included in the solid.

The inverse solutions of surface temperature and heat flux on cylindrical coordinate can be finally expressed as,

$$\overline{\theta}_w=\overline{f}_1(s)K_{1,2}(s)-\overline{f}_2(s)K_{1,1}(s)-(\theta_0(\xi_1)/s+q_0/s^2)K_{1,2}(s)$$
$$+(\theta_0(\xi_2)/s+q_0/s^2)K_{1,1}(s)+(a_0+a_2)/s+q_0/s^2 \tag{18}$$

$$\overline{\Phi}_w=\overline{f}_1(s)K_{2,2}(s)-\overline{f}_2(s)K_{2,1}(s)-(\theta_0(\xi_1)/s+q_0/s^2)K_{2,2}(s)$$
$$+(\theta_0(\xi_2)/s+q_0/s^2)K_{2,1}(s)-(a_1+q_0/2)/s \tag{19}$$

where $K_{1,1}(s)$, $K_{1,2}(s)$, $K_{2,1}(s)$, $K_{2,2}(s)$ are called "the kernels" of Eqs. (18) and (19) (See the Appendix and Table A2).

For spherical coordinate, likewise, the surface temperature and heat flux are also expressed as:

$$\overline{\theta}_w = \overline{f}_1(s)K_{1,2}(s) - \overline{f}_2(s)K_{1,1}(s) - (\theta_0(\xi_1)/s + q_0\xi_1/s^2)K_{1,2}(s) + (\theta_0(\xi_2)/s + q_0\xi_2/s^2)K_{1,1}(s) + (a_0 + a_1 + q_0/6)/s + q_0/s^2 \quad (20)$$

$$\overline{\Phi}_w = \overline{f}_1(s)K_{2,2}(s) - \overline{f}_2(s)K_{2,1}(s) - (\theta_0(\xi_1)/s + q_0\xi_1/s^2)K_{2,2}(s) + (\theta_0(\xi_2)/s + q_0\xi_2/s^2)K_{2,1}(s) + (a_1 - q_0/3)/s \quad (21)$$

where $K_{1,1}(s)$, $K_{1,2}(s)$, $K_{2,1}(s)$, $K_{2,2}(s)$ are the kernels (See the Appendix and Table A3).

It is worth mentioning, finally, that these inverse solution can be applied for cylindrical and spherical shells.

2.6 Approximate Inverse Solution for Cylindrical and Spherical Coordinates. The approximate equations for the surface temperature and the heat flux are obtained by performing the inverse transformation on Eqs. (18) and (19) for cylindrical coordinate and Eqs. (20) and (21) for spherical coordinates, resulting into the same form of Eqs. (14) and (15). Each coefficient of $C_{j,12}$, $C_{j,21}$, $D_{j,12}$, and $D_{j,21}$, and $W(q_0)$ and $Y(q_0)$ depends on the coordinates and is listed for the rectangular, cylindrical and spherical coordinates in the Appendix and Tables A1 to A3 and A5, respectively.

As for the effect of the initial temperature, let $q_0 = 0$, then all coefficients of $W(q_0)$ and $Y(q_0)$ become 0. In other words, a linear initial temperature distribution without the internal heat generation, has no influence on the inverse solution which estimates the surface temperature and the heat flux from the temperature measured at two points. It is worth mentioning finally that the inverse solutions for constant initial and linear temperature distributions become identical.

2.7 Approximate Solution for Semi-Infinite Body. General solution for a semi-infinite body is easily obtained by setting $A = 0$, $a_1 = q_0 = 0$ in Eq. (5), since there is no initial temperature distribution at steady state. The finite and semi-infinite plates are different with regard to the number of unknown variables, the former has two and the latter has one. Therefore, one measuring point is enough for the semi-infinite plate. Now, when the temperature distribution is given by, for example, Eq. (12) at $\xi = \xi_1$, one can determine the representative function of the unknown constant B. The equations for surface temperature and heat flux can be given as follows:

$$\overline{\theta}_w(\tau) = \frac{1}{2\pi i}\int_{c-i\infty}^{c+i\infty} e^{s(\tau-\tau_1^*)}e^{p\xi_1}\sum_{k=0}^{N} b_{k,1}/s^{(k/2+1)}ds \quad (22)$$

$$\overline{\Phi}_w(\tau) = \frac{1}{2\pi i}\int_{c-i\infty}^{c+i\infty} e^{s(\tau-\tau_1^*)}pe^{p\xi_1}\sum_{k=0}^{N} b_{k,1}/s^{(k/2+1)}ds \quad (23)$$

We first expand the integrand $e^{p\xi_1}$ in a series around $s = 0$, and then we perform inverse Laplace transformation to give the surface temperature and heat flux as:

$$\theta_w(\tau) = \sum_{j=-1}^{N} U_j(\tau-\tau_1^*)^{j/2}/\Gamma\left(\frac{j}{2}+1\right) \quad (24)$$

$$\Phi_w(\tau) = \sum_{j=-1}^{N} V_j(\tau-\tau_1^*)^{j/2}/\Gamma\left(\frac{j}{2}+1\right) \quad (25)$$

A semi-infinite body can also be considered in cylindrical and spherical coordinates, but the discussion of these cases would be made in a future work.

3 Procedure to Determine Coefficients in Eq. (12)

The coefficients, $b_{k,n}$, in Eq. (12) can be determined from the measured temperature, for example, by the least mean square method. The coefficients are subject to round off of the data and precision of the measured values, the level of the data accuracy becomes important. Generally speaking, the measured temperature includes some uncertainty. Therefore, the simulated temperature calculated from the exact solution can be expressed as:

$$\theta(\xi_n,\tau) = \theta_{\text{exact}}(\xi_n,\tau)(1 + 0.005\varepsilon), \quad n = 1,2 \quad (26)$$

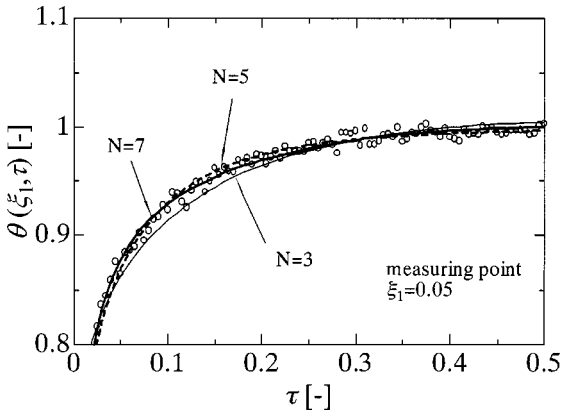

Fig. 2 Approximate solution, Eq. (12) for temperature change at a point (heavy solid line: exact solution, *o*: data with uncertainties)

Table 1 Boundary condition and dimensionless parameters (for all case, finite body)

Case	Boundary condition ($0<\tau$)	Parameters
1 (1st type B.C.)	$\theta(\tau)=1$: $\xi=0$ $\theta(\tau)=0$: $\xi=1$ $\theta=0$: $\tau=0$	$\theta = T/T_0$ $\Phi = qL/\lambda T_0$
2 (1st type B.C.)	$\theta(\tau)=\tau$. $\xi=0$ $\theta(\tau)=0$: $\xi=1$ $\theta=0$: $\tau=0$	$\theta = T/T_0$ $\Phi = qL/\lambda T$
3 (2nd type B.C.)	$\Phi(\tau)=1$: $\xi=0$ $\theta(\tau)=0$: $\xi=1$ $\theta=0$: $\tau=0$	$\theta = T\lambda/q_0L$ $\Phi = q/q_0$
4 (3rd type B.C.) ($\theta_\infty(\tau)=1$)	$\frac{\partial\theta}{\partial\xi} = \text{Bi}(\theta-\theta_\infty(\tau))$: $\xi=0$ $\frac{\partial\theta}{\partial\xi}=0$: $\xi=1$ $\theta=0$: $\tau=0$	$\theta = T/T_0$ $\Phi = qL/\lambda T_0$
5 (1st type B.C. with I.C.)	$\theta(\tau)=1$: $\xi=0$ $\theta(\tau)=0$: $\xi=1$ $\theta=\xi^2$: $\tau=0$	$\theta = T/T_0$ $\Phi = qL/\lambda T_0$

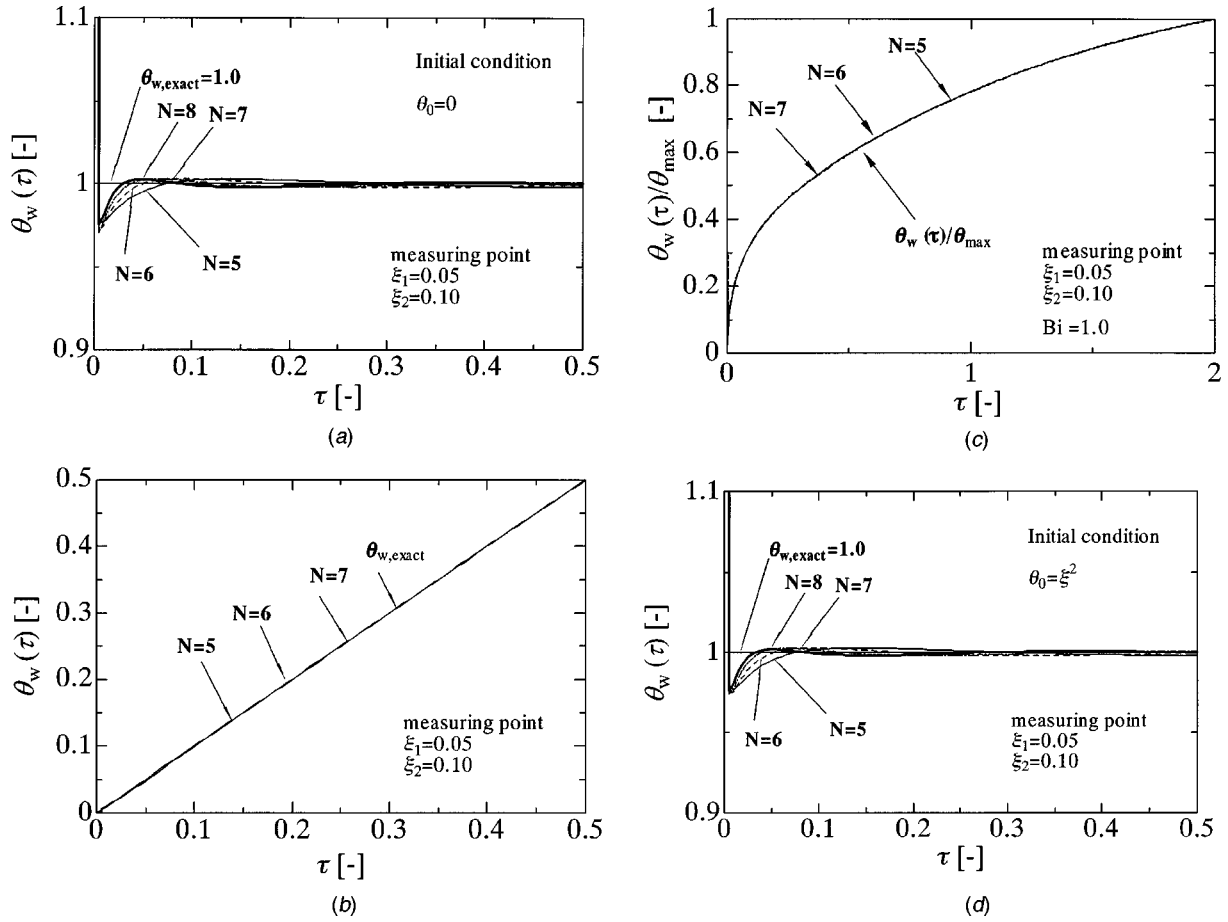

Fig. 3 (*a*) Estimated surface temperature Case 1; (*b*) Estimated surface temperature Case 2; (*c*) Estimated surface temperature Case 4; and (*d*) Estimated surface temperature Case 5.

where $\theta_{\text{exact}}(\xi_n, \tau)$ is the exact solution for the corresponding boundary conditions, and ε is a random value whose average is 0 and standard deviation is unity. It should be noted that temperature measured by thermocouples is generally expected to be accurate to only 2 or 3 significant digits and corresponds to standard deviation, $\sigma=0.001$ for the values of $\theta_{\text{exact}}(\xi_n, \tau)$.

Another method is to truncate at the second decimal place, commonly used to employ Eq. (26) by superimposing a certain disturbance on the exact solution. However, the solution obtained by Eq. (26) is worse than the truncation approach [13].

Figure 2 shows the temperature response measured at $\xi=0.05$ and the approximate curves given by Eq. (12). From Fig. 2, the approximate solution is improved with an increase in N, but becomes saturated around $N=5\sim7$ beyond which improvement is minimal. Therefore, the order of the approximate equation can be considered to be $N=7$ at most.

4 Inverse Solution and Representative Problems

4.1 Method for Calculation. The procedure to solve the inverse problems described previously is

1) Determine each coefficient of $b_{k,n}$ in Eq. (12) using the measured temperature at ξ_1 or ξ_2 by the least mean square method.
2) Expand the kernels of solution obtained by performing Laplace transformation around $s=0$ in a series whose coefficients are summarized in the Appendix.
3) Calculate coefficients given by multiplying coefficients in Eq. (12) and the coefficients of the kernel, which are summarized in the Appendix.
4) Perform inverse Laplace transformation, and calculate explicitly the surface temperature and heat flux using Eqs. (14) and (15), (18) and (19), (20) and (21).

4.2 Representative Problems and Inverse Solution. The approximating solutions for several boundary conditions are reported by Monde [13] and Monde et al. [14]. We investigated five representative combinations of initial temperature distributions and boundary conditions as listed in Table 1, which were not included in our papers [13,14].

Figures 3(*a*) to (*d*) show comparisons between the exact solution of surface temperatures and the corresponding estimated solutions for the cases 1, 2, 4, and 5. The solutions for the test Case 3 that corresponds to the heat flux boundary conditions at both $\xi=0$ and $\xi=1$ are shown in Fig. 4(a). The estimate for the boundary heat flux in the test Case 4 is represented in Fig. 4(b). The number of N in Figs. 3(*a*) to (*d*) and Figs. 4(*a*) to (*b*) means the order of the approximate equation and the values of ξ_1 and ξ_2 corresponding to the position of the measuring point in the solid. The temperatures at each measuring point were obtained by using Eq. (26). Figures 3 and 4 show that the estimated solutions approach to the exact solution as N increases.

5 Evaluation of Estimated Value

5.1 Minimum Predictive Time. It has been mathematically shown [1,2] that no inverse solution exists at $\tau=0$ and the solution can converge beyond a limiting time. Therefore, a minimum predictive time is an important factor in evaluating the inverse solution. One can adopt a minimum predictive time, τ_1 in which the inverse solution achieves a relative difference of 0.01 (error is less

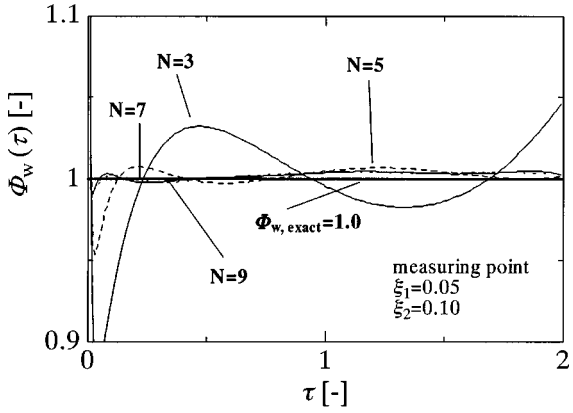

(*a*)

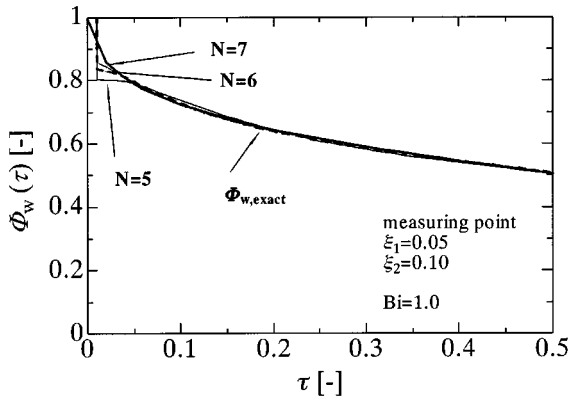

(*b*)

Fig. 4 (*a*) Estimated surface heat flux Case 3; and (*b*) Estimated surface heat flux Case 4.

than 1%) between the exact and estimated values. In a real application, the minimum predictive time may correspond to the time in which sensor takes a temperature larger than the uncertainty of temperature in a measuring equipment. Table 2 shows the minimum predictive time for every case versus the value of N. It is found from Table 2 that the minimum predictive time is hardly affected by the value of N except for cases 3 and 4. In cases 3 and 4, a value of N larger than 5 does little to influence the minimum predictive time.

5.2 Accuracy of the Estimation for Surface Temperature and Heat Flux. In order to evaluate the accuracy of the inverse solution, we introduce standard deviation as:

$$\sigma = \sqrt{\frac{1}{(\tau_2 - \tau_1)} \int_{\tau_1}^{\tau_2} (\theta_{w,\text{exact}}(\tau) - \theta_{w,\text{cal}}(\tau))^2 d\tau} \qquad (27)$$

where τ_2 is defined as 90% of the final time of the experimental data measurement. Table 3 shows a minimum standard deviation

Table 2 Minimum initial time (τ_1) estimated for error of 0.01 for ξ_1=0.05, ξ_2=0.10 (initial condition; θ=0)

N	case1	case2	case3	case4	case5
3	0.0050	0.0057	0.0233	0.0093	0.0050
4	0.0050	0.0057	0.0317	0.0067	0.0050
5	0.0050	0.0056	0.0189	0.0074	0.0050
6	0.0050	0.0047	0.0093	0.0051	0.0050
7	0.0050	0.0076	0.0059	0.0050	0.0050
8	0.0051	0.0057	0.0056	0.0050	0.0051

Table 3 Standard deviation (σ) (initial condition; θ=0)

N	case1	case2	case3	case4	case5
3	0.0029	0.0091	0.0050	0.0056	0.0030
4	0.0030	0.0093	0.0020	0.0016	0.0032
5	0.0031	0.0093	0.0018	0.0012	0.0024
6	0.0029	0.0093	0.0008	0.0007	0.0029
7	0.0026	0.0094	0.0005	0.0002	0.0025
8	0.0022	0.0094	0.0005	0.0002	0.0013

of σ=0.003 at N=6 beyond which the accuracy of prediction does not improve. Taking into account the fact that the deviation in the prediction reaches the same level as the deviation of the approximate equation, we cannot expect more accuracy in this method. In addition, Table 3 shows that the approximate equation at order N=6 gives the most accurate solution.

It can be seen from Figs. 4(*a*) and (*b*) that the inverse solutions for the surface heat flux using N=5 to 7 in Eq. (15) also agree well with the exact solutions.

5.3 Effect of Position of Temperature Measurement on Estimated Solution. Figure 5 shows the effects of temperature sensor position on the inverse solution for case 3 when N=5. The position of ξ_2=0.5 in Fig. 5 corresponds to the farthest point from the surface in a finite body.

According to Fig. 5, the inverse solutions for ξ_1=0.05 and 0.1 are in good agreement with the exact value, although for ξ_1 =0.2 and 0.3, both the solutions and the time are not recommended because of a large deviation and a delayed time.

On the other hand, the accuracy of prediction on these conditions is identical as that for ξ_1=0.05 and ξ_2=0.1, as shown in Fig. 3(*a*) and Table 2, but the minimum predictive time becomes larger for ξ_1=0.05 and ξ_2=0.1.

Consequently, it is recommended to choose the measuring points as close to the surface as possible to give a good estimation. In particular, the point ξ_1 is recommended to be ξ_1<0.1. On the other hand, we may recommend $\xi_1 \leqslant 0.2$ for the minimum prediction time.

Incidentally, when the temperature change for $0 \leqslant \xi < 1$ in cylindrical and spherical coordinates is treated with, the boundary condition at ξ=0 always becomes $\partial\theta/\partial\xi$=0. Therefore, the number of measuring points included in Eqs. (18) and (19), and Eqs. (20) and (21) are reduced to one. Consequently, these inverse solutions become simpler than Eqs. (18) and (19), and also Eqs. (20) and (21), but worse estimations are obtained. The reason is that the point of ξ=0 is the furthest from the other surface, even though the boundary condition of $\partial\theta/\partial\xi$=0 is exact at ξ=0. Therefore, it is important as shown in Fig. 5 to choose the measuring points as close to the surface as possible in getting better estimations.

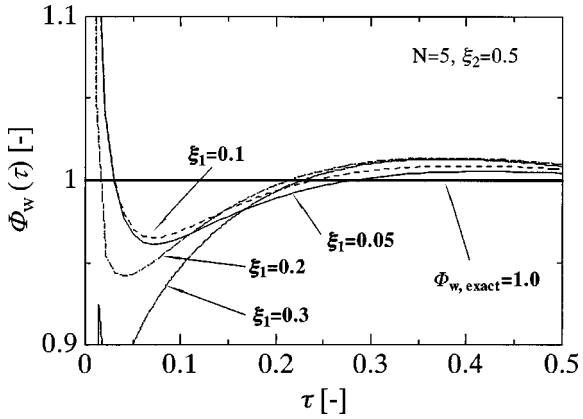

Fig. 5 Effect of measuring point on accuracy of solution (Case 3, Heat flux)

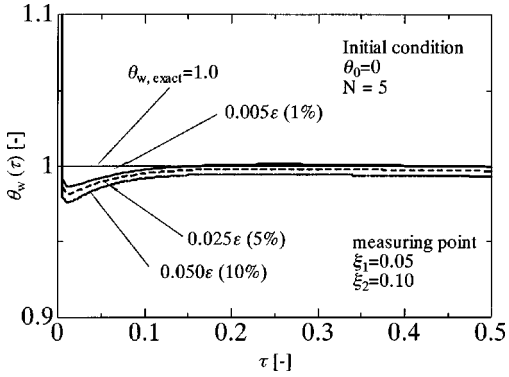

Fig. 6 Effect of data uncertainty on accuracy of solution (Case 1)

5.4 Effect of Data Uncertainties. Figure 6 shows, for example, the effects of the data uncertainties on the inverse solution for case 1 when $N=5$ and the levels of the uncertainties are tentatively chosen at 1%, 5%, and 10%. The increase in the uncertainties makes the inverse solution worse, but the surface temperature estimated using the uncertainty of 10% is still in good agreement with the given condition. It may imply that the uncertainty included in the data is smoothed during the process where the coefficients in the approximate equation, Eq. (12) are determined using the data with 10% uncertainty by the least mean square method. Table 4 lists standard deviation and minimum predicted time for the different uncertainties of 1, 5, and 10%.

5.5 Order of Approximate Equation of Eq. (12) and Its Improvement. It can be observed in Tables 2 and 3 that improvement in the accuracy of prediction and reduction in the minimum predictive time are not expected even though one increases the number of N in Eq. (12). Consequently, a value of either $N=5$ or 6 is recommended as the critical value.

When the surface condition sharply changes such as the surface temperature and heat flux have either a maximum or minimum value and the first derivative with respect to time becomes discontinuous, the inverse solutions make the estimate of the surface temperature and heat flux to degrade (see Refs. [13], [14]). The reason comes from the failure in approximating the temperature change by Eq. (12). Therefore, the present method can predict the surface conditions well only for the case in which the surface temperature presents continuous derivative. In other words, the high accurate estimation can be reached only for a smooth surface temperature change.

Either improvement in Eq. (12) approximating the temperature change or other method is required to alleviate this difficulty. We propose a new idea in which the abrupt change with time is split in partitions instead of over the whole time domain and Eq. (12) is similarly used to approximate the temperature change in each sectional time of $[\tau_i, \tau_{i+1}]$ by which the accuracy of the approximation can be achieved. The coefficients of $C_{j,12}$, $C_{j,21}$, $D_{j,12}$, and $D_{j,21}$ in Eqs. (14) and (15) for the rectangular coordinates, for example, are determined for each time interval by the same procedure as described previously. The inverse solutions for the sectional time are connected to cover the whole time.

Table 4 Standard deviation (σ) and minimum initial time (τ_1) (for the case 1)

Uncertainty	σ	τ_1
0.005 (1%)	0.00168	0.0154
0.025 (5%)	0.00288	0.0158
0.050 (10%)	0.00504	0.0162

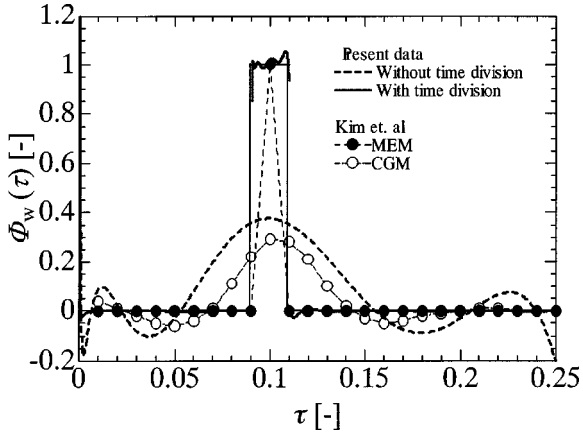

Fig. 7 Comparison between the present, MEM and CGM [17] methods for rectangular change

This method is applied to two surface conditions without heat generation in the rectangular coordinates as an example: the surface heat flux changes in triangular and rectangular shapes as given by the following equation:

For the rectangular change

$$\Phi_w=0 \quad 0<\tau<0.09, \quad 0.11<\tau<0.25$$
$$\Phi_w=1 \quad 0.09<\tau<0.11 \tag{28}$$

For the triangular change

$$\Phi_w=0 \quad 0<\tau<0.05, \quad 0.21<\tau<0.25$$
$$\Phi_w=12.5\tau-0.625 \quad 0.05<\tau<0.13 \tag{29}$$
$$\Phi_w=-12.5\tau+2.625 \quad 0.13<\tau<0.21$$

Figures 7 and 8 show the estimated surface heat flux obtained by this inverse solution with the sectional and the whole times. For a comparison, the surface heat fluxes estimated by a numerical method [17] using maximum entropy method (MEM) and conjugate gradient method (CGM) are also shown in Figs. 7 and 8. It is found that the heat flux can be predicted well by using the sectional method and the MEM. The former inverse solution method has merit in giving the continuous heat flux change, whereas the MEM shows them discrete. Another merit of this inverse solution is a better understanding of the whole trend in the surface heat flux change. In addition, this solution requires very small CPU time due to the explicit solution.

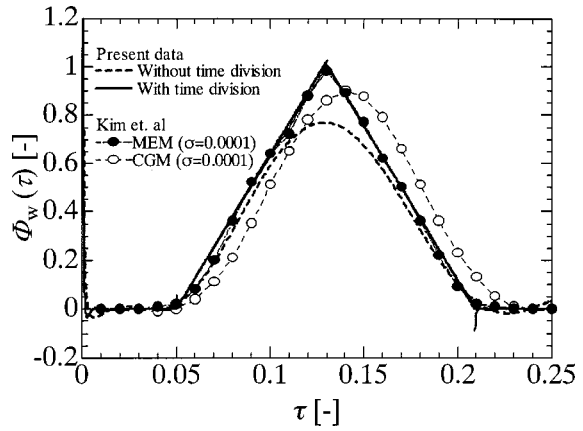

Fig. 8 Comparison between the present, MEM and CGM [17] methods for triangular change

Chantasiriwan [18] and Taler [19] applied their own methods for the IHCP, but they failed in estimating the triangular surface heat flux change, as given by Eq. (29), with the same accuracy as the present method.

6 Conclusions

A one-dimensional IHCP solution is developed for the estimation of the surface temperature and surface heat flux for three different coordinates using Laplace transformation.

1) This method is much easier to use than other existing numerical techniques such as the MEM and CGM has merit in giving the surface condition explicitly, although the software for the calculation is more complicated than that for the numerical ones.
2) The solution requires very small CPU time due to the explicit solution.
3) The surface temperature and heat flux can be easily estimated with a high accuracy even in the cases when the surface condition changes rapidly.
4) This method is also applicable in cases where an initial temperature distribution exists. A linear temperature distribution gives the same inverse solution as the constant one.

Nomenclature

a = thermal diffusivity [m^2/s]
a_0, a_1 = coefficient of initial temperature distribution
$f_1(\tau)$, $f_2(\tau)$ = function of nondimensional temperature at a point of ξ_1, ξ_2
L = characteristic length [m]
$\min(\theta)$ = minimum of significant number or minimum division of measuring equipment
N = degree of approximate polynomial
p = $\sqrt{s}$
q = heat flux [W/m^2]
$q(\xi)$ = intensity of the volumetric heat source ($=\Sigma_{n=0} q_n \xi^n$) [W/m^3]
q_o = uniform heat generation per unit volume [W/m^3]
R = characteristic length in the cylindrical and spherical coordinate [m]
s = Laplace parameter ($=p^2$)
T = temperature [K]
T_0 = characteristic temperature [K]
t = time [s]
x = x-coordinate distance [m]
W_r, W_c, W_s = influence functions of initial temperature for rectangular, cylindrical and spherical coordinates
Y_r, Y_c, Y_s = influence functions of initial temperature for rectangular, cylindrical and spherical coordinates
ε = random number varying from -1 to 1
Φ = dimensionless heat flux
$\overline{\Phi}$ = Laplace transformed value of Φ obtained by Laplace Transformation
$\Gamma(n)$ = Gamma function
λ = thermal conductivity
θ = dimensionless temperature (T/T_0)
$\overline{\theta}$ = Laplace transformed value of θ
θ_o = initial temperature (distribution)
τ = dimensionless time (Fourier number$=at/L^2$, at/R^2)
τ_1 = minimum predictive time
τ_1^* = dimensionless time lag ($\mathrm{erfc}(\xi_i/2\sqrt{\tau_i^*})=\min(\theta)$)
ξ = dimensionless length ($=x/L, r/R, \xi_1<\xi_2$)
σ = standard deviation

Subscript

1,2 = point of sensor location temperature
c = cylindrical coordinates
r = rectangular coordinates
s = spherical coordinates
w = surface

Appendix

How to expand key functions of s around $s=0$ and to calculate these coefficients is briefly explained here. The Laplace transformed form obtained after applying the Laplace transform can be abbreviated into $\overline{\theta}=\overline{f}(s)K(s)$ in which one may call the function $K(s)$ kernel. The inverse Laplace transformation of this Laplace transformed function is defined as:

$$\theta(\tau)=\frac{1}{2\pi i}\int_{c-i\infty}^{c+i\infty} e^{s\tau}\overline{\theta}(s)ds \tag{A1}$$

In the present analysis, we first expand the functions $K(s)$ around $s=0$ in a series, and then obtain the inverse solution by executing complex integration. The Laplace transformed functions of the surface temperature and heat flux can be expressed using different types of the kernel $K(s)$ depending on the coordinates and system. These concrete forms of the kernel are given in Tables A1, A2, A3, and A4.

The inverse solutions in Laplace transformed form for the surface temperature and heat flux are summarized into the following equations for three different coordinates, respectively.

(a) For Finite Body

Surface temperature.

$$\overline{\theta}=\overline{f}_1(s)K_{1,2}(s)-\overline{f}_2(s)K_{1,1}(s)-(\theta_0(\xi_1)/s+A_1/s^2)K_{1,2}(s)+(\theta_0(\xi_2)/s+A_2/s^2)K_{1,1}(s)+F(s) \tag{A2}$$

Surface Heat Flux.

$$\overline{\Phi}=\overline{f}_1(s)K_{2,2}(s)-\overline{f}_2(s)K_{2,1}(s)-(\theta_0(\xi_1)/s+A_1/s^2)K_{2,2}(s)+(\theta_0(\xi_2)/s+A_2/s^2)K_{2,1}(s)+G(s) \tag{A3}$$

where functions of $F(s)$ and $G(s)$ are related to the initial temperature distribution and the constants of A_1 and A_2, and $F(s)$ and $G(s)$ are summarized for the three coordinates into Table A5.

(b) For Semi-Infinite Body

Surface Temperature.

$$\overline{\theta}=\overline{f}_1(s)K_3(s) \tag{A4}$$

Surface Heat Flux.

$$\overline{\Phi}=\overline{f}_1(s)K_4(s) \tag{A5}$$

Table A1 Kernel $K(s)$ for finite body in rectangular coordinates, these coefficients in its series and commonly used terms in its series

	Surface temperature ($K_{1,n}(s)$)	Surface heat flux ($K_{2,n}(s)$)
Kernel $K(s)$	$\dfrac{\sinh(p\xi_n)}{\sinh\{p(\xi_2-\xi_1)\}}$	$\dfrac{p\cosh(p\xi_n)}{\sinh\{p(\xi_2-\xi_1)\}}$
Coefficients	$x_{i,n}=\dfrac{1}{(2i+1)!}\xi_n^{2i+1}$	$y_{i,n}=\dfrac{1}{(2i)!}\xi_n^{2i}$
Common terms	$g_0=\xi_2-\xi_1$, $g_i=\dfrac{(\xi_2-\xi_1)^{2i}}{(2i+1)!}$ $(i\geq 1)$	

Table A2 Kernel $K(s)$ for finite body in cylindrical coordinates, these coefficients in its series and commonly used terms in its series

	Surface temperature ($K_{1,n}(s)$)	Surface heat flux ($K_{2,n}(s)$)
Kernel $K(s)$*1	$\dfrac{Z_1(\xi_n,s)}{Z_{12}(s)}$	$\dfrac{Z_2(\xi_n,s)}{Z_{12}(s)}$
Coefficients*2	$x_{i,n}=\sum_{j=0}^{i}\{-\ln(\xi_n)a_j^\circ b_{i-j}^\circ(\xi_n)+d_j^\circ(\xi_n)a_{i-j}^\circ-c_j^\circ b_{i-j}^\circ(\xi_n)\}$	$y_{i,n}=-\sum_{j=0}^{i}\{-\ln(\xi_n)e_j^\circ b_{i-j}^\circ(\xi_n)+d_j^\circ(\xi_n)e_{i-j}^\circ-f_j^\circ b_{i-j}^\circ(\xi_n)\}$
Common terms*2	$g_0=\ln(\xi_1/\xi_2)$, $g_i=\sum_{j=0}^{i}\left\{b_j^\circ(\xi_1)b_{i-j}^\circ(\xi_2)+\dfrac{d_j^\circ(\xi_2)b_{i-j}^\circ(\xi_1)-d_j^\circ(\xi_1)b_{i-j}^\circ(\xi_2)}{\ln(\xi_1/\xi_2)}\right\}$ $(i\geqslant 1)$	

*1: Z_1, Z_2 and Z_{12} are given as:

$$Z_1(\xi_n,s)=\ln(1/\xi_n)I_0(p)I_0(p\xi_n)+X(p\xi_n)I_0(p)-X(p)I_0(p\xi_n)$$

$$Z_2(\xi_n,s)=\ln(1/\xi_n)I_1(p)I_0(p\xi_n)+X(p\xi_n)I_1(p)-\{X'(p)-I_0(p)\}I_0(p\xi_n)$$

$$Z_{12}(s)=\ln(\xi_1/\xi_2)I_0(p\xi_1)I_0(p\xi_2)+X(p\xi_2)I_0(p\xi_1)-X(p\xi_1)I_0(p\xi_2)$$

where

$$I_0(p\xi_n)=\sum_{j=0}^{\infty}\frac{s^j\xi_n^{2j}}{2^{2j}(j!)^2},\quad I_0(p)=\sum_{j=0}^{\infty}\frac{s^j}{2^{2j}(j!)^2},\quad I_1(p)=\sum_{j=1}^{\infty}\frac{(2j)s^j}{2^{2j}(j!)^2}$$

$$X(p\xi_n)=\sum_{j=1}^{\infty}\frac{s^j\xi_n^{2j}}{2^{2j}(j!)^2}\sum_{m=1}^{j}\frac{1}{m},\quad X(p)=\sum_{j=1}^{\infty}\frac{s^j}{2^{2j}(j!)^2}\sum_{m=1}^{j}\frac{1}{m},\quad X'(p)=\sum_{j=1}^{\infty}\frac{(2j)s^j}{2^{2j}(j!)^2}\sum_{m=1}^{j}\frac{1}{m}$$

where, I_0 and I_1 are modified Bessel functions of the first kind.

*2The coefficients of a_j° through f_j° are summarized as:

$$a_j^\circ=\frac{1}{2^{2j}(j!)^2},\quad b_j^\circ(\xi_n)=\frac{1}{2^{2j}(j!)^2}(\xi_n)^{2j},\quad c_j^\circ=a_j^\circ\sum_{m=1}^{j}\frac{1}{m},\quad d_j^\circ(\xi_n)=b_j^\circ(\xi_n)\sum_{m=1}^{j}\frac{1}{m}$$

$$e_j^\circ=(2j)a_j^\circ,\quad f_j^\circ=a_j^\circ\left(2j\sum_{m=1}^{j}\frac{1}{m}-1\right)$$

Table A3 Kernel $K(s)$ for finite body in spherical coordinates, these coefficients in its series and commonly used terms in its series

	Surface temperature ($K_{1,n}(s)$)	Surface heat flux ($K_{2,n}(s)$)
Kernel $K(s)$	$\dfrac{\sinh\{p(\xi_n-1)\}}{\sinh\{p(\xi_2-\xi_1)\}}$	$\dfrac{p\cosh\{p(\xi_n-1)\}+\sinh\{p(\xi_n-1)\}}{\sinh\{p(\xi_2-\xi_1)\}}$
Coefficients	$x_{i,n}=\dfrac{1}{(2i+1)!}(\xi_n-1)^{2i+1}$	$y_{i,n}=\dfrac{1}{(2i)!}(\xi_n-1)^{2i}+\dfrac{1}{(2i+1)!}(\xi_n-1)^{2i+1}$
Common terms	$g_0=\xi_2-\xi_1$, $g_i=\dfrac{(\xi_2-\xi_1)^{2i}}{(2i+1)!}$ $(i\geqslant 1)$	

(1) How to Expand the Kernel for a Finite Body. Expansions of the kernel $K_{1,n}(s)$, $K_{2,n}(s)(n=1,2)$ in Eqs. (*A*2) and (*A*3) around $s=0$ in a series are equally given for any coordinate as:

Table A4 Kernel $K(s)$ for semi-infinite body in rectangular coordinate and its coefficients in its series

	Surface temperature ($K_1(s)$)	Surface heat flux ($K_2(s)$)
Kernel $K(s)$	$e^{p\xi_1}$	$pe^{p\xi_1}$
Coefficients	$u_i=\dfrac{\xi_1^i}{i!}$	$v_i=\dfrac{\xi_1^i}{i!}$

$$K_{1,n}(s)=\sum_{j=0}^{\infty}c_{j,n}s^j\quad n=1,2 \tag{A6}$$

$$K_{2,n}(s)=\sum_{j=0}^{\infty}d_{j,n}s^j\quad n=1,2 \tag{A7}$$

Let the coefficients $c_{j,n}$ and $d_{j,n}$ be:

$$c_{j,n}=\frac{1}{g_0}\sum_{i=0}^{j}x_{i,n}h_{j-i}\quad n=1,2 \tag{A8}$$

$$d_{j,n}=\frac{1}{g_0}\sum_{i=0}^{j}y_{i,n}h_{j-i}\quad n=1,2 \tag{A9}$$

Table A5 Summary of functions and constants related to initial temperature with constant heat generation

	Rectangular coordinates	Cylindrical coordinates	Spherical coordinates
A_1	q_0	q_0	$q_0\xi_1$
A_2	q_0	q_0	$q_0\xi_2$
$F(s)$	$a_0/s+q_0/s^2$	$(a_0+q_0/4)/s+q_0/s^2$	$(a_0+a_1+q_0/6)/s+q_0/s^2$
$G(s)$	$-a_1/s$	$-(a_1+q_0/2)/s$	$(a_1-q_0/3)/s$
W	$-q_0(c_{1,2}-c_{1,1})$	$-q_0(c_{1,2}-c_{1,1})$	$-q_0(c_{1,2}\xi_1-c_{1,1}\xi_2)$
Y	$-(q_0/2)(c_{0,2}\xi_1^2-c_{0,1}\xi_2^2)$	$-(q_0/4)(c_{0,2}\xi_1^2-c_{0,1}\xi_2^2-1)$	$-(q_0/6)(c_{0,2}\xi_1^3-c_{0,1}\xi_2^3-1)$
	$-q_0(d_{1,2}-d_{1,1})$	$-q_0(d_{1,2}-d_{1,1})$	$-q_0(d_{1,2}\xi_1-d_{1,1}\xi_2)$
	$-(q_0/2)(d_{0,2}\xi_1^2-d_{0,1}\xi_2^2)$	$-(q_0/4)(d_{0,2}\xi_1^2-d_{0,1}\xi_2^2+2)$	$-(q_0/6)(d_{0,2}\xi_1^3-d_{0,1}\xi_2^3+2)$

The coefficients of $c_{i,j}$ and $d_{i,j}$ are defined in the Appendix(1) and the constants of a_0, a_1 and q_0 are given as initial condition.

where the coefficients $x_{i,,n}$ and $y_{i,n}$ are defined in Tables A1, A2, and A3 for the three coordinates and the value of h_j is also defined by using functions of g_i, which are listed in Tables A1, A2, and A3.

$$\begin{aligned} h_0&=1\\ h_1&=-g_1\\ h_2&=-g_2+g_1^2\\ h_3&=-g_3+2g_1g_2-g_1^3\\ h_4&=-g_4+(2g_1g_3+g_2^2)-3g_1^2g_2+g_1^4\\ h_5&=-g_5+2(g_1g_4+g_2g_3)-3(g_1^2g_3+g_1g_2^2)+4g_1^3g_2-g_1^5 \end{aligned} \tag{A10}$$

We can express the surface temperature $\overline{\theta_w}(s)$ and heat flux $\overline{\Phi}_w(s)$ using these coefficients in the Laplace transformed form as:

$$\overline{\theta}_w=e^{-s\tau_1^*}\sum_{i=0}^{N}\frac{b_{i1}}{s^{i/2+1}}\sum_{j=0}^{\infty}c_{j,2}s^j-e^{-s\tau_2^*}\sum_{i=0}^{N}\frac{b_{i2}}{s^{i/2+1}}\sum_{j=0}^{\infty}c_{j,1}s^j$$

$$=e^{-s\tau_1^*}\sum_{j=-1}^{N}\frac{C_{j,12}}{s^{j/2+1}}-e^{-s\tau_2^*}\sum_{j=-1}^{N}\frac{C_{j,21}}{s^{j/2+1}} \tag{A11}$$

where

$$\begin{aligned} C_{-1,lm}&=\sum_{k=0}^{Nk}b_{2k+1,l}c_{k+1,m},\quad Nk=\mathrm{Int}\{(N-1)/2\}\\ &\quad l,m=1,2\ \text{ or }\ 2,1\\ C_{j,lm}&=\sum_{k=0}^{Nk}b_{2k+j,l}c_{k,m},\quad j\geqslant 0, Nk=\mathrm{Int}\{(N-j)/2\}\\ &\quad l,m=1,2\ \text{ or }\ 2,1 \end{aligned} \tag{A12}$$

and

$$\overline{\Phi}_w=e^{-s\tau_1^*}\sum_{j=-1}^{N}\frac{D_{j,12}}{s^{j/2+1}}-e^{-s\tau_2^*}\sum_{j=-1}^{N}\frac{D_{j,21}}{s^{j/2+1}} \tag{A13}$$

where

$$\begin{aligned} D_{-1,lm}&=\sum_{k=0}^{Nk}b_{2k+1,l}d_{k+1,m},\quad Nk=\mathrm{Int}\{(N-1)/2\}\\ &\quad l,m=1,2\ \text{ or }\ 2,1\\ D_{j,lm}&=\sum_{k=0}^{Nk}b_{2k+j,l}d_{k,m},\quad j\geqslant 0, Nk=\mathrm{Int}\{(N-j)/2\}\\ &\quad l,m=1,2\ \text{ or }\ 2,1 \end{aligned} \tag{A14}$$

As for the inverse solutions of $W(q_o)$ and $Y(q_o)$, these are easily obtained by following the same procedure and are summarized in Table A5.

(2) Expansion of the Kernel for Semi-Infinite Body. Expansions of the kernel $K_1(s)$, $K_2(s)$ in Eqs. (*A*4) and (*A*5) around $s=0$ in a series are given as:

$$K_1(s)=\sum_{i=0}^{\infty}u_is^i \tag{A15}$$

$$K_2(s)=\sum_{i=0}^{\infty}v_is^i \tag{A16}$$

where u_i and v_i are given in Table A4

We can express the surface temperature $\overline{\theta_w}(s)$ and heat flux $\overline{\Phi}_w(s)$ using these coefficients in the Laplace transformed form as:

$$\overline{\theta}_w=e^{-s\tau_1^*}\sum_{i=0}^{N}\frac{b_{i,1}}{s^{i/2+1}}\sum_{j=0}^{\infty}u_js^j=e^{-s\tau_1^*}\sum_{j=-1}^{N}\frac{U_j}{s^{j/2+1}} \tag{A17}$$

where

$$\begin{aligned} U_{-1}&=\sum_{k=0}^{Nk}b_{k,1}u_{k+1},\quad Nk=N\\ U_j&=\sum_{k=0}^{Nk}b_{k+j,1}u_k,\quad j\geqslant 0, Nk=N-j \end{aligned} \tag{A18}$$

and

$$\overline{\Phi}_w=e^{-s\tau_1^*}\sum_{i=0}^{N}\frac{b_{i,1}}{s^{i/2+1}}\sum_{j=0}^{N}v_js^j=e^{-s\tau_1^*}\sum_{j=-1}^{N}\frac{V_j}{s^{j/2+1}} \tag{A19}$$

where

$$\begin{aligned} V_{-1}&=\sum_{k=0}^{Nk}b_{k,1}v_k,\quad Nk=N\\ V_j&=\sum_{k=0}^{Nk}b_{k+j+1,1}v_k,\quad j\geqslant 0,\ Nk=N-j-1 \end{aligned} \tag{A20}$$

The inverse solutions of Eqs. (24) and (25) can be derived by the above-described procedure.

References

[1] Alifanov, O. M., 1994, *Inverse Heat Transfer Problems*, Springer-Verlag, pp. 5–8.

[2] Beck, J. V., Blackwell, B., and Clair, C. R., 1985, *Inverse Heat Conduction*, Wiley-Interscience.

[3] Hsieh, C. K., and Su, K. C., 1980, "A Methodology of Predicting Cavity Geometry Based on Scanned Surface Temperature Data—Prescribed Surface

Temperature at the Cavity Side,'' ASME J. Heat Transfer, **102**(2), pp. 324–329.
[4] Bell, G. E., 1984, ''An Inverse Solution for the Steady Temperature Field within a Solidified Layer,'' Int. J. Heat Mass Transf., **27**(12), pp. 2331–2337.
[5] Lithouhi, B., and Beck, J. V., 1986, ''Multinode Unsteady Surface Element Method with Application to Contact Conductance Problem,'' ASME J. Heat Transfer, **108**(2), pp. 257–263.
[6] Shoji, M., and Ono, N., 1988, ''Application of the Boundary Element to the Inverse Problem of Heat Conduction (in Japanese),'' Trans. Jpn. Soc. Mech. Eng., Ser. B, **54–506**, pp. 2893–2900.
[7] Frankel, J. I., 1997, ''A Global Time Treatment for Inverse Heat Conduction Problems,'' ASME J. Heat Transfer, **119**(4), pp. 673–683.
[8] Burggraf, O. R., 1964, ''An Exact Solution of the Inverse Problem in Heat Conduction Theory and Application,'' ASME J. Heat Transfer, **86**, pp. 373–382.
[9] Sparrow, E. M., Haji-Sheikh, A., and Lundgren, T. S., 1964, ''The Inverse Problem in Transient Heat Conduction,'' ASME J. Appl. Mech., **86**, pp. 369–375.
[10] Imber, M., and Khan, J., 1972, ''Prediction of Transient Temperature Distributions With Embedded Thermo-couples,'' AIAA J., **10**(6), pp. 784–789.
[11] Imber, M., 1974, ''Temperature Extrapolation Mechanism for Two-Dimensional Heat Flow,'' AIAA J., **12**(8), pp. 1089–1093
[12] Shoji, M., 1978, ''Study of Inverse Problem of Heat Conduction (in Japanese),'' Trans. Jpn. Soc. Mech. Eng., **44**(381), pp. 1633–1643.
[13] Monde, M., 2000, ''Analytical Method in Inverse Heat Transfer Problem Using Laplace Transform Technique,'' Int. J. Heat Mass Transf., **43**, pp. 3965–3975.
[14] Monde, M., Arima, H., and Mitsutake, Y., 2000, ''Analytical Method In Inverse Heat Transfer Problem Using Laplace Transform Technique—Second And Third Boundary Conditions,'' 3rd European thermal Science Conference 2000, Sept. 10–13, Heidelberg .
[15] Monde, M., and Mitsutake, Y., 2001, ''A New Estimation Method of Thermal Diffusivity Using Analytical Inverse Solution for One Dimensional Heat Conduction,'' Int. J. Heat Mass Transf., **44**(16), pp. 3169–3177.
[16] Carslaw, H. S., and Jaeger, J. C., 1959, *Conduction of Heat in Solids*, Oxford Univ. Press.
[17] Kim, S. K., and Lee, W. I., 2002, ''Solution of Inverse Heat Conduction Problems Using Maximum Entropy Method,'' Int. J. Heat Mass Transf., **45**(2), pp. 381–391.
[18] Chantasiriwan, S., 1999, ''Comparison of Three Sequential Function Specification Algorithms for the Inverse Heat Conduction Problem,'' Int. Commun. Heat Mass Transfer, **16**(1), pp. 115–124.
[19] Taler, J., 1996, ''A Semi-Numerical Method for Solving Inverse Heat Conduction Problem,'' Heat Mass Transfer, **31**, pp. 105–111.

Shape Identification by Inverse Heat Transfer Method

Chin-Hsiang Cheng
e-mail: cheng@ttu.edu.tw

Mei-Hsia Chang

Department of Mechanical Engineering,
Tatung University,
40 Chungshan N. Road, Sec. 3,
Taipei, Taiwan 10451,
R.O.C.

The aim of this study is to investigate the performance of the inverse heat transfer method in application to the shape identification problem. The approach is constructed by combining the curvilinear grid generation scheme, the direct problem solver, the conjugate gradient optimization method, and the redistribution method. A number of practical cases are considered, in which shape identification for an inner void within a solid body based on the data of the outer surface temperature of the solid body is performed. These cases are divided into five kinds of geometrical configurations. Results show that the profile of the inner void can be identified by using the inverse heat transfer approach, and the accuracy of the shape identification is dependent on the uncertainty of the outer surface temperature data, the Biot number, size of the inner void, and the geometrical configuration as well. [DOI: 10.1115/1.1560152]

Keywords: Heat Transfer, Image Processing, Inverse, Numerical Methods, Optimization

Introduction

During the past several decades, development of the inverse heat transfer problem (IHTP) has progressed more rapidly, with the help of a combination of the advent of high technologies, new mathematical achievements and modern computational facilities. It is known that the space program, starting from about 1956, gave considerable impetus to the studies of the inverse heat transfer problems (IHTP). One of the earliest papers dealing with the IHTP was reported by Stolz [1] in 1960. The author calculated heat transfer rates during quenching of bodies of simple finite shapes. Considering semi-infinite geometries, Mirsepassi [2,3] had used a similar technique both numerically and graphically for several years prior to 1960. A Russian paper by Shumakov [4] on the IHTP was translated in 1957. Up to now, using the method of the IHTP can successfully estimate the unknown boundary conditions, such as temperature [5], heat flux [6,7], internal heat generation [8], and contact resistance [9], by utilizing the transient temperature measurements taken within the objects. One additional kind of applications of the IHTP is the determination of thermal properties such as thermal conductivity and specific heat of the materials. For example, Terrola [10] estimated temperature dependence of the thermal conductivity according to the measured temperature profiles and obtained the solution by using an optimization method. Lin [11] developed a similar method that could be used to simultaneously estimate the thermal conductivity, the heat capacity, and the heat transfer coefficient on the surface of the solid slab based on the one-point temperature measurement data.

In addition, the inverse problem has been extended to the applications in thermal design. Kennon and Dulikravich [12] and Dulikravich [13] devoted to design the thermal cooling system by determining the size, shape, number, and location of the coolant fluid passages within the turbine blades. The problem of optimizing the fin profile in order to satisfy the specific thermal requirements is studied by a number of several researchers. For instance, Sinder and Kraus [14] presented the optimal fin profile for the heat remover longitudinal fins, in order that the system may dissipate the highest power at the smallest volume.

Recently, shape identification problems constitute an important kind of IHTP problems. Huang and Chao [15] addressed the development in the numerical schemes, including both the Levenberg-Marquardt and the conjugate gradient algorithms, which are applied for identifying the unknown boundary profiles for the steady problems. Huang and Tsai [16] extended the study to a transient problem of which the task is to identify the irregular boundary configurations based on the external temperature measurements. In these two reports [15,16], a function of particular form is assumed in advance to define the unknown boundary profile, and hence the boundary configuration to predict may be essentially restricted by the assumed function form. Therefore, a relatively complicated boundary configuration, for example, a zigzag boundary, may not be predicted accurately. On the other hand, the external temperature measurements required in the inverse heat transfer analysis can be performed by using thermal image method. The thermal image method has gradually become one of the useful tools suitable for thermographic nondestructive evaluation (NDE) [17,18] which has received increasing attention from the IHTP investigators.

The present study is concerned with the development of an IHTP approach which is suitable to the shape identification for the complicated boundary configuration. Therefore, the feasibility of the inverse heat transfer method presented by Cheng and Wu [19] and Lan, Cheng, and Wu [20] for the shape identification is investigated. The approach combines the curvilinear grid generation, the direct problem solver, the conjugate gradient method, and the redistribution method for shape identification problem, as described in Refs. [19,20]. According to results presented in Refs. [19,20], it has been found that the approach is robust and the direct numerical sensitivity analysis applied avoids the complexity in mathematical implementation so that the application range can be extended. In addition, the approach performed direct adjustment for the X and Y coordinates of individual surface points, not for the parameters of a prescribed function which must be prescribed beforehand to express the unknown shape profile. In this manner, the approach is able to deal with any unusual shape profiles which are not easily handled by other methods.

In this study, a number of practical cases with various geometrical configurations are studied. The physical model of the test problems for shape identification is shown in Fig. 1. A solid body with given outer surface profile dissipates heat to the ambient air at temperature T_a by convection. The heat transfer coefficient (h) on the outer surface of the solid body may be given as a constant or a function of x. Somewhere within the solid body, there exist an inner void. The boundary of the inner void is just the inner surface of the solid body. It is assumed that the inner surface is maintained at a higher temperature T_w. However, neither shape nor location of the inner surface is known. Now, the problem is: Is it

Contributed by the Heat Transfer Division for publication in the JOURNAL OF HEAT TRANSFER. Manuscript received by the Heat Transfer Division September 4, 2001; revision received November 1, 2002. Associate Editor: G. S. Dulikravich.

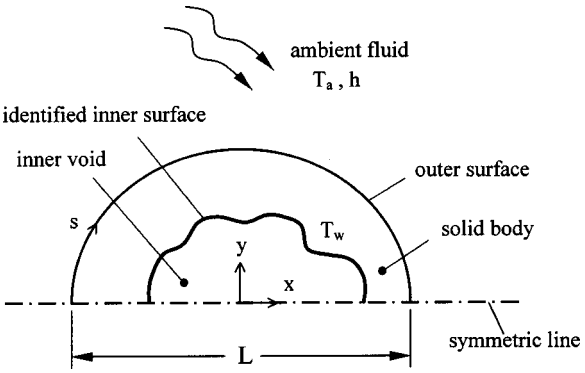

Fig. 1 A solid body of which the shape of inner void is to be identified

possible to identify the shape profile and the location of the inner surface simply based on the outer surface temperature measurements? In other words, the goal of the inverse problem is to predict the geometry of the unknown inner surface by using the measurable temperature information on the outer surface. Note that the temperature information may be collected simply by using the thermocouples installed on the outer surface of the object.

Five kinds of geometrical configurations for the test problems are considered in this study. The geometrical configurations are categorized in accordance with the shape profiles for the outer and the inner surfaces. These configurations considered are: (1) outer ellipse-inner ellipse, (2) outer ellipse-inner eccentric ellipse, (3) outer ellipse-inner circle, (4) outer circle-inner rectangle, and (5) outer circle-inner circle. The accuracy of the shape identification is found to be dependent on the configuration, and detailed information will be given later. Table 1 gives these five geometrical configurations considered.

Shape Identification Methods

Heat Conduction Problem Solver and Numerical Grid Generator. Considering a homogeneous, isotropic solid body, the heat conduction equation for the temperature solution can be expressed as

$$\nabla^2 T = 0, \text{ in } \Omega \tag{1}$$

Table 1 Five kinds of configurations considered

Case	Outer profile	Inner profile (exact)	Geometry
1	Ellipse	Ellipse	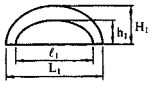
2	Ellipse	Eccentric ellipse	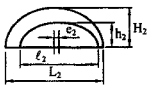
3	Ellipse	Circle	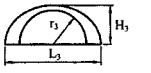
4	Circle	Rectangle	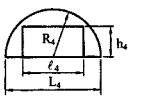
5	Circle	Circle	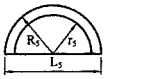

where T is the solid temperature and Ω is the solution domain. Note that a two-dimensional steady-state heat conduction equation is investigated for the test problems. That is, transient behavior of the temperature field is not taken into account in the present analysis.

The body-fitted coordinate transformation technique, which was originally proposed by Thompson et al. [21,22] is applied to generate the curvilinear grid for computation at each iteration that accommodates the variation of the shape of the solution domain during the optimization process. The coordinate transformation functions $\xi=\xi(X,Y)$ and $\eta=\eta(X,Y)$ are obtained numerically by solving two elliptic-type partial differential equations, as was suggested by Thompson et al. [21,22]. Using the curvilinear coordinate obtained, the heat conduction equation and the boundary conditions are then transformed and solved in the computation domain (ξ,η). By introducing the following group of dimensionless parameters,

$$X=\frac{x}{L}, \quad Y=\frac{y}{L}, \quad \theta=\frac{T-T_a}{T_w-T_a}, \quad \mathrm{Bi}=\frac{hL}{k_s} \tag{2}$$

the transformed steady heat conduction equation is derived from Eq. (1) as

$$\bar{\alpha}\frac{\partial^2\theta}{\partial\xi^2}-2\bar{\beta}\frac{\partial^2\theta}{\partial\xi\partial\eta}+\bar{\gamma}\frac{\partial^2\theta}{\partial\eta^2}=-Ja^2\left(F_1\frac{\partial\theta}{\partial\xi}+F_2\frac{\partial\theta}{\partial\eta}\right) \tag{3}$$

where $\bar{\alpha}=(\partial X/\partial\eta)^2+(\partial Y/\partial\eta)^2$, $\bar{\beta}=(\partial X/\partial\xi)(\partial X/\partial\eta)+(\partial Y/\partial\xi)(\partial Y/\partial\eta)$, $\bar{\gamma}=(\partial X/\partial\xi)^2+(\partial Y/\partial\xi)^2$, $Ja=(\partial X/\partial\xi)\times(\partial Y/\partial\eta)-(\partial X/\partial\eta)(\partial Y/\partial\xi)$, and F_1 and F_2 are two functions which are defined to artificially adjust the density of the grids locally.

The dimensionless boundary conditions associated with Eq. (3) become

$$\theta=1 \quad \text{at} \quad \eta=0 \quad \text{(inner surface)} \tag{4a}$$

$$\frac{\partial\theta}{\partial\xi}=0 \quad \text{at} \quad \xi=0 \quad \text{and} \quad 1 \quad \text{(symmetric line)} \tag{4b}$$

$$-\frac{\partial\theta}{\partial N}=\mathrm{Bi}\theta \quad \text{at} \quad \eta=1 \quad \text{(outer surface)} \tag{4c}$$

where N represents the dimensionless outward normal coordinate to the outer surface. In this study, the Biot number on the outer surface is prescribed by Bi=1 typically and the normal heat flux on the outer surface is calculated with the normal temperature gradient as

$$\frac{\partial\theta}{\partial N}=\frac{\bar{\gamma}\dfrac{\partial\theta}{\partial\eta}-\bar{\beta}\dfrac{\partial\theta}{\partial\xi}}{Ja\sqrt{\bar{\gamma}}} \tag{5}$$

However, results at a smaller Biot number (Bi=0.1) are also presented herein to illustrate the effects of the Biot number on the performance of shape identification.

Shape profile functions of the identified inner surface, $X_d(\xi)$ and $Y_d(\xi)$, are updated during the iterative optimization process. Based on the updated shape profile functions, a grid that accommodates the variation of the shape profile at each iteration is generated. Then with the help of Eqs. (3) to (5), the temperature distribution on the curvilinear computation domain can be solved on the curvilinear grid.

Conjugate Gradient Method. Let $X^n_{i,d}$ and $Y^n_{i,d}$ $(i=1,2,\ldots,N)$ be the nth iterative values of the identified shape functions $X_d(\xi)$ and $Y_d(\xi)$ for grid point i on the inner surface. The shape profile of the medium domain represented by the shape functions on the identified surface $X_d(\xi)$ and $Y_d(\xi)$ is varied in order that the objective function, defined by

$$J=\sum_{i=1}^{N}(\theta_{i,M}-\overline{E}_i)^2 \tag{6}$$

is minimized, where $\overline{E}_i$ is the curve-fitted simulated experimental temperature data on the outer surface after regression, and $\theta_{i,M}$ is the dimensionless outer surface temperature.

Minimization of the objective function J is achieved by using the conjugate gradient method. The conjugate gradient method evaluates the gradients of the objective function and sets up a new conjugate direction for the updated solutions with the help of a sensitivity analysis. In general, in a finite number of iterations the convergence can be attained by the conjugate gradient scheme. General descriptions and further details of the method are available in Refs. [19,20].

Redistribution Method. The distribution method proposed by Lan et al. [20] is also employed in this study to facilitate the convergence of the shape identification process. It is assumed that the shape profile of the identified surface should be a smooth and continuous curve in physical reality. Thus, the ill-ordered grid patterns, such as twisted or out-of-alignment grids, are not desirable. Four major steps are included in the redistribution method: (1) detection, (2) alignment, (3) segmentation, and (4) redistribution. Detailed information about the redistribution method can been found in Ref. [20].

Simulated Input Errors. In this study, simulated experimental outer surface temperature data (E_i) are collected by adding a perturbation to the exact values. That is

$$E_i=\theta_{\text{ex}}+\sigma\mathbf{r}_i \tag{7}$$

where θ_{ex} is the exact outer surface temperature calculated by the heat conduction problem solver for the case having a particular inner void profile of interest; $\mathbf{r}_i$ is a random number evenly distributed between -1 and 1 and is provided by a random number generator; and σ is a value given to simulate the uncertainty of experiments. The value of σ is assigned to be 0, 0.001 and 0.01 in this report. Note that at $\sigma=0$, the exact outer surface temperature data (θ_{ex}) are used directly for the shape identification.

A regression analysis for the simulated experimental outer surface temperature data is first made after they have been collected. Data regression may be performed with any mathematical tool available. In this study, a commercial software, CurveExpert 1.3, which was released by Daniel Hyams and Microsoft Corporation in 1993, is used. The data regression yields a curve best fitted by the surface temperature data. A set of input data ($\overline{E}_i$) can then be obtained based on the function of the fitted curve.

It is noted that the adjustment for $X_{i,d}^n$ and $Y_{i,d}^n$ by the conjugate gradient method is sensitive to the perturbation added to the exact values. Direct introduction of the original simulated experimental outer surface temperature data may lead to excessive grid skewness and ill-ordered grid patterns on the inner surface. In that case, the identified shape profile cannot be a smooth and continuous curve as expected. This can be treated as a limitation of the present methodology.

The flow chart regarding the iterative optimization process in search of the shape profile is shown in Fig. 2. In the present study, the convergence criterion is satisfied as the objective function reaches a minimization in the iterating process.

Numerical Check. Typically, a grid system of 41×21 grids for the solution domain is adopted in this analysis. However, a careful check has been made to ensure the grid-independence of the numerical predictions. For this purpose, two grid systems, 41×21 and 51×31 grids, are tested. Figure 3 shows the comparison in shape identifications yielded by these two grid systems, for case 2 with $L_2=1$, $H_2=0.4$, $\ell_2=0.8$, $h_2=0.25$, $e_2=0.05$, and $\sigma=0$. It is found in Fig. 3 that the discrepancy between the solutions obtained by adopting 41×21 and 51×31 grids is negligibly small. Tests for other typical cases show a similar result.

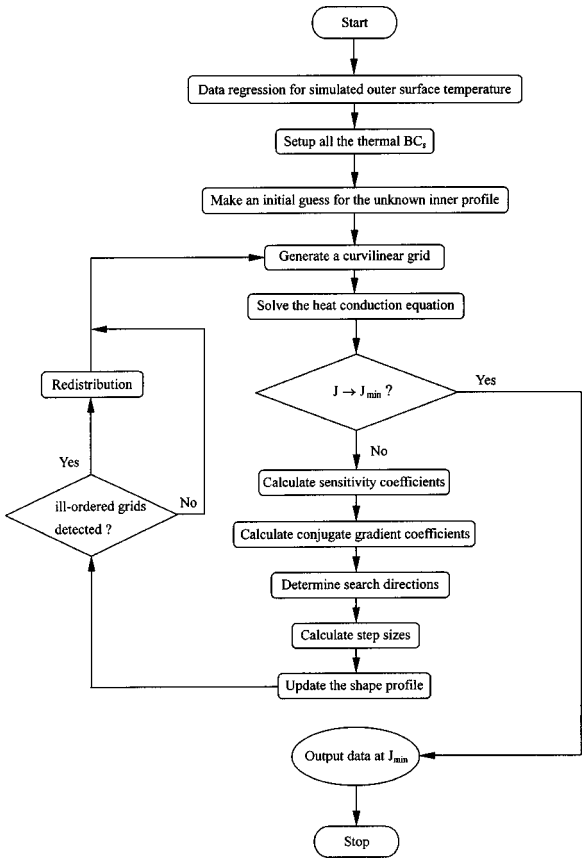

Fig. 2 Flow chart of the process for shape identification

Results and Discussion

Figure 4 displays the effects of the uncertainty of the simulated experimental outer surface temperature data (σ) on the shape identification for case 1 at $L_1=1$, $H_1=0.4$, $\ell_1=0.8$, and $h_1=0.25$. The uncertainty (σ) is set to be 0, 0.001, and 0.01. Presented in the left and the right plots of Fig. 4 are the data of outer surface temperature (θ_{os}) and the shape identified at various uncertainties. In the left plots, the original and the curve-fitted surface temperature data are given. The goal of the optimization method is to identify the unknown inner surface profile according to the outer surface temperature data. The temperature data associated with the curve identified is the final surface temperature

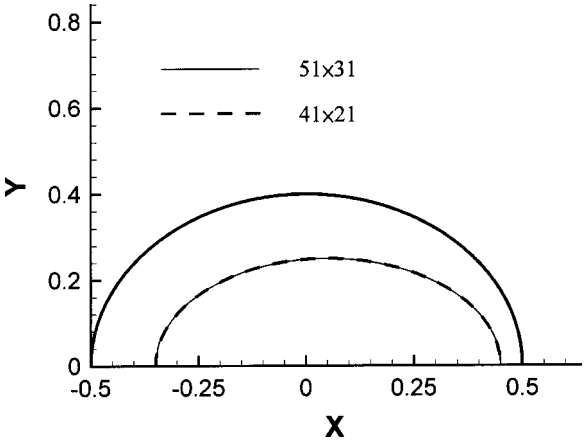

Fig. 3 Grid independence check, for case 2 with $L_2=1$, $H_2=0.4$, $\ell_2=0.8$, $h_2=0.25$, and $e_2=0.05$, at $\sigma=0$ and Bi=1

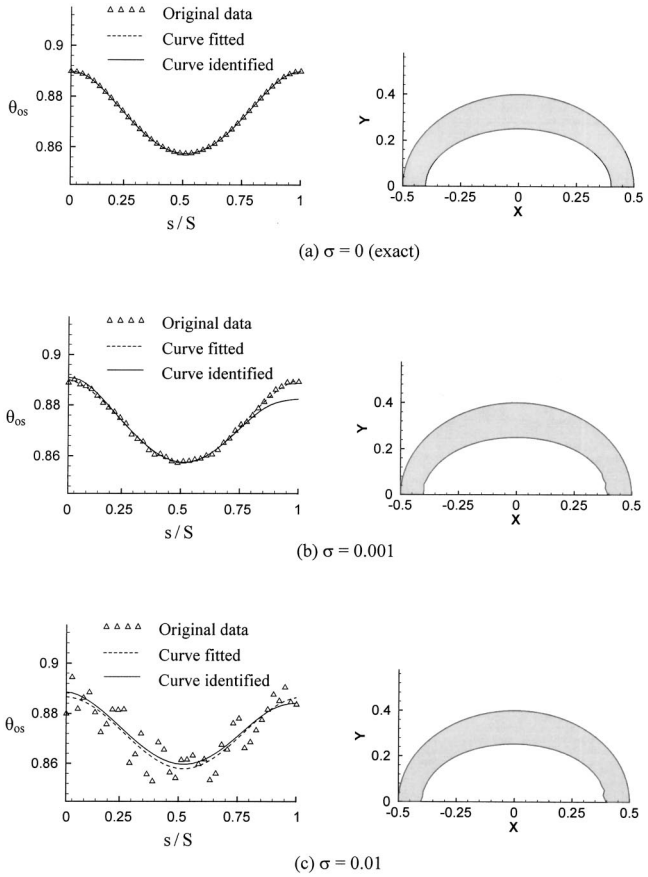

Fig. 4 Effects of uncertainty on inner surface identification, for case 1 at Bi=1 with $L_1=1$, $H_1=0.4$, $\ell_1=0.8$, and $h_1=0.25$

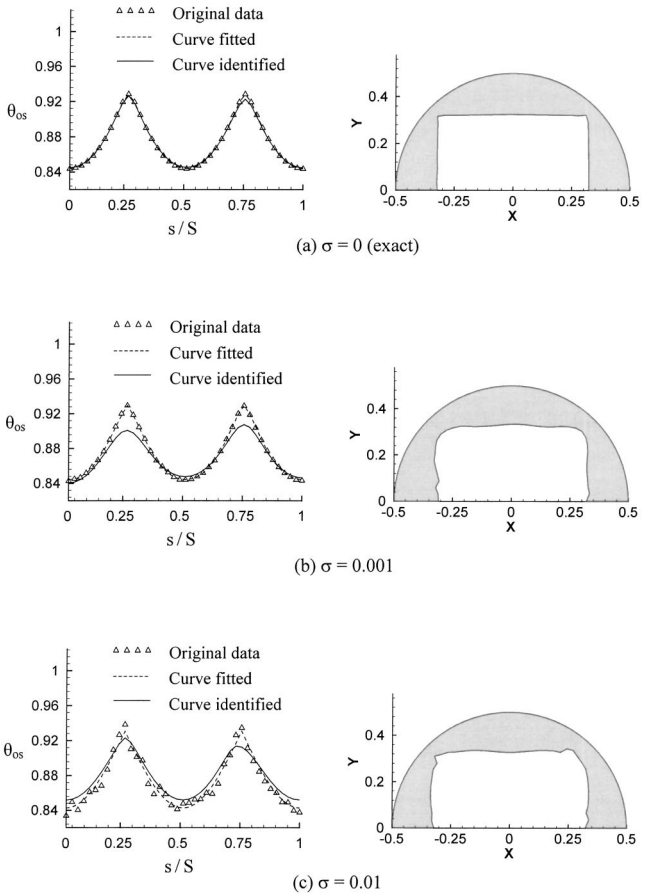

Fig. 5 Effects of uncertainty on inner surface identification, for case 4 at Bi=1 with $R_4=0.5$, $\ell_4=0.64$, and $h_4=0.32$

distribution accompanying the minimum objective function. For the case at $\sigma=0$ shown in Fig. 4(*a*), the original data, the curve-fitted data, and the curve-identified data are coincident, and thus a prefect inner surface identification is obtained. When an uncertainty is introduced into the original temperature data, as for the cases at $\sigma=0.001$, and 0.01 shown in Figs. 4(*b*) and (*c*), respectively, it is found that the disagreement between the curve-fitted data and the final curve-identified data apparently exists, and the profile identified by the optimization methods is blurred due to the uncertainty, especially for the portions adjacent to the symmetric lines. The disagreement between the curve-fitted and the curve-identified temperature data increases with the uncertainty, whereas the identified shape of the inner surface is only slightly blurred as σ is elevated to 0.01.

Attention is now drawn to the case having a rectangular inner void, case 4. The rectangular inner void features two sharp corners; therefore, the capability for the optimization method in dealing with the sharp corners is examined. Figure 5 shows the results of shape identification for case 4 with $R_4=0.5$, $\ell_4=0.64$, and $h_4=0.32$. At $\sigma=0$, the rectangular inner surface is clearly identified based on the outer surface temperature data. However, the shape identification is rather sensitive to the magnitude of the uncertainty. At $\sigma=0.001$ and 0.01, the identified shape of the rectangular inner surface is obviously blurred, and the sharp corners are smeared. Nevertheless, the rectangular outline of the inner void can still be recognized even though σ of 0.01 is introduced.

To quantify the accuracy of the shape identification, an error norm of the prediction of the shape profile is defined based on the area difference between the identified and the exact profiles as

$$\|N\| = |A - A^*| = \sum |(Y_{i,\mathrm{ex}} - Y_{i,d}^n)\Delta X_{i,\mathrm{ex}}| \tag{8}$$

where A and A^* denote the areas of the exact and the identified profiles, respectively, and $\Delta X_{i,\mathrm{ex}} = X_{i+1,\mathrm{ex}} - X_{i,\mathrm{ex}}$. Relative error norm can be expressed in terms of $\|N\|/A$. Table 2 shows the error and the relative error norms as functions of the uncertainty σ for various configurations. It is observed that the error norm of prediction increases with σ for all cases. In general, the relative error norm is approximately 2% as σ is assigned to be 0.01. However,

Table 2 Norms of errors of shape identification for various configurations

Case	σ	$\|N\|$	$\|N\|/A(\%)$
Case 1 with $L_1=1$, $H_1=0.4$, $\ell_1=0.8$, $h_1=0.25$, and Bi=1	0	1.072×10^{-3}	0.68
	0.001	1.418×10^{-3}	0.90
	0.01	2.434×10^{-3}	1.55
Case 2 with $L_2=1$, $H_2=0.4$, $\ell_2=0.8$, $h_2=0.25$, $e_2=0.05$, and Bi=1	0	3.349×10^{-4}	0.21
	0.001	2.342×10^{-3}	1.49
	0.01	4.147×10^{-3}	2.64
Case 3 with $L_3=1$, $H_3=0.4$, $r_3=0.35$, and Bi=1	0	4.243×10^{-4}	0.22
	0.001	1.526×10^{-3}	0.79
	0.01	2.742×10^{-3}	1.42
Case 4 with $R_4=0.5$, $\ell_4=0.64$, $h_4=0.32$, and Bi=1	0	2.074×10^{-3}	1.01
	0.001	9.313×10^{-3}	4.55
	0.01	1.393×10^{-2}	6.80
Case 5 with $R_5=0.5$, $r_5=0.4$, and Bi=1	0	1.675×10^{-4}	0.07
	0.001	1.092×10^{-3}	0.43
	0.01	6.403×10^{-4}	0.25

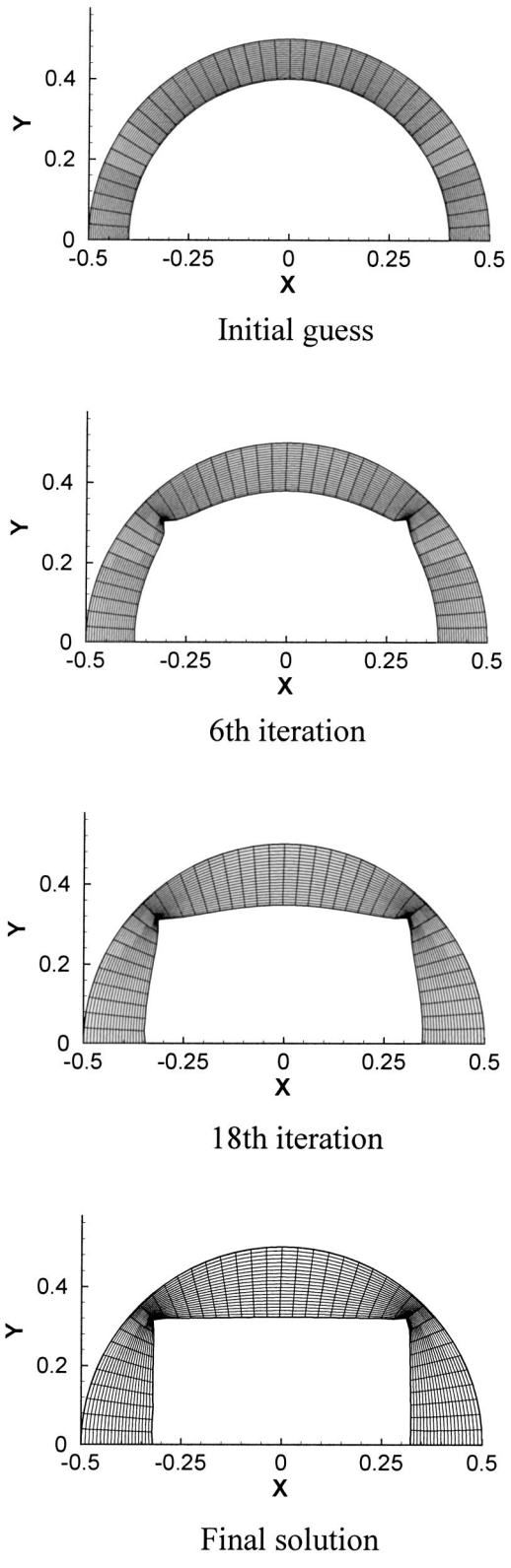

Fig. 6 Convergence process of shape identification, for case 4 at Bi=1 with $R_4=0.5$, $\ell_4=0.64$, and $h_4=0.32$ at $\sigma=0$

the predictions for case 4 are accompanied by a higher relative error up to 7% at $\sigma=0.01$. For this case, one can expect a higher relative error than for other cases observing the blurred and smeared rectangular corners with the identified profile shown in Fig. 5.

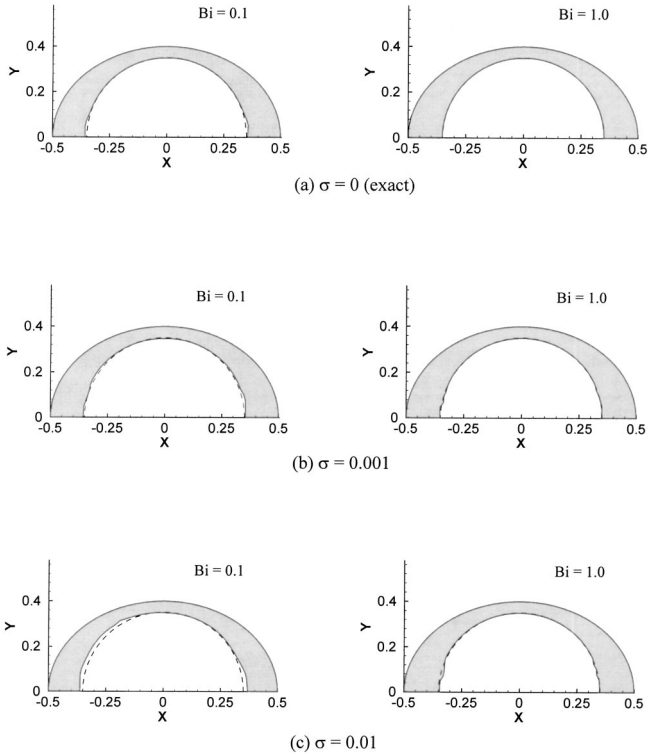

Fig. 7 Effects of uncertainty on inner surface identification, for case 3 with $L_3=1$, $H_3=0.4$, and $r_3=0.35$, at Bi=0.1 and 1

The convergence process for shape identification for case 4 with $R_4=0.5$, $\ell_4=0.64$, $h_4=0.32$, and $\sigma=0$ is displayed in Fig. 6. For this particular case, the initial guess of the inner surface profile is a circle, while the desired shape is a rectangle. The grid systems generated numerically by the body-fitted grid generator for all iterations are also displayed. The sharp corners are clearly visible at the sixth iteration, and eventually in approximately forty iterations, the rectangular inner surface profile is completely formed. Note that the number of iteration required to reach the final shape is essentially dependent on the step sizes (β_i) calculated and the magnitude of the under-relaxation factor as well. A smaller step size or under-relaxation factor will definitely lead to a larger number of iterations. Typically, twenty to sixty iterations are needed to yield the final shape with sufficiently small objective functions.

Results at different Biot numbers are provided to illustrate the effects of the Biot number on the performance of shape identification. Figure 7 shows the inner surface identification results at Bi=0.1 and 1, for case 3 with $L_3=1$, $H_3=0.4$, and $r_3=0.35$. A lower Biot number tends to increase the uniformity of temperature distribution within the solid body. Therefore, at lower Biot number a small change in the inner shape profile may not lead to an appreciable change in the temperature gradient along the outer surface. When the simulated experimental outer surface temperature data is used to identify the inner surface profile, it is expected that the error of shape identification shall be increased by a decrease in Bi. In Fig. 7, the left and the right portions of this figure illustrate the results for Bi=0.1 and 1.0, respectively. A higher error of shape identification is hence observed for the case at Bi=0.1 even though the circular inner surface profile can still be identified for various values of σ.

The size of the inner void (or say, the thickness of the solid body) to identify is also an influential factor affecting the accuracy of shape identification. Figure 8 conveys the thickness effects for case 4 at Bi=1 and $\sigma=0$. It is obvious that the error of shape identification increases with the thickness. Error of shape identi-

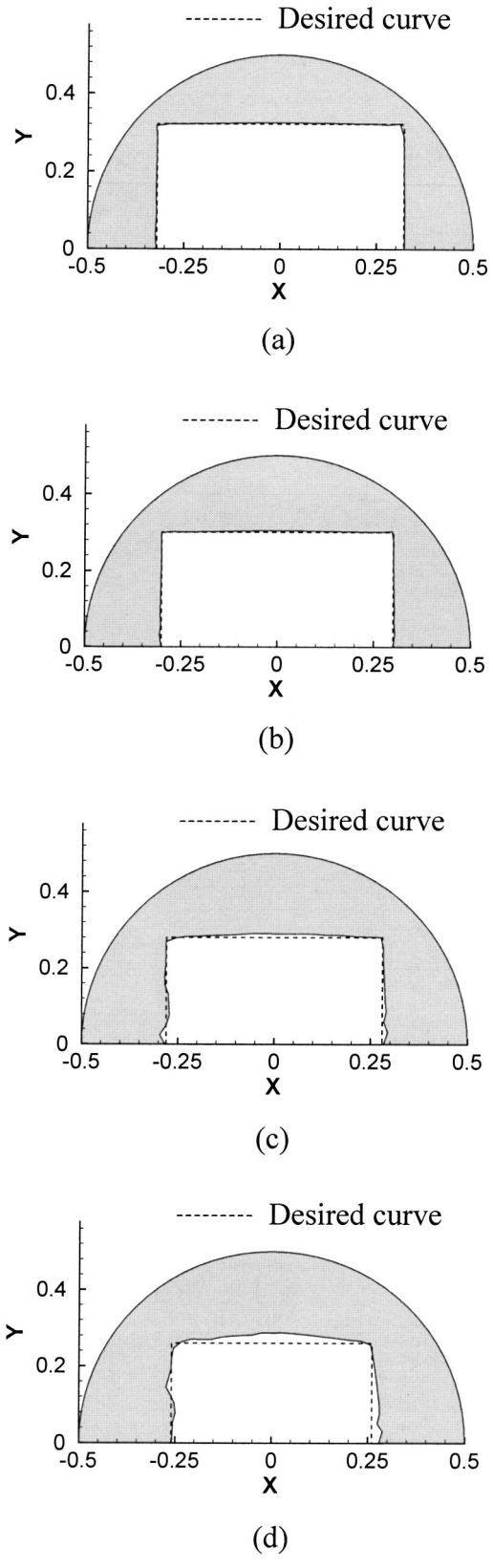

Fig. 8 Thickness effects on the accuracy of shape identification, for case 4 at Bi=1 and σ=0: (*a*) ℓ_4=0.64 and h_4=0.32; (*b*) ℓ_4=0.6 and h_4=0.3; (*c*) ℓ_4=0.56 and h_4=0.28; and (*d*) ℓ_4 =0.52 and h_4=0.26

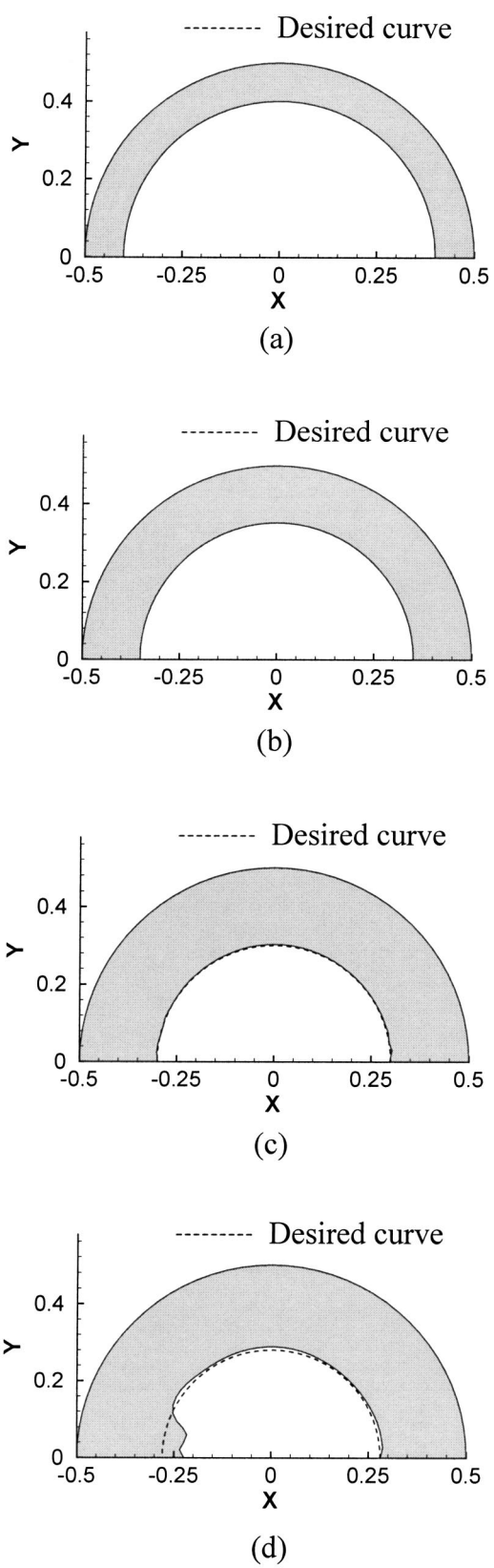

Fig. 9 Thickness effects on the accuracy of shape identification, for case 5 at Bi=1 and σ=0: (*a*) r_5=0.4, (*b*) r_5=0.35, (*c*) r_5=0.3; and (*d*) r_5=0.28

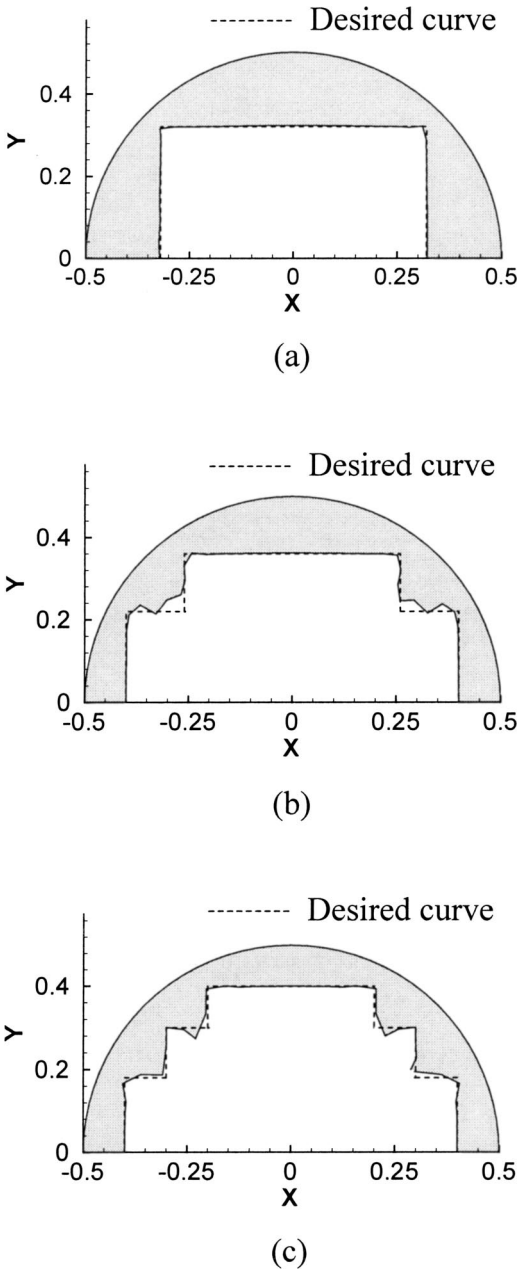

Fig. 10 Shape identification for inner surfaces with fine structures. The outer surface temperature data are given at Bi=1 and σ=0.

fication may be observed based on the values of error norms or the order of magnitude of the minimum objective function. Even for the same case, local thickness still exhibits great influence on the accuracy of local identification. The thick portion of the profile is easier to be blurred than the thin one.

The results shown in Fig. 9 considering case 5 at Bi=1 and σ=0 exhibit a similar trend. The dashed curves shown in Figs. 8 and 9 indicate the desired curve (exact solution) to identify. These dashed curves are used for comparison to reveal the discrepancy between the identified and the desired shape profiles.

The capability for the optimization process of identifying the shape profiles with fine structures has been tested. Presented in Fig. 10 are the results of shape identification for the cases stemming from case 4 and having a multiple-step rectangular inner surface. The purpose of dealing with the cases is to investigate the capability of the shape identification method of identifying the small steps. Again, the dashed lines are given to indicate the desired curves. Results plotted in Figs. 10(*b*) and (*c*) show that the major geometrical features are identified; however, the identification for the small steps is obviously blurred and not clear. The blur on the fine structures may probably be attributed to two factors. The first factor probably is due to the limitation of the grid density. In this study, there are 41 grids distributed on the inner surface for identifying the shape profile. Number of the grid points may not increase the resolution of identification for cases 1 to 5 in which the geometry of the inner void is relatively simple. However, for the present case with fine structures, a larger number of the grid points will definitely improve the resolution of identification and eliminate the blur. The other factor may be the capability for the grid generation method of handling the surfaces with convex or concave structures. The capability of the elliptic grid generation method in handling this kind of surfaces is limited since the grid density is inevitably too low on a concave surface and too high on a convex surface. The problem can only be resolved by improving the uniformity of local grid density in the area near the convex or concave surface.

It is important to mention that the present approach provides a method of shape identification simply based on the surface thermal data. These thermal data may be collected by using the thermocouples. Therefore, the average cost for the shape identification can be greatly reduced as compared with the commonly used X-ray or the ultrasonic scanning systems.

Concluding Remarks

The present study is concerned with the application of the inverse heat transfer approach for shape identification problem. To quantify the accuracy of the shape identification, an error norm of the prediction of the shape profile is defined based on the area difference between the identified and the exact profiles.

In this study, shape identification for an inner void within a solid body based on the outer surface temperature data is performed. Five kinds of geometrical configurations are tested. Results show that the inner voids are accurately identified by the approach. Accuracy of the shape identification is found to be dependent on the uncertainty of the outer surface temperature measurements, the Biot number, size of the inner void, and the geometrical configuration as well. In general, the relative error norm is approximately 2% as the uncertainty σ is assigned to be 0.01. However, the predictions for some particular cases are accompanied by a higher relative error up to 7% at σ=0.01. Meanwhile, it is observed that the error of shape identification is increased by a decrease in the Biot number or a decrease in the size of inner void. This is because a lower Biot number tends to increase the uniformity of temperature distribution within the solid body. Thus, at lower Biot number a small change in the inner shape profile may not lead to an appreciable change in the temperature gradient along the outer surface. It then becomes more difficult to accurately evaluate the sensitivity of outer surface temperature to a change in the inner shape profile. In addition, the size of the inner void to identify is also an influential factor affecting the accuracy of shape identification. It is found that the error of shape identification increases with the thickness and local thickness exhibits great influence on the accuracy of local identification.

Further increase in number of the grid points may not increase the resolution of identification for cases 1 to 5 in which the geometry of the inner void is relatively simple. However, for the case with fine structures, a larger number of the grid points will definitely improve the resolution of identification and eliminate the blur.

The present approach provides a method of shape identification simply based on the surface thermal data. These thermal data may be collected by using the thermocouples. Therefore, the average cost for the shape identification can be greatly reduced as compared with the commonly used X-ray or the ultrasonic scanning systems.

Nomenclature

A = dimensionless area of exact inner void
A^* = dimensionless area of identified inner void
Bi = Biot number ($=hL/k_s$)
E_i = simulated experimental outer surface temperature data of nodal point i
$\overline{E_i}$ = curve-fitted simulated experimental outer surface temperature data of nodal point i
h = heat transfer coefficient
J = objective function
k_s = thermal conductivity
L = length of solid body
$\|N\|$ = norm of error of shape identification
$\mathbf{r}_i$ = random number varied between -1 and 1
s = coordinate along outer surface
S = dimensionless coordinate along outer surface
t = time
T = temperature of solid body
T_a = temperature of ambient fluid
T_w = temperature on inner surface
x, y = Cartesian coordinates
X, Y = dimensionless Cartesian coordinates
X_d, Y_d = shape functions of identified surface profile
$X_{i,d}$, $Y_{i,d}$ = coordinates of grid point i on identified surface

Greek Symbols

θ = dimensionless temperature of solid body
θ_{ex} = exact outer surface temperature
θ_{os} = dimensionless outer surface temperature of solid body
ξ, η = dimensionless curvilinear coordinates
σ = uncertainty
Ω = solution domain

Subscripts

i, j = grid indices
n = iteration number
N = number of grid points in the ξ-direction
M = number of grid points in the η-direction
ex = exact profile or solution

References

[1] Stolz, G., Jr., 1960, ''Numerical Solutions to an Inverse Problem of Heat Conduction for Simple Shape,'' ASME J. Heat Transfer, **82**, pp. 20–26.
[2] Mirsepassi, T. J., 1959, ''Heat-Transfer Charts for Time-Variable Boundary Conditions,'' Br. Chem. Eng., **4**, pp. 130–136.
[3] Mirsepassi, T. J., 1959, ''Graphical Evaluation of a Convolution Integral,'' Math. Tables Aids Comput., **13**, pp. 202–212.
[4] Shumakov, N. V., 1957, ''A Method for the Experimental Study of the Process of Heating a Solid Body,'' Sov. Phys. Tech. Phys., (Translated by American Institute of Physics), **2**, pp. 771–781.
[5] Huang, C. H., and Chen, C. W., 1998, ''A Boundary-Element-Based Inverse Problem of Estimating Boundary Conditions in an Irregular Domain with Statistical Analysis,'' Numer. Heat Transfer, Part B, **33**, pp. 251–268.
[6] Prud'homme, M., and Nguyen, T. H., 1998, ''On the Iterative Regularization of Inverse Heat Conduction Problems by Conjugate Gradient Method,'' Int. Commun. Heat Mass Transfer, **25**, pp. 999–1008.
[7] Huang, C. H., and Wang, S. P., 1999, ''A Three-Dimensional Inverse Heat Conduction Problem in Estimating Surface Heat Flux by Conjugate Gradient Method,'' Int. J. Heat Mass Transf., **42**, pp. 3387–3403.
[8] Park, H. M., and Chung, O. Y., 1999, ''An Inverse Natural Convection Problem of Estimating the Strength of a Heat Source,'' Int. J. Heat Mass Transf., **42**, pp. 4259–4273.
[9] Huang, C. H., Ozisik, M. N., and Sawaf, B., 1992, ''Conjugate Gradient Method for Determining Unknown Conduct Conductance during Metal Casting,'' Int. J. Heat Mass Transf., **35**, pp. 1779–1786.
[10] Terrola, P., 1989, ''A Method to Determine the Thermal Conductivity from Measured Temperature Profiles,'' Int. J. Heat Mass Transf., **32**, pp. 1425–1430.
[11] Lin, T. P., 1998, ''Inverse Heat Conduction Problem of Simultaneously Determining Thermal Conductivity, Heat Capacity and Heat Transfer Coefficient,'' Master thesis, Department of Mechanical Engineering, Tatung Institute of Technology, Taipei, Taiwan.
[12] Kennon, S. R., and Dulikravich, G. S., 1985, ''Inverse Design of Internally Cooled Turbine Blades,'' ASME J. Eng. Gas Turbines Power, **107**, pp. 123–126.
[13] Dulikravich, G., S., 1992, ''Inverse Design of Proper Number, Shapes, Sizes and Locations of Coolant Flow Passages,'' in *Proc. 10th Annual Workshop for Computational Fluid Dynamics Applications in Rocket Propulsion*, ed. R. W. Williams, NASA MSFC, Huntsville, AL, NASA CP-3163, Part 1, pp. 467–486.
[14] Snider, A. D., and Kraus, A. D., 1987, ''Quest for the Optimum Longitudinal Fin Profile,'' Heat Transfer Eng., **8**, pp. 19–25.
[15] Huang, C. H., and Chao, B. H., 1997, ''An Inverse Geometry Problem in Identifying Irregular Boundary Configurations,'' Int. J. Heat Mass Transf., **40**, pp. 2045–2053.
[16] Huang, C. H., and Tsai, C. C., 1998, ''A Transient Inverse Two-Dimensional Geometry Problem in Estimating Time-Dependent Irregular Boundary Configurations,'' Int. J. Heat Mass Transf., **41**, pp. 1707–1718.
[17] Hsieh, C. K., and Su, K. C., 1980, ''A Methodology of Predicting Cavity Geometry Based on Scanned Surface Temperature Data—Prescribed Surface Temperature at the Cavity Side,'' ASME J. Heat Transfer, **102**, pp. 324–329.
[18] Kassab, A. J., and Pollard, J. E., 1994, ''Cubic Spline Anchored Grid Pattern Algorithm for High-Resolution Detection of Subsurface Cavities by the IR-CAT Method,'' Numer. Heat Transfer, Part B, **26**, pp. 63–77.
[19] Cheng, C. H., and Wu, C. Y., 2000, ''An Approach Combining Body-Fitted Grid Generation and Conjugate Gradient Methods for Shape Design in Heat Conduction Problems,'' Numer. Heat Transfer, Part B, **37**, pp. 69–83.
[20] Lan, C. H., Cheng, C. H., and Wu, C. Y., 2001, ''Shape Design of Heat Conduction Problems Using Curvilinear Grid Generation, Conjugate Gradient, and Redistribution Methods,'' Numer. Heat Transfer, Part A, **39**, pp. 487–510.
[21] Thompson, J. F., Thames, F. C., and Mastin, C. W., 1974, ''Automatic Numerical Generation of Body-Fitted Curvilinear Coordinate System for Fields Containing Any Number of Arbitrary Two-Dimensional Bodies,'' J. Comput. Phys., **15**, pp. 229–319.
[22] Thompson, J. F., Thames, F. C., and Mastin, C. W., 1976, ''Boundary-Fitted Curvilinear Coordinate System for Solution of Partial Differential Equation on Fields Containing Any Number of Arbitrary Two-Dimensional Bodies,'' *NASA CR-2729*.

Heat Transfer in Two-Pass Rotating Rectangular Channels (AR=2) With Five Different Orientations of 45 Deg V-Shaped Rib Turbulators

Luai AL-Hadhrami*
Research Assistant

Todd Griffith
Research Assistant

Je-Chin Han
M.C. Easterling Endowed Chair
e-mail: jchan@mengr.tamu.edu

Turbine Heat Transfer Laboratory,
Department of Mechanical Engineering,
Texas A&M University,
College Station, Texas 77843-3123, USA

An experimental study was made to obtain heat transfer data for a two-pass rectangular channel (aspect ratio=2:1) with smooth and ribbed surfaces for two channel orientations (90 deg and 135 deg with respect to the plane of rotation). The V-shaped ribs are placed on the leading and trailing surfaces. Five different arrangements of 45 deg V-shaped ribs are studied. The Reynolds number and rotation number ranges are 5000–40000, and 0.0–0.21, respectively. The rib height to hydraulic diameter ratio (e/D) is 0.094; the rib pitch-to-height ratio (P/e) is 10; and the inlet coolant-to-wall density ratio ($\Delta\rho/\rho$) is maintained around 0.115 for every test. The results show that the rotation-induced secondary flow enhances the heat transfer of the first pass trailing surface and second pass leading surface. However, the first pass leading and the second pass trailing surfaces show a decrease in heat transfer with rotation. The results also show that parallel 45 deg V-shaped rib arrangements produce better heat transfer augmentation than inverted 45 deg V-shaped ribs and crossed 45 deg V-shaped ribs, and a 90 deg channel orientation produces greater rotating effect on heat transfer than a 135 deg orientation.
[DOI: 10.1115/1.1561455]

Keywords: Enhancement, Finned Surfaces, Heat Transfer, Rotating, Turbines

Introduction

To achieve high thermal efficiency in a gas turbine engine, the turbine inlet gas temperature should be increased. However, the penalty is a high thermal load, which affects the durability of the turbine components. Therefore, improved cooling techniques such as film cooling and internal cooling are applied to turbine blades. Internal cooling is achieved by circulating low enthalpy air in multi-pass flow channels inside the blade structure. To increase the heat transfer of the internal cooling, the internal surfaces usually are roughened by angled ribs to trip the boundary layer and increase turbulence. As the turbine blade rotates, Coriolis and buoyancy forces cause different heat transfer behavior between the leading and trailing surfaces.

Over the past few decades numerous studies have been made experimentally on the flow field and heat transfer in the internal coolant passages of gas turbine rotor blades. Metzger et al. [1] studied forced convection in a non-rotating two-pass smooth rectangular channel by varying the divider location and the gap at the 180 deg turn. Fan et al. [2] extended the Metzger et al. [1] work by varying the channel width and concluded that increasing the channel aspect ratio resulted in smaller azimuthal heat transfer variations and increased overall channel heat transfer. Han and Park [3] performed experimental studies on heat transfer characteristics in a non-rotating rib-roughened rectangular channel. Han et al. [4] studied the effect of the rib angle orientation on heat transfer distributions and pressure drop in a non-rotating square channel with two opposite in-line ribbed walls. They found that the 60 deg and 45 deg V-shaped ribs performed better than the 60 deg and 45 deg parallel ribs and, subsequently, better than the 60 deg and 45 deg crossed ribs and the 90 deg rib. The V-shaped ribs produced the highest heat transfer augmentation, while the crossed ribs had the lowest heat transfer enhancement. Taslim et al. [5] measured heat transfer and friction in channels roughened with angled V-shaped and discrete ribs on two opposite walls. Ekkad and Han [6] performed a detailed study on heat transfer distributions in a non-rotating square ribbed channel using a liquid crystal technique. The results show that the 60 deg, V-shaped ribbed channel produced more heat transfer enhancement than 60 deg and 90 deg angled ribbed channels. Kiml et al. [7] investigated heat transfer enhancement mechanisms in a rectangular channel with V- and Λ-shaped ribs. They used a flow visualization technique to examine the secondary flow behaviors created by the V-shaped ribs.

Recently, experiments with rotation have been conducted to closely model turbine blade cooling environments. Wagner et al. [8,9] conducted a detailed experimental study to determine the effects of rotation (buoyancy and Coriolis forces) on the local heat transfer of a multi-pass square channel with smooth walls. They concluded that in the first pass with radially outward flow, rotation created a thinner boundary layer with higher heat transfer on the trailing surface and a thicker boundary layer with lower heat transfer on the leading surface. In the second pass with radially inward flow, opposite heat transfer results were obtained. Johnson et al. [10,11] performed a systematic investigation of the effects of buoyancy and Coriolis forces on the heat transfer coefficient distribution of a four-pass square channel with 45 deg ribs angled to the flow. They concluded that both the rotation and channel orientation with respect to the axis of rotation could change the leading and trailing surface heat transfer coefficients of the ribbed channel. Han et al. [12] investigated an uneven wall temperature effect on local heat transfer in a rotating two-pass square channel with smooth walls. Zhang et al. [13] analyzed the heating condition effects in a two pass square channel with 60 deg angled rib

*Current address: Assistant Professor, King Fahd University, Saudi Arabia.

Contributed by the Heat Transfer Division for publication in the JOURNAL OF HEAT TRANSFER. Manuscript received by the Heat Transfer Division January 25, 2002; revision received November 8, 2002. Associate Editor: H. S. Lee.

turbulators with rotation. They suggested that an uneven wall temperature had a significant impact on the local heat transfer coefficients. Parsons et al. [14,15] studied the effects of channel orientation and wall heating condition on the local heat transfer coefficient in a rotating two-pass square channel with ribbed walls. They found that the effects of the Coriolis force were reduced as the channel orientation changed from a normal (β=90 deg) to an angled orientation (β=135 deg). Dutta and Han [16] also investigated the local heat transfer coefficients in rotating smooth and ribbed two-pass square channels with three channel orientations. Dutta et al. [17] presented experimental heat transfer results for turbulent flows through a rotating two-pass rib-roughened triangular channel, with two channel orientations with respect to the direction of rotation. Taslim et al. [18,19] studied the heat transfer characteristics in rib-roughened square and rectangular orthogonal rotating channels. They used a liquid crystal technique to study the effect of rotation on heat transfer distributions on the walls. They found that rotational effects were more pronounced in rib-roughened channels, with a higher channel aspect ratio and a lower rib blockage ratio. Prabhu and Vedula [20] investigated the pressure drop distribution in a rotating rectangular channel with transverse ribs on one wall. They found that a rib array with a pitch-to-height ratio of 5 caused the largest pressure drop. In addition, Park et al. [21] conducted experimental work using Naphthalene sublimation to study the effects of the Coriolis force, 180 deg turn, channel orientation, and the different rib arrangements on local heat/mass transfer distributions on the leading and trailing walls of a two-pass square channel. Azad et al. [22] experimentally investigated the heat transfer distribution in two-pass rotating rectangular channels (AR=2:1) connected by a 180 deg turn. The results showed that parallel 45 deg angled ribs produced higher heat transfer distribution than crossed 45 deg angled ribs. For a more comprehensive compilation of turbine blade cooling research, please see the book by Han et al. [23].

Following the above-mentioned research, few papers can be found in the open literature studied the rectangular cross section channel with rotation condition. Hence, the first aim was to study two pass rectangular channels (AR=2:1) that are connected by a sharp 180 deg turn. The second motivation was to find different rib configurations that trip the boundary layer and promote more heat transfer inside the two-pass rectangular channels. However, it was found from a previous study by Han et al. [4] that the 45 deg V-shaped ribs show higher heat transfer performance in a one-pass non-rotating square duct compared to other rib configurations (45 deg angled ribs or transverse 90 deg ribs). Thus, we have chosen 45 deg V-shaped ribs to be placed on the leading and trailing surfaces of the two-pass rotating rectangular channels since they have shown a potential for higher heat transfer enhancement. A comprehensive study was conducted to cover five different arrangements of 45 deg V-shaped ribs and a comparison with 45 deg V-shaped crossed rib case. In addition, the effect of the channel orientation with respect to the axis of rotation was investigated for two positions β=90 deg and β=135 deg. Such experimental data is not available in the open literature. Our research shows the combined effect of the 45 deg V-shaped rib induced secondary flow and rotation induced secondary flow on the heat transfer distribution in the two-pass rectangular cross-sectional channels.

Description of the Experiment

The experimental test rig used by Azad et al. [22] is employed in this study. Figure 1 shows the schematic of the experimental test rig. Compressed air goes through a filter and an orifice meter, then passes through a rotary seal and a hollow-rotating shaft to feed the test section. The test section is mounted in a horizontal plane. Air travels outward in the first pass and inward in the second pass, and then exhausts into the atmosphere. Slip rings transfer thermocouple outputs to the data logger and power input from transformers to strip heaters, which are fixed under the copper plates. An electric motor with an adjustable frequency controller rotates the test section. A digital photo tachometer measures the rotational speed of the rotating shaft.

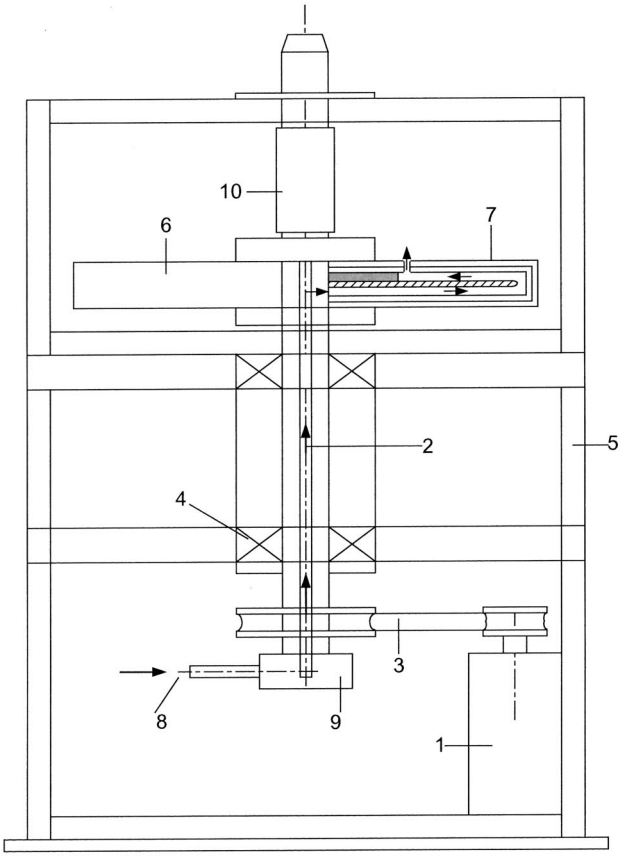

1. Electircal Motor with Controller
2. Rotating Shaft
3. Belt Drive Pulley System
4. Bearing Support System
5. Steel Table
6. Rotating Arm
7. Test Section
8. Compressor Air
9. Rotary Seal
10. Slip Ring

Fig. 1 Schematic of the rotating test rig

Figure 2 shows a cross sectional view of the test section. The test section has two passes. Each pass is 12.7 mm by 25.4 mm in cross section. The first pass starts with an unheated nylon entrance channel to establish a fully developed flow at the entrance to the heated channel. It has twelve (12) hydraulic diameter lengths to achieve the task. The heated channel length-to-hydraulic diameter (L/D) ratio is 18, while each pass length-to-hydraulic diameter (L/D) ratio is 9, connected by a sharp 180 deg turn. The ratio of the mean rotating arm radius to the channel hydraulic diameter (R/D) is 30. The flow in the first pass is radially outward and the flow in the second pass is radially inward. The heated section is divided into twelve longitudinal sections, six sections in the first pass and six in the second pass, to obtain regionally average heat transfer coefficients. Each longitudinal section has four copper plates on four walls (one per wall) of the channel. Each copper plate is surrounded circumferentially by a thin nylon strip that has a 1.59 mm thickness for insulation from neighboring plates. The copper plates are mounted in a nylon substrate, which comprises the bulk of the test section. Pre-fabricated flexible heaters are installed beneath the leading and trailing surfaces. The side walls are each heated by a wire-wound resistance heater, which is also installed beneath the copper plates. All heaters supply steady, uniform heat flux to the copper plates. Sufficient power is supplied in order to maintain a maximum wall temperature of nearly 65 deg for the corresponding section. This corresponds to an inlet

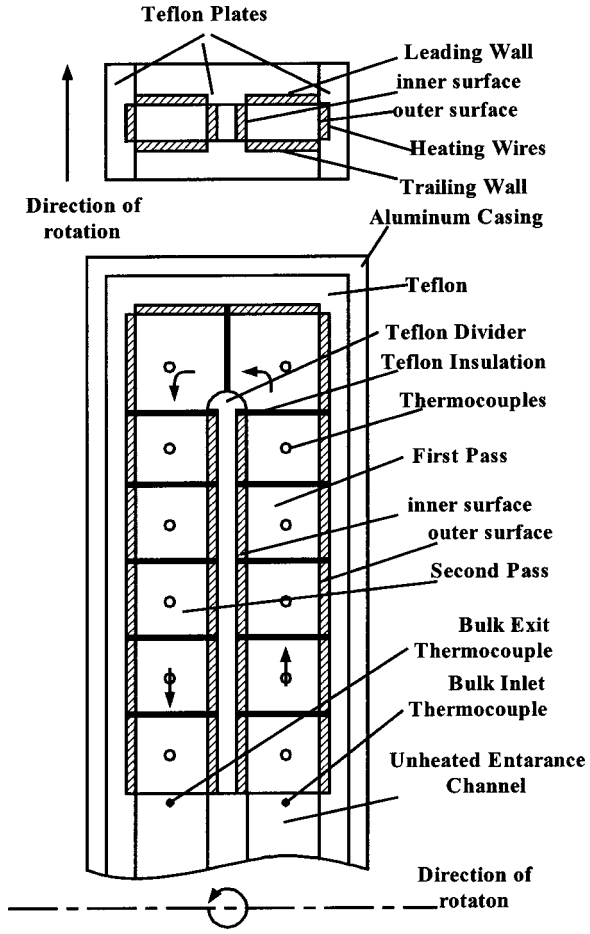

Fig. 2 Cross sectional view of the two-pass rectangular test section

coolant-to-wall density (temperature) ratio ($\Delta\rho/\rho$) of 0.115 for every test. Each 1/8 in. (0.318 cm) thick copper plate has a 1/16 in. (0.159 cm) deep blind hole drilled into its backside in which a copper-constantan thermocouple is installed 1/16 in. (0.159 cm) from the plate surface with thermal conducting glue. The inlet and exit bulk temperatures are measured by thermocouples. The 45 deg V-shaped ribs with a square cross section are made of brass and are glued on the wider walls (leading and trailing surfaces) of the rotating channel. A thin layer of conductive glue is used so that it creates a negligible thermal insulation effect between the brass ribs and the copper plates. The rib-increased surface area is 25 percent with respect to the smooth wall. The entire test duct is surrounded by insulating nylon material and fits in a hollow cylindrical arm for structural rigidity.

Data Reduction

The local heat transfer coefficient is calculated from

$$h = q_{\text{net}}/[A(T_w - T_{bx})] \tag{1}$$

Local net heat transfer rate is the electrical power generated from the heater ($q = VI$) minus losses. Losses were determined by supplying electrical power to the test section until a steady state condition is achieved for a no flow (without any airflow) condition. This is done for several power inputs to obtain a relation between the total heat loss from each surface and the corresponding surface temperature. To place the results on a common basis, the heat transfer area used in Eq. (1) was always that of a smooth wall. The local wall temperature is obtained from thermocouples that impeded in each copper plate. The bulk mean air temperatures entering and leaving the test section are measured by thermocouples. The local bulk mean temperature (T_{bx}) used in Eq. (1) is calculated from the linear interpolation between the measured inlet and exit air bulk temperatures. The bulk mean temperature rise at the lowest Reynolds number is around 20 deg. Another way to find the local bulk mean air temperature is determined by marching along the test section and calculating the temperature rise from the local net heat input through each set of four heated surfaces. The difference between the calculated and measured outlet bulk mean temperature is between 1–2 deg in all of the cases.

Local Nusselt number is normalized by the Nusselt number for the fully developed turbulent flow in a smooth stationary circular pipe to reduce the influence of the flow Reynolds number on the heat transfer coefficient. Local Nusselt number normalized by the Dittus-Boelter/McAdams correlation is:

$$\text{Nu}/\text{Nu}o = (hD/K)/[0.023^* \text{Re}^{0.8} {}^* \text{Pr}^{0.4}] \tag{2}$$

The Prandtl number (Pr) for air is 0.71. Air properties are taken based on the mean bulk air temperature.

The uncertainty of the local heat transfer coefficient depends on the uncertainties in the local wall and bulk air temperature difference and the net heat input for each test run. The uncertainty increases with the decrease of both the local wall to bulk air temperature difference and the net heat input. The temperature uncertainty is around 0.5 deg. The flowrate uncertainty is less than 4 percent. Based on the method described by Kline and McClintock [24], the typical uncertainty in the Nusselt number is estimated to be less than 9 percent for Reynolds number larger than 10,000. The maximum uncertainty, however, could be up to 23 percent for the lowest heat transfer coefficient at the lowest Reynolds number tested (Re=5000).

Results and Discussion

Figure 3 shows the 45 deg angled rib that was divided at the centerline to make the 45 deg V-shaped rib. There are two different orientations of the V-shaped rib. The first orientation is called the 45 deg V-shaped rib and the second orientation is called the inverted 45 deg V-shaped rib. Figure 3 also shows the conceptual view of secondary flow induced by the 45 deg angled rib, the 45 deg V-shaped rib, and the inverted V-shaped rib. The 45 deg angled rib induces a secondary flow that moves parallel to the rib from the left side to the right side and returns back to the left side making a counter rotating vortex. The conjectured counter rotating vortex induced by the 45 deg angled ribs has been confirmed from numerical calculations by Al-Qahtaini et al. [25].

It is further conjectured that the 45 deg V-shaped rib creates two counter rotating vortices. As the fluid approaches the

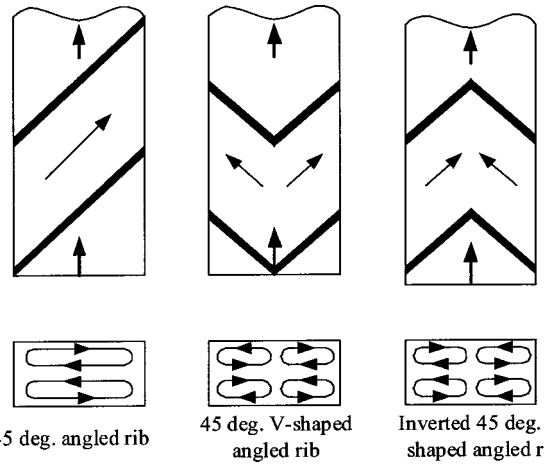

Fig. 3 Conceptual view of secondary flow vortices induced by 45 deg angled ribs and 45 deg V-shaped ribs

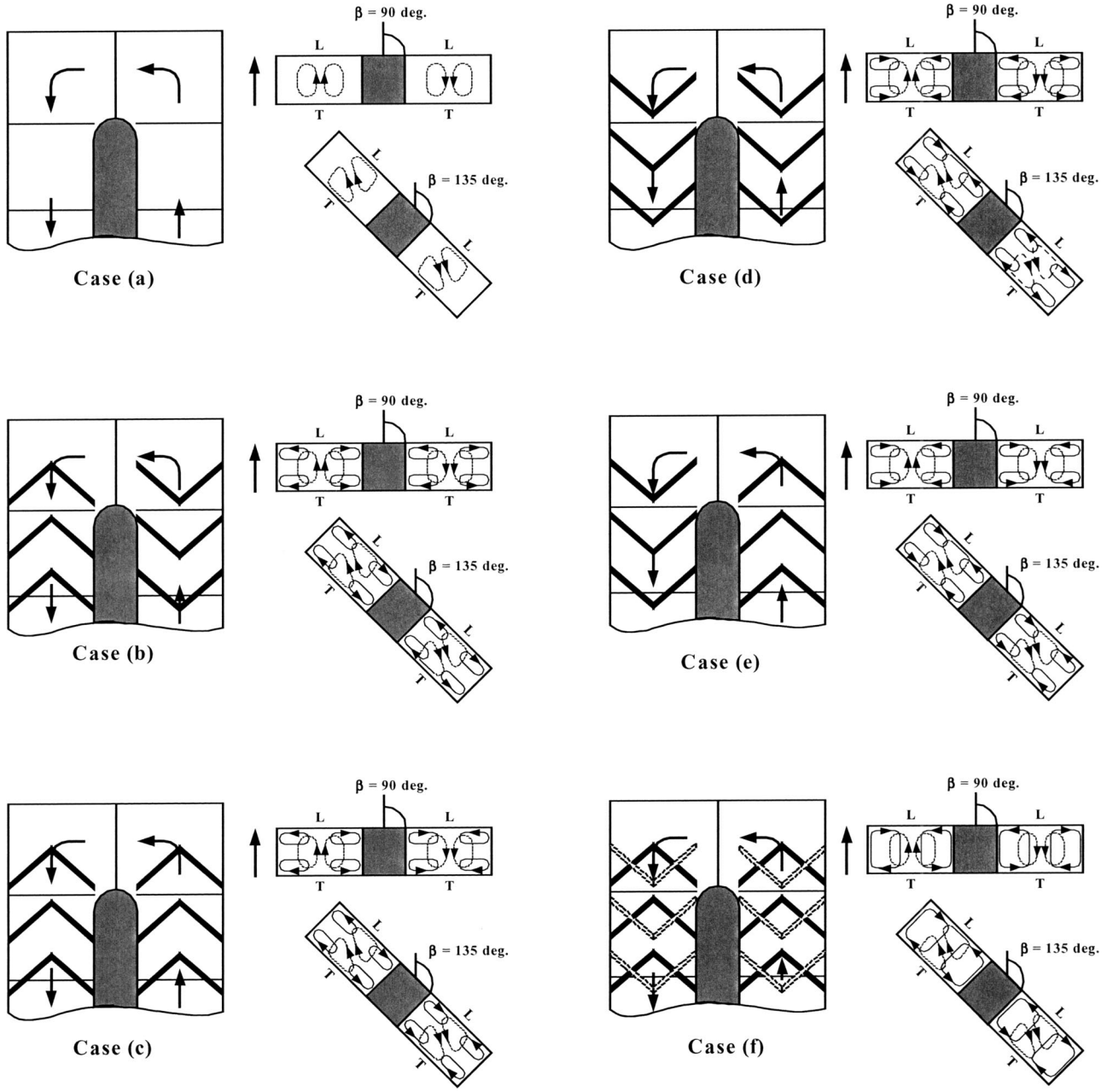

Fig. 4 Conceptual view of the secondary flow vortices induced by rotation, ribs, and channel orientation (dash line: rotation-induced vortices, solid line: rib-induced vortices)

V-shaped rib, it splits into two streams. Each one moves parallel to the rib from the centerline to either the left side or the right side and returns back to the centerline making a counter-rotating vortex. Another observation can be drawn that as the 45 deg V-shaped rib is half the 45 deg angled rib, the boundary layer thickness for the fluid that moves parallel to one side of the 45 deg V-shaped rib is thinner than produced by the 45 deg angled rib. Therefore, since the 45 deg V-shaped rib produces two counter rotating vortices that promote more mixing in the bulk main stream and at the same time produce a thinner boundary layer near the heated surface, a higher heat transfer rate is expected when compared to the 45 deg angled rib. However, a different situation can be observed in the inverted 45 deg V-shaped rib. As the fluid approaches the near surface of the inverted 45 deg V-shaped rib, it starts moving simultaneously from the left side and right side to the centerline, interacting with each other, and then returns back to the starting positions creating two counter rotating vortices. The vortices' interaction may weaken the two counter rotating vortices. Thus, the 45 deg V-shaped rib is expected to perform better than the inverted 45 deg V-shaped rib in the non-rotating condition.

Figure 4 shows conceptual views for the secondary flow patterns of a smooth and ribbed rotating two-pass rectangular channel. Figure 4(*a*) shows the smooth channel that rotates at β=90 deg with respect to the direction of rotation. Two symmetrical cells of counter rotating secondary flow (dotted line) appear due to the Coriolis force. In the first pass of the channel, the fluid moves in a radially outward direction, and the effect of the Coriolis force directs the coolant from the core toward the trailing surface. This causes an increase of the heat transfer from the trailing surface and a decrease in the heat transfer from leading surface. However, in the second pass, the opposite situation can be seen: the fluid moves in a radially inward direction, and the Coriolis force directs the coolant toward the leading surface, causing an increase of heat transfer from the leading surface and a decrease in the heat trans-

fer from trailing surface. When the channel is positioned at the $\beta=135$ deg orientation, the secondary flow vortices are asymmetric and migrate diagonally away from the corner region of the inner-leading surface toward the center in the first passage, and from the corner region of the inner-trailing surface toward the center in the second passage.

Figures 4(b) through 4(e) show four different arrangements of the parallel 45 deg V-shaped ribs. These parallel arrangements are attached to leading and trailing surfaces in a parallel fashion so that they are directly opposite to each other. Figure 4(*b*) shows that the 45 deg V-shaped ribs are attached to the leading and trailing surfaces in both passes. Also, it shows the secondary flow (dotted line) induced by rotational forces and the secondary flow (solid line) induced by the 45 deg V-shaped ribs. As the channel angle changes to $\beta=135$ deg, the rib secondary flow is unchanged, but the rotational secondary flows are shared between the principle surfaces (trailing, and leading) and side surfaces. Figure 4(*c*) shows the same channel except that the first pass rib orientation is reversed to become inverted 45 deg V-shaped ribs to the mean stream flow. Consequently, all secondary flows that are induced by rotational forces or ribs are the same as case (b) except the rib secondary flow in the first pass is reversed due to the changing in the rib orientation in the first pass. For case (d), as seen in Figure 4(*d*), the first pass has 45 deg V-shaped rib, and the second pass has inverted 45 deg V-shaped rib. Figure 4(*e*) shows the first pass and second pass to have inverted 45 deg V-shaped.

Figure 4(f) shows the crossed rib case (the ribs on the leading and trailing surfaces of the cooling channels are in crossed orientation). The crossed orientation of the 45 deg V-shaped ribs coalesces the two pairs of counter rotating vortices into one pair of counter rotating vortices. This reduction in number of rib-induced secondary flow vortices limits the mixing between the near wall flow (hot fluid) and the core flow (cold fluid), which causes less heat transfer. In case of rotation, a pair of rotating-induced secondary flow vortices appears and moves in the opposite direction the vortices generated by crossed ribs. This negative interaction minimizes the rotation effect by suppressing flow impingement on the first pass trailing and second pass leading surfaces and restricts mixing with the core for both leading and trailing surfaces in both passes, which causes low heat transfer enhancement.

Figures 5–10 show the regionally average Nusselt number ratios (Nu/Nuo) from leading and trailing surfaces for four Reynolds number (5000, 10000, 25000, 40000), rotating and non-rotating, and two channel orientations ($\beta=90$ deg, 135 deg).

Smooth Case Results. Figure 5 shows the results of Nusselt number ratios from leading and trailing surfaces for the smooth case. For the stationary case, the Nusselt number ratio decreases monotonically for both leading and trailing surfaces in the first pass. This continuous decrease is due to the developing thermal boundary layer. As the flow approaches the 180 deg turn, the Nusselt number increases due to secondary flows induced by the 180 deg turn. The Nusselt number reaches the peak value at the entrance of the second pass and then decreases as the flow moves to the exit of the second pass. This is due to the diminishing of the 180 deg turn-induced secondary flows. However, in the rotation case, the Nusselt number ratios from the first pass trailing and second pass leading surfaces are higher than in the non-rotating case, while those from the first pass leading and second pass trailing surfaces are lower. This is due to the rotation-induced secondary flow vortices as shown in Fig. 4(*a*). At channel orientation $\beta=90$ deg, rotational secondary flow vortices produced by the Coriolis forces are impinging normally on the trailing surface of the first pass and the leading surface of the second pass. However, at channel orientation $\beta=135$ deg, the rotation secondary flow vortices are impinging on the first pass trailing-side corner and the

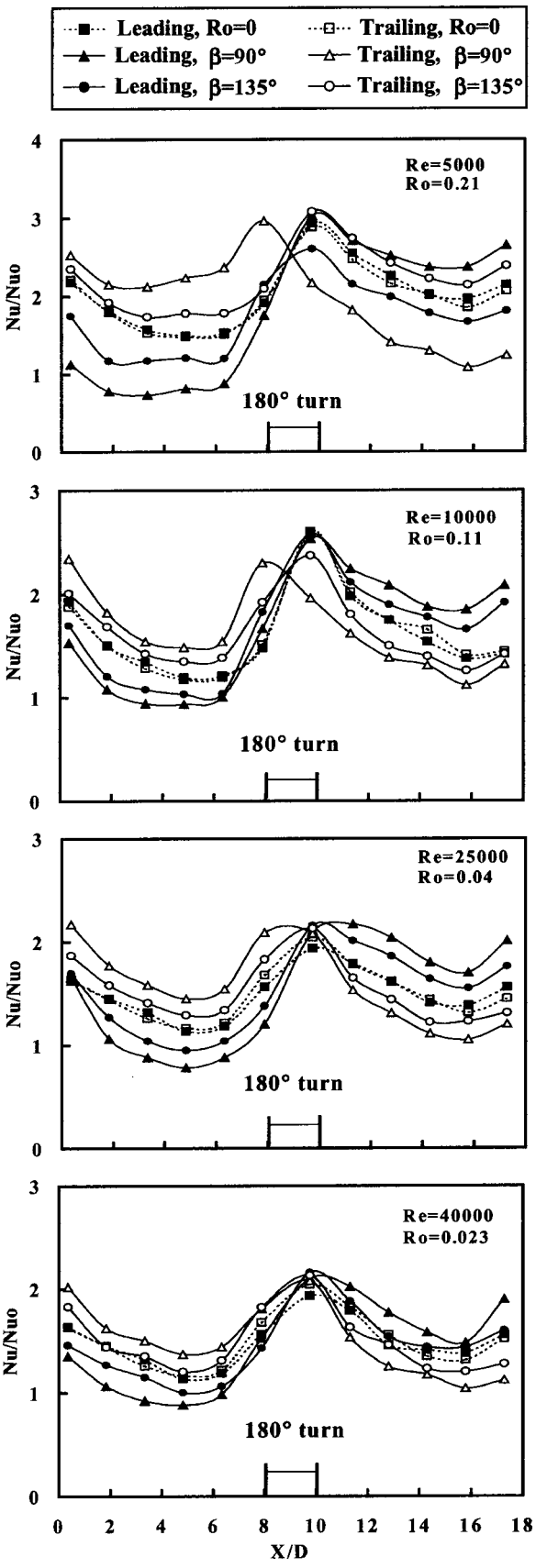

Fig. 5 Nusselt number ratio distribution for case (a)

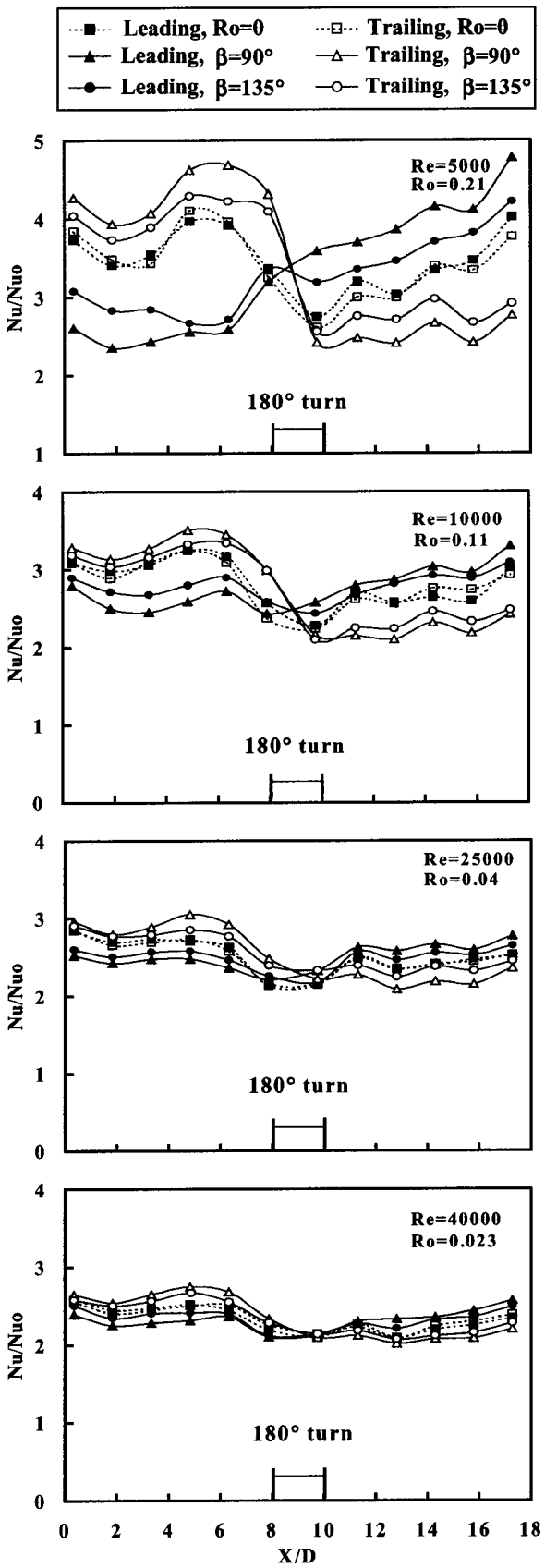

Fig. 6 Nusselt number distribution for case (b)

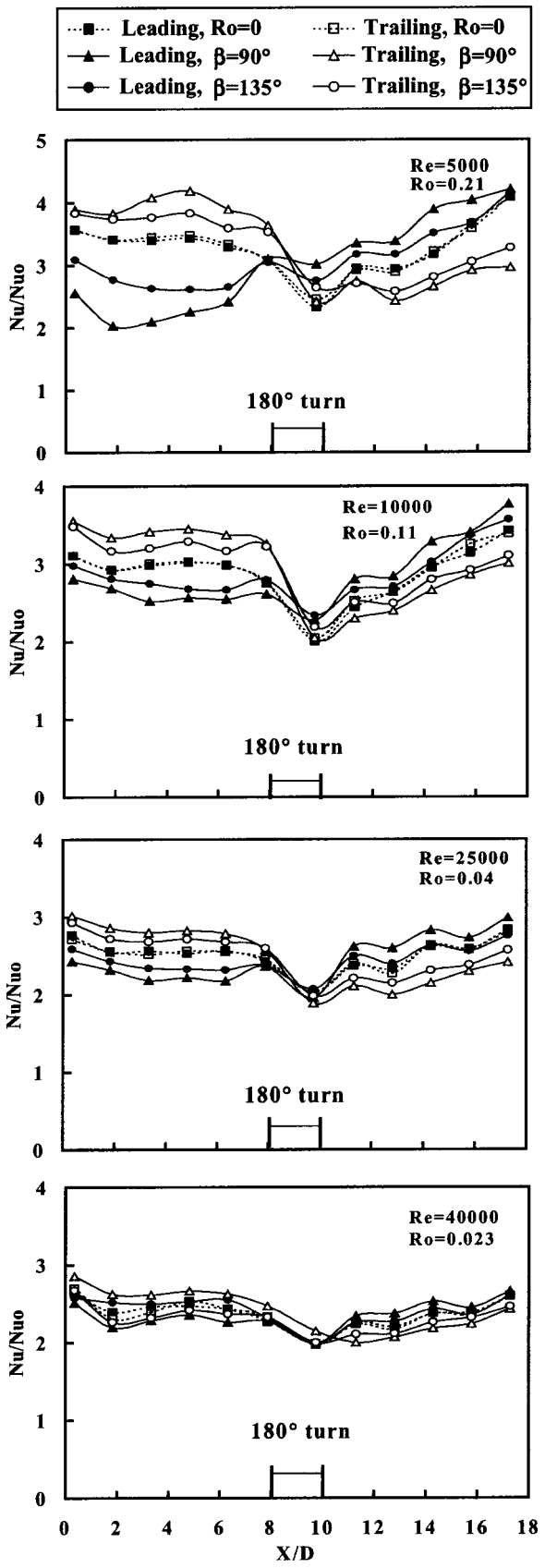

Fig. 7 Nusselt number distribution for case (c)

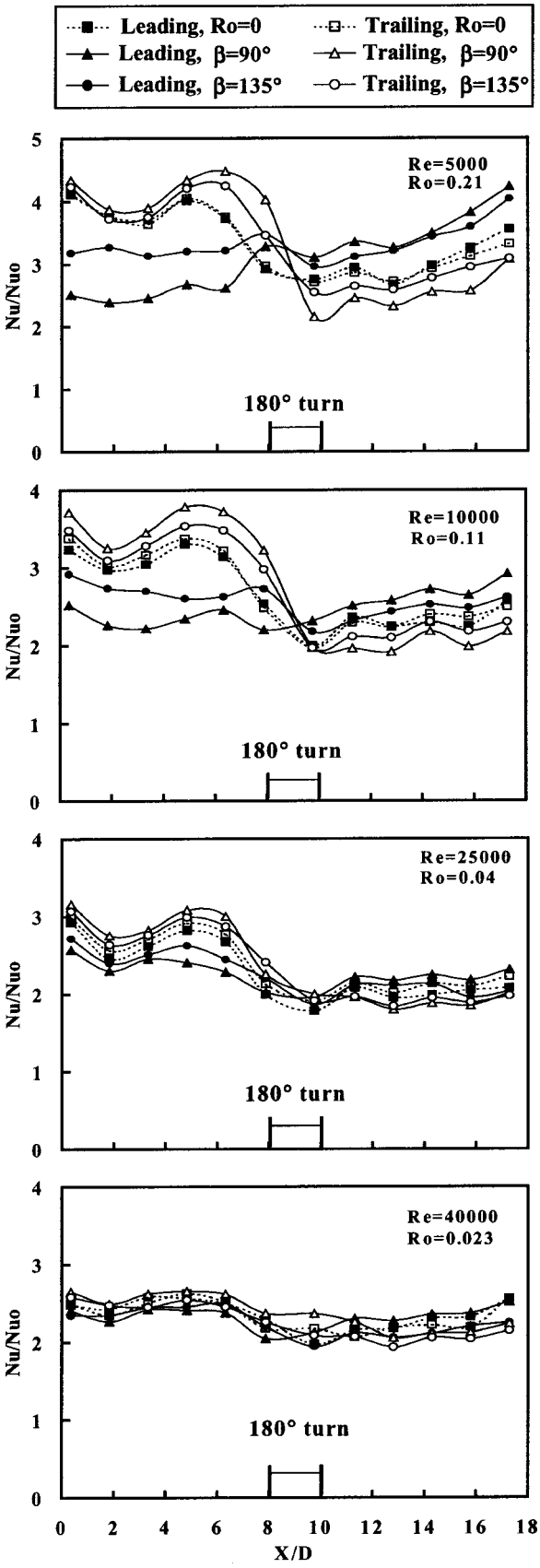

Fig. 8 Nusselt number distribution for case (d)

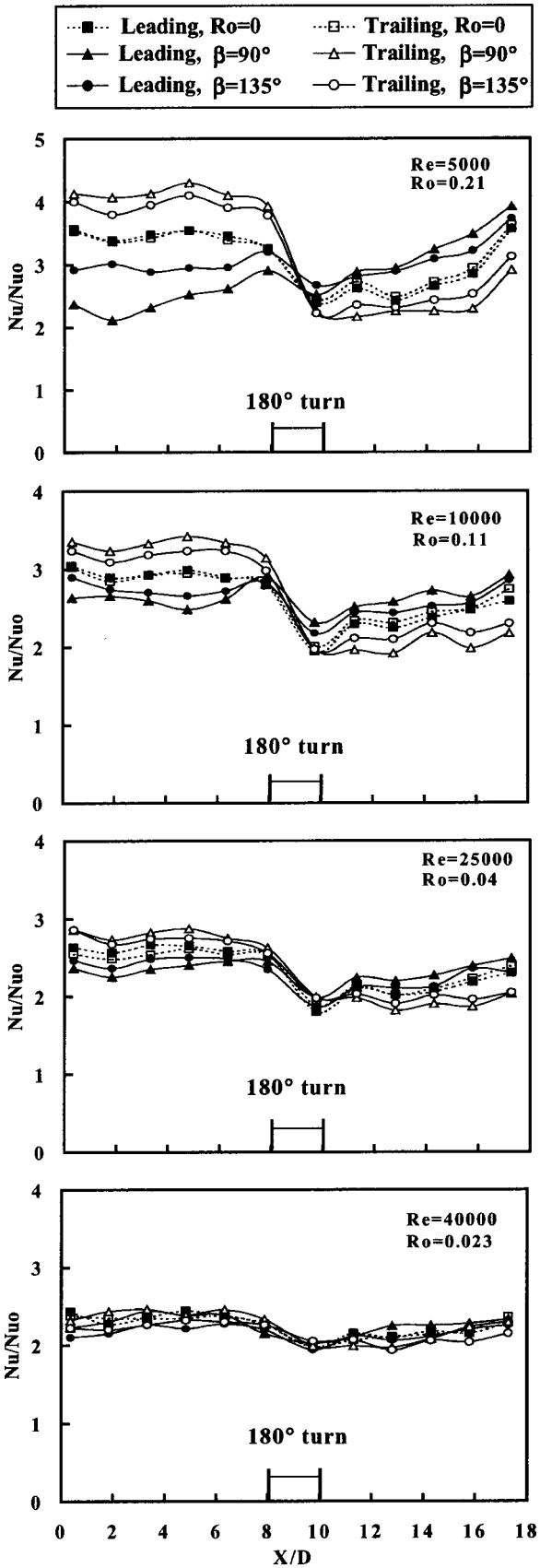

Fig. 9 Nusselt number distribution for case (e)

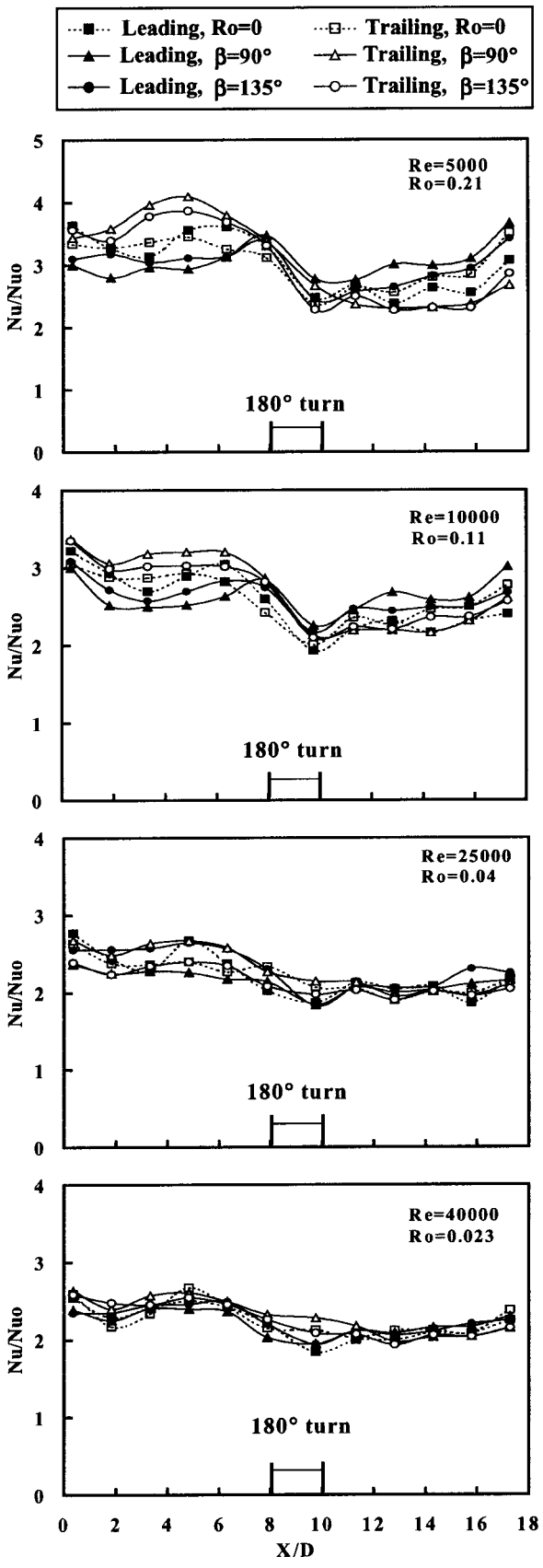

Fig. 10 Nusselt number distribution for case (f)

second pass leading-side corner, as shown in Fig. 4(*a*). Thus, the Nusselt number ratio for the trailing surface of the first pass and the leading surface of the second pass for channel orientation $\beta=135$ deg are lower than the ratios for channel orientation $\beta=90$ deg. The opposite situation is observed in the leading surface of the first pass and the trailing surface of the second pass. The results also show that the effect of rotation decreases with increasing Reynolds number (or decreasing rotation number). The abovementioned results are consistent with the previous study (see Azad et al. [22]).

Parallel 45 deg V-Shaped Rib Cases. Figure 6 shows the Nusselt number distribution for case (b). The stationary case results show that the peak Nusselt number ratio occurs at the downstream location of the inlet rather than at the entrance region of the first pass as in the smooth case. This is due to the two pairs of counter rotating secondary flow vortices that are generated by the parallel 45 deg V-shaped ribs, as shown in Fig. 4(*b*). But, the Nusselt number ratio decreases as the vortices are suppressed by the 180 deg turn. Then, the Nusselt number ratio increases again downstream of the second pass inlet as the secondary flow vortices induced by the parallel 45 deg V-shaped ribs start to develop.

The results show that rotation significantly increases the Nusselt number ratio on the first pass trailing surface and the second pass leading surface, but significantly decreases the Nusselt number ratio on the first pass leading and second pass trailing surfaces. This is because of the combined effect of the rib-induced secondary flow and the rotation-induced secondary flow vortices, as explained in Fig. 4(*b*). The results of the 135 deg channel also show that rotation enhances the heat transfer in the first pass trailing and second pass leading surfaces, whereas the heat transfer decreases in the first pass leading and second pass trailing surfaces. However, the differences in Nusselt number ratios between leading and trailing surfaces are not as significant for the 135 deg orientation as they are for the 90 deg orientation as explained in Fig. 4(*b*). The results also show that the rotational effect decreases with an increasing Reynolds number (or decreasing rotation number).

Figure 7 shows the Nusselt number ratio for case (c). Case (c) is generated from case (b) by changing the parallel 45 deg V-shaped ribs in the first pass of case (b) to inverted 45 deg V-shaped ribs. The stationary results show that the first pass Nusselt number ratio behaves differently from that in case (b) at lower Reynolds numbers. This is because, as shown in Fig. 4(*c*), the inverted 45 deg V-shaped rib vortices tend to interact with each other and reduce the surface heat transfer enhancement. However, the effect diminishes at higher Reynolds numbers. The second pass behavior is similar to case (b) due to the same V-shaped orientation. The results also show that the rotation effect decreases with an increasing Reynolds number (or decreasing rotation number).

Figure 8 shows the Nusselt Number ratio for case (d). In case (d), as explained in Figure 4(*d*), the Nusselt number ratio distribution in the first pass case (d) is similar to the case (b) first pass because they both have parallel 45 deg V-shaped ribs. In the second pass of case (d), inverted 45 deg V-shaped ribs were placed. The Nusselt number distribution shows lower values compared to the case (b) or case (c) second passes, which have parallel 45 deg V-shaped ribs.

Figure 9 shows the Nusselt number distribution for case (e). Both passes have inverted 45 deg V-shaped ribs as explained in Figure 4(*e*). The Nusselt number distribution in the first pass is similar to the Nusselt number distribution in the first pass of case (c) and the Nusselt number distribution in the second pass is similar to the Nusselt number distribution in the second pass of case (d).

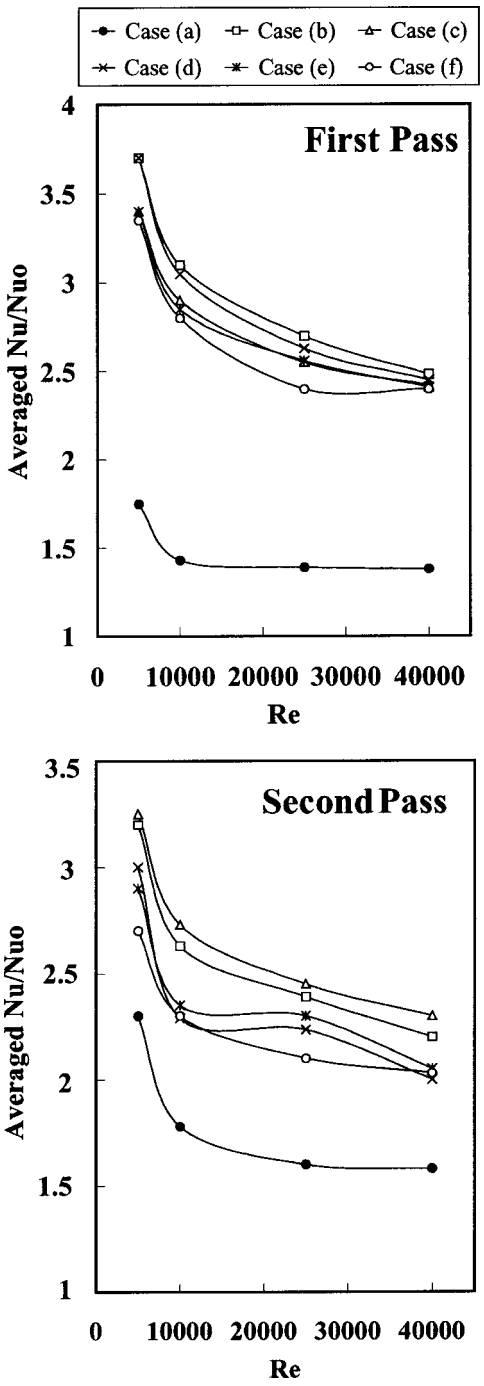

Fig. 11 Averaged Nusselt number distribution for non-rotating (ω=0) cases

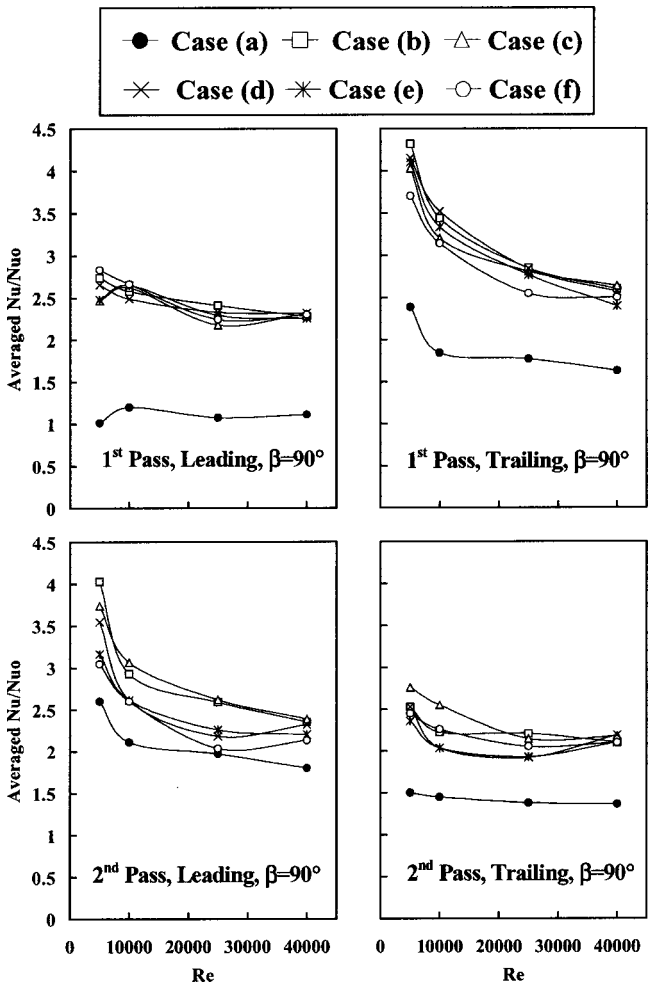

Fig. 12 Averaged Nusselt number distribution for leading and trailing surfaces with rotation (ω=550 rpm) for β=90 deg

Crossed 45 deg V-Shaped Rib Case. Figure 10 shows the Nusselt number distribution for the crossed rib case as can be seen in Figure 4(f). The results show that the non-rotating Nusselt number ratios are unlike the parallel rib case results. Both leading and trailing surfaces show different Nusselt number ratio distributions in each pass. This variation is due to the different orientations of the 45 deg V-shaped ribs that are placed on the leading and trailing surfaces Their Nusselt number ratios are lower than those of all previous parallel and inverted 45 deg V-shaped rib cases, as explained in Fig. 4(f).

Channel-Averaged Nusselt Number Ratio. Figure 11 presents the averaged Nusselt number ratio distribution for smooth and five different arrangements of the 45 deg V-shaped ribs in the two pass rectangular channels for the stationary case. The Nusselt number ratios in Fig. 11 are the average values of the leading and trailing surfaces for all cases. The results show that the ribbed surfaces provide higher Nusselt number ratios in both passes compared to the smooth surfaces. In the first pass, case (b) and case (d) show higher averaged Nusselt number ratios compared to case (c) and case (e). This is because the 45 deg V-shaped rib induces a stronger secondary flow than the inverted 45 deg V-shaped rib. In the second pass, case (b) and case (c) show better averaged Nusselt number ratios compared to other cases due to the same reason. The crossed V-shaped rib case (f) results show lower averaged Nusselt number ratios compared to the parallel V-shaped rib cases. The crossed V-shaped ribs induce a pair of counter rotating vortices, while the parallel V-shaped ribs induce two pairs of counter rotating vortices, which promote more mixing with the core flow.

Figure 12 shows the channel averaged Nusselt number ratio with respect to Reynolds number for ω=550 rpm on each pass leading and trailing surfaces for β=90 deg. All Nusselt number ratio results exhibit a decreasing trend with increasing Reynolds number. Ribbed cases provide better Nusselt number ratio enhancement compared to the smooth case. In general, Nusselt number ratios in the first pass leading surfaces are about the same for all V-shaped cases. However, Nusselt number ratios for the V-shaped rib cases (b) and (d) are higher than other cases in the first pass trailing surfaces. A noticeable variation can be seen in the second pass due to the 180 deg turn effect. Cases (b) and (c) of

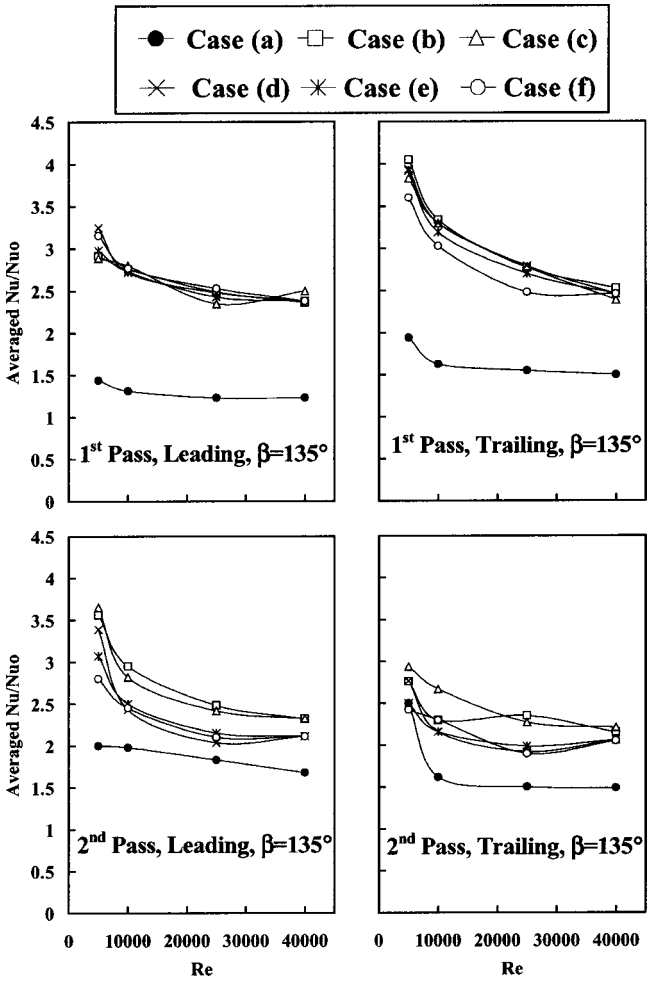

Fig. 13 Averaged Nusselt number distribution for leading and trailing surfaces with rotation (ω=550 rpm) for β=135 deg

the V-shaped rib show greater values of Nusselt number ratios than cases (d), (e), and (f) (the inverted V-shaped rib and crossed rib).

Figure 13 shows the channel averaged Nusselt number ratio on the leading and trailing surfaces for β=135 deg. The results are similar to β=90 deg in trend except that the Nusselt number ratios on the first pass trailing and the second pass leading are lower because of the oblique angle of the flow impinging on the surfaces.

Conclusions

The influences of 45 deg V-shaped rib arrangements and channel orientation on the leading and trailing Nusselt number ratios in a two-pass rectangular channel have been reported for rotation numbers from 0 to 0.21 and Reynolds numbers from 5000 to 40000. The findings are:

1) The general trend of the rotation effect shows an increase in the Nusselt number ratio in the first pass trailing surface and second pass leading surface, while the opposite situation can be observed in the first pass leading surface and second pass trailing surface. This is due to the Coriolis and buoyancy forces, which are generated by rotation. However, the differences between the Nusselt number distributions on the second pass leading and trailing surfaces are smaller than that of the first pass due to the opposite effects of the Coriolis and buoyancy forces.

2) The effects of the Coriolis force and cross-stream flow are reduced as the channel orientation changes from β=90 deg to β=135 deg. Thus, the Nusselt number ratios for the β=135 deg first pass trailing and second pass leading surfaces decrease when compared to their corresponding Nusselt number ratios for the β=90 deg orientation. The Nusselt number ratios for β=135 deg first pass leading and second pass trailing surfaces increase when compared to their corresponding Nusselt number for β=90 deg.

3) Both orientations of the 45 deg V-shaped rib induce two pairs of counter rotating vortices, but the inverted 45 deg V-shaped rib vortices tend to interact with each other. Therefore, the 45 deg V-shaped rib results in better heat transfer enhancement than the inverted 45 deg V-shaped rib for both non-rotating and rotating conditions.

4) The parallel 45 deg V-shaped rib arrangements provide a higher heat transfer enhancement compared to the crossed 45 deg V-shaped rib arrangement for both rotating and non-rotating conditions. The crossed rib arrangement shows less rotational effect compared to the parallel rib cases. This is because the parallel 45 deg V-shaped rib develops two pair of counter rotating vortices of secondary flows, while the crossed 45 deg V-shaped rib develops only one single pair of counter rotating vortices.

5) For all cases studied here, results show relatively low heat transfer enhancement in the 180 deg turn region. This is because the vortices induced by the V-shaped rib are suppressed by the 180 deg turn and there is no 45 deg V-shaped rib placed at the middle of the 180 deg turn.

6) For all cases studied here, results show that the heat transfer enhancement decreases with increasing Reynolds number.

Acknowledgments

The leading author, Luai AL-Hadhrami, received a fellowship from King Fahd University of Petroleum and Minerals, Saudi Arabia, for his Ph.D. study at Texas A&M University. This work was supported by the DOE Advanced Gas Turbine Systems Research (AGTSR) program through project number SR-094. The support of the above institutions is greatly appreciated.

Nomenclature

D = hydraulic diameter (m)
e = rib height (m)
h = heat transfer coefficient (W/m^{2}K)
k = thermal conductivity of coolant (W/mK)
Nu = local Nusselt number, hD/k
Nu_o = Nusselt number in fully-developed turbulent non-rotating tube flow with smooth wall
P = rib pitch (m)
Pr = Prandtl number
q_{net} = net heat at wall (W)
A = surface area of the copper plate (m^2)
R = radial distance from axis of rotation to heated test section's mean radius
Re = Reynolds number, $\rho VD/\mu$
R_o = rotation number, $\Omega D/V$
T_{bx} = local coolant temperature (degC)
T_{bi} = coolant temperature at inlet (degC)
T_w = wall temperature (degC)
V = bulk velocity in streamwise direction (m/s)
β = angle of channel orientation with respect to the axis of rotation
Ω = rotational speed (rad/s)
ω = rotational speed (rpm)
α = rib angle
μ = dynamic viscosity of coolant (Pa-s)
ρ = density of coolant (kg/m^3)
$\Delta\rho/\rho$ = inlet coolant-to-wall density ratio, $(T_w-T_{bi})/T_w$

References

[1] Metzger, D. E., and Sahm, M. K., 1986, "Heat Transfer Around Sharp 180 deg Turns in Smooth Rectangular Channels," ASEM J. Heat Transfer, **113**, pp. 500–506.
[2] Fan, C. S., and Metzger, D. E., 1987, "Effects of Channel Aspect Ratio on

Heat Transfer in Rectangular Passage Sharp 180 deg Turn,'' ASME Paper No. 87-GT-113.
[3] Han, J. C., and Park, J. S., 1988, ''Developing Heat Transfer in Rectangular Channels With Rib Turbulators,'' Int. J. Heat Mass Transf., **31**(1), pp. 183–195.
[4] Han, J. C., Zhang, Y. M., and Lee, C. P., 1991, ''Augmented Heat Transfer in Square Channels With Parallel, Crossed, and V-Shaped Angled Ribs,'' ASME J. Heat Transfer, **113**, pp. 590–596.
[5] Taslim, M. E., Li, T., and Kercher, D. M., 1994, ''Experimental Heat Transfer and Friction in Channels Roughened With Angled V Shaped and Discrete Ribs on Two Opposite Walls,'' ASME Paper 94-GT-163.
[6] Ekkad, S. V., and Han, J. C., 1997, ''Detailed Heat Transfer Distribution in Two-Pass Square Channels With Rib Turbulators,'' Int. J. Heat Mass Transf., **40**(11), pp. 2525–2537.
[7] Kiml, R., Mochizuki, S., and Murata, A., 2001, ''Heat Transfer Enhancement Mechanism in a Rectangular Passage with V- and Λ-Shaped Ribs,'' Journal of Flow Visualization and Image Processing, **8**, pp. 51–68.
[8] Wagner, J. H., Johnson, B. V., andHajek, T. J., 1991, ''Heat Transfer in Rotating Passage With Smooth Walls and Radial Outward Flow,'' ASME J. Turbomach., **113**, pp. 42–51.
[9] Wagner, J. H., Johnson, B. V., and Kooper, F. C., 1991b, ''Heat Transfer in Rotating Serpentine Passage With Smooth Walls,'' ASME J. Turbomach., **113**(3), pp. 321–330.
[10] Johnson, B. V., Wagner, J. H., Steuber, G. D., and Yeh, F. C., 1994, ''Heat Transfer in Rotating Serpentine Passage With Trips Skewed to the Flow,'' ASME J. Turbomach., **116**, pp. 113–123.
[11] Johnson, B. V., Wagner, J. H., Steuber, G. D., and Yeh, F. C., 1994, ''Heat Transfer in Rotating Serpentine Passage With Selected Model Orientations for Smooth or Skewed Trip Walls,'' ASME J. Turbomach., **116**, pp. 738–744.
[12] Han, J. C., Zhang, Y. M., and Kalkuehler, K., 1993, ''Uneven Wall Temperature Effect on Local Heat Transfer in a Rotating Two-Pass Square Channel With Smooth Walls,'' ASME J. Heat Transfer, **115**(4), pp. 912–920.
[13] Zhang, Y. M., Han, J. C., Parsons, J. A., and Lee, C. P., 1995, ''Surface Heating Effect on Local Heat Transfer in a Rotating Two-Pass Square Channel With 60 deg Angled Rib Turbulators,'' ASME J. Turbomach., **117**, pp. 272–280.
[14] Parsons, J. A., Han, J. C., and Zhang, Y. M., 1994, ''Wall Heating Effect on Local Heat Transfer in a Rotating Two-Pass Square Channel With 90 deg Rib Turbulators,'' Int. J. Heat Mass Transf., **37**(9), pp. 1411–1420.
[15] Parsons, J. A., Han, J. C., and Zhang, Y. M., 1995, ''Effects of Model Orientation and Wall Heating Condition on Local Heat Transfer in a Rotating Two-Pass Square Channel With 90 deg Rib Turbulators,'' Int. J. Heat Mass Transf., **38**(7), pp. 1151–1159.
[16] Dutta, S., and Han, J. C., 1996, ''Local Heat Transfer in Rotating Smooth and Ribbed Two-Pass Square Channels With Three Channel Orientations,'' ASEM J. Heat Transfer, **118**, pp. 578–584.
[17] Dutta, S., and Han, J. C., and Lee, C. P., 1996, ''Local Heat Transfer in a Rotating Two-Pass Ribbed Triangular Duct With Two Model Orientations,'' Int. J. Heat Mass Transf., **39**, pp. 707–715.
[18] Taslim, M. E., Rahman, A., and Spring, S. D., 1991, ''An Experimental Investigation of Heat Transfer Coefficients in a Spanwise Rotating Channel With Two Opposite Rib-Roughened Walls,'' ASME J. Turbomach., **113**, pp. 75–82.
[19] Taslim, M. E., Bondi, L. A., and Kercher, D. M., 1991b, ''An Experimental Investigation of Heat Transfer in an Orthogonally Rotating Channel Roughened With 45 deg Criss-Cross Ribs on Two Opposite Walls,'' ASME J. Turbomach., **113**, pp. 346–353.
[20] Prabhu, S. V., and Vedula, R. P., 1997, ''Pressure Drop Distribution in a Rotating Rectangular Channel With One Ribbed Surface,'' *ASME Paper No. 97-AA-118*.
[21] Park, C. W., Yoon, C., and Lau, S. C., 2000, ''Heat (Mass) Transfer in a Diagonally Oriented Rotating Two-Pass Channel with Rib-Roughened Walls,'' ASME J. Heat Transfer, **122**, pp. 208–211.
[22] Azad, G. M. S., Uddin, M. J., Han, J. C., Moon, H. K., and Glezer, B., 2002, ''Heat Transfer in Two-Pass Rectangular Rotating Channels with 45 deg Parallel and Crossed rib Turbulators,'' ASME J. Turbomach., **124**, pp. 251–259.
[23] Han, J. C., Dutta, S., and Ekkad, S. V., 2000, *Gas Turbine Heat Transfer and Cooling Technology*, Taylor & Francis, Inc., New York, ISBN #1-56032-841-X.
[24] Kline, S. J., and McClintock, F. A., 1953, ''Describing Uncertainties in Single-Sample Experiments,'' Mech. Eng. (Am. Soc. Mech. Eng.), **75**, pp. 3–8.
[25] Al-Qahtani, M., Jang, Y., Chen, H., and Han, J. C., 2002, ''Prediction of Flow and Heat Transfer in Rotating Two-Pass Rectangular Channels with 45 deg Rib Turbulators,'' ASME J. Turbomach., **124**, pp. 242–250.

L. B. Y. Aldabbagh

I. Sezai[1]

Mechanical Engineering Dept.,
Eastern Mediterranean University,
G. Magosa,
Mersin 10,
Turkey

A. A. Mohamad

Dept. of Mechanical and Manufacturing Engineering,
The University of Calgary,
Calgary, AB, T2N 1N4,
Canada

Three-Dimensional Investigation of a Laminar Impinging Square Jet Interaction With Cross-Flow

The flow and heat transfer characteristics of an impinging laminar square jet through cross-flow have been investigated numerically by using the three-dimensional Navier-Stokes and energy equations in steady state. The simulations have been carried out for jet to cross-flow velocity ratios between 0.5 and 10 and for nozzle exit to plate distances between 1D and 6D, where D is the jet width. The complex nature of the flow field featuring a horseshoe vortex has been investigated. The calculated results show that the flow structure is strongly affected by the jet-to-plate distance. In addition, for jet-to-plate spacing of one jet width and for jet to cross-flow velocity ratios less than 2.5 an additional peak occurs at about three-dimensional downstream of the jet impingement point. For high jet to cross-flow ratios two horseshoe vortices form around the jet in the case of small jet-to-plate spacings. [DOI: 10.1115/1.1561815]

Keywords: Heat Transfer, Impingement, Jets, Laminar, Three-Dimensional

Introduction

Impinging jets in a cross-flow are important in a number of engineering applications including tempering of glass, drying of paper and textiles, and the cooling of the metal sheets, microelectronic components and turbine blades. The impingement of a jet on the surface of a plate results in the formation of a wall jet, which flows radially away from the collision point along the plate surface. The interaction of this wall jet with the free-stream results in a complex flow field, which plays an important role in the cooling performance. Often, the jets are used in submerged arrays for cooling large surface areas. In such cases exhaust from the upstream jets imposes a cross-flow on the downstream jets. Therefore, a three-dimensional study of a single impinging jet through a cross-flow may provide a basis for understanding the essential dynamics of the complex practical flow fields, which cannot be predicted by two-dimensional simulations.

The experimental and theoretical investigations on jets in cross-flow are mostly related with turbulent jets. Although many applications involve turbulent jets, laminar jets are also encountered when the fluid is viscous or the geometry is miniature as in microelectronics. Several investigators have studied the effect of cross-flow on the heat transfer characteristics of impinging turbulent jets. Goldstein and Behbahani [1] experimentally investigated the impingement of a circular jet through a cross-flow on a heated plate. They found that for a large jet-to-plate spacing of 12 jet diameters the cross-flow decreases the maximum heat transfer while for a smaller spacing of 6 jet diameters, cross-flow can increase the maximum heat transfer. The impingement of confined single and twin turbulent jets though a cross-flow have been studied experimentally and numerically by Barata et al. [2] and Barata [3] to examine the characteristics of vortex and upwash flows generated by multiple jets in a cross-flow. The experiments were performed using Laser-Doppler measurements for the jet exit, 5 jet diameters above the ground plate and for a velocity ratio between the jets and the cross-flow of 30. Their results show the presence of a complex three-dimensional scarf vortex formed around each impinging jet and a fountain upwash flow due to the collision of the wall jets. A two dimensional numerical model was used by Chuang et al. [4] to determine the flow characteristics associated with an unsteady, compressible impinging twin slot jets between two plates coupled with cross-flow. The calculated results show that several recirculating zones are distributed around the flow field. Their size and location are closely related to the jet exit height above the ground, the nozzle spacing and the strength of cross-flow. Kim and Benson [5] employed a turbulent model to simulate the three-dimensional impingement of multiple jets with cross-flow. Their results show that the row of jets in the cross-flow is characterized by a highly complex flow field that includes a horseshoe vortex and two helical vortices whose secondary velocity components are co-rotating in space.

There is a considerable body of literature dealing with flow and heat transfer in laminar jets combined with cross-flow. Kercher and Tabakoff [6] measured the influence of spent air on the average heat transfer to a square array of round jets in a semi-closed environment and concluded that increasing cross-flow decreases the heat transfer performance. Obot and Trabold [7] observed that the degradation in heat transfer with partial and complete cross-flow, for a given mass flow rate of air, is more pronounced as the number of jets over a fixed target area increases. The numerical result of Al-Sanea [8] on single jet combined with cross-flow show that a cross-flow degrades the favorable characteristics of impinging jets, and can reduce the nominal Nusselt number by 60 percent. In addition, the local Nusselt number at a distance of one jet width downstream of the stagnation point is not affected by the initial velocity profile of the jet. Kelso et al. [9] by using the flow visualization techniques and flying-hot-wire measurements identified the structure of round jets in a cross-flow for the jet to free-stream velocity ratio from 2 to 6. Their results show that the flow field of the jet in a cross-flow includes a horseshoe vortex originating just upstream of the jet and a wake vortex system at the downstream side of the jet. Flow visualization technique was used by Gogineni et al. [10] to investigate the flow field induced by a jet in a cross-flow for a jet to cross-flow velocity ratio of one and for Reynolds number 618 based on the width of the square jet. They reported that the fluid in the wake of the jet was mixed and transported by the counter-rotating stream-wise vortex pair that is formed along the span-wise edges of the jet column.

Although most of the industrial applications of the jets in industry are in the turbulent regime, the three-dimensional nature of the flow structure resulting from laminar jets in cross-flow is far from being fully understood. Moreover, numerical simulation of

[1]E-mail address: ibrahim.sezai@emu.edu.tr

Contributed by the Heat Transfer Division for publication in the JOURNAL OF HEAT TRANSFER. Manuscript received by the Heat Transfer Division March 27, 2002; revision received November 14, 2002. Associate Editor: M. Faghri.

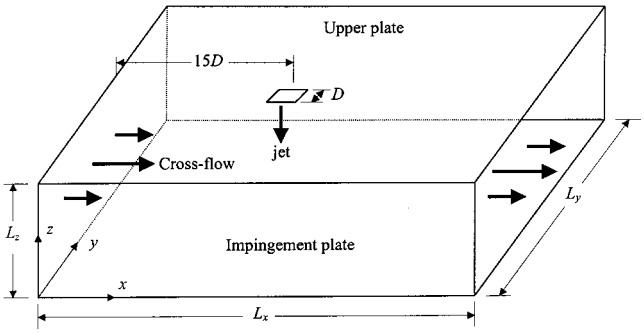

Fig. 1 Definitions of geometric parameters and the coordinate system

impinging jets using different turbulence models lacks generality owing to the absence of a very wide range of scales in the model. The present work deals with laminar, three-dimensional, analysis of a single square jet in a cross-flow (Fig. 1).

The structure of the flow field and its effect on the heat transfer characteristics are investigated numerically for Reynolds numbers between 100 and 500 with jet to cross-flow velocity ratios, R, from 0.5 to 10.

Computational Scheme

The steady-state, three-dimensional, Navier-Stokes and energy equations for incompressible flows in Cartesian coordinates are used for this study. The velocity and lengths are non-dimensionalized by jet-exit velocity and jet width, respectively. The buoyancy effect has been neglected.

The non-dimensional continuity, momentum and energy equations for steady laminar flow with constant properties can be written as:

$$\frac{\partial U}{\partial X}+\frac{\partial V}{\partial Y}+\frac{\partial W}{\partial Z}=0 \tag{1}$$

$$U\frac{\partial U}{\partial X}+V\frac{\partial U}{\partial Y}+W\frac{\partial U}{\partial Z}=-\frac{\partial P}{\partial X}+\frac{1}{\mathrm{Re}}\nabla^2 U \tag{2}$$

$$U\frac{\partial V}{\partial X}+V\frac{\partial V}{\partial Y}+W\frac{\partial V}{\partial Z}=-\frac{\partial P}{\partial Y}+\frac{1}{\mathrm{Re}}\nabla^2 V \tag{3}$$

$$U\frac{\partial W}{\partial X}+V\frac{\partial W}{\partial Y}+W\frac{\partial W}{\partial Z}=-\frac{\partial P}{\partial Z}+\frac{1}{\mathrm{Re}}\nabla^2 W \tag{4}$$

$$U\frac{\partial T}{\partial X}+V\frac{\partial T}{\partial Y}+W\frac{\partial T}{\partial Z}=\frac{1}{\mathrm{Re\,Pr}}\nabla^2 T \tag{5}$$

where, T is the non-dimensional temperature, $(t-t_j)/(t_w-t_j)$.

Boundary conditions for velocities: the cross-flow velocity is assumed to have a parabolic profile at the inlet. The outlet boundary is located far enough downstream for conditions to be substantially developed, accordingly the following conditions are imposed at inlet and outlet of the cross-flow stream:

$$V=W=0 \qquad \text{at } X=0$$

$$\frac{\partial U}{\partial X}=\frac{\partial V}{\partial X}=\frac{\partial W}{\partial X}=0 \quad \text{at } X=A_x$$

All walls are stationary and impervious therefore no slip boundary condition are used for the front, rear, top and bottom solid walls except for the W velocity at the jet exit cross section at the top wall, where it is assumed to be uniform and is set to be equal to unity. Hence,

$$U=V=W=0 \qquad \text{at } Y=0,\ Y=A_y$$

$$U=V=W=0 \qquad \text{at } Z=0,\ Z=A_z \quad \text{except at nozzle exit,}$$

$$U=V=0,\ W=-1 \qquad \text{at nozzle exit.}$$

Boundary conditions for temperature: if the fluid exits the domain the first derivative of temperature is set to zero and if the fluid flows from surroundings into the domain then the fluid temperature is set to the surrounding temperature. That is

$$\text{At } X=0 \qquad T=0$$

$$\text{At } X=A_x \qquad \frac{\partial T}{\partial X}=0$$

Adiabatic boundary conditions are imposed on the top, front, and rear walls, except at the nozzles exit cross section where it was set to be equal to that of ambient. The bottom wall is set to a higher temperature than the ambient,

$$\text{At } Y=0,\ Y=A_y \quad \frac{\partial T}{\partial Y}=0$$

$$\text{At } Z=0 \qquad T=1$$

$$\text{At } Z=A_z \qquad \frac{\partial T}{\partial Z}=0 \quad \text{except at nozzle exit}$$

$$T=0 \qquad \text{at nozzle exit.}$$

Method of Solution

The governing equations are discretized by using the finite volume method in staggered, nonuniform grids. The grids are generated such that denser grid clustering is obtained in the vicinity of the jet in x and y-directions. In the z-direction a sine function distribution is employed, yielding denser grids near the top and near the impingement plate. A grid independence test has been made for Re=300, $A_z=1$, and $R=2.5$ in order to determine the effect of number of grids on the final results. The maximum difference between the result obtained by using $251\times151\times51$ and $201\times101\times51$ grids is 2.66 percent for the local Nusselt number, which occurs near the exit section of the cross-flow. The difference in local Nusselt number at the jet impingement is only 0.4 percent. The corresponding differences between $201\times101\times51$ and $151\times75\times35$ grids is 27.7 percent and 0.73 percent. Hence, the $201\times101\times51$ grid system is used for all runs. The solution domain in x and y-directions has $L_x=40D$ and $L_y=15D$ respectively. QUICK scheme (Leonard [11]) with ULTRA-SHARP flux limiting strategy (Leonard and Mokhtari [12]; Leonard and Drummond [13]) was used to calculate the convection of a scalar term (ϕ) at a control volume face. The extra neighboring points resulting from the application of QUICK scheme is written as the sum of the upwind face value plus a correction term involving the values from the previous iteration. The correction term is added to the source term in accordance with deferred correction procedure (Leonard and Drummond [13]) so that the numerical stability is increased, while keeping the seven diagonal structure of the coefficient matrix. The Bi-CGSTAB (Van der Vorst [14]) iterative method with SSOR preconditioning (Saad [15]) is applied to the pressure correction and energy equations in the sequential procedure of the SIMPLEC (Van Doormaal and Raithby [16]) algorithm. An under relaxation factor of 0.8 for Re=100 and 200 and 0.7 for Re=300, 400 and 500 is used for momentum and energy equations in all calculations. Iterations are continued until the second norm of the residuals for all equations are reduced below 10^{-6}, where no significant variations are observed at this residual level.

The assumption of steadiness has been tested by including the time dependent terms in the code for two cases. One case is Re =500, which is the highest Reynolds number used in the study, with $A_z=1$, $R=2.5$ and the other is the case involving the highest jet-to-crossflow velocity ratio, $R=10$, with $A_z=1$ and Re=300.

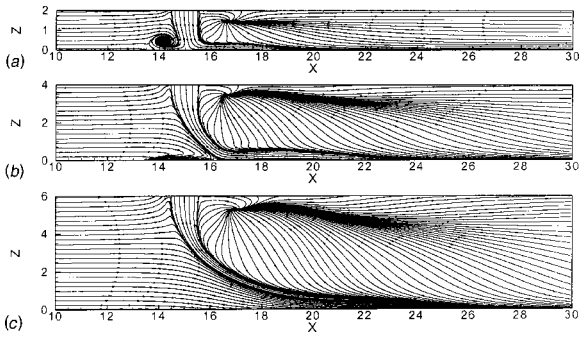

Fig. 2 Projection of flow lines on mid *x*-*z* plane for Re=200, and *R*=2.5 at jet-to-plate spacing (a) $A_z=2$, (b) $A_z=4$, and (c) $A_z=6$

In both cases the unsteady simulations have been carried out using a reduced number of grids, namely, $101\times51\times25$ in order to reduce the excessive computing time required. In both cases the flow reached steady state suggesting that the flow is steady for the values of the parameters used in the study.

Results and Discussions

Air is used as the working fluid, having a Prandtl number of 0.71. The analysis is performed for the following aspect ratios, A_z: 1, 2, 3, 4, 5 and 6. The jet to cross-flow velocity ratios used are, $R=0.5$, 1.0, 1.5, 2.5, 5, 7.5 and 10. The jet centerline was fixed at a distance of 15*D* from the entrance of the duct. The distance from the center of the jet to the duct exit is fixed to be 25*D* in order to insure a fully developed flow at the outlet. The cross section of the nozzle is taken to be square and the velocity distribution at the exit of the nozzles is assumed to have a flat profile. The cross-flow velocity at inlet is assumed to have a parabolic profile.

Flow Structure

Figure 2(*a*, *b*, and *c*) shows the projection of flow lines of the predicted velocity field on the mid vertical *x*-*z* plane, for Re $=200$, $R=2.5$ and $A_z=2$, 4 and 6. The projection of flow lines on an *x*-*z* plane are obtained from the *U* and *W* components of the velocity vectors on that plane. At the upper plate the jet exits from the nozzle perpendicular to the free stream direction and then it deflects downstream away from the stagnation point. Upon impingement a wall jet is formed on the bottom plate which spreads radially outward. The forward flowing wall jet interacts with the cross-flow and forms a ground horseshoe vortex close to the impingement plate, which wraps around the impinging jet like a scarf. The horseshoe vortex is also observed in incompressible turbulent circular single jet in cross-flow (Barata et al. [2], Barata [3], Abdon and Sunden [17]). At large jet-to-plate spacings (Fig. 2(*b*) and 2(*c*)) the jet deflection increases while the ground vortex diminishes. For higher jet-to-plate spacings (Fig. 2(*c*)), the jet is bent under the influence of the cross-flow such that no wall jet can form in the reverse direction of the cross-flow at the bottom plate. As a result, a ground vortex cannot form in front of the jet. The deflected jet becomes almost parallel to the bottom plate and exhibits a behavior similar to that of a radial jet. Downstream of the jet exit there appears to be a node which resides a short distance downstream of the edge of the nozzle from where the flow lines appear to be originating. The numerical simulation of a turbulent jet in cross-flow by Sykes et al. [18] also showed a node downstream of the jet, although it was located at the flat wall. The simulation, however, used a free-slip boundary condition at the flat wall and took no account of the flat-wall boundary layer. The node is also reported in the experimental study of Kelso et al. [9] for laminar and turbulent round jets in cross-flow. Figures 3 and 4 show the flow profiles at different *y*-*z* and *x*-*y* planes, respectively, corresponding to the case shown in Fig. 2(c). As soon as the jet exits from the nozzle, a negative pressure is induced around the jet, which drags the fluid from the surrounding into the jet, forming a vortex on the periphery of the jet (Fig. 3(*b*)). Figure 3(*c*) corresponds to a cross section where the flow lines start at the node shown in Fig. 2(*c*). The node marks the separation point of the upper pair of vortices near the top plate with the vortex pair formed in the horseshoe vortex at a lower elevation. Secondary vortices can be observed on the outer edges of the horseshoe vortex at $X=18$ (Fig. 3(*d*)). The flow structure in the wake of the jet can be better analyzed through projection of flow lines on different horizontal planes. The flow profile shown in Fig. 4(*a*) corresponds to a horizontal plane passing through the node depicted in Fig. 3(*c*). At this plane, which is close to nozzle exit, the cross-flow is deflected sideways by the penetration of the jet and cause a recirculation region behind the jet column similar to the

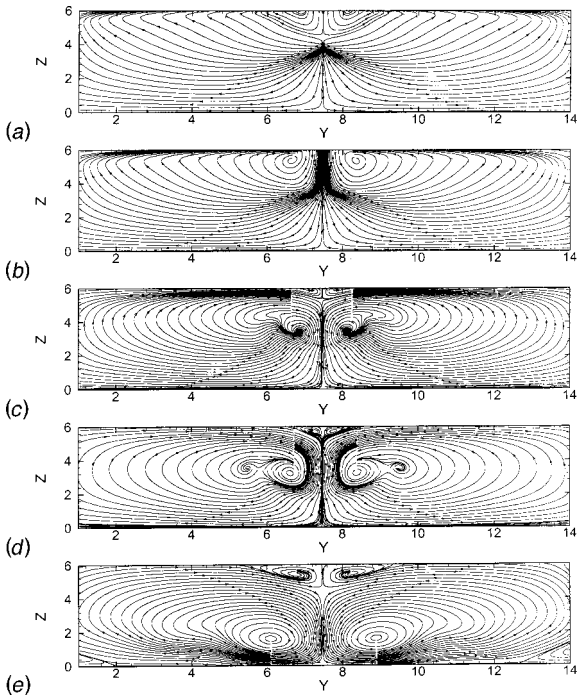

Fig. 3 Projection of flow lines for Re=200, $A_z=6$, and $R=2.5$ at vertical cross sections of (a) $X=14.5$, (b) $X=15$, (c) $X=16.8$, (d) $X=18$, and (e) $X=27$

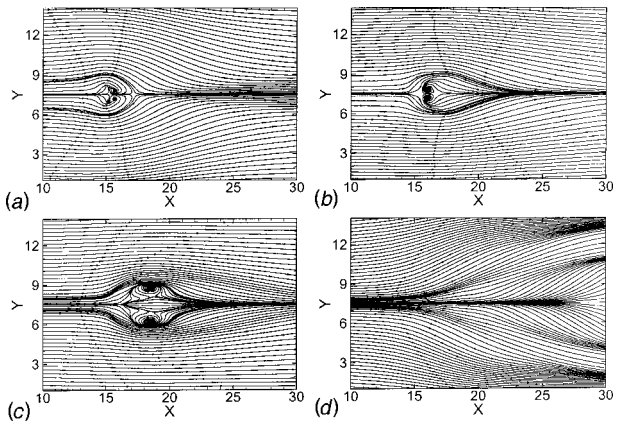

Fig. 4 Projection of flow lines for Re=200, $A_z=6$, and $R=2.5$ on horizontal cross section at (a) $Z=5.4$, (b) $Z=4.2$, (c) $Z=3$, and (d) $Z=0.6$

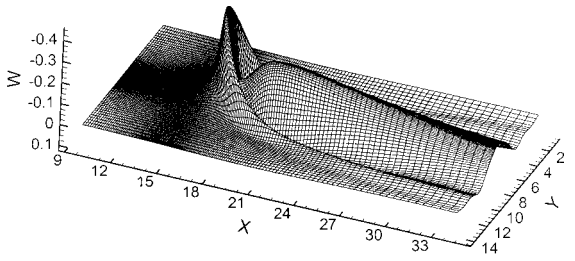

Fig. 5 The three-dimensional plots of the *W*-velocity for Re =200, A_z=6, and *R*=2.5 at the horizontal cross section *Z*=1.8

vortex formed behind a cylinder in cross-flow. The node shown earlier in Fig. 2(*c*) corresponds to the separation point from the cross-flow at the backside of the jet column at $X=16.8$, where the fluid flow is reversed. The counter rotating vortex pair, which is formed behind the jet, moves downstream together with the jet core at lower elevations (Figs. 4(*b*) and (*c*)). Close to the bottom plate the vortices disappear and the cross-flow diverges away from the centerline towards the sidewalls. A carpet plot of the vertical component of the velocity at the horizontal section at $Z=1.8$ is shown in Fig. 5, where the jet has a single peak at the jet core and is deflected downstream from the jet axis.

The effect of the jet to cross-flow velocity ratio, *R*, is shown in Fig. 6 through the projection of flow lines at mid vertical *x*-*z* plane, for Re=300 and $A_z=1$. At this small separation distance between the jet and impingement plate the jet is deflected by the cross-flow for $R<2.5$. The upstream wall jet interacts with the cross-flow and forms a horseshoe vortex close to the bottom plate for $R>0.5$, which wraps around the impinging jet. The horseshoe vortex grows in size as *R* increases and at $R=5$ it fills the whole space between the plates (Fig. 6(*e*)). At higher jet to cross-flow ratios two horseshoe vortices form upstream of the jet as shown in Figs. 6 (*e*, *f*, and *g*). Two horseshoe vortices have also been observed by Fric and Roshko [19] in free jet flows close to jet exit plane through flow visualization, but at much higher flow velocities (Re=3800 and $R=10$). The flow profiles in the larger horseshoe vortex are shown in Fig. 7 at different *y*-*z* planes along the

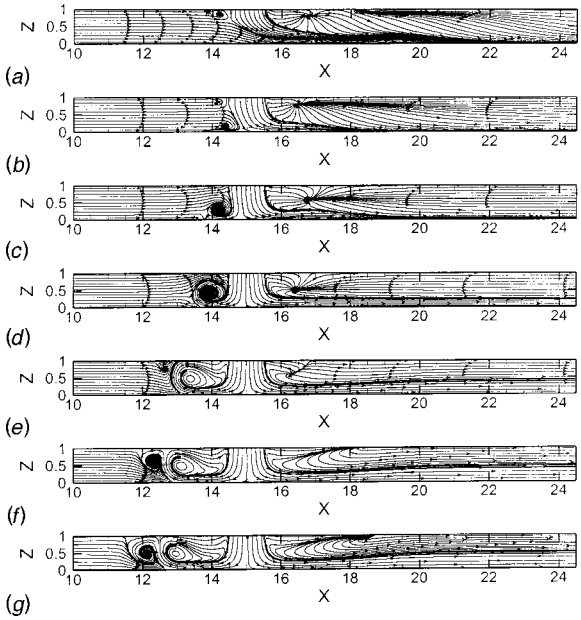

Fig. 6 Projection of flow lines on mid *x*-*z* plane for Re=300, A_z=1, and for jet to cross-flow velocity ratio (a) *R*=0.5, (b) *R* =1.0, (c) *R*=1.5, (d) *R*=2.5, (e) *R*=5, (f) *R*=7.5, and (g) *R*=10

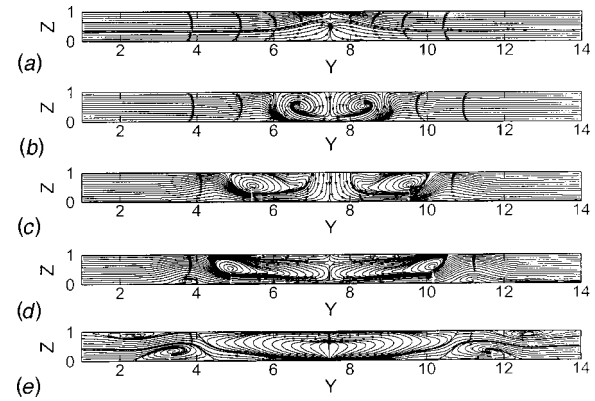

Fig. 7 Projection of flow lines for Re=300, A_z=1, and *R*=7.5 at vertical cross sections of (a) *X*=12.3, (b) *X*=13.5, (c) *X* =15, (d) *X*=16, and (e) *X*=18

cross-flow direction corresponding to case (*f*) in Fig. 6. The counter rotating vortices in the horseshoe vortex are elongated downstream the cross-flow and finally and at $X=18$ they combine and form a complex flow field with secondary vortices appearing near the top and bottom plates. The flow lines at different horizontal planes corresponding to the case (*f*) of Fig. 6 are depicted in Fig. 8. Close to the top plate an outer horseshoe vortex surrounds the inner horseshoe vortex (Figs. 8(*a*) and (*b*)). For $Z<0.5$ the outer horseshoe vortex disappears and only the inner horseshoe vortex wraps around the jet.

Heat Transfer

The local convection heat transfer coefficient is defined as

$$h=\frac{q''_w}{t_w-t_j} \tag{6}$$

and the local Nusselt number is defined in terms of the jet width, *D*, as

$$\mathrm{Nu}=\frac{hD}{k} \tag{7}$$

where it is also equal to the non-dimensional heat flux and calculated from $\mathrm{Nu}(x,y)=\partial T/\partial Z|_{\mathrm{wall}}$. At rather low jet-to-plate spacings the Nusselt number may have four off-center peaks as shown in Fig. 9. The four off-center peaks in the Nusselt number distribution curve also appear in the *W* velocity profile (not shown),

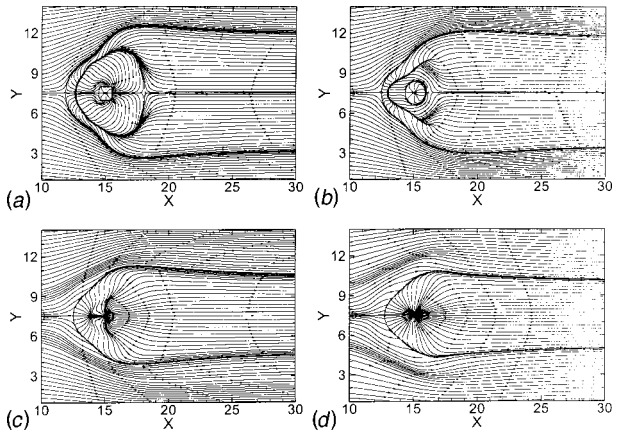

Fig. 8 Projection of flow lines for Re=300, A_z=1, and *R*=7.5 on horizontal cross section at (a) *Z*=0.9, (b) *Z*=0.5, (c) *Z* =0.3, and (d) *Z*=0.05

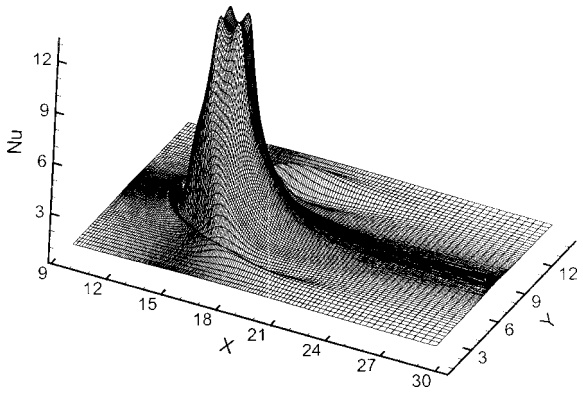

Fig. 9 The three-dimensional plot of the Nusselt number for Re=300, $A_z=1$, and $R=7.5$

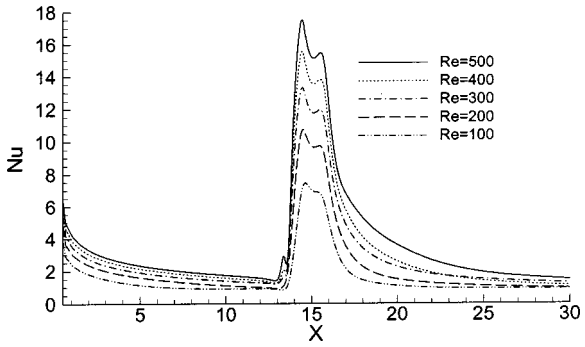

Fig. 11 Effect of Reynolds number on local Nusselt number for $A_z=1$ and $R=2.5$

which indicates that the jet velocity distribution plays a significant role in impingement cooling. The four off-center peaks are also, reported in laminar square single jet with small jet-to-plate spacing with no cross-flow by Sezai and Mohamad [20]. It is interesting to note that no such off-center peaks of the Nusselt number could be observed for the cases studied in this work when a parabolic jet velocity is used instead of a flat profile. With the parabolic jet velocity profile, Nu exhibits a maximum value at the stagnation point and sharply decreases to less than half of its value at a distance one jet width from the stagnation point. After this point, Nu curve coincides with that of the uniform jet. The maximum Nusselt number is about 100 percent higher when a parabolic jet exit profile is used. Previous results by others had shown the same effect [8,21,22]. This is a result of higher velocity and momentum of the issuing jet at the center for a parabolic profile. On the other hand the vortical flow structure formed around the jet is qualitatively similar to that of a jet with uniform velocity profile.

The effect of jet to cross-flow velocity ratio, R, on the variation of local Nusselt number along x-direction at the mid-section ($Y=7.5$) is shown in Fig. 10 for Re=300 and $A_z=1$. For this small jet-to-plate spacing, the magnitude of the local Nusselt number at the stagnation point is found to be rather insensitive to the velocity ratio for $R\geqslant 5$. For lower velocity ratios the maximum Nusselt number is higher. This is a result of the jet being squeezed into a narrower cross section by the cross flow stream as observed from Fig. 6. In practice lower R values are encountered for jets in an array system downstream of the central jet, where the fluid added by the upstream jets increase the cross-flow velocity. As the jet-to-cross flow velocity ratio decreases to 1.5 the second peak of the Nusselt number, downstream the maximum peak, decreases slightly. But a third peak appears at about 3.5 D downstream the jet axis, where the boundary layer formed by the wall jet on the bottom plate gets thinner. For $R=1$, the second peak of the Nusselt number disappears completely, while the magnitude of the third peak increases. For the case where cross-flow velocity is greater than the jet exit velocity, ($R=0.5$), the magnitude of the Nusselt number decreases and its position shifts to about 0.5D downstream the jet axis due to deflection of the jet by the cross flow. The maximum Nusselt number is not a result of jet impingement since the jet is unable to reach the bottom plate at this point, but it results due to the squeezing of the cross flow by the jet which forms a boundary layer on the bottom plate, (Fig. 6(a)). A second peak of the Nusselt number appears at $X=22.5$, which corresponds to the position of the jet impingement on the bottom plate. At low R values, the higher cross-flow velocities produce larger heat transfer coefficients at far downstream locations.

The effect of Reynolds number on the variation of local Nusselt number along x-direction at the mid x-z plane ($Y=7.5$) is shown in Fig. 11 for $A_z=1$ and $R=2.5$. The jet stagnation areas are clearly distinguishable as local high Nusselt number regions. Heat transfer decreases steeper away from the stagnation point in the upstream direction. For Re$\geqslant$300 a small peak is formed at a location upstream of the jet as a result of the interaction between the upstream lower wall jet and cross-flow. The magnitude of the local Nusselt number at the interaction point is expected to increase more when Reynolds number is increased further. In general the local Nusselt number found to increases as the Reynolds numbers increase. The effect of nozzle-to-plate spacing on the local Nusselt number along x-direction at the mid x-z plane (Y

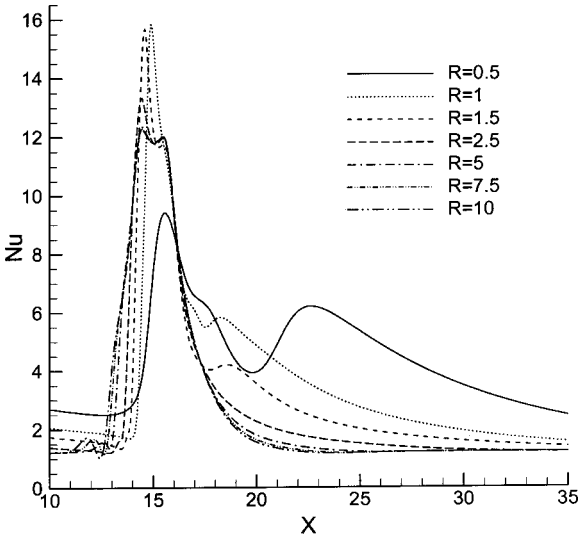

Fig. 10 Effect of jet to cross-flow velocity ratio on Nusselt number variation for Re=300 and $A_z=1$

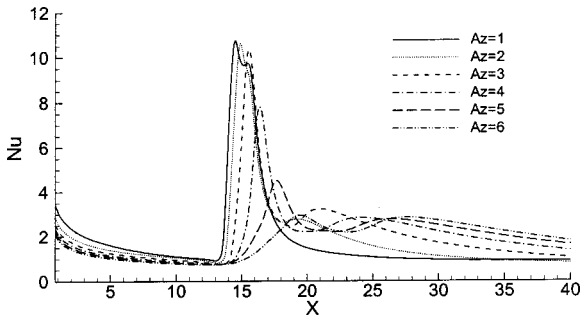

Fig. 12 Effect of aspect ratio A_z on Nusselt number variation in x-direction for Re=200, and $R=2.5$

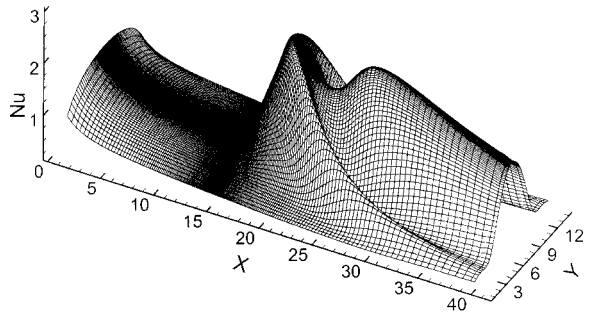

Fig. 13 The three-dimensional plot of the Nusselt number for Re=200, $A_z=6$, and $R=2.5$

$=7.5$) is shown in Fig. 12 for $R=2.5$ and Re$=200$. The location of the maximum Nusselt number is shifted downstream the jet exit plane as a result of deflection of the jet by the cross-flow. For $A_z \geqslant 2$ the local Nusselt number is found to have a second peak far downstream from the jet axis. A carpet plot of the local Nusselt number showing the two peaks for $A_z=6$ is depicted in Fig. 13. The first peak occurs at a distance about $5D$ downstream from the nozzle axis and is a result of deflection of the cross-flow towards the lower plate by the jet as observed in Fig. 2(c). The second peak in Nusselt number is found about $12D$ downstream the nozzle axis where the deflected jet impinges on the lower plate.

Conclusions

A three-dimensional numerical study has been undertaken to determine the flow and heat transfer characteristics of a single jet of square cross section combined with a cross-flow. The results indicate a rather complex flow field with one or two horseshoe vortices formed around the jet. For the jet-to-plate spacing of one jet width the horseshoe vortex fills the whole spacing between the plates while for $2 \leqslant A_z \leqslant 4$ an outer horseshoe vortex is formed near the upper plate encircling the inner horseshoe vortex. The size and location of the horseshoe vortex vary with jet-to-plate spacing and jet to cross-flow velocity ratio. At large nozzle-to-plate spacings ($L_z > 4D$), no reverse wall jet can form on the bottom plate where the jet is deflected by the cross-flow such that it impinges almost parallel to the plate like a radial jet at a location far away downstream from the jet centerline.

Heat transfer is strongly affected by the jet-to-plate spacing and the best degree of the uniformity was found at large jet-to-plate spacings ($L_z \geqslant 5D$). For a jet to plate spacing of one jet width and for $R<2.5$ the local Nusselt number was found to have an additional peak, which occurs downstream the jet impingement point of which the magnitude and position depend on jet to cross flow velocity ratio. A similar behavior is observed for jet to plate spacing greater than one nozzle width for $R=2.5$. For a nozzle to plate spacing of one nozzle width, the uniform jet velocity profile at the nozzle exit is transformed into non-uniform profile having four off-center velocity peaks downstream the nozzle. These peaks result in the formation of four off-center peaks in the Nusselt number profile at the impingement plate.

Nomenclature

A_x, A_y, A_z = aspect ratios in x, y, and z direction, L_x/D, L_y/D, L_z/D
D = jet width
h = heat transfer coefficient (W/m^2 K)
k = thermal conductivity (W/m K)
L_x = length of heated surface, in x-direction (m)
L_y = length of heated surface, in y-direction (m)
L_z = distance from jet exit to impingement plate (m)
Nu = local Nusselt number, (hD/k)
p = pressure
P = nondimensional pressure $(p/\rho u_j^2)$
Pr = Prandtl number (ν/α)
q''_w = local convective heat flux on the impingement surface
R = jet to cross flow velocity ratio (u_j/U_c)
Re = jet Reynolds number $(u_j D/\nu)$
t = temperature
T = nondimensional temperature, $(t-t_j)/(t_w-t_j)$
u, v, w = Cartesian velocities
u_j = jet exit velocity (m/s)
U = nondimensional Cartesian velocity, in x-direction (u/u_j)
U_c = center line velocity of the cross-flow
V = nondimensional Cartesian velocity, in y-direction (v/u_j)
W = nondimensional Cartesian velocity, in z-direction (w/u_j)
x, y, z = Cartesian coordinates
X, Y, Z = nondimensional Cartesian coordinates, x/D, y/D, z/D respectively

Greek Symbols

α = thermal diffusivity (m^2/s)
ν = kinematic viscosity (m^2/s)
ρ = density (kg/m^3)
ϕ = U, V, W, P, or T field

Subscripts

j = jet exit
w = wall

References

[1] Goldstein, R. J., and Behbahani, A. I., 1982, "Impingement of a Circular Jet With and Without Cross Flow," Int. J. Heat Mass Transf., **25**, pp. 1377–1382.
[2] Barata, J. M. M., Durao, D. F. G., and Heitor, M. V., 1991, "Impingement of Single and Twin Turbulent Jets Through a Crossflow," AIAA J., **29**(4), pp. 595–602.
[3] Barata, J. M. M., 1996, "Fountain Flows Produced by Multiple Impinging Jets in a Crossflow," AIAA J., **34**(12), pp. 2523–2530.
[4] Chuang, S. H., Chen, M. H., Lii, S. W., and Tai, F. M., 1992, "Numerical Simulation of Twin-jet Impingement on a Flat Plate Coupled With Cross-Flow," Int. J. Numer. Methods Fluids, **14**, pp. 459–475.
[5] Kim, S. W., and Benson, T. J., 1993, "Fluid Flow of a Row of Jets in Crossflow—A Numerical Study," AIAA J., **31**(5), pp. 806–811.
[6] Kercher, D. M., and Tabakoff, W., 1970, "Heat Transfer by a Square Array of Round Air Jets Impinging Perpendicular to a Flat Surface Including the Effect of Spent Air," ASME J. Eng. Power, **92**, pp. 73–82.
[7] Obot, N. T., and Trabold, T. A., 1987, "Impingement Heat Transfer Within Arrays of Circular Jets: Part 1—Effects of Minimum Intermediate, and Complete Crossflow for Small and Large Spacings," ASME J. Heat Transfer , **109**, pp. 872–879.
[8] Al-Sanea, S., 1992, "A Numerical Study of the Flow and Heat Transfer Characteristics of an Impinging Laminar Slot Jet Including Crossflow Effects," Int. J. Heat Mass Transf., **35**(10), pp. 2501–2513.
[9] Kelso, R. M., Lim, T. T., and Perry, A. E., 1996, "An Experimental Study of Round Jets in Cross-Flow," J. Fluid Mech., **306**, pp. 111–144.
[10] Gogineni, S., Goss, L., and Roquemore, M., 1998, "Manipulation of a Jet in a Crossflow," Exp. Therm. Fluid Sci., **16**, pp. 209–219.
[11] Leonard, B. P., 1979, "A Stable and Accurate Convective Modelling Procedure Based on Quadratic Upstream Interpolation," Comput. Methods Appl. Mech. Eng., **19**, pp. 59–98.
[12] Leonard, B. P., and Mokhtari, S., 1990, "Beyond First Order Upwinding: The ULTRA-SHARP Alternative for Nonoscillatory Steady-State Simulation of Convection," Int. J. Numer. Methods Eng., **30**, pp. 729–766.
[13] Leonard, B. P., and Drummond, J. E., 1995, "Why you should not use 'Hybrid,' 'Power Law' or related Exponential schemes for convective modelling. There are much better alternatives," Int. J. Numer. Methods Fluids, **20**, pp. 421–442.
[14] Van der Vorst, H. A. V., 1989, "BICGSTAB: A Fast and Smoothly Converging Variant of Bi-CG for the Solution of Non-Symmetric Linear Systems," SIAM (Soc. Ind. Appl. Math.) J. Sci. Stat. Comput., **10**, pp. 1174–1185.
[15] Saad, Y., 1996, *Iterative Methods for Sparse Linear Systems*, PSW Publ. Co., Boston.
[16] Van Doormaal, J. P., and Raithby, G. D., 1984, "Enhancements of the SIMPLE Method for Predicting Incompressible Fluid Flows," Numer. Heat Transfer, **7**, pp. 147–163.
[17] Abdon, A., and Sunden, B., 2001, "Numerical Simulation of Impinging Jet

Heat Transfer in the Presence of Crossflow,'' *Proc. 2nd Int. Conf. On Adv. Compu. Heat Transfer*, Australia, **1**, pp. 631–638.
[18] Sykes, R. I., Lewellen, W. S., and Parker, S. F., 1986, ''On the Vorticity Dynamics of a Turbulent Jet in a Crossflow,'' J. Fluid Mech., **80**, pp. 49–80.
[19] Fric, T. F., and Roshko, A., 1994, ''Vortical Structure in the Wake of a Transverse Jet,'' J. Fluid Mech., **279**, pp. 1–47.
[20] Sezai, I., and Mohamad, A. A., 1999, ''3-D Simulation of Laminar Rectangular Impinging Jets, Flow Structure and Heat Transfer,'' ASME J. Heat Transfer, **121**, pp. 50–56.
[21] Van Heiningen, A. R. P., Mujumdar, A. S., and Douglas, W. J. M., 1976, ''Numerical Prediction of the Flow Field and Impingement Heat Transfer Caused by a Laminar Slot Jet,'' ASME J. Heat Transfer, **98**, pp. 654–658.
[22] Sparrow, E. M., and Lee, L., 1975, ''Analysis of Flow Field and Impingement Heat/Mass Transfer Due to a Nonuniform Slot Jet,'' ASME J. Heat Transfer, **97**, pp. 191–197.

Three-Dimensional Heat Transfer of a Confined Circular Impinging Jet With Buoyancy Effects

Koichi Ichimiya
e-mail: ichimiya@ccn.yamanashi.ac.jp
Department of Mechanical Systems Engineering,
Yamanashi University,
Takeda-4, Kofu, Yamanashi 400-8511,
Japan

Yoshio Yamada
Sanshin Industry Co. Ltd.,
Shinbashimachi-1400, Hamamatsu,
Shizuoka 432-8528,
Japan

This paper describes the heat transfer and flow characteristics of a single circular laminar impinging jet including buoyancy force in a comparatively narrow space with a confined wall. Temperature distribution and velocity vectors in the space were obtained numerically by solving three-dimensional governing equations for the Reynolds number $Re(=u_mD/\nu)=400-2000$ and the dimensionless space, $H(=h/D)=0.25-1.0$. After impingement, heat transfer behavior on the impingement surface is divided into a forced convection region, a mixed convection region, and a natural convection region in the radial direction. The local heat flux corresponding to these three regions was visualized using a thermosensitive liquid crystal. Moreover, with the increase in Reynolds number, Re, and dimensionless space, H, the recirculation flow on the impingement surface moves downstream and its volume increases correspondingly. The Nusselt number averaged from $r=0$ to the minimum point of peripherally averaged Nusselt number, Num, was evaluated as a function of Re and H. [DOI: 10.1115/1.1527901]

Keywords: Analytical, Heat Transfer, Impingement, Jets, Mixed Convection, Visualization

Introduction

An impinging jet can be applied to improve the local heat transfer and local mass transfer. Recently, impinging jets are reported to contribute to the cooling of electronic equipment [1–3], film drying [4,5], and mass transfer [6] in a narrow space corresponding to a compact facility with low power, low noise and low vibration. Therefore, the heat transfer and flow features of impinging jets should be investigated in a narrow space.

There are many studies referring to local heat transfer in the flow direction in a large space for two-dimensional jets with six or seven times the nozzle diameter. Gardon and Akfirat [7], for example, measured the local and average heat transfer coefficients between an isothermal flat plate and impinging two-dimensional jets. Goldstein and Behbahani [8] reported that in a large jet-to-plate spacing the cross flow diminishes the peak heat transfer coefficient and in a small spacing the cross flow can increase the peak heat transfer coefficient for an impinging air jet. Goldstein and Timmers [9] measured the heat transfer coefficient distribution on a flat plate for either a single jet or an array of jet using a liquid crystal. Hrycak [10] correlated the stagnation point heat transfer with space and Reynolds number on turbulent jet impingement heat transfer for a comparatively large space. Streigl and Diller [11] developed an analytical model of entrained fluid on the local heat transfer to a single plane, turbulent impinging jet. Kataoka et al. [12] estimated experimentally that the large-scale structure of the impingement region becomes doubly-periodic due to the alternate impingement of fast-and-slow moving core fluids and the sway motion of the jet axis. Popiel and Trass [13] visualized toroidal vortex initiation, vortex pairing and the fluid entrainment process for a free and impinging round jet by the smoke wire method. Saad et al. [14] obtained the flow and heat transfer characteristics for geometric parameters to define the relationship between multiple jet systems and single jets. Sheriff and Zumbrunnen [15,16] studied the effect of flow pulsation on local time-averaged convective heat transfer to an impinging water jet, and indicated that the heat transfer distributions become more uniform in response to pulsation, but that heat transfer is not enhanced. Narayanan et al. [17] designed a slot jet reattachment nozzle and investigated the heat transfer characteristics. Arjocu and Liburdy [18] discussed naturally occurring large-scale structures and some turbulent characteristics near the impingement surface. Lee et al. [19] observed the local heat transfer for an ambient air jet with a fully developed velocity profile and a uniform wall heat flux thermal boundary. They obtained the relationship between Nusselt number and Reynolds number in the wall region. Meola et al. [20] measured the coherent structures and recirculation current affecting the distribution of heat transfer coefficients. They discussed the spatial distribution and averaged values of the Nusselt number. San et al. [21] measured the local Nusselt number of a confined circular air jet vertically impinging on a flat plate. They found that the transition from the impingement region to the wall jet region depends on the nozzle diameter and that the Nusselt number is due to the flow recirculation and mixing on the impingement surface. El-Glenk and Huang [22] performed a heat transfer experiment using circular jets for various nozzle diameters. Both the local and average Nusselt numbers within the jet diameters increased with radial distance from the stagnation point. Behnia et al. [23] simulated numerically the flow and heat transfer in circular confined and unconfined impinging configurations using an elliptic relaxation turbulence model. They presented the effect of confinement at very low nozzle-to-plate distances, and showed that the flow characteristics in the nozzle remarkably affect the heat transfer rate.

There have been some reviews published on the impingement heat transfer. Martin [24] systematically reviewed the heat transfer and mass transfer of a gas impinging jet. Jamubunathan [25] focussed on a single circular jet impingement heat transfer and the correlation for local heat transfer derived from the literature. Viskanta [26] examined the heat transfer characteristics of single and multiple isothermal turbulent air and flame jets impinging on surfaces and the effective features for an impinging jet. Webb and Ma [27] demonstrated the theoretical considerations, along with the hydraulic and thermodynamic characteristics of the impinging liquid jets, submerged jets and free jets. In most of these references, the radial heat transfer and two-dimensional flow have been

Contributed by the Heat Transfer Division for publication in the JOURNAL OF HEAT TRANSFER. Manuscript received by the Heat Transfer Division December 10, 2001; revision received April 15, 2002. Associate Editor: C. Amon.

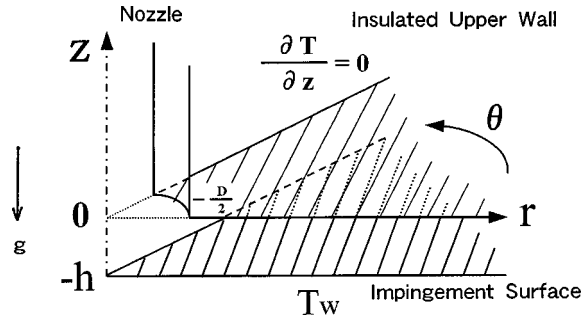

Fig. 1 Co-ordinate system

evaluated. However, the heat transfer and flow of a circular impinging jet change in three-dimensional form, radially, peripherally and vertically.

In the present study, the heat transfer and flow of a single circular impinging jet including buoyancy force in a comparatively narrow space were analyzed numerically in three-dimensional form, and the temperature distribution and velocity vectors were visualized. The mean Nusselt number was expressed by a function of the Reynolds number and the space between the nozzle and the impingement surface. Moreover, the local heat flux was visualized by a thermosensitive liquid crystal and the flow by the dye-injection method.

Description of the Problem

Figure 1 shows the co-ordinate system used in the analysis. Fluid impinges on the isothermal flat plate in a space with an insulated confined wall and flows in the radial direction. The system is a three-dimensional circular coordinate (r, θ, z) with a confined wall designed to examine the three dimensional behavior of the fluid. The gravitational force is exerted along the negative direction of the z axis. The nozzle diameter is $D=20$ mm, the length of flow passage $r=240-300$ mm, and the circumferential angle $\theta=0-90$ deg. The computational domain was previouly checked for $\theta=0-45$ deg, 0–90 deg, 0–135 deg, and 0–360 deg. In the case of $\theta=45$ deg, the local heat transfer and flow were affected by the peripheral boundary condition. However, in the case of $\theta=90$ deg, they were sufficiently equivalent to the results in $\theta=0-135$ deg and 0–360 deg. The space between the nozzle and the impingement surface is less than and equal to the nozzle diameters ($h=5$, 10, 15, and 20 mm) needed to obtain the heat transfer and flow behavior in comparatively narrow spaces after impingement. This model corresponds to the test section for the visualization except for the radial length. In the analysis, the buoyancy force was estimated by a Boussinesq approximation, which agreed with ρg within 10 percent at most under the present conditions. We considered the effects of temperature dependence of thermal conductivity and kinematic viscosity because they affected the temperature and velocity distributions compared with constant properties.

Numerical Analysis

The governing equations are as follows:

Continuity Equation.

$$\frac{\partial ru}{r\partial r}+\frac{\partial v}{r\partial\theta}+\frac{\partial w}{\partial z}=0 \tag{1}$$

Momentum Equations.

$$\frac{\partial u}{\partial t}+\frac{\partial ruu}{r\partial r}+\frac{\partial vu}{r\partial\theta}+\frac{\partial wu}{\partial z}-\frac{vv}{r}=\frac{-\partial p}{\rho\partial r}+\frac{\partial r\tau_{rr}}{r\partial r}+\frac{\partial\tau_{\theta r}}{r\partial\theta}+\frac{\partial\tau_{rz}}{\partial z}-\frac{\tau_{\theta\theta}}{r} \tag{2}$$

$$\frac{\partial v}{\partial t}+\frac{\partial ruv}{r\partial r}+\frac{\partial vv}{r\partial\theta}+\frac{\partial wv}{\partial z}-\frac{uv}{r}=\frac{-\partial p}{\rho r\partial\theta}+\frac{\partial r\tau_{r\theta}}{r\partial r}+\frac{\partial\tau_{\theta\theta}}{r\partial\theta}+\frac{\partial\tau_{z\theta}}{\partial z}-\frac{\tau_{r\theta}}{r} \tag{3}$$

$$\frac{\partial w}{\partial t}+\frac{\partial ruw}{r\partial r}+\frac{\partial uw}{r\partial\theta}+\frac{\partial ww}{\partial z}=\frac{-\partial p}{\rho\partial z}+\frac{\partial r\tau_{rz}}{r\partial r}+\frac{\partial\tau_{\theta z}}{r\partial\theta}+\frac{\partial\tau_{zz}}{\partial z}-g\beta(T-T_o) \tag{4}$$

where

$$\tau_{rr}=2\nu\frac{\partial u}{\partial r}$$

$$\tau_{\theta\theta}=2\nu\left(\frac{\partial v}{r\partial\theta}+\frac{u}{r}\right)$$

$$\tau_{zz}=2\nu\frac{\partial w}{\partial z}$$

$$\tau_{r\theta}=\tau_{\theta r}=\nu\left(\frac{\partial v}{\partial r}-\frac{v}{r}+\frac{\partial u}{r\partial\theta}\right)$$

$$\tau_{\theta z}=\tau_{z\theta}=\nu\left(\frac{\partial w}{r\partial\theta}+\frac{\partial v}{\partial z}\right)$$

$$\tau_{zr}=\tau_{rz}=\nu\left(\frac{\partial u}{\partial z}+\frac{\partial w}{\partial r}\right)$$

Energy Equation.

$$C_p\rho\left(\frac{\partial T}{\partial t}+\frac{\partial ruT}{r\partial r}+\frac{\partial vT}{r\partial\theta}+\frac{\partial wT}{\partial z}\right)=\frac{\partial rq_r}{r\partial r}+\frac{\partial q_\theta}{r\partial\theta}+\frac{\partial q_z}{\partial z} \tag{5}$$

where

$$q_r=\lambda\frac{\partial T}{\partial r},\quad q_\theta=\lambda\frac{\partial T}{r\partial\theta},\quad q_z=\lambda\frac{\partial T}{\partial z}$$

Initial Conditions. At $t=0$, the fluid is distilled and the fluid temperature is 20°C (293 K).

Boundary Conditions. At the nozzle exit, the fluid velocity has a laminar fully developed distribution (Reynolds number from 400 to 2000) and the fluid temperature is 20°C (293 K); at the impingement surface, the fluid velocity is zero and the surface temperature is 30°C (303 K); at the exit of the flow passage, the second derivative of the velocity and temperature is zero; the upper wall is insulated thermally and the peripheral gradient of temperature is zero at $\theta=0$ deg and 90 deg where the flow slips. The unsteady three-dimensional governing equations were solved numerically with the control volume method. The velocity and pressure were obtained by SIMPLE algorithm [28] and the QUICK scheme with the third order upper wind method [29] was implemented to calculate the convection flux through the cell face of a control volume. The number of meshes were $150(r)\times90(\theta)\times10(z)$. The time step Δt was 0.005 sec for numerical stability. Solution accuracy was studied from solutions on successively refined grids. The root mean square error defined by Fletcher [30] was less than 0.05 for a grid employed to predict the velocity and temperature. The numerical results were evaluated at steady conditions. Heat transfer and flow characteristics in the transient process will be reported in a subsequent study.

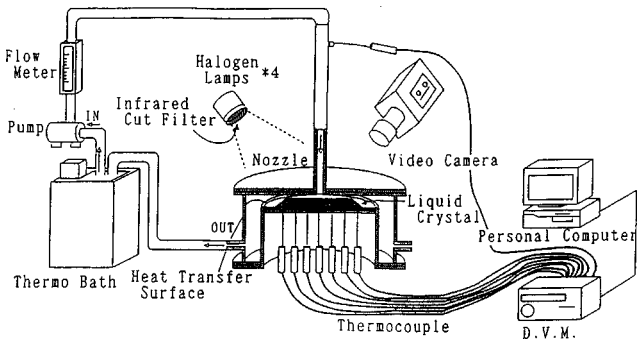

Fig. 2 Experimental apparatus

Experimental Apparatus for Visualization

Figure 2 shows the experimental apparatus for visualization. Water as a working fluid flows from a constant temperature water bath to a circular nozzle via a flow meter. The circular nozzle (inner diameter $D=20$ mm) was made of transparent acrylic material and had an entrance length of 1000 mm. Flow was almost fully developed at the nozzle exit. The size of the impingement surface made of aluminum was 330 mm in diameter and 15 mm thick. A rubber heater with a maximum power of 2 W/cm^2 was placed at the back of the impingement surface. Seven thermocouples indicated that the impingement surface temperatures were almost uniform (within ± 0.2 K) because of the high thermal conductivity (237 W/mK at 300 K) and the large heat capacity of aluminum. A kiralnematic-type thermosensitive liquid crystal sheet was set on the impingement surface. Four halogen lamps with infrared cut filters were placed at a height of 400 mm and a 45 deg angle to illuminate the liquid crystal sheet. The sheet construction consisted of a protective film, the liquid crystal layer and a black film. A temperature difference was generated by setting a thermal resistance layer between the uniform temperature wall and the liquid crystal [31]. As a result, this temperature difference distribution corresponded to the local heat flux. The thermosensitive temperature region of the present liquid crystal ranged from 28°C (301 K) to 34°C (307 K), and the temperature resolution and accuracy were 0.05°C and 0.1°C, respectively. Flow was visualized using the dye injection method.

Numerical Results and Visualization

Effect of Reynolds Number. Figures 3(*a*) and (*b*) show the effect of Re for temperature distribution and velocity vectors near the heated (impingement) surface at the space $h=10$ mm. The temperature at one mesh away from the impingement T is expressed,

$$T=Tw-(q\,\delta/\lambda) \tag{6}$$

where q is the local heat flux, δ one-mesh away from the impingement surface, and λ the thermal conductivity of water. Therefore, T corresponds to q. Consequently, the color distribution near the impingement surface (one mesh away) presents not only temperature distribution, but also heat flux distribution. The color red means low temperature, namely, high heat flux, while violet indicates high temperature, namely, low heat flux. The position $r=0$ denotes the area beneath the nozzle. In the case of Re=400, after the fluid impinged on the heat transfer surface, its flow direction changed perpendicularly. The color distribution ranges coaxially from $r=0$ to $r=60$ mm and denotes two-dimensionality, where forced convection is dominant. After that, thin blue lines and wide pink lines appear alternately in the peripheral direction, which indicates three-dimensional behavior. This is a mixed convection region composed of rising and falling flows. The thin lines denote upward motion from the high temperature surface and the thick lines the downward motion of the cooler fluid. In the case of Re =1000, the two-dimensional forced convection region and the transient region expand in the radial direction. The Richardson number ($=\mathrm{Gr}/\mathrm{Re}^2$) near the transition region was about 80. This agrees with the value Incropera et al. [32] obtained experimentally for mixed convection in a parallel plate duct.

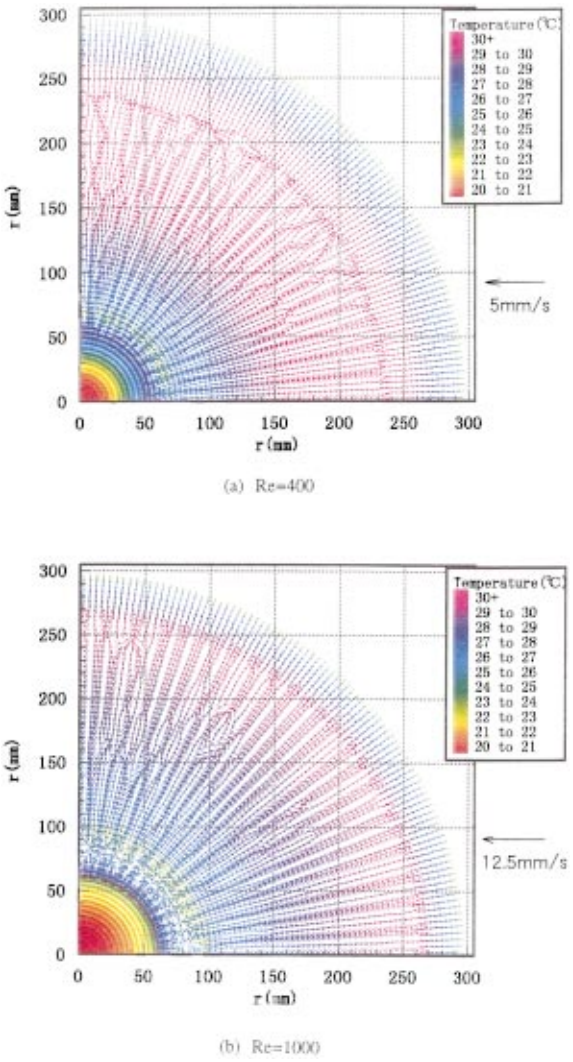

Fig. 3 Velocity vectors and temperature distribution near the heated wall ($h=10$ mm): (*a*) Re=400; and (*b*) Re=1000.

Numerical results were compared with experimental results by visualization using the thermosensitive liquid crystal shown in Fig. 4. For Re=400 and $h=10$ mm, fluid from the protruding nozzle in the figure impinges on the isothermal plate and flows in the radial direction. Color distribution changes coaxially from red at $r=0$ mm to green at $r=50$ mm. The dark green and yellow green thereafter appear alternately and peripherally. These correspond to the two-dimensional forced convection region and the three-dimensional mixed convection region, respectively. For Re =1000, the transition from a two-dimensional forced convection region to a three-dimensional mixed convection region appears as a dark green area and expands in the radial direction.

Figure 5 shows the rising and falling flows in a mixed convection region by flow visualization at Re=400 and $h=10$ mm. A plane figure of the parabolic behavior of the flow at $r=70$ mm is observed from the exit. Peripheral convex and concave flows can be seen alternately. This agrees well with the behavior of the mixed convection region in the numerical results and the heat flux visualization (Fig. 3 and 4).

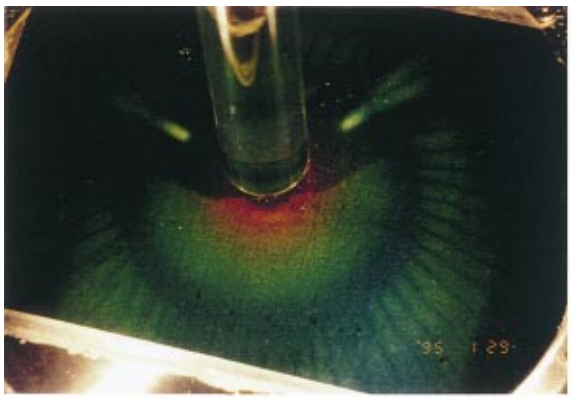

(a) Re=400

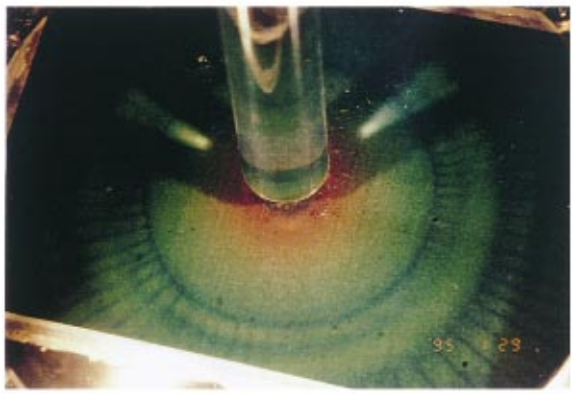

(b) Re=1000

Fig. 4 Heat flux visualization by thermosensitive liquid crystal (*h*=10 mm): (*a*) Re=400; and (*b*) Re=1000.

Figures 6(*a*), (*b*), (*c*) and (*d*) show the temperature distribution and velocity vectors in (*r*,*z*) cross section for θ=45 deg at various Reynolds numbers. A coordinate $(r,z)=(0,0)$ denotes the nozzle center and $z=-10$ mm the impingement surface. For Re=400, a recirculating flow is generated on the upper wall, and the flow near the impingement surface is accelerated. The fluid temperature near the impingement surface increases slightly because of the rising flow due to a bouncing phenomenon. From $r=80$ mm, the fluid flows downstream. For Re=1000, a large recirculating flow on the upper wall expands, and a small recirculating flow on the impingement surface moves downstream, corresponding to the transition from the forced convection region to the mixed convection region.

Figures 7(*a*) and (*b*) show the peripheral velocity vector and temperature distribution, respectively, at $r=160$ mm. The rising thin line and falling thick line exist as a pair. The number of pairs does not depend on Re.

Figure 8 shows the peripherally averaged Nusselt number Nua as a parameter Re for $h=10$ mm. *Nua* is defined by

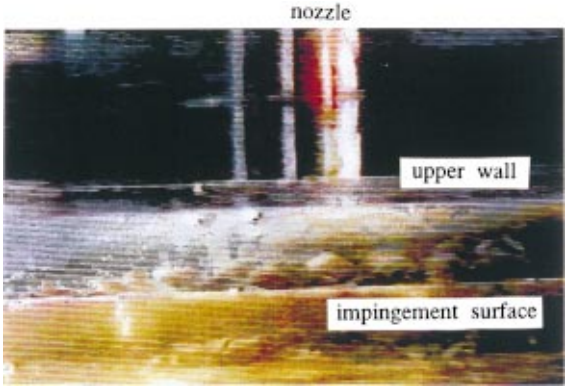

Fig. 5 Flow visualization across the $\theta-z$ section (*h*=10 mm, Re=400)

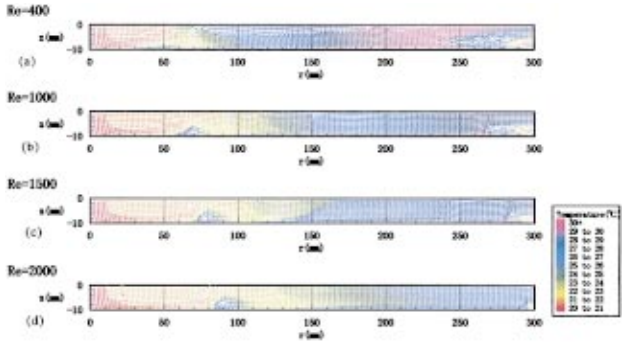

Fig. 6 Velocity vectors and temperature distribution across the $r-z$ section (θ=45 deg): (*a*) Re=400; (*b*) Re=1000; (*c*) Re=1500; and (*d*) Re=2000.

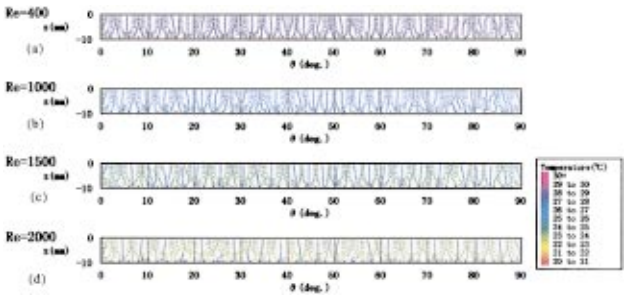

Fig. 7 Velocity vectors and temperature distribution across the $\theta-z$ section (r=160 mm): (*a*) Re=400; (*b*) Re=1000; (*c*) Re=1500; and (*d*) Re=2000.

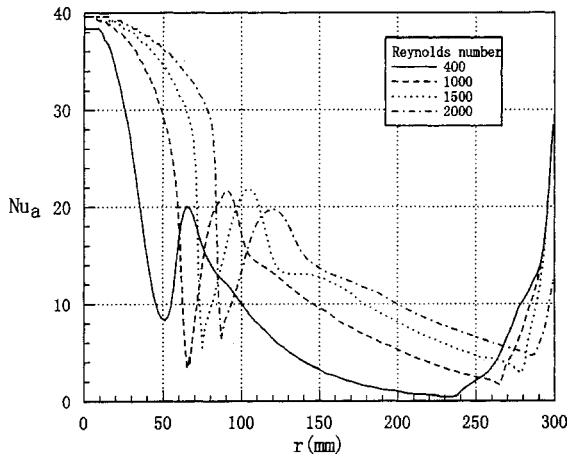

Fig. 8 Peripherally averaged Nusselt number along the radial direction (*h*=10 mm)

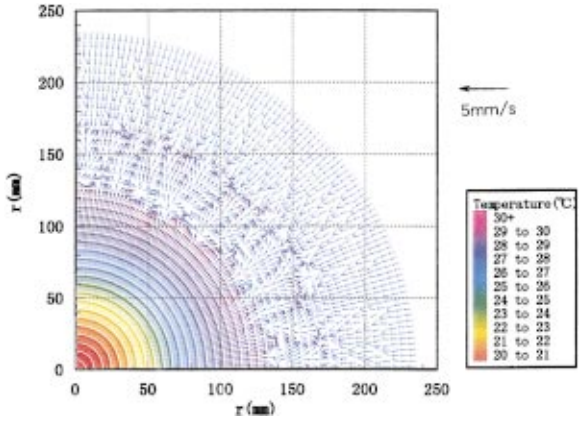

Fig. 9 Velocity vectors and temperature distribution near the heated wall (h=20 mm, Re=1000)

$$Nua = \frac{\sum_{j=1}^{m} Nuj}{m} \tag{7}$$

Nua takes the minimum corresponding to the small recirculating flow on the impingement surface as shown in Fig. 6, and peaks at the fluid reattachment position. These positions move downstream, and the absolute values increase with the increase in Re. However, at Re=2000, though the absolute value decreases, the variant width of *Nua* increases, meaning that the longitudinal gradient of the *Nua* weakens. The increase in *Nua* at the exit is due to the backflow of low-temperature fluid.

Effect of Space Between Nozzle and Impingement Surface. Figure 9 shows the velocity vector and temperature distribution at $h=20$ mm and Re=1000. The average velocity at $h=20$ mm is less than that at $h=10$ mm because of the large space. The alternate peripheral stripe lines do not appear, and the flow moves from the forced convection region to a flow region dominated by natural convection with the increase in temperature. Visualization was done using a thermosensitive liquid crystal in this condition was performed (Fig. 10). The coaxial structure can be seen beneath the nozzle, but the stripe structure does not appear clearly.

Figures 11(*a*), (*b*), (*c*), and (*d*) show the radial isothermal line and velocity vector for various spaces at Re=1000 and θ=45 deg. The small recirculating flow on the impingement surface moves downstream. At $h=20$ mm, the recirculating flow on the upper wall increases in size, but the small recirculating flow does not appear on the impingement surface. The flow rises from $r=140$ ~150 mm and behaves irregularly. Figures 12(*a*), (*b*), (*c*), and (*d*) simultaneously present the peripheral temperature distribution and velocity vectors at $r=150$ mm. The fluid ascends and descends across the section from $h=5$ mm to 15 mm. At $h=20$ mm, the periodicity of the peripheral rising and falling flow disappears and three-dimensional instability can be seen.

Figure 13 shows the peripherally averaged Nusselt number *Nua* in the radial direction for various spaces at Re=1000. The peak value of *Nua* decreases with an increase in the space and the maximum moves downstream. In the case of $h/D=0.25$ (h

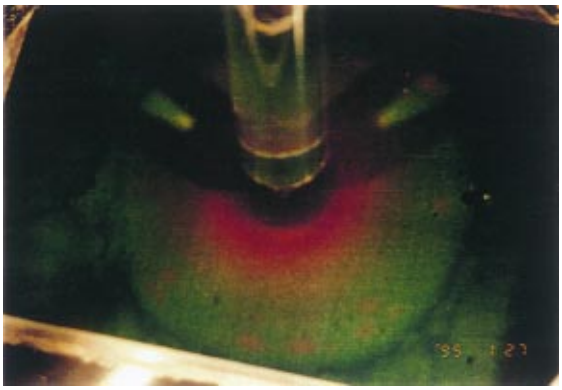

Fig. 10 Heat flux visualization by thermosensitive liquid crystal (h=20 mm, Re=1000)

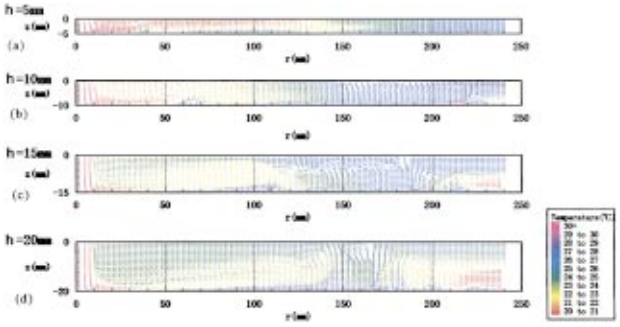

Fig. 11 Velocity vectors and temperature distribution across the $r-z$ section (θ=45 deg): (*a*) h=5 mm; (*b*) h=10 mm; (*c*) h=15 mm; and (*d*) h=20 mm.

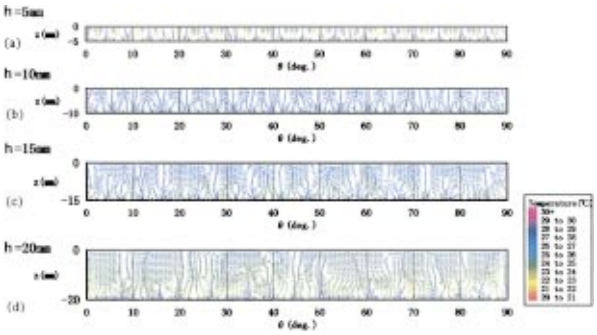

Fig. 12 Velocity vectors and temperature distribution across the $\theta-z$ section (r=150 mm): (*a*) h=5 mm; (*b*) h=10 mm; (*c*) h=15 mm; and (*d*) h=20 mm.

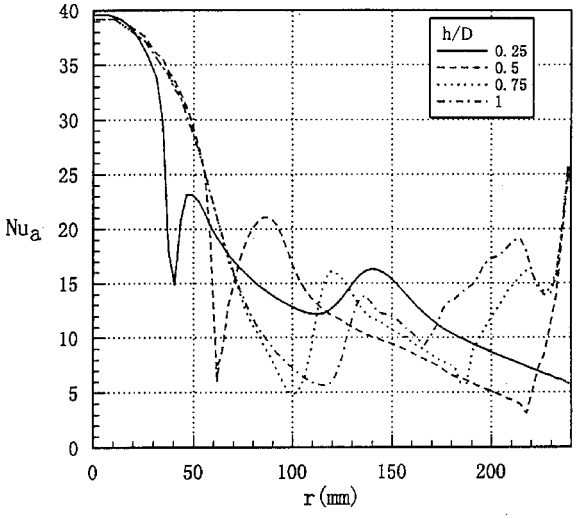

Fig. 13 Peripherally averaged Nusselt number along the radial direction (Re=1000)

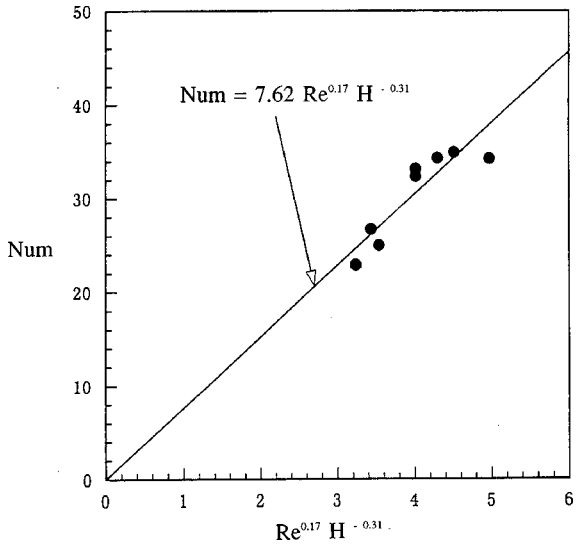

Fig. 14 Averaged Nusselt number

$=5$ mm), the second peak of *Nua* appears at $r=140$ mm. This depends on the impingement of low temperature fluid on the impingement surface. In the case of $h/D=0.5$, 0.75, and 1.0, the second peak is due to the backflow from the exit.

Average Nusselt Number. The effective region of an impinging jet is assumed to be the two-dimensional forced convection region from the center of the nozzle to a small recirculation flow on the impingement surface. *Nua* is averaged from $r=0$ mm to the minimum point of *Nua* in Fig. 8 and Fig. 13, and the Nusselt number *Num* is defined by

$$Num=\frac{\sum_{i=1}^{n} Nuai}{n} \tag{8}$$

Num is related to Re and h/D in Fig. 14. As a result, *Num* depends on $\mathrm{Re}^{0.17}$ and $(h/D)^{-0.31}$. The experimental equation of *Num* is expressed as follows:

$$Num=7.62\,\mathrm{Re}^{0.17}\,(h/D)^{-0.31} \tag{9}$$

The solid line denotes the above equation. The values are scattered within ± 15 percent.

In some practical applications, such as heat removal from an electric device, the cooling of gas turbine blades and so on, the space between the nozzle and impingement surface may be narrow. In this connection, the Nusselt number may change significantly. The average Nusselt number *Num* increases with a decrease in space within the present conditions. The effective region expands with the Reynolds number. These results can be employed by the designer as basic data to promote the heat transfer and determine the nozzle pitch of multi-jets.

Conclusions

We performed a numerical estimation and visualization of heat transfer and flow of the impinging jet including buoyancy effect by a single circular nozzle in a comparatively narrow space with a confined wall using a thermosensitive liquid crystal and the dye injection method.

1. After impingement, the heat transfer and flow were classified into three regions, a two-dimensional forced convection region, a three-dimensional mixed convection region and a three-dimensional natural convection region. In the mixed convection region, streak lines due to rising and falling flows peripherally appear on the impingement surface.
2. In the constant space between the nozzle and impingement surface, a small recirculation flow on the impingement surface moves downstream with the increase in Reynolds number. Downstream of the recirculating flow, the streak lines appear in the mixed convection region. The average Nusselt number depends on $\mathrm{Re}^{0.17}$.
3. At a constant Reynolds number, a recirculating flow on the impingement surface moves downstream with the increase of space. However, in a large space the recirculating flow does not appear clearly, and the forced convection region moves directly to the natural convection region. The average Nusselt number *Num* depends on $(h/D)^{-0.31}$.

Nomenclature

C_P = specific heat at constant pressure [J/(kg K)]
D = nozzle diameter [mm]
h = space between nozzle and impingement surface [mm]
H = dimensionless space, $H=h/D$
(Nu) = Nusselt number, $\mathrm{Nu}=\alpha D/\lambda$
Nua = peripherally averaged Nusselt number, Eq. (7)
Num = mean Nusselt number, Eq. (8)
p = pressure [Pa]
r, θ, z = circular coordinate
Re = Reynolds number, $\mathrm{Re}=u_m D/\nu$
t = time [sec]
T = temperature [°C, K]
To = fluid temperature at nozzle exit [°C, K]
Tw = impingement surface temperature [°C, K]
u_m = average velocity at nozzle exit [m/sec]
α = heat transfer coefficient [W/(m^2 K)]
β = coefficient of volume expansion [1/K]
δ = one-mesh size [mm]
λ = thermal conductivity of fluid [W/(mK)]
ν = kinematic viscosity of fluid [m^2/sec]
ρ = density of fluid [kg/m^3]

References

[1] Hollworth, B. R., and Durbin, M., 1992, "Impingement Cooling of Electronics," ASME Journal of Heat Transfer, **114**, pp. 607–613.
[2] Hamadah, T. T., 1989, "Impingement Cooling of a Simulated Electronics Package with a Square Array of Round Air Jets," *Proceedings of the National Heat Transfer Conference*, HTD-Vol. 111, pp. 107–112.
[3] Ichimiya, K., 1995, "Heat Transfer and Flow Characteristics of an Oblique Turbulent Impinging Jet within Confined Walls," ASME Journal of Heat Transfer, **117**, pp. 316–322.
[4] Loo, E., and Mujumdar, A. S., 1984, "A Simulation Model for Combined Impingement and Through Drying Using Superheated Steam as the Drying Medium," *Drying '84*, pp. 264–280.
[5] Law, H., and Masliyah, J. H., 1984, "Mass Transfer Due to a Confined Laminar Impinging Two-dimensional Jet," Int. J. Heat Mass Transf., **27**, pp. 529–539.
[6] Popiel, Cz. O., and Boguslawski, L., 1986, "Mass or Heat Transfer in Impinging Single, Round Jets Emitted by a Bell-shaped Nozzle and Sharp-ended Orifice," *Proceedings of 8th International Heat Transfer Conference* (San Francisco), **3**, pp. 1187–1192.
[7] Gardon, R. and Akfirat, J. C., 1966, "Heat Transfer Characteristics of Impinging Two-Dimensional Air Jets," ASME Journal of Heat Transfer, **88**, pp. 101–108.
[8] Goldstein, R. J., and Behbahani, A. I., 1982, "Impingement of a Circular Jet with and without Cross Flow," Int. J. Heat Mass Transf., **25**, pp. 1377–1382.
[9] Goldstein, R. J., and Timmers, J. F., 1982, "Visualization of Heat Transfer from Arrays of Impinging Jets," Int. J. Heat Mass Transf., **25**, pp. 1857–1868.
[10] Hrycak, P., 1983, "Heat Transfer from Round Impinging Jets to a Flat Plate," Int. J. Heat Mass Transf., **26**, pp. 1857–1865.
[11] Streigl, S. A., and Diller, T. E., 1984, "The Effect of Thermal Entrainment on Jet Impingement Heat Transfer," ASME Journal of Heat Transfer, **106**, pp. 27–33.
[12] Kataoka, K., Suguro, M., Degawa, H., Maruo, K., and Mihata, I., 1987, "Effect of Surface Renewal Due to Large-Scale Eddies on Jet Impingement Heat Transfer," ASME Journal of Heat Transfer, **30**, pp. 559–567.
[13] Popiel, C. O., and Trass, O., 1991, "Visualization of a Free and Impinging Round Jet," Exp. Therm. Fluid Sci., **4**, pp. 253–264.
[14] Saad, N. R., Polat, S., and Douglas, J. M., 1992, "Confined Multiple Impinging Slot Jets without Crossflow Effects," Int. J. Heat Mass Transf., **13**(1), pp. 2–14.
[15] Sheriff, H. S., and Zumbrunnen, D. A., 1994, "Effect of Flow Pulsations on

the Cooling Effectiveness of an Impinging Jet,'' ASME Journal of Heat Transfer, **116**, pp. 886–895.
[16] Sheriff, H. S., and Zumbrunnen, D. A., 1999, ''Local and Instantaneous Heat Transfer Characteristics of Arrays of Pulsating Jets,'' ASME Journal of Heat Transfer, **121**, pp. 341–348.
[17] Narayanan, V., Seyed-Yagoobi, J., and Page, R. H., 1998, ''Heat Transfer Characteristics of a Slot Jet Reattachment Nozzle,'' ASME Journal of Heat Transfer, **120**, pp. 348–356.
[18] Arjocu, S. C., and Liburdy, J. A., 1999, ''Near Surface Characterization of an Impinging Elliptic Jet Array,'' ASME Journal of Heat Transfer, **121**, pp. 384–390.
[19] Lee, D., Greif, R., Lee, S. J., and Lee, J. H., 1995, ''Heat Transfer from a Flat Plate to a Fully Developed Axisymmetric Impinging Jet,'' ASME Journal of Heat Transfer, **117**, pp. 772–776.
[20] Meola, C., Luca, L. D., and Carlomagno, G. M., 1996, ''Influence of Shear Layer Dynamics on Impingement Heat Transfer,'' Exp. Therm. Fluid Sci., **13**, pp. 29–37.
[21] San, J. Y., Huang, C. H., and Shu, M. H., 1997, ''Impingement Cooling of a Confined Circular Air Jet,'' Int. J. Heat Mass Transf., **40**, pp. 1355–1364.
[22] El-Glenk, M. S., and Huang, L., 1999, ''An Experimental Investigation of the Effect of the Diameter of Impinging Air Jets on the Local and Average Heat Transfer,'' Heat and Technology, **17**, pp. 3–12.
[23] Behnia, M., Parneix, S., Shabany, Y., and Durbin, P. A., 1999, ''Numerical Study of Turbulent Heat Transfer in Confined and Unconfined Impinging Jets,'' Int. J. Heat Fluid Flow, **20**, pp. 1–9.
[24] Martin, H., 1977, ''Heat and Mass Transfer Between Impinging Gas Jets and Solid Surfaces,'' *Advances in Heat Transfer*, Hartnett, J. P., and Irvine, T. F., eds., Academic Press, London, pp. 1–60.
[25] Jamubunathan, K., Lai, E., Moss, M. A., and Button, B. L., 1992, ''A Review of Heat Transfer Data for Single Circular Jet Impingement,'' Int. J. Heat Fluid Flow, **13**(2), pp. 106–115.
[26] Viskanta, R., 1993, ''Heat Transfer to Impinging Isothermal Gas and Flame Jets,'' Exp. Therm. Fluid Sci., **6**, pp. 111–134.
[27] Webb, B. W., and Ma, C. F., 1995, ''Single-Phase Liquid Jet Impingement Heat Transfer,'' *Advances in Heat Transfer*, Hartnett, J. P., and Irvine, T. F., eds., Academic Press, London, pp. 105–217.
[28] Patankar, S. V., 1980, *Numerical Heat Transfer and Fluid Flow*, Hemisphere Publishing Corp., London.
[29] Leonard, B. P., 1980, ''The QUICK Algorithm,'' *Computer Methods in Fluids*, Pentech Press, Plymouth.
[30] Fletcher, C. A. J., 1988, *Computational Techniques for Fluid Dynamics 1*, Springer Series in Computational Physics, Springer, Berlin.
[31] Akino, N., and Kubo, S., 1995, ''Heat Flux Visualization Using Liquid Crystal Sheet,'' *Proceedings of 23rd Visualization Symposium of Japan*, **15**(1), pp. 67–70.
[32] Incropera, F. P., Knox, A. L., and Maughan, J. R., 1987, ''Mixed Convection Flow and Heat Transfer in the Entry Region of a Horizontal Rectangular Duct,'' ASME Journal of Heat Transfer, **109**, pp. 434–439.

Erick A. Siba
Dell Corp.,
One Dellway,
Roundrock, TX 78682

M. Ganesa-Pillai
5505 Stonehenge Drive,
Richardson, TX 75082

Kendall T. Harris

A. Haji-Sheikh

Department of Mechanical and Aerospace Engineering,
The University of Texas at Arlington,
Arlington, TX 76019-0023

Heat Transfer in a High Turbulence Air Jet Impinging Over a Flat Circular Disk

This study concerns the flow and heat transfer characteristics of a turbulent submerged circular air jet impinging on a horizontal flat surface when free stream turbulence exceeds 20 percent. The turbulent fluctuations of the free stream velocity are the primary aerodynamics influencing heat transfer. Two regions with distinct flow characteristics are observed: the stagnation region, and the wall-jet region. According to the linear form of the energy equation, the surface heat flux may be decomposed into laminar and turbulent components. An inverse methodology can determine the turbulent component of the heat transfer coefficient in the stagnation region and in the wall-jet region as a function of the root mean square value of the fluctuating component of velocity in the bulk flow direction.
[DOI: 10.1115/1.1469523]

Keywords: Analytical, Boundary Layer, Conjugate, Flow, Forced Convection, Heat Transfer, High Temperature, Impingement, Inverse, Jets, Laminar, Thermal, Turbulence, Unsteady

Introduction

Impinging jets are often used where high rates of heat transfer are recommended. A jet impingement device can produce a flow field that can achieve relatively high local heat transfer rates over a surface area to be cooled or heated. One major application of jet impingement is in electronic cooling. Other industrial uses of impinging air jets include tempering of glass, annealing of metal and plastic sheets, drying of paper and textiles and cooling of turbine blades. Due to the many industrial uses for impinging jets, extensive research has been conducted to understand the heat transfer characteristics. The heat transfer rate to or from a jet impinging onto a surface is a complex function of many parameters: Nusselt number (Nu), Reynolds number (Re), Prandtl number (Pr), non-dimensional nozzle-to-plate spacing (z_o/D), free stream turbulence intensity (Tu), and non-dimensional displacement from the stagnation point (r/D). A majority of reported studies that consider the effect of these parameters on the heat transfer rate focus on a region extending a few nozzle diameters from the stagnation point.

Bollen [1] and Zapp Jr. [2] reveal that over a wide range of turbulence intensities and Reynolds numbers the heat transfer increased with an increase in turbulence intensity. Kestin and Maeder [3] show that a change in the intensity of turbulence in the free stream affects the local rate of heat transfer. Their results also show that the local heat transfer can be strongly influenced by the transition to a turbulent boundary layer. Martin [4] contributed extensively to the literature on submerged jet impingement and its heat transfer characteristics by compiling experimental data from various studies that have lead to many correlations. The effect of free stream turbulence on heat transfer from heated cylinders in cross flow is reported by Lowery and Vachon [5] where, at the stagnation point, the heat transfer is related to the turbulence intensity by

$$\mathrm{Nu}/\mathrm{Re}^{1/2} = 0.686 + 0.043\mathrm{Tu}\,\mathrm{Re}^{1/2}, \quad 0 < \mathrm{Tu}\,\mathrm{Re}^{1/2} < 10 \tag{1}$$

Further research by Simonich and Bradshaw [6], Pedisius et al. [7], Blair [8], and Hancock [9] on the effect of free stream turbulence on heat transfer show a complex relation between the local heat transfer and turbulence parameters.

Maciejewski and Moffat [10] used a wind tunnel to study the effect of free stream turbulence on the heat transfer coefficient over a flat plate. Using data from various independent sources concluded ''the free stream turbulence of 20 to 60 percent intensity results in Stanton number 1.8 to 4 times that would be predicted locally using accepted correlations for turbulent boundary layers at the same enthalpy thickness Reynolds number''. In an accompanying paper, Maciejewski and Moffat [11] theorized that the Stanton number, St,′ within an error band of ±15 percent, is a weak function of the Reynolds number but depends on the Prandtl number by the relation

$$\begin{aligned} \mathrm{St}'/f(\mathrm{Pr}) &= 0.024 + 0.012\exp\left[-\left(\frac{(\mathrm{Tu}-0.1)}{0.055}\right)^2\right] \\ f(\mathrm{Pr}) &= \mathrm{Pr}^{0.6}, \quad \mathrm{Pr} > 3 \\ &= 0.75, \quad \mathrm{Pr} = 0.71 \end{aligned} \tag{2}$$

where u' is the maximum value of the root mean square of turbulent fluctuations within the boundary layer in the bulk flow direction, with Tu the corresponding turbulence. When the local heat transfer coefficient is $h' \cong h$, then $\mathrm{St}' = h/(\rho C_p u')$ is the turbulence Stanton number, According to Eq. (2), when Tu>0.2, there is a nearly linear relationship between the local heat transfer coefficient, h, and u'. This approximate linear relationship between h and u' is

$$\mathrm{St}' = h/(\rho C_p u') \cong \text{constant} \tag{3}$$

The study by Maciejewski and Moffat [10] was based on flow over a flat plate with uniform thermal boundary conditions.

According to Eq. (2), for a given Pr, the turbulence intensity locally sets the heat transfer coefficient and there is no parameter describing the flow geometry. Al-Salam et al. [12] studied the effect of free stream turbulence on heat transfer in stagnation flow where the heat transfer coefficient has a strong laminar component. They summarized their high turbulence data and those from Hoogendoorn [13], and Lowery and Vachon [5] to conclude that, instead of the local heat transfer coefficient, h, its turbulent component, $h' = h_{\mathrm{tur}}$, is a function of u',

$$h_{\mathrm{tur}} = 226(1 - e^{-0.1u'}) \tag{4}$$

Contributed by the Heat Transfer Division for publication in the JOURNAL OF HEAT TRANSFER. Manuscript received by the Heat Transfer Division March 28, 2000; revision received November 2, 2001. Associate Editor: M. Hunt.

When Tu>0.2 and Pr=0.71, Eq. (2) yields $St' \cong 0.018$, while under the same conditions, Eq. (4) yields $St' = h'/(\rho c_p u') \cong 0.019$ at the lower range of u' and at a mean temperature of 300 K. This is well within the ±15 percent error band for Eq. (2). Even for turbulence exceeding 20 percent, it can be deduced from these studies that, for flow over different-shaped bodies, the primary aerodynamics that influence the heat transfer are due to the maximum turbulent fluctuation, u', in the boundary layer.

The objective of this work is to investigate the effect of u' on the heat transfer coefficient and to ascertain if modifications are necessary for different flow dynamics. The flow regime selected for this study is a single-phase turbulent jet of air normally impinging on a flat circular surface. Because of the spreading of the fluid, away from the stagnation zone, this provides a different flow dynamics than in reported cases leading to Eqs. (2) and (4). The heat transfer coefficient has a relatively large laminar component at the stagnation point and gradually decreases as the radial distance increases.

It is desirable to have a test model maintained at a constant temperature that would provide an accurate measure of the surface heat flux at various locations. Since, this is not easily attainable for a large, surface, an alternative method is employed. A test model is constructed and temperatures are measured internally near the surface of the test model. The interior temperature data are analyzed by an inverse technique in order to provide the local surface heat flux and surface temperature within the stagnation and the wall-jet regions. The inverse heat conduction method is a non-intrusive method of calculating both the surface heat flux and surface temperature because there is no measurement probe on the surface to impede the surface phenomena. The thermal boundary conditions of the surface are non-uniform. Initially, the disk is heated 30 to 40°C above ambient temperature and then cooled down by the air jet. The temperatures at interior sites within the disk and flow rate are collected at predetermined time intervals. For any uniform nozzle flow rate, the inverse technique yields the local heat transfer coefficient and a hot wire anemometer provides experimental data consisting of the mean and fluctuating velocity components of air.

Experimental Setup

The experimental setup is designed to perform two concurrent studies. The first study uses an inverse technique to determine the local heat transfer coefficient from the measured temperature within a test model. The second experimental study uses a constant temperature hot-wire anemometer to identify the local mean velocity, $\overline{u}$ and the root mean square of its fluctuations, u'.

An impinging air jet offers a simple flow field capable of generating very high local turbulence. The mean velocity is distributed across the jet from a maximum value on the centerline to a zero value in the surrounding air. The turbulence intensity increases dramatically near the outer edge. A relative turbulence intensity of up to 50 percent, based on local mean velocity, can easily be found. A variable velocity air jet facility produces a wide range of local mean velocities and turbulence intensities. The present experiments are conducted by placing a non-isothermal heat transfer surface under a turbulent jet that is impinging on that surface. The test surface is located at a distance of 10 nozzle diameters downstream of the jet exit plane to ensure a monotonic variation of the heat transfer coefficient (Gardon and Akfirat, [14]). For all the experiments described below, the disk is aligned with the centerline axis of the jet. The jet stream is produced by an air jet system (Model PAC-71C-23, FTS Systems, Inc.) with a holding arm used to position the flow. The circular jet nozzle has an inside diameter of 11.176 mm (0.44 inch). The system has a temperature controller and uses a variable flow rate to provide uniform flow. Three volumetric flow rates are selected for the experiments: 2.24 m^3s^{-1}, 3.30 m^3s^{-1}, 4.13 m^3s^{-1} and are set by using the flow rate controller on the air jet system.

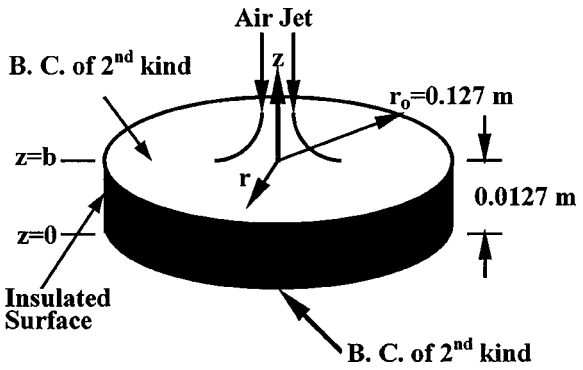

Fig. 1 Schematic of the 304 stainless steel geometry and boundary conditions

The experimental model selected to study heat transfer is a SS304C stainless steel disk of radius, $r_o = 127$ mm (5 inches) and thickness, $b = 12.7$ mm (0.5 inch). The disk is insulated around the circumference, and at the bottom. Polyethylene foam materials of very low thermal conductivity thermally insulate the bottom surface and the edges. Type-T thermocouples are located at six radial locations to measure the internal temperatures. The thermocouple holes are drilled from the bottom surface of the disk, at the center, and at radial locations of 12.7 mm, 25.4 mm, 38.1 mm, 63.5 mm, and 114.3 mm. All the thermocouples are at an axial location of $z = 11.94$ mm, i.e., 0.76 mm below the top surface. The top surface of the disk is exposed to the impinging jet. Figure 1 gives a schematic of the test disk with the geometry and boundary conditions used for the calculations (note that, for clarity, the thermocouples are not shown).

The gauge pressure for an external air supply is set to 310 kPa, to obtain the desired flow rates. A heater is held against the top surface of the test disk to heat the surface. The temperatures are monitored as the disk is heated and, once a pre-determined temperature is reached, the heater is removed and an insulating pad is used to cover the disk surface. The temperatures are allowed to stabilize, so that the six thermocouples record a nearly uniform temperature. The top insulation is then removed, the impinging air jet hits the surface, and the specimen is cooled to the desired temperature range. The temperatures at all internal locations are recorded, and the surface heat flux and temperature are determined from these measurements by the inverse heat conduction method, which is discussed in the next section.

The velocity and turbulence in the stagnation zone, and in the wall-jet region, are measured using a three-channel, constant-temperature hot-wire anemometer (DANTEC Model 56C17 CTA). Although the turbulence generated by the flow under investigation is anisotropic, the qualitative characteristics of the flow near the heat transfer surface allow some simplification in the aerodynamics. In the present experiment, u' can reasonably characterize the state of all three components of the turbulent fluctuations in the free stream, as suggested by Maciewjewski et al. [10]. The velocity signals received from the anemometer are passed through an analog-to-digital converter to data-acquisition software that analyzes this data and calculates mean-velocities $\overline{u}_{\text{mean}}$, intensity of turbulence Tu, and u'. All velocities and turbulence measurements are taken at atmospheric pressure and ambient temperature of 25°C. The hot-wire anemometer probe is attached to a traversing mechanism that allows radial and axial positioning. Instantaneous velocities and their fluctuating components are measured at a sample rate of 1/2 kHz, consisting of 8192 samples. The velocities and turbulence properties are measured at eleven radial and different axial positions for three flow rates.

Inverse Heat Conduction Analysis

The inverse heat conduction problem (IHCP) refers to the prediction of the boundary conditions or thermophysical properties from the solution of the conduction equation and the temperature history at some internal sites. Here the IHCP is solved to calculate the temperature and heat flux on the surface. The fundamentals of inverse heat conduction are discussed in Beck et al. [15]. The governing equation and the boundary conditions for the geometry that is being discussed are given by

$$\frac{\partial^2 T}{\partial r^2}+\frac{1}{r}\frac{\partial T}{\partial r}+\frac{\partial^2 T}{\partial z^2}+\frac{g}{k}=\frac{1}{\alpha}\frac{\partial T}{\partial t} \tag{5}$$

$$k\frac{\partial T}{\partial r}=0 \quad \text{at } r=0 \quad \text{and} \quad r=r_o$$

$$k\frac{\partial T}{\partial z}=0 \quad \text{at } z=0$$

$$-k\frac{\partial T}{\partial z}=q(r,t) \quad \text{at } z=b \tag{6}$$

$$T(r,z,0)=T_o$$

These equations assume that the temperature $T=T(r,z,t)$ is independent of the angular coordinate. This is justified since the jet is circular, nearly uniform, and hits the disk at the center. The disk material is assumed to be isotropic; therefore, the thermal conductivity k is independent of direction. The parameter g represents the heat generation per unit volume that includes the surface heat flux. The solution to Eq. (5) is

$$\theta(r,z,t)=T(r,z,t)-T_o$$
$$=\frac{\alpha}{k}\int_0^{r_o}\int_0^b\int_0^t G(r,z,t|r',z',\tau)$$
$$\times\{q(r',\tau)\delta(z'-b)\}\times 2\pi r'\,dr'\,dz'\,d\tau \tag{7}$$

where $G(r,z,t|r',z',\tau)=G_r(r,t|r',\tau)\times G_z(z,t|z',\tau)$ is the Green's function for the geometry in Fig. 1 and its boundary conditions. The Green's functions are taken from Beck et al. [16], Eq. (X22.3) for $G_z(\cdot)$ and Eq. (R02.1) for $G_r(\cdot)$).

The next step is to assume a profile for the unknown heat flux $q(r,t)$. A linear combination of polynomials in r and t would suffice, i.e.,

$$q(r,t)=\sum_{j=1}^{M_1\times M_2} c_j f_j \tag{8}$$

where

$$f_j=r^{j-1}, j=1,\ldots M_1$$
$$f_j=r^{j-(M_1+1)}\times t, j=M_1+1,\ldots 2M_1$$
$$f_j=r^{j-(2M_1+1)}\times t^2, j=2M_1+1,\ldots 3M_1 \tag{9}$$
$$\vdots \quad \vdots \qquad \vdots \quad \vdots$$
$$f_j=r^{j-(M_1(M_2-1)+1)}\times t^{M_2-1}, j=M_1(M_2-1)+1,\ldots M_1\times M_2$$

The maximum number of spatial functions permitted should not exceed the number of locations at which the temperature is measured. When the number of functions approaches this maximum, the solution tends to be more oscillatory about the true solution. Based on this guideline, $M_1=4$ and $M_2=4$ are chosen for the top surface where heat flux changes rapidly. The choice of $M_1=4$ means that four spatial functions describe the heat flux at the top surface, including the constant, i.e., a cubic variation for $q(r,t)$ with r. Note that the temperature is measured at $L=6$ locations near the top surface. Also, $M_2=4$ is chosen to recover the true variation of the boundary condition with time since the behavior of $q(r,t)$ is not known a priori. The total number of functions that describe the heat flux at the top surface is $M=M_1M_2=16$. Substituting these profiles into Eq. (7) and integrating in the z-direction results in the following expression:

$$\theta(r,z,t)=\sum_{j=1}^{M} c_j F_j \tag{10}$$

where

$$F_j(r,z,t)=\frac{\alpha}{k}\int_0^t d\tau\{G_z(z,t|z',\tau)|_{z'=b}\}$$
$$\times\int_0^{r_o} G_r(r,t|r',\tau)f_j(r',\tau)2\pi r'\,dr' \tag{11}$$

The function $F_j(r,z,t)$ on the right-hand-side of Eq. (10) can be evaluated for each $f_j(r,t)$. If the temperature measurements are taken at N time instants, there will be N equations for each location, totaling to $K=N\times L$ equations. Equation (10) is numerically calculated so that the first N equations represent the temperature at N time instants for the first thermocouple location, the next N equations for the next thermocouple, and so on until the Lth location. Then, the matrix form of Eq. (10) is

$$\mathbf{F}\cdot\mathbf{C}=\boldsymbol{\Theta} \tag{12}$$

where $\boldsymbol{\Theta}$ and $\mathbf{C}$ are $K\times 1$ and $M\times 1$ vectors and $\mathbf{F}$ is a $K\times M$ matrix. This set of equations is solved by the method of least squares to provide the vector $\mathbf{C}$ as

$$\mathbf{C}=(\mathbf{F}^T\cdot\mathbf{F})^{-1}\cdot(\mathbf{F}^T\cdot\boldsymbol{\Theta}) \tag{13}$$

Once the c_j's are calculated, the heat flux $q(r,t)$ at $z=b$ can be determined from Eq. (8). A measure of a good fit is the standard deviation of the error given by

$$\sigma=\sqrt{\frac{(\boldsymbol{\Theta}-\mathbf{F}\cdot\mathbf{C})^T\cdot(\boldsymbol{\Theta}-\mathbf{F}\cdot\mathbf{C})}{K}} \tag{14}$$

This measure is equivalent to the root mean square of the error between the measured temperatures and those obtained from the solution of the direct problem at those locations. A low value of σ is indicative of the robustness of the inverse estimation of surface heat flux.

Results and Discussion

Hydrodynamics of the Impinging Flow. A turbulent axisymmetric air jet impinging normal to the surface of a disk produces the flow field. Since the diameter is large compared to that of the jet exit diameter, the flow field is subdivided into different regimes. Based on the flow characteristics, as shown in Fig. 2, three regions are identified: (i) The free jet region develops from the exit of the nozzle and becomes turbulent at large Z_o/D; (ii) The impingement or stagnation region, where the strong interaction of the jet with the surface produces a deceleration as it approaches the surface, resulting in an increase in pressure. This helps to form and stabilize the hydrodynamic and thermal boundary layer. The flow then changes direction and starts accelerating away from the stagnation point. (iii) The wall-jet region where the flow leaving the stagnation region begins to decelerate in a direction parallel to the targeted test surface. It is also termed the parallel flow zone. In the wall-jet region, the deceleration of the mean velocity helps the transition to turbulence to occur generally at a distance $1.2D$ from the stagnation region, whereas the stabilizing effect of acceleration helps keep the boundary layer laminar in the stagnation zone, Kestin et al. [3]. Moreover, the transition is triggered by the disappearance of the pressure gradients that exist in the vicinity of the stagnation point and serve to stabilize the laminar boundary layer, despite the presence of high local turbulence

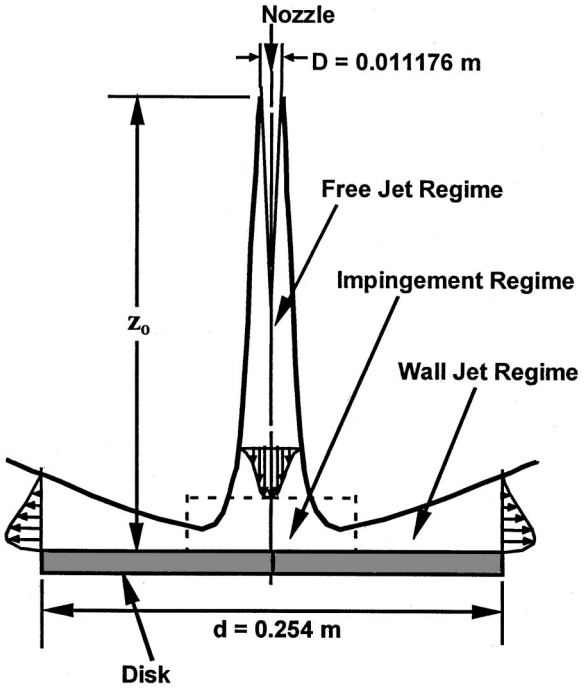

Fig. 2 Schematic of flow developing from a nozzle and impinging on a surface

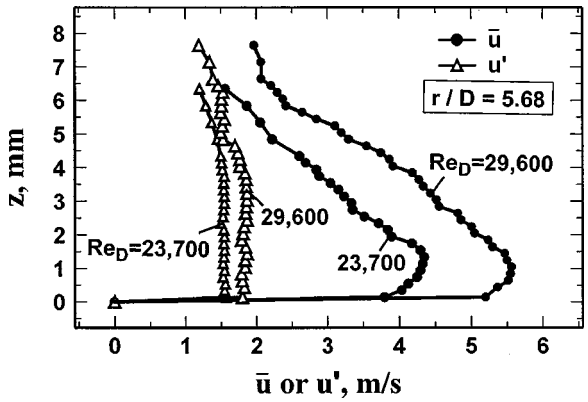

Fig. 4 The $\bar{u}$ and u' profiles at $r/D=5.68$ and for $Re_D=23{,}700$ and $Re_D=29{,}600$

levels in the free stream. Thus, it is only at the outer edge of the jet deflection region that conditions are conducive for a transition to a turbulent boundary layer.

The experiments are carried out at three values of the mean velocity at the jet exit nozzle, $W_o=22.9\,\mathrm{ms}^{-1}$, 33.7 ms^{-1}, and 42.1 ms^{-1}. The corresponding values of the Reynolds number, based on the inner diameter of the nozzle, are 16,100, 23,700, and 29,600, respectively. The mean velocity and turbulence properties are measured at nine stations along the r direction. A single-wire probe is used for this purpose. At each radial location, the probe is traversed vertically to different heights. Samples of measured data, Figs. 3 and 4, show the behavior of the velocity field. The experimental data depict the variation of u' and $\bar{u}$ as a function of z. Figure 3 shows $\bar{u}$ and u' as a function of the height z for two Reynolds numbers at $r/D=7.95$. The data are for $Re_D=16{,}100$ and $Re_D=29{,}600$; they illustrate the effect of the Reynolds number on u' and $\bar{u}$. For the low Reynolds number, $Re_D=16{,}100$, spreading and decay of the boundary layer is more pronounced than for the higher Reynolds number $Re_D=29{,}600$. A similar trend is observed at other locations; Fig. 4 shows $\bar{u}$ and u' profiles at $r/D=5.68$ for $Re_D=23{,}700$ and 29,600. Figures 3 and 4 demonstrate the growth and spreading of the boundary layer, measured at two radial locations and for three Reynolds numbers. The mean velocity profiles show the effect of wall friction on one side and jet mixing on the other side. Also, they show that the value of u' is nearly constant inside the boundary layer whereas the mean radial velocity, $\bar{u}$, increases with z, attains a maximum within the boundary layer, and then reduces. However, both u' and $\bar{u}$ monotonically reduce as r increases. The radial velocity and u' are found to have their highest values near the impingement surface for all Re_D values.

The boundary layer was traversed to obtain u' and $\bar{u}$ data similar to those in Figs. 3 and 4. The velocity data are summarized in Figs. 5 and 6. The maximum value of u', within the boundary layer, is plotted in Fig. 5 for all the Reynolds numbers mentioned earlier. The data are collected at two radial locations in the stagnation flow region and at nine locations in the wall-jet region. In general, the maximum u' in wall jet region, within experimental uncertainties, is located where $\bar{u}$ is maximum. The corresponding turbulence data, in Fig. 6, represent Tu, the ratios of the maximum u' to maximum $\bar{u}$ in the boundary layer. From this point forward, u' refers to the maximum value of the local u' in the boundary layer. The Tu data in Fig. 6 display a sharp rise near $r/D=3.5$ for $Re_D=16{,}100$ and $Re_D=23{,}700$, indicating a transition from predominantly laminar to predominantly turbulent flow. This transition occurs earlier at $r/D=2.25$ for $Re_D=29{,}600$, Fig. 6. The radial location of transition is likely to be dependent on the Reynolds number; however, this deserves a separate investigation.

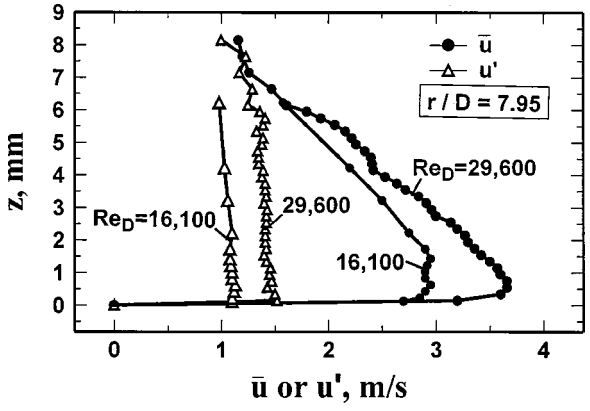

Fig. 3 The $\bar{u}$ and u' profiles at $r/D=7.95$ for $Re_D=16{,}100$ and $Re_D=29{,}600$

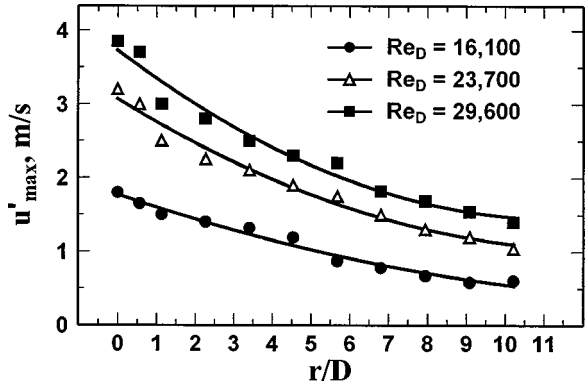

Fig. 5 Variation of u'_{max} as a function of r/D for three Reynolds numbers

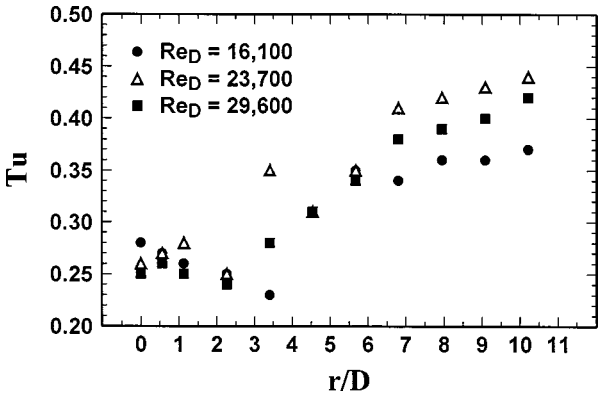

Fig. 6 Measured Tu as a function of *r/D* for three Reynolds numbers

Further away from the stagnation region the intensity of turbulence, Tu, increases since the mean radial velocity, $\bar{u}$, decreases faster than u'.

Heat Transfer Measurements

A test begins by heating the disk to a pre-selected temperature. The disk is cooled using the pre-selected flow rates. An inverse technique is then used to find the surface heat flux and surface temperature. Figure 7 shows a sample of computed surface temperature data to illustrate the behavior of the impinging jet for Re_D=23,700. The data for the other flow rates follow the same trend, but are not shown, for brevity. In Fig. 8, the computed surface heat flux is also shown for the same flow rate. Figure 9 compares the measured temperatures and those calculated by the direct solution using the estimated boundary conditions. The standard deviation of the error is about 3°C, which is within ±6 percent of $(T_o - T_{amb})$.

The computed surface heat flux is plotted versus the difference in temperatures between the wall and the ambient temperature; see Fig. 10. The heat transfer coefficient, defined by $h = q/(T_{sur} - T_{amb})$, is calculated, averaged over the entire duration of the experiment, and plotted in Fig. 11 for three flow rates. Note that the general character of these curves follows the behavior discussed previously; that is, the stagnation region heat transfer coefficient is relatively high compared to that of the wall-jet region when the dimensionless distance (jet exit plane to plate) $z/D \geqslant 10$. Because of the great difference between the behaviors of the heat transfer at and near the stagnation point, and in the developed wall-jet, it is convenient to discuss the measurements in these regions separately.

The primary interest is in the distribution of heat transfer under an impinging submerged jet. Therefore, an attempt is made to study the dependence of local heat transfer rates on the hydrody-

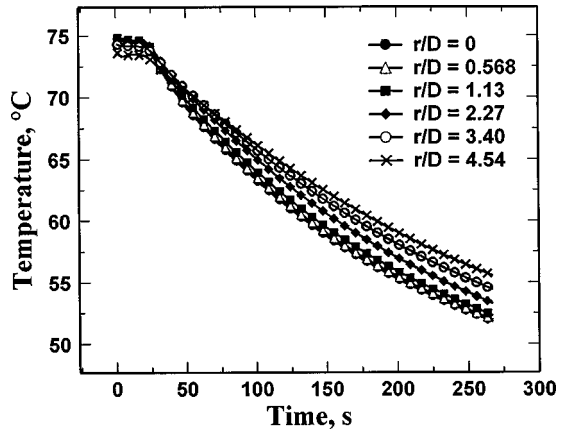

Fig. 7 Surface temperatures at different *r/D* locations for Re_D=23,700

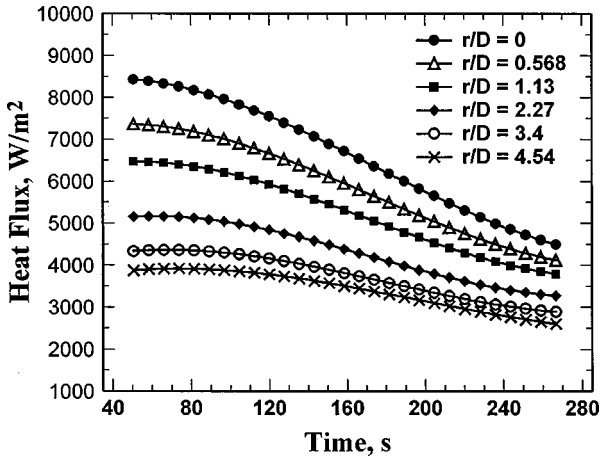

Fig. 8 Surface heat flux at different *r/D* locations for Re_D=23,700

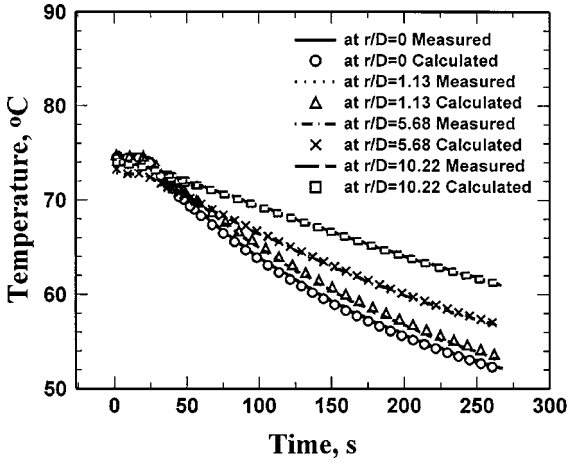

Fig. 9 Comparison of measured and recalculated temperatures at different thermocouple locations at Re_D=23,700

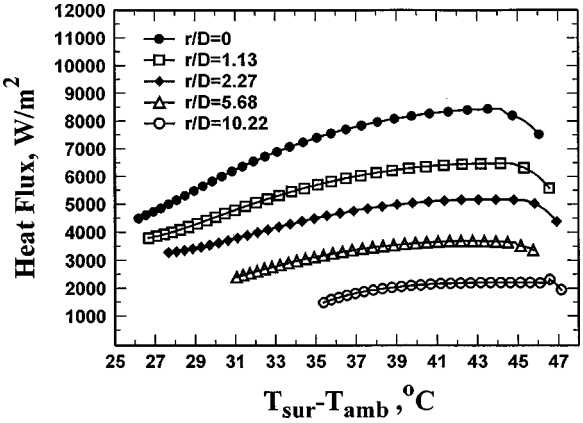

Fig. 10 Surface heat flux at different *r/D* locations for Re_D=23,700

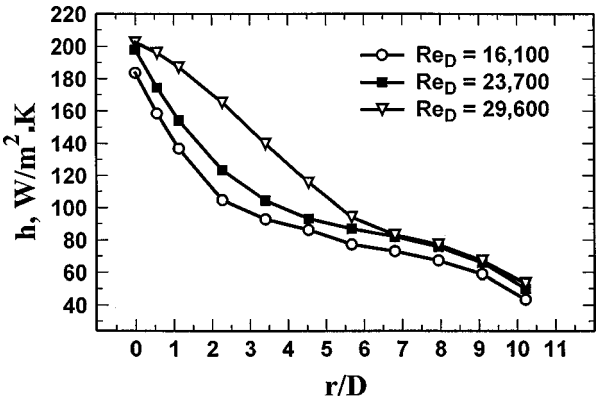

Fig. 11 Heat transfer coefficient as a function of r/D for three Re_D values

namic properties of the jet in the stagnation region and in the wall-jet region. The data recorded are, u', $\overline{u}$, Tu, and the heat transfer coefficient, h. They are calculated at eleven radial locations. Figure 11 shows the average values of h versus r/D over the entire disk for the three experiments.

Stagnation Flow Region

The stagnation region, based on data available in the literature, is defined as a circular region with a radius equal to $1.2D$ from the center of the disk. As stated earlier, for high values of the free-stream turbulence, Tu≥20 percent, Maciejewski and Moffat [11] observed that, for air, the heat transfer coefficient, h, is directly proportional to the standard deviation of the local stream-wise velocity. Using empirical reasoning, Al-Salam et al. [12], hypothesized that h, has a laminar component, h_{lam}, and a turbulent component, h_{tur}, that depends on w'. This hypothesis for fluids with constant thermophysical properties is mathematically verified in the Appendix; therefore, near the stagnation point,

$$h = h_{\text{lam}} + h_{\text{tur}} \tag{15}$$

The laminar component of the heat transfer coefficient at the stagnation point depends on the mean velocity, $\overline{w}$, outside of the boundary layer and can be written as

$$h_{\text{lam}} = c_1\sqrt{|\overline{w}|} \tag{16}$$

where c_1 is a constant that includes the dependence of h_{lam} on the Prandtl number Pr, geometry, and thermophysical properties of the fluid. Equation (16) assumes that changes in the velocity profile within the boundary layer due to turbulence have a weak influence on c_1, see Appendix. At or near the stagnation point, a single wire probe provides a velocity that is approximately normal to the wall, $\overline{w}$, and its fluctuating component, w'. When Tu>0.2, for a relatively small range of w', it is assumed there is a linear relationship between h_{tur} and w', therefore, h_{tur} is written as

$$h_{\text{tur}} = c_2 w' \tag{17}$$

where c_2 is a constant to be determined. Now, the total heat transfer coefficient, h, at the stagnation region, can be written in the following form:

$$h = c_1\sqrt{|\overline{w}|} + c_2 w' \tag{18}$$

The next task is to use the experimental data to extract the contribution of laminar and turbulent components. Rewriting Eq. (18) with the data at or near the stagnation point

$$\mathbf{U}\cdot\mathbf{C} = \mathbf{H} \tag{19}$$

where $\mathbf{U}$ is a matrix and $\mathbf{C}$ and $\mathbf{H}$ are column vectors,

Table 1 Comparison of present h_{lam} with h_{lam} (Liu et al. [17])

Re_D	h_{lam} (present)	h_{lam} (Liu et al.)
16100	115.74	113.1
23700	115.37	112.5
29600	130.12	126.9

$$\mathbf{U} = \begin{bmatrix} \sqrt{|\overline{w}_1|} & w_1' \\ \vdots & \vdots \\ \sqrt{|\overline{w}_6|} & w_6' \end{bmatrix},\quad \mathbf{C} = \begin{bmatrix} c_1 \\ c_2 \end{bmatrix},\quad \text{and}\quad \mathbf{H} = \begin{bmatrix} h_1 \\ \vdots \\ h_6 \end{bmatrix}, \tag{20}$$

results in an over-determined linear system. The variable $|\overline{w}_i|$ stands for $|\overline{w}|$ at the ith combination of flow rate and location. Since there are two locations inside the stagnation region and the data is collected for three flow rates, then $i=1,2,\ldots,6$. Solving for c_1 and c_2, the method of least squares gives $c_1=37.82$ and $c_2=17.75$. Now Eq. (18) becomes:

$$h = 37.82\sqrt{|\overline{w}|} + 17.75w' \tag{21}$$

The error between the experimental heat transfer coefficient and that calculated using Eq. (21) is less than 10 percent.

To validate the earlier assumption that changes in $\overline{u}$ and $\overline{w}$ due to turbulence do not appreciably affect h_{lam}, the laminar component of Eq. (21) need to be compared against established data. For h_{lam} at the stagnation region, the following correlation obtained by Liu et al. [17],

$$\text{Nu}_D = 0.715\,\text{Re}_D^{1/2}\,\text{Pr}^{0.4},\quad \text{for}\ \ 0<r/D<0.787$$
$$\text{and}\quad 0.15<\text{Pr}<3 \tag{22}$$

is used. Although Eq. (22) is for a free jet, this comparison is appropriate for flow near stagnation point since heat transfer coefficient for a given Pr depends on Re_D alone. Moreover, the Prandtl number in this study is within the range Prandtl numbers in Eq. (22). The error in the calculated h_{lam} compares remarkably well with the correlation of Liu et al. [17], less than 2 percent (See Table 1) and this close agreement verifies the earlier assumptions concerning h_{lam}.

The turbulent component of Eq. (21) is also compared against the correlation obtained by Al-Salam et al. [12], Eq. (4). Figure 12 compares the present data with Eq. (4) in the stagnation region. The error between data from Eq. (4) and the present experimental results is within 10 percent. The agreement is very satisfactory although, in this study, the velocity components were measured

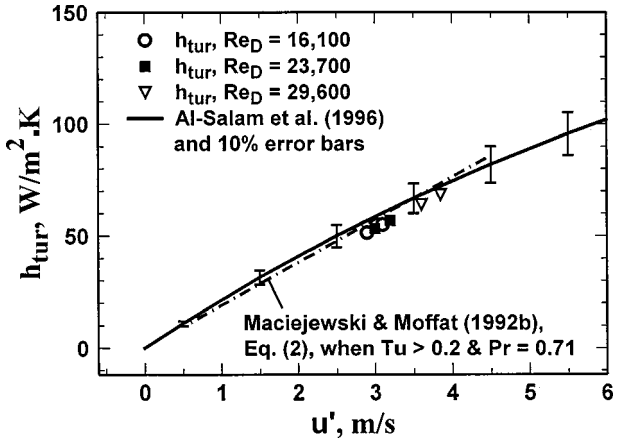

Fig. 12 Turbulent heat transfer coefficient as a function of u' at the stagnation region

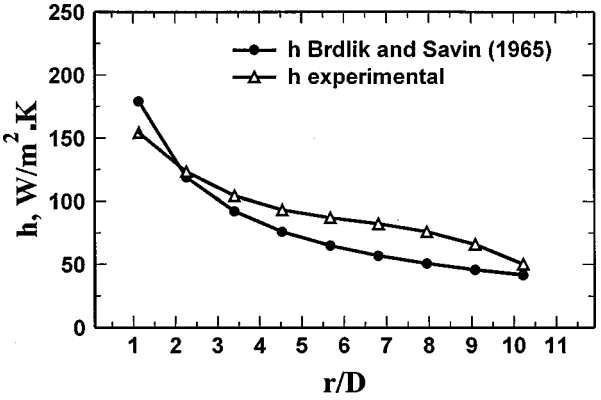

Fig. 13 Heat transfer coefficient as a function of r/D for Re_D=23,700 in the wall-jet region

with the test model in place whereas Hoogendoorn [13] and Lowery and Vachon [5] and Al-Salam et al. [12] reported removing the test models prior to measurements.

Generally, there is a high laminar component of h due to a favorable pressure gradient in the stagnation region. Despite the high laminar component, when Tu is large (greater than 20 percent) in the stagnation region, the root mean square of the fluctuating component of the local stream-wise velocity determines the turbulent component h_{tur}.

Wall-Jet Region. The success of the simple correlation suggested by Eq. (15), encourages one to attempt the same formulation in order to obtain a description of the behavior of jet impingement heat transfer in the wall-jet region. To validate this approach, the total heat transfer coefficient is obtained experimentally and needs to be compared against established data for h in the wall-jet region. The analysis of Brdlik and Savin [18] is based on laminar theory, but their experimental investigation dealt with a region far away from the stagnation region where the velocity at the outer edge of the boundary layer is decreasing with r, and the free stream, Tu, is relatively high. The same trend is also observed in the present experiments. The following semi-empirical correlation, obtained by Brdlik and Savin [18], uses data from experiments where the flow in the wall-jet region is essentially turbulent

$$\mathrm{Nu}_r = 1.18\mathrm{Pr}^{1/3}\,\mathrm{Re}_{D_o}^{1/2}\left(\frac{\bar{r}^2}{1+\bar{r}}\right)\left[\bar{r}\left(\frac{1}{2}\bar{r}-1\right)+\ln(1+\bar{r})\right]^{-1/2} \tag{23}$$

where $\bar{r}=r/D$. Figure 13 compares the correlation obtained by Brdlik and Savin [18] with the present heat transfer coefficient in the wall-jet region. The total heat transfer coefficient, h, follows the same trend as Eq. (23), Brdlik and Savin [18], but differs by about 20 percent. The higher values of measured h in Fig. 13 are attributed to higher u'. The other flow rates, not shown, also show the same trend.

The mean heat transfer coefficients is computed over a time interval when radial changes in temperature are relatively small, see Fig. 7. The results for three Reynolds numbers are plotted in Fig. 14 using open circular symbols. The data are plotted for the same radial locations where u'_{max} is plotted in Fig. 5. Since h in the present experiments follows the same trend observed by Brdlik and Savin [18] but at a higher value, Fig. 13, the next step is to describe the variation of h in the wall-jet region with u'. Also, the heat transfer in the wall-jet exhibits higher levels compared to parallel flow as noted by Dup. Donaldson et al. [19]. This appears to be due to the higher level of turbulence generated by the shear between the wall-jet and the ambient air, which is transported to the boundary layer at the heat transfer test surface.

As stated earlier, Eq. (15) can describe the total heat transfer coefficient in the wall-jet region. The computed temperature at

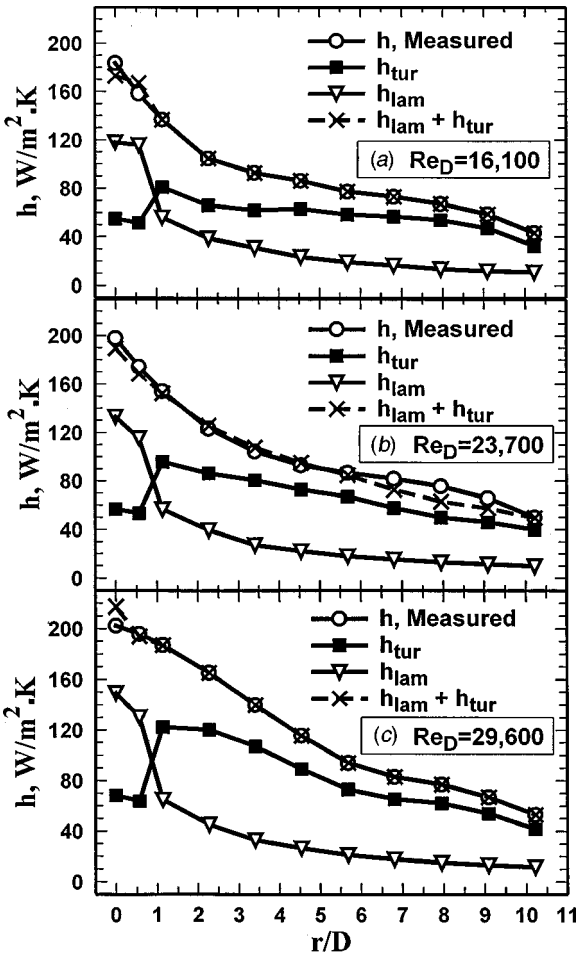

Fig. 14 Variation of h, h_{lam}, and h_{tur} as functions of r/D at: (*a*) Re_D=16,100, (*b*) Re_D=23,700, and (*c*) Re_D=29,600

any r/D in Fig. 7 shows that dT/dt is small and a quasi-steady state assumption is valid. One can infer from Eq. (*A*.2) in the Appendix that the laminar heat transfer coefficient in the wall-jet region is inversely proportional to $r^{1/2}$. Therefore, assuming velocity profiles are similar and neglecting the higher-order contribution of dT_{sur}/dr since h_{lam} is small (See Fig. 7), then the laminar component of h in the wall-jet region can be written as

$$h_{lam} = c_3\sqrt{\frac{\overline{u}_{max}}{r}} \tag{24}$$

The constant c_3 includes the dependence of h on the Prandtl number, the influence of turbulence on $\overline{u}$ and $\overline{w}$, and any secondary effect due to departure from non-uniform surface temperature condition. Maintaining Eq. (17) to be valid in the wall-jet region when Tu>0.2, one can write

$$h_{tur} = c_4 u' \tag{25}$$

where c_4 is a constant expressing the physical properties of the fluid. Therefore, using Eqs. (24) and (25), Eq. (15) can be written as

$$h = c_3\sqrt{\frac{\overline{u}_{max}}{r}} + c_4 u' \tag{26}$$

Rewriting Eq. (26) with the data recorded in the wall-jet region and employing the method described by Eqs. (19) and (20) leads to the computation of c_3 and c_4. A least squares method yields c_3=2.12 and c_4=38.27 and Eq. (26) becomes:

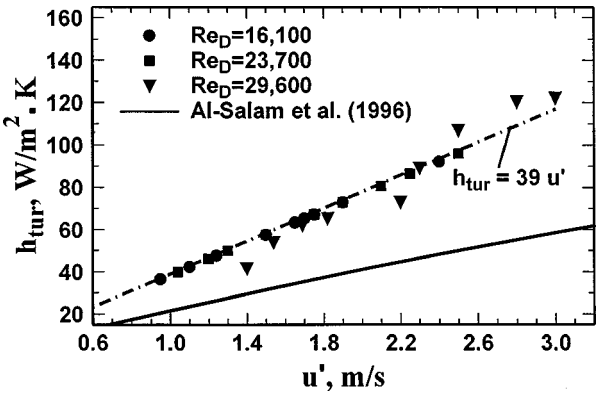

Fig. 15 Variation of h_{tur} as a function of u' in the wall-jet region for Re_D=16,100, 23,700, and 29,600, and comparison with Al-Salam et al. [12]

$$h = 2.12\sqrt{\frac{\overline{u}_{max}}{r}} + 38.37u' \tag{27}$$

Discussion

Figure 14 shows the laminar and turbulent components of h. The computed laminar component when $r/D<1$ is nearly constant only for Re_D=16,100 as suggested by Eq. (22) Liu et al. [17]. However, the variations of h_{lam} when $r/D<1$ for other two Re_D values are within ±10 percent from their mean. The value of $h_{lam}+h_{tur}$ is also plotted in Fig. 14 for the three Reynolds numbers. The error between the experimental value of h and $h_{lam}+h_{tur}$ calculated using Eq. (27) is generally less than 10 percent and slightly larger for a few data points when Re_D=23,700. As in the stagnation region, for validation, the laminar and turbulent components of Eq. (27) need to be compared against established data. Generally, the flow in the wall-jet region is turbulent and therefore no data on heat transfer in laminar flow is cited in the literature for comparison with calculated h_{lam}. Figure 15 illustrates the turbulent component of the heat transfer coefficient in the wall-jet region. The correlation obtained by Al-Salam et al. [12] for the stagnation flow region, Eq. (4), is also plotted in Fig. 15 for comparison. Figure 16 compares the stagnation flow and wall jet with the Maciejewski and Moffat [11] correlation, Eq. (2). The stagnation flow data fall within the error band specified in Maciejewski and Moffat [11]. Also, the data in the wall jet region

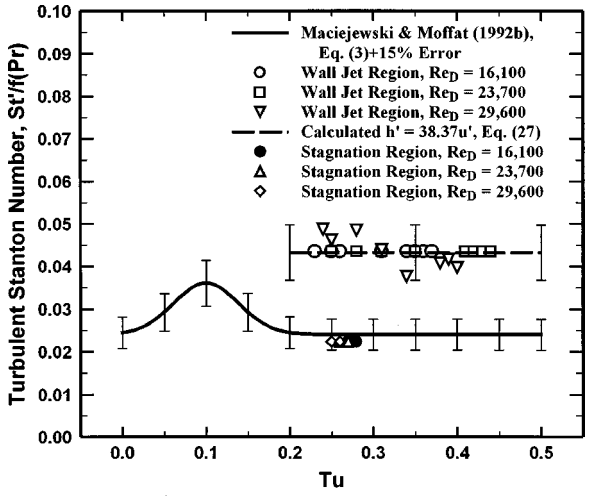

Fig. 16 A comparison between Maciewjewski and Moffat [11] correlation and the data from present study

are plotted in Fig. 16. The data for Re_D=16,100 and 23,700 are quite smooth but the data for Re_D=29,600 have noise within 10 percent of the mean. For the measured wall-jet-region data, the mean value of $St'/f(Pr)$ is 0.043 instead of 0.024. This increase is attributed to a much higher turbulent component, h_{tur}, that can be predicted from flat plate data, and it is in line with the hydrodynamics of the flow in the wall regime. It is likely that a thinning of the laminar sublayer, occurring in the wall-jet region as the radius increases, is responsible for this increase. Figures 3 and 4 validates the thinning boundary layer assumption because, when Re_D=29,600, the peak $\overline{u}_{max}$ moves closer to the wall as r/D increases. This phenomenon can reduce the thermal resistance of the sublayer and increase the rate of heat transfer across this layer.

Conclusions

In the stagnation region, the heat transfer coefficient has a high laminar component for all the Reynolds numbers studied. Figure 12 shows that these results agree well with the summary of stagnation-flow data for different shaped bodies in Al-Salam et al. [12]. The measured data are within the error band of ±10 percent specified in Al-Salam et al. [12]. Figure 16 shows that the stagnation flow data fall within the 15 percent error band, as specified in Maciejewski and Moffat [11]. Accordingly, one can conclude that Eq. (2) and Eq. (4) can adequately describe the contribution of the fluctuating component of the stream wise velocity on the heat transfer coefficient, h_{tur} while the laminar flow theory can provide h_{lam} at or near the stagnation point.

Special care is needed to account for the effect of stream-wise turbulence in the wall jet region. Because the contribution of the laminar component is small, the free stream turbulence can have a profound effect on the heat transfer coefficient. This confirms the Maciejewski and Moffat [10] assertion that the classical Reynolds number based correlations can produce information with large errors depending on relative value of u'. Figure 16 compares the data in the wall-jet region with Eq. (2). When Tu>0.2, there is a significant departure from the asymptotic value of 0.024 in Eq. (2). Accordingly, for a turbulent flow in the wall jet region, one needs to modify Eq. (2) in order to account for the contribution of the fluctuating component of the stream wise velocity on the heat transfer coefficient.

Nomenclature

b = thickness of the disk, m
c_j = coefficient
$\mathbf{C}$ = array of coefficients
C_p = specific heat, J/kg.K
D = nozzle diameter at exit, m
f = a function of Pr
$\mathbf{F}$ = matrix, Eq. (12)
h = heat transfer coefficient, W/m^2.K
h' = turbulent heat transfer coefficient, W/m^2.K
k = thermal conductivity, W/m.K
Nu = Nusselt number, hr/k_f
Pr = Prandtl number
r = radial coordinate
$\overline{r}$ = r/D
r_o = radius of the disk, m
Re_D = Reynolds number, $\rho W_o D/\mu$
St = Stanton number, $St=h/(\rho C_p u)$
St$'$ = turbulence Stanton number, $St'=h'/(\rho C_p u')$
t = time, s
T = temperature, °C
T_o = initial temperature, °C
Tu = turbulence intensity, u'/u (percent)
u = radial velocity, m/s
u' = root mean square value of the fluctuating component of u, m/s
$\overline{u}$ = temporal mean of radial velocity, m/s
w = axial velocity, m/s

w' = root mean square value of the fluctuating component of w, m/s
$\overline{w}$ = temporal mean of axial velocity, m/s
W_o = velocity at nozzle exit, m/s
z = axial coordinate, m
α = thermal diffusivity, m^2/s
μ = viscosity coefficient, $N \cdot s/m^2$
θ = temperature after transformation, $T - T_o$
Θ = array of measured θ
ρ = density of SS304C steel, kg/m^3
σ = standard deviation

Subscripts and Superscripts

amb = ambient
lam = laminar
max = maximum in the boundary layer
sur = surface
tur = turbulent

Appendix

The residency of most fluid particles over a 0.127 m disk radius is typically less than 50 milliseconds. An examination of transient temperature in Fig. 7 shows that the cooling process in the test model is sufficiently slow so that the temperature in the air can be classified as quasi-steady state. Therefore, the fluid boundary conditions are classified as prescribed nonuniform temperature distribution at $z=0$ and constant ambient temperature far away from the surface. For a steady state incompressible boundary layer flow, the two-dimensional form of the energy equation is

$$\rho c_p \left(\overline{u} \frac{\partial \overline{T}}{\partial r} + \overline{w} \frac{\partial \overline{T}}{\partial z} \right) = k \frac{\partial^2 \overline{T}}{\partial z^2} + S \qquad (A1)$$

where S is the contribution of the fluctuating components of T and w and can be viewed as a sink/source in Eq. (*A*1). One can decompose the temperature $\overline{T}(r,z)$ into two components: $\overline{T}(r,z) = \overline{T}_1(r,z) + \overline{T}_2(r,z)$ so that $\overline{T}_1(r,z)$ satisfies equation

$$\rho c_p \left(\overline{u} \frac{\partial \overline{T}_1}{\partial r} + \overline{w} \frac{\partial \overline{T}_1}{\partial z} \right) = k \frac{\partial^2 \overline{T}_1}{\partial z^2} \qquad (A2)$$

and $\overline{T}_2(r,z)$ satisfies equation

$$\rho c_p \left(\overline{u} \frac{\partial \overline{T}_2}{\partial r} + \overline{w} \frac{\partial \overline{T}_2}{\partial z} \right) = k \frac{\partial^2 \overline{T}_2}{\partial z^2} + S \qquad (A3)$$

The boundary conditions for $\overline{T}_1(r,z)$ are linear and identical to boundary conditions for $\overline{T}(r,z)$ while the boundary conditions for $\overline{T}_2(r,z)$ are homogeneous. Therefore, once Eq. (*A*2) and (A3) are satisfied, the Eq. (*A*1) and the corresponding boundary conditions are satisfied. The surface heat flux is

$$q = -k \left. \frac{\partial \overline{T}}{\partial z} \right|_{z=0} = \left(-k \left. \frac{\partial \overline{T}_1}{\partial z} \right|_{z=0} \right) + \left(-k \left. \frac{\partial \overline{T}_2}{\partial z} \right|_{z=0} \right) \qquad (A4)$$

Equation (*A*2) has a form similar to the energy equation for laminar although $\overline{u}$ and $\overline{w}$ are different. Therefore, the function $-k \partial T_1 / \partial z$ at $z=0$ serves as the laminar component of the surface heat flux, q_{lam}. Because $\overline{T}_1(r,z)$ has the same boundary conditions as $\overline{T}(r,z)$, one can set $q = h(T_{\text{sur}} - T_{\text{amb}})$ and $q_{\text{lam}} = h_{\text{lam}}(T_{\text{sur}} - T_{\text{amb}})$. Accordingly, Eq. (*A*4) can be rewritten as

$$\begin{aligned} q_{\text{tur}} &= -k \left. \frac{\partial \overline{T}_2}{\partial z} \right|_{z=0} = \left(-k \left. \frac{\partial \overline{T}}{\partial z} \right|_{z=0} \right) - \left(-k \left. \frac{\partial \overline{T}_1}{\partial z} \right|_{z=0} \right) \\ &= h(T_{\text{sur}} - T_{\text{amb}}) - h_{\text{lam}}(T_{\text{sur}} - T_{\text{amb}}) \\ &= (h - h_{\text{lam}})(T_{\text{sur}} - T_{\text{amb}}) = h_{\text{tur}}(T_{\text{sur}} - T_{\text{amb}}) \end{aligned} \qquad (A5)$$

where $h_{\text{tur}} = h - h_{\text{lam}}$. Since the boundary conditions for $\overline{T}_2(r,z)$ are homogeneous, the nonhomogeneous boundary conditions have secondary effects on effect $\overline{T}_2(r,z)$ and consequently on h_{tur}.

References

[1] Bollen, W., 1949, "Effect of Turbulence on Heat Transfer Coefficient Distribution Around a Cylinder Normal to Air Flow," Master's thesis, Oregon State College, Corvallis, OR.
[2] Zapp, G., Jr., 1950, "The Effect of Turbulence on Local Heat Transfer Coefficient Around a Cylinder Normal to Air Flow," Master's thesis, Oregon State College, Corvallis, OR.
[3] Kestin, J., Maeder, P. F., and Sogin, H. H., 1961, "The Influence of Turbulence on the Transfer of Heat to Cylinders Near the Stagnation Point," Z. Agnew. Math. Phys., **12**, pp. 115–132.
[4] Martin, H., 1977, "Heat and Mass Transfer Between Impinging Gas Jets and Solid Surfaces," Adv. Heat Transfer, **13**, pp. 1–60.
[5] Lowery, G. W., and Vachon, P. I., 1975, "The Effect of Turbulence on Heat Transfer from Heated Cylinders," Int. J. Heat Mass Transf., **18**, pp. 1229–1242.
[6] Simonich, J. C., and Bradshaw, P., 1978, "Effect of Free-Stream Turbulence on Heat Transfer Through a Turbulent Boundary Layer," ASME J. Heat Transfer, **100**, p. 673.
[7] Pedisius, A. A., Kazimekas, P. V. A., and Slanciauskas, A. A., 1979, "Heat Transfer From a Plate to a High-Turbulence Air Flow," Heat Transfer-Sov. Res., **11**(5), p. 125.
[8] Blair, M. F., 1983, "Influence of Free-Stream Turbulence on Turbulent Boundary Layer Heat Transfer and Mean Profile Development: Part II—Analysis of Results," ASME J. Heat Transfer, **105**, p. 41.
[9] Hancock, P. E., and Bradshaw, P., 1983, "The Effect of Free-Stream Turbulence on Turbulent Boundary Layers," ASME J. Fluids Eng., **105**, p. 284.
[10] Maciejewski, P. K., and Moffat, R. J., 1992, "Heat Transfer With Very High Free-Stream Turbulence: Part 1—Experimental Data," ASME J. Heat Transfer, **114**(4), pp. 827–833.
[11] Maciejewski, P. K., and Moffat, R. J., 1992, "Heat Transfer with Very High Free-Stream Turbulence: Part II—Analysis of Results," ASME J. Heat Transfer, **114**(4), pp. 834–839.
[12] Al-Salam, H., Haji-Sheikh, A., and You, S. M., 1996, "Effect of Turbulence on Heat Transfer in Stagnation Flow," J. Thermophys. Heat Transfer, **10**(2), pp. 290–296.
[13] Hoogendoorn, C. J., 1977, "The Effect of Turbulence on Heat Transfer at a Stagnation Point," Int. J. Heat Mass Transf., **20**, pp. 1333–1338.
[14] Gardon, P., and Akfirat, J. C., 1965, "The Role of Turbulence in Determining the Heat-Transfer Characteristics of Impinging Jets," Int. J. Heat Mass Transf., **8**, pp. 1261–1272.
[15] Beck, J. V., Kole, K. D., Haji-Sheikh, A., and Litkouhi, B., 1992, *Heat Conduction Using Green's Functions*, Hemisphere Publishing Corporation, Washington, D.C.
[16] Beck, J. V., Blackwell, B., and St. Clair Jr., C. R., 1985, *Inverse Heat Conduction*, Wiley-Interscience Publication, New York.
[17] Liu, X., Lienhard V, J. H., and Lombara, J., 1991, "Convective Heat Transfer by Impingement of Circular Liquid Jets," ASME J. Heat Transfer, **113**, pp. 571–582.
[18] Brdlik, P. M., and Savin, V. K., 1965, "Heat Transfer Between an Axi-Symmetric Jet and a Plate Normal to the Flow," J. Eng. Phys., **8**, pp. 91–98.
[19] Dup. Donaldson, C., Snedekker, R. S., and Margolis, D. P., 1971, "A Study of Free Jet Impingement: Part 2—Free Jet Turbulent Structure and Impingement Heat Transfer," J. Fluid Mech., **45**, pp. 477–512.

Juan E. Velásquez
e-mail-jvelasquezv@colorquimica.com.co
Instituto de Energía y Termodinámica,
Univ. Pontificia Bolivariana,
Medellín, Colombia

Farid Chejne
e-mail: fchejne@perseus.unalmed.edu.co
Escuela de Procesos y Energía,
Univ. Nacional de Colombia,
Medellín, Colombia

Alan F. J. Hill
Instituto de Energía y Termodinámica,
Univ. Pontificia Bolivariana,
Medellín, Colombia

Mathematical Model and Simulation of a Thermal Diffusion Column

A two-dimensional mathematical model, in stationary state was developed for the separation of species in a thermal diffusion column working with total reflux. The model was applied to a gas mixture of CO_2 *and* N_2*. The existence of convective currents along the column was verified, the separation of species due to the temperature gradient was predicted and the effect of the thermal gradient and of the operation pressures on the composition profiles was analyzed.* [DOI: 10.1115/1.1560150]

Keywords: Heat Transfer, Mass Transfer, Modeling, Natural Convection, Non-Equilibrium

1 Introduction

Irreversible phenomena in nature can act simultaneously [1] in such a way that under certain conditions imperceptible effects become perceptible. A typical example of the phenomena is the separation of a two specie gaseous mixture in two interconnected recipients when a significant temperature difference is produced between them [2]. This irreversible phenomena is known as thermal diffusion, which accompanied by ordinary diffusion, due to concentration gradients, produces heat and mass flows simultaneously.

Substances separation due to temperature gradients, was used first in an efficient way, in 1938, when Klaus Clusius and Gerhard Dickel [3,4] demonstrated that the introduction of a convective laminar flow in a gas mixture, subjected to a temperature gradient, achieves the species separation with high yields. The Clusius–Dickel Thermal Diffusion Column (TDC) (Fig. 1) consists on a vertical tube refrigerated outside by means of water and with a electrical resistance located in its central axis as a heater. Therefore, a radial temperature gradient originates radial thermal diffusion and axial mass convection currents. The thermal diffusion process produces radial species separation and the presence of convective laminar flow causes a longitudinal separation of species. Consequently, an accumulation of the lightest component in the top and the heaviest one in the bottom of the column is normally placed. A qualitative experimental evidence of the operation of the TDC is obtained using a homogeneous mixture of Bromine and Nitrogen [5].

The concentric tubes column, in which the central tube is usually conformed by an electric heating element, is the TDC more commonly used in the separation of gas mixtures [4]. However, the parallel plates TDC is used for liquid mixture separations, because it guaranty a gap less than one mm between the hot wall and the cold one [3].

The TDC can be used to separate mixtures which are difficult or impossible by the common methods, such as distillation and extraction. Recent studies have shown that it can be separated by the above procedure biological solutions and suspensions; aqueous, isotopic and polymeric solutions; organic geometric isomers and organic mixtures (as raw petroleum and mixtures of high molecular weight alcohol), etc. [6–8]. Also, a plant has been designed for the production of high viscosity oil lubricant [9].

Contributed by the Heat Transfer Division for publication in the JOURNAL OF HEAT TRANSFER. Manuscript received by the Heat Transfer Division June 6, 2002; revision received November 1, 2002. Associate Editor: H. Bau.

Since the thermal diffusion process is thermodynamically irreversible, probably it is not an economically profitable process such as other separation methods with high production levels. However, since the TDC is simple, relatively cheap and it can work for long periods of time without supervision, the process can be competitive when small quantities of special substances are produced.

From Clusius and Dickel's TDC developments a lot of studies about the gas mixture behavior in the column have been made. In 1939, Furry, Jones and Onsanger [10] published a theory about the plane wall TDCs by employing kinetic theories to find the fluid properties values. In 1946, Furry and Jones [11] extended the theory in order to apply it to the extreme cylinder TDC (hot filament column). In the following decades, studies were continued to obtain more general and complete models. They included the arbitrary dependence of properties with temperature and the consideration of more realistic kinetic models for gases—Srivastava [12], McInteer and Reisfeld [13], Saxena and Raman [14], among others. Simplified analytic models based on experimental data for the properties in either batch or continuous systems have been developed more recently [15–21]. However, these models are characterized by simplifications that allow easy analytic solutions, but also exclude some important aspects.

More realistic models, with numerical solutions employing computational machines [22,23] to simulate the column behavior and to optimize the design parameters of TDC with flows have been developed. Employing the above models, the pressure operation [24,25], the separation between the surfaces [15,26–28] and the optimal feeding point of columns [29] have been found for continuous columns.

In order to allow a higher species separation efficiency; a lot of column designs have been made. Examples of them are interconnected column systems [27,30–32], inclined columns [31,33,34], rotational columns [35,36], packed columns [35,37], and columns with barriers [38,39].

A new mathematical model for a batch TDC from analytical and numerical data is presented in this paper. The temperature and velocity profiles are evaluated from the analytical solution of the energy and momentum equations due to their simplicity. The concentration profiles are obtained by the numerical solution of the mass conservation equation. The model allows to predict the gaseous mixture pattern of several variables at the inside of a thermal diffusion column without flow. Also, the model can predict the composition inversion due to convective phenomena.

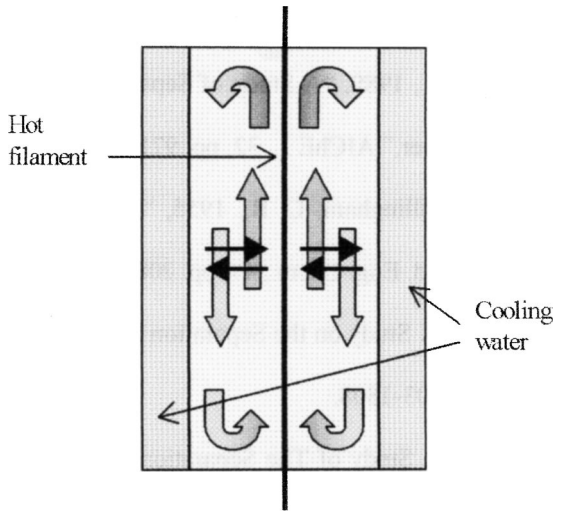

Fig. 1 Clusius-Dickel Column

2 Mathematical Model

A two-dimensional and time independent mathematical model, for describing the separation of a binary gas mixture in a TDC, subjected to a temperature gradient between two cylindrical surfaces (Fig. 2) was developed.

The temperature difference between the walls of the column generates a radial temperature profile, which can be obtained by solving the energy conservation equation. The temperature and the global *z*-direction velocity are only function of *r*-dimension due to a fully developed flow and the assumption that the thermal conductivity is a constant. If it is only considered a time independent problem, from the energy balance it can be obtained the following expression

$$-\left(\frac{1}{r}\frac{\partial}{\partial r}(rq_r)+\frac{1}{r}\frac{\partial q_z}{\partial z}\right)+\mu\left(\frac{\partial V_Z}{\partial r}\right)^2=0 \tag{1}$$

Assumptions that are made in order to simplify the above equation are that the effects of viscous dissipation are negligible since the velocity in natural convection processes is low; the contribution of the Dufour heat (heat flow due to concentration gradients) to heat transfer rate is small and it could be considered that it does not have an important effect in the temperature profile; temperature is not exactly equal along the whole hot wall of the TDC [18], but it may be assumed as constant in *z*-direction since the column is very long compared with its width. With the previous considerations, Eq. (1) can be written as

$$\frac{d}{dr}\left(rk\frac{dT}{dr}\right)=0 \tag{2}$$

subject to the following boundary conditions

$$r=R_C \quad T=T_C \tag{3}$$

$$r=R_H \quad T=T_H \tag{4}$$

where the sub-indexes *H* and *C* are used to denote the hot and the cold walls respectively.

By integrating Eq. (2) and considering the thermal conductivity at mean temperature and composition, the temperature profile is obtained

$$T=\frac{T_H-T_C}{\ln\left(\frac{R_H}{R_C}\right)}\ln\left(\frac{r}{R_C}\right)+T_C \tag{5}$$

which gives the temperature at any point in the column.

Due to the existence of the *r*-direction temperature profile, a convective flow in *z*-direction is generated. The velocity profile can be obtained by solving the momentum conservation equation

$$\frac{1}{r}\frac{d}{dr}\left(r\mu\frac{dV_Z}{dr}\right)-\rho g-\frac{dP}{dz}=0 \tag{6}$$

The effects at the column ends leading to a two-dimensional profile are neglected, because they appear only in a narrow region [18].

The pressure gradient may be obtained by considering the whole system at average temperature ($\overline{T}$) and gas composition ($\overline{x}$) and at zero mean velocity

$$\frac{dP}{dz}=-\overline{\rho}g \tag{7}$$

where $\overline{\rho}$ is the fluid mean condition density. In natural convection, the velocity gradients are only generated by the existence of temperature or a non-homogeneous composition field and the fluid movement is generally very slow. Eq. (7) is a good approach, also for the fluid in movement [40].

The density is a function of temperature and composition, and its dependence can be obtained by means of an expansion in Taylor series around the mean Temperature ($\overline{T}$) and composition ($\overline{w}$) values. Rejecting the second and greatest terms for the temperature and composition variable, the density can be expressed as

$$\rho=\overline{\rho}-\overline{\rho}\overline{\beta}(T-\overline{T})-\overline{\rho}\overline{\zeta}(w-\overline{w}) \tag{8}$$

where $\overline{\beta}$ is the thermal expansion coefficient and $\overline{\zeta}$ is a coefficient that represent the density variation with respect to the composition (analogous to $\overline{\beta}$) calculated at mean conditions.

From. (7) and (8) in (6)

$$\frac{d}{dr}\left(\mu r\frac{dV_Z}{dr}\right)+\overline{\rho}\overline{\beta}g(T-\overline{T})r+\overline{\rho}\overline{\zeta}g(w-\overline{w})r=0 \tag{9}$$

subjected to the following boundary conditions

$$r=R_H \quad V_Z=0 \tag{10}$$

$$r=R_C \quad V_Z=0 \tag{11}$$

It can be seen from (9) that the buoyancy force depends on mean temperature and mass composition. In some cases the buoyancy force is positive and in others it is negative. The last term in the Eq. 9 can be omitted because the solute buoyancy force is negligible to the temperature one in a thermal diffusion column. Sup-

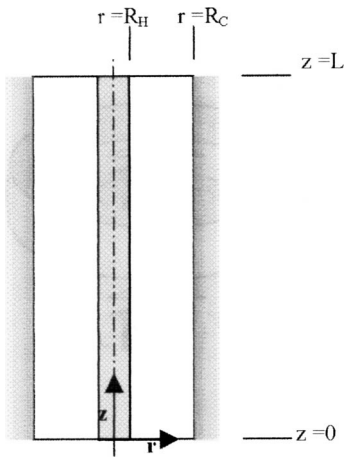

Fig. 2 Concentric Tubes TDC Scheme

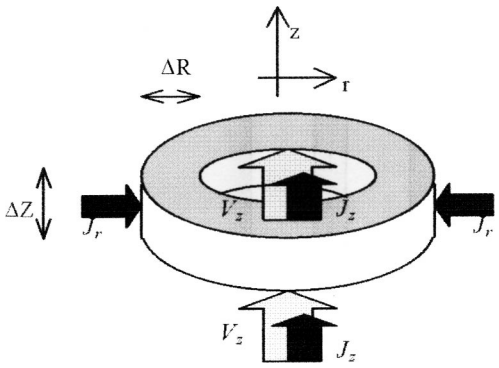

Fig. 3 Control volume for mass balance

posing the viscosity as a constant and with the temperature profile (Eq. 5), Eq. (9) may be integrated to obtain an expression for the velocity profile

$$V_Z = V_m V_Z^* \tag{12}$$

$$V_m = \frac{\overline{\rho}\overline{\beta} g}{4\mu}(T_H - T_C)(R_C^2 - R_H^2) \tag{13}$$

$$V_Z^* = \left(\frac{r^2 - R_C^2}{R_C^2 - R_H^2}\right)\frac{\ln(r/R_H)}{\ln(R_C/R_H)} + \left(\frac{R_H^2 - r^2}{R_C^2 - R_H^2}\right)\frac{1}{\ln(R_C/R_H)} + \frac{\ln(r/R_H)}{(\ln(R_C/R_H))^2} - \frac{T_H - \overline{T}}{T_H - T_C}\left(\frac{r^2 - R_H^2}{R_C^2 - R_H^2} - \frac{\ln(r/R_H)}{\ln(R_C/R_H)}\right) \tag{14}$$

The net mass flow in each cross section is zero, since there is no mass accumulation and the stationary state must be satisfied. Therefore,

$$\int_{R_H}^{R_C} \rho V_Z r\, dr = 0 \tag{15}$$

Substituting Eqs. (12) to (14) in (15), an equation for the mean temperature is found. In order to solve the integral, the density is considered as a constant and a numerical method is used.

To obtain the concentration profile of the heaviest component (*i*) along the column, a mass balance on a control volume in a ring shape is made (Fig. 3)

$$\frac{1}{r}\frac{\partial}{\partial r}(r j_r) + V_Z \frac{\partial \rho_i}{\partial z} + \frac{\partial j_z}{\partial z} = 0 \tag{16}$$

The mass diffusive flows are given by

$$j_r = -\rho D \frac{\partial w_i}{\partial r} - \frac{\rho D^T}{T}\frac{dT}{dr} \tag{17}$$

$$j_z = -\rho D \frac{\partial w_i}{\partial z} \tag{18}$$

Substituting Eqs. (17) and (18) in (16)

$$\frac{1}{r}\frac{\partial}{\partial r}\left(\rho D r \frac{\partial w_i}{\partial r}\right) + \frac{1}{r}\frac{\partial}{\partial r}\left(\rho D^T r \frac{d\ln T}{dr}\right) - V_Z\frac{\partial \rho_i}{\partial z} + \frac{\partial}{\partial z}\left(\rho D \frac{\partial w_i}{\partial z}\right) = 0 \tag{19}$$

Equation (19) can be written in a different way using the following dimensionless parameters

$$W^* = \frac{w_i - w_{\sup}}{w_{\inf} - w_{\sup}}, \quad T^* = \frac{\ln T - \ln T_C}{\ln T_H - \ln T_C}, \quad Z^* = \frac{z}{L},$$
$$R^* = \frac{r}{R_C}, \quad \rho^* = \frac{\rho}{\rho_{i-C}}, \quad D^* = \frac{D}{D_H}, \quad D_T^* = \frac{D^T}{D_H^T} \tag{20}$$

where $w_{\sup}$, $w_{\inf}$ are respectively the mass fractions of the *i*-component at the top and bottom end of the column, ρ_{i-C} is the density of the *i*-component at the cold wall, D_H is the diffusivity at the hot wall and D_H^T is the maximum thermal diffusion coefficient at the hot wall.

With the expressions (20), the differential Eq. (19) can be written as follows

$$\frac{1}{R^*}\frac{\partial}{\partial R^*}\left(\rho^* D^* R^* \frac{\partial W^*}{\partial R^*}\right) + \frac{Cl}{R^*}\frac{\partial}{\partial R^*}\left(\rho^* D_T^* R^* \frac{dT^*}{dR^*}\right) - PeGV_Z^*\frac{\partial(\rho^*(W^* + W_m))}{\partial Z^*} + G^2 D^* \frac{\partial}{\partial Z^*}\left(\rho^* \frac{\partial W^*}{\partial Z^*}\right) = 0 \tag{21}$$

In Eq. (21) four dimensionless numbers appear. The first one is the Clusius Number in honor to one of the inventors of the thermal diffusion column and it is given by

$$Cl = \frac{D_H^T}{D_H}\frac{\ln(T_H/T_C)}{(w_{\inf} - w_{\sup})} \tag{22}$$

The Clusius Number provides information about how the separation of a binary mixture is executed in a thermal diffusion column. The second dimensionless number is the Peclet Number

$$\mathrm{Pe} = \mathrm{Gr}\cdot Sc = \frac{V_m R_C}{\nu}\frac{\nu}{D_H} \tag{23}$$

where Gr is the Grashof Number, Sc Schmidt Number, and ν the Cinematic viscosity. The Peclet number provides information about the relation between convective and diffusive forces.

The other numbers are a geometric and a separation factors given by

$$G = \frac{R_C}{L}, \quad W_m = \frac{w_{\sup}}{w_{\inf} - w_{\sup}} \tag{24}$$

The boundary conditions to solve the differential equation are

$$r = R_H \ \text{ or } \ R^* = \frac{R_H}{R_C}, \quad j_r = 0 \tag{25}$$

$$r = R_C \ \text{ or } \ R^* = 1, \quad j_r = 0 \tag{26}$$

$$z = 0 \ \text{ or } \ Z^* = 0, \quad j_z = 0 \tag{27}$$

$$z = L \ \text{ or } \ Z^* = 1, \quad j_z = 0 \tag{28}$$

With the above boundary conditions, the solution of the model is not possible because in the system solution any composition value could be true. Then, Eqs. (27) and (28) must be in terms of known composition values at the neighborhood of the end and the top of the column. These values can be obtained from separation relations taken from the literature [3,4,15]. In consequence,

$$z = 0 \ \text{ or } \ Z^* = 0, \quad w_i = w_{\inf} \ \text{ or } \ W^* = 1 \tag{29}$$

$$z = L \ \text{ or } \ Z^* = 1, \quad w_i = w_{\sup} \ \text{ or } \ W^* = 0 \tag{30}$$

Additionally, it is necessary some relationships among properties, i.e., for the diffusivity

$$D = D_o\left(\frac{T}{T_o}\right)^{3/2}\left(\frac{P_o}{P}\right) \tag{31}$$

where D_o is the reference diffusivity at temperature T_o and pressure P_o.

For the thermal diffusion coefficient,

$$D^T = \alpha_T D w_i (1 - w_i) \tag{32}$$

where α_T is a thermal diffusion factor which is a function of temperature

$$\alpha_T = a - \frac{b}{T} \tag{33}$$

where a and b are experimental constants that depend on the type of the gaseous binary mixture and on pressure. Further a and b are practically independent of composition [3].

The density can be expressed as a function of temperature and molecular weight by using the ideal gas law, which is valid at low pressures

$$\rho = \frac{PM}{R_g T} \tag{34}$$

where R_g is the universal gas constant.

The dependence of the viscosity of a pure gas with temperature can be expressed by a third degree polynomial expression

$$\mu = a + bT + cT^2 + dT^3 \tag{35}$$

and the dependence with pressure is assumed to be negligible.

For a gas mixture, the viscosity can be expressed by means of the Wilke's experimental correlation [40]

$$\mu_{\text{mixture}} = \sum_{i=1}^{2} \frac{x_i \mu_i}{\Sigma_{j=1}^{2} x_i \Phi_{ij}} \tag{36}$$

where

$$\Phi_{ij} = \frac{1}{8^{0.5}} \left(1 + \frac{M_i}{M_j}\right)^{-0.5} \left[1 + \left(\frac{\mu_i}{\mu_j}\right)^{0.5} \left(\frac{M_j}{M_i}\right)^{0.25}\right]^2 \tag{37}$$

and i, j denote the chemical species which are presents.

3 Numerical Solution

Differential Eq. (21) together with the boundary conditions (25), (26), (29), and (30) can be solved for the mass fraction by using the finite volume method [41]. It consists of dividing the system in small control volumes which do not overlap on each volume, in such a way that a nodal point exists inside each volume. The differential equation is integrated on each one of the volumes.

The thermal diffusion column (Fig. 2) can be divided in finite volumes of a ring shape (Fig. 3) with their nodal points settled at the shell center except the top and bottom ones (boundary nodes).

Integrating Eq. (21) over the control volume and then applying Gauss divergence theorem over some terms in order to find a new surface integral, the Eq. *can* be discretized at each nodal point as follows

$$A_P W_P^* = A_E W_E^* + A_W W_W^* + A_N W_N^* + A_S W_S^* + B \tag{38}$$

where,

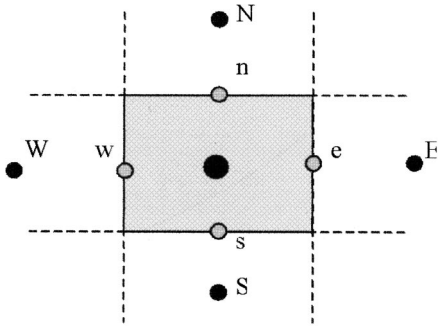

Fig. 4 Selected mesh scheme

Table 1 Thermo-physical properties of the gas mixture $CO_2'N_2$

Property	Correlation
Viscosity CO_2, μ_{CO_2}(N s/m^2)	$a=2.2460e-6$, $b=4.0315e-8$, $c=9.1141e-12$, $d=-1.2893e-14$.
Viscosity N_2, μ_{N_2}(N s/m^2)	$a=1.5696e-6$, $b=6.4705e-8$, $c=-3.8999e-11$, $d=1.2732e-14$.
Diffusivity, D(m^2/s)	$D_o=1.67e-5$ m^2/s, $T_o=298$ K, $P_o=1$ atm.
Thermal diffusion factor, α_T	$a=0.09870$, $b=17.7433$.

$$A_E = \rho_e^* D_e^* R_e^* \frac{\Delta Z^*}{\Delta R^*} \tag{39}$$

$$A_W = \rho_w^* D_w^* R_w^* \frac{\Delta Z^*}{\Delta R^*} \tag{40}$$

$$A_N = PeG\rho_n^* R_P^* \Delta R^* \max(-V_Z^*, 0) + G^2 \rho_n^* D_n^* R_P^* \frac{\Delta R^*}{\Delta Z^*} \tag{41}$$

$$A_S = PeG\rho_s^* R_P^* \Delta R^* \max(V_Z^*, 0) + G^2 \rho_s^* D_s^* R_P^* \frac{\Delta R^*}{\Delta Z^*} \tag{42}$$

$$A_P = A_E + A_W + G^2 \rho_n^* D_n^* R_P^* \frac{\Delta R^*}{\Delta Z^*} + G^2 \rho_s^* D_s^* R_P^* \frac{\Delta R^*}{\Delta Z^*} + PeG\rho_n^* R_P^* \Delta R^* \max(V_Z^*, 0) + PeG\rho_s^* R_P^* \Delta R^* \max(-V_Z^*, 0) \tag{43}$$

$$B = ClC_e^* D_{Te}^* R_e^* \frac{\Delta Z^*}{\Delta R^*}(T_E^* - T_P^*) + ClC_w^* D_{Tw}^* R_w^* \frac{\Delta Z^*}{\Delta R^*}(T_W^* - T_P^*) - PeG\rho_n^* R_P^* \Delta R^* V_Z^* W_m + PeG\rho_s^* R_P^* \Delta R^* V_Z^* W_m \tag{44}$$

The sub-indexes E, W, N, S, and P denote east, west, north, south and central nodes in the finite volume respectively, while e, w, n, and s denote east, west, north and south nodes touching each finite volume surface respectively (Fig. 4). The operator max compares several real inputs in order to get the biggest value among them.

The convective term in Eqs. (38) to (44) is approached by means of the upwind scheme [41], in which is assumed that the value of the composition in a finite volume surface has the same value that the corresponding location at the contiguous up stream nodal point.

Gas compositions inside the column can be calculated at the nodal points by solving the algebraic equation system once the original differential equation is discretized.

4 Results

A software developed in FORTRAN 90 was employed in order to solve the mathematical model for a gaseous mixture of CO_2/N_2. The data for viscosity, diffusivity, and for the thermal diffusion factor were taken from Incropera and DeWitt [42],

Table 2 Thermal diffusion column Operation conditions data

Parameter	Value
T_H (K)	900.0
T_C (K)	300.0
R_H (m)	0.001
R_C (m)	0.006
L (m)	1.0
w_{sup}	0.10
w_{inf}	0.90

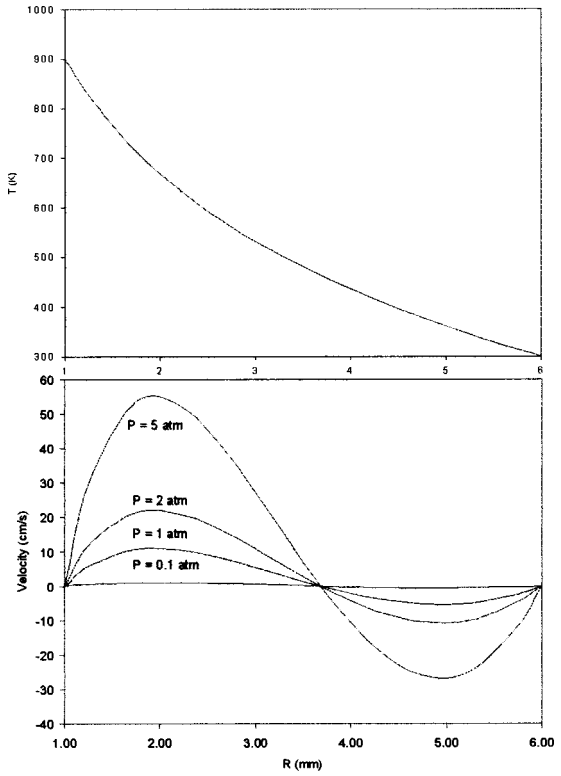

Fig. 5 Temperature and velocity profiles

Hinex and Maddox [43] and from Grew and Ibbs [3] respectively. The thermophysical properties of the mixture are presented in Table 1 and the operation conditions in Table 2.

The temperature and velocity profiles are shown in Fig. 5. A variation of temperature is observed along the radius, and the highest slopes are presented in the neighborhood of the hot surface ($r = 1$ mm). Velocity only changes with radius and not with height. The inside fluid portion flows up and the outside fluid flows down, producing convective streams between the bottom and the top ends.

It is noticed that as the pressure inside the tube increases, the speed of the ascending fluid next to the hot surface is proportionally increased. The same occurs with the descending velocity next to the cold surface.

In Fig. 6 the concentration profiles with the height (at the left) and the radius (at the right) of the column, for pressures of 0, 1 atm (at the bottom) and 5 atm (at the top) are shown.

A variation of the mass fraction is seen with the radius and the height, demonstrating the separation due to the thermal diffusion and the convective effects.

The higher effects of thermal diffusion are at low pressures, in which the heavy component (CO_2) is concentrated in the cold wall (Fig. 7). At high pressures the convective effects cause the heavy component to concentrate on the hot wall because the fluid circulation is increased (Fig. 5). Although, the effect of profile inversion due to an alpha sign change has been reported in the literature [3], for the analyzed gas mixture the effect is caused by the convective flow.

When the thermal diffusion phenomena controls the process, the concentration of the heavy component varies smoothly throughout the radius of the tube. An opposite situation is observed when the convective phenomena controls the process; the heaviest species concentration varies in appreciable way, mainly

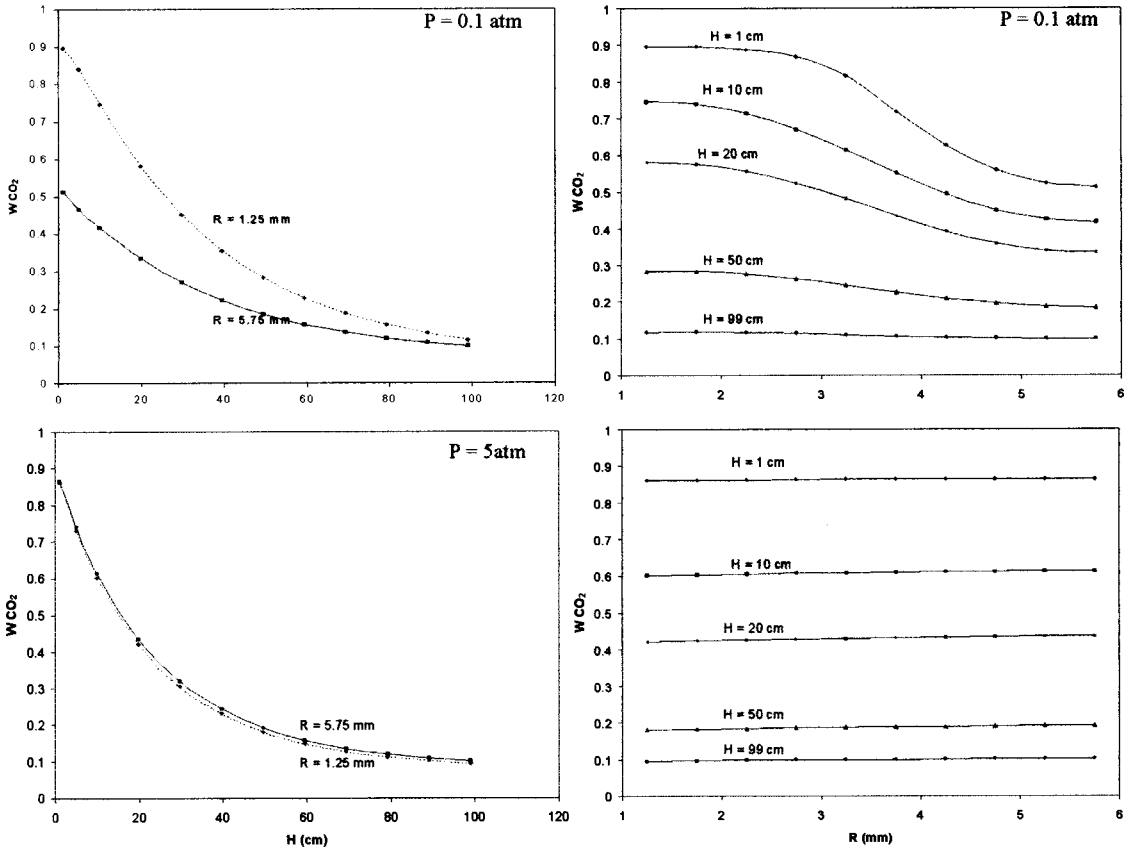

Fig. 6 Mass fraction profiles

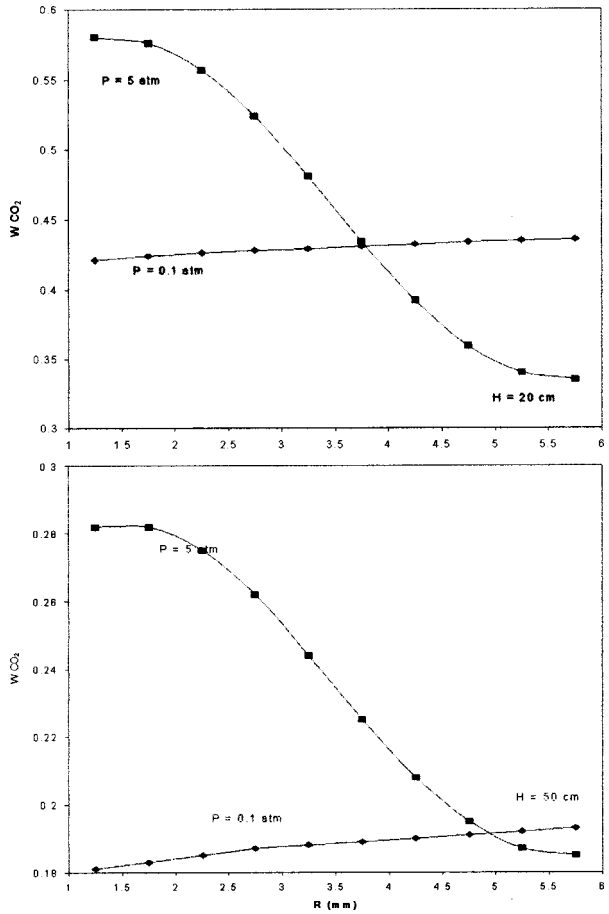

Fig. 7 Effect of the pressure in the mass fraction profiles

in the bottom of the column ($z<20$ cm). Also, it is observed that the inflection point of the concentration profile happens exactly in the inflection point of the velocity.

Due to the drastic change in the gas composition with the radius at high pressures, the gaseous mixture is only partially purified in the neighborhood of the column bottom. For example, at 5 cm of height, the CO_2 average mass fraction at a pressure of 5 atm is 0, 65, whereas at a pressure of 0, 1 atm it is 0, 75. So, the separation is more efficient at low pressures. However, if the column operates at low pressures, the processed amount of gas is smaller. Then, the optimal working pressure is selected on the bases of two criteria: required purity and quantity of processed gas.

Similarly to the operation pressure, the mathematical model could be used to determine under specific conditions of separation (gas concentrations at the column ends), other optimal parameters of operation and design, as temperature gradient, diameters and column height.

In order to find the point where the convective and diffusive phenomena are equally important, Fig. 8 was constructed. In this figure a minimum of the heavy species concentration is observed at a pressure near 1 atm, showing that the accumulation of the heavy species at the bottom of the column is greater than at other pressures. Due to the existence of a minimum, at this value of the pressure the convective phenomenon starts to control the phenomena.

5 Conclusions

A stationary two-dimensional model was developed to describe the separation of a gas mixture subjected to a temperature gradient. The model allows to determine optimal operation parameters and design of a TDC from conditions of required gases purity.

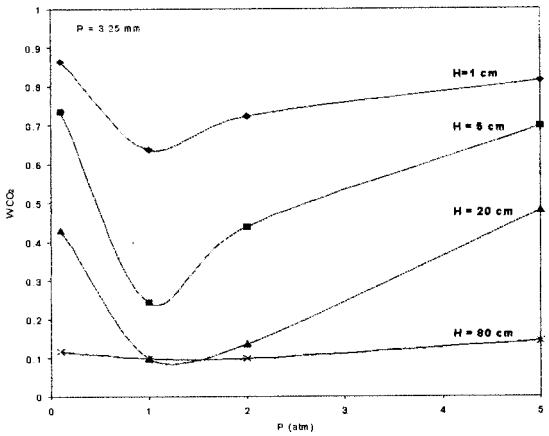

Fig. 8 Mass fraction versus pressure at different heights along the column

In situations at low pressures (less than 1 atm) the lightest specie, in this case N_2, is concentrated in the warm zone and the weightiest specie, in this case CO_2, is concentrated in the cold zone. At high pressures (over 1 atm), an opposite situation is observed, but a separation of the species is placed.

Acknowledgments

The authors wish to acknowledge W. Flórez (Energy and Thermodynamic Institute) for giving advices in the numerical solution of the model. Also, we wish to thank COLCIENCIAS (Colombian Government Sponsor), COLORQUIMICA S.A. and Universidad Pontificia Bolivariana for supporting this research.

Nomenclature

- A = term of the discretized equations
- a = parameter of the equation for the thermal diffusion factor and of the correlation for the viscosity [=] $N\cdot s/m^2$
- B = term of the discretized equations
- b = parameter of the equation for the thermal diffusion factor and of the correlation for the viscosity [=] $N\cdot s/m^2\cdot K$
- c = parameter of the correlation for the viscosity [=] $N\cdot s/m^2\cdot K^2$
- Cl = Clusius number
- D = coefficient of ordinary diffusion [=] m^2/s
- d = parameter of the correlation for the viscosity [=] $N\cdot s/m^2\cdot K^3$
- D^T = thermal diffusion coefficient [=] m^2/s
- D^* = dimensionless ordinary diffusion coefficient
- D_T^* = dimensionless thermal diffusion coefficient
- G = dimensionless geometric number of the column
- g = gravity acceleration [=] m/s^2
- Gr = Grashof number
- j_r = radial component of the diffusive flow [=] $kg/m^2\cdot s$
- j_z = axial component of the diffusive flow [=] $kg/m^2\cdot s$
- k = thermal conductivity at average conditions [=] $W/m\cdot K$
- L = thermal diffusion column height [=] m
- P = pressure [=] Pa
- Pe = Peclet number for mass transfer with natural convection
- q_r = radial component of the heat density flux vector [=] $J/m^2\cdot s$
- q_z = axial component of the heat density flux vector [=] $J/m^2\cdot s$
- R = radius [=] m

r = radial coordinate
R_g = universal gas constant [=] J/kmol·K
R^* = dimensionless normalized radial coordinate
Sc = Schmidt number
T = temperature [=] K
t = time [=] s
$\overline{T}$ = average temperature [=] K
T^* = dimensionless normalized temperature
V = Velocity vector [=] m/s
V_m = Parameter of the velocity profile [=] m/s
V_Z = Axial component of the velocity vector [=] m/s
V_Z^* = Dimensionless parameter of the velocity profile
w = Mass fraction
$\overline{w}$ = Average mass fraction
W_m = Dimensionless mass fraction
W^* = Normalized molar fraction
z = Axial coordinate
Z^* = Dimensionless normalized axial coordinate

Greek Letters

α_T = thermal diffusion factor
β = thermal expansion coefficient at average conditions [=] 1/K
Φ = parameter of the viscosity correlation
μ = absolute or dynamic viscosity [=] N·s/m^2
ν = cinematic Viscosity [=] m^2/s
ρ = density [=] kg/m^3
ρ^* = dimensionless density
$\overline{\rho}$ = density at average conditions [=] kg/m^3
ζ = coefficient of density variation with respect to the composition

Subscripts

C = cold wall
E = east node in discretized equations
e = east bound in discretized equations
H = hot wall
inf = bottom of the column
N = north node in discretized equations
n = north bound in discretized equations
P = central node in discretized equations
S = south node in discretized equations
s = south bound in discretized equations
sup = top of the column
W = west node in discretized equations
w = west bound in discretized equations

References

[1] Onsanger, L., 1931, Phys. Rev., **37**, p. 405.
[2] Prigogine, I., 1988, *Introduction To Thermodynamics Of Irreversible Processes*, 3 ed., Interscience Publishers, USA.
[3] Grew, K. E., and Ibbs T. L., 1952, *Thermal Diffusion in Gases*, Cambridge University Press, Cambridge UK.
[4] Vasaru, G., Müller, G., Reinhold, G., and Fodor, T., 1969, *The Thermal Diffusion Column*, Veb Deutscher Verlag Der Wissenschaften, Berlin.
[5] Español, C., 1964, ''La Difusión Térmica en Gases como Método de Separación de Isótopos Estables,'' Ciencia y Técnica, **133**, pp. 329–353.
[6] Jones, A. L., and Milberger, E. C., 1953, ''Separation of Organic Liquid Mixtures by Thermal Diffusion,'' Ind. Eng. Chem., **45**(12), pp. 2689–2696.
[7] Vasaru, G., and Bratu, C., 1988, ''Thermal Diffusion Column: Status and Prospects,'' Rev. Roum Physiol., **33**, pp. 977–980.
[8] Muller, G., and Vasaru, G., 1988, ''The Clusius-Dickel Thermal Diffusion Columna—50 Years After its Invention,'' Isotopenpraxis, **24**(11–12), pp. 455–464.
[9] Jones, A. L., and Foreman, R. W., 1952, ''Liquid Thermal Diffusion of Tall Oil,'' Ind. Eng. Chem., **44**, pp. 2249–2253.
[10] Furry, W. H., Jones, R. C., and Onsanger, L., 1939, Phys. Rev., **55**, p. 1083.
[11] Furry, W. H., and Jones, R. C., 1946, Phys. Rev., **69**, p. 459.
[12] Srivastava, B. N., and Srivastava, R. C., 1954, Physica, **20**, p. 237.
[13] McInteer, B. B., and Reisfled, M. J., 1960, Physics, **33**, p. 570.
[14] Saxena, S. C., and Raman, S., 1962, Rev. Mod. Physics, **34**, p. 252.
[15] Leyarovski, J. K., Georgiev, J. K., and Zahariev, A. L., 1990, ''Influence of the Thermodynamic Parameters and Geometry on the Degree of Separation and Energy Consumption in a Gas Thermal Diffusion Column under Static Conditions,'' Sep. Sci. Technol., **25**, pp. 557–580.
[16] Yamamoto, I., and Kanagawa, A., 1990, ''Approximate Column Constants Expressed in Terms of Design Parameters for Hot Wire Thermal Diffusion Column,'' J. Nucl. Sci. Technol., **27**, pp. 48–55.
[17] Yeh, H. M., and Lin, W. H., 1991, ''Thermal Diffusion in an Ideal Column,'' Sep. Sci. Technol., **26**, pp. 395–407.
[18] Yamamoto, I., Shibata, A., and Kanagawa, A., 1994, ''Simple Model for Prediction of Changes in Hot Wire Temperature Caused by Convection at Top and Bottom of Thermal Diffusion Column,'' J. Nucl. Sci. Technol., **31**, pp. 222–227.
[19] Yeh, H. M., Ho, C. D., Huang, W. K., and Yan, Y. L., 1999, ''Simplified Analysis of the Enrichment of Heavy Water in a Batch Thermal Diffusion Column,'' Sep. Sci. Technol., **16**, pp. 205–211.
[20] Georgiev, J. K., and Zahariev, A. L., 1992, ''Degree of Separation in a Gas Thermal Diffusion Column Depending on the Parameters of the Gas Mixture, the Geometry, and the Column Productivity,'' Sep. Sci. Technol., **27**, pp. 717–740.
[21] Georgiev, J. K., and Zahariev, A. L., 1992, ''Optimization and Calculation of Gas Thermal Diffusion Column,'' Sep. Sci. Technol., **27**, pp. 917–936.
[22] Yamamoto, I., Kanoh, K., and Kanagawa, A., 1985, ''Numerical Solution of Two-Dimensional Axisymmetric Free Convection within Isotope Separating Thermal Diffusion Column,'' J. Nucl. Sci. Technol., **22**, pp. 469–483.
[23] Yamamoto, I., Yamagishi, K., and Kanagawa, A., 1987, ''Numerical Calculation of Concentration Profiles within Thermal Diffusion Column with Continuous Feed and Draw-Offs,'' J. Nucl. Sci. Technol., **24**, pp. 393–403.
[24] Yamamoto, I., Makino, H., and Kanagawa, A., 1990, ''Optimum Pressure for Total—Reflux Operated Thermal Diffusion Column for Isotope Separation,'' J. Nucl. Sci. Technol., **27**, pp. 149–156.
[25] Yamamoto, I., and Kanagawa, A., 1993, ''Similarity in Pressure Dependence among Separation Factors of Thermal Diffusion Column in Total—Reflux Operation,'' J. Nucl. Sci. Technol., **30**, pp. 831–833.
[26] Yeh, H. M., 1994, ''The Optimum Plate—Spacing for the Best Performance in Flat—Plate Thermal Diffusion Columns,'' Chem. Eng. Sci., **49**, pp. 2027–2029.
[27] Yeh, H. M., 1995, ''The Best Performance of Inclined Flat—Plate Thermal Diffusion Columns,'' Seperations Technology, **5**, pp. 115–120.
[28] Yeh, H. M., 1998, ''The Optimum Plate Aspect Ratio for the Best Performance in a Flat—Plate Thermal Diffusion Column with Transverse Sampling Streams,'' Sep. Sci. Technol., **33**, pp. 227–240.
[29] Yamamoto, I., Makino, H., and Kanagawa, A., 1995, ''Optimum Feed Point for Isotope Separating Thermal Diffusion Column,'' J. Nucl. Sci. Technol., **32**, pp. 200–205.
[30] Yeh, H. M., and Yang, S. C., 1987, ''Thermal Diffusion of the Frazier Scheme with Columns Inclined for Improved Performance,'' J. Chin. Inst. Chem. Eng., **18**, pp. 249–254.
[31] Yeh, H. M., 1994, ''Thermal Diffusion in Inclined Flat—Plate Columns of the Frazier Scheme,'' Can. J. Chem. Eng., **72**, pp. 815–821.
[32] Yeh, H. M., 1999, ''Optimum Design of Inclined Frazier Scheme Thermal Diffusion Columns for Enriching Heavy Water,'' Sep. Pur. Technol., **17**, pp. 243–247.
[33] Chueh, P. L., and Yeh, H. M., 1967, ''Thermal Diffusion in a Flat—Plate Column Inclined for Improved Performance,'' AIChE J., **13**, pp. 37–41.
[34] Yeh, H. M., Tsai, S. W., and Lin, C. S., 1989, ''A Study of Separation Efficiency in Thermal Diffusion Columns with Permeable Vertical Barrier,'' AIChE J., **32**, pp. 971–980.
[35] Sullivan, L. J., Ruppel, T. C., and Willingham, C. B., 1955, ''Rotary and Packed Thermal Diffusion Fractionating Columns for Liquids,'' Ind. Eng. Chem., **47**, pp. 208–212.
[36] Yeh, H. M., and Cheng, S. M., 1973, ''A Study on the Separation Efficiency of Rotary Thermal Diffusion Columns,'' Chem. Eng. Sci., **28**, pp. 1803–1808.
[37] Yeh, H. M., and Chu, T. Y., 1974, ''A Study of The Separation Efficiency of Continuous Type Packed Thermal Diffusion Columns,'' Chem. Eng. Sci., **29**, pp. 1421–1425.
[38] Yeh, H. M., 1989, ''Separation Theory of an Inclined Thermal Diffusion Column with Fixed Operating Expense,'' J. Chin. Inst. Chem. Eng., **20**, pp. 263–267.
[39] Tsai, S. W., and Yeh, Y. M., 1989, ''Improvement in Separation of the Batch Type Thermal Diffusion Column with Impermeable Barriers Inserted Between the Plates,'' Can. J. Chem. Eng., **67**, pp. 589–594.
[40] Bird, R. B., Stewart, W. E., and Lightfoot, E. N., 1996, *Fenómenos de Transporte*, Reverté, México.
[41] Versteeg, H. K., and Malalasekera, W., 1995, *An Introduction to Computational Fluid Dynamics the Finite Volume Method*, Longman, England.
[42] Incropera, F. P., and DeWitt, D. P., 1999, *Fundamentos de Transferencia de Calor*, Prentice Hall, México.
[43] Hines, A. L., and Maddox, R. N., 1987, *Transferencia de Masa: Fundamentos y Aplicaciones*, Prentice Hall, México.

Integral Solutions for Transient Temperature Profiles in Stably-Stratified Open Enclosures

K. O. Homan
e-mail: khoman@umr.edu
Assoc. Member ASME,
Department of Mechanical and Aerospace Engineering, and Engineering Mechanics,
University of Missouri-Rolla,
Rolla, MO 65409-0050

The stably-stratified filling of an enclosure produces an interfacial layer, or thermocline, separating the hot and cold fluid volumes which is transported through the vessel with the bulk flow. The evolution of this interfacial layer is characterized by profile asymmetries and growth rates not explained by simple molecular diffusion. The present paper presents integral solutions to the horizontally-averaged energy equation with variable diffusivities exhibiting these same characteristics. The formulation requires only two parameters in addition to those of the uniform diffusivity case. The solutions are compared to published data to illustrate determination of the empirical constants and show that key characteristics of the model, specifically a constant fill-line temperature and symmetric growth rates, are satisfied for a range of moderate flow rates. At higher flow rates, the layers are seen to exhibit an increasingly higher degree of growth rate asymmetry.
[DOI: 10.1115/1.1527911]

Keywords: Enclosure Flows, Heat Transfer, Mixed Convection, Storage, Transient

Introduction

Buoyant convection in enclosures encompasses a wide variety of applications and has traditionally focused on the steady-state behavior of closed systems, that is, systems for which there is no mass flow through the enclosure. For such systems, the energy transfer to and from the enclosure provides the only driving mechanism for the internal flow. Several comprehensive reviews of the related research are available [1,4,5,21,22] including a review of closed systems with time-dependent boundary conditions by Hyun [13].

The present focus is on a related but distinct class of problems for which the enclosure is open and the internal flow is driven through a combination of mass and energy flows, i.e., mixed convection. This class of problems is encountered in applications such as thermal energy storage [6], building ventilation [16], reservoir flows [27], and electronic equipment [8]. Although the steady-state behavior is of primary interest in several of these applications, only the transient behavior is of interest in thermal energy storage devices since both the charging and discharging processes are inherently transient. The optimal performance of these devices depends, in turn, on the transient behavior as shown for fully-mixed storage storage vessels [2,3,14,20]. Interestingly, for perfectly-stratified behavior in which there is no thermal contact between the hot and cold fluid volumes, Krane and Krane [15] have shown that optimal performance has no dependence on the time of operation. However, since real thermal storage systems invariably exhibit a significant degree of thermal contact between the fluid volumes, as evidenced by the presence of a thermocline, the optimal performance depends intimately on the evolution of the thermal contact.

Despite the ubiquity of liquid-sensible thermal storage applications, only a relatively small number of simplified models exist due to the difficulty of determining suitable characterizations for the multi-dimensional, thermal mixing effects. Zurigat et al. [30] have described a numerical model based on the one-dimensional convective energy equation with an eddy diffusivity fixed in time, but varied over the height of the vessel. Truman et al. [24] introduced a numerical model which accounted for mixing effects by averaging nodal temperatures over a fraction of the tank height. In each case, the difficulty of predicting the temperature profile evolution over the filling process was noted.

In the present work, integral solutions to the horizontally-averaged energy equation with non-uniform and time-dependent diffusivities have been developed which reproduce observed transient behaviors. The model predictions are compared with several sources of published data to illustrate their determination and quantify their variation with key flow parameters.

Formulation

Consider a vertical vessel of height H and cross-sectional area A_c with an inflow of constant temperature fluid occurring at the lower boundary of the vessel and an outflow at the upper boundary occurring at an identical rate so that the mass inventory is constant. Provided it is the low temperature fluid which flows into the lower portion of the vessel or the higher temperature fluid into the upper portion of the vessel, the temperature field in the enclosure will be stably stratified. The flowfield observed in such an enclosure is dictated by the geometry of the respective inlet and outlet diffusers, the vessel geometry, the imposed through-flow rate, and the stabilizing effect of gravity. Even at relatively low mass flow rates both the velocity and the temperature field are multi-dimensional and time-dependent. A schematic of the vessel geometry and a representative vertical temperature profile are illustrated in Fig. 1.

After decomposing the full temperature field, $T(t,\mathbf{x})$, into a horizontally-averaged component, $\overline{T}(t,y)$, and a perturbation, $T'(t,\mathbf{x})$, the horizontally-averaged energy equation [12] simplifies to

$$\frac{\partial \overline{T}}{\partial t} + v(t)\frac{\partial \overline{T}}{\partial y} = \frac{\partial}{\partial y}\left(\frac{1}{\mathrm{Pe}}\frac{\partial \overline{T}}{\partial y} - \int_{A_c} v'T'\,dA\right), \tag{1}$$

where $v(t) \equiv \overline{v}/v_o$ and $\mathrm{Pe} \equiv v_o H/\alpha$. The length, time and velocity scales used in the non-dimensionalization of Eq. (1) are H, (H/v_o), and v_o, respectively. The dimensional velocity v_o is a representative scale for $\overline{v}$, the dimensional, instantaneous area-averaged velocity. The area-averaged velocity is related to the dimensional mass flow rate through the system by $\overline{v} = (\dot{m}/\rho)/\hat{A}_c = \dot{V}/\hat{A}_c$. In general, $\overline{v}$ will be time-dependent and the present formulation encompasses this potentiality. The temperature scale

Contributed by the Heat Transfer Division for publication in the JOURNAL OF HEAT TRANSFER. Manuscript received by the Heat Transfer Division February 13, 2001; revision received August 26, 2002. Associate Editor: B. T. F. Chung.

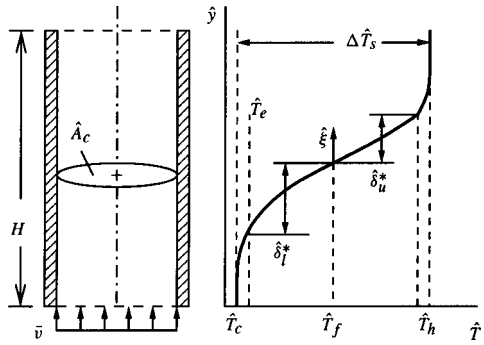

Fig. 1 Schematic of a thermal storage vessel and a representative instantaneous vertical temperature profile

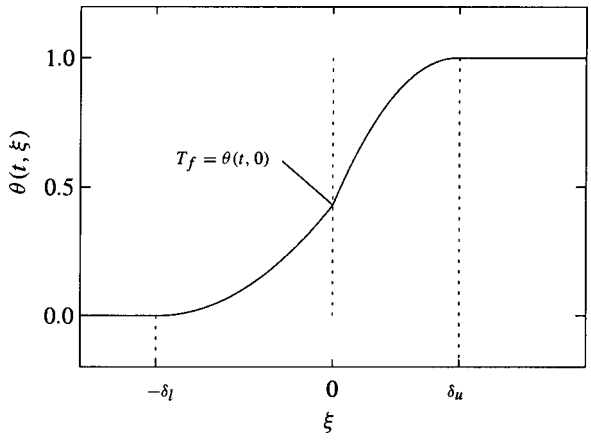

Fig. 2 Schematic of a composite boundary layer profile

is taken as the characteristic temperature difference of the storage device, $\Delta\hat{T}_s$, which is the nominal difference between the high and low temperatures in the system. Consideration of the possibility that the perturbation integral is proportional to the gradient in the mean temperature suggests a convective thermal diffusivity, ε, defined as

$$\frac{\varepsilon}{v_o H}\frac{\partial \overline{T}}{\partial y} = -\int_{A_c} v'T'\,dA, \tag{2}$$

after Homan and Soo [12]. Upon substitution of Eq. (2) into Eq. (1), the energy equation simplifies to

$$\frac{\partial \overline{T}}{\partial t} + v(t)\frac{\partial \overline{T}}{\partial y} = \frac{\partial}{\partial y}\left(\frac{\alpha+\varepsilon}{v_0 H}\frac{\partial \overline{T}}{\partial y}\right). \tag{3}$$

Defining a convective thermal-mixing factor as $\kappa \equiv 1+\varepsilon/\alpha$, the energy equation can finally be expressed as

$$\frac{\partial \overline{T}}{\partial t} + v(t)\frac{\partial \overline{T}}{\partial y} = \frac{\partial}{\partial y}\left(\frac{\kappa}{\mathrm{Pe}}\frac{\partial \overline{T}}{\partial y}\right). \tag{4}$$

The utility of this model hinges upon the assumption implied in the definition of the convective thermal diffusivity, Eq. (2), and an appropriate characterization of ε or, alternatively, κ. The present paper examines several possible variations of κ and their comparison to published empirical data.

The bars appearing in Eq. (4) will hereafter be dropped, although it remains a description of the horizontally averaged temperature field which is being sought.

Coordinate Transformation. From mass conservation, the horizontally-averaged vertical velocity can be at most a function of time, $v(t)$. As a result, a coordinate system is selected which moves with the contact line between the hot and cold fluid volumes, the position of which is specified by

$$y_f(t) = \int_0^t v(t)dt. \tag{5}$$

The transformation from a fixed coordinate system originating from the bottom of the vessel to one moving with the fill line is therefore $\xi = y - y_f(t)$, and the relation of the desired temperature distribution to the corresponding solution in transformed coordinates, $\theta(t,\xi)$, is $T(t,y) = \theta(t, y-y_f(t))$. This coordinate system is illustrated in Fig. 2.

In terms of $\theta(t,\xi)$, the energy equation of Eq. (1) then simplifies to

$$\frac{\partial \theta}{\partial t} = \frac{\partial}{\partial \xi}\left(\frac{\kappa}{\mathrm{Pe}}\frac{\partial \theta}{\partial \xi}\right). \tag{6}$$

Integral Energy Equation. Empirical observations of the vertical temperature distribution in stratified, liquid sensible storage devices generally indicate a strongly asymmetric temperature profile [19] and thermocline growth rates which vary with operating parameters and design parameters. In order to model such characteristics, the domain is divided into two regions, separated by the fill line, y_f, as shown in Fig. 2. The extent of the gradient layer on either side of the fill line is denoted by the boundary layer scale, $\delta(t)$, the size of which will differ between the upper and lower regions (the "upper" region refers to $\xi > 0$).

For the upper region, $0^+ \leqslant \xi \leqslant \delta_u(t)$, the integration of Eq. (6) over this interval yields

$$\int_{0^+}^{\delta_u}\frac{\partial \theta}{\partial t}d\xi = \left[\frac{\kappa_u}{\mathrm{Pe}}\frac{\partial \theta}{\partial \xi}\bigg|_{\xi=\delta_u} - \frac{\kappa_u}{\mathrm{Pe}}\frac{\partial \theta}{\partial \xi}\bigg|_{\xi=0^+}\right]. \tag{7}$$

Applying the boundary conditions,

$$\theta(t, \xi=\delta_u) = 1, \tag{8}$$

$$\frac{\partial \theta}{\partial \xi}(t, \xi=\delta_u) = 0, \tag{9}$$

and Liebnitz' Rule, the equation simplifies to

$$\frac{d}{dt}(\psi_u - \delta_u) = -\frac{1}{\mathrm{Pe}}\left[\kappa_u\frac{\partial \theta}{\partial \xi}\right]_{\xi=0^+}, \tag{10}$$

where

$$\psi_u \equiv \int_{0^+}^{\delta_u(t)}\theta(t,\xi)d\xi. \tag{11}$$

In a similar manner, integration of the energy equation over the lower region, $-\delta_u(t) \leqslant \xi \leqslant 0^-$, yields

$$\frac{d}{dt}(\psi_l) = \frac{1}{\mathrm{Pe}}\left[\kappa_l\frac{\partial \theta}{\partial \xi}\right]_{\xi=0^-}, \tag{12}$$

where

$$\psi_l \equiv \int_{-\delta_u(t)}^{0^-}\theta(t,\xi)d\xi, \tag{13}$$

with the boundary conditions

$$\theta(t, \xi=-\delta_l) = 0, \text{ and} \tag{14}$$

$$\frac{\partial \theta}{\partial \xi}(t, \xi=-\delta_l) = 0. \tag{15}$$

Temperature Profiles. As indicated in the development of the integral energy equations, Eqs. (10) and (12), the natural boundary conditions include the specification of the temperature and a zero gradient at the end of each layer, $\xi = \delta_u$ and ξ

$=-\delta_l$. In addition, the temperature profiles must satisfy matching conditions for temperature and heat flux at the interface, $\xi=0$. Symbolically, these conditions require

$$\theta_l(t,\xi=0^-)=\theta_u(t,\xi=0^+), \tag{16}$$

and

$$\left[k_{t,l}\frac{\partial\theta_l}{\partial\xi}\right]_{\xi=0^-}=\left[k_{t,u}\frac{\partial\theta_u}{\partial\xi}\right]_{\xi=0^+}, \tag{17}$$

where k_t is the total conductivity, consistent with Eq. (3). Since the molecular properties of the liquid are uniform across the two regions, the flux-matching boundary condition may be rewritten in terms of the respective thermal mixing factors as

$$\left[\kappa_l\frac{\partial\theta_l}{\partial\xi}\right]_{\xi=0^-}=\left[\kappa_u\frac{\partial\theta_u}{\partial\xi}\right]_{\xi=0^+}. \tag{18}$$

Considering polynomial profiles of up to the fourth order in each of the two regions, the general form of the solution for θ will be $\theta=\Sigma_{j=0}^{J}m_j\xi^j$ with $J=2$, 3, or 4. The matching conditions require

$$m_{0,l}=m_{0,u}, \tag{19}$$

and

$$\frac{\kappa_l}{\kappa_u}m_{1,l}=m_{1,u}. \tag{20}$$

The first of the two matching conditions serves to determine the interfacial (fill-line) temperature, T_f, defined as

$$T_f=\theta_l(t,\xi=0^-)=\theta_u(t,\xi=0^+). \tag{21}$$

The matching conditions, along with the previously mentioned boundary conditions at the edges of the two regions, are sufficient to determine the six unknown coefficients and the interfacial temperature, T_f, for the quadratic profiles

$$\theta_l=T_f+2T_f\left(\frac{\xi}{\delta_l}\right)+T_f\left(\frac{\xi}{\delta_l}\right)^2, \text{ and} \tag{22a}$$

$$\theta_u=T_f+2(1-T_f)\left(\frac{\xi}{\delta_u}\right)-(1-T_f)\left(\frac{\xi}{\delta_u}\right)^2. \tag{22b}$$

For a cubic or quartic profile, additional constraints are required. After Goodman [9], a ''derived'' boundary condition is obtained from the differential equation, Eq. (6). Evaluating the differential equation at the far end of the two regions and upon recognizing that θ is independent of time at these locations, one obtains

$$\left.\frac{\partial^2\theta_l}{\partial\xi^2}\right|_{\xi=-\delta_l}=\left.\frac{\partial^2\theta_u}{\partial\xi^2}\right|_{\xi=\delta_u}=0. \tag{23}$$

The cubic profiles resulting from the application of these additional constraints are given in Homan [10]. These profiles are applicable irrespective of whether the interfacial temperature is constant or a function of time.

For the more restrictive case, in which T_f is independent of time, two additional profiles may be obtained. An additional constraint on the profile may then be derived from application of the governing differential equation at $\xi=0$, in a manner identical to that of Eq. (23). Application of both derived boundary conditions produces quartic profiles given by

$$\theta_l=T_f+2T_f\left(\frac{\xi}{\delta_l}\right)-2T_f\left(\frac{\xi}{\delta_l}\right)^3-T_f\left(\frac{\xi}{\delta_l}\right)^4, \text{ and} \tag{24a}$$

$$\theta_u=T_f+2(1-T_f)\left(\frac{\xi}{\delta_u}\right)-2(1-T_f)\left(\frac{\xi}{\delta_u}\right)^3+(1-T_f)\left(\frac{\xi}{\delta_u}\right)^4. \tag{24b}$$

For each profile, the second matching condition, Eq. (18), requires that the interfacial temperature satisfies

$$T_f=\frac{\delta_l\kappa_u}{\delta_u\kappa_l+\delta_l\kappa_u}, \qquad =(1+\beta)^{-1}, \tag{25}$$

where

$$\beta\equiv\frac{\kappa_l}{\kappa_u}\frac{\delta_u}{\delta_l}. \tag{26}$$

As will be seen, this corresponds to the parameter defined as $\beta=(k_1/k_2)\sqrt{\alpha_1/\alpha_2}$ in the solution for a two-layer medium using the method of Laplace transforms by Özişik [23].

Results and Discussion

The solutions to the integral equations are examined for diffusivities uniform across both regions, with differing magnitudes in each of the two regions, and finally with identical time-dependency but differing magnitude. The model results are then compared to several sources of empirical data. For all of the results presented, a uniform through-flow rate, $v(t)=1$, has been assumed.

Uniform Diffusivity. For the integral solution, the interfacial temperature is determined by the matching condition, Eq. (18), and is a constant for time-independent diffusivities. In the case of a uniform diffusivity across both regions, T_f is identically equal to 1/2. Since the interfacial temperature is constant, the assumed profiles for θ can be substituted into the respective integrated energy equations to produce an ordinary differential equation for each of the boundary layer scales, $\delta_u(t)$ and $\delta_l(t)$. Assuming zero initial thickness for the thermal layers, the solutions are of the form

$$\delta_n=\left[\frac{a\kappa_n t}{\mathrm{Pe}}\right]^{1/2}=f(t;\mathrm{Pe}/\kappa_n). \tag{27}$$

where the subscript n denotes either of u or l as is appropriate to the region under consideration. The constant a appearing in Eq. (27) takes on different values for each of the assumed profiles, $a=12$ for the quadratic profile ($J=2$) in Eq. (22), and $a=(40/3)$ for the quartic profile ($J=4$) in Eq. (24).

For two semi-infinite regions in perfect thermal contact with a uniform conductivity across both regions, the well-known analytical solution [23] also predicts an interfacial temperature T_f identically equal to 1/2. Özişik [23] has shown that the quartic profile, Eq. (24), provides the most accurate prediction of the interfacial heat flux relative to the analytical solution. In the context of stratified sensible storage, a quantity of greater interest is the thickness of the thermocline which in turn has direct relation to the degree of thermal mixing. The selection of a particular definition for the extent of the thermocline takes on physical significance if the edge is chosen as the limiting temperature for the usable fraction of the storage volume. For cool storage applications, the usable portion of the fluid volume is typically considered to be that portion at a temperature of less than 5–25 percent of the overall storage temperature difference. For heat storage applications, the fluid volume above 75–95 percent of the storage temperature difference [11,17,18,29] is typically considered usable in most applications. The thermocline thickness, δ_n^*, is therefore computed as the distance between the fill line, y_f and the location at which the profile equals a particular edge temperature, T_e. The thicknesses are defined, implicitly, according to $\theta_l(t,\xi=-\delta_l^*)=T_e$, and $\theta_u(t,\xi=\delta_u^*)=1-T_e$. In the case of a uniform diffusivity, $\kappa_l/\kappa_u\equiv1$ and $\delta_l^*\equiv\delta_u^*$. The variation of the apparent thermocline thickness, δ^*, in time is shown in Fig. 3.

The $t^{1/2}$ growth of the layer thickness is untouched by the choice of the edge temperature, T_e. For each edge temperature,

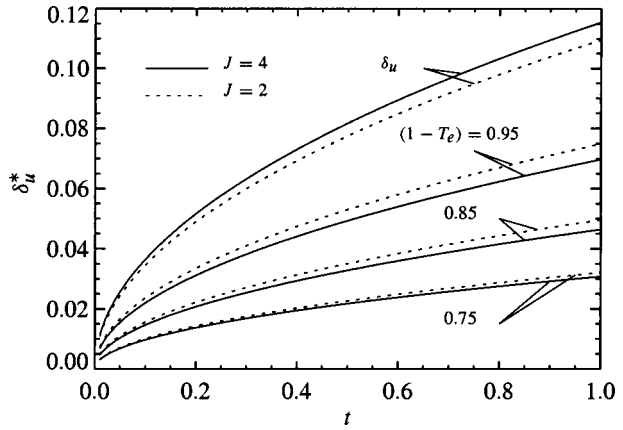

Fig. 3 Upper boundary layer growth, $\delta_u^*(t)$, for several edge temperatures, T_e, at Pe$=10^3$

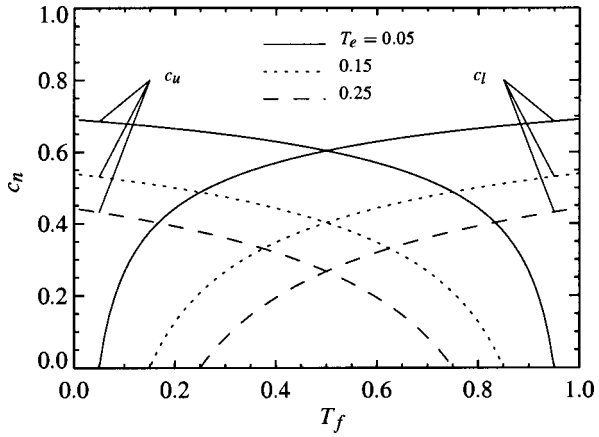

Fig. 5 Ratio of thermocline thickness to boundary layer scale versus interfacial temperature for several edge definitions

the apparent thermocline thickness is greater in the quadratic profile than in the quartic profile. However, the boundary layer scale, δ, is larger in the quartic profile than in the quadratic profile as indicated by the previously indicated coefficient values. Based on comparison to the analytical solution for uniform diffusivity, the quadratic profile gives a slightly more accurate prediction of the $T_e=0.05$ edge whereas, for the 0.15 and 0.25 edges, the quartic profile provides the closest agreement [10]. The results presented in the remainder of this paper will therefore utilize the quartic profile.

Non-Uniform Diffusivity. Considering the case in which the diffusivity is constant in time, but of different magnitude in each of the two regions, the solutions for the boundary layer scales remain of the form shown in Eq. (27). Defining a thermal mixing factor ratio as $\kappa_r \equiv \kappa_l/\kappa_u$, the boundary layer scales can be expressed in the form $\delta_u = f(t;\mathrm{Pe}/\kappa_u)$ and $\delta_l = f(t;(\mathrm{Pe}/\kappa_u)/\kappa_r)$.

The interfacial temperature is then given by

$$T_f = (1+\beta)^{-1} = (1+\sqrt{\kappa_r})^{-1}, \tag{28}$$

since $\beta = (\kappa_l/\kappa_u)(\delta_u/\delta_l) = \sqrt{\kappa_r}$.

Interestingly, increasing κ_r results in an increase in both δ_u^* and δ_l^* at fixed Pe/κ_u. The upper layer thickness increases slightly because the interfacial temperature decreases with increasing κ_r. The increase in δ_l^* with κ_r, however, is much greater. The growth in time for δ_u^* and δ_l^* at several κ_r values is shown in Fig. 4.

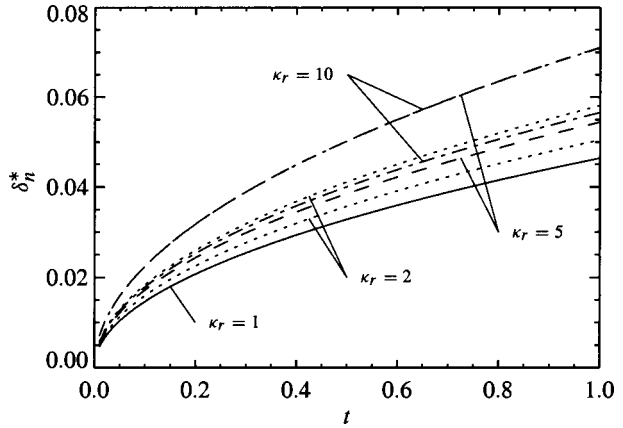

Fig. 4 Growth of the upper and lower boundary layers, δ_u^* and δ_l^*, for $T_e=0.15$ and $(\mathrm{Pe}/\kappa_u)=10^3$. In each case, $\delta_l^* > \delta_u^*$ except for the case $\kappa_r \equiv 1$, where $\delta_l^* \equiv \delta_u^*$.

The difference between the two thicknesses increases for $\kappa_r \leq 5$, but at $\kappa_r = 10$ has clearly decreased. Qualitatively, the explanation is that the boundary layer scale, δ_n, is independent of the interfacial temperature, whereas one or the other of the apparent thermocline thicknesses, δ_n^*, must vanish as T_f approaches either T_e or $(1-T_e)$. Quantitatively, the behavior may be understood by comparing the ratio of the respective thicknesses to their boundary layer scale. Symbolically, this ratio is computed as

$$c_n = \frac{\delta_n^*}{\delta_n(t)}. \tag{29}$$

These ratios are shown versus the interfacial temperature for selected T_e in Fig. 5.

The shape of the curve serves to explain the behavior observed in Fig. 4. Observe that as T_f is decreased from one-half, c_u increases slightly and therefore the upper thermocline thickness δ_u^* takes on an ever larger fraction of the boundary layer scale, δ_u. On the other hand, c_l decreases rapidly as T_f approaches T_e. Thus, δ_l^* becomes an ever smaller fraction of δ_l, which does increase according to $\sqrt{\kappa_r}$.

Transient Diffusivity. Physical reasoning suggests that the effective diffusivity observed at the thermocline will vary in time since the thermocline is transported away from the inlet at the bulk velocity. Since gravity serves to restore and maintain equilibrium in the stably-stratified case, it is only the inflow and outflow which drive the departure from equilibrium (in the absence of heat transfer in or through the tank walls). The effective thermal diffusivity must therefore be a function of time if the thermocline thickness is to grow at anything other than the $t^{1/2}$ rate prodicted by a constant diffusivity. Consider, therefore, a thermal mixing factor of the form

$$\kappa(t) = \tilde{\kappa}(1+b)t^b. \tag{30}$$

Provided that the exponent b is identical for both the lower and upper regions, the interfacial temperature remains constant and the solutions for the boundary layer scale are of the form

$$\delta_n = \left[\frac{a\tilde{\kappa}_n t^{(1+b)}}{\mathrm{Pe}}\right]^{1/2}, \tag{31}$$

where the subscript n again refers to either of u or l. The thermocline thickness will therefore have a simple power law dependence on b. The constant a in Eq. (31) remains as earlier. The interfacial temperature, T_f, also remains equal to $(1+\beta)^{-1}$, except that now $\beta = \sqrt{\tilde{\kappa}_l/\tilde{\kappa}_u} \equiv \sqrt{\kappa_r}$.

The growth in time of the upper layer thickness, δ_u^*, is shown in Fig. 6 for several values of b. The constant diffusivity case, b

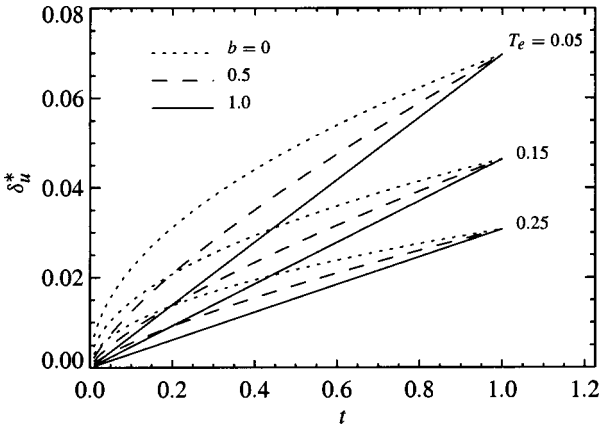

Fig. 6 Growth of the upper boundary layer thickness, $\delta_u^*(t)$, for $\kappa_{o,r}=1$ at $(\mathrm{Pe}/\kappa_{o,u})=10^3$ for several b values

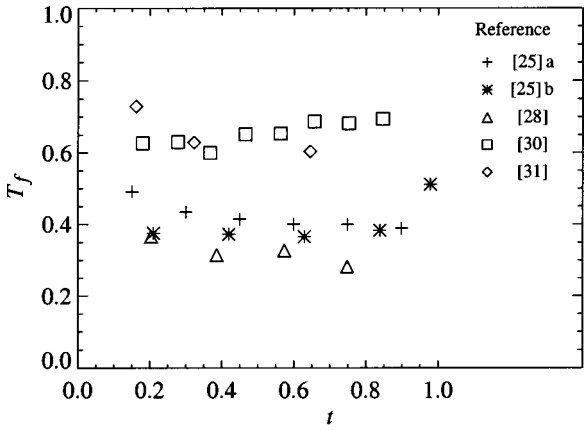

Fig. 7 Variation of the fill-line temperature in time for empirical data from several references

$=0$, is seen to produce the familiar $\delta \sim t^{1/2}$ growth whereas the $b=1$ limit shows $\delta \sim t$. The relation between the upper and lower thicknesses, δ_u^* and δ_l^*, remains identical to that of the constant diffusivity case since T_f remains constant with respect to time.

Comparison To Empirical Data. The distinguishing characteristics of the diffusivity variations considered in the present formulation are (1) a constant fill-line temperature and (2) a constant thermocline growth rate for all edge temperatures, both above and below the fill line. Several sources of empirical data have therefore been selected to demonstrate the validity of these basic hypotheses and are shown in Table 1 along with the corresponding experimental conditions. The sources cover a wide range of enclosure volumes and include temperature ranges corresponding to both hot and cool storage. The data of Truman et al. [25], Wildin and Sohn [28] and Zurigat et al. [31] consist of temperature profiles at several instants in time whereas the data of Zurigat et al. [30] consists of time series data for each of several sensors. All of the references except for that of Zurigat et al. [30] correspond to a bottom inflow of lower temperature water.

The time variation of the fill-line temperature for each of the data sets are shown in Fig. 7.

In each case, except possibly for the data of Zurigat et al. [31], the fill-line temperature is essentially uniform in time. The last data point of Truman et al. [25] departs from the trend otherwise indicated and is likely due to the influence of the outlet since it corresponds to the point at which essentially an entire tank volume has been drawn through the vessel.

The growth of the upper and lower thermocline thicknesses are shown in Figures 8, 9 and 10 for Truman et al. [25], Wildin and Sohn [28], and Zurigat et al. [31], respectively. In each case, the growth rates are, to a good approximation, identical for each of the edge temperatures although a clear asymmetry in the thermocline thickness may be observed on either side of the fill line. Estimated thermocline growth rates from the data in these figures are in the range $t^{0.33}$ to $t^{0.43}$. Interestingly, the data also makes clear that a higher degree of mixing does not necessarily manifest itself in a larger thermocline thickness at all edge temperatures. For example, Figures 8 and 9 show $\delta_l^* < \delta_u^*$ for $T_e=0.25$ and 0.75, respectively. In effect, the higher degree of mixing erodes the lower edges of the thermocline thereby transporting it throughout a broader region, resulting in the long tails often observed in these profiles [19]. Since the data presented in these figures exhibit both a nominally uniform fill-line temperature and constant growth rates for all edge temperatures, there is good agreement with the basic tenets of the present formulation.

To illustrate the quantitative determination of the empirical constants in the present formulation, the data of Zurigat et al. [30] and Zurigat et al. [31] will be examined in detail. The latter has both a relatively constant fill-line temperature and thermocline growth rates whereas the former has strongly varied thermocline growth rates.

The data of Zurigat et al. [31] consists of vertical temperature profiles, $\hat{T}(\hat{y})$, recorded at three times during the discharging of a heat storage device. From these profiles, the instantaneous fill-line temperatures and thermocline thicknesses can be directly determined. These quantities are shown in Table 2.

Based on T_f, the mixing factor ratio may be determined from Eq. (28), which is equally applicable to any of the diffusivity variations considered. Then, having selected a representative value for T_f, values for κ_n may be computed from each thermocline thickness using Eq. (24) and Eq. (27). Additionally, the plot of $\delta_n^*(t)$, Fig. 10, may then be used to estimate a value for b since the slope of the curve is equal to $(1+b)/2$. Values for $\tilde{\kappa}_n$

Table 1 Empirical data sources and associated experimental conditions.

Reference	$\dot{V}$ (Lpm)	V (L)	H (m)	D_h (m)	Pe	$\hat{T}_c$ (°C)	$\Delta\hat{T}_s$ (°C)
Truman et al. [25a][1]	2.0	561	0.91	0.78	357	6	9.9
Truman et al. [25b][1]	5.6	561	0.91	0.78	999	6.2	9.6
Wildin and Sohn [28][2]	13.0	1,990	0.91	1.32	645	12	10.9
Zurigat et al. [30][3]	5.72	188	1.45	0.406	7010	24.6	26
Zurigat et al. [31][4]	12.1	2,250	2.1	1.16	2750	22.5	18.1

[1]Temperature profile data taken from Figures 11 and 14, respectively.
[2]Temperature profile data taken from Figure 14.
[3]Temperature profile data taken from Figure 6.
[4]Temperature profile data taken from Figure 12.

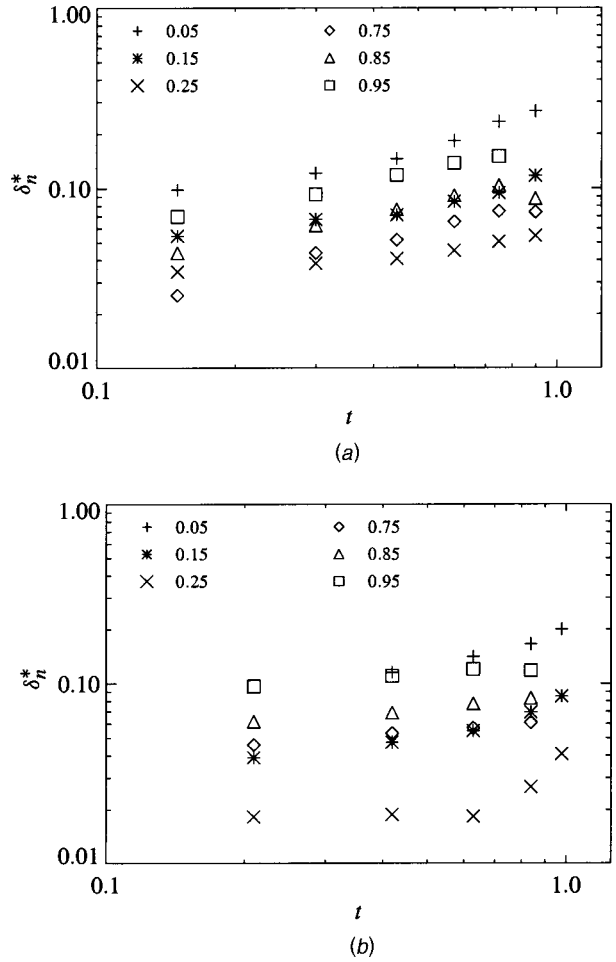

Fig. 8 Growth of the thermocline thickness for the indicated edge temperatures taken from the data of Truman et al. [25] at Peclet numbers of 357 and 999, respectively. The lower edge temperatures correspond to the inlet side of the thermocline.

may then be determined for each of the thermocline thicknesses using Eq. (24) and Eq. (31). The values for $\tilde{\kappa}_n$ are also shown in Table 2. Solution profiles based on the data in the table are shown overlayed with the temperature data in Fig. 11.

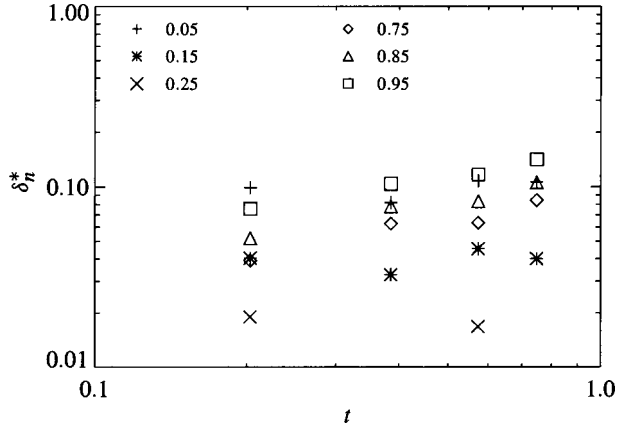

Fig. 9 Growth of the thermocline thickness for the indicated edge temperatures taken from data of Wildin and Sohn [28] with a Peclet number of 645. The lower edge temperatures correspond to the inlet side of the thermocline.

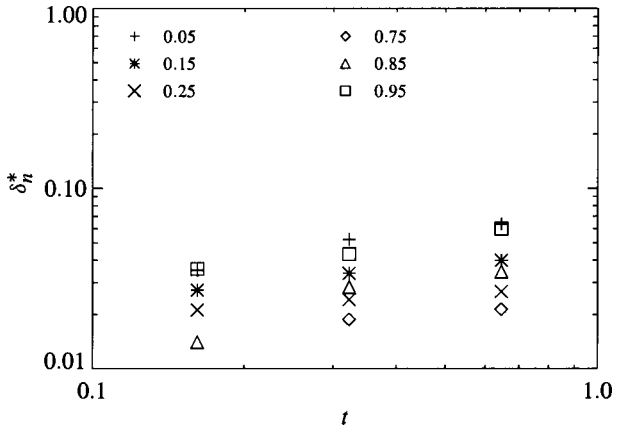

Fig. 10 Growth of the thermocline thickness for the indicated edge temperatures taken from data of Zurigat et al. [31] with a Peclet number of 2750. The lower edge temperatures correspond to the inlet side of the thermocline.

Three solution profiles are shown corresponding to uniform, non-uniform, and transient non-uniform diffusivities. The uniform diffusivity model is clearly inadequate for predicting the growth of the upper layer while the non-uniform ($\kappa_r \neq 1$) and transient ($\tilde{\kappa}_r \neq 1, b \neq 0$) diffusivities provide increasingly better agreement throughout the duration of the filling process.

Finally, the data of Zurigat et al. [30] is examined which consists of time series data, $\hat{T}(\hat{t})$, at each of several temperature sensors distributed vertically in the enclosure throughout the charging process of a heat storage vessel. The vertical coordinate,

Table 2 Fill-line temperatures, thermocline thicknesses and mixing factor coefficients computed from the temperature profiles of Zurigat et al. [31]

	t		
Parameter	0.161	0.323	0.645
T_f	0.729	0.629	0.603
κ_r , $\tilde{\kappa}_r$	0.138	0.348	0.433
	$T_e = 0.05$[a]		
δ_i^*	0.0352	0.0522	0.0635
κ_i	3.93	4.31	3.19
$\tilde{\kappa}_i$	2.07	2.90	2.74
	$T_e = 0.15$[a]		
δ_i^*	0.0273	0.0338	0.0399
κ_i	4.65	3.55	2.48
$\tilde{\kappa}_i$	2.45	2.39	2.12
	$T_e = 0.25$[a]		
δ_i^*	0.0212	0.0242	0.0268
κ_i	5.20	3.38	2.07
$\tilde{\kappa}_i$	2.74	2.27	1.78
	$T_e = 0.75$[a]		
δ_0^*	0.00612	0.0188	0.0214
κ_0	1.77	8.32	5.40
$\tilde{\kappa}_0$	0.933	5.60	4.63
	$T_e = 0.85$[a]		
δ_0^*	0.0140	0.0284	0.0345
κ_0	2.37	4.87	3.60
$\tilde{\kappa}_0$	1.25	3.28	3.09
	$T_e = 0.95$[a]		
δ_0^*	0.0358	0.0433	0.0598
κ_0	5.30	3.87	3.69
$\tilde{\kappa}_0$	2.80	2.60	3.17

[a]The convective mixing factor, κ_n, and coefficient $\tilde{\kappa}_n$ are computed based on $T_f = 0.63$.

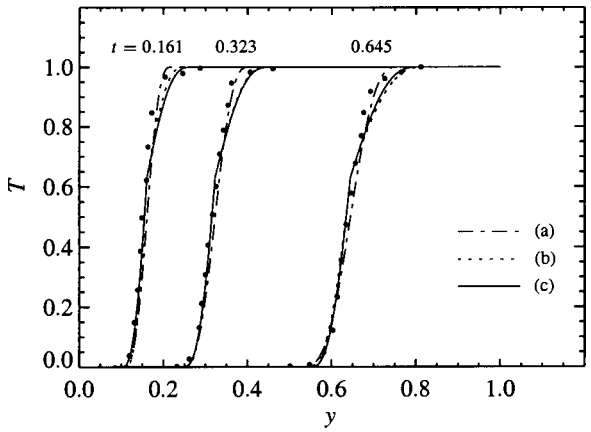

Fig. 11 Comparison of the analytical model for (*a*) $b=0$, $\kappa_i=4$, and $\kappa_r=1$, (*b*) $b=0$, $\kappa_i=3.5$, and $\kappa_r=0.34$, and (*c*) $b=-0.35$, $\tilde{\kappa}_i=2.5$, and $\tilde{\kappa}_r=0.34$ with empirical profile data of Zurigat et al. [31]

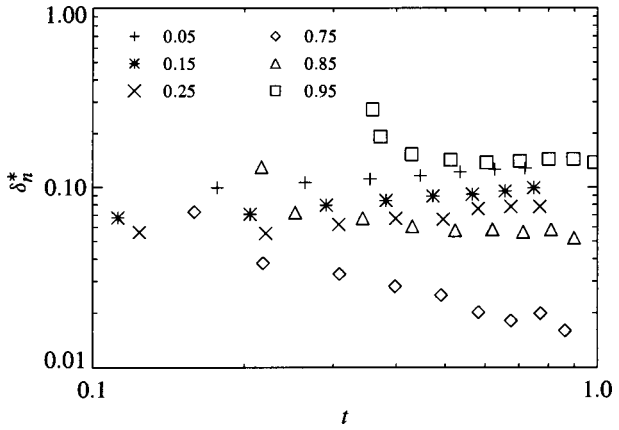

Fig. 12 Growth of the thermocline thickness for the indicated edge temperatures taken from data of Zurigat et al. [30] with a Peclet number of 7010. The higher edge temperatures correspond to the inlet side of the thermocline.

x, is aligned with the direction of bulk flow such that $x=1-y$ where y is the coordinate originating from the bottom of the vessel. The fill-line temperature is then the temperature at each sensor when y_f equals the sensor position. In the x-coordinate system

Table 3 Fill-line temperatures, thermocline thicknesses and mixing factor coefficients computed from the temperature profiles of Zurigat et al. [30]

	$\hat{x}/H$			
Parameter	0.276	0.466	0.657	0.847
T_f	0.630	0.652	0.687	0.694
t_f	0.276	0.466	0.657	0.847
κ_r, $\tilde{\kappa}_r$	2.90	3.51	4.82	5.14
	$T_e=0.05$[a]			
δ_0^*	0.0994	0.111	0.122	0.128
t	0.177	0.355	0.535	0.719
κ_0	72.0	44.8	35.9	29.4
$\tilde{\kappa}_0$	22.8	22.5	23.7	23.6
	$T_e=0.15$[a]			
δ_0^*	0.0708	0.0843	0.0913	0.0991
t	0.205	0.382	0.566	0.748
κ_0	60.7	46.2	36.5	32.6
$\tilde{\kappa}_0$	21.2	24.4	25.0	26.9
	$T_e=0.25$[a]			
δ_0^*	0.0554	0.0670	0.0759	0.0780
t	0.221	0.399	0.581	0.769
κ_0	62.1	50.3	44.3	35.4
$\tilde{\kappa}_0$	22.8	27.3	30.9	29.7
	$T_e=0.75$[a]			
δ_i^*	0.0330	0.0251	0.0181	0.0160
t	0.309	0.491	0.675	0.863
κ_i	102.2	37.2	14.1	8.6
$\tilde{\kappa}_i$	46.9	23.2	10.8	7.8
	$T_e=0.85$[a]			
δ_i^*	0.0673	0.0576	0.0563	0.522
t	0.343	0.524	0.713	0.899
κ_i	75.6	36.3	25.5	17.4
$\tilde{\kappa}_i$	37.2	23.6	20.3	16.2
	$T_e=0.95$[a]			
δ_i^*	0.153	0.137	0.144	0.138
t	0.429	0.603	0.801	0.985
κ_i	97.2	55.5	46.1	34.4
$\tilde{\kappa}_i$	55.4	39.6	39.8	34.1

[a]The convective mixing factor, κ_n, and coefficient $\tilde{\kappa}_n$ are computed based on $T_f=0.66$.

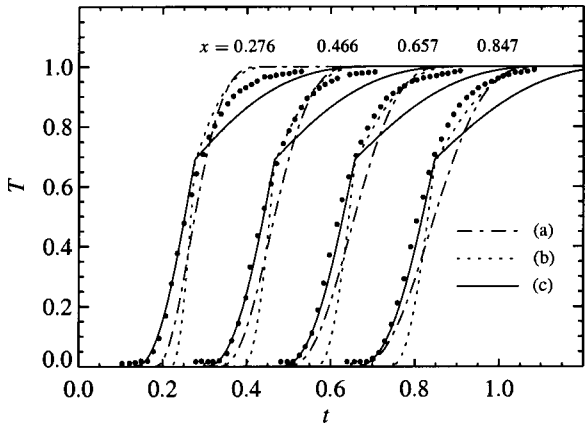

Fig. 13 Comparison of the analytical model for (*a*) $b=0$, $\kappa_i=30$, and $\kappa_r=1$, (*b*) $b=0$, $\kappa_i=40$, and $\kappa_r=4.5$, and (*c*) $b=-0.665$, $\tilde{\kappa}_i=40$, and $\tilde{\kappa}_r=5.0$ with empirical time series data of Zurigat et al. [30]

$T_f=\beta/(\beta+1)$, in contrast to Eq. (25), since the "upper" and "lower" designation is reversed. Determination of the thermocline thicknesses is considerably more tedious than for the instantaneous profile data since each thermocline edge crosses a given sensor at a different time. The instantaneous thickness is then the difference between the sensor position and the instantaneous fill-line position. The fill-line temperatures and thermocline thickness data so determined are shown in Table 3.

As with the time series data, an estimate of T_f is sufficient to determine the κ_n values shown in Table 3. In order to determine the parameters of the transient diffusivity model, the power law exponent must also be estimated. The thermocline thickness variation in time for this data is shown in Fig. 12. The variation is clearly more complex than observed in the previous data sets with marked differences in the thermocline growth rate of the upper (outlet) and lower (inlet) side. Based on the outlet side thicknesses, a value for b is estimated as -0.665. Fig. 13 shows solution profiles overlaying the empirical data for each of the uniform, non-uniform and transient diffusivity models. Neither the uniform nor the non-uniform diffusivity models provide a good prediction of the data throughout the filling process. However, having estimated b from the time variation of the outlet-side thicknesses, the transient diffusivity provides an excellent prediction of the outlet-side segment of the profile. The inlet-side has a much lower growth rate, however, and the transient diffusivity model therefore overpredicts its growth. Although not encompassed by the present

formulation, this behavior is consistent with the higher flow inertia for this case and the observed sharpening of a fixed gradient layer undergoing interaction with an imposed turbulent field [7,26].

Conclusions

The stably-stratified top- or bottom-filling of an enclosure produces an interfacial layer, or thermocline, reflecting the internal mixed-convection flow. The evolution of this thermocline largely determines the performance of the stratified thermal storage system. Integral solutions to the horizontally-averaged energy equation with non-uniform and time-dependent diffusivities are presented which exhibit profile asymmetries and growth rates consistent with empirical observations of thermocline evolution. Analysis of published data from several sources shows good agreement with the present model over the duration of the filling process at moderate flow rates corresponding to Peclet numbers from order 10^2 to 10^3. At these Peclet numbers, the profiles are characterized by nominally uniform (1) fill-line temperatures and (2) thermocline growth rates on either side of the fill line. Thermocline growth rates of the form $\delta^* \sim t^b$ with b-values ranging from 0.33 to 0.43 are observed, in contrast to the $t^{1/2}$ growth rate predicted by simple molecular diffusion. Empirical diffusivities of up to several orders of magnitude larger than the molecular diffusivity are also observed. At higher flow rates, Peclet numbers of order 10^4, the evolution of the thermocline exhibits increasingly different growth rates on either side of the thermocline, a characteristic not encompassed by the diffusivity variations considered in the present paper.

Acknowledgments

This research was supported in part by the American Society of Heating, Refrigerating and Air Conditioning Engineers (ASHRAE) under the New Investigator Award. In addition, the constructive comments of the anonymous reviewers are gratefully acknowledged.

Nomenclature

Dimensional variables are denoted by a hat, e.g., $\hat{y}$

- $\hat{A}_c$ = vessel cross-sectional area (dimensional)
- a = constant in boundary scale solution, see Eq. (27)
- b = power law exponent, see Eq. (30)
- c = ratio of δ^* to δ, see Eq. (29)
- D_h = hydraulic diameter
- H = vessel height (dimensional)
- k = thermal conductivity
- m = general polynomial coefficient, see Eq. (18)
- Pe = Peclet number, see Eq. (1)
- $\Delta\hat{T}_s$ = storage temperature differential
- T = temperature
- T_f = interfacial or fill-line temperature, see Eq. (20)
- V = volume
- v = dimensionless vertical velocity
- $\overline{v}$ = vertical velocity (dimensional)
- $\dot{V}$ = volumetric flow rate
- v_o = vertical velocity scale (dimensional)
- y_f = fill-line position

Greek

- α = molecular thermal diffusivity
- β = constant, see Eq. (26)
- δ = boundary layer scale
- δ^* = thermocline thickness
- ε = convective thermal diffusivity, see Eq. (1)
- θ = solution in transformed coordinates, see Eq. (5)
- κ = convective mixing factor, see Eq. (2)
- κ_r = ratio of thermal mixing factors, κ_l / κ_u
- $\tilde{\kappa}$ = transient diffusivity coefficient, see Eq. (30)
- ξ = spatial coordinate relative to fill-line, see Eq. (5)
- ψ = time-dependent function, see Eq. (11)

Subscripts

- c = cold
- e = edge
- f = fill-line
- h = hot
- l = lower region
- t = total (molecular and convective), see Eq. (17)
- u = upper region

References

[1] Anderson, R., and Kreith, F., 1987, "Natural Convection in Active and Passive Solar Thermal Systems," *Advances in Heat Transfer*, T. F. Irvine, Jr. and J. P. Hartnett, eds., **18**. Academic Press, San Diego, CA, pp. 1–86.

[2] Bejan, A., 1978, "Two Thermodynamic Optima in the Design of Sensible Heat Units for Energy Storage," ASME J. Heat Transfer, **100**, pp. 708–712.

[3] Bejan, A., 1996, *Entropy Generation Minimization*, CRC Press, Boca Raton, FL.

[4] Buchberg, H., Catton, I., and Edwards, D. K., 1976, "Natural Convection in Enclosed Spaces—A Review of Application to Solar Collection," ASME J. Heat Transfer, **98**, pp. 182–188.

[5] Catton, I., 1978, "Natural Convection in Enclosures," *Proceedings of the Sixth International Heat Transfer Conference*, **6**.

[6] Clark, J. A., 1985, "Thermal Energy Storage," *Handbook of Heat Transfer Applications*, W. M. Rohsenow, J. P. Hartnett, and E. N. Ganic', eds., McGraw-Hill, New York, pp. 8-1–8-40.

[7] Fernando, H. J. S., 1991, "Turbulent Mixing in Stratified Fluids," Annu. Rev. Fluid Mech., **23**, Annual Reviews Inc., pp. 455–493.

[8] Gebhart, B., Jaluria, Y., and Sammakia, R. L. M. B., 1988, *Buoyancy-Induced Flows and Transport*, Hemisphere, New York.

[9] Goodman, T. R., 1964, "Application of Integral Methods to Transient Nonlinear Heat Transfer," *Advances in Heat Transfer*, T. F. Irvine and J. P. Hartnett, eds., **1**, Academic Press, San Diego, CA, pp. 51–122.

[10] Homan, K. O., 2001, "Approximate Analytical Solutions for the Transient Temperature Profiles in Stratified Liquid Sensible Storage," *Proceedings of the 2001 National Heat Transfer Conference*, T. L. Bergman and C. B. Panchal, eds., ASME, New York; **1**, pp. 313–322.

[11] Homan, K. O., Sohn, C. W., and Soo, S. L., 1996, "Thermal Performance of Stratified Chilled Water Storage Tanks," HVAC&R Res., **2**, pp. 158–170.

[12] Homan, K. O., and Soo, S. L., 1998, "Laminar Flow Efficiency of Stratified Chilled-Water Storage Tanks," Int. J. Heat Fluid Flow, **19**, pp. 69–78.

[13] Hyun, J. M., 1994, "Unsteady Buoyant Convection in an Enclosure," *Advances in Heat Transfer*, T. F. Irvine, Jr., J. P. Hartnett, and Y. I. Cho, eds., **24**, Academic Press, San Diego, CA, pp. 277–320.

[14] Krane, R. J., 1987, "A Second Law Analysis of the Optimum Design and Operation of Thermal Energy Storage Systems," Int. J. Heat Mass Transf., **30**, pp. 43–57.

[15] Krane, R. J., and Krane, M. J. M., 1992, "The Optimum Design of Stratified Thermal Energy Storage Systems—Part II: Completion of the Analytical Model, Presentation and Interpretation of the Results," ASME J. Energy Resour. Technol., **114**, pp. 204–208.

[16] Kuehn, T. H., Ramsey, J. W., and Threlkeld, J. L., 1998, *Thermal Environmental Engineering*, 3rd ed., Prentice-Hall, Englewood Cliffs, NJ.

[17] Lavan, Z., and Thompson, J., 1977, "Experimental Study of Thermally Stratified Hot Water Storage Tanks," Sol. Energy, **19**, pp. 519–524.

[18] Mackie, E. I., 1987, "Influence of Discharge Characteristics on Design of Chilled Water Storage," *Cool Storage*, **3**. ASHRAE Technical Data Bulletin.

[19] Mavros, P., Belessiotis, V., and Haralambopoulos, P., 1994, "Stratified Energy Storage Vessels: Characterization of Performance and Modeling of Mixing Behavior," Sol. Energy, **52**, pp. 327–336.

[20] Moran, M. J., and Keyhani, V., 1982, "Second Law Analysis of Thermal Energy Storage Systems," *Proceedings of the Seventh International Heat Transfer Conference*, **6**.

[21] Ostrach, S., 1972, "Natural Convection in Enclosures," *Advances in Heat Transfer*, T. F. Irvine, Jr. and J. P. Hartnett, eds., **8**. Academic Press, San Diego, CA, pp. 161–227.

[22] Ostrach, S., 1982, "Natural Convection Heat Transfer in Cavities and Cells," *Proceedings of the Seventh International Heat Transfer Conference*, **1**.

[23] Özişik, M. N., 1980, *Heat Conduction*, John Wiley and Sons, New York.

[24] Truman, C. R., Roybal, L. G., and Wildin, M. W., 1985, "A Finite Difference Model for Stratified Chilled Water Thermal Storage Tanks," *Proceedings/Communications of ENERSTOCK85*, Toronto.

[25] Truman, C. R., Wildin, M. W., and Yoo, J., 1985, "Scale Modeling of Stratified Water Thermal Storage Tanks," *Proceedings of Symposium on Modeling Environmental Flows*, ASCE/ASME Mechanics Conference.

[26] Turner, J. S., 1979, *Buoyancy Effects in Fluids*, Cambridge University Press.

[27] Valentine, D. T., and Tannous, A. G., 1985, "Stratification of a Two-Dimensional Reservoir Produced by a Buoyant Inflow," *Proceedings of Symposium on Modeling Environmental Flows*, ASCE/ASME Mechanics Conference.

[28] Wildin, M. W., and Sohn, C. W., 1993, "Flow and Temperature Distribution in

a Naturally Stratified Thermal Storage Tank,'' USACERL Technical Report FE-94/01, U.S. Army Construction Engineering Research Laboratories.
[29] Wildin, M. W., and Truman, C. R., 1985, ''A Summary of Experience With Stratified Chilled Water Tanks,'' ASHRAE Trans., **92**, pp. 956–976.
[30] Zurigat, Y. H., Liche, P. R., and Ghajar, A. J., 1991, ''Influence of Inlet Geometry on Mixing in Thermocline Thermal Energy Storage,'' Int. J. Heat Mass Transf., **34**, pp. 115–125.
[31] Zurigat, Y. H., Maloney, K. J., and Ghajar, A. J., 1989, ''A Comparison Study of One-Dimensional Models for Stratified Thermal Storage Tanks,'' ASME J. Sol. Energy Eng., **111**, pp. 204–210.

Natural Convection Heat Transfer From a Cylinder With High Conductivity Permeable Fins

Bassam A/K Abu-Hijleh
Mem. ASME
Department of Mechanical
and Manufacturing Engineering,
RMIT University,
Bundoora East Campus,
PO Box 71, Bundoora 3083,
Victoria, Australia
e-mail: Bassam.Abu-Hijleh@RMIT.edu.au

The problem of laminar natural convection from a horizontal cylinder with multiple equally spaced high conductivity permeable fins on its outer surface was investigated numerically. The effect of several combinations of number of fins and fin height on the average Nusselt number was studied over a wide range of Rayleigh number. Permeable fins provided much higher heat transfer rates compared to the more traditional solid fins for a similar cylinder configuration. The ratio between the permeable to solid Nusselt numbers increased with Rayleigh number, number of fins, and fin height. This ratio was as high as 8.4 at Rayleigh number of 10^6, non-dimensional fin height of 2.0, and with 11 equally spaced fins. The use of permeable fins is very advantageous when high heat transfer rates are needed such as in today's high power density electronic components.
[DOI: 10.1115/1.1532013]

Keywords: Computational, Finned Surfaces, Heat Transfer, Natural Convection

Introduction

Laminar convection from a heated cylinder is an important problem in heat transfer. It is used to simulate a wide range of engineering applications as well as provide a better insight into more complex systems of heat transfer. Accurate knowledge of the overall natural convection heat transfer around circular cylinders is important in many fields, including heat exchangers, passive cooling of electronic components, hot water and steam pipes, heaters, refrigerators and electrical conductors. Because of its industrial importance, this class of heat transfer has been the subject of many experimental and analytical studies. The problem has received continuous attention since the early work of Morgan [1] and Churchill and Chu [2]. The most widely referenced work in this area is that of Kuehn and Goldstein [3] which included the first numerical solution of the full elliptic governing equations. Although more recent work and more accurate work has been reported in the literature since then [4–6] the work of Kuehn and Goldstein [3] is still being referenced [7,8]. A more extensive review can be found in a recent paper by Eckert et al. [9].

Fins have always been used as a passive method of enhancing the convection heat transfer from cylinders [7]. The presence of the solid fins has an effect on both the aerodynamic as well as the thermal characteristics of the flow. The fins tend to obstruct the natural convection currents near the cylinder surface, thus reducing the heat transfer from the cylinder to the surrounding fluid. On the other hand, the fins increase the heat transfer area resulting in an increase in the heat transfer from the cylinder to the surrounding fluid. The net result of these two opposing effects depend on the combination of number of fins, fin height, and Rayleigh number. Previous work by the author has shown that increasing the number of uniformly spaced solid fins beyond a Rayleigh number dependent value can result in a reduction in the Nusselt number [10]. Permeable fins can offer less resistance to the natural convection currents around the cylinder while still offering the increased heat transfer surface area of solid fins. Such fins are expected to offer much enhanced heat transfer rates from a cylinder than solid fins. Stewart and Burns [11] reported enhanced convection heat transfer characteristics in a concentric annulus with heat generating porous media when using a permeable inner boundary. Zhao and Liao [12] and Zhao and Song [13] showed that forced convection heat transfer in a cavity can be significantly enhanced using permeable walls. No published work could be located that discusses the use of permeable fins on the natural convection heat transfer from a horizontal cylinder.

This paper details the changes in the Nusselt number due to the use of different number of equally spaced high conductivity permeable fins placed at the cylinder's outer surface. The fluid under consideration is Air. The elliptic momentum and energy equations were solved numerically using the stream function-vorticity method on a stretched grid. This detailed study included varying the Rayleigh number from 10^3 to 10^6, number of fins from 1 to 11, and the non-dimensional fin height from 0.25 to 2. This range of values is based on the experience gained from a previous work using uniformly spaced solid fins for the same configuration [10]. Due to symmetry, the computations were carried on half the physical domain making use of the vertical symmetry plane passing through the center of the cylinder. The number of fins reported herein is that on one half of the cylinder. No fins were located at the symmetry plane.

Mathematical Analysis. The steady-state equations for two-dimensional laminar convection over a cylinder, including the Boussinesq approximation, are given by:

$$\frac{1}{r}\frac{\partial(ru)}{\partial r}+\frac{1}{r}\frac{\partial v}{\partial \theta}=0 \tag{1}$$

$$u\frac{\partial u}{\partial r}+\frac{v}{r}\frac{\partial u}{\partial \theta}-\frac{v^2}{r}=\frac{1}{\rho}\left[\rho g\beta(T-T_\infty)\sin(\theta)-\frac{\partial p}{\partial r}\right]+\nu\left[\frac{\partial^2 u}{\partial r^2}+\frac{1}{r}\frac{\partial u}{\partial r}-\frac{u}{r^2}+\frac{1}{r^2}\frac{\partial^2 u}{\partial \theta^2}-\frac{2}{r^2}\frac{\partial v}{\partial \theta}\right] \tag{2}$$

$$u\frac{\partial v}{\partial r}+\frac{v}{r}\frac{\partial v}{\partial \theta}+\frac{uv}{r}=\frac{1}{\rho}\left[\rho g\beta(T-T_\infty)\cos(\theta)-\frac{1}{r}\frac{\partial p}{\partial \theta}\right]+\upsilon\left[\frac{\partial^2 v}{\partial r^2}+\frac{1}{r}\frac{\partial v}{\partial r}-\frac{v}{r^2}+\frac{1}{r^2}\frac{\partial^2 v}{\partial \theta^2}+\frac{2}{r^2}\frac{\partial u}{\partial \theta}\right] \tag{3}$$

Contributed by the Heat Transfer Division for publication in the JOURNAL OF HEAT TRANSFER. Manuscript received by the Heat Transfer Division March 22, 2002; revision received October 8, 2002. Associate Editor: K. S. Ball.

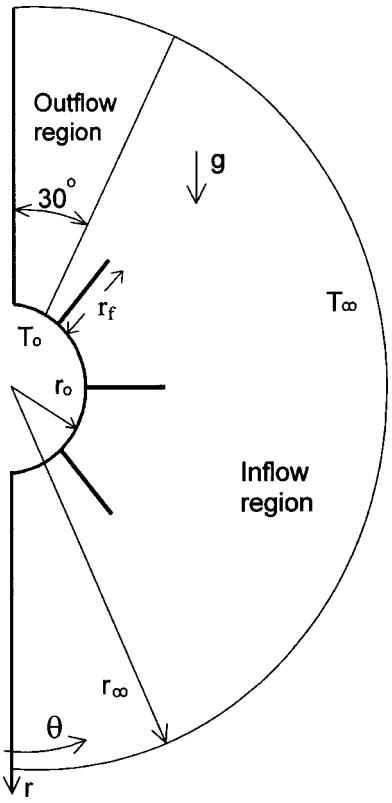

Fig. 1 Schematic of the problem, showing a case with non-uniform fin distribution

$$u\frac{\partial T}{\partial r}+\frac{v}{r}\frac{\partial T}{\partial \theta}=\alpha\nabla^2 T \tag{4}$$

where,

$$\nabla^2\equiv\left[\frac{\partial^2}{\partial r^2}+\frac{1}{r}\frac{\partial}{\partial r}+\frac{1}{r^2}\frac{\partial^2}{\partial\theta^2}\right]$$

Equations (1)–(4) are subject to the following boundary conditions:

1 On the cylinder surface, i.e., $r=r_o$; $u=v=0$ and $T=T_o$.

2 Far-stream from the cylinder, i.e., $r\to\infty$; $\partial v/\partial r=0$. As for the temperature, and following the work of Kuehn and Goldstein [3] and Abu-Hijleh et al. [8], the far-stream boundary condition is divided into an inflow ($\theta\leqslant 150$deg) and an outflow (θ

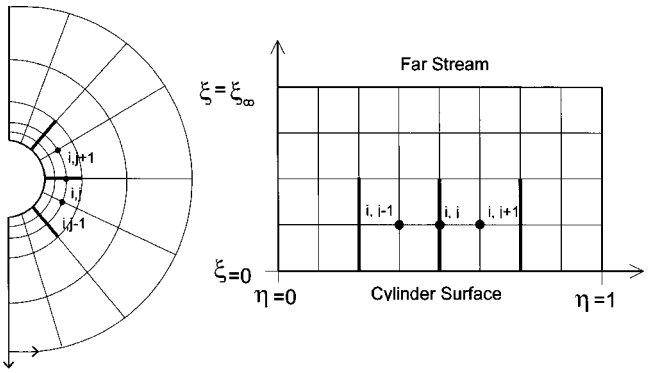

Fig. 2 Schematic of the computational grid in the physical (left) and computational (right) domains, showing a case with uniform fin distribution

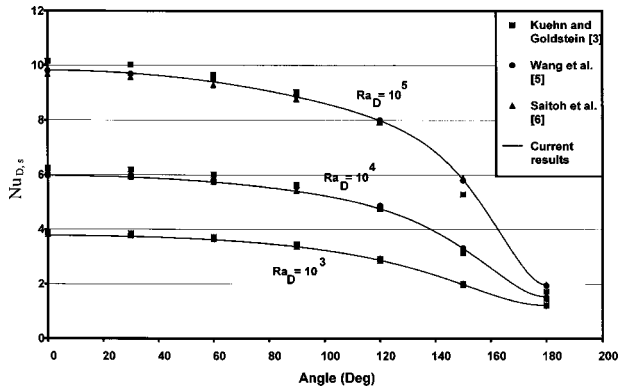

Fig. 3 Comparison of the local Nusselt number for the case of a cylinder without fins

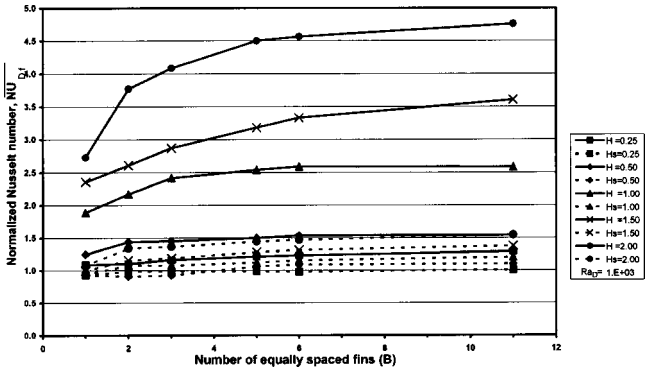

Fig. 4 Change in the normalized Nusselt number of the permeable fins (solid lines) and solid fins (broken lines), at $Ra_D=10^3$

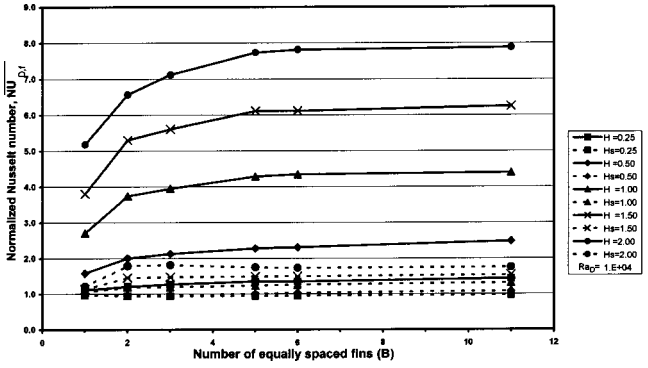

Fig. 5 Change in the normalized Nusselt number of the permeable fins (solid lines) and solid fins (broken lines), at $Ra_D=10^4$

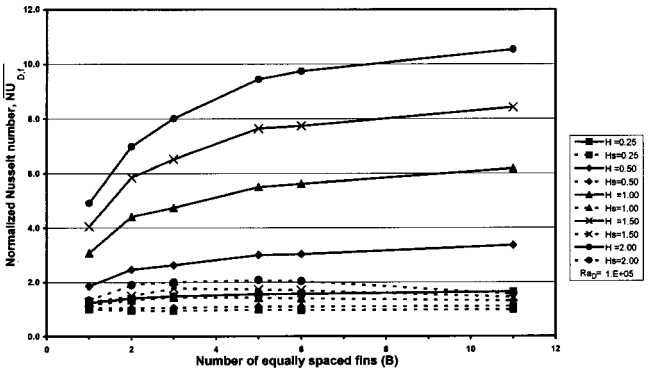

Fig. 6 Change in the normalized Nusselt number of the permeable fins (solid lines) and solid fins (broken lines), at $Ra_D=10^5$

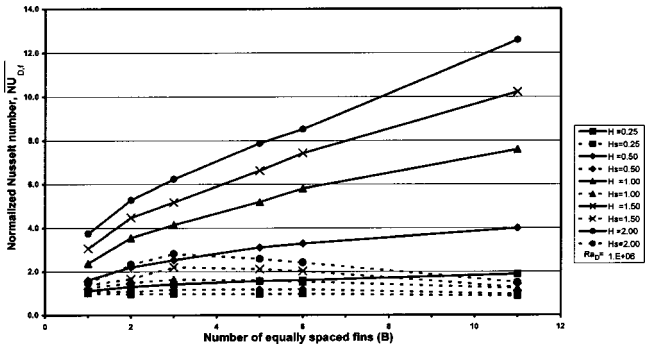

Fig. 7 Change in the normalized Nusselt number of the permeable fins (solid lines) and solid fins (broken lines), at $Ra_D=10^6$

>150deg) regions, Fig. 1. The far-stream temperature boundary conditions are $T=T_\infty$ and $\partial T/\partial r=0$ for the inflow and outflow regions, respectively.

3. Plane of symmetry; $\theta=0$ and $\theta=180$degrees; $v=0$ and $\partial u/\partial\theta=\partial T/\partial\theta=0$.

4. On the permeable fin surface; $u=0$. The least restrictive permeable boundary condition is that of no resistance to the velocity normal to the fin surface, i.e., $v=\text{constant}\equiv\partial v/\partial\theta=0$ [11]. The fins are assumed to be very thin and of very high conductivity, thus the temperature along the fin will be equal to that of the cylinder's surface, i.e., $T_{\text{fin}}=T_o$.

The major assumptions made regarding the fins' boundary conditions above are: fin thickness$\rightarrow$0, fin thermal conductivity $\rightarrow\infty$, and fin flow resistance$\rightarrow$0. These assumptions we introduced in order to simplify the solution of the problem and will give the ''best case scenario'' effect of using permeable fins. ''Real'' fins will have a finite thickness and thermal conductivity. If this is to be taken into account, the problem will become that of conjugated conduction—convection heat transfer. This will greatly complicate the solution procedure as well as introduce two new parameters that need to be considered, i.e. fin thickness and fin thermal conductivity. Neglecting the fin's flow resistance will only change the velocity gradient boundary condition at the fin but will not affect the computational procedure. Still this will introduce another parameter that need to be addressed. The inclusion of any of these parameters will greatly increase the number of different cases that need to be simulated and will further expand the size of this paper. Thus as a first attempt at studying the benefits of permeable fins, the author made a conscious decision to introduce the above mentioned simplifying assumptions. With the ''ideal'' performance of permeable fins established, future work can focus on real fin effects such as the fin's flow resistance, thickness, and thermal conductivity.

The local Nusselt number, based on diameter, on the cylinder surface is given by:

$$\text{Nu}_{D,s}(\theta)=\frac{Dh(\theta)}{k}=-\frac{D}{(T_o-T_\infty)}\frac{\partial T(r_o,\theta)}{\partial r} \tag{5}$$

The local Nusselt number at the fin, based on diameter, is given by:

$$\text{Nu}_{D,f}(\theta_f)=\int_1^{\text{fin}}-\frac{D}{(T_o-T_\infty)}\frac{1}{r}\left[\left.\frac{\partial T(r,\theta_f)}{\partial\theta}\right|_{\text{top}}+\left.\frac{\partial T(r,\theta_f)}{\partial\theta}\right|_{\text{bottom}}\right]dr \tag{6}$$

The effective average Nusselt number, including the effect of the fin(s) is given by:

$$\overline{\text{Nu}_{D,f}}=\int_0^{\pi}\text{Nu}_{D,s}(\theta)d\theta+\sum_1^{N_f}\text{Nu}_{D,f}(\theta_f) \tag{7}$$

The following nondimensional groups are introduced:

$$R\equiv\frac{r}{r_o},\quad U\equiv\frac{u}{(\alpha/r_o)},\quad V\equiv\frac{v}{(\alpha/r_o)},\quad \phi\equiv\frac{(T-T_\infty)}{(T_o-T_\infty)},$$
$$P\equiv\frac{(p-p_\infty)}{\frac{1}{2}\rho(\alpha/r_o)^2},\quad H\equiv\frac{r_{\text{fin}}-r_o}{r_o} \tag{8}$$

Using the stream function-vorticity formulation, the nondimensional form of Eqs. (1)–(4) is given by:

$$\omega=\nabla^2\psi \tag{9}$$

$$U\frac{\partial\omega}{\partial R}+\frac{V}{R}\frac{\partial\omega}{\partial\theta}=\text{Pr}\nabla^2\omega+\text{RaPr}\left[\sin(\theta)\frac{\partial\phi}{\partial R}+\frac{\cos(\theta)}{R}\frac{\partial\phi}{\partial\theta}\right] \tag{10}$$

$$U\frac{\partial\phi}{\partial R}+\frac{V}{R}\frac{\partial\phi}{\partial\theta}=\nabla^2\phi \tag{11}$$

where,

$$U\equiv\frac{1}{R}\frac{\partial\psi}{\partial\theta},\quad V\equiv-\frac{\partial\psi}{\partial R},\quad \text{Ra}=\frac{g\beta r_o^3(T_o-T_\infty)}{\alpha\nu},$$
$$\text{Ra}_D=\frac{g\beta D^3(T_o-T_\infty)}{\alpha\nu},\quad \text{Pr}=\frac{\nu}{\alpha} \tag{12}$$

The new non-dimensional boundary conditions for Eqs. (9)–(11) are given by:

1. On the cylinder surface, i.e., $R=1.0$; $\psi=\partial\psi/\partial R=0$, $\omega=\partial^2\psi/\partial R^2$, and $\phi=1.0$.
2. Far-stream form the cylinder, i.e., $R\rightarrow\infty$; $\partial^2\psi/\partial R^2=0$ and $\omega=-(1/R^2)(\partial^2\psi/\partial\theta^2)$. For the nondimensional temperature, $\phi=0$, and $\partial\phi/\partial R=0$, for the inflow and outflow regions, respectively.
3. Plane of symmetry; $\psi=\omega=\partial\phi/\partial\theta=0$.
4. On the fin surface; $\partial^2\psi/\partial R\partial\theta=0$, and $\phi_{\text{fin}}=1.0$.

In order to accurately resolve the boundary layer around cylinder, a grid with small radial spacing is required. It is not practical to use this small spacing as we move to the far-stream boundary. Thus a stretched grid in the radial direction is needed [14]. This will result in unequally spaced nodes and would require the use of more complicated and/or less accurate finite difference formulas. To overcome this problem, the unequally spaced grid in the physical domain (R,θ) is transformed into an equally spaced grid in the computational domain (ξ,η) [14], Fig. 2. The two domains are related as follows:

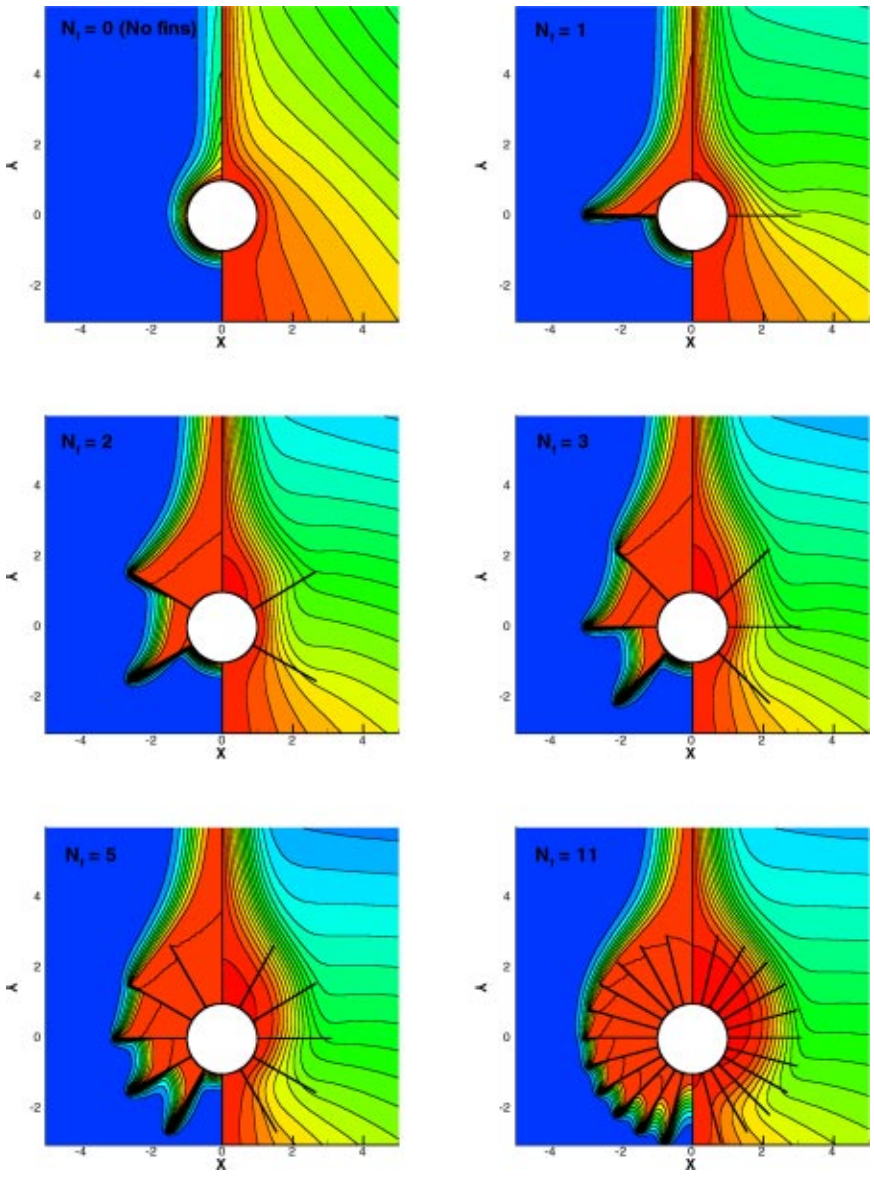

Fig. 8 Streamlines (right) and isotherms (left) for the case $Ra_D=10^4$ and $H=2.00$ for different number of permeable fins

$$R=e^{\pi\xi}, \quad \theta=\pi\eta \tag{13}$$

Equations (9)–(11) along with the corresponding boundary conditions need to be transformed into the computational domain. In the new computational domain, the current problem is given by:

$$\omega=\frac{1}{E^2}\left[\frac{\partial^2\psi}{\partial\xi^2}+\frac{\partial^2\psi}{\partial\eta^2}\right] \tag{14}$$

$$\frac{\partial^2\omega}{\partial\xi^2}+\frac{\partial^2\omega}{\partial\eta^2}=\frac{1}{\mathrm{Pr}}\left[\frac{\partial\psi}{\partial\eta}\frac{\partial\omega}{\partial\xi}-\frac{\partial\psi}{\partial\xi}\frac{\partial\omega}{\partial\eta}\right]-E\mathrm{Ra}\left[\sin(\pi\eta)\frac{\partial\phi}{\partial\xi}+\cos(\pi\eta)\frac{\partial\phi}{\partial\eta}\right] \tag{15}$$

$$\frac{\partial^2\phi}{\partial\xi^2}+\frac{\partial^2\phi}{\partial\eta^2}=\left[\frac{\partial\psi}{\partial\eta}\frac{\partial\phi}{\partial\xi}-\frac{\partial\psi}{\partial\xi}\frac{\partial\phi}{\partial\eta}\right] \tag{16}$$

where,

$$E=\pi e^{\pi\xi} \tag{17}$$

The transformed boundary conditions are given by:

1. On the cylinder surface, i.e., $\xi=0$; $\psi=\partial\psi/\partial\xi=0$, $\omega=(1/\pi^2)(\partial^2\psi/\partial\xi^2)$, and $\phi=1.0$.
2. Far-stream form the cylinder, i.e., $\xi\rightarrow\infty$; $\partial^2\psi/\partial\xi^2=0$ and $\omega=-(1/E^2)(\partial^2\psi/\partial\eta^2)$. For the nondimensional temperature $\phi=0$ and $\partial\phi/\partial\xi=0$, for the inflow and outflow regions, respectively.
3. Plane of symmetry; i.e., $\eta=0$ and $\eta=1$; $\psi=\omega=\partial\phi/\partial\eta=0$.
4. On the fin surface; $\partial^2\psi/\partial\xi\partial\eta=0$, and $\phi_{\mathrm{fin}}=1.0$.

The effect of adding the fin(s) on the convection heat transfer from the cylinder will be presented in terms of the normalized Nusselt number ($\overline{\mathrm{NU}_{D,f}}$) which shows the relative change in the Nusselt number compared to the case of a smooth cylinder, Eq. (18) below. The ratio of ($\overline{\mathrm{NU}_{D,f}}$) permeable fins to ($\overline{\mathrm{NU}_{D,f}}$) solid fins will be used to gage the enhancement in heat transfer due to the use of permeable fins in place of solid fins, ($\overline{R\ \mathrm{NU}_{D,f}}$), Eq. (19) below.

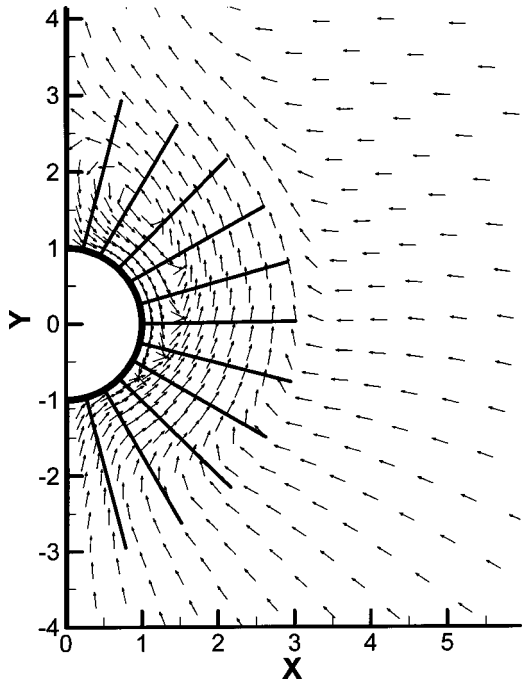

Fig. 9 Velocity vector plot for the case of $Ra_D=10^4$, $H=2.00$, and $N_f=11$ (constant length vectors are use, i.e., vector's length does not represent the magnitude of the velocity vector)

$$\overline{\mathrm{NU}_{D,f}}=\overline{\mathrm{Nu}_{D,f}}/\overline{\mathrm{Nu}_{D,o}} \tag{18}$$

$$\overline{R\ \mathrm{NU}_{D,f}}=(\overline{\mathrm{NU}_{D,f}})_{\mathrm{Permeable}}/(\overline{\mathrm{NU}_{D,f}})_{\mathrm{solid}} \tag{19}$$

The resulting system of elliptic PDEs along with the corresponding boundary conditions were discretized using the finite difference method. The resulting system of algebraic equations was solved using the hybrid scheme [15]. Such a method proved to be numerically stable for convection-diffusion problems. The finite difference form of the equations was checked for consistency with the original PDEs [15]. The iterative solution procedure was carried out until the error in all solution variables (ψ,ω,ϕ) became less than a predefined error level $(\in)$. Other predefined parameters needed for the solution method included the placement of the far-stream boundary condition (R_∞) and the number of grid points in both radial and tangential directions, N and M, respectively. Extensive testing was carried out in order to determine the effect of each of these parameters on the solution.

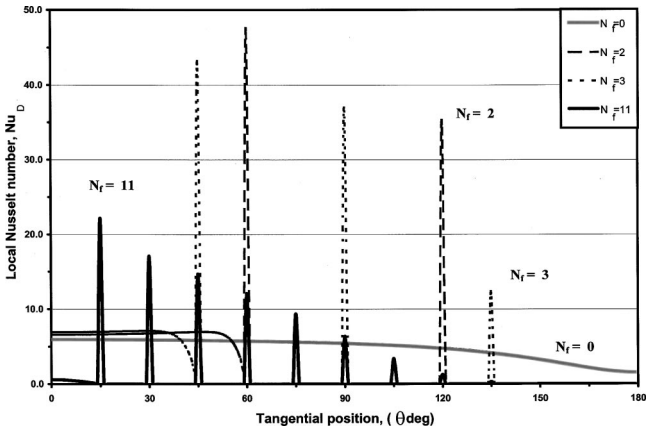

Fig. 10 Variation of the local Nusselt number for different number of permeable fins at $Ra_D=10^4$ and $H=2.00$

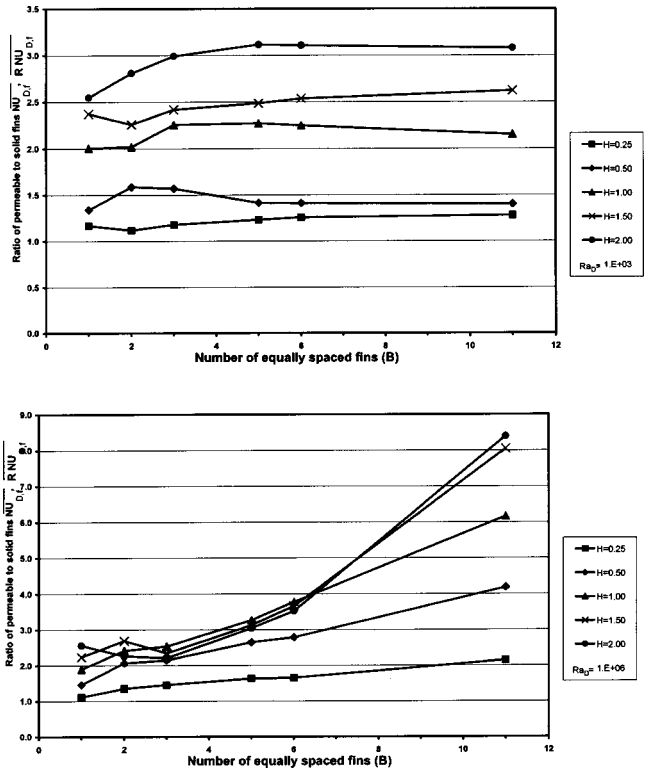

Fig. 11 Change in the ratio of the normalized permeable to solid fins Nusselt number at $Ra_D=10^3$ (top) and $Ra_D=10^6$ (bottom)

This was done to insure that the solution obtained was independent of the predefined value of each of these parameters. The testing included varying the value of $\in$ from 10^{-3} to 10^{-6}, R_∞ from 5 to 50, N from 60 to 150, and M from 60 to 144. For the case of a smooth cylinder at $Ra_D=10^5$, using $\in=10^{-5}$ and changing the grid size $(N\times M)$ from 60×60 to 120×90 to 140×120 to 150×144 resulted in average Nusselt number values of 7.7352, 7.7925, 7.7951, and 7.7948, respectively. These numbers indicate that a 120×90 grid size is fine enough to resolve the fluid and thermal boundary layers. Still the next size up grid (140×120) was chosen to allow for the changes in the flow and thermal fields that will rise as a result of adding the fins. For the same case $(Ra_D=10^5)$ and a grid size of (140×120), changing the predefined error level $(\in)$ from 10^{-3} to 10^{-4} to 10^{-5} to 10^{-6} resulted in average Nusselt number values of 8.5035, 8.0972, 7.7951, and 7.7943, respectively. The results reported herein are based on the following combination: $N\times M=140\times120$, $R_\infty=13.19$, and $\in=10^{-5}$. The accuracy of the local Nusselt number calculations, $\mathrm{Nu}_{D,s}(\theta)$, is another measure of the accuracy of the numerical code. Figure 3 shows very good agreement between the profiles of the local Nusselt number calculated by the current code and the data reported by Kuehn and Goldstein [3], Wang et al. [5], and Saitoh et al. [6], for the case of a cylinder with no fins.

In the previous work for uniformly spaced fins [10], the number of grid points was varied in the radial $(N=133-141)$ and tangential $(M=105-120)$ directions in order to insure that all fins coincided with one of the grid's radial lines and that the fins end coincided with one of the grid's tangential lines, Fig. 2. The need for the fins to coincide with the grid was also observed in this study but in a different fashion. In order to avoid any changes that might result from using different grids for different combinations of number fin(s) and fin height, a fixed size grid was used for combinations in this study (140×120). In this study the fin's tangential location was varied in 15 deg increments between 15–

165 deg. Thus using $M=120$ insured that the tangential grid resolution was suitable for all tangential fin locations. The hardest part was adjusting the radial grid resolution to insure that the fin's end coincided with one of the radial grid points. In this study the nominal fin heights (H) used were: 0.25, 0.5, 1.0, 1.5, and 2.0. The combination of $N=140$ and $R_\infty=13.19$ resulted in a difference of less that 1 percent between the actual fin height and the nominal fin height used in the current study. The actual height being that of the fin used in the calculation with the fin's end coinciding with the closest radial grid point while using a fixed radial grid resolution ($N=140$).

Results. Figures 4–7 show the change in $\overline{\mathrm{NU}_{D,f}}$ for the cases of $\mathrm{Ra}_D=10^3-10^6$, respectively. The solid curves indicate the results of permeable fins while the broken line curves indicate the results of solid fins. The solid fin cases were recomputed using the current fixed size grid, not the results of the previous work [10], and are intended to show the heat transfer enhancement due to the use of permeable fins. It can be seen that the use of permeable fins results in a significant heat transfer enhancement over solid fins under the same geometric and flow conditions. Under no condition does the increase of the number of permeable fins result in a reduction in the Nusselt number as opposed to case of using solid fins, Figs. 5–7. This clearly shows that permeable fins perform the function of increasing the heat transfer area without the penalty of reducing the convection currents, as is the case of solid fins [10]. At low Rayleigh number, the value of ($\overline{\mathrm{NU}_{D,f}}$) levels off at large number of permeable fins. As the air flows through the permeable fins it gets heated and creates a thermal wake behind the fin. This wake renders part of the next fin ineffective as the temperature gradient between the next fin and the incoming hot air is small and thus not conducive to significant convection heat transfer. As the air flows through more fins the ineffective portion of each subsequent fin becomes larger. As the number of fins increases the spacing between the fins becomes smaller. This causes part of the hot air to get ''trapped'' between the fins resulting in a recirculation region which further increases the ineffective portion of the fins. Also as the number of fins increases the surrounding cold air cannot penetrate radially deep into the smaller hot air pockets formed by the larger number of fins. This can be seen form the streamlines and isotherms shown in Fig. 8 for the case of $\mathrm{Ra}_D=10^4$ and $H=2.0$ at different number of fin configurations. The reduction in the effective portion of the fins is clearly visible from the isotherms while the increase in the radial size and tangential span of the recirculation zone can be deduced from the streamlines. Figure 9 shows the velocity vector plot for the case of $\mathrm{Ra}_D=10^4$, $H=2.0$, and $N_f=11$. In this figure, constant length vectors are used. The use of vectors whose length is proportional to the magnitude of the velocity would have rendered the slow speed recirculation zone not visible. Figure 9 clearly shows the reduction in the cool surrounding air's ability to penetrate between the subsequent fins. The size of the recirculation zone is also visible. Figure 10 shows the tangential distribution of the local Nusselt number around the cylinder for the same conditions in Fig. 8 but limited to four cases in order to improve readability. The reduction in the heat transfer from each subsequent fin is clearly visible. Also visible is the reduction in the individual fin contribution as the total number of fins is increased from $N_f=2$ to 3 to 11.

Figure 11 shows the ratio of ($\overline{\mathrm{NU}_{D,f}}$) permeable fins to ($\overline{\mathrm{NU}_{D,f}}$) solid fins, ($\overline{R\ \mathrm{NU}_{D,f}}$), at $\mathrm{Ra}_D=10^3$ and 10^6. The ratio ($\overline{R\ \mathrm{NU}_{D,f}}$) increased with increasing number of fins, fin height, and Rayleigh number and was as high as 8.4 at $\mathrm{Ra}_D=10^6$, $H=2.0$, and $B=11$. Such high heat transfer rates can only be achieved by using fan induced mixed or forced convection heat transfer when coupled with solid fins. The use of permeable fins is an excellent passive method for providing high heat transfer rates for electronic components in a small, light weight, low maintenance, and energy free package. This figure indicates that the use of permeable fins is more beneficial when using long fins. This is logical since long solid fins tend to significantly suppress the convection currents around the cylinder. It is in such circumstances that the aerodynamic advantages of permeable fins become prevalent. The significant increase in permeable fin heat transfer compared to that of solid fins at large number of fins and high Rayleigh is mainly due to the reduction in ($\overline{\mathrm{NU}_{D,f}}$) of solid fins at combinations of large number of long solid fins and high Rayleigh numbers, Figs. 5–7.

Conclusions

The problem of laminar natural convection heat transfer from a horizontal cylinder with uniformly spaced permeable high conductivity fins was studied numerically over a range of Rayleigh numbers and for different configurations of number of fins and fin height. The use of permeable fins resulted in much higher Nusselt number values than for cases of similar cylinder/fin configurations but with solid fins. Permeable fins increased the heat transfer area without suppressing the convection currents, as is the case of solid fins. The ratio between the permeable to solid fins Nusselt number increased, up to 8.4, with Rayleigh number, fin height, and number of fins. At low Rayleigh numbers, $\mathrm{Ra}_D\leqslant 10^4$, the Nusselt number of permeable fins did not increase much for $N_f\geqslant 5$. The results indicate that permeable fins can be very useful in situations which require higher heat transfer rates than what can be achieved by the use of regular solid fins.

Nomenclature

D = cylinder diameter (meters), $2\,r_o$
E = parameter in computational domain, $\pi e^{\pi\xi}$
g = gravity
H = nondimensional fin height
h = local convection heat transfer coefficient
k = conduction heat transfer coefficient
M = number of grid points in the tangential direction
N = number of grid points in the radial direction
N_f = number of fins
$\mathrm{Nu}_{D,s}$ = local Nusselt number on the cylinder surface based on diameter
$\mathrm{Nu}_{D,f}$ = local Nusselt number over the length of the fin based on diameter
$\overline{\mathrm{Nu}_{D,0}}$ = average Nusselt number based on cylinder diameter, reference case with no fins
$\overline{\mathrm{Nu}_{D,f}}$ = average Nusselt number based on cylinder diameter, including effect of (f) number of fins
$\overline{\mathrm{NU}_{D,f}}$ = normalized average Nusselt number based on cylinder diameter, including effect of (f) fins
P = nondimensional pressure
p = pressure
Pr = Prandtl number
R = nondimensional radius
r = radius
r_f = fin radius
r_o = cylinder radius
Ra = Rayleigh number based on cylinder radius, $g\beta(T_o-T_\infty)r_o^3/\alpha v$
Ra_D = Rayleigh number based on cylinder diameter, $g\beta(T_o-T_\infty)D^3/\alpha v$
$\overline{\mathrm{R\ NU}_{D,f}}$ = Ratio of the normalized Nusselt number for the case of permeable fins to that of solid fins
T = temperature
U = nondimensional radial velocity
u = radial velocity
V = nondimensional tangential velocity
v = tangential velocity
α = thermal diffusivity
β = coefficient of thermal expansion
$\in$ = measure of convergence of numerical results

η = independent parameter in computational domain representing tangential direction
θ = angle
ν = kinematic viscosity
ξ = independent parameter in computational domain representing radial direction
ρ = density
ϕ = nondimensional temperature
ψ = stream function
ω = vorticity function

Subscripts

D = value based on cylinder diameter
f = value at fin
o = value at cylinder surface
∞ = free stream value

References

[1] Morgan, V. T., 1975, ''The Overall Convective Heat Transfer From Smooth Circular Cylinders,'' Adv. Heat Transfer, **11**, pp. 199–264.
[2] Churchill, S. W., and Chu, H. H. S., 1975, ''Correlating Equations for Laminar and Turbulent Free Convection From a Horizontal Cylinder,'' Int. J. Heat Mass Transf., **18**, pp. 1049–1053.
[3] Kuehn, T. H., and Goldstein, R. J., 1980, ''Numerical Solutions to the Navier-Stokes Equations for Laminar Natural Convection About a Horizontal Cylinder,'' Int. J. Heat Mass Transf., **23**, pp. 971–979.
[4] Farouk, B., and Guceri, S. I., 1981, ''Natural Convection From a Horizontal Cylinder-Laminar Regime,'' J. Heat Transfer, , **103**, pp. 522–527.
[5] Wang, P., Kahawita, R., and Nguyen, T. H., 1990, ''Numerical Computation of the Natural Convection Flow About a Horizontal Cylinder Using Splines,'' Numer. Heat Transfer, Part A, **17**, pp. 191–215.
[6] Saitoh, T., Sajik, T., and Maruhara, K., 1993, ''Benchmark Solutions to Natural Convection Heat Transfer Problem Around a Horizontal Circular Cylinder,'' Int. J. Heat Mass Transf., **36**, pp. 1251–1259.
[7] Chai, J. C., and Patankar, S. V., 1993, ''Laminar Natural Convection in Internally Finned Horizontal Annuli,'' Numer. Heat Transfer, Part A, **24**, pp. 67–87.
[8] Abu-Hijleh, B. A/K, Abu-Qudais, M., and Abu-Nada, E., 1998, ''Entropy Generation Due to Laminar Natural Convection From a Horizontal Isothermal Cylinder,'' J. Heat Transfer, , **120**, pp. 1089–1990.
[9] Eckert, E. R. G., Goldstein, R. J., Ibele, W. E., Patankar, S. V., Simon, T. W., Kuehn, T. H., Strykowski, P. J., Tamman, K. K., Bar-Cohen, A., Heberlein, J. V. R., Davidson, J. H., Bischof, J., Kulacki, F. A., Kortshagenm, U., and Garrick, S., 2000, ''Heat Transfer—A Review of 1997 Literature,'' Int. J. Heat Mass Transf., **43**, pp. 2431–2528.
[10] Abu-Hijleh, B. A/K, 2001, ''Natural Convection and Entropy Generation From a Cylinder with high Conductivity Fins,'' J. Numer. Heat Transfer, **39**, pp. 405–432.
[11] Stewart, W. E., and Burns, A. S., 1992, ''Convection in a Concentric Annulus with Heat Generating Porous Media and a Permeable Inner Boundary,'' Int. Commun. Heat Mass Transfer, **19**, pp. 859–868.
[12] Zhao, T. S., and Liao, Q., 2000, ''On Capillary-Driven Flow and Phase-Change Heat Transfer in a Porous Structure Heated by a Finned Surface: Measurements and Modeling,'' Int. J. Heat Mass Transf., **43**, pp. 1141–1155.
[13] Zhao, T. S., and Song, Y. J., 2001, ''Forced Convection in a Porous Medium Heated by a Permeable Wall Perpendicular to Flow Direction: Analyses and Measurements,'' Int. J. Heat Mass Transf., **44**, pp. 1031–1037.
[14] Anderson, J. D., 1994, *Computational Fluid Dynamics: The Basics with Applications*, McGraw Hill, New York.
[15] Patankar, S. V., 1980, *Numerical Heat Transfer of Fluid Flow*, McGraw Hill, New York.

Line Plume Approximation on Atrium Smoke Filling With Thermal Stratified Environment

J. Li

W. K. Chow

Department of Building Services Engineering,
The Hong Kong Polytechnic University,
Hong Kong, China

Upward motion of a balcony spill plume in an atrium with a thermal stratified layer will be simulated. This is aimed at answering the question on whether a smoke plume can move up an atrium to reach the ceiling. The gradient of air density in the atrium is taken as a constant negative value. The plume motion under this condition is compared with the case without a thermal stratified layer. It is noted that the effect of stratification is not obvious in regions near to the fire. But for the upper region of the plume, the effect is significant. In this way, the plume might not be able to reach the ceiling of an atrium with a hot enough thermal stratified layer. The maximum plume rise under this condition will also be calculated. [DOI: 10.1115/1.1532009]

Keywords: Enclosure Flows, Entrainment, Fire, Heat Transfer, Plumes, Stratified

1 Introduction

Knowledge on how a balcony spill plume flows out of a shop to fill up an atria is important in determining the fire safety measures with some works reported in the literature ([1–4]). Based on earlier experimental results ([5,6]), correlations on air entrainment into a two-dimensional spill plume were developed ([7,8]) using dimensional analysis with the line plume theory ([9]) and Computational Fluid Dynamics (CFD) ([10,11]). In those works, the plume and the fire under the balcony were treated separately. The spill plume was considered as a two-dimensional flow emerging from under the balcony with the atrium temperature taken as a constant.

However, there might be a thermal stratified layer inside an atrium with glazed ceiling due to solar heating. The magnitude of the vertical temperature gradient depends on the geometry and the architectural features of the atrium ([12–14]). Buoyancy acting on the fire-induced plume might be reduced if the ambient temperature increases with height. The plume cannot travel up to the roof as shown in Fig. 1 if the temperature of the plume is lower than the ambient due to cool air entrainment. Sprinkler heads and thermal detectors installed at the atrium ceiling might not be activated. Further, smoke management systems [e.g., ([14–16])] such as natural vents might not be effective in extracting smoke. The effects of the thermal stratified layer on the development of the plume should be considered carefully and will be discussed in this paper.

2 Review on Line Plume Theory in Uniform Environment

One of the earliest works on line plumes might be due to Lee and Emmons [9] with assumptions:

- Turbulent flow is fully developed with negligible molecular diffusion
- Local density variations are small compared with the reference density in the field
- Acceleration along the horizontal direction is small compared with that along the vertical direction
- The rate of entrainment at the edge of the plume is proportional to the centerline velocity at that height

A set of key equations can be derived (as shown in Appendix A) from the integral forms of the conservation equations on a line plume. Gaussian profile assumptions are taken for vertical velocity and temperature rise.

- The vertical velocity along the centerline w_m is:

$$w_m=\sqrt{2}\left(\frac{\sqrt{1+\lambda^2}}{4}\right)^{1/3}\frac{1}{(\alpha L)^{1/3}}F_0^{1/3}=\left(\frac{\sqrt{1+\lambda^2}}{\sqrt{2}}\right)^{1/3}\frac{1}{\alpha^{1/3}}\left(\frac{g\dot{Q}_c'}{\rho_a C_p T_a}\right)^{1/3} \tag{1}$$

- The Gaussian half-width of the plume b is:

$$b=\frac{2\alpha}{\sqrt{\pi}}z \tag{2}$$

- The density difference $\Delta\rho_m$ is given by:

$$\frac{\Delta\rho_m}{\rho_a}=\frac{(\sqrt{2})^{1/3}(\sqrt{1+\lambda^2})^{2/3}}{2\alpha^{2/3}}\frac{1}{\lambda g}\left(\frac{g\dot{Q}_c'}{\rho_a C_p T_a}\right)^{2/3}z^{-1} \tag{3}$$

- The volume flux per unit length N/L is:

$$\frac{N}{L}=2\cdot\left(\frac{\sqrt{1+\lambda^2}}{\sqrt{2}}\right)^{1/3}\alpha^{2/3}F_0'^{1/3}z=2\cdot\left(\frac{\sqrt{1+\lambda^2}}{\sqrt{2}}\right)^{1/3}\alpha^{2/3}\left(\frac{g\dot{Q}_c'}{\rho_a C_p T_a}\right)^{1/3}z \tag{4}$$

- The mass flux $\dot{m}$ can be expressed as:

$$\dot{m}=2^{5/6}\alpha^{2/3}(\sqrt{1+\lambda^2})^{1/3}L\rho_a\left(\frac{g\dot{Q}_c'}{\rho_a C_p T_a}\right)^{1/3}z \tag{5}$$

Dividing $\dot{m}$ by L gives:

$$\dot{m}/L=2^{5/6}\alpha^{2/3}(\sqrt{1+\lambda^2})^{1/3}\rho_a\left(\frac{g\dot{Q}_c'}{\rho_a C_p T_a}\right)^{1/3}z \tag{6}$$

In the above equations,

$$F_0=\frac{g\dot{Q}_c}{\rho_a C_p T_a} \tag{7}$$

$$F_0'=F_0/L \tag{8}$$

Contributed by the Heat Transfer Division for publication in the JOURNAL OF HEAT TRANSFER. Manuscript received by the Heat Transfer Division February 13, 2002; revision received September 25, 2002. Associate Editor: K. S. Ball.

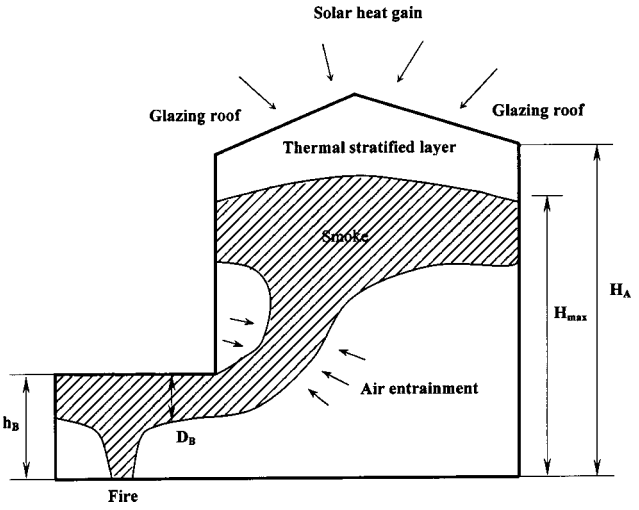

Fig. 1 Geometry of the problem

$$\dot{Q}_c' = \dot{Q}_c / L \tag{9}$$

$$\Delta\rho_m = \rho_a - \rho_m \tag{10}$$

ρ_a, C_p, and T_a are the density, specific heat and temperature of the ambient gas; α is the entrainment constant; λ is the ratio of the widths of buoyancy and velocity profiles; L is the length of the plume; z is the distance above the source; $\dot{Q}_c$ is the rate of heat release by the fire transferring to the plume, and the subscript m designates the local value along the plume axis.

As given by Eqs. (1) to (6), width of the plume induced by a line heat source will increase linearly with the elevation. The vertical velocity along the centerline is independent on the elevation, but the density difference is inversely proportional to the height.

3 Line Plume in a Thermal Stratified Layer

A similar approach can be applied to study a line plume in a thermal stratified layer as that for a plume rising in an atmosphere with constant density. A constant negative density gradient is assumed to simplify the analysis. For more complicated density gradients, the set of equations concerned had to be solved numerically.

Suppose the ambient fluid has a constant density gradient, dT_a/dz denoted by γ:

$$\gamma = -\frac{1}{\rho_{a0}}\frac{d\rho_a}{dz} \approx \frac{1}{T_{a0}}\frac{dT_a}{dz} \tag{11}$$

where ρ_{a0} is the standard density in the environment, T_{a0} is the corresponding temperature, and $d\rho_a/dz$ is the ambient density gradient.

Following similar analyses on buoyant point source plume by Morton and Turner [17–19], the conservation equations of mass, momentum and buoyancy can be reduced to the form:

$$\frac{d(\sqrt{\pi} L w_{sm} b_s)}{dz} = 2\alpha L w_{sm} \tag{12}$$

$$\frac{d\left(\sqrt{\frac{\pi}{2}} L w_{sm}^2 b_s\right)}{dz} = gL\lambda b_s \sqrt{\pi}\frac{\Delta\rho_{sm}}{\rho_{a0}} \tag{13}$$

$$\frac{d\left(\sqrt{\frac{\lambda^2}{1+\lambda^2}}\cdot\sqrt{\pi}\cdot b_s L\cdot g w_{sm}\frac{\Delta\rho_{sm}}{\rho_{a0}}\right)}{dz} = -\sqrt{\pi} b_s L w_{sm}\left(-\frac{g}{\rho_{a0}}\frac{d\rho_a}{dz}\right) \tag{14}$$

In the above equations,

$$\Delta\rho_{sm} = \rho_{sm} - \rho_a \tag{15}$$

$$\rho_a = \rho_{a0}(1-\gamma z) \tag{16}$$

Quantities with the subscript s refer to those for the stratified environment. The density gradient in the environment is described by the last term in Eq. (14).

Introducing:

$$G = -\frac{g}{\rho_{a0}}\frac{d\rho_a}{dz} \tag{17}$$

Solving the above conservation equations (as shown in Appendix B) would give the following in terms of φ:

$$\varphi = \sin^{-1}\left(\frac{M_s}{F_0\sqrt{\frac{\sqrt{1+\lambda^2}}{\sqrt{2}G}}}\right) \tag{18}$$

where

$$M_s = \sqrt{\frac{\pi}{2}} b_s L\cdot w_{sm}^2 \tag{19}$$

and

$$0 \leqslant \varphi \leqslant \pi \tag{20}$$

- The plume width b_s is given by:

$$\frac{b_s}{z} = \frac{3\alpha}{\sqrt{\pi}} f_1(\varphi) \tag{21}$$

where

$$f_1(\varphi) = \frac{(\varphi - \sin\varphi\cos\varphi)^{2/3}}{\sin\varphi\cdot\int_0^{\varphi}\frac{\sin\varphi d\varphi}{(\varphi-\sin\varphi\cos\varphi)^{1/3}}} \tag{22}$$

- The centerline upward velocity w_{sm} is:

$$\frac{w_{sm}}{z} = (\sqrt{1+\lambda^2})^{1/2} G^{1/2} f_2(\varphi) \tag{23}$$

where

$$f_2(\varphi) = \frac{\sin\varphi}{(\varphi-\sin\varphi\cos\varphi)^{1/3}\int_0^{\varphi}\frac{\sin\varphi d\varphi}{(\varphi-\sin\varphi\cos\varphi)^{1/3}}} \tag{24}$$

- The density difference is:

$$\frac{\Delta\rho_{sm}}{\rho_{a0}} z = \frac{\sqrt{2}}{6^{2/3}}\frac{(\sqrt{1+\lambda^2})^{2/3}}{\lambda g}\frac{F_0^{2/3}}{(\alpha L)^{2/3}} f_3(\varphi) \tag{25}$$

where

$$f_3(\varphi) = \frac{\cos\varphi}{(\varphi-\sin\varphi\cos\varphi)^{1/3}}\int_0^{\varphi}\frac{\sin\varphi d\varphi}{(\varphi-\sin\varphi\cos\varphi)^{1/3}} \tag{26}$$

- The volume flux N_s/z is expressed as:

$$\frac{N_s}{z} = \frac{6^{2/3}}{\sqrt{2}}(\sqrt{1+\lambda^2})^{1/3}(\alpha L)^{2/3} F_0^{1/3} f_4(\varphi) \tag{27}$$

where

$$f_4(\varphi)=\frac{(\varphi-\sin\varphi\cos\varphi)^{1/3}}{\int_0^{\varphi}\frac{\sin\varphi d\varphi}{(\varphi-\sin\varphi\cos\varphi)^{1/3}}} \tag{28}$$

- The plume elevation z is given as:

$$z=\frac{2}{6^{1/3}\cdot(\sqrt{2})^{3/2}(\sqrt{1+\lambda^2})^{1/6}}\cdot\frac{1}{(\alpha L)^{1/3}}\cdot\left(\frac{1}{G}\right)^{1/2}F_0^{1/3}\int_0^{\varphi}\frac{\sin\varphi d\varphi}{(\varphi-\sin\varphi\cos\varphi)^{1/3}} \tag{29}$$

- The mass flow rate of the plume is given by:

$$\dot{m}_s=\int_{-\infty}^{\infty}\rho w\cdot Lxdx\approx\rho_{a0}\left(1-\frac{G}{g}z\right)N_s$$

$$=\frac{6^{1/3}(\sqrt{1+\lambda^2})^{1/6}}{(\sqrt{2})^{1/2}}\rho_{a0}\left(1-\frac{G}{g}z\right)(\alpha L)^{1/3}\times\left(\frac{1}{G}\right)^{1/2}F_0^{2/3}(\varphi-\sin\varphi\cos\varphi)^{1/3} \tag{30}$$

Combining with Eq. (29) gives:

$$\frac{\dot{m}_s}{z}=\frac{6^{2/3}}{\sqrt{2}}(\sqrt{1+\lambda^2})^{1/3}\rho_{a0}\left(1-\frac{G}{g}z\right)(\alpha L)^{2/3}F_0^{1/3}f_4(\varphi) \tag{31}$$

4 Maximum Elevation

Characteristics of the plume in stratified ambient can be analyzed by the above Eqs. (21) to (31). The mean centerline velocity would decrease with the increase in height. For w_{sm} to approach zero:

$$\frac{\sin\varphi}{(\varphi-\sin\varphi\cos\varphi)^{1/3}}\to 0 \tag{32}$$

and $\varphi\to\pi$.

Vertical motion of the plume flow would be stopped, and the plume would reach its maximum elevation $z_{\max}$. Integrating Eq. (29) with φ tends to π, the maximum elevation $z_{\max}$ that the plume can reach is:

$$z_{\max}=\frac{2}{6^{1/3}\cdot(\sqrt{2})^{3/2}(\sqrt{1+\lambda^2})^{1/6}}\cdot\frac{1}{(\alpha L)^{1/3}}\cdot\left(\frac{1}{G}\right)^{1/2}F_0^{1/3}\int_0^{\pi}\frac{\sin\varphi d\varphi}{(\varphi-\sin\varphi\cos\varphi)^{1/3}}$$

$$=1.56\cdot(1+\lambda^2)^{-1/12}\alpha^{-1/3}F_0'^{1/3}G^{-1/2} \tag{33}$$

For $\lambda=1$,

$$z_{\max}=1.47\cdot\alpha^{-1/3}F_0'^{1/3}G^{-1/2} \tag{34}$$

Volume flux per unit length at height $z_{\max}$ can be calculated as:

$$N_s|_{z=z_{\max}}/L=1.435\cdot(\sqrt{1+\lambda^2})^{1/3}\cdot\alpha^{2/3}F_0'^{1/3}z_{\max} \tag{35}$$

Comparing with the volume flux in uniform environment at the same height,

$$N/N_s=1.24 \tag{36}$$

Therefore, air entrained from the stratified ambient is less than that entrained from the uniform environment at the same height. The buoyancy of the plume would be negative rather than positive at regions above the height with $\Delta\rho_{sm}/\rho_{a0}=0$.

For $\Delta\rho_{sm}/\rho_{a0}=0$, $\varphi\to\pi/2$,

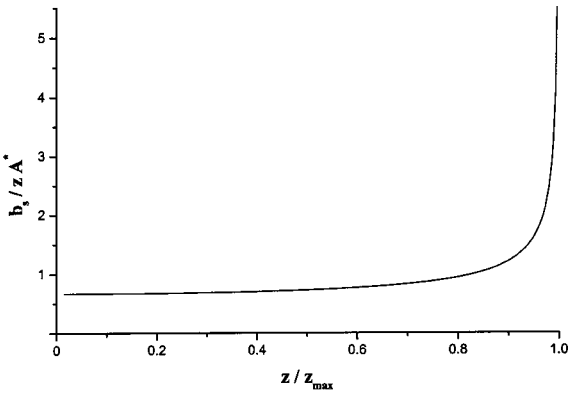

Fig. 2 Variation of the plume width with height

$$z_{\text{cri}}=\frac{2}{6^{1/3}\cdot(\sqrt{2})^{3/2}(\sqrt{1+\lambda^2})^{1/6}}\cdot\frac{1}{(\alpha L)^{1/3}}\cdot\left(\frac{1}{G}\right)^{1/2}F_0^{1/3}\int_0^{\pi/2}\frac{\sin\varphi d\varphi}{(\varphi-\sin\varphi\cos\varphi)^{1/3}}$$

$$=1.07\cdot(1+\lambda^2)^{-1/12}\alpha^{-1/3}F_0'^{1/3}G^{-1/2} \tag{37}$$

$$z_{\text{cri}}=0.69z_{\max} \tag{38}$$

That means the direction of buoyancy would change from upward to downward when the plume reaches 69 percent of the maximum height it can travel. In comparing with the plume induced by a point source, buoyancy would change the direction at 76 percent of the height it can rise ([18–22]). However, the upward velocity at that height would keep it moving up until decelerated by the downward buoyancy to reach $z_{\max}$ where the upward velocity becomes zero.

5 Numerical Examples

Numerical solutions of Eqs. (21), (23), (25), and (27) would give characteristics of the plume. The variations of plume width, centerline density difference and centerline vertical velocity as a function of height are shown in Figs. 2–4 respectively, with constants A^*, B^*, and C^* in these figures given by:

$$A^*=\frac{3\alpha}{\sqrt{\pi}} \tag{39}$$

$$B^*=\frac{\sqrt{2}}{6^{2/3}}\frac{(\sqrt{1+\lambda^2})^{2/3}}{\lambda g}\frac{F_0^{2/3}}{(\alpha L)^{2/3}} \tag{40}$$

$$C^*=(\sqrt{1+\lambda^2})^{1/2}G^{1/2} \tag{41}$$

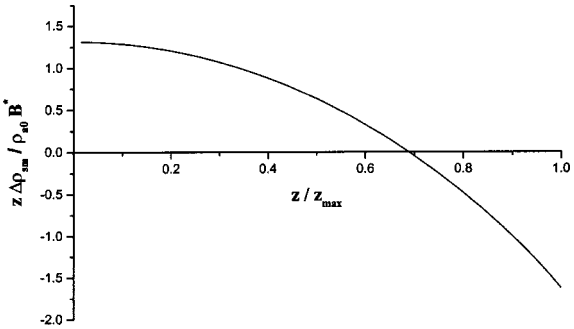

Fig. 3 Variation of the plume centerline density difference with height

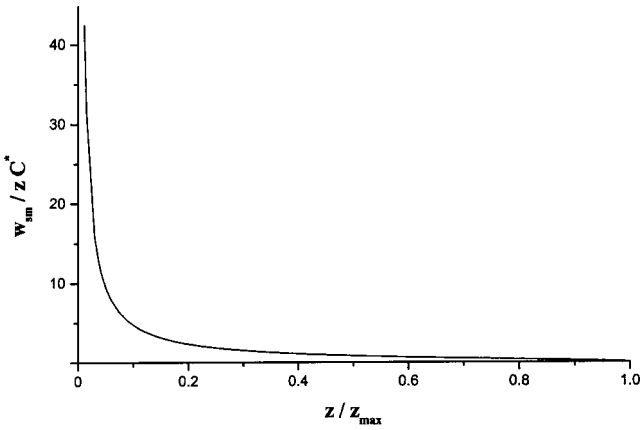

Fig. 4 Variation of the plume centerline velocity with height

Defining the nondimensional value of volume flux N'^*, and centerline density difference $\Delta\rho_m^*$ as:

$$N'^* = \frac{N'}{\left(\frac{g}{\rho_a C_p T_a}\right)^{1/3} \dot{Q}_c'^{1/3} z} \tag{42}$$

$$\Delta\rho_m^* = \frac{\Delta\rho_m}{\left(\frac{\rho_a}{g C_p^2 T_a^2}\right)^{1/3} \dot{Q}_c'^{2/3} z^{-1}} \tag{43}$$

In a constant temperature environment, N'^* and $\Delta\rho_m^*$ are constant; but in a stratified ambient, their values will change with height. Comparisons of plume width, nondimensional volume flux and nondimensional centerline density difference with the results predicted in uniform environment, described by $(b_s/z)/(b/z)$, $N_s'^*/N'^*$ and $\Delta\rho_{sm}^*/\Delta\rho_m$ respectively, are shown in Fig. 5.

For buoyant plumes induced by a point source rising in an environment with weak density gradient, the effects of stratification is relatively smaller near the source, but would dominate at the upper regions of the plume ([18–22]). A similar conclusion can be drawn for the line plumes. As shown in Figs. 2 to 5, the shape of the plume is similar to that predicted for a uniform environment at a lower height.

$$b_s \propto z \tag{44}$$

$$\Delta\rho_{sm}/\rho_{a0} \propto 1/z \tag{45}$$

and

$$w_{sm} \propto z^0 \tag{46}$$

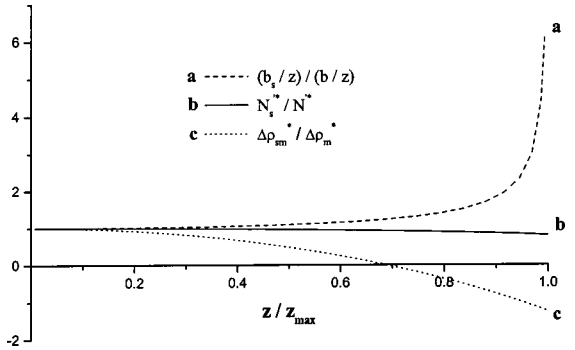

Fig. 5 Comparison of the plume rising in stratified environment with that rising in uniform ambient

However, with the increase in height, the effects of stratification would become more significant. Buoyancy would be reduced to zero at the height of 0.69 z_{max}, rather than 0.76 z_{max} in the point source plume ([18–22]), then become negative above it. Numerical results showed that the plume width would increase rapidly while approaching the maximum plume rise. The centerline velocity would decrease rapidly at the lower height and approach zero at the maximum rise. Volume flux of the plume under the two different environments would have almost the same tendency at all heights.

With a constant density gradient, the minimum convective heat release rate $\dot{Q}_{c\,\min}'$ required to drive the plume from the source to the ceiling can be found by:

$$\dot{Q}_{c\,\min}' = 0.264 \cdot \alpha(1+\lambda^2)^{1/4} \left(\frac{\rho_{a0} C_p T_{a0}}{g}\right) G^{3/2} H^3 \tag{47}$$

where H is the height of the room.

The increase in ambient temperature ΔT_a from the fire source to the ceiling to prevent a plume of strength $\dot{Q}_c'$ to reach the ceiling can be deduced from Eq. (33):

$$\frac{\Delta T_a}{T_{a0}} = 2.43 \cdot \frac{1}{(1+\lambda^2)^{1/6}} \frac{1}{\alpha^{2/3} g} \left(\frac{g\dot{Q}_c'}{\rho_{a0} C_p T_{a0}}\right)^{2/3} H^{-1} \tag{48}$$

For $\lambda = 1$,

$$\frac{\Delta T_a}{T_{a0}} = 2.166 \cdot \frac{1}{\alpha^{2/3} g} \left(\frac{g\dot{Q}_c'}{\rho_{a0} C_p T_{a0}}\right)^{2/3} H^{-1} \tag{49}$$

For comparison, the centerline temperature rise ΔT_m generated by a fire plume in a constant temperature environment at the ceiling level given by Eq. (3) can be expressed as:

$$\frac{\Delta T_m}{T_{a0}} = \frac{\Delta\rho_m}{\rho_{a0}} = 0.707 \cdot \frac{1}{\alpha^{2/3} g} \left(\frac{g\dot{Q}_c'}{\rho_{a0} C_p T_{a0}}\right)^{2/3} H^{-1} \tag{50}$$

$$\Delta T_{sm}/\Delta T_m \approx 3.06 \tag{51}$$

If the ambient temperature rise from the fire source to the ceiling is 3 times greater than the ceiling temperature rise predicted for a fire in a uniform environment, the plume cannot rise up to the ceiling. Remedial works, such as cooling down the stratified layer, should be considered to give smoke management system which can be more effective in controlling smoke.

Equations which describe the line plume characteristics in a stratified environment were derived theoretically through the conservation equations of mass, momentum and energy. λ and α are constants describing the flow before the plume rises to its maximum height in which local density variations are small ([18,19]). These constants are determined experimentally. Retaining λ and α in these equations might not affect the accuracy of these equations, as long as these values were determined experimentally. Different values of λ and α were proposed from different experiments in the past years ([26–29]). As in axisymmetric plumes for different cases, it appears that no universal values of λ and α can be derived. Suitable values should be chosen for fire engineering application, but have to be verified by full-scale burning tests.

6 Balcony Spill Plume in Stratified Environment

As described earlier, the balcony spill plume can be considered as two-dimensional flows emerging from under the balcony. As discussed by Poreh et al. [8], the balcony spill plume can be considered as a two-dimensional line plume with its virtual source located at the height of z_0 below the balcony. This is because only a small amount of air would be entrained into the turning region of the smoke flow from the horizontal to the vertical at the balcony edge. z_0 is given in terms of the depth of the buoyant layer beneath the balcony D_B and the mass flux beneath the balcony spill edge $\dot{m}_B$ by:

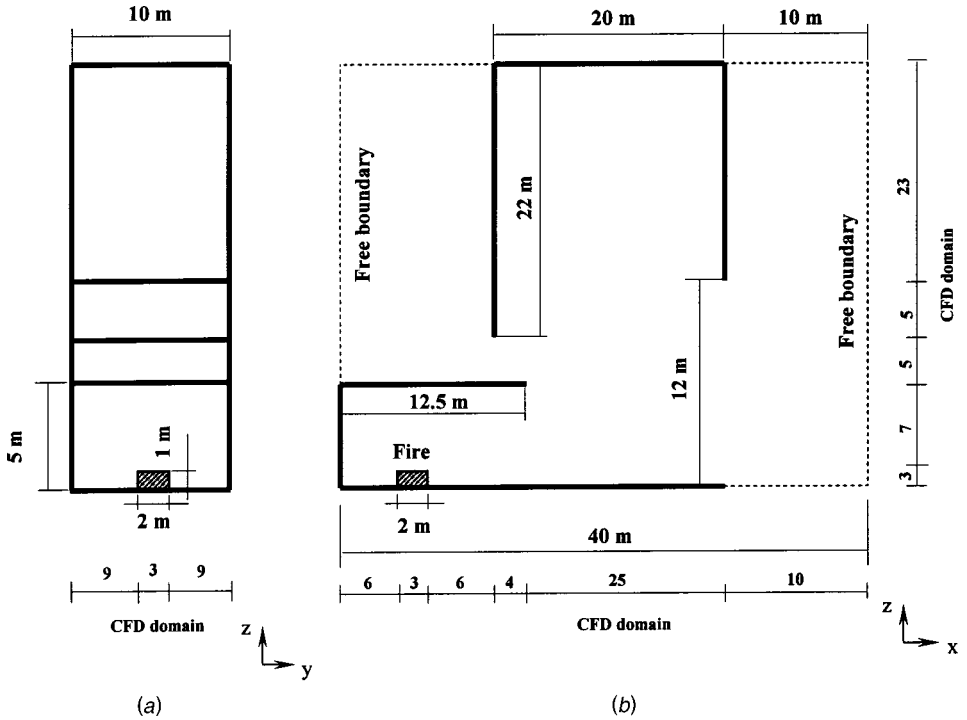

Fig. 6 Geometry for numerical experiments: (*a*) plane *y-z*; and (*b*) elevation

$$z_0 = D_B + \dot{m}_B / (C \dot{Q}_c'^{1/3}) \tag{52}$$

where

$$C = 2^{5/6} \alpha^{2/3} (\sqrt{1+\lambda^2})^{1/3} \rho_{a0} \left(\frac{g}{\rho_{a0} C_p T_{a0}} \right)^{1/3} \tag{53}$$

Based on the results predicted by the above theoretical derivation for a line plume in stratified environment, as shown in Fig. 5, at the lower level below the maximum rise, the behavior of the plume in weakly stratified atmosphere is similar to that predicted for a uniform environment, and the effects of stratification would only dominate at the upper region of the plume. Therefore, the buoyant spill plume rising in the atrium with constant density gradient could be taken as a line plume rising in the weakly stratified ambient with the source located at the height of z_0 below the balcony.

The maximum elevation which the balcony spill plume can reach is:

$$H_{\max} = z_{\max} - z_0 + h_B \tag{54}$$

where h_B is the height of the balcony, and $z_{\max}$ can be calculated by Eq. (33).

Assuming the height of the atrium is H_A, the minimum convective heat release rate to drive the spill plume from the source to the atrium ceiling can be calculated by Eq. (47) with

$$H = H_A - h_B + z_0 \tag{55}$$

Similarly, the ambient temperature rise which could just prevent a plume of strength $\dot{Q}_c'$ from reaching the ceiling can be calculated by Eq. (48).

The mass flux of the balcony spill plume in the stratified environment can be expressed as:

$$\frac{\dot{m}_{sA}}{z_A} = \frac{6^{2/3}}{\sqrt{2}} (\sqrt{1+\lambda^2})^{1/3} \rho_{a0} \left(1 - \frac{G}{g} z_A \right) (\alpha L)^{2/3} F_0^{1/3} f_4(\varphi) \tag{56}$$

In the above equation,

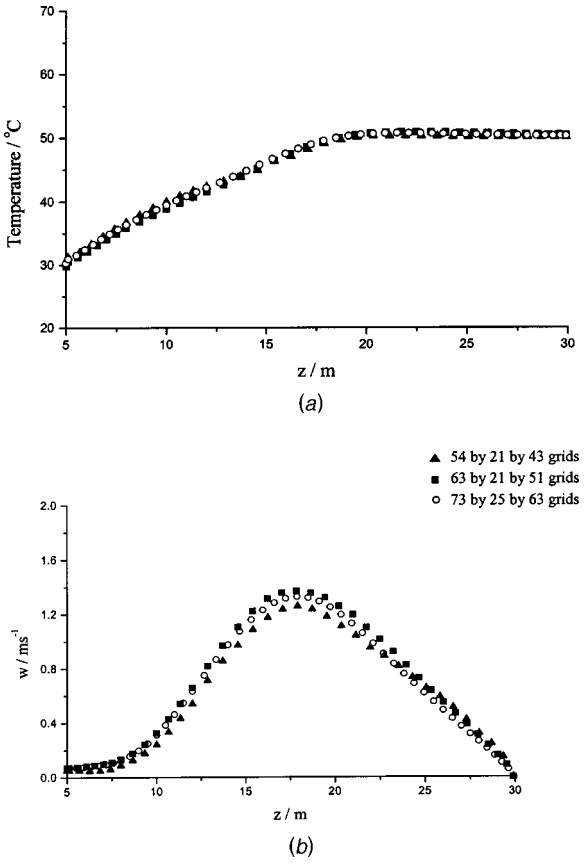

Fig. 7 Sensitivity studies on the grid size: (*a*) temperature distribution; and (*b*) vertical velocity distribution.

$$z_A = \frac{2}{6^{1/3}\cdot(\sqrt{2})^{3/2}(\sqrt{1+\lambda^2})^{1/6}}\cdot\frac{1}{(\alpha L)^{1/3}} \cdot\left(\frac{1}{G}\right)^{1/2} F_0^{1/3}\int_0^{\varphi}\frac{\sin\varphi d\varphi}{(\varphi-\sin\varphi\cos\varphi)^{1/3}} = f(\varphi) \qquad (57)$$

where $z_A \geqslant z_0$, $z_A - z_0 + h_B \leqslant H_{\max}$.

7 Numerical Simulation on Balcony Spill Plume

Smoke filling in an atrium with height 30 m, length 20 m and width 10 m due to a balcony spill plume resulted from an adjacent fire compartment was simulated. The dimensions of the compartment are 10 m by 10 m and 5 m high. The ceiling of the compartment was extended a distance of 2.5 m into the atrium. A fire of size 2 m×2 m×1 m with constant heat release rate of 2.0 MW was located at the center of the compartment.

The physical model was simulated with the free boundaries extended to outside, giving the entire computing domain of 40 m×10 m×30 m. Cartesian coordinate system was used in the simulations with z-axis taken to be opposite to the direction of gravity.

To save effort in developing CFD code from "scratch," PHOENICS ([23]) was selected as the simulator. This code has routines accessible for checking so that equations and parameters in the models can be modified. There is a module FLAIR ([23]) designed for simulating the fire-induced air flow by taking the fire as a heat and mass source. Verification works on applying this CFD code to simulate free plumes and flows induced by enclosure fires were reported [e.g., ([34–37])]. The predicted results agreed satisfactorily with the experiment, giving confidence in applying this CFD code to study line plumes.

The two-equation k-ε model with buoyancy modification ([30]) was used in the simulation. The governing equations are discretized into finite difference forms by the finite-volume method in a staggered grid system with the hybrid differencing scheme. The algorithm SIMPLEST was used for solving the velocity-pressure linked equations ([23]). The convergence criterion is to check whether the sum of normalized absolute residuals in each control volume for all variables is less than 10^{-3}. The fire was taken as a volumetric heat source. Combustion was not included in the simulation. This is sufficient to study the smoke movement in enclosure fires ([31–33]).

Nonuniform grids were used in the simulations. Coarse or fine grids were used at different positions to give the solutions within reasonable computing time. Time steps were initially taken as 0.1 s, and then increased to 0.5 s after 600 time steps. Comparisons of temperature and velocity profiles at several locations showed that the results will be the same when using grid distributions of 54 by 21 by 43. Results on the predicted vertical velocity w and temperature T at x of 20.2 m and y of 5 m for grid systems of 54 by 21 by 43, 63 by 21 by 51 and 73 by 25 by 63 as shown in Fig. 7 indicated that the results are the same. Further reduction in grid size did not give different results. Geometry of the atrium and the distributions of grids are shown in Fig. 6.

Two cases were simulated by taking the ambient air temperature as 20°C.

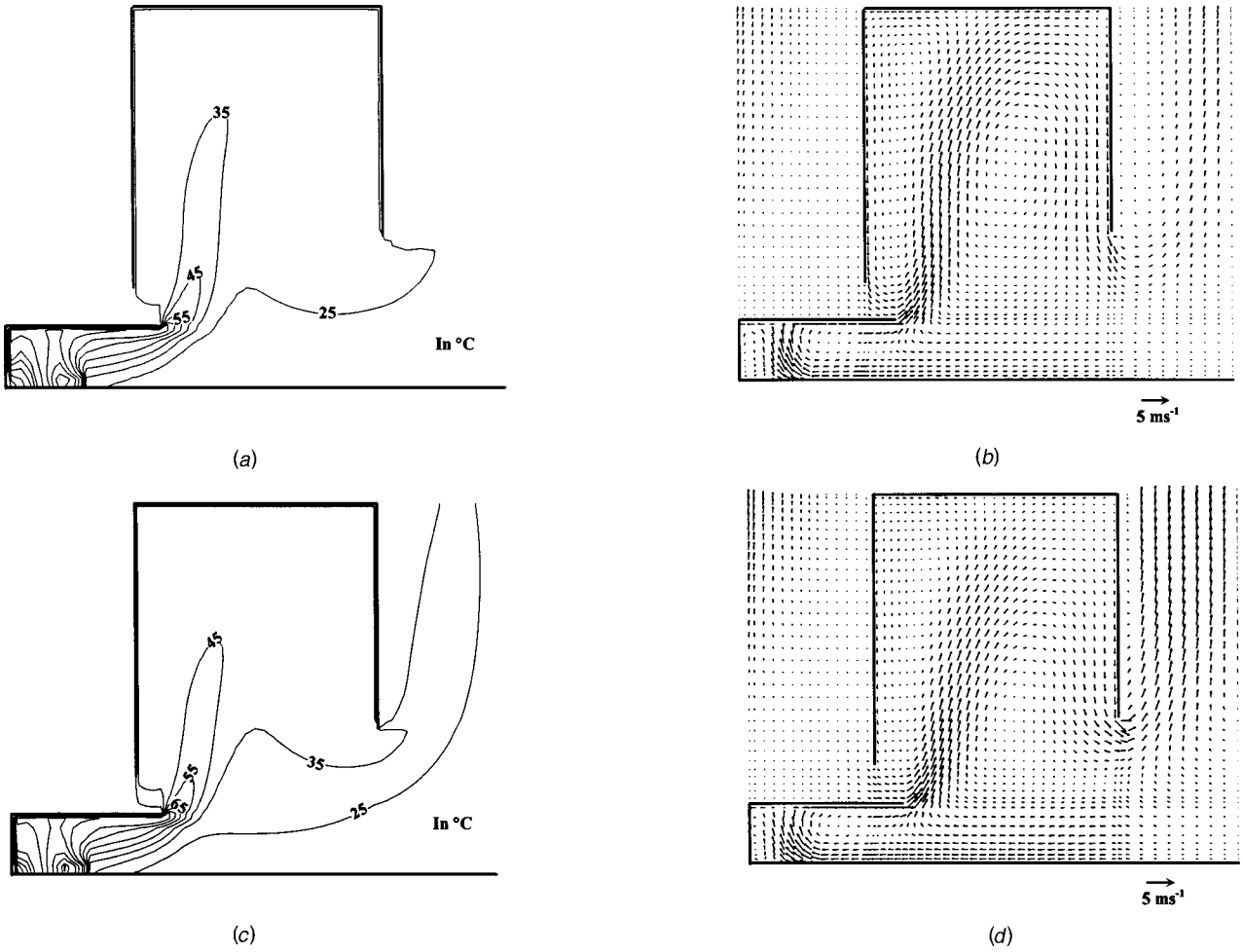

Fig. 8 Results for case NTS: (*a*) temperature at 50 s; (*b*) velocity at 50 s; (*c*) temperature at 150 s; and (*d*) velocity at 150 s

Case NTS: No Thermal Stratification. The initial conditions were taken as those of normal ambient at 20°C, all the walls and the ceiling of the atrium were adiabatic in the simulations. Temperature contours and velocity vectors for NTS at the central x-z plane are shown in Fig. 8.

For the case of constant temperature environment, the plume was observed to reach the ceiling rapidly by its buoyancy force, and a ceiling jet was formed after reaching the ceiling. The thickness of the hot air layer under the ceiling increased with time as the plume brought more hot fluid into the layer, and eventually the ceiling jet was totally submerged into the warm upper layer.

Case WTS: With Thermal Stratification. There was a thermal stratified layer in the atrium, with the initial temperature distribution as shown in Fig. 9. The ceiling of the atrium was at constant temperature of 80°C, other walls were adiabatic. Such a high temperature at the roof glazing has been observed in hot summer of tropical areas such as Hong Kong.

Numerical results were only used to show the hot spill plume filling process in thermal stratified ambient. Numerical results at 25 s and 50 s, 100 s and 150 s across the central x-z plane are shown in Fig. 10 and Fig. 11, respectively.

It is observed from WTS simulations that with the spill plume moving up in the atrium with a hot stratified air layer, smoke spreading into the atrium would be cooled down rapidly at the early stage of a fire. The plume cannot move up to the high level at this stage because its average density is larger than the density in the upper layer, as shown in Fig. 10, at 25 s and 50 s.

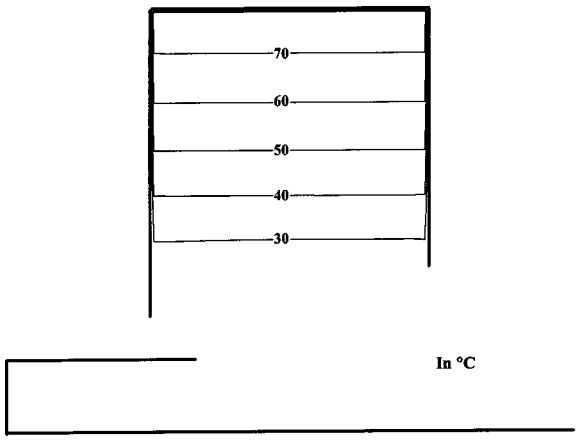

Fig. 9 Thermal stratification assumed for WTS

For regions near the centerline of the plume with higher temperature and vertical velocity, the plume there is able to penetrate the hot air layer interface when its density is smaller than that of the ambient air there. Buoyancy forces and initial momentum of the plume flow will act on this region and cause the plume to rise up to the ceiling. Associated with the entrainment of ambient ''cool'' air is a decrease in the upward velocity and temperature of

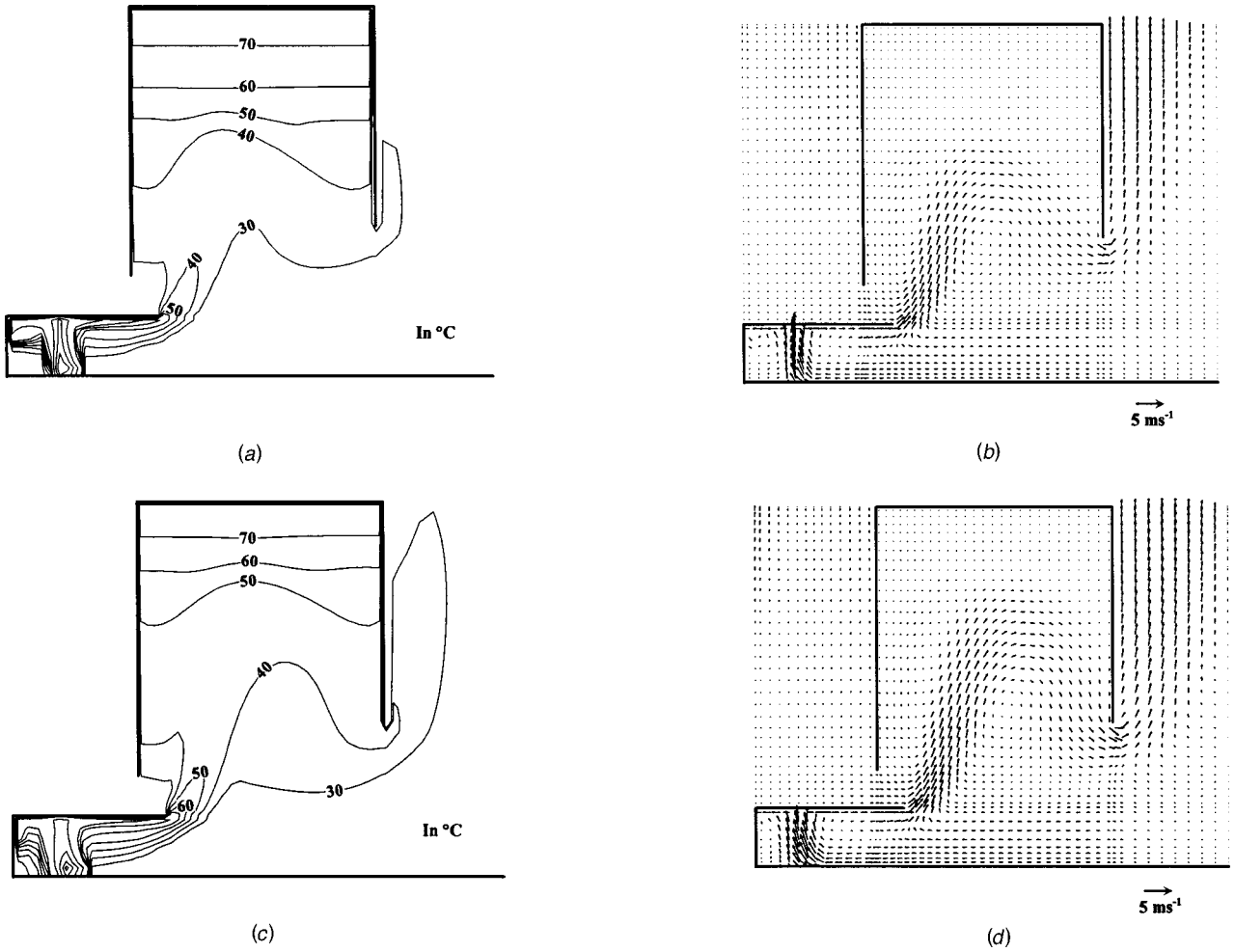

Fig. 10 Numerical results at 25 s and 50 s for case WTS: (*a*) temperature at 25 s; (*b*) velocity at 25 s; (*c*) temperature at 50 s; and (*d*) velocity at 50 s

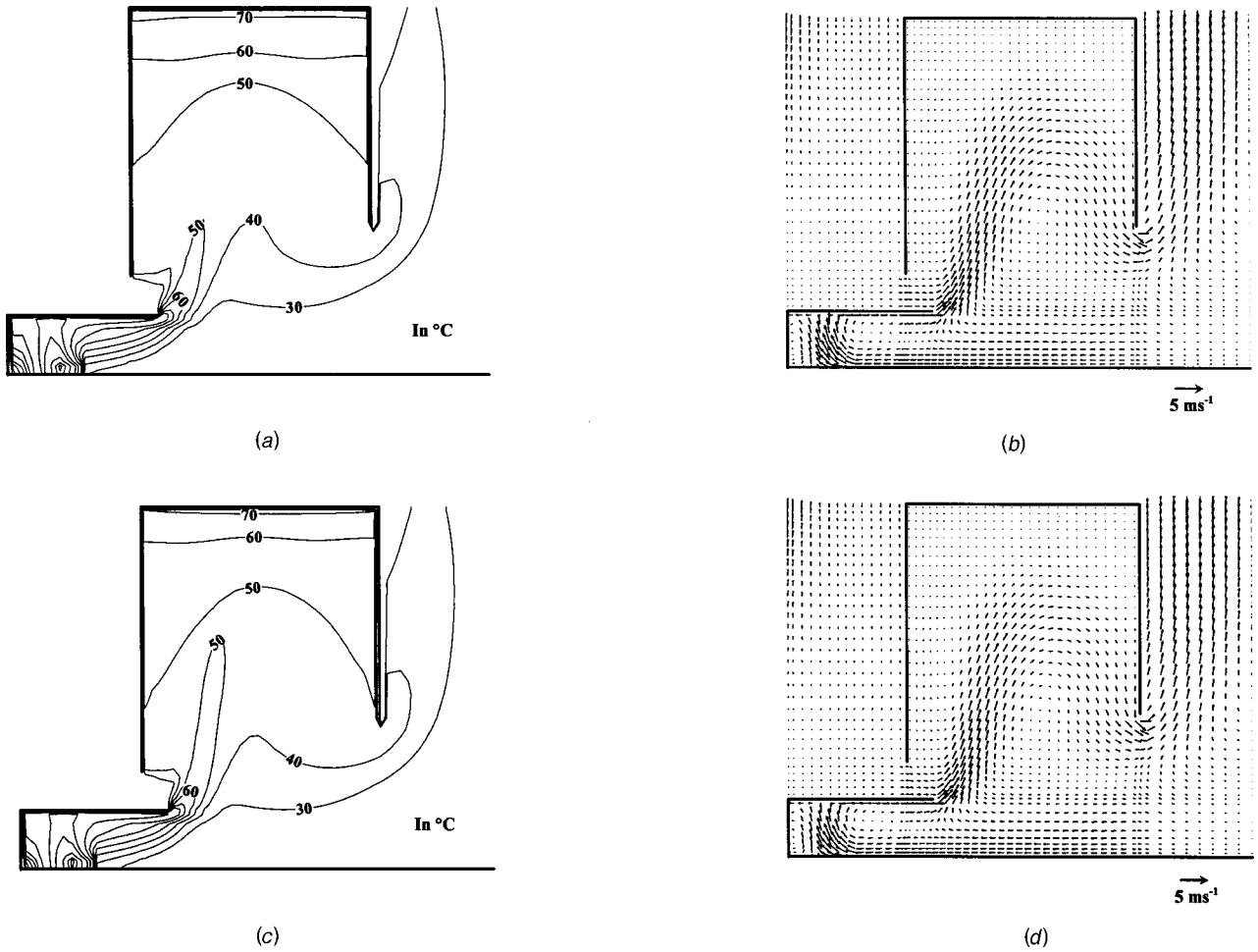

Fig. 11 Numerical results at 100 s and 150 s for case WTS: (*a*) temperature at 100 s; (*b*) velocity at 100 s; (*c*) temperature at 150 s; and (*d*) velocity at 150 s

the plume. When the plume reaches the height z_{cri}, where the ambient temperature is higher than the maximum temperature of the plume, the buoyancy driving the plume up will change its sign. Above this elevation, the plume will continue to rise until the negative buoyancy reduces its momentum to zero, and the plume would reach its maximum elevation z_{max} at that stage. As the fire grows, temperature of the plume will rise to give hotter smoke with sufficient buoyancy to move up to the higher level in the atrium. This process will continue until the smoke ''strata'' have become sufficiently mixed to rise up as a single ''bulk of smoke.'' Taking the smoke front to be the surface where the vertical velocity is zero, the development of the smoke front at the central x-z plane is shown in Fig. 12. The time for the plume to reach the ceiling is extended in comparing with in an atrium of constant temperature ambient.

8 Conclusion

The behavior of a line plume rising up in an atrium with a thermal stratified hot air layer was studied. Based on this study and earlier research work in the literature ([8]), some characteristics of the balcony plume rising in an atrium with such a thermal environment were predicted. The following can be concluded:

- The effects of thermal stratification should be considered carefully at the upper region of the atrium, but might be ignored at the lower region.
- The minimum heat release rate of a fire that the plume can reach the ceiling is given by Eq. (47). For fires of heat release rate smaller than that value, smoke cannot reach the ceiling.
- The maximum height that the plume can reach and the associated mass flow rate can be calculated. These results will be useful for designing smoke control systems in atria. Note that only the stratification effects for plumes induced by a point source are given in NFPA 92B ([14]). Results given by Eqs. (54) and (56) in this paper can be worked out in complementary to those design guides [e.g., ([14])].
- Numerical simulations were carried out on the smoke filling process to support the argument. The results showed that the time for the smoke to reach the ceiling might be delayed due to the thermal stratified layer. But for some cases, such as the volume of the atrium was very large or the fire size was too small, smoke cannot reach the atrium roof.
- Smoke failed to rise might spread to other areas adjacent to the atrium. More occupants will be exposed to smoke to give a shorter available safe egress time (ASET). Smoke detectors installed at the ceiling cannot be activated. If the hot air cannot be extracted immediately, the evacuation plan will be disturbed.

All the above should be considered carefully in designing smoke management systems for atria. New alternatives, such as beam smoke detectors ([15,16]) and video smoke detection system might be assessed for suitability. Further, verification of the derived equations should be carried out with full-scale burning tests. Such tests will be conducted at the PolyU/USTC Atrium ([24]) and the results will be reported later.

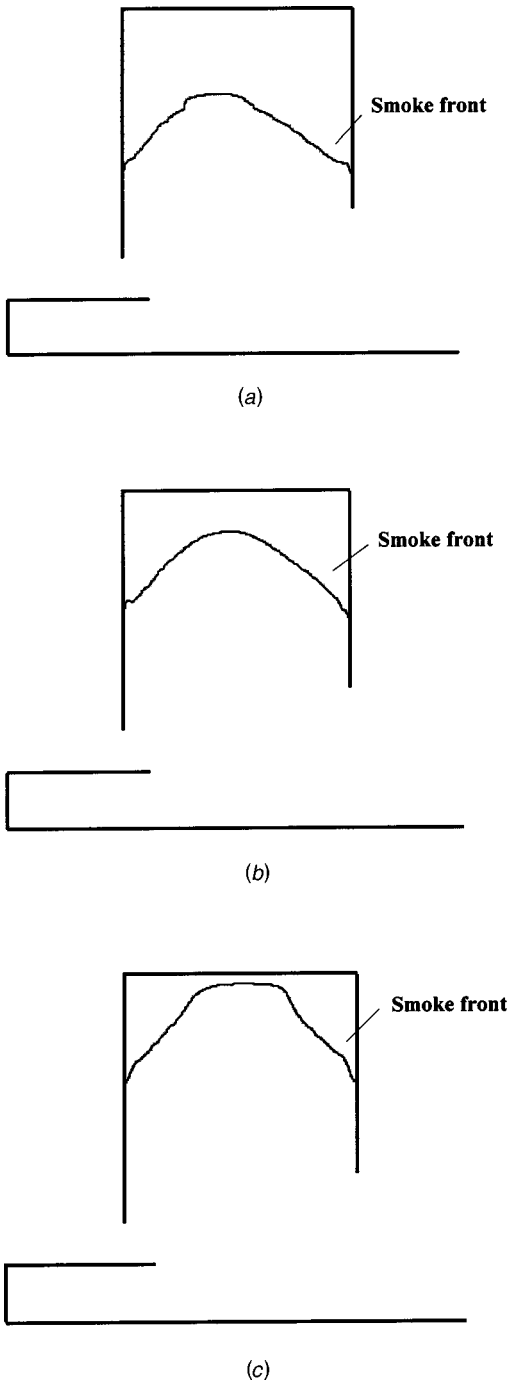

Fig. 12 Smoke front at central *x-z* plane for case WTS: (*a*) 25 s; (*b*) 50 s; and (*c*) 100 s

Acknowledgements

This project is funded by the Research Grants Council of Hong Kong with account number B-Q063.

Nomenclature

b = plume width in uniform ambient, m
b_s = plume width in stratified ambient, m
C_p = specific heat capacity of air at constant pressure, kJ/kg·K
D_B = smoke layer thickness under the balcony, m
F = buoyancy flux in uniform ambient, m^4/s^3
F_0 = buoyancy flux from the source, m^4/s^3
F_0' = F_0/L, m^3/s^3
Fs = buoyancy flux in stratified ambient, m^4/s^3
G = the square of local buoyancy, $1/s^2$
g = acceleration due to gravity, m/s^2
H_A = height of the atrium, m
H_{max} = maximum rise of the plume in an atrium, m
h_B = height of the space under the balcony, m
L = width of the balcony spill plume, m
N = volume flux of the plume in a uniform environment, m^3/s
N' = N/L, m^2/s
N_s = volume flux of the plume in a stratified environment, m^3/s
N_s' = N_s/L, m^2/s
M = momentum flux in a uniform environment, m^4/s^2
M_s = momentum flux of the plume in a stratified environment, m^4/s^2
$\dot{m}_B$ = mass flux of smoke layer flowing out under the balcony, kg/s
$\dot{m}_A$ = entrainment rate in the balcony spill plume, kg/s
$\dot{m}_s$ = mass flux above the fire in a stratified ambient, kg/s
$\dot{Q}_c$ = convective heat release of fire source, kW
$\dot{Q}_c'$ = $\dot{Q}_c/L$, kW/m
T_a = temperature of the ambient air, K
T_{a0} = temperature of the ambient air at the level of the fire source, K
w = vertical velocity of the plume, m/s
w_m = centerline velocity of the plume, m/s
w_{sm} = centerline velocity in stratified ambient, m/s
z = height above the fire source, m
z_0 = virtual source height, m
z_A = height above the virtual source in the atrium, m
z_{max} = maximum rise of the plume, m

Greek Symbols

α = entrainment constant
γ = constant of the ambient density gradient
φ = defined as Eq. (18)
λ = ratio of the widths of buoyancy and vertical profiles
ρ_a = density of the ambient air, kg/m^3
ρ_{a0} = density of the ambient air at the level of the fire source, kg/m^3
ρ_m = density of the plume on centerline, kg/m^3
ρ_{sm} = density of the plume on centerline in the stratified environment, kg/m^3
ΔT_a = increase in ambient temperature from the level of the fire source to the ceiling, K
ΔT_{Aa} = increase in ambient temperature from the level of the virtual source to the ceiling in the atrium, K
ΔT_m = $T_m - T_a$
ΔT_{sm} = $T_{sm} - T_a$
$\Delta \rho_m$ = $\rho_a - \rho_m$
$\Delta \rho_{sm}$ = $\rho_a - \rho_{sm}$

Subscripts

a = ambient
m = local values along the plume axis
s = stratified environment

Appendix A

Derivation of Key Equations of Lee and Emmons [9]. The conservation equations for a line buoyant plume can be written in integral form as:

Continuity.

$$\frac{d}{dz}\left[\int_{-\infty}^{\infty}\rho L w dx\right] = 2\rho_a \lim_{x\to\infty}(Lv) \qquad (A1)$$

Momentum.

$$\frac{d}{dz}\left[\int_{-\infty}^{\infty}\rho L w^2 dx\right]=g\int_{-\infty}^{\infty}\Delta\rho L dx \tag{A2}$$

Energy.

$$\frac{d}{dz}\left[\int_{-\infty}^{\infty}\rho C_p \Delta T w L dx\right]=\frac{d\dot{Q}_c}{dz} \tag{A3}$$

Buoyancy.

$$\frac{d}{dz}\left[\int_{-\infty}^{\infty} g\frac{\Delta\rho}{\rho_a} w L dx\right]=0 \tag{A4}$$

where $\Delta\rho$ and ΔT are the density and temperature difference, respectively:

$$\Delta\rho=\rho_a-\rho \tag{A5}$$

$$\Delta T=T-T_a \tag{A6}$$

Taking the rate at which the fluid entrained into the plume is proportional to the vertical velocity on the axis of the plume through an entrainment constant α ([9,17–19]):

$$-\lim_{x\to\infty}(Lv)=\alpha w_m L \tag{A7}$$

With the Gaussian profiles assumption, vertical velocity and temperature difference at height z can be expressed as:

$$w(x,z)=w_m(z)\exp\left(-\frac{x^2}{b^2}\right) \tag{A8}$$

$$\Delta T(x,z)=\Delta T_m(z)\exp\left(-\frac{x^2}{\lambda^2 b^2}\right) \tag{A9}$$

where λ is the ratio of the widths of buoyancy and velocity profiles, b is the Gaussian half-width for velocity profile, and the subscript m designates the local value along the plume axis.
Ideal gas law gives:

$$\rho T=\rho_a T_a \tag{A10}$$

Combining with the second assumption,

$$\frac{\Delta\rho}{\rho_a}=\frac{\Delta T}{T_a} \tag{A11}$$

Integrating Eqs. (*A*1) to (*A*4) with the profiles in Eqs. (*A*8) and (*A*9) gives:

$$\frac{d(\sqrt{\pi}L w_m b)}{dz}=2\alpha L w_m \tag{A12}$$

$$\frac{d\left(\sqrt{\frac{\pi}{2}}L w_m^2 b\right)}{dz}=gL\lambda b\sqrt{\pi}\frac{\Delta\rho_m}{\rho_a} \tag{A13}$$

$$\frac{d\left(\sqrt{\frac{\pi}{1+\lambda^2}}\lambda b w_m L\frac{\Delta T_m}{T_a}\right)}{dz}=\frac{d\left(\frac{\dot{Q}_c}{\rho_a C_p T_a}\right)}{dz} \tag{A14}$$

$$\frac{d\left(\sqrt{\frac{\lambda^2}{1+\lambda^2}}\cdot\sqrt{\pi}\cdot bL\cdot g w_m\frac{\Delta\rho_m}{\rho_a}\right)}{dz}=0 \tag{A15}$$

To solve the above equations, ''mass flux'' N, ''momentum flux'' M and buoyancy flux F are introduced:

$$N=\sqrt{\pi}L w_m b \tag{A16}$$

$$M=\sqrt{\frac{\pi}{2}}bL\cdot w_m^2 \tag{A17}$$

$$F=\sqrt{\frac{\lambda^2}{1+\lambda^2}}\cdot\sqrt{\pi}\cdot bL\cdot w_m g\frac{\Delta\rho_m}{\rho_a} \tag{A18}$$

Thus,

$$\frac{dN}{dz}=2\sqrt{2}\alpha L\frac{M}{N} \tag{A19}$$

$$\frac{dM}{dz}=\frac{\sqrt{1+\lambda^2}}{\sqrt{2}}\cdot\frac{NF}{M} \tag{A20}$$

By eliminating z and integrating with the boundary conditions, $N=0$ at $z=0$ and $M=0$ at $z=0$. This gives:

$$N=\left(\frac{4}{\sqrt{1+\lambda^2}}\frac{\alpha L}{F}\right)^{1/3}M \tag{A21}$$

From Eqs. (*A*16) and (*A*17),

$$w_m=\left(\frac{\sqrt{1+\lambda^2}}{\sqrt{2}}\right)^{1/3}\frac{1}{\alpha^{1/3}}\left(\frac{g\dot{Q}_c'}{\rho_a C_p T_a}\right)^{1/3} \tag{A22}$$

$$b=\frac{2\alpha}{\sqrt{\pi}}z \tag{A23}$$

$$\frac{\Delta\rho_m}{\rho_a}=\frac{(\sqrt{2})^{1/3}(\sqrt{1+\lambda^2})^{2/3}}{2\alpha^{2/3}}\frac{1}{\lambda g}\left(\frac{g\dot{Q}_c'}{\rho_a C_p T_a}\right)^{2/3}z^{-1} \tag{A24}$$

$$\frac{N}{L}=2\cdot\left(\frac{\sqrt{1+\lambda^2}}{\sqrt{2}}\right)^{1/3}\alpha^{2/3}F_0'^{1/3}z$$

$$=2\cdot\left(\frac{\sqrt{1+\lambda^2}}{\sqrt{2}}\right)^{1/3}\alpha^{2/3}\left(\frac{g\dot{Q}_c'}{\rho_a C_p T_a}\right)^{1/3}z \tag{A25}$$

In the above equations,

$$F_0'=F_0/L \tag{A26}$$

$$\dot{Q}_c'=\dot{Q}_c/L \tag{A27}$$

The mass flux for the line plume is given by:

$$\dot{m}=\int_{-\infty}^{\infty}\rho w\cdot Lx dx$$

$$=\sqrt{\pi}\rho_a w_m b L$$

$$=2^{5/6}\alpha^{2/3}(\sqrt{1+\lambda^2})^{1/3}L\rho_a\left(\frac{g\dot{Q}_c'}{\rho_a C_p T_a}\right)^{1/3}z \tag{A28}$$

Appendix B:

Line Plume Equations in a Thermal Stratified Environment. Three conservation equations for mass, momentum and buoyancy for the line plume rising in a thermal stratified environment can be given as:

$$\frac{d(\sqrt{\pi}L w_{sm} b_s)}{dz}=2\alpha L w_{sm} \tag{B1}$$

$$\frac{d\left(\sqrt{\frac{\pi}{2}}L w_{sm}^2 b_s\right)}{dz}=gL\lambda b_s\sqrt{\pi}\frac{\Delta\rho_{sm}}{\rho_{a0}} \tag{B2}$$

$$\frac{d\left(\sqrt{\frac{\lambda^2}{1+\lambda^2}}\cdot\sqrt{\pi}\cdot b_s L\cdot g w_{sm}\frac{\Delta\rho_{sm}}{\rho_{a0}}\right)}{dz}$$

$$=-\sqrt{\pi}b_s L w_{sm}\left(-\frac{g}{\rho_{a0}}\frac{d\rho_a}{dz}\right) \tag{B3}$$

Quantities with the subscript s refer to those for the stratified environment.
Let

$$N_s=\sqrt{\pi}Lw_{sm}b_s \tag{B4}$$

$$M_s=\sqrt{\frac{\pi}{2}}b_s L\cdot w_{sm}^2 \tag{B5}$$

$$F_s=\sqrt{\frac{\lambda^2}{1+\lambda^2}}\cdot\sqrt{\pi}\cdot b_s L\cdot w_{sm}g\frac{\Delta\rho_{sm}}{\rho_{a0}} \tag{B6}$$

$$G=-\frac{g}{\rho_{a0}}\frac{d\rho_a}{dz} \tag{B7}$$

Substituting the above equations into the conservation equations gives:

$$\frac{dN_s}{dz}=2\sqrt{2}\alpha L\frac{M_s}{N_s} \tag{B8}$$

$$\frac{dM_s}{dz}=\frac{\sqrt{1+\lambda^2}}{\sqrt{2}}\cdot\frac{N_s F_s}{M_s} \tag{B9}$$

$$\frac{dF_s}{dz}=-N_s G \tag{B10}$$

Integrating the above equation with the boundary condition at $z=0$:

$$F_s=F_0=2\lambda b_{s0}L\cdot w_{s0}g\frac{\Delta\rho_{sm0}}{\rho_{a0}}=\frac{g\dot{Q}_c}{\rho_{a0}C_pT_{a0}} \tag{B11}$$

$$M_s=M_{s0} \tag{B12}$$

This gives:

$$M_s=\left[-\frac{\sqrt{1+\lambda^2}}{\sqrt{2}}\frac{(F_s^2-F_0^2)}{G}+M_{s0}^2\right]^{1/2} \tag{B13}$$

$$F_s=\left[-\frac{\sqrt{2}G}{\sqrt{1+\lambda^2}}(M_s^2-M_{s0}^2)+F_0^2\right]^{1/2} \tag{B14}$$

Integrating Eq. (*B*8) with z gives:

$$N_s^3=\frac{6\alpha L}{(\sqrt{1+\lambda^2})^{1/2}(\sqrt{2}G)^{1/2}}\left\{-M_s\left[\left(M_0^2+\frac{\sqrt{1+\lambda^2}}{\sqrt{2}G}F_0^2\right)-M_s^2\right]^{1/2}+\left(M_{s0}^2+\frac{\sqrt{1+\lambda^2}}{\sqrt{2}G}F_0^2\right)\times\sin^{-1}\left(\frac{M_s}{\sqrt{M_{s0}^2+\frac{\sqrt{1+\lambda^2}}{\sqrt{2}G}F_0^2}}\right)\right\}+3C \tag{B15}$$

where

$$C=\frac{N_{s0}^3}{3}-\frac{6\alpha L}{(\sqrt{1+\lambda^2})^{1/2}(\sqrt{2}G)^{1/2}}\left[-\left(\frac{\sqrt{1+\lambda^2}}{\sqrt{2}G}\right)^{1/2}M_{s0}F_{s0}+\left(M_{s0}^2+\frac{\sqrt{1+\lambda^2}}{\sqrt{2}G}F_0^2\right)\sin^{-1}\left(\frac{M_{s0}}{\sqrt{M_{s0}^2+\frac{\sqrt{1+\lambda^2}}{\sqrt{2}G}F_0^2}}\right)\right] \tag{B16}$$

For the line source, at $z=0$,

$$N_{s0}=0 \tag{B17}$$

$$M_{s0}=0 \tag{B18}$$

Let

$$\sin\varphi=\frac{M_s}{F_0\sqrt{\frac{\sqrt{1+\lambda^2}}{\sqrt{2}G}}} \tag{B19}$$

Then,

$$M_s=F_0\sqrt{\frac{\sqrt{1+\lambda^2}}{\sqrt{2}G}}\sin\varphi \tag{B20}$$

$$N_s=\frac{6^{1/3}\cdot(\sqrt{1+\lambda^2})^{1/6}(\alpha L)^{1/3}}{(\sqrt{2})^{1/2}G^{1/2}}F_0^{2/3}(-\sin\varphi\cos\varphi+\varphi)^{1/3} \tag{B21}$$

From Eq. (*B*8),

$$z=\int_0^N\frac{1}{2\sqrt{2}\alpha L}\frac{N_s dN_s}{M_s}=\frac{2}{6^{1/3}\cdot(\sqrt{2})^{3/2}(\sqrt{1+\lambda^2})^{1/6}}\cdot\frac{1}{(\alpha L)^{1/3}}\cdot\left(\frac{1}{G}\right)^{1/2}F_0^{1/3}\int_0^{\varphi}\frac{\sin\varphi d\varphi}{(\varphi-\sin\varphi\cos\varphi)^{1/3}} \tag{B22}$$

$$b_s=\frac{N_s^2}{\sqrt{2\pi}M_s L}=\frac{6^{2/3}}{(\sqrt{2})^{3/2}(\sqrt{1+\lambda^2})^{1/6}\sqrt{\pi}}\frac{(\alpha L)^{2/3}}{L}\left(\frac{1}{G}\right)^{1/2}\times F_0^{1/3}\frac{(\varphi-\sin\varphi\cos\varphi)^{2/3}}{\sin\varphi} \tag{B23}$$

$$w_{sm}=\sqrt{2}\frac{M_s}{N_s}=\frac{\sqrt{2}(\sqrt{1+\lambda^2})^{1/3}}{6^{1/3}}\cdot\frac{1}{(\alpha L)^{1/3}}F_0^{1/3}\frac{\sin\varphi}{(\varphi-\sin\varphi\cos\varphi)^{1/3}} \tag{B24}$$

$$\frac{\Delta\rho_{sm}}{\rho_{a0}}=\frac{\sqrt{1+\lambda^2}}{\lambda g}\frac{F_s}{N_s}=\frac{(\sqrt{2})^{1/2}}{6^{1/3}}\frac{(\sqrt{1+\lambda^2})^{5/6}}{\lambda g}\frac{F_0^{1/3}G^{1/2}}{(\alpha L)^{1/3}}\frac{\cos\varphi}{(\varphi-\sin\varphi\cos\varphi)^{1/3}} \tag{B25}$$

The mass flow rate of the plume at height z is computed as:

$$\dot{m}_s = \int_{-\infty}^{\infty} \rho w \cdot L x dx$$

$$\approx \rho_{a0}\left(1 - \frac{G}{g}z\right)N_s$$

$$= \frac{6^{1/3}(\sqrt{1+\lambda^2})^{1/6}}{(\sqrt{2})^{1/2}}\rho_{a0}\left(1 - \frac{G}{g}z\right)(\alpha L)^{1/3}\left(\frac{1}{G}\right)^{1/2}F_0^{2/3}(\varphi - \sin\varphi\cos\varphi)^{1/3} \quad (B26)$$

References

[1] Thomas, P. H., 1987, ''On the Upward Movement of Smoke and Related Shopping Mall Problems,'' Fire Saf. J., **12**, pp. 191–203.

[2] Law, M., 1986, ''A Note on Smoke Plumes from Fires in Multi-Level Shopping Malls,'' Fire Saf. J., **10**, pp. 197–202.

[3] Law, M., 1995, ''Measurements of Balcony Smoke Flow,'' Fire Saf. J., **24**, pp. 189–195.

[4] Morgan, H. P., and Marshall, N. R., 1975, ''Smoke Hazards in Covered Multi-Level Shopping Malls: An Experimentally Based Theory for Smoke Production,'' Building Research Establishment Current Paper CP48/75, Building Research Establishment, Garston, UK.

[5] Hansell, G. O., Morgan, H. P., and Marshall, N. R., 1993, ''Smoke Flow Experiments in a Model Atrium,'' Building Research Establishment Occasional Paper OP55, Building Research Establishment, Garston, UK.

[6] Marshall, N. R., and Harrison, R., 1996, ''Experimental Studies of the Thermal Spill Plumes,'' Building Research Establishment Occasional Paper OP1, Building Research Establishment, Garston, UK.

[7] Thomas, P. H., Morgan, H. P., and Marshall, N., 1998, ''The Spill Plume in Smoke Control Design,'' Fire Saf. J., **30**, pp. 21–46.

[8] Poreh, M., Morgan, H. P., Marshall, N. R., and Harrison, R., 1998, ''Entrainment by Two-Dimensional Spill Plumes,'' Fire Saf. J., **30**, pp. 1–19.

[9] Lee, L., and Emmons, H. W., 1961, ''A Study of Natural Convection above Line Fires,'' J. Fluid Mech., **11**, pp. 353–368.

[10] Chow, W. K., and Cui, E., 1998, ''CFD Simulations on Balcony Spill Plume,'' J. Fire Sci., **16**(6), pp. 468–485.

[11] Miles, S., Kumar, S., and Cox, G., 1997, ''The Balcony Spill Plume—Some CFD Simulations,'' *Fire Safety Science—Proceedings of the Fifth International Symposium*, International Association for Fire Safety Science, Melbourne, pp. 237–247.

[12] Hansell, G. O., and Morgan, H. P., 1994, ''Design Approaches for Smoke Control in Atrium Buildings,'' Building Research Establishment Report BR258, Building Research Establishment, Garston, UK.

[13] Morgan, H. P., Ghosh, B. K., and Garrad, G., 1999, ''Design Methodologies for Smoke and Heat Exhaust Ventilation,'' Building Research Establishment Report BR368, Building Research Establishment, Garston, UK.

[14] NFPA 92B, 1995, ''Guide for Smoke Management Systems in Malls, Atria and Large Areas,'' (design guide), National Fire Protection Association, Quincy, MA, USA.

[15] Klote, J. H., ''Method of Predicting Smoke Movement in Atria with Application to Smoke Management,'' NISTIR 5516, National Institute of Standards and Technology, Gaithersburg, MD.

[16] Klote, J. H., 2000, ''New Development in Atrium Smoke Management,'' ASHRAE Trans., **106**, Part I, pp. 620–626.

[17] Morton, B. R., Taylor, G. I., and Turner, J. S., 1956, ''Turbulent Gravitational Convection from Maintained and Instantaneous Sources,'' Proc. R. Soc. London, Ser. A, **A234**, pp. 1–23.

[18] Morton, B. R., 1959, ''Forced Plumes,'' J. Fluid Mech., **5**, pp. 151–163.

[19] Turner, J. S., 1973, *Buoyancy Effects in Fluids*, Cambridge University Press, London, UK.

[20] Heskestad, G., 1989, ''Note on Maximum Rise of Fire Plumes in Temperature-Stratified Ambients,'' Fire Saf. J., **15**, pp. 271–276.

[21] Bloomfield, L. J., and Kerr, R. C., 1998, ''Turbulent Fountains in Stratified Fluid,'' J. Fluid Mech., **358**, pp. 335–356.

[22] Cardoso, S. S. S., and Woods, A. W., 1993, ''Mixing by a Turbulent Plume in a Confined Stratified Region,'' J. Fluid Mech., **250**, pp. 277–305.

[23] *The PHOENICS 3.2 POLIS*, 1998, CHAM Ltd., Wimbledon Village, London, UK.

[24] Chow, W. K., Li, Y. Z., Cui, E., and Huo, R., 2001, ''Natural Smoke Filling in Atrium with Liquid Pool Fires up to 1.6 MW,'' Build. Environ., **36**(1), pp. 121–127.

[25] Batchelor, G. K., 1954, ''Heat Convection and Buoyancy Effects in Fluids,'' Quart. J. Roy. Met. Soc., **80**, pp. 339–358.

[26] Rouse, H., Yih, C. S., and Humphreys, H. W., 1952, ''Gravitational Convection from a Boundary Source,'' Tellus, **4**, pp. 201–210.

[27] Yuan, L. M., and Cox, G., 1996, ''An Experiment Study of Some Line Fires,'' Fire Saf. J., **27**, pp. 123–139.

[28] Chen, C. J., and Rodi, W., 1975, ''A Review of Experimental Data of Vertical Turbulent Buoyant Jets,'' University of Karlsruhe Report SFB 80/T/69.

[29] Yokoi, S., 1960, ''Study on the Prevention of Fire Spread Caused by Hot Upward Current,'' Building Research Report **34**, Japanese Ministry of Construction.

[30] Rodi, W., 1984, *Turbulence Models and Their Application in Hydraulics*, second revised edition, IAHR, Netherlands, pp. 9–46.

[31] Markatos, N. C., Malin, M. R., and Cox, G., 1982, ''Mathematical Modelling of Buoyancy-Induced Smoke Flow in Enclosures,'' Int. J. Heat Mass Transf., **25**(1), pp. 63–75.

[32] Xue, H., Ho, J. C., and Cheng, Y. M., 2001, ''Comparison of Different Combustion Models in Enclosure Fire Simulation,'' Fire Saf. J., **36**, pp. 37–54.

[33] Chow, W. K., 1995, ''Use of Computational Fluid Dynamics for Simulating Enclosure Fires,'' J. Fire Sci., **13**, pp. 300–333.

[34] Nam, S., and Bill, R. G., 1993, ''Numerical Simulation of Thermal Plumes,'' Fire Saf. J., **21**(3), pp. 231–256.

[35] Chow, W. K., 1995, ''Use of Computational Fluid Dynamics for Simulating Enclosure Fires,'' J. Fire Sci., **13**, pp. 300–333.

[36] Chow, W. K., 1995, ''A Comparison of the Use of Fire Zone and Field Models for Simulating Atrium Smoke-filling Process,'' Fire Saf. J., **25**, pp. 337–353.

[37] Yang, K. T., 1994, ''Recent Development in Field Modelling of Compartment Fires,'' JSME Int. J., Ser. B, **37**(4), pp. 702–717.

An Adaptive Angular Quadrature for the Discrete Transfer Method Based on Error Estimation

Hendrik K. Versteeg
e-mail: H.K.Versteeg@Lboro.ac.uk

Jonathan C. Henson[1]
e-mail: J.C.Henson@Lboro.ac.uk

Weeratunge Malalasekera
e-mail: W.Malalasekera@Lboro.ac.uk

Loughborough University, U.K.

The ray effect is a serious problem in radiative heat transfer computations. Continuously varying radiation fields are approximated numerically by sampling a limited number of angular directions. The discrete transfer method (DTM) is a conceptually simple technique suitable for general-purpose calculations of thermal radiation in complex geometries. Over the years a large variety of quadratures based on fixed ray firing patterns has been suggested for use in conjunction with the DTM. Arguably, in absence of a comprehensive error analysis, the efficacy of all these quadratures has only been proved for limited collections of radiation problems. Recently, sharp error bounds for the heat flux integral in the DTM have been established for irradiation distributions of three different continuity classes: smooth fields, fields with discontinuous angular derivatives and piecewise constant fields. The resulting error formulas have paved the way for a new adaptive quadrature strategy. Results are presented of its application to an idealized jet flame and to radiative exchanges inside a cube-shaped enclosure, along with brief comments on the viability of this approach in general-purpose CFD/radiation computations. In this paper, the following capabilities of the new adaptive angular quadrature are demonstrated: Evaluation of DTM heat flux integrals to a pre-specified tolerance for any intensity distribution; Excellent accuracy with very low ray numbers for irradiation due to small view factor sources; and Good heat flux estimates for piecewise constant sources, provided that the starting mesh is selected carefully. [DOI: 10.1115/1.1560148]

Keywords: Computational, Heat Transfer, Numerical Methods, Radiation

Introduction

The discrete transfer method (DTM) is a conceptually simple algorithm for the computation of radiative heat transfer problems. The technique was originally developed by Shah [1] and has since been applied successfully to coupled CFD/radiation problems in complex geometries involving 3D body-fitted and unstructured meshes. The DTM computes the irradiation of enclosure surfaces at the midpoints of elements of a surface mesh. The hemisphere about such a midpoint is subdivided into solid angle elements. A ray is fired through the centroid of each solid angle element and traced from its origin to the irradiated point. Its contribution to the irradiation is computed by assuming that the intensity of the centroid ray applies throughout the entire solid angle element. An error arises due to the fact that the actual intensity generally varies within each element. Sampling of a varying intensity field along a limited number of centroid ray directions causes this error, which is commonly known as the ''ray effect''. It is a serious problem in radiative heat transfer computations with the DTM and other algorithms [2]. The original DTM [1,3] involves discretization of the hemisphere by means of uniform intervals $\Delta\phi$ and $\Delta\theta$ in the azimuthal (ϕ) and polar (θ) directions of a spherical polar coordinate system. This leads to a distribution of rays with nonuniform solid angles and a bias towards the pole.

Over the years, various improved integration rules or quadratures, based on fixed ray firing patterns, have been suggested for use in conjunction with the DTM. The more recent contributions are briefly reviewed. Cumber [4] discussed an unbiased ray distribution (due to Guilbert) with uniform solid angles throughout the hemisphere. He also proposed a higher-order (Newton-Cotes) quadrature rule to improve the accuracy of the DTM. Cumber's rule is exact for locally constant and bilinear intensity distributions and was tested for the case of a jet flame. Andersen [5] compared Shah's method with a variety of other quadratures including Gauss-Legendre rules in spherical coordinates and in two different transformed coordinate systems for a test case involving a cylindrical pipe with cold walls and filled with a hot absorbing/emitting medium. He also investigated the discrete ordinates quadratures S-2, S-4, S-6 and S-8. Andersen found that the Gauss-Legendre rule implemented in the μ-ϕ coordinate system (where $\mu=\cos\theta$) was the most accurate for his test case. Li et al. [6] developed ray distributions by subdividing the θ-direction into equal intervals. This produced a series of azimuthal bands on the hemisphere surface. The band nearest the pole was equipped with 1 ray per octant. The second azimuthal band was given 2 rays per octant and so forth, giving n rays per octant within the nth azimuthal band (or $4n$ rays on the entire hemisphere in each band). Bressloff et al. [7] suggested an unbiased ray distribution consisting of elements with (almost) equal solid angles based on the projection of a cylindrical coordinate system onto the hemisphere.

All the above techniques have fixed ray directions and weighting coefficients. Most recently, Cumber [8] has made an important step forward by proposing an adaptive quadrature for the DTM. The technique involves a coarse starting mesh and simultaneous bisection of each solid angle element in both angular directions until the estimated local relative error is smaller than a pre-set tolerance. The computed irradiation due to a jet fire using fixed and adaptive angular meshes was compared with radiation measurements. Cumber's adaptively refined mesh achieved similar accuracy as a fixed angular mesh using around half the number of rays. In spite of considerable progress, most authors have only demonstrated the efficacy of their method for a fairly narrow range of radiation problems. Generalization of such findings has

[1]Presently at Alstom Power, Whetstone, Leics., UK. e-mail: Jonathan.Henson@power.alstom.com

Contributed by the Heat Transfer Division for publication in the JOURNAL OF HEAT TRANSFER. Manuscript received by the Heat Transfer Division March 28, 2002; revision received October 25, 2002. Associate Editor: S. T. Thynell.

thus far been problematic due to the absence of a systematic analysis of the errors associated with each numerical method. In recent work [9,10], Versteeg et al. have established sharp error bounds for the heat flux integral in the DTM for irradiation distributions of three different continuity classes: (i) smooth fields, (ii) fields with discontinuous angular derivatives, and (iii) piecewise constant fields. The resulting error formulas have paved the way for the new adaptive angular quadrature that is presented in this paper. The method is applied to two radiation problems: an idealised jet flame and radiative exchanges inside a cube-shaped enclosure. Brief comments are also given on the computational resource implications of the adaptive method and on the viability of adaptive strategies in general purpose computations involving coupled CFD/radiation.

Absolute Error Estimates

Following Shah [1], an angular mesh on the surface of the hemisphere around an irradiated point defined in terms of spherical angular coordinates (θ,ϕ) is considered. The DTM computes the incident heat flux as a sum of heat flux contributions $\delta q^-_{i,j}$ due to solid angle elements (i,j), where i is the index in the θ-direction and j is the index in the ϕ-direction:

$$q^-_{\text{actual}} \cong \sum_{i,j} (\delta q^-_{i,j})_{\text{DTM}} = \sum_{i,j} \frac{1}{2} I_{i,j} \sin(2\theta_i)\sin(\Delta\theta_{i,j})\Delta\phi_{i,j} \tag{1}$$

In Eq. (1), $I_{i,j}$ denotes the intensity at the centroid (θ_i,ϕ_j) of solid angle element (i,j); the interval size in angular directions θ and ϕ is denoted by $\Delta\theta_{i,j}$ and $\Delta\phi_{i,j}$, respectively.

Versteeg et al. [9,10] used Taylor series expansions to develop estimates of the local absolute error associated with $(\delta q^-_{i,j})_{\text{DTM}}$ in Eq. (1) assuming that $\Delta\theta_{i,j}$ and $\Delta\phi_{i,j}$ are sufficiently small, and that the intensity is a smooth, infinitely differentiable function of θ and ϕ:

$$\delta\varepsilon_{i,j} = (\delta q^-_{i,j})_{\text{actual}} - (\delta q^-_{i,j})_{\text{DTM}} = (\Delta\theta_{i,j}\Delta\phi_{i,j})^2 F_{i,j} \tag{2a}$$

where

$$F_{i,j} = c^{\theta}_{i,j} AR + c^{\phi}_{i,j}/AR \tag{2b}$$

$$c^{\theta}_{i,j} = \frac{1}{12}\cos(2\theta_i)\left.\frac{\partial I}{\partial\theta}\right|_{i,j} + \frac{1}{48}\sin(2\theta_i)\left.\frac{\partial^2 I}{\partial\theta^2}\right|_{i,j} \tag{2c}$$

$$c^{\phi}_{i,j} = \frac{1}{48}\sin(2\theta_i)\left.\frac{\partial^2 I}{\partial\phi^2}\right|_{i,j} \tag{2d}$$

$$AR = \Delta\theta_{i,j}/\Delta\phi_{i,j} \tag{2e}$$

The total absolute error ε associated with the DTM heat flux in Eq. (1) can be computed by summing the elemental errors over the entire hemisphere. Thus,

$$\varepsilon = \sum_{i,j} \delta\varepsilon_{i,j} \tag{3}$$

Coefficients $c^{\theta}_{i,j}$ and $c^{\phi}_{i,j}$ in Eqs. (2*c*–*d*) contain derivatives of the intensity field in the angular directions. If the size of an element (i,j) is sufficiently small, the derivatives can be approximated by means of finite differences. In principle, the intensity at the centroids of element (i,j) and its nearest neighbors could be used. However, in an adaptive meshing procedure this requires the evaluation of finite differences on irregular angular meshes after one or more refinement cycles. Here, a less economical, but conceptually simpler method is proposed for the computation of the relevant finite differences using four additional rays.

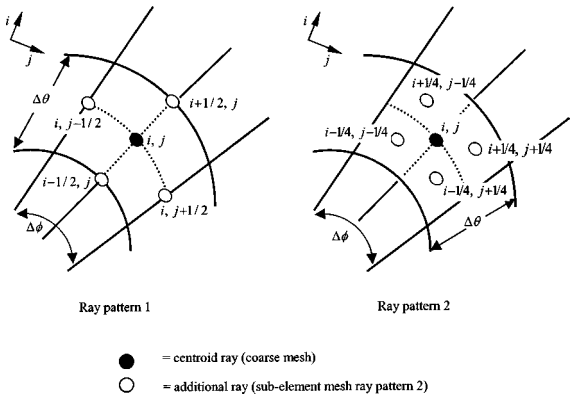

Fig. 1 Mesh element (i,j) with centroid ray and additional rays for gradient estimation

Figure 1 illustrates two alternative ray configurations. Ray pattern 1 is recommended for intensity fields that may that contain jump discontinuities, e.g., due to radiation source patches. Ray pattern 2 can only be used in conjunction with intensity distributions without discontinuities, but it will be shown later that it has advantageous error properties, since it allows Richardson extrapolation between the coarse mesh and the (quartered) sub-element mesh.

The intensity gradients in Eqs. (2*c*–*d*) are computed using the expressions given below. For ray pattern 1 in Fig. 1, the following expressions are used:

$$\left.\frac{\partial I}{\partial\theta}\right|_{i,j} \cong \frac{I_{i+1/2,j} - I_{i-1/2,j}}{\Delta\theta_{i,j}} \tag{4a}$$

$$\left.\frac{\partial^2 I}{\partial\theta^2}\right|_{i,j} \cong \frac{I_{i+1/2,j} - 2I_{i,j} + I_{i-1/2,j}}{(\Delta\theta_{i,j})^2/4} \tag{4b}$$

$$\left.\frac{\partial^2 I}{\partial\phi^2}\right|_{i,j} \cong \frac{I_{i,j+1/2} - 2I_{i,j} + I_{i,j-1/2}}{(\Delta\phi_{i,j})^2/4} \tag{4c}$$

For ray pattern 2:

$$\left.\frac{\partial I}{\partial\theta}\right|_{i,j} \cong \frac{(I_{i+1/4,j+1/4} + I_{i+1/4,j-1/4}) - (I_{i-1/4,j+1/4} + I_{i-1/4,j-1/4})}{\Delta\theta_{i,j}} \tag{5a}$$

$$\left.\frac{\partial^2 I}{\partial\theta^2}\right|_{i,j} \cong \frac{I_{i+1/4,j+1/4} + I_{i+1/4,j-1/4} - 4I_{i,j} + I_{i-1/4,j+1/4} + I_{i-1/4,j-1/4}}{(\Delta\theta_{i,j})^2/8} \tag{5b}$$

$$\left.\frac{\partial^2 I}{\partial\phi^2}\right|_{i,j} \cong \frac{I_{i+1/4,j+1/4} + I_{i-1/4,j+1/4} - 4I_{i,j} + I_{i+1/4,j-1/4} + I_{i-1/4,j-1/4}}{(\Delta\phi_{i,j})^2/8} \tag{5c}$$

Refinement Criterion

First, it is necessary to define a maximum relative error $\varepsilon_{R,\text{tol}}$ associated with DTM heat flux estimate given by Eq. (1). The task in hand is to design a subdivision of the hemisphere into solid

angle elements (i,j) such that the absolute error in the DTM heat flux q_{DTM} does not exceed $\varepsilon_{R,\mathrm{tol}}\bar{q}_{\mathrm{DTM}}$. Thus, the requirement is that

$$\varepsilon=\sum_{i,j}\ \delta\varepsilon_{i,j}\leqslant\varepsilon_{R,\mathrm{tol}}\bar{q}_{\mathrm{DTM}} \tag{6}$$

Equations (2) shows that the magnitude of the elemental error contributions $\delta\varepsilon_{i,j}$ depends on the intensity gradients. Hence, if the incident intensity distribution $I(\theta,\phi)$ is nonuniform the most economical hemisphere mesh to achieve objective of Eq. (6) might well be non-uniform with smaller solid angle elements in areas of large intensity gradients.

The fraction occupied by solid angle element (i,j) in the θ-direction is equal to $\Delta\theta_{i,j}/(\pi/2)$ and in the ϕ-direction, it is equal to $\Delta\phi_{i,j}/(2\pi)$. The maximum allowable local error contribution due to each element $(\delta\varepsilon_{i,j})_{\max}$ is made proportional to the interval sizes in both angular directions. Thus,

$$(\delta\varepsilon_{i,j})_{\max}^{(r+1)}=\frac{\Delta\theta_{i,j}\Delta\phi_{i,j}}{\pi^2}\varepsilon_{R,\mathrm{tol}}(\bar{q}_{\mathrm{DTM}})^{(r)} \tag{7}$$

Superscripts (r) and $(r+1)$ indicate that at the $r+1^{\mathrm{th}}$ adaptive refinement cycle, the maximum allowable error is evaluated on the basis of a DTM heat flux estimate at the end of the r^{th} refinement cycle. Solid angle element (i,j) is refined if the current error contribution $\delta\varepsilon_{i,j}$ is greater than the maximum allowable error $(\delta\varepsilon_{i,j})_{\max}$, i.e., if their ratio R_ε exceeds unity:

$$R_\varepsilon=\frac{|\delta\varepsilon_{i,j}|}{(\delta\varepsilon_{i,j})_{\max}^{(r+1)}}=\frac{|\delta\varepsilon_{i,j}|\pi^2}{\Delta\theta_{i,j}\Delta\phi_{i,j}\varepsilon_{R,\mathrm{tol}}(\bar{q}_{\mathrm{DTM}})^{(r)}}>1 \tag{8}$$

Bi-Directional Adaptive Refinement With Fixed *AR*

It is easiest to maintain a fixed element aspect ratio AR throughout the various cycles of adaptive refinement, hence $AR^{\mathrm{new}}=AR=\Delta\theta_{i,j}/\Delta\phi_{i,j}$, where AR^{new} is the aspect ratio of the refined mesh. Cumber [8] used this technique in conjunction with successive stages of local bisection of the solid angle elements. As an alternative to the bisection method, Eq. (2) can be used to predict the interval sizes $\Delta\theta'_{i,j}=\Delta\theta_{i,j}/N$ and $\Delta\phi'_{i,j}=\Delta\phi_{i,j}/N$ of a mesh that should not require further refinement. N is the number of subdivisions in each angular direction, so there will be N^2 sub-elements and Eq. (2) shows that the error contribution $\delta\varepsilon'$ due to each sub-element is given by:

$$\delta\varepsilon'=(\Delta\theta'_{i,j}\Delta\phi'_{i,j})^2F'\cong\frac{1}{N^4}(\Delta\theta_{i,j}\Delta\phi_{i,j})^2F_{i,j}=\frac{1}{N^4}\delta\varepsilon_{i,j} \tag{9a}$$

with

$$F_{i,j}=c_{i,j}^{\theta}AR+c_{i,j}^{\phi}/AR \tag{9b}$$

and

$$F'=(c^{\theta})'AR+(c^{\phi})'/AR \tag{9c}$$

In Eqs. (9*a*–*c*) the prime $(')$ indicates properties of a sub-element. The approximate equality in Eq. (9*a*) holds good when the original solid angle elements are sufficiently small that factor F' for the sub-elements is not too different from $F_{i,j}$.

The total error $\delta\varepsilon_{i,j}^{(N)}$ associated with the sum of error contributions due to N^2 sub-elements can be approximated using the right hand side of Eq. (9*a*):

$$\delta\varepsilon_{i,j}^{(N)}=\sum_{N^2}\ \delta\varepsilon'=N^2\times\frac{1}{N^4}\delta\varepsilon_{i,j}=\frac{1}{N^2}\delta\varepsilon_{i,j} \tag{10}$$

The required number of angular sub-intervals N is calculated by inverting criterion given by Eq. (8). This yields:

$$\frac{|\delta\varepsilon_{i,j}^{(N)}|}{(\delta\varepsilon_{i,j})_{\max}}=\frac{|\delta\varepsilon_{i,j}^{(N)}|}{|\delta\varepsilon_{i,j}|/R_\varepsilon}\leqslant 1 \tag{11}$$

Finally, $\delta\varepsilon_{i,j}^{(N)}$ is replaced by the right hand side of Eq. (10). After some re-arrangement, the following expression is obtained

$$N=\frac{\Delta\theta_{i,j}}{\Delta\theta'_{i,j}}=\frac{\Delta\phi_{i,j}}{\Delta\phi'_{i,j}}\geqslant R_\varepsilon^{1/2} \tag{12}$$

The actual new sizes of the refined intervals ($\Delta\theta_{i,j}^{\mathrm{new}}$ and $\Delta\phi_{i,j}^{\mathrm{new}}$) must be integer fractions of the original interval sizes of the coarse mesh, so it is necessary to take:

$$\Delta\theta_{i,j}^{\mathrm{new}}=\frac{\Delta\theta_{i,j}}{1+\mathrm{INT}(R_\varepsilon^{1/2})} \tag{13a}$$

and

$$\Delta\phi_{i,j}^{\mathrm{new}}=\frac{\Delta\phi_{i,j}}{1+\mathrm{INT}(R_\varepsilon^{1/2})} \tag{13b}$$

where $\mathrm{INT}(x)$=integer part of real number x.

Uni-Directional Adaptive Refinement With Variable *AR*

Next, an extreme case is investigated where bi-directional refinement with fixed AR is obviously wasteful. Equations (2*a*–*d*) show that the contribution to the elemental heat flux error due to changes in one of the angular directions is zero if the intensity gradient is zero in that direction, i.e., if $c_{i,j}^{\theta}=0$ or $c_{i,j}^{\phi}=0$. In such cases, it is much more effective to refine the mesh only in the direction of the nonzero gradient. To demonstrate this idea let us assume that $c_{i,j}^{\phi}=0$ and $c_{i,j}^{\theta}\neq 0$. Now, Eqs. (2) give the following expression for the DTM error:

$$|\delta\varepsilon_{i,j}|=\Delta\phi_{i,j}\Delta\theta_{i,j}^3|c_{i,j}^{\theta}| \tag{14}$$

Since $c_{i,j}^{\phi}=0$, the value of $\Delta\phi_{i,j}$ is maintained at its current value. The required interval size $\Delta\theta'_{i,j}=\Delta\theta_{i,j}/N$ in the θ-direction is evaluated by noting that there are N sub-elements and the error contribution $\delta\varepsilon'$ due to each subelement is given by:

$$\delta\varepsilon'=\Delta\phi_{i,j}(\Delta\theta'_{i,j})^3(c_{i,j}^{\theta})'\cong\frac{1}{N^3}\Delta\phi_{i,j}\Delta\theta_{i,j}^3c_{i,j}^{\theta}=\frac{1}{N^3}\delta\varepsilon_{i,j} \tag{15}$$

If $(c_{i,j}^{\theta})'\cong c_{i,j}^{\theta}$ the total error $\delta\varepsilon_{i,j}^{(N)}$ associated with all N sub-elements of original element (i,j) can be approximated by:

$$\delta\varepsilon_{i,j}^{(N)}=\sum_{N}\ \delta\varepsilon'=N\times\frac{1}{N^3}\delta\varepsilon_{i,j}=\frac{1}{N^2}\delta\varepsilon_{i,j} \tag{16}$$

As before, the criterion given by Eq. (8) is inverted and $\delta\varepsilon_{i,j}^{(N)}$ is replaced by the right hand side of Eq. (16). Next, it is necessary to ensure that the sum of the errors $\delta\varepsilon_{i,j}^{(N)}$ due to the N sub-elements is smaller than $(\delta\varepsilon_{i,j})_{\max}$:

$$N=\frac{\Delta\theta_{i,j}}{\Delta\theta'_{i,j}}\geqslant R_{\varepsilon}^{1/2} \tag{17}$$

Again, the new interval size $\Delta\theta_{i,j}^{\text{new}}$ must be an integer fraction of the current interval. Thus,

$$\Delta\theta_{i,j}^{\text{new}}=\frac{\Delta\theta_{i,j}}{1+\text{INT}(R_{\varepsilon}^{1/2})} \tag{18}$$

Treatment of the case $c_{i,j}^{\theta}=0$ and $c_{i,j}^{\phi}\neq 0$ is analogous. The appropriate expression for the refined interval size can be obtained by interchanging θ and ϕ in Eq. (18).

Optimal Adaptive Refinement

In three-dimensional radiation problems intensity gradients will generally be nonzero, so $c_{i,j}^{\theta}\neq 0$ and $c_{i,j}^{\phi}\neq 0$. However, unidirectional mesh refinement with variable AR is likely to be superior to bi-directional refinement with fixed AR if the error $\delta\varepsilon_{i,j}$ in the elemental DTM heat flux is largely due to intensity gradients in one angular direction, i.e., if $|c_{i,j}^{\theta}|AR\gg|c_{i,j}^{\phi}|/AR$ or $|c_{i,j}^{\theta}|AR\ll|c_{i,j}^{\phi}|/AR$ in Eq. (2).

As an alternative to fixed AR refinement, a new aspect ratio AR^* is sought that makes the contributions to the error in both angular directions equal:

$$|c_{i,j}^{\theta}|AR^*=|c_{i,j}^{\phi}|/AR^* \tag{19a}$$

so

$$AR^*=\sqrt{|c_{i,j}^{\phi}/c_{i,j}^{\theta}|} \tag{19b}$$

This aspect ratio is, in fact, an excellent choice when coefficients $c_{i,j}^{\theta}$ and $c_{i,j}^{\phi}$ have opposite signs. Equation (2) shows that the local error contribution reduces to zero in this case. It can be shown that if $c_{i,j}^{\theta}$ and $c_{i,j}^{\phi}$ have the same sign, the local error contribution is minimized by AR^* of Eq. (19*b*) for fixed value of the product $\Delta\theta_{i,j}\Delta\phi_{i,j}$. This suggests that, if $AR\neq AR^*$, it would be advantageous to reduce the local error by simultaneous changes of interval size and aspect ratio. The ratio AR^*/AR is computed and the (integer) refinement parameter N_{AR} is defined as follows:

$$N_{AR}=\begin{cases}\text{NINT}(AR^*/AR) & \text{if } AR^*/AR\geqslant 1\\ \text{NINT}(AR/AR^*) & \text{if } AR^*/AR<1\end{cases} \tag{20}$$

with NINT(x)=nearest integer to real number x.

The following simple rule for optimal adaptive mesh refinement is proposed:

$N_{AR}=1$: apply bidirectional fixed AR refinement.
$N_{AR}\geqslant 2$: apply unidirectional variable AR refinement.

For unidirectional refinement ($N_{AR}\geqslant 2$) the refinement direction is governed by the magnitude of ratio AR^*/AR. If $AR^*/AR>1$, the ϕ-direction is subdivided, whereas if $AR^*/AR<1$, the θ-direction is subdivided. Finally, if the current mesh is very coarse Eq. (18) will indicate a large number of sub-intervals. This can produce values of AR beyond the optimum value AR^*. To protect against this condition the number of sub-elements is set in accordance with: $N=MIN(N,N_{AR})$.

Global Termination Criterion

Mesh refinement takes place on the basis of local relative error, so the possibility exists that an unnecessarily large amount of effort is spent attempting refinement in a solution region where the contribution to the global heat flux estimate is modest. This can be avoided by means of a global termination criterion:

- The change in the global heat flux estimates for two successive generations of mesh refinement is smaller than $f_T\times\varepsilon_{\text{R,tol}}$ (with $0<f_T\leqslant 1$).
- The magnitude of the change is smaller for the last of these two refinement generations.

A flowchart indicating the key elements of the algorithm used for the test cases in the next section is presented in the Appendix.

Final Heat Flux and Error Estimates

The adaptive refinement process is continued until $\delta\varepsilon_{i,j}<(\delta\varepsilon_{i,j})_{\max}$ for all elements (i,j). The final DTM heat flux and its error can then be computed by summing the contributions for all solid angle elements over the entire hemisphere. The DTM heat flux value on the final mesh of elements (i,j) and a sharp error bound are computed as follows:

$$\bar{q}_{DTM}=\sum_{i,j}(\delta\bar{q}_{i,j})_{\text{DTM}} \tag{21a}$$

$$\varepsilon=\sum_{i,j}\delta\varepsilon_{i,j} \tag{21b}$$

A more accurate DTM heat flux estimate and a further error based on known rate of decrease of error with element size given by Eq. (2) can be made using the four additional rays of pattern 2 and their intensities:

$$(\bar{q}_{\text{DTM}})'=\sum_{i,j}\left\{\frac{1}{4}\sum_{k=i-1/4}^{i+1/4}\sum_{l=j-1/4}^{j+1/4}I_{k,l}\sin(2\theta_k)\sin\left(\frac{1}{2}\Delta\theta_{i,j}\right)\Delta\phi_{i,j}\right\} \tag{22}$$

$$\varepsilon'=\frac{1}{4}\sum_{i,j}\delta\varepsilon_{i,j}\cong\frac{1}{4}\varepsilon \tag{23}$$

Richardson extrapolation of the results of Eqs. (21*b*) and (23) is possible if the trends are monotonic for a sequence of three results at different mesh sizes. At the cost of the additional storage required to enable this test to be performed, an extrapolated heat flux estimate can be constructed as follows:

$$\bar{q}_{\text{actual}}-\bar{q}_{\text{DTM}}=\varepsilon \tag{24a}$$

$$\bar{q}_{\text{actual}}-(\bar{q}_{\text{DTM}})'=\varepsilon'\cong\frac{1}{4}\varepsilon \tag{24b}$$

Subtraction of 1/4 times Eq. (24*a*) from Eq. (24*b*) yields an extrapolated heat flux estimate:

$$\bar{q}_{\text{actual}}=\frac{4}{3}(\bar{q}_{\text{DTM}})'-\frac{1}{3}\bar{q}_{\text{DTM}} \tag{25}$$

Results and Discussion

The error theory developed in Refs. [9,10] has shown that the most important aspects of the error behavior of the DTM are closely related to the continuity class of the irradiation distribution as a function of the angular variables θ and ϕ: infinitely differen-

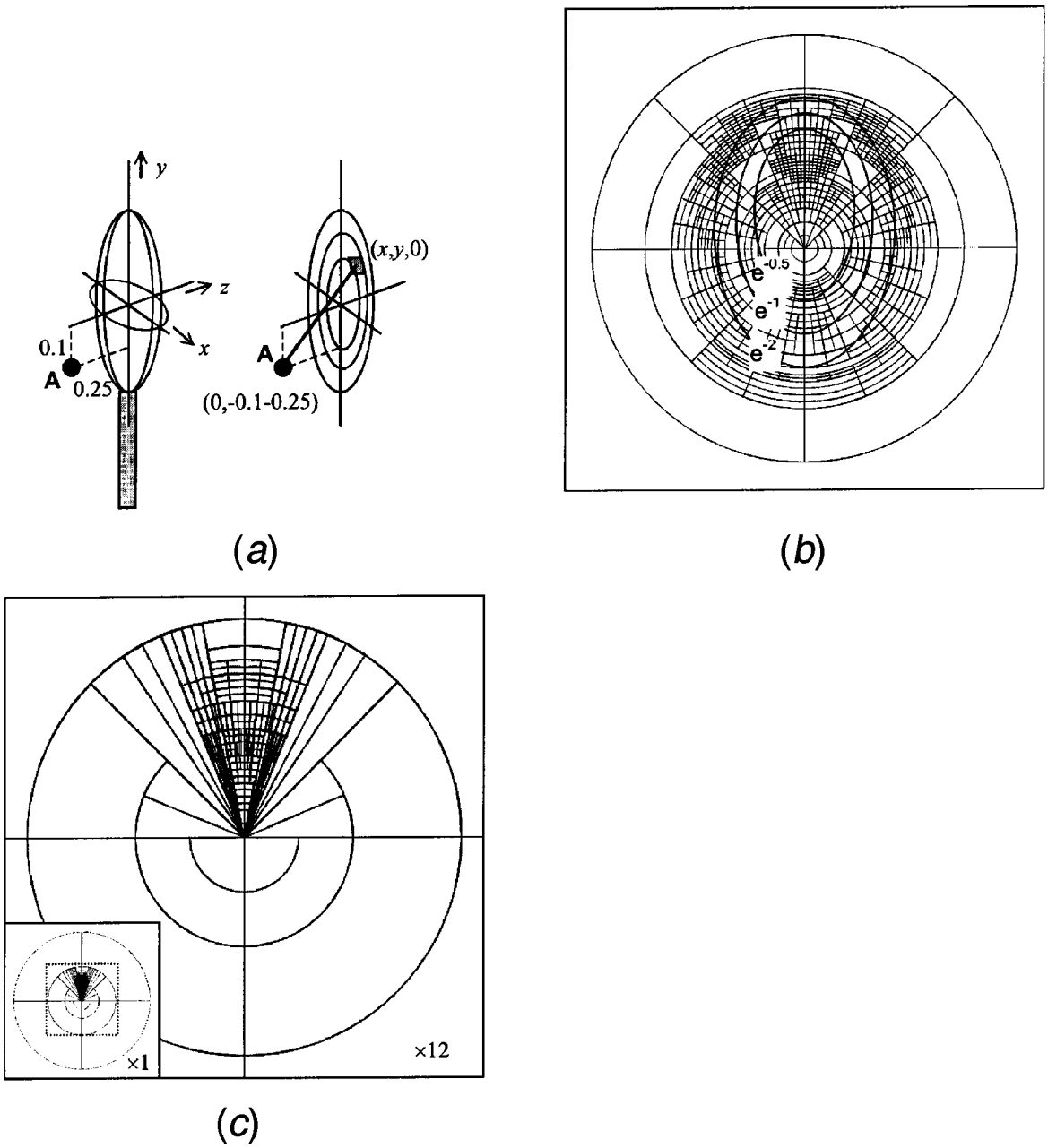

Fig. 2 (*a*) Schematic of idealized jet flame problem; (*b*) Hemisphere mesh and intensity contours for irradiated point (0, −0.1, −0.25); and (*c*) Hemisphere mesh of concentrated source; irradiated point (0, −0.1, −0.25). Inset gives full hemisphere, diagram gives region within dotted line at 12× magnification relative to inset.

tiable, piecewise constant and derivative-discontinuous. To demonstrate the application of the adaptive angular quadrature results are presented for the following test cases:

1. Irradiation due to a bivariate normal intensity distribution (infinitely differentiable distribution). This resembles a jet flame and is similar to one of the problems considered by Cumber [8].
2. Irradiation due to a small square source patch on the side face of a cube shaped enclosure filled with a transparent medium (piecewise constant distribution). This problem was considered by Versteeg et al. [9].
3. Irradiation on the cold walls of a unit cube due to a nonuniform, hot absorbing/emitting medium (combination of piecewise constant and derivative-discontinuous distributions), and is the case benchmark E1 of Hsu and Farmer [11].

The above summary shows that all the aforementioned continuity classes are considered. In each test the starting mesh was uniform, so $N_\phi = 4N_\theta$. The coarsest possible mesh $N_\theta = 1$ was always considered as a starting point, but N_θ was also varied to examine the effect of the density of the initial mesh. Two different refinement practices were tested: (i) bisection and (ii) predicted refinement using Eqs. (13*a–b*) and (18). Both methods applied unidirectional or bidirectional refinement depending on the value of N_{AR} in Eq. (20).

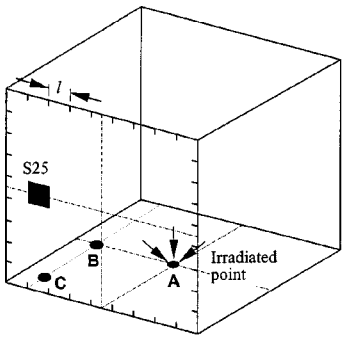

(*a*)

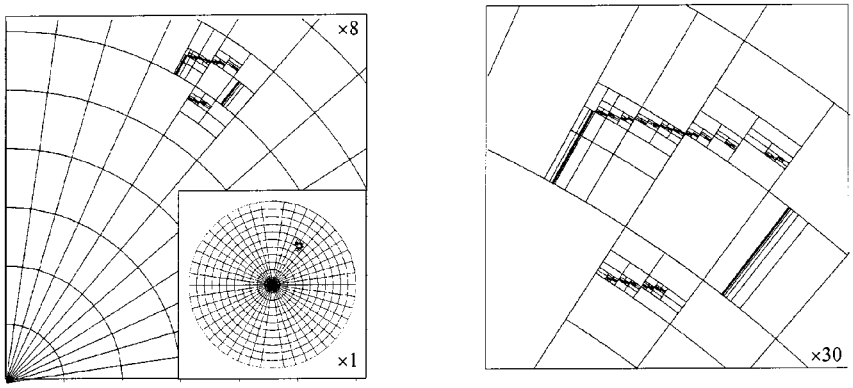

(*b*)

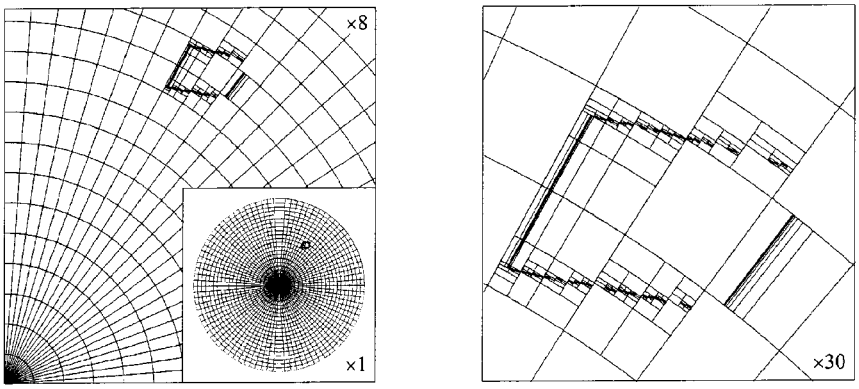

(*c*)

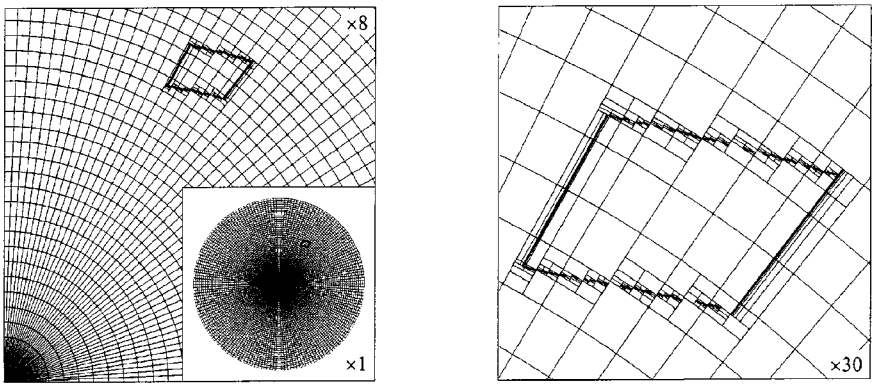

(*d*)

Fig. 3 (*a*) **Square source patch location relative to irradiated point in unit cube. Patch side length** $l=1/9$; (*b*) **Hemisphere mesh for square patch problem with starting mesh** $N_\theta=11$, $N_\phi=44$; (*c*) **Hemisphere mesh for square patch problem with starting mesh** $N_\theta=22$, $N_\phi=88$; **and** (*d*) **Hemisphere mesh for square patch problem with starting mesh** $N_\theta=44$, $N_\phi=176$.

Performance Indicators. To indicate the performance of the algorithm two sets of *element counts* N_E are presented for each test case: (a) the cumulative total number of elements at termination of the algorithm, and (b) the "minimum" cumulative element number at which the algorithm first returns heat flux values within the required error tolerance. The first result represents a "headline performance figure" for the adaptive algorithm, whereas the second figure indicates the potential for reduction of the final element count, while satisfying the original error objective, by means of fine-tuning of the numerical parameters: number of elements $N_\theta N_\phi$ in the starting mesh, local refinement criterion $\varepsilon_{R,\mathrm{tol}}$ and the factor f_T in the global termination criterion $f_T \times \varepsilon_{R,\mathrm{tol}}$.

To obtain an indication of the potential of the adaptive algorithm in coupled CFD/radiation problems, where ray tracing is overwhelmingly the largest computational cost, the cumulative element count of the adaptive algorithm is compared with the ray count of the standard DTM for similar error level. In order to generate the local error measure that drives the refinement process, the adaptive algorithm incurs the additional cost of the ray tracing associated with four sub-elements. Thus, the total *cumulative ray number* (i.e., the total storage count for each incident point) is 5 times the *cumulative number of elements* reported below. Nevertheless, the cumulative *element* counts provide an adequate basis for comparison with the standard DTM if it is borne in mind that the latter does *not* provide an error estimate. The only way to obtain an error estimate is to compare the standard DTM heat flux value at a given mesh with a DTM heat flux value computed on (at least) one further mesh with twice as many rays in each direction. This exercise would also involve four extra rays for each original one, so the total ray count for the standard DTM is also 5 times the ray count at the coarsest mesh with sufficiently accurate heat flux. Hence, a comparison of the cumulative element count for the present adaptive DTM with the ray number for the standard DTM for a similar error level provides the correct basis for a performance measure for coupled CFD/radiation problems.

Idealized Jet Flame. In jet flames the highest temperature occurs in a small core region around the combustion reaction zone, where the emissive power peaks. The intensity rapidly drops as the distance from the core increases. As an idealization of a jet flame it is assumed that the spatial distribution of irradiation at an incident points arises from a source of emissive power with roughly ellipsoidal contours around the origin of a Cartesian coordinate system. Consider the irradiation in a plane parallel to the axis of the idealized flame and perpendicular to the line of sight between the incident point and the origin of the coordinate system. Figure 2(*a*) shows a schematic sketch of the problem. In the far-field, the distribution of incident intensity will be not too far from that due to a bivariate normal intensity distribution. To demonstrate the adaptive algorithm the incident intensity at an irradiated point A, located at $(0,-0.1,-0.25)$, is assumed to take the following form:

$$I(x,y) = I_{\max} \exp\left[-\frac{1}{2}\left\{ \left(\frac{x}{\sigma_x}\right)^2 + \left(\frac{y}{\sigma_y}\right)^2 \right\} \right] \tag{26}$$

where x and y indicate the position of the radiation source and $I_{\max} = 1/(2\pi\sigma_x\sigma_y)$.

For the first test case the heat flux is computed at an irradiated point A, located at $(0,-0.1,-0.25)$ for the distribution defined in Eq. (26) taking $\sigma_x = 0.1$ and $\sigma_y = 0.2$, respectively. The adaptive algorithm was run with a coarse starting mesh with 4 elements ($N_\theta = 1$, $N_\phi = 4$), relative error tolerance $\varepsilon_{R,\mathrm{tol}} = 5 \times 10^{-3}$ and global termination factor $f_T = 0.8$. Figure 2(*b*) shows the final hemisphere mesh for the adaptive algorithm as a projection of the unit hemisphere surrounding the irradiated point onto the irradiated plane using a linear mapping of polar coordinate θ onto the radial direction (i.e., $\theta = c \times r$). In addition to the hemisphere mesh, three contours of constant intensity ($I_{\max} e^{-0.5}$, $I_{\max} e^{-1}$, and $I_{\max} e^{-2}$, labeled $e^{-0.5}$, e^{-1}, and e^{-2}, respectively, in Fig. 2(*b*) are shown to highlight that the adaptive procedure causes refinement of the hemisphere mesh in the direction of the intensity gradients. Since point A is slightly below the center of the idealized flame, the contours are slightly distorted ellipses. The result clearly illustrates that bi-directional refinement is found in regions where the contours intersect the hemisphere mesh at an angle and uni-directional refinement where the contours are aligned with one of the angular coordinate directions.

Accurate solutions of the problem were obtained with a standard DTM at high ray number ($N_R = 4 \times 10^6$) and automatic (numerical) integration using the computer code *Mathematica*®. Both methods yielded a converged heat flux value of 7.0694. The standard DTM returns solutions within the required tolerance band $7.034 < q^- < 7.105$ when the ray count exceeds 256. The element count for adaptive algorithm at termination depends on the starting mesh and the details of implementation. The bisection variant of the algorithm in conjunction with a four element starting mesh ($N_\theta = 1$, $N_\phi = 4$) produces values within the error band for $N_E \geqslant 88$ elements and terminates at a total cumulative element count of $N_E = 1{,}216$.

Reduction of the standard deviation values in Eq. (26) by a factor 10 to $\sigma_x = 0.01$ and $\sigma_y = 0.02$ yields a concentrated source with a small view factor and high intensity. The high N_R DTM and *Mathematica*® value of incident heat flux at point A is 11.833. Figure 2(*c*) shows the final mesh of the adaptive quadrature using a 4 element ($N_\theta = 1$, $N_\phi = 4$) starting mesh. The bisection variant terminated at $N_E = 1{,}004$ and first matched the required tolerance ($\varepsilon_{\mathrm{R,tol}} = 5 \times 10^{-3}$) at $N_E = 432$. The standard DTM achieves the same accuracy at $N_R = 1{,}024$.

Square Source Patch. As a second test case the irradiation was computed at the centroid of the bottom face of a unit cube due to a square radiating patch with unit intensity on one of its side faces. The cube-shaped enclosure contains a transparent medium and its walls are cold except for the patch. The position of the patch, denoted by S25, is shown in Fig. 3(*a*). Further details of the problem can be found in Versteeg et al. [9]. The exact value of the irradiation at the centroid of the bottom face of the cube can easily be found using view factor algebra and is equal to 8.252×10^{-3}. Versteeg et al. [9] showed that the standard DTM consistently achieves an absolute error of 8×10^{-5}, which corresponds to a relative error of 1 percent ($\varepsilon_{R,\mathrm{tol}} = 10^{-2}$), using around 10^6 rays. This problem is of considerable interest, since adaptivity is likely to yield improvements in ray count if the algorithm that can "recognize" the rapid intensity change at the edge of the source. However, it is not immediately obvious that the algorithm will be able to cope with the jump discontinuities in the intensity field due to a source patch, since it is based on error formulas that assume differentiable intensity fields.

The adaptive algorithm applies refinement in regions with excessively large gradients of incident intensity. For the method to work in cases with piecewise constant radiation sources, a starting mesh is required where two rays straddle each discontinuity. The present case involves one source patch, so at least one ray of the starting mesh must hit the patch, otherwise all local gradients are estimated to be zero and the procedure terminates without refinement indicating zero error. A uniform starting mesh with $N_\theta = 11$ and $N_\phi = 44$ rays ($N_\theta N_\phi = 484$ elements) generates a single hit on the source patch, so this is the minimum necessary for the adaptive procedure to start working.

Figure 3(*b–d*) shows final meshes of computations with the adaptive algorithm using different starting meshes. The results show that the method correctly interprets the intensity discontinuity at the edge of the source patch as a region of high intensity gradient. Along sections of the edges of the source the mesh is highly refined and there is clear evidence of uni-directional refine-

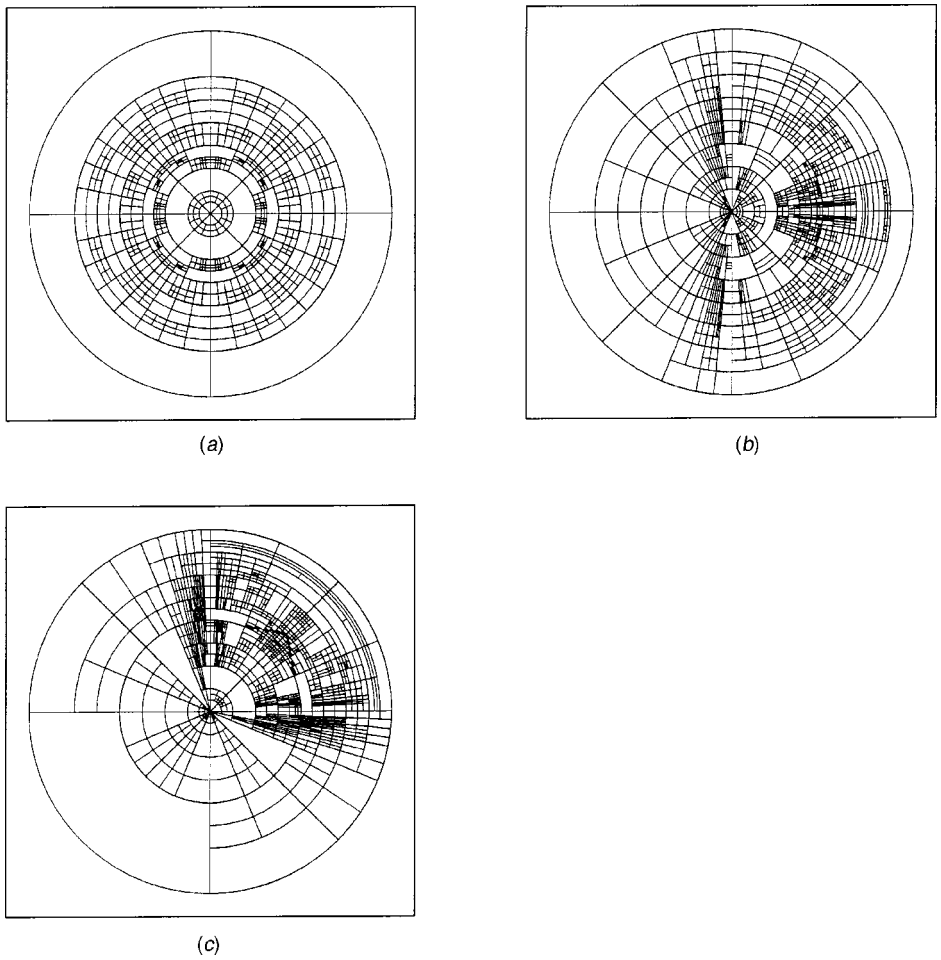

Fig. 4 (*a*) Hemisphere mesh for point A (0,0,−1/2); (*b*) Hemisphere mesh for point B (−4/9, 0,−1/2); and (*c*) Hemisphere mesh for point C (−4/9,−4/9,−1/2).

ment. Figure 3(*b*) shows clearly that early refinement cycles miss out three of the four corners of the source patch and converges to a value of 6.45×10^{-3} is obtained, which is in error by 22 percent. A starting mesh with $N_\theta=22$ and $N_\phi=88$ rays ($N_\theta N_\phi=1{,}936$) converges towards a result with 4 percent error. This rapid improvement continues with a further doubling of the starting mesh. A uniform mesh with $N_\theta=44$ and $N_\phi=176$ rays ($N_\theta N_\phi=7{,}744$) gave results within a 1 percent error band after adaptive refinement for $N_E\geqslant 8{,}030$ elements and terminates at an element count of 8480.

This test case demonstrates that this quadrature, which is based on error formulas for smooth irradiation distributions, does not break down in the presence of radiation sources with discontinuities. Moreover, modest cumulative element counts, which are two orders of magnitude smaller than the corresponding ray counts for the standard DTM for a given accuracy, can be obtained if care is taken when specifying the starting mesh.

Unit Cube With Nonhomogeneous Medium. The final case study involves the calculation of the irradiation at three points: point A at the center (0,0,−1/2), point B near the edge (−4/9,0, −1/2) and point C near one of the corners (−4/9,−4/9,−1/2) on the bottom face of a unit cube. The cube is filled with a hot absorbing/emitting medium with constant source function and nonuniform absorption coefficient. The problem corresponds to Benchmark Case E1 designed by Hsu and Farmer [11]. The geometry of the domain and the locations of the irradiated points are shown in Fig. 3(*a*). The value of the absorption coefficient is high at the center of the cube and linearly decreases towards the walls of the cube. This yields irradiation distributions with a strong bias towards the center of the cube. The medium is discretized by means of a uniform mesh with 9×9×9 control volumes. The combined effect of the shape of the enclosure and the discretization of the medium generates irradiation fields with large intensity gradients and jump discontinuities in the angular derivatives of intensity. The test case is discussed further in Versteeg et al. [10], where a DTM solution with 16×10^6 rays was reported to produce incident heat flux values of 0.193350, 0.109783, and 0.073225 for points A, B, and C, respectively. The DTM solution compared favourably with other high quality Monte-Carlo and finite-element solutions of this problem available in the literature.

The irradiation was computed at A, B, and C with the adaptive angular DTM quadrature using $\varepsilon_{R,\mathrm{tol}}=5\times10^{-3}$ and a selection of starting meshes, including the 4 element mesh ($N_\theta=1$, $N_\phi=4$). Figures 4(*a*–*c*) show the final meshes of computations with this starting mesh for all three incident points. It is evident that the adaptive quadrature concentrates the hemisphere mesh in the direction of the main source contribution around the center of the cube. At point A this is located around the pole, whereas at points B the source appears at $\theta=45°$ and $\phi=0°$ and at C it is found around $\theta=\phi=45°$. As before, the adaptive quadrature terminates giving solutions within the specified tolerance band. The cumulative element count at termination varied between 908 and 1156. The lowest cumulative element count for which the required ac-

curacy was achieved varied between 156, 320, and 228 elements for points A, B, and C, respectively. In previous work [10] it was shown that the standard DTM consistently produces solution to the same accuracy using around 196, 400, and 676 rays, respectively.

Concluding Remarks

A new adaptive hemisphere meshing strategy with a number of distinctive features has been introduced. The algorithm is supported by a rigorous error theory, which includes sharp error bounds for the irradiation integral in the DTM for irradiation distributions of different continuity classes. This enables the computation of incident heat flux estimates to a pre-specified tolerance. The combined uni and bidirectional refinement capability allows improved meshing of regions with high intensity gradients that are predominantly in one angular direction, reducing the sensitivity of the method to the aspect ratio of non-uniform starting meshes. The analytical basis of the underpinning error theory permits us to claim that, although the method has only been demonstrated for a few test cases, the algorithm can be applied to radiation problems involving arbitrary intensity distributions. The method has three free parameters: the number of elements of the starting mesh, the relative error tolerance $\varepsilon_{R,\mathrm{tol}}$ and the global termination factor f_T. For differentiable irradiation distributions and for continuous distributions with discontinuities in the intensity derivatives the algorithm does not need case-dependent empirical adjustments, unlike Cumber's adaptive algorithm. Moreover, for the most testing category of radiation problems, namely those involving piecewise constant irradiation and, hence, infinite intensity gradients, the adaptive method gave good results provided that an adequate starting mesh is chosen.

Experience with the algorithm has shown that, it is adequate to use very coarse starting meshes with four subelements ($N_\theta=1$, $N_\phi=4$) if the irradiation distribution is sufficiently smooth (e.g., such as those in test cases 1 and 3). Adaption strategies using bisection and predictive refinement were tested. This revealed that the predictive ability of Eqs. (13*a*–*b*) and (18) tends to be fairly poor unless the starting mesh is much finer. As the refinement progresses, a more accurate picture of the intensity gradients emerges gradually in most problems. It is, therefore, essential to avoid the early appearance of excessively fine meshes in regions, which are subsequently found to have only modest intensity gradients. This explains why the bisection method generally seems to work best in conjunction with coarse starting meshes.

In radiation problems involving optically thick and/or scattering media the intensity distribution is often fairly uniform without large gradients. Test cases 1 and 3 involve comparatively smooth irradiation distributions with a large view factor, which is typical of many coupled three-dimensional CFD/radiation problems. In such cases it was found that similar ray numbers are needed by the adaptive DTM and the standard DTM to achieve a given accuracy. Since adaptive meshing involves a computational overhead and also requires additional storage of the ray directions at each irradiated surface point, the adaptive quadrature does not appear to offer much benefit and fixed angular meshes are likely to be preferable in these cases. Nevertheless, the algorithm consistently achieved the specified error tolerance. Moreover, the "minimum" cumulative total element count shows there is potential for optimization of the adaptive quadrature through empirical adjustments of the starting mesh and the global termination factor f_T on a case-by-case basis.

In optically thin problems, on the other hand, very substantial benefits are possible when the algorithm is applied to radiation originating from sources with a small view factor. It is straightforward to make a rough assessment of the superiority of an adaptive approach by considering a small source, which subtends an angle $\Delta\theta_s$ in the θ-direction and $\Delta\phi_s$ in the ϕ-direction. To achieve one hit on the source requires on the order of $N_s=\pi^2/(\Delta\theta_s\Delta\phi_s)$ rays. Let the number of hits on the source to compute the heat flux to a given accuracy be N_h rays. The ray number required by the standard DTM to achieve the accuracy will then be on the order of $N_s\times N_h$, but an adaptive quadrature will need on the order of N_s+N_h elements.

Crucially, this work has shown that the adaptive quadrature does not break down when it is applied to piecewise constant intensity distributions, such as the square source patch, and achieves excellent accuracy if a starting mesh is chosen that affords 8 hits on a patch.

In conclusion, it is noted that an adaptive angular quadrature for the DTM heat flux integral has been presented with the following capabilities:

- Evaluation of DTM heat flux integrals to a pre-specified tolerance for all test cases.
- Adaptive algorithm and standard DTM use similar ray numbers for a given accuracy if the angular irradiation distribution is smoothly distributed across the hemisphere.
- Good accuracy with very low ray numbers for irradiation due small view factor sources.
- Good heat flux estimates for piecewise constant sources, provided that care is taken in the selection of the starting mesh.

Nomenclature

AR = aspect ratio of solid angle element

c^θ, c^ϕ = error coefficients (Eqs. (2*b*–*d*))

F = error multiplier (Eqs. (2*a*–*b*)).

f_T = global termination factor

I = intensity

$I_{\max}$ = peak intensity (Eq. (26))

N = number of angular sub-intervals

N_{AR} = refinement parameter (Eq. (20))

N_R = ray number

R_ε = error ratio (Eq. (8))

q^- = incident heat flux

Greek Symbols

$\delta\varepsilon$ = absolute error due to solid angle

$(\delta\varepsilon_{ij})_{\max}$ = local absolute error tolerance for hemisphere element (i,j)

δq^- = incident heat flux due to solid angle

$\Delta\theta$, $\Delta\phi$ = angle increments

ε = absolute error

$\varepsilon_{R,\mathrm{tol}}$ = local and global relative error tolerance

ϕ = azimuthal angle

θ = polar angle

Subscripts

actual = actual value

DTM = approximate (DTM) value

i = polar angle index

j = azimuthal angle index

max = maximum

Appendix

Flowchart of Adaptive DTM Algorithm

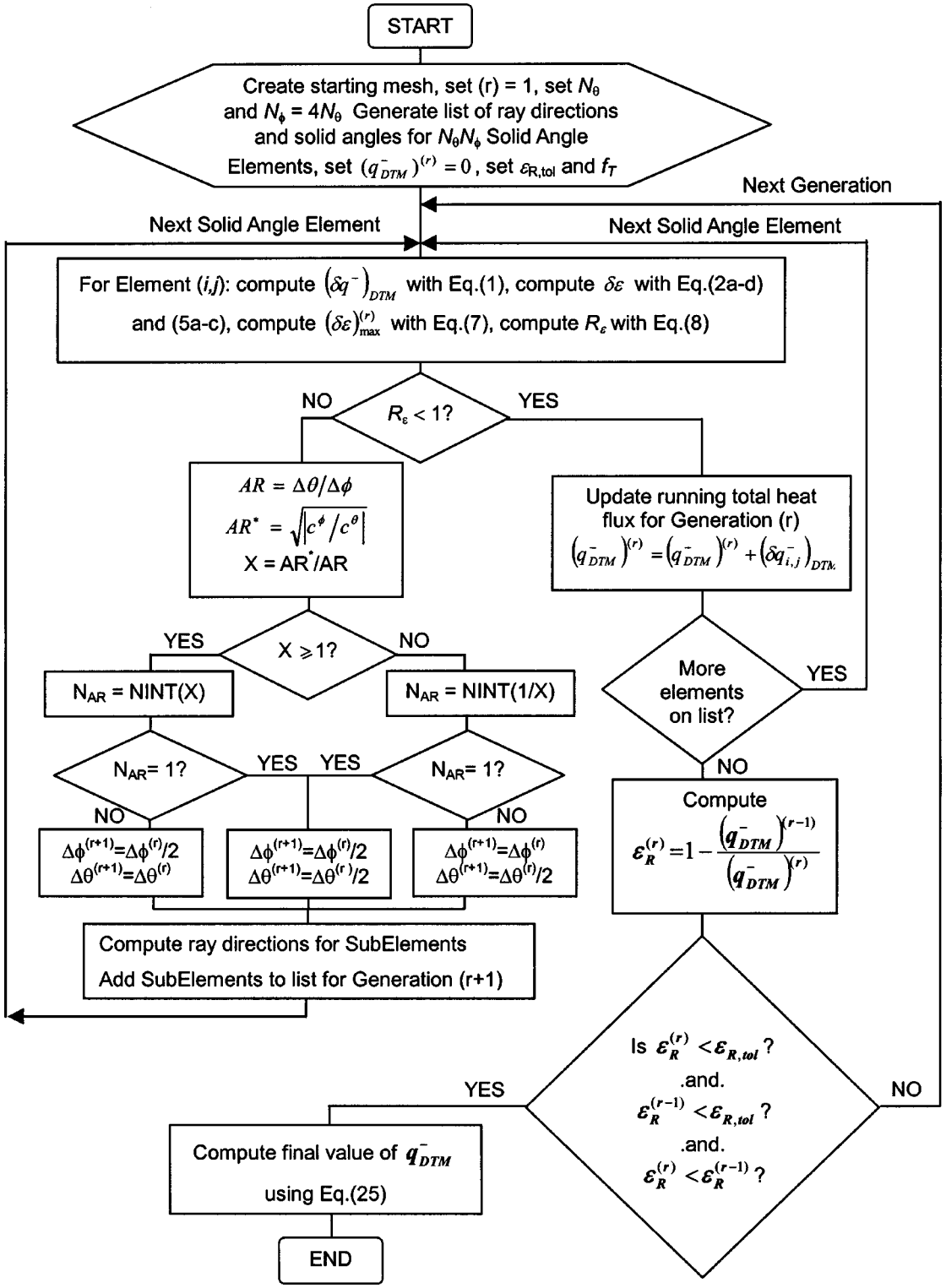

References

[1] Shah, N. G., 1979, ''New Method for the Computation of Radiation Heat Transfer in Combustion Chambers,'' Ph.D. thesis, Imperial College of Science and Technology, London.

[2] Pessoa-Filho, J. B., and Thynell, S. T., 1997, ''An Approximate Solution to the Radiative Transfer in Two-Dimensional Rectangular Enclosures,'' ASME J. Heat Transfer, **119**(4), pp. 738–745.

[3] Lockwood, F. C., and Shah, N. G., 1981, ''A New Radiation Solution Method for Incorporation in General Combustion Prediction Procedures,'' *Proc. Eighteenth Symp. (Int.) Combustion*, The Combustion Institute, Pittsburgh, PA, pp. 1405–1413.

[4] Cumber, P. S., 1995, ''Improvements to the Discrete Transfer Method of Calculating Radiative Heat Transfer,'' Int. J. Heat Mass Transf., **38**(12), pp. 2251–2258.

[5] Andersen, F. M. B., 1996, ''Comparison of Numerical Quadrature Schemes

Applied in the Method of Discrete Transfer,'' J. Thermophys. Heat Transfer, **10**(3), pp. 549–551.
[6] Li, B.-W., Tao, W.-Q., and Liu, R.-X., 1997, ''Ray Effect in Ray Tracing for Radiative Heat Transfer,'' Int. J. Heat Mass Transf., **40**(14), pp. 3419–3426.
[7] Bressloff, N. W., Moss, J. B., and Rubini, P. A., 1999, ''Application of a New Weighting Set for the Discrete Transfer Method,'' *Proc. 3rd European Conf. Industrial Furnaces and Boilers*, 18–21 April 1999, Lisbon, Portugal, pp. 208–215.
[8] Cumber, P. S., 2000, ''Ray Effect Mitigation in Jet Fire Radiation Modelling,'' Int. J. Heat Mass Transf., **43**(6), pp. 935–943.
[9] Versteeg, H. K., Henson, J. C., and Malalasekera, W. M. G., 1999, ''Approximation Errors in the Heat Flux Integral of the Discrete Transfer Method. Part 1: Transparent Media,'' Numer. Heat Transfer, Part B, **36**, Pt. 4, pp. 387–407.
[10] Versteeg, H. K., Henson, J. C., and Malalasekera, W. M. G., 1999, ''Approximation Errors in the Heat Flux Integral of the Discrete Transfer Method. Part 2: Participating Media,'' Numer. Heat Transfer, Part B, **36**, Pt. 4, pp. 409–432.
[11] Hsu, P.-F., and Farmer, J. T., 1995, ''Benchmark Solutions of Radiative Heat Transfer Within Nonhomogeneous Participating Media Using the Monte Carlo and YIX Methods,'' ASME HTD-315, **13**, ASME, New York, pp. 29–36.

Application of Adomian's Decomposition Procedure to the Analysis of Convective-Radiative Fins

Ching-Huang Chiu
Department of Vehicle Engineering,
National Huwei Institute of Technology,
Huwei, Yunlin, Taiwan 632

Cha'o-Kuang Chen
e-mail: ckchen@mail.ncku.edu.tw
Department of Mechanical Engineering,
National Cheng Kung University,
Tainan, Taiwan 701

This paper presents a method which may be used to determine the temperature distribution within a convective-radiative longitudinal fin of variable thermal conductivity, subject to convection heat transfer from a fluid of known temperature T_f through the inside face of the primary surface, and which experiences convection-radiation heat dissipation into the environment at its tip. The paper demonstrates the use of the Adomian decomposition method in generating an analytical solution of the resulting nonlinear energy balance equation with nonlinear boundary conditions. [DOI: 10.1115/1.1532012]

Keywords: Conduction, Convection, Enhancement, Finned Surfaces, Radiation

Introduction

When fins dissipate heat by convection or by radiation (or both), the performance is significantly affected by variable thermal conductivity, particularly in the case of large temperature differences. The analysis of longitudinal convective fins, frequently provided in published literature, e.g., [1–3], is based upon the assumption that the base temperature is known. However, as shown in Fig. 1, in an actual situation it is the temperature of the fluid T_f on the inside face of the primary surface which is known, rather than the fin base temperature. Therefore, to generate a more realistic analysis it is necessary to incorporate this convective boundary, and also to include the conductive resistance of the wall. In fact, Aziz [4] did adopt this more precise model in calculations of the optimization of single rectangular, and triangular fins. Although numerous studies of the heat transfer characteristics of extended surfaces may be found in published literature, e.g. [5,6], these studies neglect the effects of heat transfer from the tip of the fin, despite the fact that such losses have a significant influence when the ratio of the fin length to its transversal direction is small. The governing equation for fins that exchange heat with their surroundings via radiation, or simultaneous convection and radiation mechanisms, is given by a nonlinear heat transfer equation, as is the equation for fins having variable thermal conductivity. Furthermore, in the case where the base of the fin, or its tip, is subject to a radiation interaction, the boundary conditions are also represented by nonlinear forms.

This paper applied the Adomian decomposition method to solve a nonlinear heat transfer equation with nonlinear boundary conditions. Three different heat dissipation mechanisms are considered, namely pure convection, pure radiation, and simultaneous convection and radiation, and heat flow through the fin is considered to be in the direction away from the base, i.e., towards the tip. In contrast to many previous papers, this study takes into account the effects of heat transfer that occurs at the tip of the fin. It will be noted that since it is the temperature responses of the fin that are the basis for further analysis and optimization procedures, only these results are presented in this paper.

Contributed by the Heat Transfer Division for publication in the JOURNAL OF HEAT TRANSFER. Manuscript received by the Heat Transfer Division February 11, 2002; revision received October 8, 2002. Associate Editor: S. T. Thynell.

The Governing Equation and Boundary Condition

This study considers one-dimensional conduction in a straight fin of length b, cross sectional area A_c, and perimeter P, as shown in Fig. 1. The fin surface loses heat by a combination of convection and radiation mechanisms. Both convective heat transfer coefficient h_a and the ambient temperature T_a are assumed uniform. These conditions may not necessarily hold in all cases. Allowing the thermal conductivity of the fin to be variable, the energy balance equation may be written as:

$$\frac{d}{dx}\left(K(T)\frac{dT}{dx}\right)-\frac{Ph_a}{A_c}(T-T_a)-\frac{P\sigma}{A_c}(\varepsilon T^4-\alpha T_s^4)=0. \quad (1)$$

Let the thermal conductivity, K, of the fin's material vary linearly with temperature as follows:

$$K(T)=k_a[1+\beta(T-T_a)] \quad (2)$$

where k_a is the thermal conductivity at ambient temperature, T_a, and β is the slope of the thermal conductivity-temperature curve divided by the intercept k_a.

If the conductive thermal resistance of the primary surface wall, i.e., $\delta=0$ in Fig. 1, is ignored, then the convection boundary conditions imposed at the base and the fin tip may be expressed as follows:

$$-K(T)\frac{dT}{dx}=h_f(T_f-T), \quad x=0 \quad (3)$$

$$-K(T)\frac{dT}{dx}=h_a(T-T_a)+\sigma(\varepsilon T^4-\alpha T_e{}^4), \quad x=b, \quad (4)$$

where T_f is the fluid temperature on the inside of the primary surface, and h_f represents the convective heat transfer coefficient between the fluid and the primary surface.

The following dimensionless quantities may then be introduced:

$$\theta=T/T_a,\ \theta_f=T_f/T_a,\ \theta_s=T_s/T_a,\ X=x/b.$$

Substitution of these dimensionless quantities into Eq. (1) yields:

$$\frac{d^2\theta}{dX^2}+n_1\theta\frac{d^2\theta}{dX^2}+n_1\left(\frac{d\theta}{dX}\right)^2-n_2(\theta-1)-n_3\theta^4+n_4=0. \quad (5)$$

Similarly, the boundary conditions may now be expressed as:

$$m_1\frac{d\theta}{dX}+m_2\theta\frac{d\theta}{dX}=m_3(\theta-\theta_f), \quad X=0 \quad (6)$$

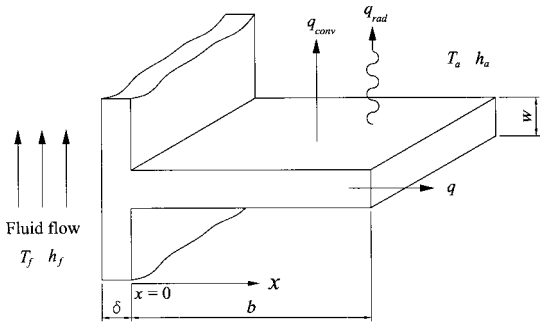

Fig. 1 Straight fin of rectangular cross section

$$m_1\frac{d\theta}{dX}+m_2\theta\frac{d\theta}{dX}+m_4\theta+m_5\theta^4=m_4+m_6,\quad X=1 \tag{7}$$

where:

$$n_1=\frac{\beta T_a}{1-\beta T_a},\ n_2=\frac{h_a P b^2}{A_c k_a(1-\beta T_a)},\ n_3=\frac{P b^2\sigma T_a^3\varepsilon}{A_c k_a(1-\beta T_a)},$$

$$n_4=\frac{P b^2\sigma {T_a}^3\alpha {\theta_e}^4}{A_c k_a(1-\beta T_a)},$$

$$m_1=1-\beta T_a,\ m_2=\beta T_a,\ m_3=\frac{h_f b}{k_a},\ m_4=\frac{h_a b}{k_a},$$

$$m_5=\frac{b\sigma T_a^3\varepsilon}{k_a},\ m_6=\frac{b\sigma T_a^3\alpha\theta_e^4}{k_a}.$$

Decomposition Method

Previous studies have proposed the use of the main algorithm within the Adomian decomposition method to solve boundary value problems, e.g., [7–10]. The double decomposition method evaluates a value of θ_o which satisfies the boundary conditions, and then adds constants of integration for each successive component, θ_n. For a detailed discussion of the double decomposition method, interested readers are invited to refer to Ref. [11].

It is possible to express Eq. (5) in an operator form, i.e.,

$$L_x\theta=-(n_2+n_4)+n_2\theta-n_1\theta\frac{d^2\theta}{dX^2}-n_1\left(\frac{d\theta}{dX}\right)^2+n_3\theta^4$$

$$=-(n_2+n_4)+n_2\theta-n_1\ NA-n_1\ NB+n_3\ NC, \tag{8}$$

where L_X is a second order differential operator.

Hence the inverse operator, L_X^{-1}, is taken to be a two-fold integral operator defined as follows:

$$L_X^{-1}(\cdot)=\int_0^X\int_0^X(\cdot)dX\ dX$$

where $\theta d^2\theta/dX^2$, $(d\theta/dX)^2$, θ^4 are nonlinear terms.

The decomposition method may be used to formally expand each of these nonlinear terms into a power series, i.e.,

$$NA=\theta\frac{d^2\theta}{dX^2}=\sum_{n=0}^{\infty}A_n,\ NB=\left(\frac{d\theta}{dX}\right)^2=\sum_{n=0}^{\infty}B_n,$$

$$NC=\theta^4=\sum_{n=0}^{\infty}C_n,$$

where A_n, B_n, and C_n are the so-called Adomian polynomials corresponding to the nonlinear terms $\theta d^2\theta/dX^2$, $(d\theta/dX)^2$, and θ^4, respectively. Using the derivation process of Adomian polynomials for any type of nonlinearity which is presented in Ref. [12], it is found that A_n, B_n, and C_n are given by the following expressions:

$$A_0=\theta_0\frac{d^2\theta_0}{dX^2},$$

$$A_1=\theta_1\frac{d^2\theta_0}{dX^2}+\theta_0\frac{d^2\theta_1}{dX^2}, \tag{9}$$

$$A_2=\theta_2\frac{d^2\theta_0}{dX^2}+\theta_1\frac{d^2\theta_1}{dX^2}+\theta_0\frac{d^2\theta_2}{dX^2},$$

$$\vdots$$

$$B_0=\left(\frac{d\theta_0}{dX}\right)^2,$$

$$B_1=2\frac{d\theta_0}{dX}\frac{d\theta_1}{dX}, \tag{10}$$

$$B_2=\left(\frac{d\theta_1}{dX}\right)^2+2\frac{d\theta_0}{dX}\frac{d\theta_2}{dX},$$

$$\vdots$$

$$C_0=\theta_0^4,$$

$$C_1=4\theta_0^3\theta_1, \tag{11}$$

$$C_2=6\theta_0^2\theta_1^2+4\theta_0^3\theta_2,$$

$$\vdots$$

Operating with L_X^{-1} on both sides of Eq. (8) yields the following:

$$L_X^{-1}L_X\theta=-L_X^{-1}(n_2+n_4)+n_2L_X^{-1}\theta-n_1L_X^{-1}NA-n_1L_X^{-1}NB+n_3L_X^{-1}NC. \tag{12}$$

Hence, $L_X^{-1}L_X\theta=\theta-\phi_X$. Let $\theta=\Sigma_{m=0}^{\infty}\theta_m$, $\phi_X=\Sigma_{m=0}^{\infty}\phi_{X,m}$ and $\phi_{X,m}=c_{0,m}+Xc_{1,m}$. Equation (12) becomes:

$$\sum_{m=0}^{\infty}\theta_m=\sum_{m=0}^{\infty}\phi_{X,m}-L_X^{-1}(n_2+n_4)+n_2L_X^{-1}\sum_{m=0}^{\infty}\theta-n_1L_X^{-1}\sum_{m=0}^{\infty}A_m-n_1L_X^{-1}\sum_{m=0}^{\infty}B_m+n_3L_X^{-1}\sum_{m=0}^{\infty}C_m. \tag{13}$$

The first component θ_o is normally taken inhomogeneous term as:

$$\theta_o=\phi_{X,0}-L_X^{-1}(n_2+n_4)=c_{0,0}+Xc_{1,0}-L_X^{-1}(n_2+n_4).$$

Higher-order terms are determined from the recursive relationship:

$$\theta_m=c_{0,m}+Xc_{1,m}+n_2L_X^{-1}\theta_{m-1}-n_1L_X^{-1}A_{m-1}-n_1L_X^{-1}B_{m-1}+n_3L_X^{-1}C_{m-1},\quad m\geqslant 1 \tag{14}$$

Summing these terms, it is observed that:

$$\varphi_m=\sum_{i=0}^{m-1}\theta_i=\theta_0+\theta_1+\theta_2\cdots+\theta_{m-1}. \tag{15}$$

Thus, components of θ are determined and written as an m-terms approximation converging to θ as $m\to\infty$. It is noted that the integral constants may be retained within each component. These integral constants, denoted by $c_{0,m}$ and $c_{1,m}$ may be evaluated by satisfying the boundary conditions for each approximate solution, φ_m. It will be clear from the preceding discussion that the evaluation of these constants is no simple matter in the case of nonlinear boundary conditions.

Nonlinear Boundary Conditions

The boundary conditions presented in Eqs. (6) and (7) are of a nonlinear, inhomogeneous form, and can be expressed by an approximate solution, φ_m, as follows:

$$m_1\frac{d\varphi_m}{dX}-m_3\varphi_m+m_2\varphi_m\frac{d\varphi_m}{dX}+m_3\theta_f=0,\quad X=0 \tag{16}$$

$$m_1\frac{d\varphi_m}{dX}+m_4\varphi_m+m_2\varphi_m\frac{d\varphi_m}{dX}+m_5\varphi_m^4-m_4-m_6=0,\quad X=1 \tag{17}$$

Applying the decomposition method to these boundary operator equations, allows the nonlinear terms to be defined by the following expressions:

$$ND=\varphi_m\frac{d\varphi_m}{dX}=\sum_{n=0}^{\infty}(D_m)_n,\quad NE=\varphi_m^4=\sum_{n=0}^{\infty}(E_m)_n.$$

In accordance with Refs. [11] and [12], $(D_m)_n$ and $(E_m)_n$ may be given as follows:

$$(D_m)_0=(\varphi_m)_0\frac{d(\varphi_m)_0}{dX},$$

$$(D_m)_1=(\varphi_m)_1\frac{d(\varphi_m)_0}{dX}+(\varphi_m)_0\frac{d(\varphi_m)_1}{dX},$$

$$(D_m)_2=(\varphi_m)_2\frac{d(\varphi_m)_0}{dX}+(\varphi_m)_1\frac{d(\varphi_m)_1}{dX}+(\varphi_m)_0\frac{d(\varphi_m)_2}{dX},$$

$$\vdots$$

$$(E_m)_0=(\varphi_m)_0^4,$$

$$(E_m)_1=4(\varphi_m)_0^3(\varphi_m)_1,$$

$$(E_m)_2=4(\varphi_m)_0^3(\varphi_m)_2+6(\varphi_m)_0^2(\varphi_m)_1^2,$$

$$\vdots$$

The one-component, approximate solution is given by:

$$\varphi_1=\theta_0=c_{0,0}+Xc_{1,0}-L_X^{-1}(n_2+n_4) \tag{18}$$

Satisfying the boundary conditions for this approximate solution, enables the integral constants, $c_{0,0}$ and $c_{1,0}$, to be determined, i.e.,

$$m_1\frac{d\varphi_1}{dX}-m_3\varphi_1+m_2\sum_{n=0}^{\infty}(D_1)_n=-m_3\theta_f,\quad X=0 \tag{19}$$

$$m_1\frac{d\varphi_1}{dX}+m_4\varphi_1+m_2\sum_{n=0}^{\infty}(D_1)_n+m_5\sum_{n=0}^{\infty}(E_1)_n=m_4+m_6,\quad X=1 \tag{20}$$

Let $c_{0,0}=\Sigma_{n=0}^{\infty}(c_{0,0})_n$, $c_{1,0}=\Sigma_{n=0}^{\infty}(c_{1,0})_n$, and $\varphi_1=\Sigma_{n=0}^{\infty}(\varphi_1)_n$. Equation (18) then becomes:

$$(\varphi_1)_n=\sum_{n=0}^{\infty}(c_{0,0})_n+X\sum_{n=0}^{\infty}(c_{1,0})_n-L_X^{-1}(n_2+n_4)$$

φ_1 may be decomposed into the following terms:

$$(\varphi_1)_0=(c_{0,0})_0+X(c_{1,0})_0-L_X^{-1}(n_2+n_4),$$

$$(\varphi_1)_1=(c_{0,0})_1+X(c_{1,0})_1,$$

$$(\varphi_1)_2=(c_{0,0})_2+X(c_{1,0})_2,$$

$$\vdots$$

The first term, $(\varphi_1)_0$, is given by the solution of the linear inhomogeneous elements of Eqs. (19) and (20), i.e.,

$$m_1\left.\frac{d(\varphi_1)_0}{dX}\right|_{X=0}-m_3(\varphi_1)_0|_{X=0}=-m_3\theta_f,$$

$$m_1\left.\frac{d(\varphi_1)_0}{dX}\right|_{X=1}+m_4(\varphi_1)_0|_{X=1}=m_4+m_6.$$

Accordingly,

$$m_1(c_{1,0})_0-m_3(c_{0,0})_0=-m_3\theta_f$$

$$m_1(c_{1,0})_0-m_1(n_2+n_4)+m_4[(c_{0,0})_0+(c_{1,0})_0-\tfrac{1}{2}(n_2+n_4)]=m_4+m_6$$

Expressed in matrix form, these become:

$$\begin{bmatrix}-m_3 & m_1\\ m_1 & m_1+m_4\end{bmatrix}\begin{bmatrix}(c_{0,0})_0\\ (c_{1,0})_0\end{bmatrix}=\begin{bmatrix}(\eta_{0,0})_0\\ (\eta_{1,0})_0\end{bmatrix}$$

where

$$\begin{bmatrix}(\eta_{0,0})_0\\ (\eta_{1,0})_0\end{bmatrix}=\begin{bmatrix}-m_3\theta_f\\ (m_1+m_4/2)(n_2+n_4)+m_4+m_6\end{bmatrix}$$

If the determinant of the first matrix is non-zero, then $(c_{0,0})_0$, $(c_{1,0})_0$, and $(\varphi_1)_0$ may be determined. The second term of φ_1 given above, i.e., $(\varphi_1)_1$ is derived by solving the nonlinear homogeneous elements of Eqs. (19) and (20), i.e.,

$$m_1\left.\frac{d(\varphi_1)_1}{dX}\right|_{X=0}-m_3(\varphi_1)_1|_{X=0}+m_3(D_1)_0|_{X=0}=0$$

$$m_1\left.\frac{d(\varphi_1)_1}{dX}\right|_{X=1}+m_4(\varphi_1)_1|_{X=1}+m_2(D_1)_0|_{X=1}+m_5(E_1)_0|_{X=1}=0$$

Accordingly,

$$m_1(c_{1,0})_1-m_3(c_{0,0})_1=-m_3(D_1)_0|_{X=0}$$

$$m_1(c_{1,0})_1+m_4[(c_{0,0})_1+(c_{1,0})_1]=-m_2(D_1)_0|_{X=1}-m_5(E_1)_0|_{X=1}$$

Therefore, it is possible to determine $(c_{0,0})_1$, $(c_{1,0})_1$, and $(\varphi_1)_1$. In order to increase the accuracy of the integral constants it is necessary to further evaluate the approximant $(\varphi_1)_n$, which must still satisfy the nonlinear homogeneous boundary equations. The n-term integral constants are calculated from the following relationships:

$$m_1\left.\frac{d(\varphi_1)_n}{dX}\right|_{X=0}-m_3(\varphi_1)|_{X=0}+m_3(D_1)_{n-1}|_{X=0}=0$$

$$m_1\left.\frac{d(\varphi_1)_n}{dX}\right|_{X=1}+m_4(\varphi_1)_n|_{X=1}+m_2(D_1)_{n-1}|_{X=1}+m_5(E_1)_{n-1}|_{X=1}=0$$

Accordingly,

$$m_1(c_{1,0})_n-m_3(c_{0,0})_n=-m_3(D_1)_{n-1}|_{X=0}$$

$$m_1(c_{1,0})_n+m_4[(c_{0,0})_n+(c_{1,0})_n]=-m_2(D_1)_{n-1}|_{X=1}-m_5(E_1)_{n-1}|_{X=1}$$

The n-term integral constants $(c_{0,0})_n$ and $(c_{1,0})_n$ may therefore be determined. Finally, the integral constants can be obtained from:

$$c_{0,0}=\sum_{n=0}^{X}(c_{0,0})_n,\quad c_{1,0}=\sum_{n=0}^{X}(c_{1,0})_n. \tag{21}$$

At this point the approximate solution, φ_1, is fully solved. Therefore, the next approximation φ_2 can be determined by marching the boundary conditions to evaluate the constants, $c_{0,1}$ and $c_{1,1}$, since $\varphi_2=\varphi_1+\theta_1$ and φ_1 has been determined. In order to increase the accuracy of solution, the further evaluations of the approximant $\varphi_{m+1}=\varphi_m+\theta_m$, which must still satisfy the boundary conditions, are required.

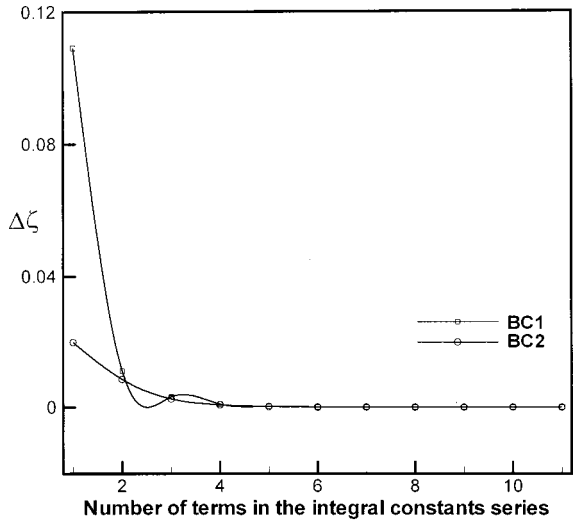

Fig. 2 Error of boundary conditions, as a function of number of terms in the integral constants series

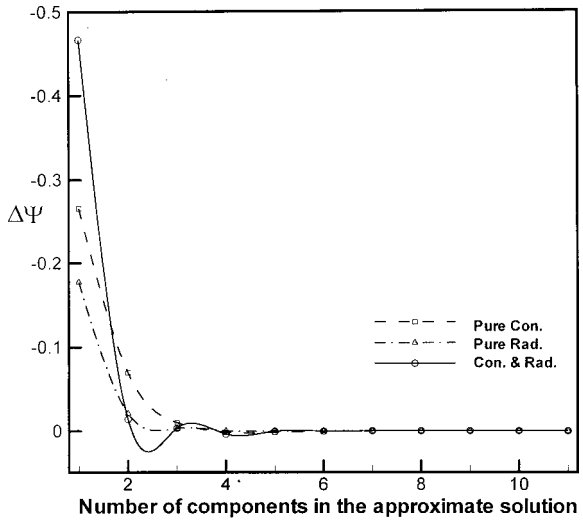

Fig. 3 Error of governing equation at $X=0.5$, as a function of number of components in the approximate solution

The Adomian decomposition solution provides an analytical solution in terms of an infinite power series. However, there is a practical need to evaluate this solution with a finite number of components of Eq. (15). The integral constants of each component are evaluated from a finite number of terms in Eq. (21). The number of terms depends on the magnitude of nonlinearity in the problem. In order to investigate the accuracy of the approximate solution, its order of error (i.e., the deviation of its result from zero) is plotted for different number of terms within the integral constants. Figure 2 shows the error, $\Delta\zeta$, when the approximate solution is substituted into the boundary conditions, i.e., Eqs. (6) and (7) for different number of terms, n, in the integral constants series. Figure 3 shows the error, $\Delta\Psi$ obtained by substituting the approximate solution with varying number of components, m, into the governing equation, i.e., Eq. (5). Figure 3 presents the results for three different heat dissipation mechanisms, namely convection-conduction, pure convection and pure radiation. Observation of Fig. 2 shows that the error $\Delta\zeta$ decreases asymptotically to zero as the number of terms increases; in fact when $n \geqslant 5$ the difference never exceeds 0.0003. Figure 3 shows oscillations of decreasing amplitude in the case of convection-radiation, and that the difference decreases asymptotically to zero as the number of components, m, in the approximate solution increases. When $m \geqslant 6$ it is found that the maximum difference never exceeds 0.0008 for any of the dissipation mechanisms. Therefore, it may be concluded that the use of 5-terms for the integral constants of each component, and the use of 6-components within the approximate solution will yield sufficiently accurate results.

In order to verify the accuracy of the proposed method, its results are compared with those presented by Yu and Chen [13]. In their study the temperature distribution of a simultaneous convective-radiative rectangular fin with variable thermal conductivity at $T_f = 600$ K was calculated using the Taylor transformation method. The values of the m component approximations, φ_m, for $m = 1,2,\ldots,M$ $(M = 11)$ used are presented in Table 1, and represent the case of convection-radiation. If φ_m is plotted against m, it will be seen that the oscillations decrease in amplitude, and assume a uniform value as the number of components, m, in the approximate solution increases.

Table 1 Node temperature of a convective-radiative fin at $T_f = 600$ K, as a function of components in the approximate solution

	X				
φ_m	0	1/4	1/2	3/4	1
φ_1	2.03076	2.04070	2.04202	2.03472	2.01881
φ_2	1.83901	1.77652	1.72909	1.69677	1.67938
φ_3	1.83177	1.76761	1.72020	1.68841	1.67140
φ_4	1.82692	1.76157	1.71398	1.68235	1.66551
φ_5	1.82762	1.76276	1.71573	1.68451	1.66778
φ_6	1.82744	1.76257	1.71560	1.68442	1.66770
φ_7	1.82755	1.76274	1.71581	1.68464	1.66792
φ_8	1.82753	1.76271	1.71577	1.68459	1.66787
φ_9	1.82754	1.76272	1.71579	1.68461	1.66788
φ_{10}	1.82754	1.76272	1.71578	1.68460	1.66787
φ_{11}	1.82754	1.76272	1.71578	1.68460	1.66787
Yu [13]	1.82900	1.76500	1.71800	1.68700	1.68155

Results and Discussion

The usefulness of the proposed method will now be illustrated by means of a worked example. Consider a rectangular profile, longitudinal fin made of the alloy AISI 1010 subject to convection-radiation heat dissipation. The following values are

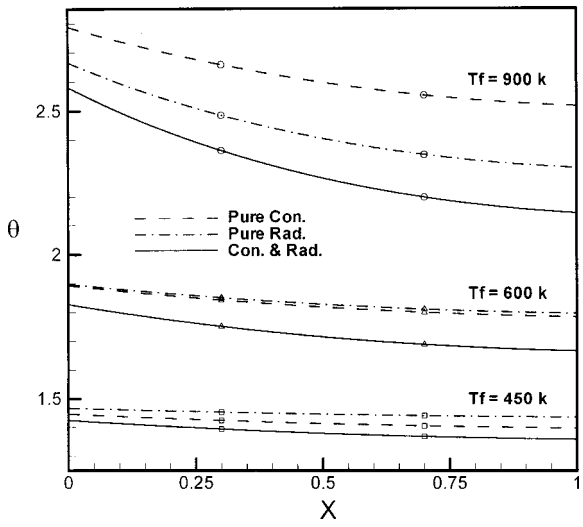

Fig. 4 Temperature distributions of a rectangular fin for pure convection, pure radiation and convection-radiation, at the fluid temperature $T_f = 450$ K; 600 K; 900 K, respectively

assumed: $k_a = 63.9$ W/mK, $\beta = -0.0007582$ K^{-1}, $T_a = T_s = 300$ K, $T_f = 450$ K; 600 K; 900 K, $V = 0.003$ m^3, $A_p = 0.003$ m^2, $h_a = 20$ W/m^2 K, $h_f = 1000$ W/m^2 K, $\alpha = 1.0$, $\varepsilon = 1.0$, and the Stefan-Boltzmann constant is taken to be $\sigma = 5.67 \times 10^{-8}$ W/m^2 K^4.

The nondimensional temperature distributions along the fin are shown in Fig. 4 for fluid temperatures $T_f = 450$ K; 600 K; 900 K, respectively. The figures present the results for pure convection, pure radiation and simultaneous convection-radiation heat transfer. It will be observed that the dimensionless fin temperature always decreases monotonically from the base of the fin towards the tip, and that the temperature distribution is the lowest in the case of simultaneous convection-radiation heat transfer. For $T_f = 450$ K, it can be seen that the temperature distribution is lower in the case of pure convection than for the pure radiation case. For $T_f = 600$ K, the two temperature distributions are very similar for pure convection heat transfer and pure radiation heat transfer. As before, the temperature distribution is lower in the case of pure convection. However, in the case of $T_f = 900$ K it can be seen that the temperature distribution for pure radiation is lower than in the case of pure convection, i.e., the observed results are reversed. Regarding the maximum temperature difference between the pure convection and the simultaneous convection-radiation cases, it will be seen that this difference is about 3 percent for $T_f = 450$ K, 7 percent when $T_f = 600$ K, and 17 percent for $T_f = 900$ K. The maximum temperature difference between the pure radiation and the simultaneous convection-radiation cases is approximately 6 percent at $T_f = 450$ K, 7.7 percent for $T_f = 600$ K, and 7 percent when $T_f = 900$ K. The results presented above indicate that convection heat transfer is the most effective dissipation mechanism at lower fluid temperatures, and is the only mechanism which needs to be considered. However, for higher fluid temperatures, radiation effects assume the greatest importance.

Conclusions

This paper has presented an essentially closed form solution for a convective-radiative rectangular fin with temperature-dependent thermal conductivity. These solutions have taken into consideration the effects of convection-radiation heat transfer from the fin tip. It has been shown that both the governing heat energy equation and the boundary conditions are of a nonlinear form. The Adomian decomposition method has been applied to the nonlinear differential equation with nonlinear inhomogeneous boundary conditions, and has been shown to be effective in dealing with this type of nonlinear problem. It is a valuable tool in the solution of nonlinear problems associated with complex conditions presented by fin boundaries and geometries.

Nomenclature

A_c = cross sectional area of the fin
A_m = Adomian's polynomial
A_p = profile area of the fin
b = fin length
c = integral constant
h = heat transfer coefficient
k = thermal conductivity
L = the highest order derivate
L^{-1} = inverse operator of L
P = fin perimeter
T = temperature
T_s = the effective sink temperature of the radiation surface
N_u = nonlinear terms
V = volume of the fin
w = fin thickness
x = axial distance measured from fin tip
X = dimensionless distance x/b

Greek Symbols

α = absorptivity
β = slop of the thermal conductivity-temperature divided by the intercept k_a
ε = emissivity
θ = dimensionless temperature T/T_a
σ = Stefan-Boltzmann constant
φ = the approximate solution

Subscripts

a = ambient
b = base of the fin
m = number of components in the approximate solution
n = number of terms in the integral constants series
f = fluid on the inside face of the primary surface

References

[1] Kern, Q. D., and Kraus, D. A., 1972, *Extended Surface Heat Transfer*, McGraw-Hill, New York.
[2] Chung, B. T. F., Abdalla, M. H., and Liu, F., 1989, "Optimization of Convective Longitudinal Fins of Trapezoidal Profile," Chem. Eng. Commun., **80**, pp. 211–223.
[3] Chu, H. S., Chen, C. K., and Weng, C. I., 1983, "Transient Response of Circular Pins," ASME J. Heat Transfer, **105**, pp. 205–208.
[4] Aziz, A., 1985, "Optimization of Rectangular and Triangular Fins With Convective Boundary Condition," Int. Commun. Heat Mass Transfer, **12**, pp. 479–482.
[5] Aziz, A., and Hug, S. M. Enamul, 1975, "Perturbation Solution for Convecting Fin With Variable Thermal Conductivity," ASME J. Heat Transfer, **97**, pp. 300–301.
[6] Razelos, P., 1986, "The Optimum Dimensions of Convective Pin Fins With Internal Heat Generation," J. Franklin Inst., **321**, pp. 1–19.
[7] Adomian, G., 1991, "A Review of the Decomposition Method and Some Recent Results for Nonlinear Equations," Comput. Math. Appl., **21**, pp. 101–127.
[8] Adomian, G., and Rach, R., 1993, "Analytic Solution of Nonlinear Boundary-Value Problems in Several Dimensions by Decomposition," J. Math. Anal. Appl., **174**, pp. 118–137.
[9] Adomian, G., 1993, "A New Approach to the Heat Equation—An Application of Decomposition Method," J. Math. Anal. Appl., **113**, pp. 202–209.
[10] Adomian, G., 1986, *Nonlinear Stochastic Operator Equation*, Kluwer Academic, Dordrecht.
[11] Adomian, G., 1994, *Solving Frontier Problems in Physics: The Decomposition Method*, Kluwer Academic, Dordrecht.
[12] Adomian, G., 1988, *Nonlinear Stochastic System Theory and Application to Physics*, Kluwer Academic, Dordrecht.
[13] Yu, L. T., and Chen, C. K., 1998, "Application of Taylor Transformation to Optimize Rectangular Fins With Variable Thermal Parameters," Appl. Math. Model., **22**, pp. 11–21.

An Experimental Investigation on Flow Boiling of Ethylene-Glycol/ Water Mixtures

Satish G. Kandlikar
ASME Fellow
e-mail: sgkeme@rit.edu

Murat Bulut

Mechanical Engineering Department,
Rochester Institute of Technology,
Rochester, NY 14623

*Mixtures of ethylene glycol and water are used in cooling the engines in automotive applications. Heat is transferred essentially under subcooled flow boiling conditions as the mixture flows over the hot surfaces, which are at temperatures well above the local saturation temperature of the mixture. Very little information is available in the literature on the subcooled flow boiling characteristics of this mixture. The present work focuses on obtaining experimental heat transfer data for water and its mixtures containing ethylene-glycol (0 to 40 percent mass fraction, limited by the maximum allowable temperature in the present setup) in the subcooled flow boiling region. The experimental setup is designed to obtain local heat transfer coefficients over a small circular aluminum heater surface, 9.5-mm in diameter, placed at the bottom 40-mm wide wall of a rectangular channel 3-*mm$\times$*40-*mm *in cross-section. Available models for (a) subcooled flow boiling of pure liquids and (b) saturated flow boiling of binary mixtures are extended to model the subcooled flow boiling of binary mixtures.* [DOI: 10.1115/1.1561816]

Keywords: Binary, Boiling, Evaporation, Flow, Heat Transfer

Introduction

Subcooled flow boiling of ethylene-glycol/water mixtures occurs over hot surfaces in the engine coolant passages in automotive cooling application. Efficient cooling of these hot surfaces is important in avoiding localized dryout in these regions (Finlay et al., [1]). Although this mixture has been used for over several decades, there is very little information available in the open literature on its heat transfer characteristics under these conditions. The present work is aimed toward obtaining experimental flow boiling data and characterizing the mixture effects on the heat transfer performance.

Subcooled flow boiling of binary mixtures involves the combination of two phenomena that are quite extensively studied: subcooled flow boiling of pure components, and flow boiling of binary mixtures. A brief overview of these topics is presented here.

Subcooled Flow Boiling of Pure Components. Figure 1 shows the heat transfer characteristics during subcooled flow boiling of a pure liquid. Heat flux is plotted as a function of the local wall temperature. The plot represents the conditions existing at a certain location in a uniformly heated tube with constant liquid subcooling. As the heat flux is increased, path A-B-C-E-G is followed. Initially the heat transfer is by single-phase mode in the region A-B-C where an increase in the flow velocity or a decrease in the local fluid temperature causes an increase in the heat transfer rate. At location C in the plot, the local wall superheat is sufficient to cause nucleation (Onset of Nucleate Boiling, ONB) for the given set of flow conditions (hysteresis delays nucleation to D in some cases). Following the ONB condition, heat transfer is by combined nucleation and convection modes in the region C-E (Partial Boiling). Finally, beyond E, Fully Developed Boiling (FDB) is established in the region E-G, and heat transfer is entirely by nucleate boiling mode. In the single phase region A-B, the single-phase correlations apply, while specific correlations are developed for the FDB and the partial boiling regions. Kandlikar [2] provides further details of various regions.

The FDB correlation plotted in Fig. 1 represents a line that is approached as an asymptote from the partial-boiling region. Kandlikar [2] used the nucleate boiling component in the Kandlikar [3] flow boiling correlation to predict the fully developed flow boiling heat transfer with pure liquids. He compared experimental data from several sources with predictive models by McAdams et al. [4], Jens and Lottes [5], Thom et al. [6], Mikic and Rohsenow [7], and Shah [8] and found good agreement between his model and the data as well as the trends in their parametric relationships. The boiling curves for different mass fluxes and subcooling merged into a single FDB curve at higher heat fluxes. This was also noted by Vandervort et al. [9] through their extensive experiments with water.

Heat transfer in the partial boiling region covers the region between the ONB and the location where FDB is established. Various schemes are available in literature for predicting heat transfer in this region, e.g. Shah [8]. However the scheme presented by Kandlikar [10] provides a comprehensive methodology covering the single-phase, partial boiling, and fully developed boiling regions. This scheme resulted in good agreement (within 15 percent) with water and refrigerant data from earlier investigators.

Flow Boiling of Binary Mixtures. Heat transfer under flow boiling of binary mixtures consists of two components, convective boiling component and nucleate boiling component. The convective component for mixtures is similar to that for pure liquids and can be predicted from the existing pure component correlations using mixture properties. The nucleate boiling component, however, is affected by the nucleation of bubbles and their growth in the surrounding liquid mixture. The difference in the liquid and vapor phase compositions during evaporation sets off a mass diffusion process that increases the saturation temperature at the evaporating interface and presents an additional resistance to heat transfer. The resulting suppression in the nucleate boiling component depends on the thermodynamic properties and the nature of the vapor-liquid equilibrium curves (bubble point and dew point) for the mixture.

Calus et al. [11], Bennett and Chen [12] and Jung [13] presented flow boiling correlations for binary mixtures. More recently, Wettermann and Steiner [14] presented a new correlation scheme to represent their own data for binary mixtures of refrig-

Contributed by the Heat Transfer Division for publication in the JOURNAL OF HEAT TRANSFER. Manuscript received by the Heat Transfer Division March 21, 1999; revision received November 14, 2002. Associate Editor: S. S. Sadhal.

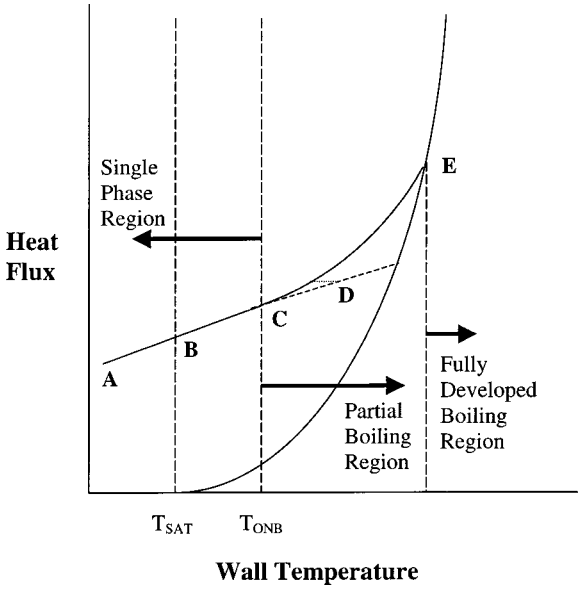

Fig. 1 Heat flux dependence on wall superheat at constant local subcooling during subcooled flow boiling

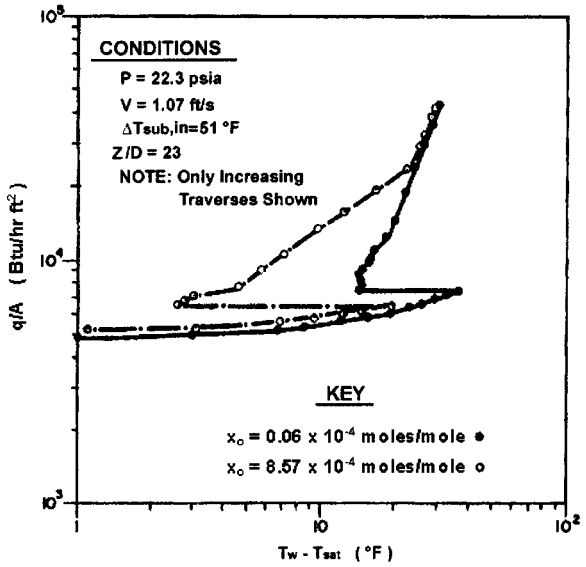

Fig. 2 Effect of dissolved gases on flow boiling heat transfer of R-113, Murphy and Bergles [25], reproduced with permission

erants. Barbosa et al. [15] present a review of the existing correlation schemes to predict the heat transfer with binary mixtures.

Kandlikar [10,16] presents a review of the previous work done with mixtures in pool boiling as well as flow boiling and offers a comprehensive treatment of the phenomena. He classifies the level of heat transfer suppression into three regions: near azeotropic region (heat transfer characteristics are similar to that for a pure liquid), mild diffusion-induced suppression region, and severe diffusion-induced suppression region. The correlations presented by Kandlikar [16] for these regions along with the subcooled flow boiling correlations by Kandlikar [10] are extended in this paper to model subcooled flow boiling of binary mixtures.

Subcooled Flow Boiling of Ethylene-Glycol/Water and Propylene-Glycol/Water Mixtures. Finlay et al. [1] conducted experiments with 50/50 mixture by volume of ethylene-glycol/water covering an operating range for coolant velocities of 0.1 to 5.5 m/s, pressures of 1.15, 1.4, and 2 atm, and for heat fluxes up to 140 W/cm^2 using copper and aluminum tubing and cast-iron sections. From their literature review, Finlay et al. noted that in many automotive engines the coolant is pressurized to 2 atm, and the thermostat is set at 85°C to 95°C. In the high heat flux regions of the cylinder head, the heat transfer is under subcooled flow boiling mode. They also noted that the heat transfer is dominated by nucleate boiling at lower velocities, while convective boiling was dominant at higher velocities. Their results indicate that there is a need for better predictive methods for correlating the heat transfer data, especially in the high heat-flux region (corresponding to FDB).

Recently there has been an increased thrust to switch to propylene-glycol/water mixtures. Propylene glycol is less toxic than ethylene glycol, possesses very similar heat transfer characteristics, and appears to be an ideal replacement. Ambrogi et al. [17] presented a comparison of the two coolants under a wide range of heat flux and mass flux conditions.

McAssey et al. [18], Bhowmick et al. [19,20], and McAssey and Kandlikar [21] conducted experiments to compare the performance of propylene-glycol/water and ethylene-glycol/water mixtures in the engine cooling application. The flow velocity ranged from 0.4 m/s to 2.5 m/s, and the maximum heat flux employed was 1.8 MW/m^2. The investigation covered subcooled and saturated flow boiling. Under these conditions, the performance with the two mixtures was very similar. Bhowmick et al. [20] modified the Chen [22] correlation to correlate their data.

McAssey and Kandlikar [21] compared the ethylene glycol/water mixture data obtained from automotive engine cooling application with the FDB correlation for mixtures (see Eq. (2)) and found the agreement to be within ± 30 percent. They also indicated that the prediction accuracy would improve with the incorporation of accurate F_{fl} for ethylene glycol, inclusion of the factor F_D, and the extension of the Kandlikar's [2] partial boiling methodology to mixtures.

Effect of Dissolved Gases on Flow Boiling Heat Transfer. The solubility of dissolved gases in liquids decreases with an increase in liquid temperature. This causes release of dissolved gases as the liquid temperature is raised resulting in an early nucleation at temperatures well below saturation temperature. The effect of dissolved gases on boiling heat transfer of water was studied by McAdams et al. [4]. Their results indicate that the dissolved gases have no effects on the single-phase heat transfer. In the partial boiling region, the heat transfer coefficient increases due to increased nucleation activity. However, this effect completely disappears at higher wall superheats as fully developed boiling conditions are established. This is well illustrated by Rohsenow et al. [23] in a figure that shows no effect of dissolved gases in the fully developed boiling region between completely degassed water and water with a very high dissolved air content. Similar results were obtained by Behar et al. [24] with water.

A detailed study on the effect of dissolved gases on the heat transfer in an R-113 system was performed by Murphy and Bergles [25]. Nucleation was initiated when the wall temperature exceeded the saturation temperature corresponding to the partial pressure of water in the air-water vapor mixture. The effect of dissolved gases is seen to disappear quickly at higher wall temperatures as the fully developed boiling conditions approach. This was observed even for the case with very high levels of dissolved gas content. Figure 2, reproduced from Murphy and Bergles [25], clearly shows this trend.

Objectives of the Peresent Work

In the present work, the subcooled flow boiling heat transfer performance for ethylene-glycol/water mixtures is obtained experimentally using a rectangular flow channel and a localized spot

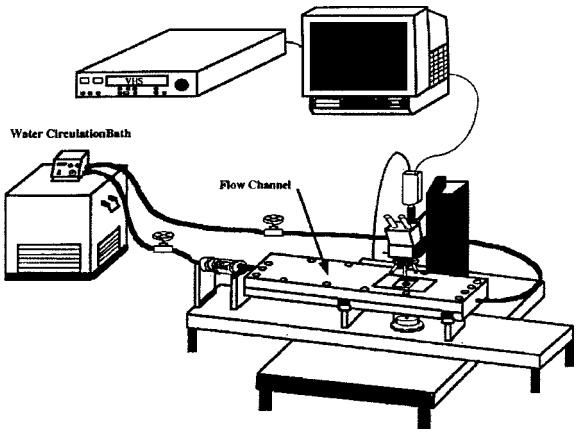

Fig. 3 Schematic of the experimental setup

heater. The heat transfer characteristics in the partial boiling region and early part of the fully developed boiling region are studied, and a correlation scheme is proposed for heat transfer for binary mixtures in these regions.

Experimental Setup

The experimental apparatus used in this study consists of a horizontal channel in which ethylene-glycol/water mixture flows over a 9.5-mm circular heater surface mounted flush in the wall. Kandlikar and Spiesman [26] used a similar experimental setup as shown in Fig. 3. The test section is fabricated from 6061-T6 aluminum with the flow channel c/s of 3-mm×40-mm (channel hydraulic diameter of 5.58-mm). A two-piece polycarbonate window is provided for visual observation of boiling on the heater surface. The heater assembly, shown in Fig. 4, is made of 2024-T3 aluminum. Four thermocouples, TT-E-36-type, are placed along the length of the 9.5-mm diameter section as shown in Fig. 4. One thermocouple is placed in the flow before the test section to measure the incoming fluid temperature. A torlon bushing is used to insulate the heater element from the test section. The working fluid is circulated through the test section using a VWR Scientific model 1167 constant temperature circulation bath. The flow rate was measured with an Omega FL-1503A rotameter.

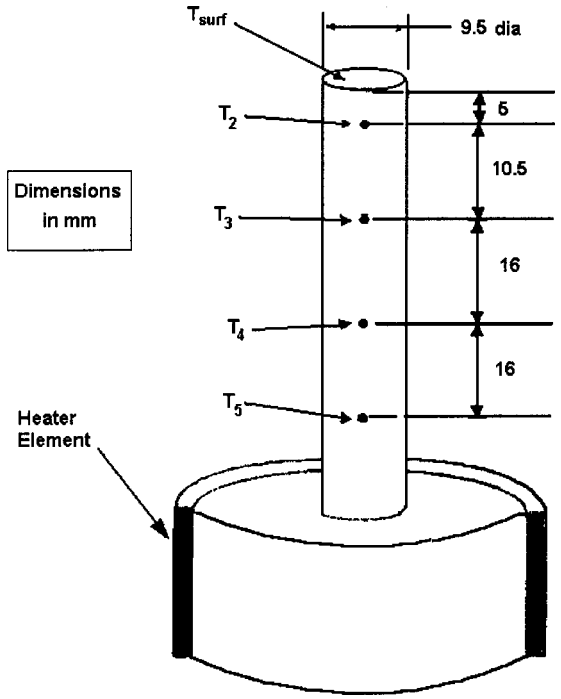

Fig. 4 Details of heater assembly

Experimental Procedure

The experiments were performed with pure water and mixtures of ethylene-glycol/water in the mass concentration range from 0 to 40 percent ethylene-glycol (limited by the maximum allowable temperature in the setup). For the initial test runs, distilled water was used as the working fluid in the system. After each run, ethylene-glycol was added systematically to yield the desired concentration for the next run. At the beginning of the data collection sessions, the water bath was filled, and the pump and the heater were turned on. The water circulation bath was equipped with two internal pumps, one on the delivery side and one on the suction side. Using the two valves across the test section, the pressure at the test section was maintained at the local atmospheric pressure value (as shown in Fig. 3). The mixture was heated to a temperature of 90°C and allowed to circulate through the system for 3 hours prior to each test with a given concentration. During this period, the immersion heater in the circulation bath produced boiling in the liquid pool. The cover of the tank of lightly covered throughout the experiments. Boiling around the heater, with the liquid subcooled by only five to fifteen degrees would result in a very low dissolved gas content in the liquid. The power to the heater and the flow rate were set to the desired values. It was noted that the system reached steady state conditions within 20 minutes. Temperatures along the heater length and inside the flow channel were recorded after 30 minutes. From the temperature measurements in the heater at known locations, the heat flux, the temperature of the heated surface, and the heat transfer coefficient were determined.

The tests were performed by powering the heaters and systematically increasing the heat flux between the successive runs. The experiments were then repeated by systematically decreasing the heat flux from the maximum value to assess the hysteresis effect. The results presented here are for decreasing heat flux values unless otherwise stated.

The heater surface was placed flush with the torlon housing. The video images of boiling on the entire surface indicated that there was very little activity present due to rogue sites at the interface between the aluminum heater and the torlon housing.

Error Analysis

The surface heat flux, the surface temperature, and the heat transfer coefficient are calculated by measuring the temperature profile along the length of the circular aluminum heater. The error associated with the measurement of distances between the thermocouple locations is 0.25 mm. The flow rate is measured with a flow meter with an accuracy of ± 0.5 percent of the full-scale value. The thermocouples and the data acquisition system are calibrated at steam point and ice point, and yield values within 0.1 K at these two conditions. The saturation temperature is calculated from the local pressure measurement and the barometer reading. The estimated accuracy in the calculation of the saturation temperature is 0.1 K. In order to calculate the standard deviations associated with the measurement of precision of various quantities, readings were taken for a few sample runs for every three minutes over a period of 2 hours.

The surface heat flux and the surface temperature are calculated by extrapolating the heater temperature measurements. The validity of this approach was confirmed through a detailed numerical analysis using an ANSYS model.

The uncertainty analysis was performed according to the ASME Policy on Reporting Uncertainties in Experimental Measurements and Results. Table 1 shows the bias and precision limits obtained from the instrument data, calibration experiments, and statistical data obtained (40 readings at the same setting). The results of the

Table 1 Bias limits and precision limits

Bias Limit
Temperature measurement—±0.1 K
Saturation temperature—±0.2 K
Thermocouple location—±0.25 mm
Flow velocity measurement—±0.006 m/s
Water temperature measurement—±0.1 K
Precision limits derived from 50 samples
Heater thermocouples—±0.2 K
Water temperature—±0.025 K

analysis are shown in Fig. 5. The uncertainty is high at the lower values of the heat transfer coefficient near the single phase region due to the small temperature difference between the wall and the fluid. In the region of interest, the uncertainty is between 3–10 percent.

Effect of Dissolved Gases

In the present experiments, the circulation bath was heated with an immersion heater that kept the water temperature above 90°C. The difference in the dissolved gas content corresponding to 90°C and the actual saturation temperature is quite small. For pure water, the difference in solubility is only 0.6 percent higher at 100°C than that at 90°C. In the fully developed boiling region, the effect of dissolved gases completely disappears as found by earlier investigators as seen from Fig. 2 by Murphy and Bergles [25].

Results and Discussion

The study was primarily focused on studying the effect of concentration on heat transfer performance. Experimental results are obtained for pure water and ethylene glycol mass fractions of 1%, 2%, 3%, 4%, 5%, 6%, 7%, 8%, 10%, 11%, 12%, 14%, 20%, 25%, 30%, 35%, and 40%. Two flow velocities of 0.129 m/s and 0.387 m/s are employed. The differences in the saturation temperature at different concentrations and the resulting differences in heat losses in the piping for each run made it difficult to keep the subcooling constant, and a range of 5–25 K in inlet subcooling was obtained. Note that the saturation temperature of the mixture (bubble point temperature) increases with increasing concentration of ethylene glycol as shown in Fig. 6.

Figure 7 shows a comprehensive plot of heat flux versus wall superheat for a mean flow velocity of 0.129 m/s. To avoid overcrowding the plot, results for water and only seven other concentrations are shown. As the properties change with ethylene glycol concentration, the flow Reynolds number changes for each concentration. Individual values of Reynolds number and inlet subcooling for the respective runs are also shown in Fig. 7. All properties are calculated at the saturation temperature (bubble point temperature) of the mixture.

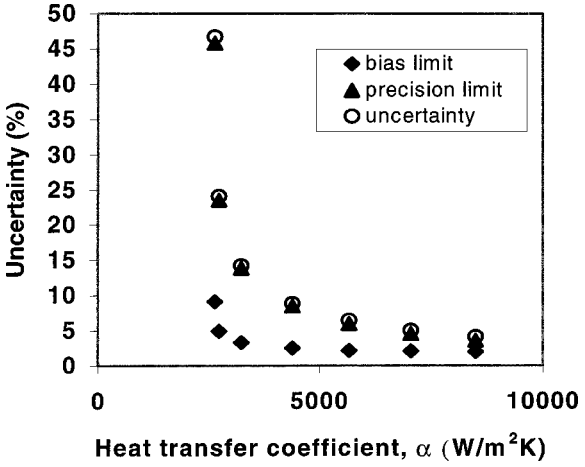

Fig. 5 Uncertainty estimates in the experimental results

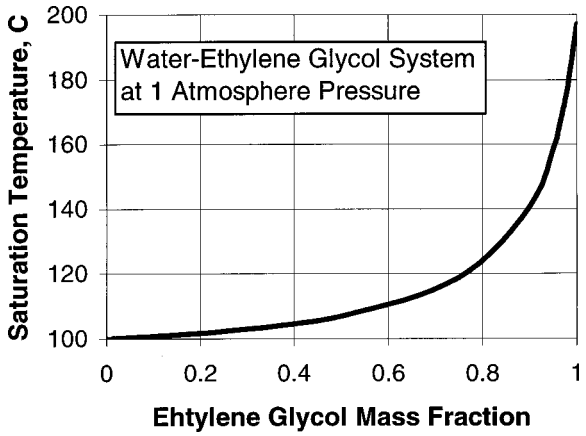

Fig. 6 Variation of saturation temperature for ethylene glycol/water mixture at atmospheric pressure

Figure 7 shows that as the ethylene glycol concentration increases, the heat transfer performance deteriorates (larger superheat is needed at the same heat flux) in the partial boiling and FDB regions for the same flow rate. Addition of just 1 percent ethylene glycol resulted in a reduction in heat transfer compared to pure water. As the concentration of ethylene glycol increased, the curves systematically shifted to the right.

The results from Fig. 7 are redrawn with heat transfer coefficient versus wall superheat axes in Fig. 8. At lower heat fluxes, the heat transfer coefficient corresponds to the single-phase value. Boiling occurs at higher heat fluxes beyond ONB. Comparing different curves, it is seen that as the concentration of ethylene glycol increases, heat transfer coefficient at a given wall superheat decreases. It should be noted that the saturation temperature (bubble point temperature) for each concentration is different, and has been accounted for in the calculation of the wall superheat and

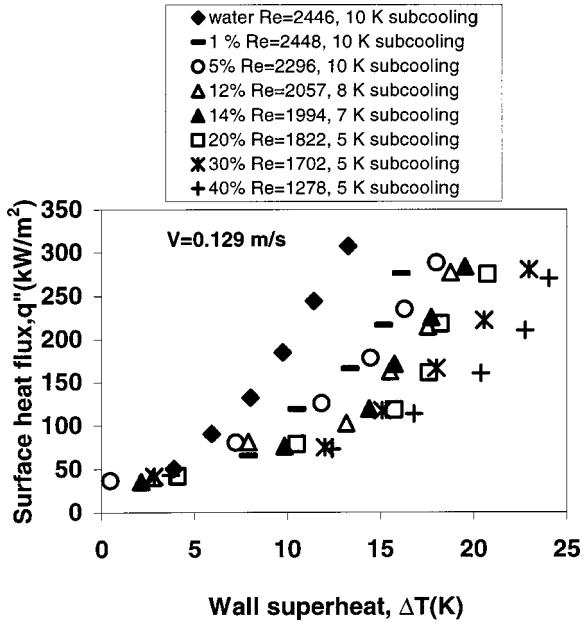

Fig. 7 Surface heat flux versus wall superheat for flow boiling of water/ethylene glycol mixtures at $V=0.129$ m/s and atmospheric pressure

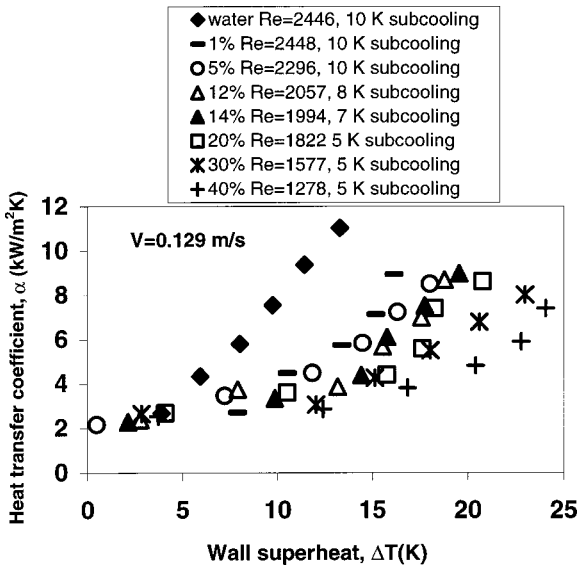

Fig. 8 Heat transfer coefficient versus wall superheat for flow boiling of water/ethylene glycol mixtures at $V=0.129$ m/s and atmospheric pressure

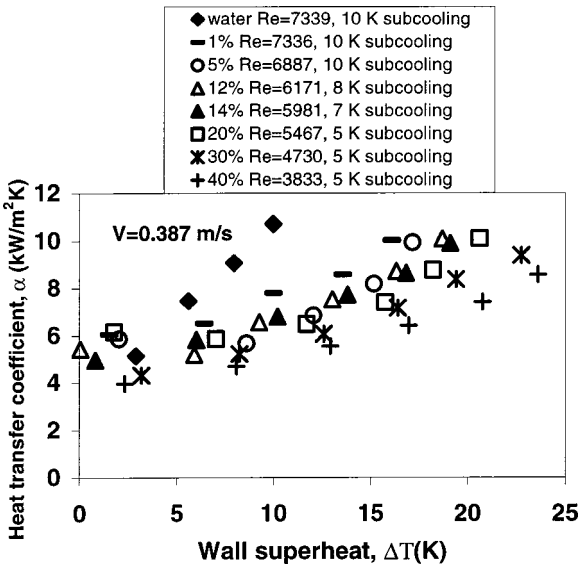

Fig. 10 Heat transfer coefficient versus wall superheat for flow boiling of water/ethylene glycol mixtures at $V=0.387$ m/s and atmospheric pressure

the liquid subcooling. Similar results are obtained for a higher flow velocity of 0.387 m/s and are shown in Figs. 9 and 10.

The effect of hysteresis is also investigated in the present work. The data presented in Figs. 7–10 are obtained for decreasing value of heat fluxes. To see the effect of hysteresis, experiments were conducted for both increasing and decreasing heat fluxes. The hysteresis effects were most significant at the start-up (not shown here). Once the highest heat flux was employed, the hysteresis effect disappeared in the subsequent runs. The results presented here correspond to the heater performance after several cycles of increasing and decreasing heat fluxes. For low velocity runs, a slight hysteresis effect (10 percent difference in heat flux) was observed for mixtures in the region 0–10 K wall superheat. This effect was very small for high velocity (0.387 m/s) runs.

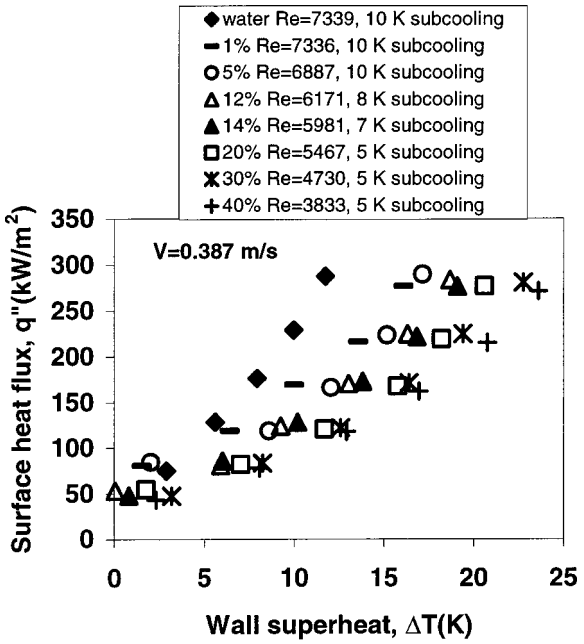

Fig. 9 Surface heat flux versus wall superheat for flow boiling of water/ethylene glycol mixtures at $V=0.387$ m/s and atmospheric pressure

Figures 11 and 12 show such plots for pure water and 6% concentrations of ethylene glycol at a flow velocity of 0.387 m/s.

In the present investigation, a high speed video camera, Kodak Ektapro 1000, was employed to study the nucleation behavior. The departing bubble sizes in the present investigation are typically less than 0.1 mm. Earlier investigators reported the presence of rogue sites surrounding spot heaters. The crevices between the heater and the surrounding torlon in the preset setup produced very few rogue sites. The nucleation on the surface of the heater was seen to be very intense with hardly any interaction with the bubbles generated at the rogue sites. Similar observations were made from their experiments by Kandlikar and Stumm [27] and Kandlikar and Howell [28].

Comparison With Correlations in the Fully Developed and Partial Boiling Regions. Heat transfer during subcooled flow boiling is classified into partial boiling and fully developed boiling regions. Kandlikar [2] presented a comprehensive methodology to predict heat transfer in these regions for pure liquids. One of the major aspects of his methodology is the prediction of the heat transfer coefficient in the fully developed boiling region using the nucleate boiling component of the Kandlikar [3] correlation. Heat transfer in the fully developed boiling region for pure liquid is given by:

$$q''=h_{TP}(T_w-T_f)=h^*(T_w-T_{\text{sat}})=1058\text{Bo}^{0.7}F_{fl}h_{lo}(T_w-T_{\text{sat}}) \quad (1)$$

h_{TP} in Eq. (1) is based on (T_w-T_f), where T_f is the bulk liquid temperature, and h^* is based on (T_w-T_{sat}). According to Eq. (1), there is no effect of subcooling on heat transfer in the fully developed boiling region. F_{fl} is a fluid-dependent factor in the Kandlikar [3] correlation, which is employed in the subsequent correlations by Kandlikar [2,16]. F_{fl} for mixtures is obtained as a mass fraction-averaged value of the respective pure component F_{Fl} values. Since the value of F_{fl} is not available for ethyleneglycol, it is used as 1 (same as water) in the present work. The error introduced by this assumption is quite small at lower ethylene glycol concentrations because the F_{fl} value for mixtures is the mass-fraction averaged value of the respective pure component F_{fl} values.

Kandlikar [16] presented a methodology for predicting heat transfer during saturated flow boiling of binary mixtures. He identified three regions to describe the level of mixture effects: (*a*) In

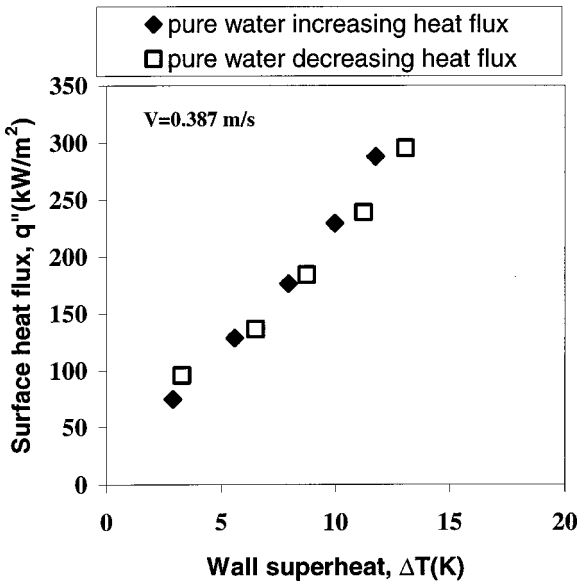

Fig. 11 Effect of hysteresis on flow boiling heat transfer for pure water at $V=0.387$ m/s and atmospheric pressure

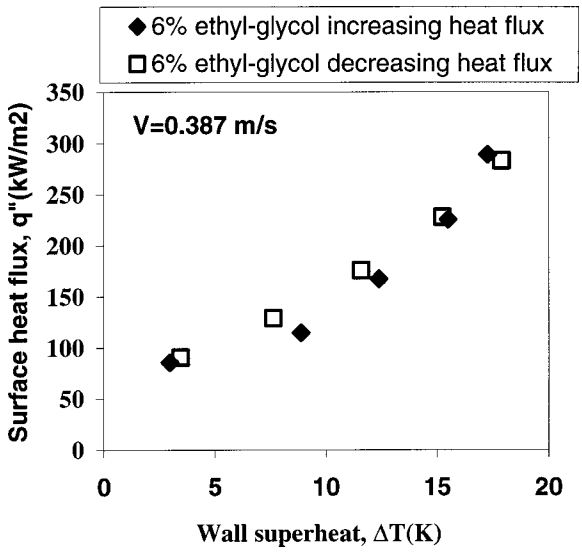

Fig. 12 Effect of hysteresis on flow boiling heat transfer for 6% ethylene-glycol/water mixture at $V=0.387$ m/s and atmospheric pressure

the near-azeotropic region, the mass transfer effects are negligible, and the heat transfer is given by the pure component equation; (*b*) In the moderate suppression region, nucleation is suppressed to some extent and the heat transfer is described by the equation applicable in the convective boiling dominant region; and (*c*) In the severe suppression region, the heat transfer is further reduced and a factor F_D is introduced in the nucleate boiling term to represent the mass diffusion effects.

Extending the above models to subcooled flow boiling of binary mixtures, the heat transfer in the fully developed boiling region can also be classified depending on the level of suppression. In the near-azeotropic region, Eq. (1) is expected to apply. In the moderate suppression region, the nucleate boiling term from the equation applicable to the convective boiling dominant region is used. It is given by:

$$q''=66.7.2\mathrm{Bo}^{0.7}F_{fl}h_{LO}(T_w-T_{\mathrm{sat}}) \tag{2}$$

In the severe suppression region, the heat transfer is further reduced by a factor F_D. The final expression in the fully developed nucleate boiling region is given by

$$q''=1058\mathrm{Bo}^{0.7}F_{fl}h_{LO}(T_w-T_{\mathrm{sat}})F_D \tag{3}$$

The diffusion induced suppression factor F_D is given by:

$$F_D=0.678\left[1+\left(\frac{c_{p,L}}{\Delta h_{LG}}\right)^{1/2}\left(\frac{dT}{dx_1}\right)(x_1-y_1)\right]^{-1} \tag{4}$$

dT/dx_1 is the slope of the temperature versus liquid concentration curve, and y_1 is the equilibrium vapor concentration. A volatility parameter V_1, defined in the nomenclature section, is used by Kandlikar [10,16] to describe the suppression effects. According to Kandlikar [16], for $V_1<0.03$, the mixture can be treated as a pure component, moderate suppression region covers $0.03<V_1\leq 0.2$ (and $\mathrm{Bo}>1\times10^{-4}$), and severe suppression region extends beyond $V_1>0.2$.

Figure 13 shows the variation of volatility parameter with concentration for ethylene-glycol/water mixtures. Applying the criteria described above, the mixture can be treated as a pure component below a concentration of 0.13, and Eq. (1) applies in the fully developed boiling region. For concentrations between 0.13 and 0.4, the mixture falls under moderate suppression and the lower end of severe suppression regions. The estimation of the volatility parameter at lower concentrations may be in considerable error due to errors in estimating the slope of the bubble point curve near $x_1=0$. Therefore, the near-azeotropic range may be considered to be from 0 to 0.15 as seen from Fig. 13.

In the partial boiling region, the following method by Kandlikar [2] is modified (in Eq. (6)) and is presented below.

Heat Flux at ONB (location *C* in Fig. 1):

$$q''_{\mathrm{ONB}}=[\lambda_l i_{LG}/(8\sigma\nu_{LG}T_{\mathrm{Sat}})][\Delta T_{\mathrm{Sat,ONB}}]^2 \tag{5}$$

The heat flux q''_F at the intersection of the single phase line ABC and the fully developed boiling curve is given by the following equation:

$$CF_{fl}(Gi_{LG})^{-0.7}q''_F-q''^{0.3}_F-Ch_{LO}F_{fl}(Gi_{LG})^{-0.7}\Delta T_{\mathrm{Sub}}=0 \tag{6}$$

where $C=1058$ in the near azeotropic region, $C=667.2$ in the moderate suppression region, and $C=1058\,F_D$ in the severe suppression region.

Location of *E*:

$$q''_E=1.4q''_F \tag{7}$$

Partial Boiling Region, C-E.

$$q''=a+b(T_w-T_{\mathrm{Sat}})^m \tag{8}$$

where,

$$b=\frac{q''_E-q''_C}{(\Delta T_{\mathrm{Sat},E})^m-(\Delta T_{\mathrm{Sat},C})^m} \tag{9}$$

$$a=q''_C-b(\Delta T_{\mathrm{Sat},C})^m \tag{10}$$

The exponent *m* is obtained as follows:

$$m=n+pq'' \tag{11}$$

where,

$$p=(1/0.3-1)/(q''_E-q''_C) \tag{12}$$

and

$$n=1-pq''_C \tag{13}$$

Note that *m*, *a*, and *b* in Eqs. (8–11) are dependent on the heat flux; hence an iterative scheme is needed to evaluate the heat flux at a given wall superheat location between points *C* and *E* in Fig. 1 corresponding to the partial boiling region.

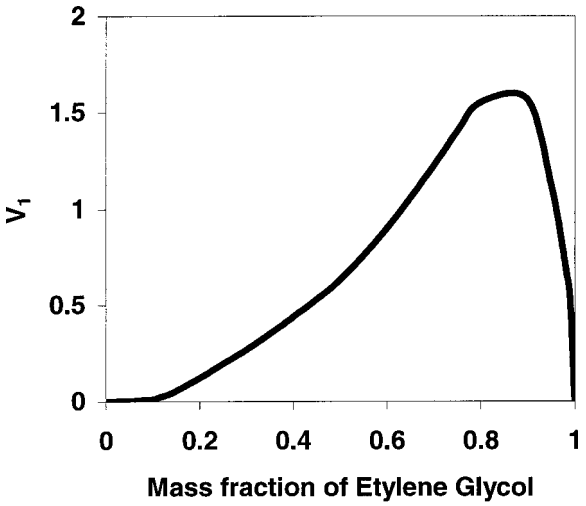

Fig. 13 Variation of the volatility parameter in the Kandlikar [2] correlation for binary mixtures of ethylene glycol/water at atmospheric pressure

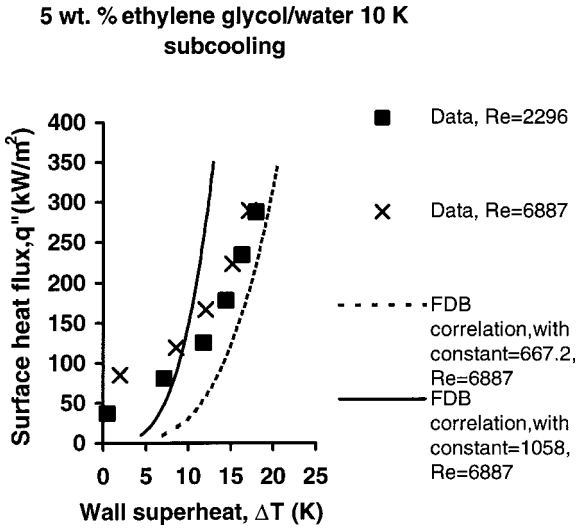

Fig. 15 Comparison of the present data with the FDB correlation (asymptote to data at high superheats), Eqs. (1) and (2), 5 percent solution of ethylene glycol in water at atmospheric pressure

Comparison With Data. Figure 12–18 present the comparison of the partial boiling and fully developed boiling correlations presented in Eqs. (1–13) with the experimental data obtained in the present investigation.

Figure 14 shows the comparison of data for pure water at Re =7339 with Kandlikar's [2] FDB correlation given by Eq. (1) and Eqs. (5–13) in the partial boiling region with $C=1058$. The data covers only the partial boiling region and the early part of the FDB region. It can be seen that the agreement is quite good between the data and the correlations.

Figure 15 shows the experimental data for 5% ethylene glycol solution at Re=6887. Also shown in the figure are the predictions from Eqs. (1) and (2). Two sets of FDB curves are presented, FDB_1 using $C=1058$ applicable in the nucleate boiling dominant region, and FDB_2 with $C==667.2$ for the convective boiling dominant region. As the concentration of ethylene glycol increases, the curves are expected to shift from FDB_1 for pure water to FDB_2. The data for 5 percent ethylene glycol concentration lies in between the two curves. Again, the wall superheat is not high enough to enter the FDB region.

The results for the three concentrations of 14 percent, 20 percent, and 30 percent are plotted on a single plot in Fig. 16. Although the Reynolds number is somewhat different, a systematic shift to the right is noted for both data and predictive correlation.

For a concentration of 14 percent, the results shown in Fig. 16 indicate a better agreement between the data in the FDB region with the correlation at high wall superheats. The FDB curve in this plot uses $C=667.2$. The agreement in the partial boiling region is quite good.

For the case of ethylene glycol concentration of 20 percent, the diffusion effects are expected to be somewhat higher, and Eq. (2) should be applicable. The FDB curve is drawn with $C=667.2$. At

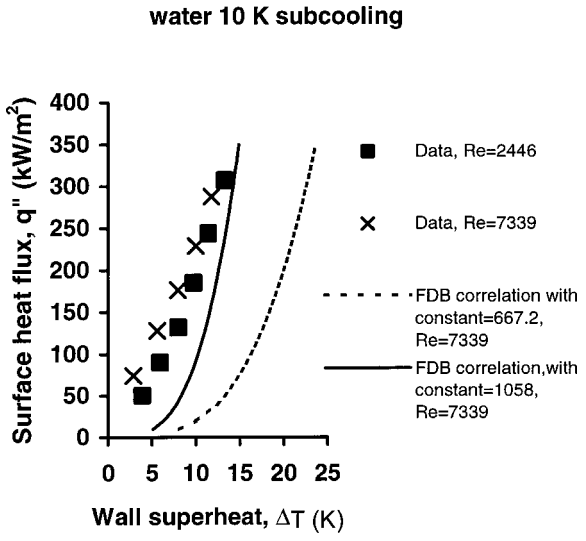

Fig. 14 Comparison of the present data with the FDB correlation (asymptote to data at high superheats), Eqs. (1) and (2), water at atmospheric pressure

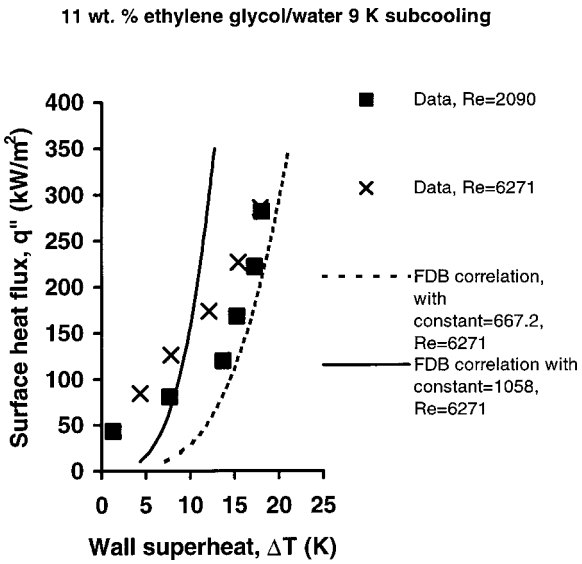

Fig. 16 Comparison of the present data with the FDB correlation (asymptote to data at high superheats), Eqs. (1) and (2), 11 percent solution of ethylene glycol in water at atmospheric pressure

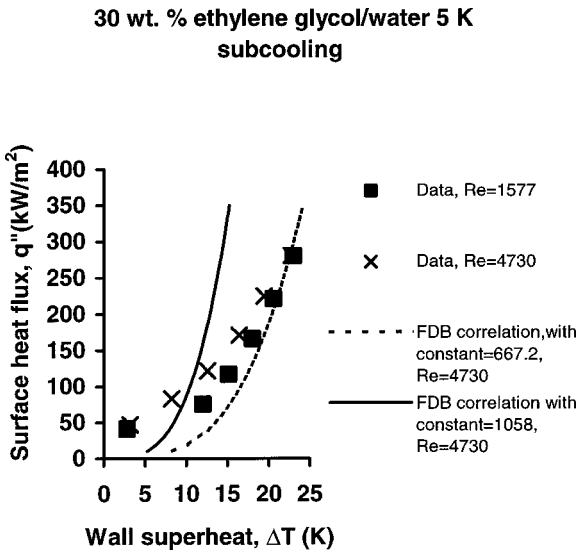

Fig. 17 Comparison of the present data with the FDB correlation (asymptote to data at high superheats), Eqs. (1) and (2), 30 percent solution of ethylene glycol in water at atmospheric pressure

higher wall superheats, the data is expected to follow the FDB curve. However, such data could not be obtained due to limits on the available heater power.

The results for 30 and 40 percent ethylene glycol solutions are shown in Figs. 17 and 18. In both plots, the data exhibit a tendency to go beyond the FDB curve using $C=667.2$. This indicates that the suppression is higher and Eq. (3) with appropriate suppression factor F_D is warranted. Since the high wall superheat data is not available, the FDB curve in the severe suppression region using the additional suppression factor is not plotted. Accurate values of F_{fl} are also needed at higher ethylene glycol concentrations. Further work on obtaining high wall superheat data for pure ethylene glycol and for the mixtures is recommended.

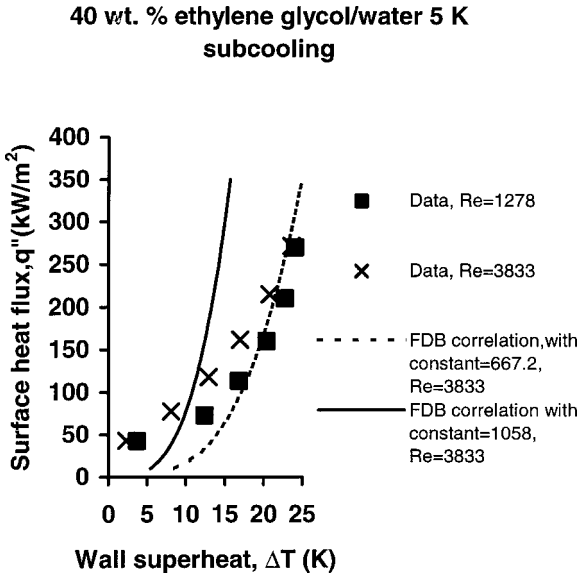

Fig. 18 Comparison of the present data with the FDB correlation (asymptote to data at high superheats), Eqs. (1) and (2), 40 percent solution of ethylene glycol in water at atmospheric pressure

Conclusions and Future Work

The following conclusions are drawn on the basis of the present study.

1. An experimental investigation is conducted to study the subcooled flow boiling heat transfer of aqueous ethylene glycol solutions. Experimental results are obtained for surface heat flux as a function of wall superheat by systematically varying the mass concentration of ethylene glycol in the range of 0 to 40 percent. The flow configuration is a rectangular flow channel, 3-mm $\times$40-mm in cross-section, with a circular heater of 9.5-mm diameter placed centrally on the 40 mm side.
2. The results for flow boiling of pure water in the partial boiling and early stages of the Fully Developed Boiling regions are in good agreement (Fig. 14) with the Kandlikar [2] model. The data approaches the fully developed curve asymptotically as the wall superheat increases. Higher wall superheat data is needed to further confirm the model in the FDB region.
3. As the concentration of ethylene glycol increases, the heat transfer performance deteriorates due to the adverse effects of mass diffusion on the nucleate boiling heat transfer. The moderate suppression region starts at much lower concentrations than predicted by using the volatility parameter (Fig. 13) criterion given by Kandlikar [16]. The error in calculating the slope dT/dx_1 required in evaluating V_1 in this region is suspected to be the main reason for this discrepancy. Further evaluation is needed to establish this range accurately for subcooled flow boiling of mixtures. Similar work with other binary mixture systems is also recommended.
4. The heat transfer model in the partial boiling region given by Eqs. (5–13), with an appropriate FDB correlation from Eqs. (1–3), is able to correlate the present subcooled flow boiling data for ethylene-glycol/water system at low concentrations well as seen from Figs. 14–18.
5. The fully developed boiling model for binary mixtures, Eqs. (1–3), seems to be applicable for subcooled flow boiling of binary mixtures as well. However additional data at higher wall superheats and over the entire range of concentration are needed to further validate and refine the subcooled flow boiling model.

Nomenclature

a = constant defined by Eq. (10)
Bo = Boiling number$=q''/Gi_{LG}$
b = constant defined by Eq. (9)
C = constant in Eq. (6)
$c_{p,L}$ = specific heat of liquid, J/kgK
D_{12} = diffusion coefficient of 1 (ethylene glycol) in 2 (water), m^2/s
D_h = hydraulic diameter of the flow channel, m
dT/dx_1 = slope of the bubble point curve at concentration x_1, K
F_D = Mass diffusion induced suppression factor, Eq. (4)
F_{fl} = fluid-surface parameter in Kandlikar [3] correlation, represents the nucleation characteristics of the surface with the given fluid
G = mass flux, kg/m^2s
h_{TP} = two-phase heat transfer coefficient defined with wall to fluid temperature difference, Eq. (1).
h^* = heat transfer coefficient defined with wall to saturation temperature difference, Eq. (1).
I_{LG} = latent heat of vaporization, J/kg
m = constant defined by Eq. (11)
n = constant defined by Eq. (13)
p = constant defined by Eq. (12)
q'' = heat flux, W/m^2
Re = Reynolds number, $\rho VD_h/\mu_L$
T = temperature, K
ΔT_{Sat} = wall superheat, K
ΔT_{Sub} = liquid subcooling, K

V = flow velocity, m/s
V_1 = Volatility parameter, defined by Kandlikar [10], $=(c_{p,L}/i_{LG})(\kappa/D_{12})^{0.5}(x_1-y_1)dT/dx_1$; represents the mass diffusion effects in the liquid surrounding a nucleating bubble
v = specific volume, m^3/kg
v_{LG} = v_G-v_L, m^3/kg
x_1 = liquid mass fraction of ethylene glycol in aqueous solution
y_1 = vapor mass fraction of ethylene glycol in aqueous solution

Greek Letters

h = heat transfer coefficient, W/m^2K
h_{LO} = heat transfer coefficient with all flow as liquid in Kandlikar [3] correlation, calculated from Gnielinski [29] and Petukhov and Popov [30] correlations, W/m^2K
h^* = h based on (T_w-T_{sat}), Eq. (1)
κ = thermal diffusivity, $=\lambda/(\rho c_{p,L})$, m^2/s
λ = thermal conductivity, W/mK
μ = viscosity, $N\text{-}s/m^2$
ρ = density, kg/m^3
σ = surface tension, N/m

Subscripts

conv = convective component
f = bulk fluid
G = vapor
L = liquid
LG = latent
lo = entire flow as liquid
nb = nucleate boiling component
Sat = saturation value
Sub = subcooling
tp = two phase
W = wall

References

[1] Finlay, I. C., Boyle, R. J., Pirault, J. P., and Biddulph, T., 1987, ''Nucleate and Film Boiling of Engine Coolants Flowing in a Uniformly Heated Duct of Small Cross Section,'' SAE Technical Paper Series, No. 870032.

[2] Kandlikar, S. G., 1998, ''Heat Transfer and Flow Characteristics in Partial Boiling, Fully Developed Boiling, and Significant Void Flow Regions of Subcooled Flow Boiling,'' ASME J. Heat Transfer, **120**, pp. 395–401.

[3] Kandlikar, S. G., 1990, ''A General Correlation for Two-Phase Flow Boiling Heat Transfer Coefficient Inside Horizontal and Vertical Tubes,'' ASME J. Heat Transfer, **102**, pp. 219–228.

[4] McAdams, W. H., Minden, C. S., Carl, R., Picornell, D. M., and Dew, J. E., 1949, ''Heat Transfer at High Rates to Water with Surface Boiling,'' Ind. Eng. Chem., **41**(9), pp. 1945–63.

[5] Jens, W. H., and Lottes, P. A., 1951, ''Analysis of Heat Transfer, Burnout, Pressure Drop and Density Data for High Pressure Water,'' U.S. AEC Report ANL-4627.

[6] Thom, J. R. S., Walker, W. M., Fallon, T. A., and Reising, G. F. S., 1965, ''Boiling in Subcooled Water During Flow up Heated Tubes or Annuli,'' paper presented at the Symposium on Boiling Heat Transfer in Steam Generating Units and Heat Exchangers, Manchester, Sept. 15–16, **180** (Part 3C) Institute of Mech. Eng., London.

[7] Mikic, B. B., and Rohsenow, W. M., 1969, ''New Correlation of Pool Boiling Data Including the Effect of Heating Surface Characteristics,'' ASME J. Heat Transfer, **91**, pp. 241–250.

[8] Shah, M. M., 1977, ''A General Correlation for Heat Transfer During Subcooled Boiling in Pipes and Annuli,'' ASHRAE J., **83**, Part 1, pp. 205–215.

[9] Vandervort, C. L., Bergles, A. E., and Jensen, M. K., ''An Experimental Study of Critical Heat Flux in Very High Heat Flux Subcooled Boiling,'' Int. J. Heat Mass Transf., **37**, Suppl. 1, pp. 54–57.

[10] Kandlikar, S. G., 1998, ''Boiling Heat Transfer in Binary Systems: Part I-Pool Boiling,'' ASME J. Heat Transfer, **120**, pp. 380–387.

[11] Calus, W. F., di Montegnacco, A., and Kenning, D. B. R., ''Heat Transfer in a Natural Circulation Single Tube Reboiler, Part II: Binary Liquid Mixtures,'' Chem. Eng. J., **6**, pp. 251–264.

[12] Bennett, D. L., and Chen, J. C., 1980, ''Forced Convection Boiling in Vertical Tubes for Saturated Pure Components and Binary Mixtures,'' AIChE J., **26**(3), pp. 454–461.

[13] Jung, D. S., 1988, ''Horizontal Flow Boiling Heat Transfer Using Refrigerant Mixtures,'' Ph.D. dissertation, University of Maryland.

[14] Wettermann, M., and Steiner, D., 2000, ''Flow Boiling Heat Transfer of Wide-Boiling Binary and Ternary Mixtures,'' Boiling 2000, Phenomena and Emerging Applications, Proceedings of the Engineering Foundation Conference, Anchorage, Alaska, April 30–May 5, pp. 684–697.

[15] Barbosa, J. R., Wadekar, V. V., and Hewitt, G. F., 2000, ''A Review of Heat and Mass Transfer in Flow Boiling of Binary Mixtures,'' Boiling 2000, Phenomena and Emerging Applications, Proceedings of the Engineering Foundation Conference, Anchorage, Alaska, April 30–May 5, pp. 754–771.

[16] Kandlikar, S. G., 1998, ''Boiling Heat Transfer in Binary Systems: Part II-Flow Boiling,'' ASME J. Heat Transfer, **120**, pp. 388–394.

[17] Ambrogi, G., McAssey, E. V., Cozzone, G., and Hoover, C., 1997, ''The Effect of Off-Design Operation on the Thermal Performance of Propylene-glycol and Ethylene-glycol Engine Coolants,'' SAE Paper No. 971827, Vehicle Thermal Management Conference, Indianapolis, IN, pp. 441–448.

[18] McAssey, E. V., Stinson, C., and Gollin, M., 1995, ''Evaluation of Engine Coolants Under Flow Boiling Conditions,'' Proceedings of the ASME Heat Transfer Division, M. Ebadian and M. Kaviany, eds., HTD-Vol. 317-1, pp. 193–200.

[19] Bhowmick, S., Branchi, C., Gollin, M., and Cozzone, G., 1997, ''Prediction of Heat Transfer in Engine Cooling Systems,'' Experimental Heat Transfer, Fluid Mechanics, and Thermodynamics 1997, June 1997, **1**, M. Giot, F. Mayinger, and G. P. Celata, eds., Brussels, Belgium, pp. 387–392.

[20] Bhowmick, S., Branchi, C. McAssey, E. V., Gollin, M., and Cozzone, G., 1997, ''Prediction of Heat Transfer in Engine Cooling Systems,'' Proceedings of the 4th World Conference on Experimental Heat Transfer, Fluid Mechanics, and Thermodynamics, Brussels, Belgium.

[21] McAssey E. V., Jr., and Kandlikar, S. G., 1999, ''Convective Heat Transfer of Binary Mixtures Under Flow Boiling Conditions,'' Two-Phase Flow Modelling and Experimentation 1999, Proceedings of the 2nd International Symposium on Two-phase Flow Modeling and Experimentation, Pisa, Italy, May 23–26, 1999, Eds. Celata, G. P., Di Marco, P., and Shah, R. K., pp. 271–278.

[22] Chen, J. C., 1966, ''A Correlation for Boiling Heat Transfer to Saturated Fluids in Convective Flow,'' Ind. Eng. Chem. Process Des. Dev., **5(3)**, pp. 322–329.

[23] Rohsenow, W. M., Hartnett, J. P., and Ganic, E. N., 1985, *Boiling*, Handbook of Heat Transfer Fundamentals, p. 12, Chap. 12.

[24] Behar, M., Courraud, M., Ricque, R., and Semeria, R., 1966, ''Fundamental Aspects of Subcooled Boiling With an Without Dissolved Gases,'' Proceedings of the Third International Heat Transfer Conference, AIChE-ASME, **4**, pp. 1–11.

[25] Murphy, R. M., and Bergles, A. E., 1971, ''Subcooled Flow Boiling of Fluocarbons,'' M.I.T. Engineering Projects Laboratory Report No. DSR 71903-72.

[26] Kandlikar, S. G., and Spiesman, P. H., 1997, ''Effect of Surface Characteristics on Flow Boiling Heat Transfer,'' paper presented at the Engineering Foundation conference on Convective and Pool Boiling, F. Mayinger and M. Lehner, eds., Irsee, Germany, May 18–25, pp. 191–197.

[27] Kandlikar, S. G., and Stumm, B. S., 1995, ''A Control Volume Approach to Predict Departure Bubble Diameter in Flow Boiling,'' ASME J. Heat Transfer, **117**, pp. 990–997.

[28] Kandlikar, S. G., and Howell, M. J., 1996, ''Investigation of Nucleation Characteristics and Heat Transfer on Microfin Surfaces,'' Proceedings of the Second European Thermal-Sciences and 14th UIT National Heat Transfer Conference, Rome, Italy, May 29–31, G. P. Celata, P. DiMarco, and A. Mariani, eds., **1**, pp. 241–246.

[29] Gnielinski, V., 1976, ''New Equations for Heat and Mass Transfer in Turbulent Pipe and Channel Flow,'' Int. Chem. Eng. **16**, pp. 359–368.

[30] Petukhov, B. S., and Popov, V. N., 1963, ''Theoretical Calculation of Heat Exchanger in Turbulent Flow in Tubes of an Incompressible Fluid with Variable Physical Properties,'' High Temp., **1(1)**, pp. 69–83.

The Effect of Dissolving Salts in Water Sprays Used for Quenching a Hot Surface: Part 1—Boiling of Single Droplets

Qiang Cui

Sanjeev Chandra
e-mail: chandra@mie.utoronto.ca

Susan McCahan

Department of Mechanical
and Industrial Engineering,
University of Toronto,
Toronto, Ontario M5S 3G8, Canada

We conducted experiments on the effect of dissolving three different salts sodium chloride (NaCl), sodium sulfate (Na_2SO_4) and magnesium sulfate ($MgSO_4$) in water droplets boiling on a hot stainless steel surface. Substrate temperatures were varied from 90°C to 220°C. We photographed droplets as they evaporated, and recorded their evaporation time. At surface temperatures that were too low to initiate nucleate boiling all three salts were found to reduce droplet evaporation rates because they lower the vapor pressure of water. In the nucleate boiling regime, low concentrations (<0.1 mol/l) of Na_2SO_4 and $MgSO_4$ enhanced heat transfer because they prevented coalescence of vapor bubbles and produced foaming in the droplet, significantly reducing droplet lifetimes. Increasing the salt concentration further did not produce a corresponding increase in droplet boiling rate. Dissolved salts prevent bubble coalescence because they increase surface tension and stabilize the liquid film separating bubbles, and because electric charge that accumulates on the surfaces of bubbles produces a repulsive force, preventing them from approaching each other. Na_2SO_4 and $MgSO_4$, which have high ionic strengths, produced a large amount of foaming in droplets and increased their boiling rate significantly. NaCl, which has low ionic strength, had little effect on droplet boiling.
[DOI: 10.1115/1.1532010]

Keywords: Cooling, Droplet, Enhancement, Heat Transfer, Impingement, Sprays

Introduction

When measuring heat transfer from a hot surface quenched by a spray, researchers typically use water that has been carefully distilled so as to remove any dissolved impurities. It is well known that even trace contaminants in water can produce large variations in boiling heat flux. But the water used in engineering spray applications, which the laboratory tests hope to simulate, is rarely purified with such care. Industrial users know that the water they employ for cooling contains significant amounts of dissolved salts and gases, since it is too expensive to remove them, even though the effect they have on spray cooling effectiveness is poorly understood.

The effect of additives on pool boiling heat transfer has received much more attention than their role in spray cooling. Pool boiling studies done by Jamiliahmadi et al. [1] and Najibi et al. [2] showed that dissolved salts precipitate on the heater surface during boiling. This initially enhances boiling, since the deposits act as bubble nucleation sites, but eventually the insulating salt layer decreases heat transfer. Surfactants also have an important effect on pool boiling [3–5]: they promote bubble nucleation and foaming in the liquid and significantly enhance heat transfer.

The use of additives in water sprays has been the subject of a few studies published in the fire safety literature, since there is anecdotal evidence that some additives can greatly enhance the fire suppression capabilities of water. To quantify this effect Finnerty [6] measured the time required to put out a liquid pool fire, using water sprays in which a variety of organic and inorganic salts were dissolved. The time to extinguish the fire varied by an order of magnitude, depending on the salt used, but the reason for this large difference was not understood. The salts may modify the combustion chemistry, or they may alter the physical properties of water and affect evaporation of droplets.

Boiling in droplets deposited on a hot surface differs from that observed in a liquid pool, since heat transfer depends on the contact area between the droplets and substrate. Any additive that increases this area will also enhance heat transfer. Qiao and Chandra [7,8] found that dissolving traces of a surfactant in the spray water significantly enhanced heat transfer. The surfactant reduced the liquid-solid contact angle and produced foaming in boiling droplets; both these effects increased the solid area wetted and enhanced surface cooling. King et al. [9] observed the evaporation of salt solution droplets placed on a hot stainless steel plate, at temperatures below those required to trigger boiling. They found that the dissolved salts reduced the vapor pressure of water and therefore decreased the droplet evaporation rate. Cui et al. [10] examined the effect of dissolving either a gas (carbon dioxide) or salts (sodium carbonate or sodium bicarbonate) in water droplets boiling on a hot surface. They established that the gas had little effect on boiling: it came out of solution and escaped soon after a droplet landed on the surface. The salts, however, prevented coalescence of vapor bubbles inside the boiling droplet, producing foaming and greatly reducing the droplet lifetime.

The ability of dissolved salts to prevent coalescence of vapor bubbles is well known: it is the reason, for example, that seawater foams more than fresh water. The phenomenon is extensively documented in the chemical engineering literature [11–18], since it is important in reactors where a gas is bubbled through a liquid. The rate of heat and mass transfer between the liquid and vapor phases is proportional to the contact area between them, which is a function of the size and number of gas bubbles. The effect has been demonstrated quite clearly in experiments [11–14] where gases were introduced into water baths in which electrolytic salts were dissolved. There was a critical solute concentration above which the frequency with which bubbles merged was sharply reduced. The mechanism by which these solutes prevent coales-

Contributed by the Heat Transfer Division for publication in the JOURNAL OF HEAT TRANSFER. Manuscript received by the Heat Transfer Division February 27, 2002; revision received October 7, 2002. Associate Editor: D. B. R. Kenning.

cence is not clearly understood [14]. Some theories [15–17] attribute it to the change in liquid surface tension produced by dissolved salts. As two bubbles approach each other the liquid film separating them thins, increasing the local salt concentration and surface tension, which stabilizes the liquid. This model does not explain the observed correlation between the ionic strength of the solute and the critical concentration required to prevent bubble coalescence. An alternate hypothesis [18] is that electrical charges accumulating on the bubble surfaces produce repulsive forces between them.

In an earlier experiment [10] we demonstrated that dissolving 1 percent by weight of either sodium carbonate or sodium bicarbonate in a water droplet boiling on a hot plate greatly reduced the droplet lifetime. The dissolved salt prevented coalescence of vapor bubbles, enlarging the boiling droplet and increasing the area in contact with the hot substrate. However, the study left us with several new unanswered questions. For example, do other salts have a larger or smaller effect on droplet boiling than the two we tested? What properties of the dissolved salt determine the magnitude of its influence on boiling? What salt concentration maximizes the boiling rate? And most importantly from a practical viewpoint, how do salts influence heat transfer in a spray, rather than just a single droplet, impacting a hot surface?

Our objective in the present study was to vary both the type and concentration of salts dissolved in water, and observe their effect on boiling of single droplets of salt solution placed on a hot stainless steel surface. In a companion study [19] we confirmed that salts that enhanced boiling of single droplets also significantly increased heat transfer to a spray of droplets quenching a hot surface.

In the experiments reported in this paper we deposited 2.0 mm diameter droplets of salt solution on a heated surface and photographed their evaporation. The surface temperature was varied from 90°C to 220°C, so that we could observe both evaporation and nucleate boiling of droplets. At surface temperatures above 220°C we earlier found [10] that bubbles grew so vigorously in salt solution droplets deposited on a hot surface that they shattered, making it impossible to define a droplet lifetime. The salts to be tested were selected after reviewing the literature on bubble coalescence in salt solutions. Lessard and Zieminki [11] demonstrated that the effectiveness of a dissolved salt in preventing coalescence depends on the valencies of its ions. Salts such as sodium chloride (NaCl), both of whose ions have valencies of 1, are the least effective. Magnesium sulfate ($MgSO_4$), with ionic valencies of 2 and 2 respectively, has a large effect. Sodium sulfate (Na_2SO_4), which has intermediate valency values (1 and 2), has an effect that lies between those of the other two salts. We selected all three of these salts (NaCl, Na_2SO_4 and $MgSO_4$) for our study, to examine the effect of valence combinations on droplet boiling. The concentration of each salt was varied from 0 to 0.4 mol/l.

Experimental Method

Water used in our experiments was first distilled and then deionized. Distilled water was deionized in a NANOpure Bioresearch Deionization System (Model #D4754, Barnstead Thermolyne Corporation) to an electrical resistivity of 18.3 MΩ-cm. Salt solutions were prepared by weighing out the required quantity of powdered salt and dissolving it in purified water at room temperature, and then allowing the solution to stand for about 12 hours to ensure complete mixing. The salt concentrations used in these tests were all well below their solubility limits in water.

A syringe pump was used to drive liquid through a 33-gauge stainless steel hypodermic needle, from whose tip the droplets detached and fell onto the test surface placed 50 mm below the needle tip. The test surface was a stainless steel plate, 50.8 mm square and 6.35 mm thick, finished with 600 grit emery cloth and metal polish. During experiments it was cleaned with a cotton swab dipped in distilled water after each test to remove any salt residue. It was bolted to a copper block in which two cartridges heaters were inserted. Chromel-Alumel thermocouples were used to measure surface temperature. Before depositing a droplet on the surface its temperature was held constant within ± 0.5°C by regulating power to the heaters using a temperature controller. Tests were done at surface temperatures ranging from 90°C to 220°C.

The diameters of water droplets in our tests, measured by photographing spherical droplets in air after they detached from the tip of the needle, were determined to be 2.0 ± 0.02 mm. Dissolving salts in the water produced no measurable change in their size, from which we concluded that solute concentrations were sufficiently low to have no appreciable effect on liquid surface tension.

After each droplet was deposited on the hot surface, its boiling was recorded using both a 35 mm camera and a video system. The Nikon F-3 camera used to take photographs was controlled by a computer based data acquisition and control system that sent pulses at pre-determined time intervals to trigger the camera motor drive, taking still photographs of successive stages of droplet impact. The resolution of these pictures was much higher than that of video images, allowing bubbles nucleating inside droplets to be clearly seen. The evaporation time of each droplet was measured from video images; the resolution of these measurements, corresponding to the duration of a single video frame, was 33 ms.

Results and Discussion

Figure 1 shows photographs of the boiling of droplets of pure water, NaCl solution and Na_2SO_4 solution on a stainless steel surface at a temperature of 130°C. The initial diameter of all the droplets was 2.0 mm. The molar concentration of both salt solutions was the same, 0.06 mol/l. Each column in Fig. 2 shows successive stages during the lifetime of a droplet, and each row shows droplets boiling at the same time (t) measured from the instant of droplet impact on the surface, as indicated besides each row of photographs. Reflections of the droplets are seen in the polished stainless steel surface.

A number of small vapor bubbles nucleated inside the droplets immediately after they touched the surface. In the pure water droplet these bubbles rapidly coalesced and burst through the liquid surface so that by $t = 0.5$ s (the second frame in Fig. 1(a)) no bubble was visible. When a water droplet is placed on a hot stainless steel plate the surface under it cools rapidly. Measurements of surface temperature variation, under conditions identical to those in our experiments [20]), showed that when a 2.0 mm water drop is placed on a polished stainless surface initially at 130°C the temperature drops by approximately 35°C in 25 ms. Consequently no more bubbles formed in the droplet because the temperature of the stainless steel substrate became too low to sustain further nucleation. The droplets were then in a state of evaporation rather than of nucleate boiling. Dissolved NaCl had little effect on evaporation of a droplet (Fig. 1(b)) except that the large vapor bubble stayed intact until $t = 2.00$ s, when it burst through the droplet surface. The droplet containing NaCl took approximately 12 s to evaporate completely, compared to 10 s for a pure water droplet; the increase in evaporation time was attributed to the vapor pressure of water being reduced by the dissolved salt.

Dissolved Na_2SO_4 had a significantly greater effect on droplet boiling than NaCl. Once a droplet containing dissolved Na_2SO_4 landed on the hot surface, many bubbles were produced inside it (Fig. 1(c)). These bubbles did not merge but grew larger, greatly expanding the bubble diameter. Consequently the contact area between the liquid and the hot surface was significantly increased. The droplet lifetime was reduced to about 5 s, only half that of pure water. A ring of deposited salt was left on the test surface (see Fig. 1(c), $t = 5.50$ s) after all the water evaporated.

Dissolved $MgSO_4$ had an effect similar to that of Na_2SO_4. Figure 2 shows the boiling of droplets of water containing dissolved $MgSO_4$ with three different concentrations: 0.01 mol/l (Fig. 2(a)), 0.06 mol/l (Fig. 2(b)), and 0.4 mol/l (Fig. 2(c)) respec-

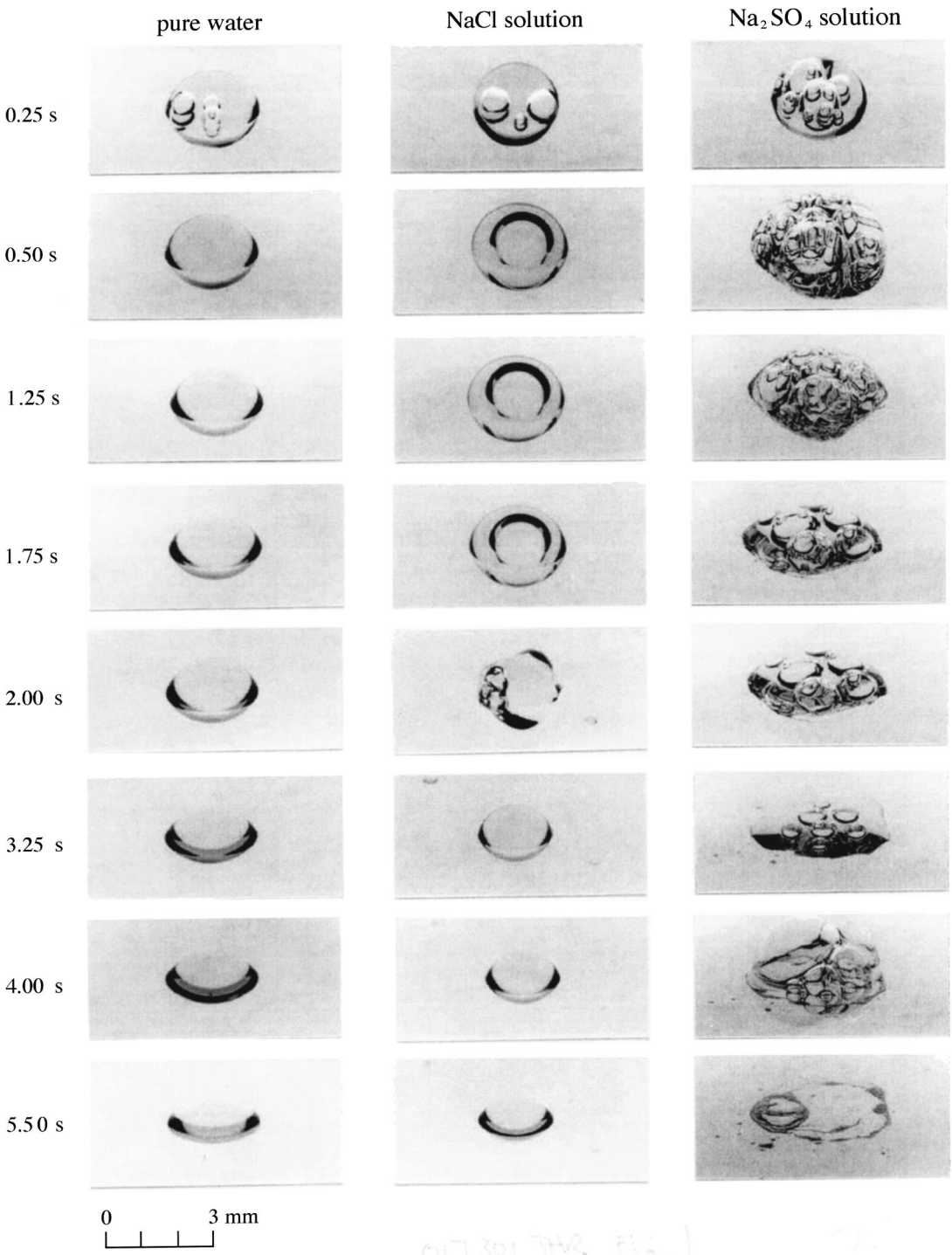

Fig. 1 Boiling of droplets of (*a*) pure water, (*b*) NaCl solution (0.06 mol/l), and (*c*) Na_2SO_4 solution (0.06 mol/l), deposited on a stainless steel surface at a temperature of 130°C

tively. Boiling in droplets containing 0.06 mol/l of $MgSO_4$ closely resembled that of droplets with the same concentration of Na_2SO_4 (compare Figs. 1(*c*) and 2(*b*)). $MgSO_4$ was slightly more effective than Na_2SO_4 in reducing droplet lifetime. When the concentration was reduced to 0.01 mol/l, there was only one large bubble inside the drop and the bubble lifetime increased (Fig. 2(*a*)). Raising the salt concentration to 0.4 mol/l increased the number of bubbles in the drop (see Fig. 2(*c*), $t=0.25$ s), but did not further diminish the droplet lifetime. In fact, the time taken for the liquid to evaporate was slightly greater for a droplet containing 0.40 mol/l of dissolved $MgSO_4$ than it was for one with 0.06 mol/l of the same salt.

Figure 3 summarizes our measurements of droplet lifetimes on a stainless steel surface with surface temperatures varying from 90°C to 220°C. Data is shown for pure water drops and those of 0.06 mol/l solutions of NaCl, Na_2SO_4, and $MgSO_4$. Each data point represents the average of five measurements, with error bars marking the highest and lowest values. When the surface was at a

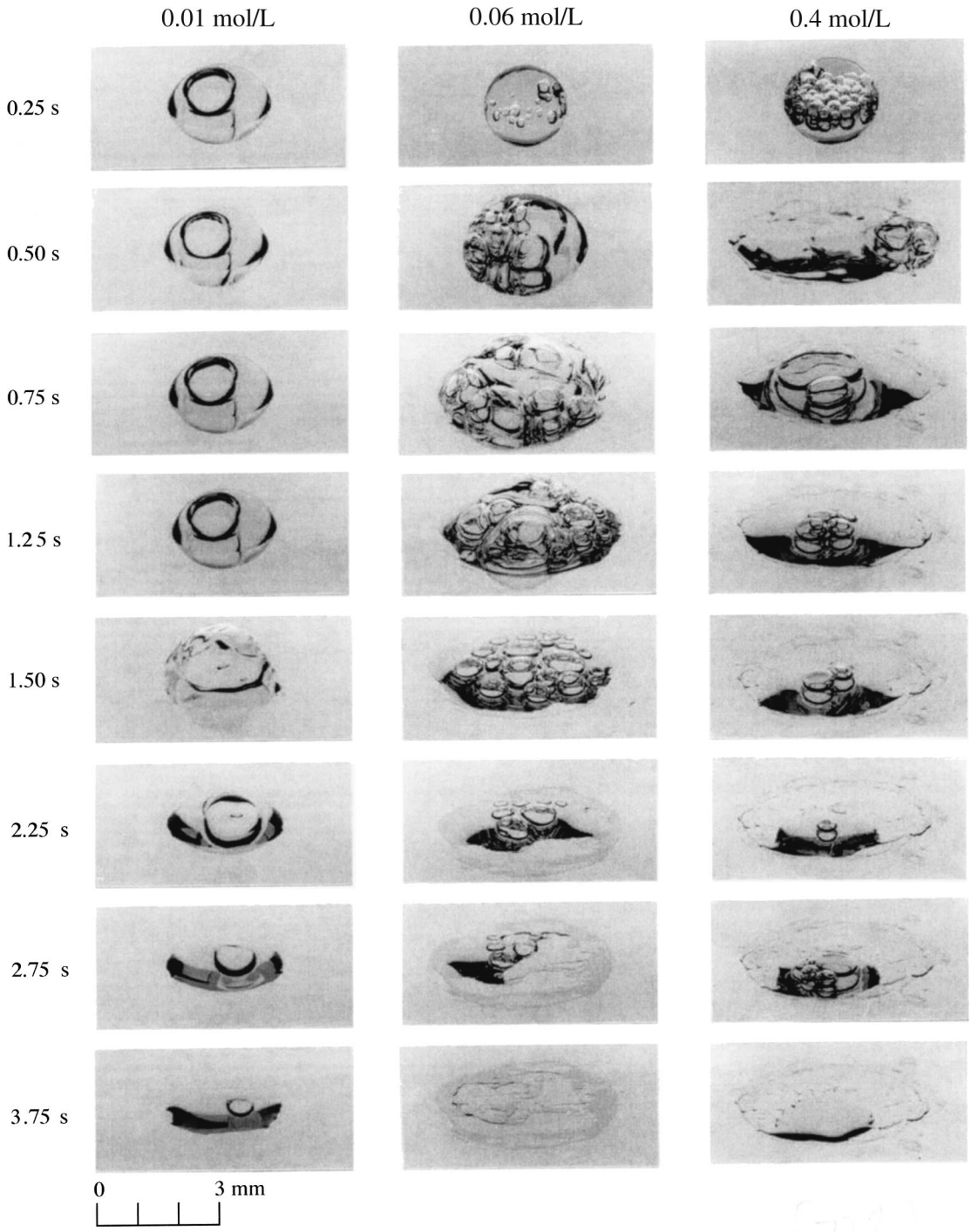

Fig. 2 Boiling of droplets of $MgSO_4$ dissolved in water with concentrations of (*a*) 0.01 mol/l, (*b*) 0.06 mol/l, and (*c*) 0.40 mol/l, deposited on a stainless steel surface at a temperature of 130°C

temperature below the saturation point of water (100°C), droplets evaporated with no nucleation of vapor bubbles in the liquid. The only effect of the dissolved salts was to decrease the vapor pressure of the drops. Calculations showed that the magnitude of this reduction was rather small (~1 kPa) for the relatively dilute (0.06 mol/l) solutions used. However, towards the end of droplet evaporation, when the volume of liquid decreased and the salt concentration increased, the vapor pressure reduction was significant enough to produce a measurable increase in droplet lifetime. King et al. [9] have previously observed the same effect.

A test surface initially at a temperature above 130°C was sufficiently superheated to trigger nucleate boiling in drops. Dissolved Na_2SO_4 and $MgSO_4$ prevented coalescence of these bubbles and increased the droplet-surface contact area sufficiently (see Figs. 1 and 2) to offset the reduction in liquid vapor pressure, decreasing the droplet lifetime by approximately 50 percent. However dissolved NaCl did not produce foaming in the drops as the other two salts did (see Fig. 1) and therefore did not enhance boiling. When the surface temperature was increased above 180°C droplet boiling was so rapid, and bubble nucleation so vigorous, that it was no longer possible to discern if any of the salts produced a reduction in droplet lifetime.

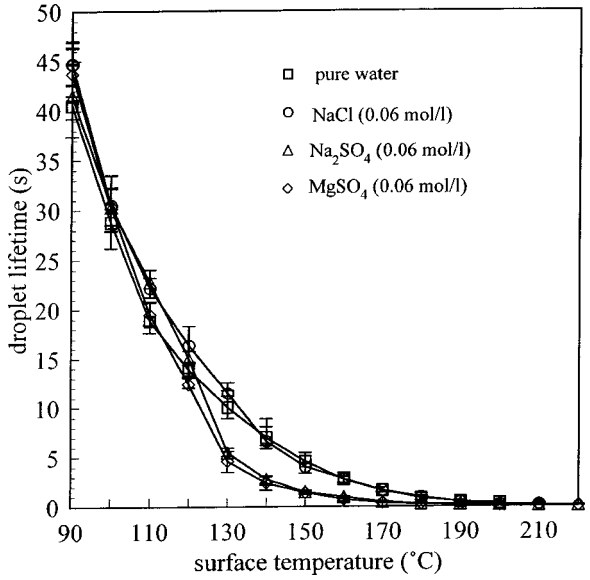

Fig. 3 Variation of the lifetime of 2.0 mm diameter droplets of water or salt solution placed on a stainless steel plate with varying surface temperature

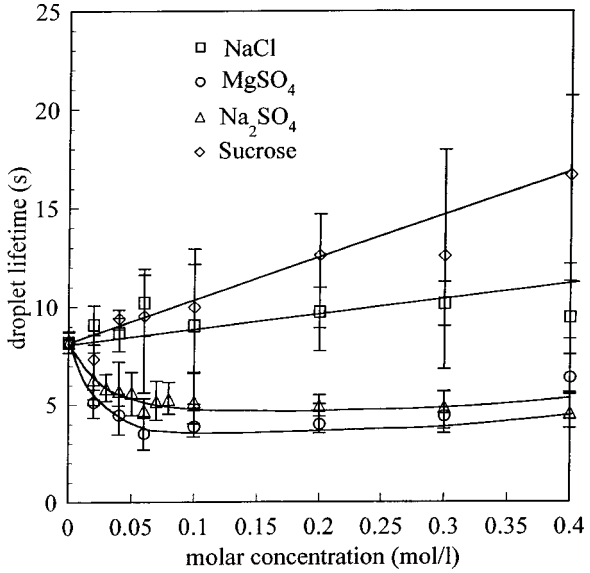

Fig. 4 Variation of droplet lifetime with solution concentration for 2.0 mm diameter water droplets containing either NaCl, Na_2SO_4, $MgSO_4$, or sucrose, deposited on a stainless steel surface at a temperature of 130°C

The effect of varying salt concentration is shown in Fig. 4, which shows measured droplet lifetimes of droplets containing between 0 and 0.4 mol/l of dissolved salt placed on a surface at 130°C. For purposes of comparison we also did a series of tests with solutions of sucrose, which is a non-ionic solute but increases liquid viscosity. Small amounts ($<$0.06 mol/l) of Na_2SO_4 and $MgSO_4$ produced a significant decrease in droplet lifetime, but further increases in salt concentration had little effect. In fact, droplet lifetime began to increase at the highest concentrations ($>$0.3 mol/l). Dissolving either NaCl or sucrose in droplets always increased droplet lifetime.

Dissolving salt in a droplet appears to influence its boiling in two ways: it prevents bubble coalescence, producing foaming and increasing heat transfer from the substrate; and it decreases the vapor pressure of water, reducing the droplet evaporation rate. Depending on which of these two effects is dominant, droplet lifetime may be increased or decreased by a solute. At surface temperatures too low to initiate bubble nucleation ($\leqslant$100°C) dissolved salts always increase droplet lifetime (see Fig. 3). At higher surface temperatures small concentrations of Na_2SO_4 and $MgSO_4$ are sufficient to promote foaming in drops and enhance boiling; adding larger amounts only reduces the droplet evaporation rate (see Fig. 4). NaCl produces little foaming (see Fig. 1), which is why it always increases droplet lifetime. Sucrose, which is non-ionic, was totally ineffective in preventing bubble coalescence and greatly reduced the evaporation rate of water.

The decrease in vapor pressure due to dissolved salts can be calculated using the method described by Cisternas et al. [21]. During boiling of a droplet the concentration of salt in it is constantly increasing; however, for the same salt concentration, dissolved $MgSO_4$ depresses the vapor pressure less than Na_2SO_4. This may be part of the reason that $MgSO_4$ was slightly more effective in reducing droplet lifetime than dissolved Na_2SO_4 (see Fig. 3).

Our experiments established that the most important effect that a dissolved salt plays in droplet boiling is in preventing nucleating bubbles from merging. Unfortunately, though the ability of dissolved salts to prevent coalescence of vapor bubbles has been extensively documented [e.g., [11–14,18,22]] the phenomenon is still not well understood. We found only one theoretical model that tried to predict the minimum concentration of dissolved salt in water required to prevent the merging of two bubbles. Originally proposed by Marruci [15], and later extended by other researchers [16,17], the model assumes that when two bubbles approach each other the liquid film separating them thins rapidly. The dissolved salt in the thinning liquid layer cannot diffuse away quickly, raising the local salt concentration and therefore the surface tension. The increased surface tension prevents draining of the liquid film and retards coalescence.

This model considers only surface tension changes and neglects electrostatic effects that may be important in ionic solutions. Electric charge accumulating on the surfaces of bubbles may produce a repulsive force, preventing them from approaching each other [18]. However, no quantitative model of such effects has yet been developed.

In the absence of any more comprehensive model we used Marruci's theory [15], as enhanced by Prince and Blanch [17], to compare with our measurements of salt concentration required to prevent bubble coalescence in boiling droplets. The model is based on a solution of the Navier-Stokes equations in the thinning liquid film between a pair of bubbles approaching each other, and neglects all electrostatic forces. It predicts that the transition salt concentration above which bubbles do not coalesce is given by [17]:

$$c_t = 1.18\nu\left(\frac{B\sigma}{r_b}\right)^{1/2} R_g T\left(\frac{\partial\sigma}{\partial c}\right)^{-2} \tag{1}$$

In Eq. (1) the transition concentration is a function of bubble size. As the radius of coalescing bubbles increases, the salt transition concentration required for inhibiting bubble coalescence decreases. Figure 5 shows the calculated variation of transition concentration with bubble radius for the three salts used in our experiments.

Bubble coalescence in boiling is a very complex phenomenon, since there is a range of bubble sizes present in droplets. From photographs we measured vapor bubbles varying in radius from 0.1 mm to 0.5 mm soon after the start of boiling (see Figs. 2 and 4, $t = 0.25$ s). To compare these values with predictions from Eq. (1), we estimated the transition concentration (c_t) from Fig. 4, as being 0.11 mol/l for Na_2SO_4 and 0.06 mol/l for $MgSO_4$. The corresponding bubble sizes from Fig. 5 are listed in Table 1.

Predicted bubble sizes seem to be significantly larger than those measured. However, the comparison is not very conclusive, since

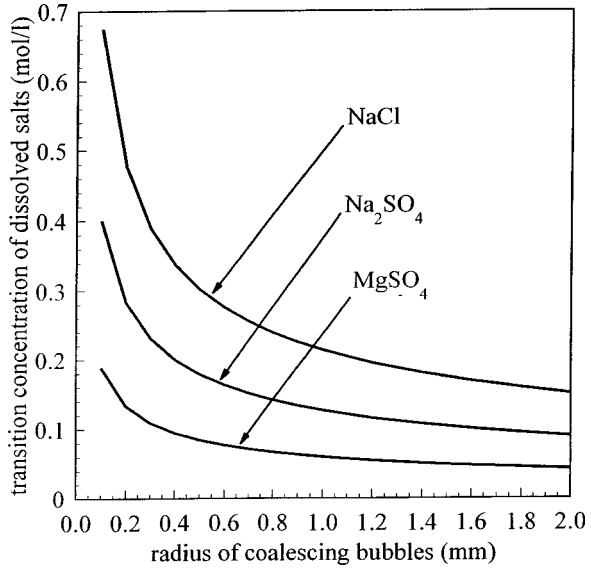

Fig. 5 Transition concentration of salt required to prevent bubble coalescence as a function of bubble radius in a salt solution at a temperature of 100°C

even small changes in estimates of c_t can produce large variations in the predicted bubble size (see Fig. 5). It is likely, though, that the model is too simple to accurately simulate the variety of physical phenomena that govern bubble coalescence in nucleate boiling. Phase change at bubble surfaces during boiling produces localized concentrations of salt, which the model does not consider. Marangoni convection, driven by concentration gradients along vapor bubble surfaces, can also affect bubble dynamics. Finally, electrostatic forces caused by ions accumulating at bubble surfaces play an important role in bubble coalescence.

Electrostatic effects in a solution are a function of its ionic strength (I), which is defined in terms of the valence of the ions present in the solution and their concentration:

$$I = 0.5 \sum_i c_i Z_i^2 \tag{2}$$

where c_i is the molar concentration (mol/l) and Z_i the valence of ionic species i. Chang et al. [23] confirmed that bubble coalescence in saline solutions decreased with increasing ionic strength. In our experiments, too, it was clear that droplet the effectiveness of dissolved salts in reducing bubble lifetime depended on their ionic strength: in Fig. 4 droplet lifetime is seen to decrease with increasing salt concentration. Also, $MgSO_4$ and Na_2SO_4, which have ions with larger valencies than NaCl and consequently greater ionic strength at the same concentration, were much more effective in producing foaming in the liquid (see Figs. 1 and 2).

Though the model used to develop Eq. (1) does not explicitly consider the effect of ionic strength, it does include it indirectly through the dependence of surface tension of salt solutions on their ionic strength. The increase of surface tension caused by dissolving a strong electrolyte in water is largely due to the repulsion of ions from the surface by electrostatic image forces [24]. The variation of surface tension with concentration ($d\sigma/dc$) listed in Table 1, which was used in Eq. (1), is therefore a function of the ionic strength of the salt solutions.

Table 1 Calculated and measured bubble sizes corresponding to the observed transition concentrations (c_t) of salts

salt	$d\sigma/dc$ (gcm^3/s^2mol)	c_t from experiments (mol/l)	bubble radius from Eq. 1 (mm)	bubble radius from experiments (mm)
NaCl	1,700	~	~	0.1–0.5
Na_2SO_4	2,700	0.11	1.3	0.1–0.5
$MgSO_4$	3,200	0.06	0.7	0.1–0.5

The rate of diffusion of a dissolved salt in water may also play an important role in droplet boiling. When a bubble grows in a salt solution, the solute concentration increases at the bubble surface when liquid evaporates, and increases the ionic strength locally. The lower the rate of diffusion of salt away from the region of high concentration, the stronger is this effect. The diffusion coefficient of NaCl in water is much higher than those of Na_2SO_4 and $MgSO_4$. The diffusion coefficients of the three salts in a 0.1 M solution at 100°C are [25]: 1.988×10^{-9} m^2/s (NaCl), 1.244×10^{-9} m^2/s (Na_2SO_4), and 0.892×10^{-9} m^2/s ($MgSO_4$). Therefore we expect much less accumulation of salt around bubbles in NaCl solution droplets, and less foaming, than in those containing Na_2SO_4 or $MgSO_4$.

Conclusions

Dissolving small amount of ionic salts in water droplets evaporating on a hot stainless steel surface had a significant effect on their evaporation and boiling. For surface temperatures that were too low to produce nucleate boiling dissolved salts always reduced the droplet evaporation rate. If the droplet was in a state of nucleate boiling, small concentrations (<0.1 mol/l) of Na_2SO_4 and $MgSO_4$ were effective in inhibiting bubble coalescence and produced foaming in the liquid, significantly reducing the droplet lifetime. Increasing salt concentration above 0.3 mol/l reduced the vapor pressure of water enough to produce an increase in droplet lifetime. Dissolved NaCl did not generate foam; it only reduced the vapor pressure of water and therefore the boiling rate. A theoretical model of bubble coalescence, which considers the variation of surface tension with salt concentration, was used to calculate the size of bubbles in foaming droplets. It predicted bubbles that were larger than those observed in our experiments. Other properties of the salts such as their ionic strengths and diffusion coefficients, which were not considered in the model, are also important in determining the effect of dissolved salts on droplet boiling.

Acknowledgments

The authors gratefully acknowledge the financial support of the Natural Sciences and Engineering Research Council of Canada for this project.

Nomenclature

B = retarded Van der Waals coefficient
c = salt concentration
c_t = transition concentration
I = ionic strength
r_b = bubble radius
R_g = gas constant
T = temperature
ν = number of ions produced upon dissociation
σ = surface tension

References

[1] Jamialahmadi, M., and Muller-Steinhagen, H., 1990, "Pool Boiling Heat Transfer to Electrolyte Solutions," Chem. Eng. Process., **28**, pp. 79–88.
[2] Najibi, S. H., Muller-Steinhagen, H., and Jamialahmadi, M., 1996, "Boiling and Non-Boiling Heat Transfer to Electrolyte Solutions," Heat Transfer Eng., **17**(4), pp. 46–63.
[3] Wu, W. T., Yang, Y. M., and Maa, J. R., 1998, "Nucleate Pool Boiling Enhancement by Means of Surfactant Additives," Electronics, **18**, pp. 195–209.
[4] Hetsroni, G., Zakin, J. L., Lin, Z., Mosyak, A., Pancallo, E. A., and Rozenblit, R., 2001, "The Effect of Surfactants on Bubble Growth, Wall Thermal Patterns and Heat Transfer in Pool Boiling," Int. J. Heat Mass Transf., **44**, pp. 485–497.
[5] Wasekar, V. M., and Manglik, R. M., 2000, "Pool Boiling Heat Transfer in

Aqueous Solutions of an Anionic Surfactant,'' ASME J. Heat Transfer, **122**, pp. 708–715.
[6] Finnerty, A. E., 1995, ''Water-Based Fire-Extinguishing Agents,'' Proceedings of Halon Options Technical Working Conference, Albuquerque, New Mexico, pp. 461–471.
[7] Qiao, Y. M., and Chandra, S., 1997, ''Experiments on Adding a Surfactant to Water Drops Boiling on a Hot Surface,'' Proc. R. Soc. London, Ser. A, **453**, pp. 673–689.
[8] Qiao, Y. M., and Chandra, S., 1998, ''Spray Cooling Enhancement by Addition of a Surfactant,'' ASME J. Heat Transfer , **120**, pp. 92–98.
[9] King, M. D., Yang, J. C., Chien, W. S., and Grosshandler, W. L., 1997, ''Evaporation of a Small Water Droplet Containing an Additive,'' *Proceedings of the 32nd National Heat Transfer Conference*, **4**, pp. 45–57.
[10] Cui, Q., Chandra, S., and McCahan, S., 2001, ''The Effect of Dissolving Gases or Solids in Water Droplets Boiling on a Hot Surface,'' ASME J. Heat Transfer, **123**, pp. 719–728.
[11] Lessard, R. R., and Zieminski, S. A., 1971, ''Bubble Coalescence and Gas Transfer in Aqueous Electrolytic Solutions,'' Ind. Eng. Chem. Fundam., **10**(2), pp. 260–269.
[12] Zieminski, S. A., and Whitemore, R. C., 1971, ''Behavior of Gas Bubbles in Aqueous Electrolyte Solutions,'' Chem. Eng. Sci., **26**, pp. 509–520.
[13] Marrucci, G., and Nicodemo, L., 1967, ''Coalescence of Gas Bubbles in Aqueous Solution of Inorganic Electrolytes,'' Chem. Eng. Sci., **22**, pp. 1257–1265.
[14] Craig, V. S. J., Ninham, B. W., and Pashley, R. M., 1993, ''The Effect of Electrolytes on Bubble Coalescence in Water,'' J. Phys. Chem., **97**, pp. 10192–10197.
[15] Marrucci, G., 1969, ''A Theory of Coalescence,'' Chem. Eng. Sci., **24**, pp. 975–985.
[16] Oolman, T. O., and Blanch, H. W., 1985, ''Bubble Coalescence in Stagnant Liquids,'' Chem. Eng. Commun., **43**, pp. 237–261.
[17] Prince, M. J., and Blanch, H. W., 1990, ''Transition Electrolyte Concentrations for Bubble Coalescence,'' AIChE J., **36**(9), pp. 1425–1429.
[18] Keitel, G., and Onken, U., 1982, ''Inhibition of Bubble Coalescence by Solutes in Air/Water Dispersions,'' Chem. Eng. Sci., **17**(11), pp. 1635–1638.
[19] Cui, Q., Chandra, S., and McCahan, S., 2002, ''The Effect of Dissolving Salts in Water Sprays Used for Quenching a Hot Surface, Part 2: Spray Cooling,'' ASME J. Heat Transfer , submitted.
[20] Qiao, Y. M., and Chandra, S., 1996, ''Boiling of Droplets on a Hot Surface in Low Gravity,'' Int. J. Heat Mass Transf., **39**, pp. 1379–1393.
[21] Cisternas, L. A., and Lam, E. J., 1991, ''An Analytic Correlation for the Vapor Pressure of Aqueous and Non-Aqueous Solutions of Single and Mixed Electrolytes. Part II. Application and Extension,'' Fluid Phase Equilib., **62**, pp. 11–27.
[22] Pashley, R. M., and Craig, V. S., 1997, ''Effect of Electrolytes on Bubble Coalescence,'' Langmuir, **13**, pp. 4772–4774.
[23] Chang, S. K., Kang, Y., and Kim, S. D., 1986, ''Mass Transfer in Two- and Three-Phase Fluidized Beds,'' J. Chem. Eng. Jpn., **19**(6), pp. 524–530.
[24] Stairs, R. A., 1995, ''Calculation of Surface Tension of Salt Solutions: Effective Polarizability of Solvated Ions,'' Can. J. Chem., **73**, pp. 781–787.
[25] Zaytsev, I. D., and Aseyev, G. G., 1992, *Properties of Aqueous Solutions of Electrolytes*, CRC Press, Inc.

The Effect of Dissolving Salts in Water Sprays Used for Quenching a Hot Surface: Part 2—Spray Cooling

Qiang Cui

Sanjeev Chandra
e-mail: chandra@mie.utoronto.ca

Susan McCahan

Department of Mechanical
and Industrial Engineering,
University of Toronto,
Toronto, Ontario M5S 3G8, Canada

The effect of adding one of three salts (NaCl, Na_2SO_4 or $MgSO_4$) to water sprayed on a hot surface was studied experimentally. A copper test surface was heated to 240°C and quenched with a water spray. The variation of surface temperature during cooling was recorded, and the surface heat flux calculated from these measurements. Surface heat flux during cooling with pure water sprays was compared with that obtained using salt solutions. Dissolved NaCl or Na_2SO_4 increased nucleate boiling heat transfer, but had little effect on transition boiling during spray cooling. $MgSO_4$ increased both nucleate and transition boiling heat flux. Enhanced nucleate boiling was attributed to foaming in the liquid film generated by the dissolved salts. $MgSO_4$ produced the largest increase in nucleate boiling heat transfer, Na_2SO_4 somewhat less and NaCl the least. A concentration of 0.2 mol/l of $MgSO_4$ produced the greatest heat flux enhancement; higher salt concentrations did not result in further improvements. During transition boiling particles of $MgSO_4$ adhered to the heated surface, raising surface roughness and increasing heat transfer. Addition of $MgSO_4$ reduced the time required to cool a hot surface from 240°C to 120°C by an order of magnitude. [DOI: 10.1115/1.1532011]

Keywords: Cooling, Droplet, Enhancement, Heat Transfer, Impingement, Sprays

Introduction

Liquid sprays are used to cool hot objects in many industrial processes. Typical applications are found in continuous casting processes in metal foundries, emergency core cooling of nuclear reactors, and cooling of electronic equipment. In heat-treating processes, rapid quenching to room temperature is used to control solute precipitation in alloys, enhancing both hardness and strength.

Much recent research has focused on finding methods of improving the effectiveness of spray cooling. It has been established that dissolving surfactants in the spray water, which promote bubble nucleation and foaming, enhances heat transfer. Qiao and Chandra [1] reported that adding surfactants to water sprays can increase nucleate boiling heat flux by up to 300 percent, and Jia and Qiu [2] confirmed this finding. But little is known about the effect of other dissolved substances, such as gases or salts, on the cooling effectiveness of water sprays.

In two earlier studies [3,4] we studied the effect of dissolving either gases or ionic salts on the boiling of water droplets deposited on a hot stainless steel surface. We found that dissolved carbon dioxide had little effect on droplet boiling: the gas came out of solution and escaped almost immediately after droplets contacted a hot surface [3]. Dissolved salts, however, prevented coalescence of vapor bubbles in a boiling droplet, produced foaming and significantly reduced droplet lifetime [3,4]. The effectiveness of any particular salt in enhancing boiling was a function of its ionic strength: sodium chloride (NaCl) produced little change whereas sodium sulfate (Na_2SO_4) and magnesium sulfate ($MgSO_4$) greatly reduced droplet evaporation time. Only small concentrations of these salts (<0.1 mol/l) were required to enhance heat transfer; greater amounts of solute decreased the vapor pressure of water and therefore the droplet boiling rate.

Contributed by the Heat Transfer Division for publication in the JOURNAL OF HEAT TRANSFER. Manuscript received by the Heat Transfer Division February 27, 2002; revision received October 7, 2002. Associate Editor: D. B. R. Kenning.

Though dissolved salts enhanced the boiling of individual water droplets, it was still not clear whether they significantly improve spray-cooling efficiencies. We undertook the present study to determine whether dissolving a salt in a water spray would influence the rate at which it quenched a hot metal surface. A hot copper surface was rapidly cooled using a spray of either pure water or salt solution. The surface temperature varied from 240°C to 95°C, so that we observed all regimes of heat transfer including film boiling, transition boiling, nucleate boiling, and forced convection. Experiments were done with the three salts (NaCl, Na_2SO_4 and $MgSO_4$) that had earlier been used in the single droplet study [4]. We measured the transient temperature distribution in the copper substrate as it cooled, and calculated the surface heat flux. We varied the water mass flux (0.5 or 3.0 kg/m^{2}s), mean impact velocity of droplets (17 to 23 m/s), and salt concentration (0.01 to 0.4 mol/l).

Experimental Method

Figure 1 shows a schematic diagram of the apparatus built to measure surface temperature during spray cooling. The apparatus was a modified version of the one used by Qiao and Chandra [1] and has been described in detail elsewhere [5]. The main components of the system were: a water delivery system, a spray nozzle, a heated copper test surface, and a data acquisition and control system to record surface temperature.

The turbine pump (CT9755, Burks Pumps, Pique, OH) supplied water through stainless steel tubing and valves to the spray nozzle. Only a portion of the total flow delivered by the pump was actually supplied to the nozzle, while any excess was re-circulated through a bypass valve back to the supply tank. The mass flow rate of water supplied to the nozzle was measured by a flow meter (GF1360, Gilmont Instruments, Barrington, IL) with a resolution of ± 1 ml/min, and controlled by adjusting a needle valve. The nozzle inlet pressure was adjusted using a pressure regulator (26 A, Watts Regulator Groups, North Andover, MA) and measured with a digital pressure gauge (OMEGA DPG-500) with an accu

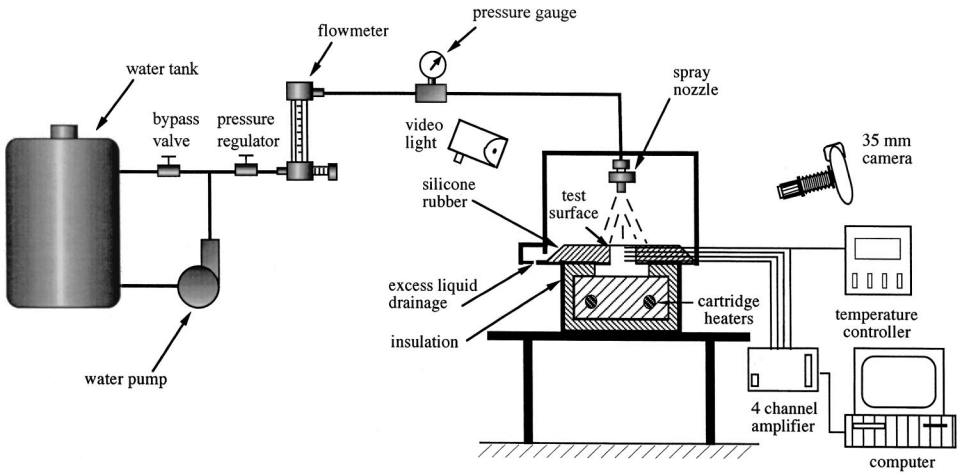

Fig. 1 Schematic diagram of experimental apparatus for spray cooling

racy of ±7 kPa. The spray nozzle was located normal to and directly above the center of the upward facing test surface.

Two commercial full cone nozzles (Unijet TG 0.6 and 0.7, Spray Systems Co., Wheaton IL) were used in this study to obtain two different mass fluxes at the surface: 0.5 and 3.0 kg/m^{2}s. They provided uniform coverage over the test surface. The mean velocity of spray droplets impinging on the test surface was estimated from the following correlation developed by Ghodhane and Holman [6] and extended by Qiao [7]

$$U_m = \left(U_0^2 + \frac{2\Delta p}{\rho} - \frac{12\sigma}{\rho d_{05}} - 2gh \right)^{1/2} \quad (1)$$

The second term dominates the right hand side of Eq. (1); neglecting the other three produces an error of less than 1 percent. The droplet impact velocity was controlled by adjusting nozzle pressure alone. Three nozzle pressures were used in the present study (138, 207 and 276 kPa) to obtain mean droplet velocities of 17, 20, and 23 m/s.

The spray mass flux was measured by replacing the test surface with a section of copper tubing with the same internal diameter as the surface and recording the volume of water flowing into the tubing in a known period of time. The measurement was estimated to be accurate within ±4 percent. The mass flux of water at the test surface was kept constant while changing nozzle pressure by raising or lowering the spray nozzle relative to the surface.

The Sauter mean diameter (d_{32}) of droplets in the sprays, obtained from the manufacturer, was approximately 0.2 mm. Addition of the low concentration of salts (0.06–0.4 mol/l) used in our tests changed the density, viscosity, and surface tension of water by less than 1 percent [8], and therefore did not affect the spray pattern. We did not find any difference between the measured mass flux of pure water or salt solution sprays for the same spray settings. Previous research [9,10] has shown that even large changes in Sauter mean diameter (in the range 0.2 to 1 mm) has little effect on spray cooling. Therefore, any observed difference in heat transfer from a hot surface to a pure water or salt solution spray can be attributed to the effect of the dissolved salts on the boiling process rather than any change in droplet size or distribution.

Experiments were done with sprays of pure water and solutions of NaCl, Na_2SO_4, and $MgSO_4$. Most tests were done with salt solutions containing 0.06 mol/l of additive, a concentration that had previously [4] been found to maximize the evaporation rate of single droplets. Other tests to ascertain the effect of varying salt concentration were done using $MgSO_4$ solutions containing 0.01 to 0.4 mol/l of solute. Fresh salt solutions were prepared before each experiment by weighing and dissolving the selected salt in distilled water.

The test surface was the flat end of a 25.4 mm diameter copper cylinder, electroplated with a 10 μm thick coating of nickel to minimize corrosion. The bottom of the cylinder was bolted to a heated copper block that housed two 500 W cartridge heaters. Four 0.5 mm diameter chromel-alumel thermocouples were inserted into holes drilled 6.35 mm apart along the axis of the copper cylinder, with the first thermocouple positioned 0.4 mm below the test surface. High thermal conductivity paste was applied to the thermocouples to ensure good contact between the copper surface and the thermocouple bead.

The test surface was cleaned prior to each experiment by washing it first with acetone and then with distilled water. It was heated to 240°C by regulating the power to the heating cartridges. Then the pump was switched on while a plastic plate was held in front of the test surface to shield it from the spray. Once the nozzle pressure reached a steady value, the power to the heaters was turned off and the plastic plate was removed to allow water from the nozzle to quench the test surface. The test surface took between 5 s to 300 s, depending on spray parameters, to cool from 240°C to 95°C. Temperatures measured by the thermocouples were continuously recorded using a digital data acquisition system. Photographs of the test surface at selected temperatures were taken using a 35 mm camera, which was driven by the data acquisition and control system.

Only transient quenching tests were done in this study. Previous studies [1] have shown that boiling curves obtained from transient spray cooling tests are almost identical to that determined from steady-state measurements.

Results and Discussion

Figure 2 displays typical temperature measurements made during spray cooling of a surface using pure water with a mass flux $m_1 = 0.5$ kg/m^{2}s and mean droplet velocity $U_m = 20$ m/s. The temperature variation recorded by each of the four thermocouples (T_1 to T_4) is shown. Prior to spray cooling, the test surface was heated to a constant temperature of 240°C. Heat conduction within the copper cylinder was high enough to give an almost uniform temperature profile along its centerline. The temperature difference between the top thermocouple and the bottom one was less than 1°C at the start of cooling, and increased during quenching to approximately 10°C. The temperature measured by the thermo

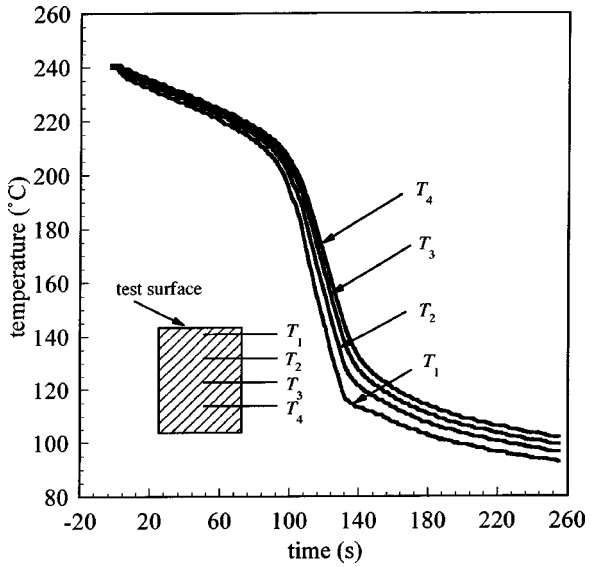

Fig. 2 Transient temperature measurements during spray cooling using pure water with mass flux $m_l = 0.5$ kg/m^{2}s and mean droplet velocity $U_m = 20$ m/s

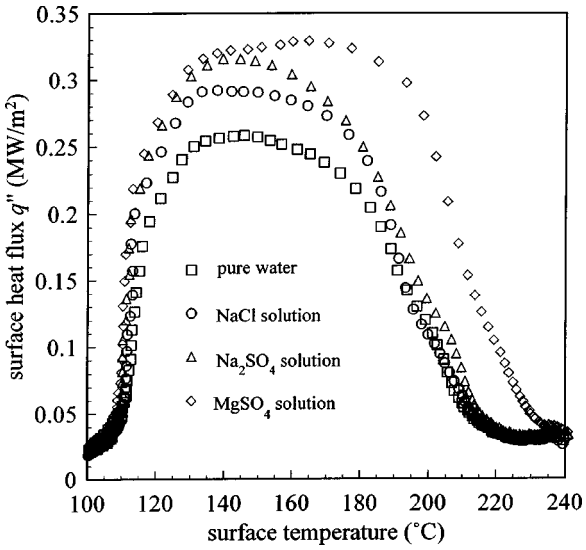

Fig. 4 The effect of dissolved salts on heat transfer during spray cooling with 0.06 mol/l concentration salt solutions. Spray mass flux $m_l = 0.5$ kg/m^{2}s and mean droplet velocity $U_m = 20$ m/s.

couple closest to the surface dropped from 240°C to 100°C in approximately 250 s, during which the bottom one dropped from 240°C to 110°C.

Surface heat flux during spray quenching was calculated from temperature measurements such as those in Fig. 2 using the sequential function specification method to solve the inverse heat conduction problem [2]. The surface temperature was determined by assuming one-dimensional heat conduction within the test block. Error analysis showed [7] the calculated heat flux to be accurate to within 10 percent, with the largest errors occurring at the start and the end of cooling where the relative magnitude of heat flux was small.

Figure 3 shows the variation of heat flux and surface temperature during spray quenching with pure water, calculated from the temperature measurements of Fig. 2. As the surface temperature decreased the mechanism of heat transfer changed, passing successively through four different regimes. At the highest surface temperatures ($T_w > 220$°C) spray droplets were in a state of film boiling where a thin vapor layer blanketed the surface, insulating it and reducing surface heat flux to a relatively low value ($q'' \approx 0.03$ MW/m^2). Better liquid-surface contact was obtained in the transition boiling regime (140°C$< T_w <$220°C); heat transfer increased significantly, reaching a maximum at the critical heat flux point ($q'' = 0.26$ MW/m^2). Heat transfer decreased rapidly with further reduction in surface temperature in the nucleate boiling regime (105°C$< T_w <$140°C). Once the surface temperature became too low ($T_w <$105°C) to sustain bubble nucleation, cooling was due to single-phase forced convection alone ($q'' \leqslant 0.05$ MW/m^2).

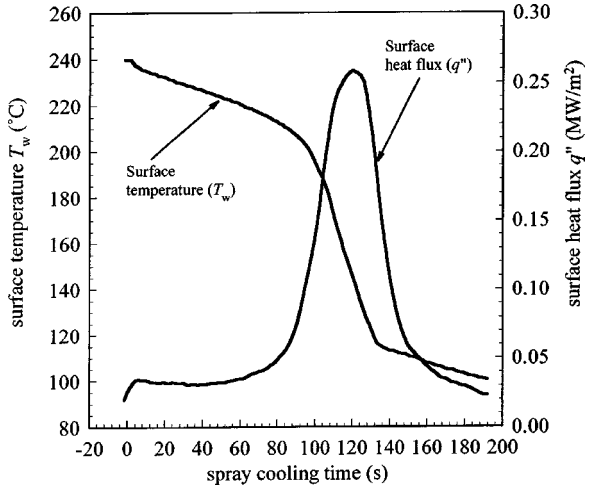

Fig. 3 Calculated surface heat flux and temperature obtained from interior temperature measurements during spray cooling using pure water with mass flux $m_l = 0.5$ kg/m^{2}s and mean droplet velocity $U_m = 20$ m/s

Plotting surface heat flux (q'') as a function of surface temperature (T_w) gives the boiling curve for spray cooling. Figure 4 shows the boiling curve for a water spray with $m_1 = 0.5$ kg/m^{2}s and $U_m = 20$ m/s. Similar boiling curves for sprays of 0.06 mol/l solutions of NaCl, Na_2SO_4 and $MgSO_4$, with the same mass flux and mean droplet velocity, are also shown in Fig. 4. All three salts enhanced nucleate boiling heat transfer and critical heat flux. The increase was greatest for $MgSO_4$, somewhat less for Na_2SO_4 and least for NaCl; previous experiments [4] had established the same ranking for the effectiveness of these salts in enhancing heat transfer to single droplets on a hot surface. Na_2SO_4 and NaCl had little effect on the temperature at which CHF occurred and on transition boiling heat transfer, whereas $MgSO_4$ increased both.

Examination of photographs of the surface taken during quenching showed that dissolving a salt in the spray water had two visible effects. First, it produced foaming during nucleate boiling of the thin liquid film on the test surface. Foaming was noticeably more pronounced in Na_2SO_4 and $MgSO_4$ solutions than in the NaCl solution, producing greater surface cooling. Secondly, during transition boiling of $MgSO_4$ solution some salt precipitated onto the test surface. Patches of deposited salt, each several millimeters in diameter, were clearly visible on the surface for $T_w <$180°C. When cleaning the test surface it was found that these particles adhered quite tenaciously. Na_2SO_4 and NaCl, which have a much higher solubility than $MgSO_4$ [8], did not accumulate on the surface. The deposited $MgSO_4$ particles effectively increased the test surface roughness, enhancing surface heat flux. During transition boiling the salt particles broke through the vapor layer insulating the heated surface and increased direct liquid-solid contact, while in nucleate boiling they provided bubble nucleation sites. Greater surface roughness also shifted the

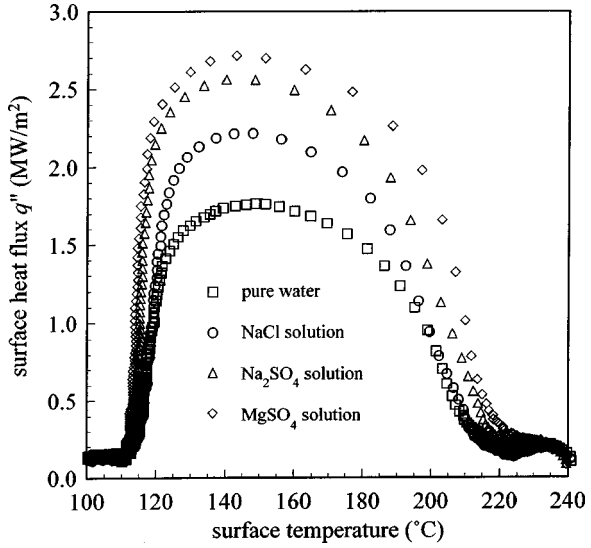

Fig. 5 The effect of dissolved salts on heat transfer during spray cooling with 0.06 mol/l concentration salt solutions. Spray mass flux $m_l = 3.0$ kg/m^{2}s and mean droplet velocity $U_m = 20$ m/s.

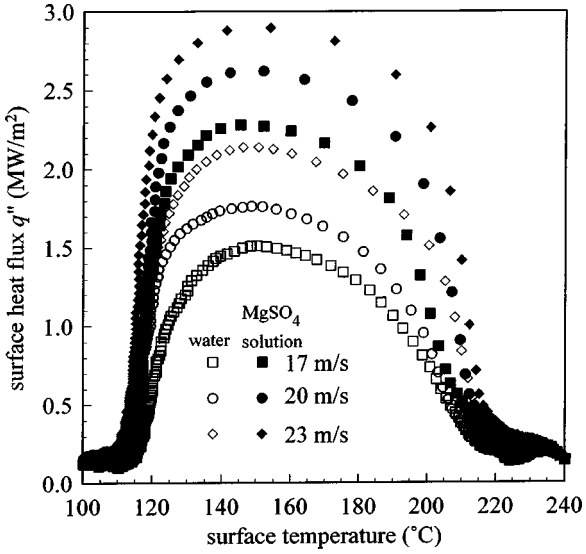

Fig. 6 The effect of dissolving 0.06 mol/l of $MgSO_4$ in water used for spray cooling at three different droplet velocities: 17 m/s, 20 m/s, and 23 m/s. Spray mass flux $m_l = 3.0$ kg/m2s.

onset of transition boiling, and therefore the critical heat flux, to a higher temperature (170°C for $MgSO_4$ solution compared to 150°C for pure water). Surface roughness is known to greatly influence the critical flux during spray cooling [12].

Dissolved salts were equally effective in enhancing heat transfer when liquid mass flux was increased. Figure 5 shows the boiling curve for quenching with pure water and salt solutions with a spray mass flux of 3.0 kg/m^{2}s. All three salts enhanced heat transfer and their relative effectiveness was in same order as previously observed at $m_1 = 0.5$ kg/m^{2}s. In this case, however, $MgSO_4$ did not increase the temperature at which critical heat flux occurred, unlike what was observed at the lower mass flux (see Fig. 4). At this high spray mass flux the surface was flooded with water and salt particles did not precipitate on the surface. The only effect of the dissolved salts was to promote foaming in the boiling water film.

Increasing the nozzle pressure, and therefore the mean droplet impact velocity in the nozzle, increases spray cooling heat transfer [1,9]. Dissolved salts further enhanced heat transfer at all droplet velocities in our tests. Figure 6 shows measured heat flux for pure water and $MgSO_4$ solution (0.06 mol/l) at three different droplet velocities: 17 m/s, 20 m/s, and 23 m/s. Comparison of the boiling curve for pure water with that of the salt solution at each velocity shows a significant increase in heat transfer at all temperatures.

All the results reported in this paper so far were those from tests done using salt solutions with a solute concentration of 0.06 mol/l. We also did experiments to investigate the effect of varying salt concentration. Figure 7 shows boiling curves for $MgSO_4$ solution sprays with concentrations varying from 0.01 mol/l to 0.4 mol/l. Surface heat flux increased with salt concentration for all temperatures, until the concentration exceeded 0.2 mol/l. Further raising the concentration to 0.4 mol/l reduced the heat transfer for $T_w < 210$°C; at higher temperatures, where droplets were in transition boiling, heat flux continued to increase with salt concentration.

Experiments on the nucleate boiling of single droplets of salt solution placed on a stainless steel surface [4] showed that there is an optimum salt concentration that minimized droplet lifetime. Increasing the amount of dissolved salt further reduced the vapor pressure of water and decreased the rate of droplet boiling. Our spray cooling data followed the same trend: a concentration of 0.2 mol/l of $MgSO_4$ maximized nucleate boiling heat transfer (see Fig. 7). At higher surface temperatures ($T_w > 210$°C) dissolved salt particles deposited on the heater surface, increasing its roughness. The salt particles disrupted film boiling of droplets and enhanced heat transfer. Surface heat flux therefore continuously increased with salt concentration.

Figure 8 shows the variation of critical heat flux with concentration of $MgSO_4$. The critical heat flux increased from 1.6 MW/m^2 for a pure water spray to a maximum value of approximately 2.9 MW/m^2 when a 0.2 mol/l solution of $MgSO_4$ was used. Further increases in salt concentration resulted in the critical heat flux being diminished.

Enhanced heat transfer due to dissolved salts can greatly reduce the time required to quench a surface with a water spray. Figure 9 shows the variation of surface temperature during the cooling of a surface with a water spray with $m_l = 3.0$ kg/m^{2}s and $U_m = 20$ m/s. When quenching with pure water the initial cooling rate

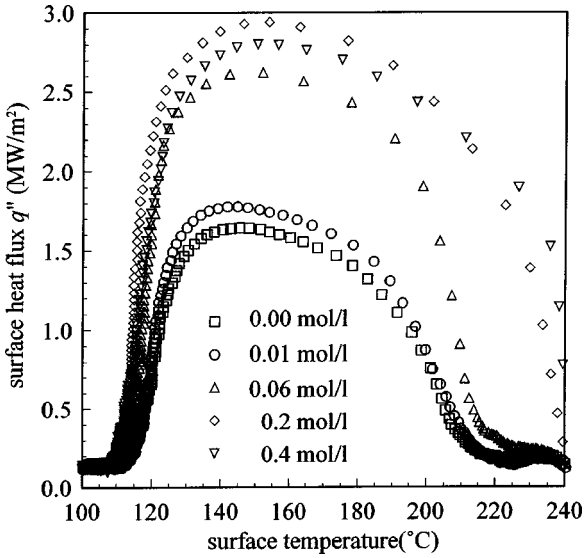

Fig. 7 The effect of varying salt concentration on heat flux during spray cooling with $MgSO_4$ solution. Spray mass flux $m_l = 3.0$ kg/m^{2}s and mean droplet velocity $U_m = 20$ m/s.

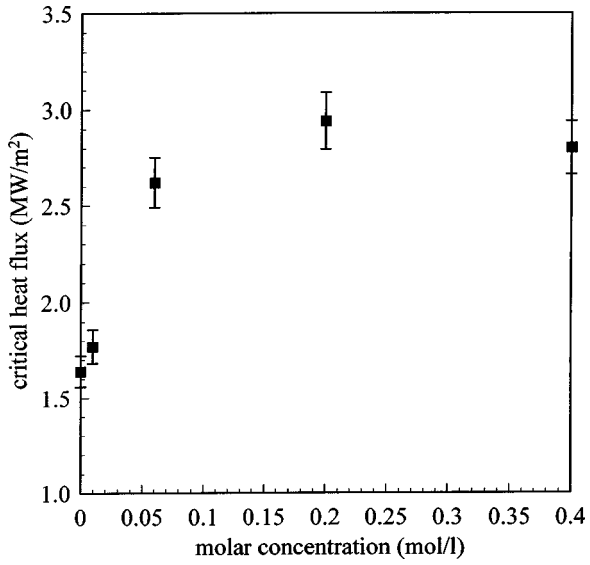

Fig. 8 The effect of dissolved salt concentration on critical heat flux during spray cooling with $MgSO_4$ solution. Spray mass flux $m_l = 3.0$ kg/m^{2}s and mean droplet velocity $U_m = 20$ m/s.

was relatively slow because spray droplets were in film boiling and rebounded off the surface after impact. It took 8 s for the surface temperature to decrease from 240°C to 210°C. Below this temperature surface heat flux increased greatly and it took only an additional 2 s for the surface to cool to 120°C. Dissolving a very small amount of $MgSO_4$ (0.01 mol/l) in the water did not have a measurable effect on the spray cooling rate, but adding 0.06 mol/l of salt significantly enhanced heat transfer: it took only 5 s to cool the surface from 240°C to 120°C. When salt concentration was increased to 0.4 mol/l surface heat flux was high even when $T_w > 210$°C (see Fig. 7), and there was no longer an initial period of slow cooling. It took only about 1 s to quench the test surface down to 120°C.

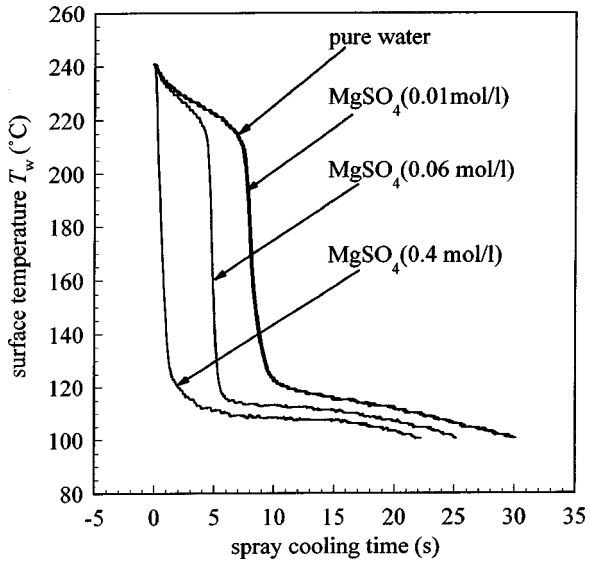

Fig. 9 The effect of salt concentration on surface temperature variation during spray cooling with $MgSO_4$ solution. Spray mass flux $m_l = 3.0$ kg/m^{2}s and mean droplet velocity $U_m = 20$ m/s.

Conclusions

We conducted experiments on the effect of dissolving one of three salts (NaCl, Na_2SO_4 or $MgSO_4$) in water sprays used for cooling of a hot surface. The results were compared with those obtained using pure water sprays. Dissolved NaCl or Na_2SO_4 increased nucleate boiling heat transfer, but had little effect on transition boiling during spray cooling. $MgSO_4$ increased both nucleate and transition boiling heat flux. Enhanced nucleate boiling was attributed to foaming in the liquid film generated by the dissolved salts. $MgSO_4$ produced the largest increase in nucleate boiling heat transfer, Na_2SO_4 somewhat less and NaCl the least. This ranking of effectiveness corresponded to that previously observed for single droplets of water boiling on a hot surface [4]. A concentration of 0.2 mol/l of $MgSO_4$ produced the greatest increase in heat flux; higher salt concentrations did not result in further improvements. During transition boiling particles of $MgSO_4$ adhered to the heated surface, raising surface roughness and increasing heat transfer. Addition of salts can reduce the time required to cool a hot surface from 240°C to 120°C by an order of magnitude.

Acknowledgments

The authors gratefully acknowledge the financial support of the Natural Sciences and Engineering Research Council of Canada for this project.

Nomenclature

d_{05} = mass median diameter, m
d_{32} = Sauter mean diameter (SMD), m
g = acceleration due to gravity, m/s^2
h_f = height of nozzle above surface, m
m_1 = spray mass flux, kg/m^{2}s
Δp = pressure drop across nozzle, N/m^2
q'' = surface heat flux, W/m^2
t = time, s
T_{max} = surface temperature at the critical heat flux
T_w = surface temperature, °C
U_m = mean droplet impact velocity, m/s
U_o = upstream velocity of the nozzle and relative velocity of the droplet to the test surface, m/s; initial droplet velocity, m/s

Greek Symbols

ρ = density, kg/m^3
σ = surface tension, N/m

References

[1] Qiao, Y. M., and Chandra, S., 1998, "Spray Cooling Enhancement by Addition of a Surfactant," ASME J. Heat Transfer, **120**, pp. 92–98.
[2] Jia, W., and Qiu, H. H., 2001, "Experimental Investigation of Droplet Dynamics and Heat Transfer in Spray Cooling," Proceedings of the 35th National Heat Transfer Conference, Paper NHTC2001-20109.
[3] Cui, Q., Chandra, S., and McCahan, S., 2001, "The Effect of Dissolving Gases or Solids in Water Droplets Boiling on a Hot Surface," ASME J. Heat Transfer, **123**, pp. 719–728.
[4] Cui, Q., Chandra, S., and McCahan, S., 2002, "The Effect of Dissolving Salts in Water Sprays Used for Quenching a Hot Surface. Part 1: Boiling of Single Droplets," ASME J. Heat Transfer, submitted.
[5] Cui, Q., 2001, "The Effect of Dissolving Salts or Gases in Water Sprayed on a Hot Surface," Ph.D. thesis, University of Toronto, Toronto, ON, Canada.
[6] Ghodbane, M., and Holman, J. P., 1991, "Experimental Study of Spray Cooling With Freon-113," Int. J. Heat Mass Transf., **34**, pp. 1163–1174.
[7] Qiao, Y. M., 1996, "Effect of Gravity and Surfactant on Spray Cooling of Hot Surfaces," Ph.D. thesis, University of Toronto, Toronto, ON, Canada.
[8] Zaytsev, I. D., and Aseyev, G. G., 1992, *Properties of Aqueous Solutions of Electrolytes*, CRC Press, Boca Raton, FL.

[9] Mudawar, I., and Valentine, W. S., 1989, ''Determination of the Local Quench Curve for Spray Cooled Metallic Surfaces,'' Journal of Heat Treating, **7**, pp. 107–121.
[10] Yao, S. C., and Choi, K. J., 1987, ''Heat Transfer Experiments of Mono-Dispersed Vertically Impacting Sprays,'' Int. J. Multiphase Flow, **13**(5), pp. 639–648.
[11] Beck, J. V., Litkouhi, B., and St. Clair, C. R., Jr., 1982, ''Efficient Sequential Solution of the Nonlinear Heat Conduction Problem,'' Numer. Heat Transfer, **5**, pp. 275–286.
[12] Pais, M. R., Chow, L. C., and Mahekey, E. T., 1992, ''Surface Roughness and Its Effects on the Heat Transfer Mechanism in Spray Cooling,'' ASME J. Heat Transfer, **114**, pp. 211–219.

Conjugate Heat Transfer and Effects of Interfacial Heat Flux During the Solidification Process of Continuous Castings

M. Ruhul Amin
e-mail: ramin@me.montana.edu

Nikhil L. Gawas
Department of Mechanical & Industrial Engineering,
Montana State University,
Bozeman, MT 59717

Multiphase fluid flow involving solidification is common in many industrial processes such as extrusion, continuous casting, drawing, etc. The present study concentrates on the study of air gap formation due to metal shrinkage on the interfacial heat transfer of a continuous casting mold. Enthalpy method was employed to model the solidification of continuously moving metal. The effect of basic process parameters mainly superheat, withdrawal velocity, mold cooling rate and the post mold cooling rate on the heat transfer was studied. The results of cases run with air gap formation were also compared with those without air gap formation to understand the phenomenon comprehensively. The current study shows that there exists a limiting value of Pe above which the effect of air gap formation on the overall heat transfer is negligible. [DOI: 10.1115/1.1560146]

Keywords: Heat Transfer, Interface, Melting, Solidification

Introduction

Thermal transport phenomenon plays an important role in engineering applications especially in manufacturing processes such as continuous casting, optical fiber drawing, hot rolling, metal wire drawing, etc. Continuous casting is a rapidly developing field and has gained prime importance in the manufacturing of ferrous and non-ferrous slabs. A substantial amount of steel is produced by continuous casting every year. In a typical continuous casting process, superheated metal enters an open ended metal mold via a tundish and a nozzle. The metal is cooled due to heat exchange with the water-cooled mold. As the metal shell forms, it is continuously withdrawn from the exit of the mold through pinch rollers. Lubrication is provided with the help of mold flux, which prevents the liquid metal from sticking to the mold wall. On exit, the metal shell is subjected to spray cooling before finally being cut off by a gas torch. Serious problems are encountered during continuous casting if the process parameters are not carefully monitored and controlled. The heat extraction rate and the withdrawal speed are critical and can lead to breakout without proper control. Breakout is a serious condition where the metal shell formed cannot withstand the ferrostatic pressure of the liquid core due to insufficient shell thickness. The solid metal breaks, spilling out hot liquid metal leading to formidable damages and repairs.

Numerical modeling of continuous casting dates back almost five decades. Primarily two numerical approaches have been adopted to solve this problem; one is the moving grid technique and the second is the fixed grid technique. The fixed grid technique takes care of the latent heat evolution by introducing nonlinearities in the specific heat or enthalpy of the material, whereas, the moving grid technique involves the change of grid points with time. The fixed grid method is easy to implement whereas the moving grid method is more accurate but difficult to implement. Phase change problems are highly non-linear due to the presence of a boundary (solidification front) across which the properties vary like a Dirac-δ-type behavior. In such problems, the numerical simulations for the temperature history and/or the location of the solidification front result in either overprediction or underprediction, as well as numerical oscillations about the true response as pointed out by Namburu and Tamma [1]. Finite difference methods were traditionally employed for analyzing the phase change problems, but lately, numerical analysts are focusing more on finite element analysis (FEA) due to their inherent advantages in handling the evolution of latent heat. By employing finite elements in conjunction with numerical integration, a reasonable accuracy can be obtained for sufficiently smooth variations of the effective heat transfer capacity [1]. In this research the enthalpy based fixed grid method has been employed to model the thermal transport accompanied by solidification.

Several parameters governing the process need to be studied carefully in order to streamline the continuous casting process. Typical parameters include superheat temperature, withdrawal velocity, mold cooling rate and post-mold cooling rate. Metal shrinkage leads to the development of an air gap at the metal mold interface causing a formidable decrease in the heat transfer rate. Air gap at the metal-mold interface results in decreased contact conductance, thus decreasing the overall effective heat transfer rate. This leads to higher mold temperatures and lower heat transfer efficiency. Mold heat transfer is governed by the size of the gap separating the solidifying shell from the wall of the cooling mold and the properties of the flux which infiltrates the gap. Application of inverse techniques was one of the common methods used to quantify the contact conductance at the metal mold interface. Inverse techniques are usually used to back calculate the heat transfer coefficient when the temperature profile is known. Mechanism of heat transfer at a metal mold interface was studied by Ho and Pehlke [2] for ingot casting. A numerical procedure was also presented which was based on the non-linear technique of Beck [3] and an implicit formulation of the enthalpy method. Three different mechanisms were expected to affect the transition of a metal-mold solid contact to an interfacial gap, namely, surface interaction of the metal and the mold, transformation of metal and mold materials and effects of the geometry. Huang et al. [4] presented the conjugate gradient method for the inverse solution to determine unknown contact conductance during metal casting. The advantage of the conjugate gradient method was that there was no need to assume a specific functional form over the specific domain. Ho [5] has characterized the metal mold interface heat transfer in continuous casting of slabs. A continuous casting model was formulated based on a spreadsheet program. This

Contributed by the Heat Transfer Division for publication in the JOURNAL OF HEAT TRANSFER. Manuscript received by the Heat Transfer Division May 2, 2002; revision received October 28, 2002. Associate Editor: C. Amon.

model was coupled with the interface model to integrate the phenomenon. A relationship characterizing the temperature dependency of mold flux viscosity was introduced and incorporated in the fluid flow equations for liquid mold flux. Isaac et al. [6] simulated the solidification of aluminum in cast iron mold using experimental values of air gap.

Investigators like Blackwell and Ockendon [7], Chidiac et al. [8], DeBellis and LeBeau [9], Kang and Jaluria [10], have carried out numerical investigation of continuous casting process using the enthalpy method which has been widely used in phase change problems. Metal-mold heat transfer has been studied by several other investigators like Kim et al. [11], Piwonka and Berry [12], Ho and Pehlke [13], Droste et al. [14]. Recently several investigators like Holzhauser et al. [15], Stone and Thomas [16] and Cho et al. [17] have performed experimental investigations on the mold-metal thermal resistance due to mold flux. Various expressions for evaluating metal-mold heat transfer coefficient have been compiled by Brimacombe et al. [18] which take into account factors like chill properties, transient effects and conjugate heat transfer.

Although a lot of information is available on the metal-mold interface heat transfer for metal ingot castings, where the inverse solution was attempted, no data could be found regarding the same in continuous castings for pure metals. Extensive studies have been conducted to include all kinds of process parameters but at the expense of computational time and space. Thus, the process of continuous casting entails efficient and simple models to simulate the phenomena realistically. Simplified formulations have to be explored and their results compared, to benchmark the adequacy of the models. The present method is simple as it employs linear 1D conduction to model the air gap formation to account for metal-mold contact conductance. The details of this method are shown at a later section. A finite element method was used to simulate the 2D solidification process coupled with conjugate heat transfer during continuous casting. Conduction and convection were the primary modes of heat transfer.

Mathematical Formulation

Figure 1 shows the geometry of the present numerical investigation. Aluminum was chosen for the cast material while the mold material was copper. The pre-mold region was assumed to be insulated whereas the mold surface and the post mold region was subjected to convective heat transfer. Aluminum was modeled as Newtonian incompressible fluid with Boussinesq approximation. The fluid flow was assumed to be laminar and two-dimensional. The symmetry of the problem allowed for modeling half of the domain for computational purpose. The left half of the domain was modeled and a transient algorithm was used. The post mold wall exit was taken as the origin. An aspect ratio, Ar=20 was used in the present research. Various mold parameters shown in Fig. 1 were, $L_3/L=0.5$, $L_1/L=0.1$, and $t_m/W=0.25$.

A commercial finite element code called Ansys [19] was used for the numerical investigation. A user routine was developed to include multiphase fluid flow accompanied by solidification. The user routine was validated with analytical and experimental information to gain confidence. The ultimate objective was to study the effect of air gap formation on the interfacial heat transfer. So, the original algorithm was modified to include interfacial heat resistance to model the air gap formation. Numerical simulations were conducted on a Silicon Graphics Inc. (SGI) Origin 200 server.

Governing Equations. The following assumptions were made to simplify the current study involving conjugate heat transfer:

1. The fluid is Newtonian, incompressible with Boussinesq approximation.
2. The fluid flow is laminar in the liquid region.
3. There is negligible change in the density with change in phase. For numerical purposes, the density was assumed to be same in both the phases. However, shrinkage was calculated based on the linear coefficient of expansion of the material.
4. Materials were considered homogeneous and isotropic.
5. Material properties were constant within individual phases.
6. Viscous work and dissipation are neglected.
7. In the phase transition zone (ΔT), the thermal conductivity of the domain is equal to the thermal conductivity of the solid phase. Phase transition zone is the temperature difference over which the evolution of latent heat takes place and is explained later.

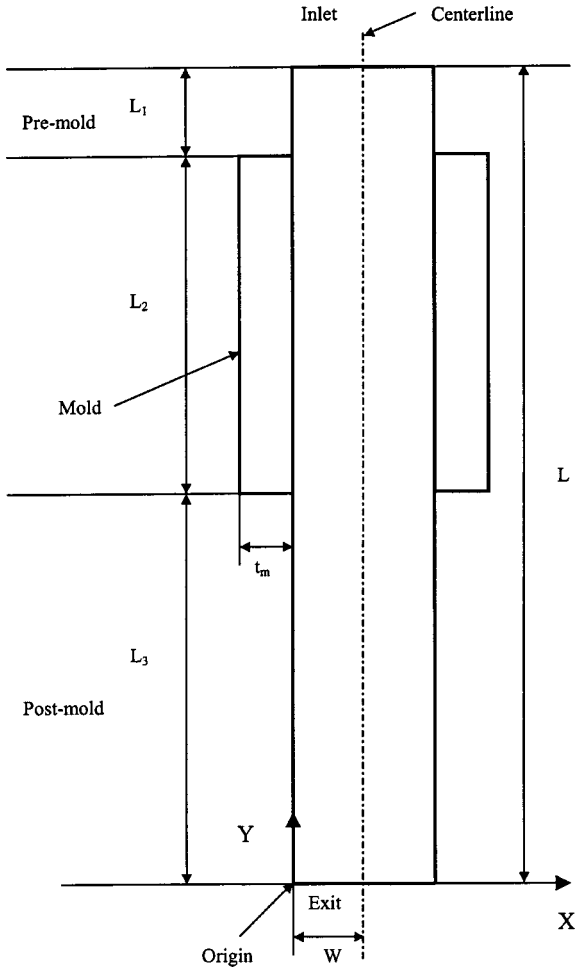

Fig. 1 Problem domain in terms of dimensional parameters

Based on these assumptions the governing equations can be expressed as follows.

Continuity Equation.

$$\frac{\partial(V_x)}{\partial x}+\frac{\partial(V_y)}{\partial y}=0 \tag{1}$$

Momentum Equations. The momentum equations in the x and y directions, commonly known as the Navier-Stokes equations, govern the fluid flow and are given by:

$$\rho\frac{\partial V_x}{\partial t}+\rho V_x\frac{\partial V_x}{\partial x}+\rho V_y\frac{\partial V_x}{\partial y}=-\frac{\partial P}{\partial x}+\mu\left[\frac{\partial^2 V_x}{\partial x^2}+\frac{\partial^2 V_x}{\partial y^2}\right] \tag{2}$$

$$\rho\frac{\partial V_y}{\partial t}+\rho V_x\frac{\partial V_y}{\partial x}+\rho V_y\frac{\partial V_y}{\partial y}=-\frac{\partial P}{\partial y}+\mu\left[\frac{\partial^2 V_y}{\partial x^2}+\frac{\partial^2 V_y}{\partial y^2}\right]+\rho g_y\beta(T-T_\infty) \tag{3}$$

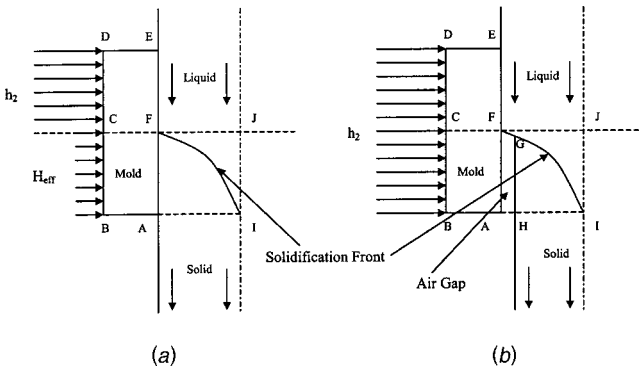

Fig. 2 (*a*), (*b*) Effective heat transfer coefficient formulation

Energy Equation.

$$\rho C\left[\frac{\partial T}{\partial t}+V_x\frac{\partial T}{\partial x}+V_y\frac{\partial T}{\partial y}\right]=k\left[\frac{\partial^2 T}{\partial x^2}+\frac{\partial^2 T}{\partial y^2}\right] \tag{4}$$

The energy equation is the thermal transport equation. As stated earlier, the density of the liquid is constant throughout the domain but subject to the Boussinesq approximation and the specific heat and the thermal conductivity are evaluated according to their respective phases in the domain. The momentum equation is coupled with the energy equation. In the liquid region, both momentum and energy equations are solved simultaneously to determine the temperature field. In the solid phase, the X component of velocity is set to zero while the withdrawal speed U_0 is substituted for the Y velocity component. Thus, the only governing equation in the solid phase is the energy equation. The solidification front position was identified by comparing the nodal temperature with the solidification temperature of the material. If the solidification front passed between two nodes then linear interpolation was used to determine its exact position. The boundary conditions are convection on the mold surfaces (Bi_2) and the post mold region (Bi_3), superheat temperature at the inlet (θ_0), zero axial thermal gradient at the exit and insulated pre-mold. The metal was assumed to enter and exit the mold with withdrawal speed whereas no slip boundary condition was applied on the wall.

A physical quantity, namely enthalpy was introduced to handle the solidification process. Enthalpy is defined as the integral of heat capacity with respect to temperature. Thus,

$$H=\int_{T_0}^{T}\rho\cdot C(T)dT \tag{5}$$

or equivalently,

$$\frac{dH}{dT}=\rho\cdot C(T) \tag{6}$$

The derivative in the above equation is numerically averaged over each element, from which the value of ρC is obtained.

The enthalpy method incorporates the latent heat in the specific heat of the material.

$$\rho\cdot C(T)=\rho\cdot C_s \qquad \text{for } T<T_1 \tag{7}$$

$$\rho\cdot C(T)=\rho\cdot C^*=\rho\cdot\left(\frac{L_h}{\Delta T}\right) \qquad \text{for } T_1<T<T_2 \tag{8}$$

$$\rho\cdot C(T)=\rho\cdot C_l \qquad \text{for } T>T_2 \tag{9}$$

Here, T_1 and T_2 are the solidus and liquidus temperatures respectively, and ΔT is the difference between them. The energy equation was formulated using temperature but for solidification process, enthalpy was incorporated using Eqs. (5) through (9).

Interface Heat Flux Model Formulation. In the present research, the air gap was modeled in terms of appropriate heat resistance. Figures 2(*a*) and (*b*) display the magnified sketch of the mold where the heat resistance due to air gap was incorporated in terms of effective convective heat transfer coefficient (H_{eff}) on the vertical face of the mold. The air gap which forms at the interface (Fig. 2(*b*)) is modeled by applying an effective heat resistance. This equivalent heat resistance is incorporated by changing the convective coefficient on the vertical mold surface. It is to be noted that the effective heat transfer coefficient, H_{eff}, which is less than mold cooling rate (h_2), is applied on the vertical surface of the mold that corresponds to the length of the air gap and is shown in Fig. 2(*a*). Thus, the heat transfer on the vertical face of the mold is governed by the effective heat transfer coefficient (H_{eff}) and the mold cooling rate (h_2). Assumptions in the formulation of the interfacial gap, based on the findings of Refs. [2], [13], are as follows:

1. Shrinkage of the solid metal is uniform based on an average temperature; the shape of the air gap is uniform and continuous.
2. The physical dimensions of the air gap formed are small enough to neglect their effect on the thermal transport due to the change in the shape of the domain.
3. Heat flow in the gap is by pure conduction.

It should be noted here that although convection may have some effect at the gap, it is neglected to keep the current model tractable. At this time it is not known the effect of neglecting the convection at the interface gap. One possibility is to have less solidification than the actual process. Future work is underway to study the effect of convection.

Referring to Fig. 2 and equating the resistances from the first principle, the following expression for effective heat transfer coefficient can be obtained

$$H_{\text{eff}}=\left(\frac{k_{\text{air}}\cdot h_2}{k_{\text{air}}+X_{\text{gap}}\cdot h_2}\right) \tag{10}$$

Air gap width is calculated based on the two-dimensional metal shrinkage in the mold region. Metal shrinkage can be calculated as follows:

$$X_{\text{gap}}=\frac{\Delta A}{L_m} \tag{11}$$

$$\Delta A=A_1\cdot\beta\cdot\delta T \tag{12}$$

where A_1=Area of the solidified metal in the mold region (Area AFJI in Fig. 2(*a*))

ΔA=shrinkage area
$\beta=2\cdot\alpha$, where α is the linear coefficient of expansion
δT=temperature difference=$(T_{\text{avg}}-T_s)$
T_{avg}=average temperature of the solidified region
T_s=solidification temperature of the material
L_m=the vertical length of the solid shell on the copper mold wall, which is equal to the length of the segment AF in Fig. 2(*a*)

Detailed derivation in this regard can be found in Gawas [20]. Equation (10) incorporates metal-mold contact conductance due to air gap formation and hence it is also representative of the interface heat flux.

Numerical Procedure

Due to the inherent symmetry of the model, half of the geometry shown in Fig. 1 was used. A commercial code called Ansys [19] was used for the numerical exercise. The computational grid comprised of non-uniform four noded elements and was denser near the mold walls because of high temperature and velocity gradients. A user algorithm was setup to model the process of continuous casting which was further modified to incorporate the interfacial heat transfer based on shrinkage. The flow diagram for

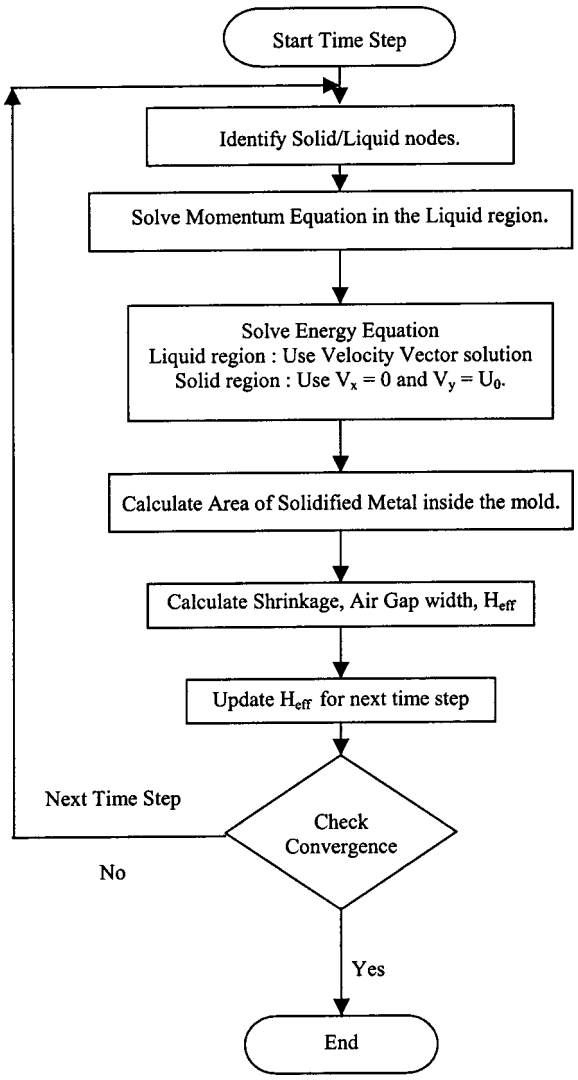

Fig. 3 Flow chart for the algorithm to incorporate effective heat resistance due to air gap

the algorithm to model the effective air gap heat resistance at the interface is illustrated in Fig. 3. The effective heat resistance was accounted for by changing the coefficient of convective heat transfer on the outer surface of the copper mold. In each time step, the effective heat transfer coefficient was calculated based on the formulation. The boundary condition, H_{eff}, on the outer surface of the mold was then updated for the next time step. Time step was carefully controlled to avoid divergence due to inherent stiffness of the problem. The following convergence criteria was used:

$$\text{Convergence Monitor} = \sum_{i=1}^{n} \frac{|\phi_i^k - \phi_i^{k-1}|}{|\phi_i^k|}$$

It represents the normalized rate of convergence for the degree of freedom variables, namely temperature and velocity, using the current kth iteration and the previous $(k-1)$th iteration. The convergence monitor was set to 10^{-6} for the current study.

Code Validation. The present code and the user algorithm was validated by comparing the results, namely the location of the solidification front, with analytical results by Siegel [21] and experimental data by Wolff and Viskanta [22]. As seen from Figs. 4 and 5, the results obtained by the present method are in good agreement with the published analytical results and experimental data. The accuracy of the present method was further validated by

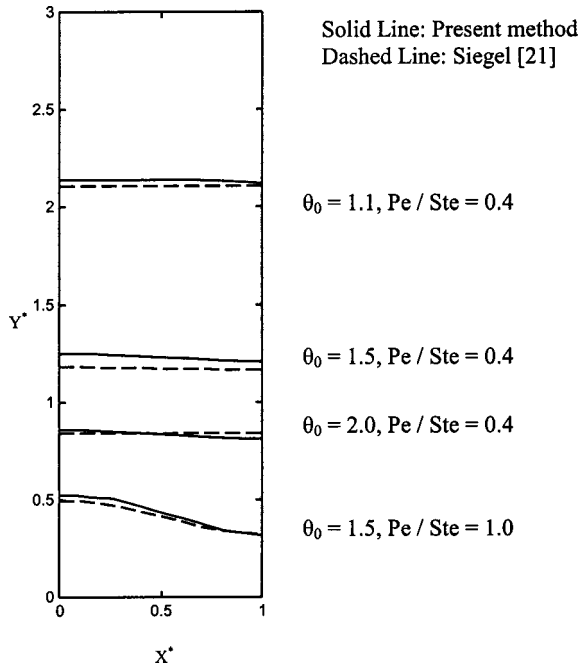

Fig. 4 Comparison of numerically obtained solidification front positions with analytical results by Siegel [21]

a grid independency test. Two different grids were examined—one with 2600 elements and the other with 5700 elements. The grids were tested by running a stiff case with high values of process parameters. It was found that the maximum temperature difference along the wall and the centerline was equal to 2 percent and 1 percent respectively. Hence, the grid with 2600 elements was used in the present study. Details in this regard can be found in [20]. It should be noted here that Ref. [21] was for solidification process of a very slowly moving metal, and Ref. [19] was for stationary liquid metal. Interfacial heat flux was not considered in these works. However, the objective here was to validate if the current method can be used to solve solidification problems.

Results and Discussion

The objective of the present research was to study the effect of air gap formation on different process parameters. Numerical investigation was performed to determine the effect of each param-

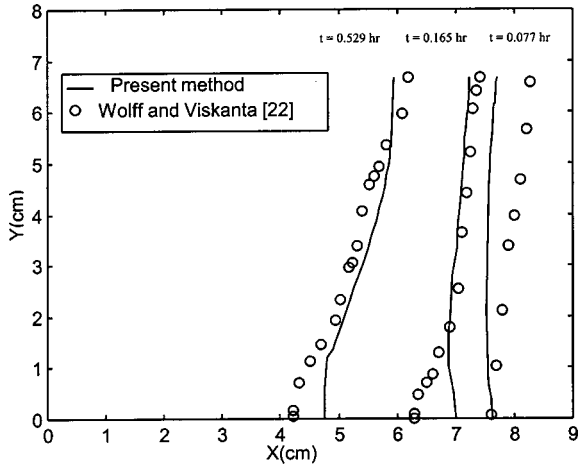

Fig. 5 Comparison of numerically obtained solidification front positions with experimental data by Wolff and Viskanta [22]

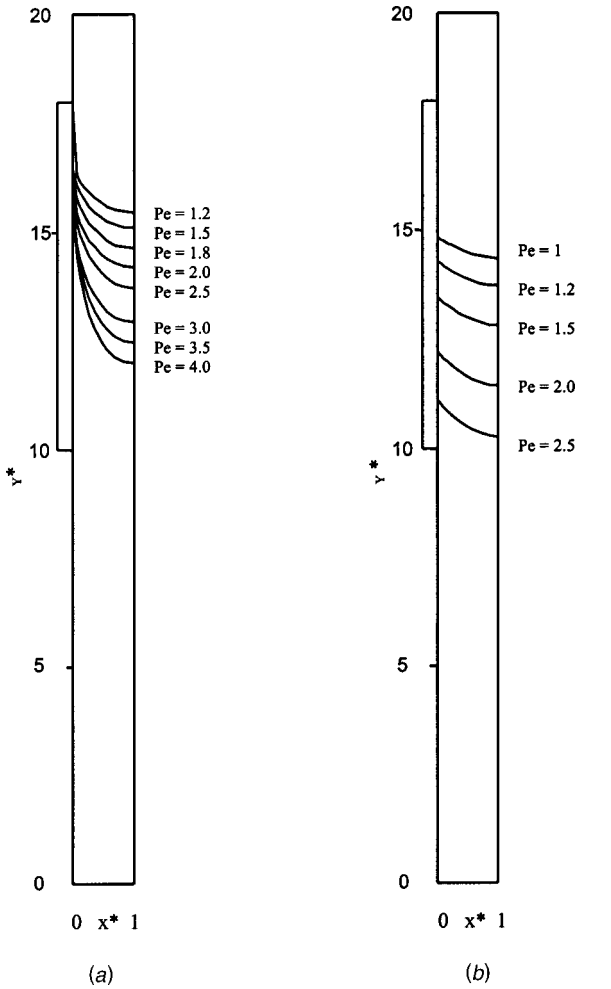

Fig. 6 Effect of withdrawal speed on solidification front: (*a*) $\theta_0=1.2$, $Bi_2=0.1$, $Bi_3=0.15$; and (*b*) $\theta_0=1.2$, $Bi_2=0.02$, $Bi_3=0.05$.

eter, namely withdrawal speed (Pe), superheat (θ_0), mold cooling rate (Bi_2) and post mold cooling rate (Bi_3). The ranges of parameters used in the present study were Pe=1–4, $\theta_0=1.2$–3.0, $Bi_2=0.02$–0.1, and $Bi_3=0.05$–0.15. The governing equations were solved in terms of primitive variables and the results obtained were non-dimensionalized with the help of various non-dimensional parameters stated in the nomenclature. The pre-mold was insulated whereas the Stefan number (St) was equal to 2.5 throughout the exercise. The cast metal and the mold were made of aluminum and copper respectively. A few cases were also investigated to compare the results of the interfacial model with the noninterfacial model, i.e., neglecting the effects of air gap formation.

Figure 6 shows the effect of withdrawal speed on the solidification front position with air gap formation. The phenomenon of continuous casting is a transient one and hence as the Peclet number (Pe) increases, the liquid metal has higher velocities and less time to cool and consequently the phase front moves down the mold. The movement of the phase front is more prominent in Case (b) as compared to Case (a), because Case (b) has relatively lower cooling rates. Also, the slope of the front becomes steeper with increase in Pe, the steepest slope is exhibited at Pe=4.0 for $\theta_0=1.2$, $Bi_2=0.1$, $Bi_3=0.15$. For higher mold cooling rates, the position of the solidification front on the wall differs by small magnitudes as compared to that with Case (b). No breakout condition was observed, in spite of high values of Peclet number.

Variation of nondimensional local heat flux along the wall for

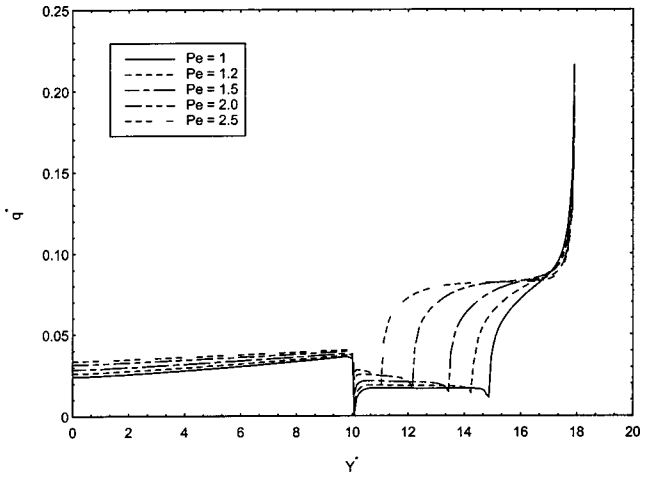

Fig. 7 Effect of withdrawal speed on non-dimensional local heat flux on the wall for $\theta_0=1.2$, $Bi_2=0.02$, $Bi_3=0.05$

$\theta_0=1.2$, $Bi_2=0.02$, $Bi_3=0.05$, Pe=1, 1.2, 1.5, 2.0, 2.5 is shown in Fig. 7. In the upstream direction there is a sharp drop in the heat flux from $Y^*=18$ (the entry of mold region) to the point of inception of the solidification front. The local heat flux remains almost constant from the solidification front position on the wall till the mold exit ($Y^*=0$). In part of the mold region ($10\leqslant Y^*\leqslant 18$), depending of the value of Pe, lower values of local heat flux along the wall are observed. This can be attributed to the air gap formation as it leads to higher thermal resistance or lower contact conductance. At $Y^*=10$, the flux increases as the metal exits the mold where the air gap ceases to exist. The discontinuity in the curves at $Y^*=10$ is due to the change in the boundary condition at the mold exit ($Bi_2\neq Bi_3$). Figure 8 shows the variation of wall temperature versus Y^*. The slope changes abruptly at $Y^*=18$ as a result of the change in the boundary condition from the pre-mold region ($Y^*=18$ to 20) to the mold region ($Y^*=10$ to 18). It can be seen from the figure that the wall temperature increases with increase in Y^*, i.e., along the upstream direction. There was a noticeable change in slope of the temperature profile at $Y^*=10$, which indicated higher mold temperatures, again due to the increased heat resistance incurred by the air gap formation. As expected, higher Peclet numbers lead to higher wall tempera-

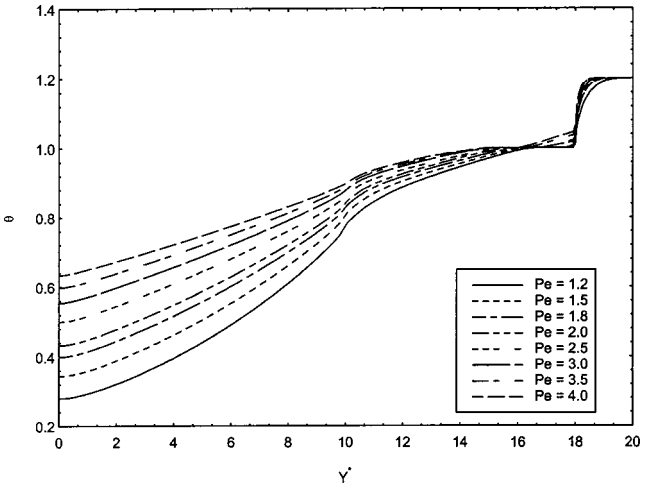

Fig. 8 Effect of withdrawal speed on wall temperature for $\theta_0=1.2$, $Bi_2=0.1$, $Bi_3=0.15$

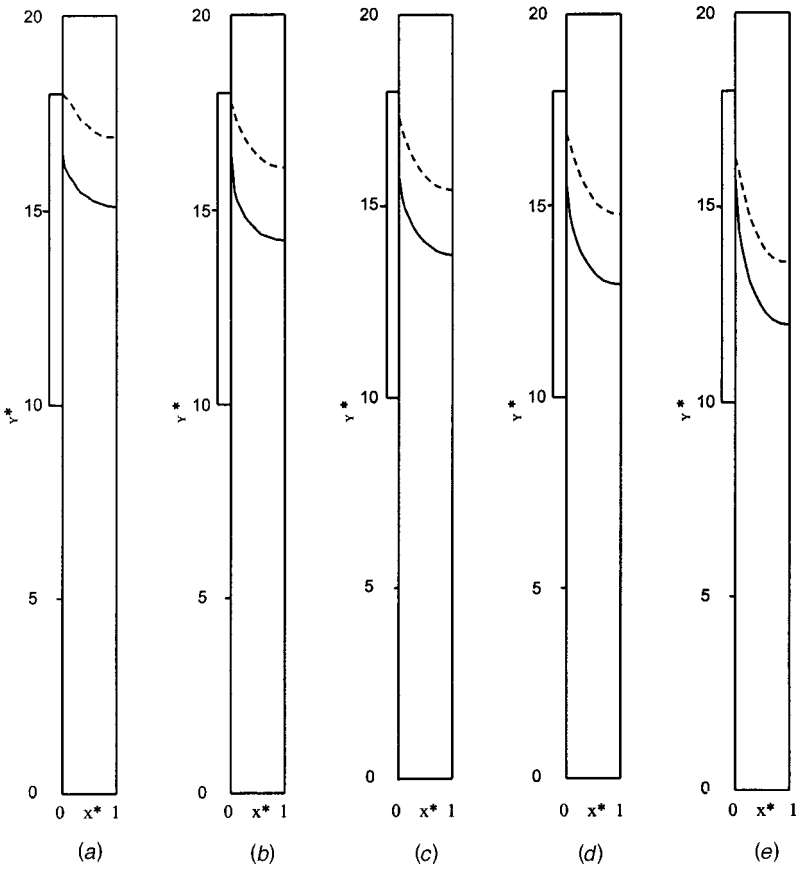

Fig. 9 Comparison of solidification front positions for $\theta_0=1.2$, $Bi_2=0.1$, $Bi_3=0.15$, (*a*) Pe=1.5, (*b*) Pe=2.0, (*c*) Pe=2.5, (*d*) Pe=3.0, and (*e*) Pe=4.0, Dotted line: Without interfacial heat flux, Solid line: With interfacial heat flux.

tures due to the transient nature of the problem. Therefore, it can be stated that the average temperature of the system increases with increase in Peclet number.

Figures 9 and 10 show the relative positions of the solidification fronts for $\theta_0=1.2$, $Bi_2=0.1$, $Bi_3=0.15$, Pe=1.5, 2.0, 2.5, 3.0, 4.0, and $\theta_0=1.2$, $Bi_2=0.02$, $Bi_3=0.05$, Pe=2.0, 2.5, respectively. In these figures the solid lines represent the results when interfacial heat flux was considered. The dotted lines in the figures are corresponding results without taking the interfacial heat flux into account. It is to be noted that with increase in the air gap width there is a decrease in the effective heat transfer coefficient H_{eff}. Consequently, it leads to lower thermal efficiency of the system relative to the initial cooling rate Bi_2. Lower heat extraction rate in the mold means hotter fluid flows through the mold. Hence the solidification front moves downstream with respect to the same cases run without interface heat flux modeling and is demonstrated in Fig. 9. It is also observed from Fig. 9 that the slope of the solidification front for the cases with interfacial heat flux was steeper with respect to that of the non-interfacial heat flux model.

Figures 10(*a*) and (*b*) show the solidification fronts for Pe=2.0 and Pe=2.5 with lower cooling rates ($\theta_0=1.2$, $Bi_2=0.02$, $Bi_3=0.05$), respectively. It can be noted that the air gap does not influence the position and the shape of the phase front significantly for the given parameters. This is because, a combination of higher withdrawal speed (Pe=2.0, Pe=2.5) and lower cooling rates ($Bi_2=0.02$, $Bi_3=0.05$) leads to the downstream movement of the solidification front. When the solidification front moves downstream, less solidified metal is in the mold. That means the volume of the solidified metal in the mold is less, leading to lesser shrinkage or smaller air gap width. It should be noted that the shrinkage is directly proportional to the volume of the solidified metal in the mold. In fact as seen in Figure 10(*b*) ($\theta_0=1.2$, Pe=2.5, $Bi_2=0.02$, $Bi_3=0.05$), the solidification fronts for both interfacial and non-interfacial models are almost indistinguishable. This is because as the air gap width tends to zero, the value of the nondimensionalized heat transfer coefficient H^* approaches the Bi_2 value which is prominently demonstrated in the present cases. Therefore, it can be said that for a given set of parameters and conditions in the study of withdrawal speed, there exists a limiting value of Pe above which the effect of air gap formation on the overall heat transfer is negligible.

Figure 11 shows the local heat flux variation for different superheat values. The air gap had a considerable effect on the local non-dimensional heat flux for the case with $\theta_0=1.2$, Pe=1.5, $Bi_2=0.1$, $Bi_3=0.15$. At this superheat value, the nondimensional effective heat transfer coefficient, H^* was 2×10^{-2}, resulting a decrease in the value of Bi_2 (due to air gap thermal resistance) by about 80 percent. This led to a drastic reduction in local heat flux which was due to a combination of low withdrawal speed, low superheat and high cooling rates. In this case the solidification front moved upstream with lower superheat and withdrawal speed ($\theta_0=1.2$, Pe=1.5), resulting in a higher value of the volume of solidified metal in the mold. Consequently, more shrinkage of the metal occurred, which led to higher values of air gap width and subsequent drastic drop in local heat flux.

Figure 12 shows the solidification front location for cases executed with and without interface heat flux modeling for different superheat values. Dashed line represents the solidification front for the respective cases run without interface heat flux modeling whereas the solid line represents the solidification front with the interface heat flux. As seen in Fig. 12, the effect of air gap forma-

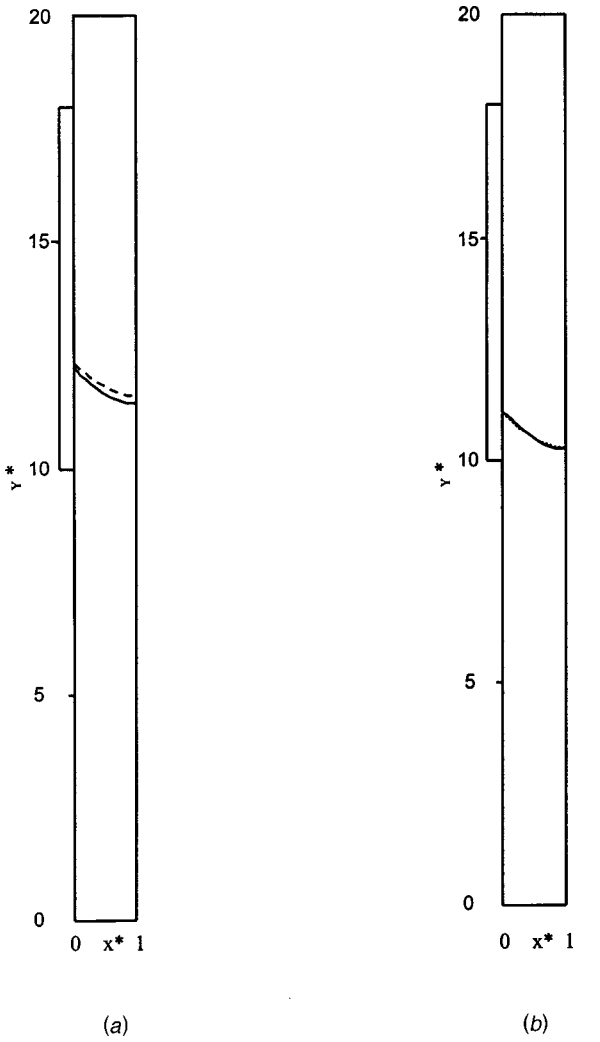

Fig. 10 Comparison of solidification front positions for $\theta_0 = 1.2$, $Bi_2 = 0.02$, $Bi_3 = 0.05$, (*a*) Pe=2.0, and (*b*) Pe=2.5, Dotted line: Without interfacial heat flux, Solid line: With interfacial heat flux.

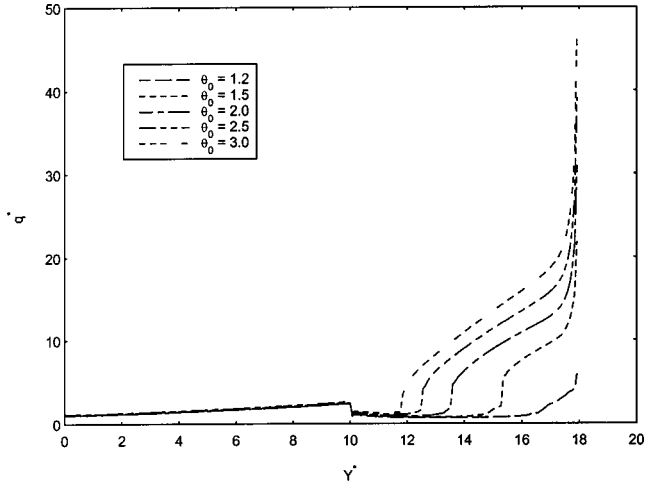

Fig. 11 Variation of local heat flux for different superheats for Pe=1.5, $Bi_2 = 0.1$, $Bi_3 = 0.15$

tion is more prominent at low superheat value ($\theta_0 = 1.2$) (Figs. 12(*a*) and (*c*)). The solidification front is significantly displaced downstream with the interface heat flux model with respect to the cases without interfacial heat flux. The difference between the front locations for interface and noninterface models considerably decreases with increase in superheat (Figs. 12(*b*) and (*d*)). Hence, it can be stated that the effect of air gap formation on the heat transfer is less significant with the increase in superheat. This is because, the volume of the solidified metal in the mold decreases with the increase in the superheat due to downstream movement of the solidification front. Less solid metal in the mold means smaller air gap, as there is a direct relationship between the shrinkage and the solid metal volume in the mold. Therefore, it can be concluded that if the solidified metal volume in the mold is considerably small, causing negligibly small air gap width, then the difference between the solidification front positions for the model with and without interfacial heat flux will be negligible.

A curve fit was obtained to yield a power law variation of the calculated non-dimensional air gap width with the superheat for various values of Pe. For both the cases, the cooling rates were set to $Bi_2 = 0.1$ and $Bi_3 = 0.15$. The corresponding graphs can be seen in Fig. 13. The diamond shaped symbol represents cases with Pe=1.5 and the corresponding equation is given by:

$$G^* = 0.0029 \cdot \theta_0^{-0.7585} \tag{13}$$

The rectangle shaped symbol represents cases with Pe=2.0 and the corresponding equation is given by:

$$G^* = 0.00211 \cdot \theta_0^{-1.1796} \tag{14}$$

The r^2 (variance) value for the Eqs. (13) and (14) was found to be equal to 0.9847 and 0.8998 respectively. The lower value of the variance for the second case is due to insufficient data points. The value of the variance turns out to be equal to unity for both cases if a polynomial curve fit is done. However, the power law curve fit equations are presented here because of its usefulness in practical applications. The previously described phenomena, that is, decrease in the air gap with increase in Pe and θ_0 is clearly visible here.

Figures 14(*a*) and (*b*) show the variation of overall nondimensional heat flux with respect to mold cooling rate, for $\theta_0 = 1.2$, Pe=2.0, $Bi_3 = 0.05$, 0.1, 0.15 and $\theta_0 = 1.2$, Pe=2.5, $Bi_3 = 0.05$, 0.1, 0.15 respectively. The overall nondimensional heat flux (Q^*) ranged from 1.01 to 2.2 for the present cases. As the mold cooling rate is increased from $Bi_2 = 0.02$ to $Bi_2 = 0.05$, the value of Q^* increases which shows that mold cooling rate is the dominant factor for heat transfer in spite of the interfacial air gap. Further increase in mold cooling rate from $Bi_2 = 0.05$ to $Bi_2 = 0.1$ results in a decrease in the value of Q^*. The maximum value of Q^* occurs at $Bi_2 = 0.05$ for the given process parameters and is seen in Figs. 14(*a*) and (*b*). This is because, increase in mold cooling rate from $Bi_2 = 0.05$ to $Bi_2 = 0.1$ leads to upstream movement of the solidification front. This means more metal is being solidified in the mold leading to more shrinkage and as such a higher value of air gap width and length. It is to be noted that both effective heat transfer coefficient (H_{eff}) and mold cooling rate (h_2) govern the overall heat flux, where, ($H_{\text{eff}} \ll h_2$). Due to the upstream movement of the solidification front, H_{eff} is applied over a significant length on the surface of the mold. Hence, the overall heat flux is dominated more by H_{eff} than h_2. Therefore, higher air gap width contributes a low value of effective heat transfer coefficient and thus reduces the heat transfer rate. This is the reason the decrease in the overall heat flux (after $\Theta_0 = 0.05$) is observed in Fig. 14. Thus the value of the volume of the solidified metal in the mold is crucial because it is directly related to the air gap width. The heat extraction efficiency of the mold is also affected in a similar way by the air gap formation.

In the current study it is observed that the solidification front location does not change significantly with the change in post mold cooling rate. This is because most of the total heat is ex-

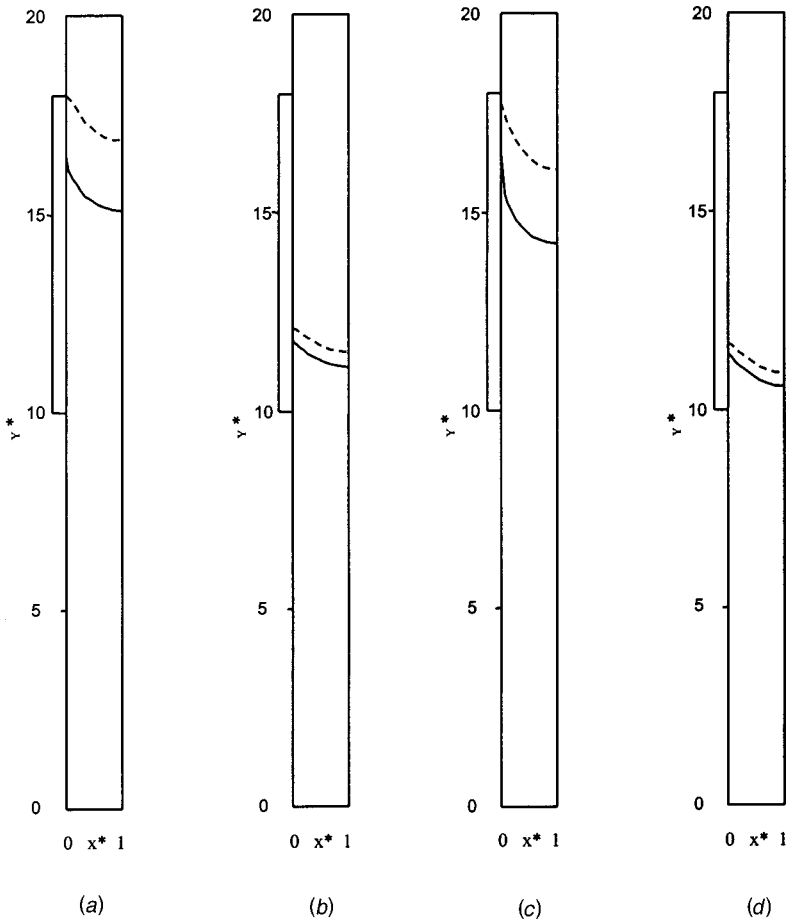

Fig. 12 Comparison of solidification front positions with and without interface heat flux modeling for $Bi_2=0.1$, $Bi_3=0.15$. (*a*) Pe=1.5, $\theta_0=1.2$, (*b*) Pe =1.5, $\theta_0=3.0$, (*c*) Pe=2.0, $\theta_0=1.2$, and (*d*) Pe=2.0, $\theta_0=2.5$, Dotted line: Without interfacial heat flux, Solid line: With interfacial heat flux.

tracted in the mold and hence the mold cooling rate dominates the cooling mechanism. The air gap modeling did not change this aspect of the process. It can be noted here that Greif [23] has also reported the negligible effect of post mold cooling rate on the solidification front position in his work, which did not take into account the air gap formation. By observing the corresponding

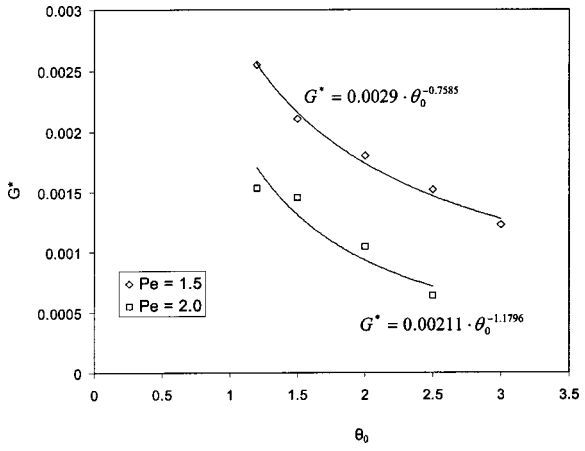

Fig. 13 Power law curve fit for the variation of nondimensional air gap width with superheat at different withdrawal speeds ($Bi_2=0.1$, $Bi_3=0.15$)

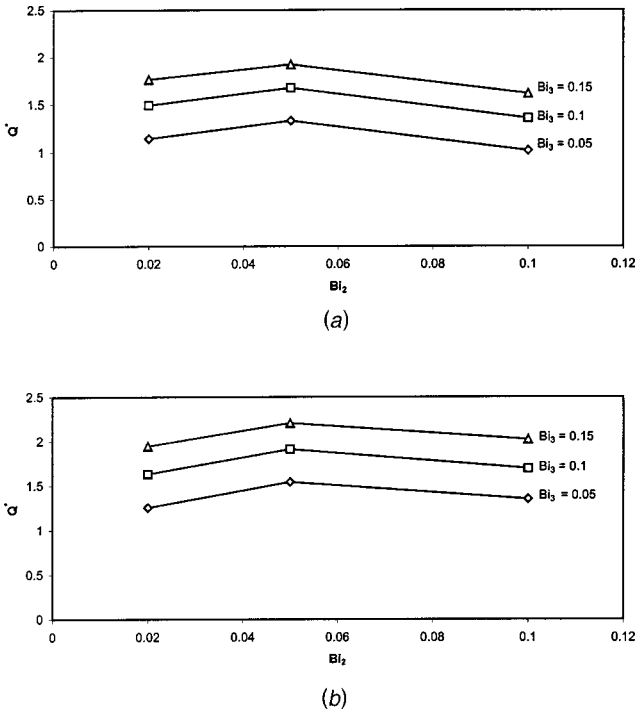

Fig. 14 Overall heat flux variation with respect to mold cooling rate for $\theta_0=1.2$, $Bi_3=0.05$, 0.1, 0.15 for different withdrawal speeds, (*a*) Pe=2.0, and (*b*) Pe=2.5

isotherms (not shown here due to space limitations), it can be concluded that the temperature distribution in the post mold region is significantly affected by change in cooling rate as more heat is removed from the withdrawn metal with the increase in Bi_3. The isotherms in the post mold region move upstream with increase in the post mold cooling rate. This was the case for all the parameters in the present study of post mold cooling rate. The temperature profile provides useful information on the metallurgical transformation of the metal and is critical in the case of alloys. It can also be stated that average temperature of the system decreases with the increase in post mold cooling. The position and the shape of the solidification front cannot be controlled by varying the post mold cooling rate. However, the temperature of the solid metal leaving the post mold region can definitely be controlled by changing the value of Bi_3. The temperature of the solid metal exiting the mold is of practical importance for subsequent metal handling operations.

Conclusions

The overall heat transfer was strongly affected by small values of air gap at the metal mold interface. The fact that air has very low conductivity explains this finding. The comparison of the results for cases run with and without interface heat flux modeling demonstrated major differences in the phase front locations, total heat flux and temperature distribution. Higher temperature in the mold region as well as sharp drop in heat flux was observed due to increased heat resistance at the solidified metal mold interface. However, in cases with higher superheat and withdrawal speed, the effect of air gap resistance, which is proportional to volume of the solidified metal in the mold, was minor.

The effect of withdrawal speed on the phase front and the temperature distribution was significant. Increase in withdrawal speed leads to steeper phase front for cases with higher cooling rates. At lower cooling rates ($Bi_2=0.02$, $Bi_3=0.05$) the solid front moves downstream, but the effect is more prominent. Higher Peclet numbers lead to more superheated fluid flowing in the mold resulting in higher heat fluxes. The effect of air gap decreases with increasing Peclet number as smaller air gap leads to lesser thermal resistance. Increase in Pe number pushes the solidification front downstream leading to smaller air gap width, and hence less effect of the inter facial heat flux on the cooling process. There exists a limiting value of Pe for a given set of process parameters beyond which the air gap does not affect the solidification front location and the local heat flux. The effect of air gap also diminishes at higher superheat temperature, as it leads to smaller air gap widths.

It was found that the overall heat flux in the mold increases with the increase in Bi_2 value from 0.02 to 0.05 and then decreases for values of Bi_2 from 0.05 to 0.1. This shows that, for the same superheat and withdrawal speed, the effective heat transfer coefficient, H_{eff}, dominates the overall heat transfer at higher mold cooling rates. Thus, a critical value of Bi_2 exists for a given set of parameters, which gives the maximum heat extraction rate. For the range of parameters studied here, critical value of Bi_2 was found to be to 0.05 for $\theta_0=1.2$, $Pe=2.0, 2.5$, $Bi_3=0.05, 0.1, 0.15$. The effect of post mold cooling rate was minor. Since most of the heat is extracted in the mold, the post mold cooling rate only affects the temperature distribution in the post mold region. The post mold cooling rate cannot be used to control the shape and the location of the solidification front.

Nomenclature

Ar = aspect ratio of cast material, L/W
Bi = Biot number, h W/k
C = specific heat
g = constant of gravity
G^* = nondimensional air gap width, X_{gap}/W
h = heat transfer coefficient
H^* = nondimensional effective heat transfer coefficient, $H_{\text{eff}}W/k_m$
H_{eff} = effective heat transfer coefficient
k = thermal conductivity
L = length of the cast material
L_h = latent heat of fusion
P = pressure
Pe = Peclet number, U_0W/α_s
q^* = nondimensional local heat flux
Q^* = average dimensionless heat flux
Ste = Stefan number, $C_s(T-T_\infty)/L_h$
t = time
T = temperature
U_0 = withdrawal speed
V_x = X component of velocity
V_y = Y component of velocity
W = half thickness of the cast material
x,y = spatial coordinates
X^*, Y^* = nondimensional spatial coordinates, x/W·y/W

Greek Symbols

α = thermal diffusivity (also coefficient of linear expansion where stated)
β = coefficient of volumetric expansion
δ = dirac-delta-function
μ = dynamic viscosity
ρ = density
θ = nondimensional temperature$=(T-T_\infty)/(T_s-T_\infty)$
θ_0 = superheat$=(T_0-T_\infty)/(T_s-T_\infty)$
Φ = degree of freedom variable

Subscripts

0 = condition at the inlet
1 = Pre-mold region property
2 = Mold region property
3 = Post mold region property
eff = effective value
gap = air gap property
l = liquid phase
m = mold property
s = solid property

References

[1] Namburu, R. R., and Tamma, K. R., 1990, ''Recent Advances, Trends and New Perspectives via Enthalpy-Based Finite Element Formulations for Applications to Solidification Problems,'' Int. J. Numer. Methods Eng., **30**, pp. 803–820.

[2] Ho, K., and Pehlke, R. D., 1984, ''Mechanisms of Heat Transfer at a Metal-Mold Interface,'' AFS Transactions, **92**, pp. 587–598.

[3] Beck, J. V., 1970, ''Nonlinear Estimation Applied to the Non-Linear Inverse Heat Conduction Problem,'' Int. J. Heat Mass Transf., **13**, pp. 703–716.

[4] Huang, C. H., Ozisik, M. N., and Sawaf, B., 1992, ''Conjugate Gradient Method for Determining Unknown Contact Conductance During Metal Casting,'' Int. J. Heat Mass Transf., **35**(7), pp. 1779–1786.

[5] Ho, B., 1992, ''Characterization of Interfacial Heat Transfer in the Continuous Slab Casting Process,'' M.S. thesis, University of Illinois, Urbana, IL.

[6] Isaac, J., Reddy, G. P., and Sharma, G. K., 1985, ''Variations of Heat Transfer Coefficients During Solidification of Castings in Metallic Moulds,'' The British Foundryman, **78**, pp. 465–468.

[7] Blackwell, J. H., and Ockendon, J. R., 1982, ''Exact Solution of a Stephan Problem Relevant to Continuous Casting,'' Int. J. Heat Mass Transf., **25**(7), pp. 1059–1060.

[8] Chidiac, S. E., Samarasekera, I. V., and Brimacombe, J. K., 1989, ''A Numerical Method for Analysis of Phase Change in the Continuous Casting Process,'' Proceedings of Numiform 89, E. C. Thompson, R. D. Wood, O. C. Zienkiewick, A. Samuelson, and A. A. Balkema, eds., The Netherlands, pp. 121–128.

[9] DeBellis, C. L., and LeBeau, S. E., 1989, ''A Verified Thermal Model for Continuous Casting Process,'' Heat Transfer in Manufacturing and Materials Processing, R. K. Shah ed., ASME 1989 National Heat Transfer Conference, NY, pp. 105–111.

[10] Kang, B. H., and Jaluria, Y., 1993, ''Thermal Modeling of the Continuous Casting Process,'' J. Thermophys. Heat Transfer, **7**(1), pp. 139–147.

[11] Kim, W. S., Ozisik, M. N., and Hector Jr., L. G., 1990, ''Inverse Problem of 1D Solidification for Determining Air-Gap Resistance to Heat Flow During Metal Casting,'' XXII ICHMT International Symposium on Manufacturing and Material Processing, Dubrovnik, Yugoslavia.

[12] Piwonka, T. S., and Berry, J. T., 1993, ''Heat Transfer at the Mold/Metal Interface in Investment Castings,'' Proceedings of the 41st Annual Technical Meeting—Investment Casting Institute, pp. 15:1–15:17.
[13] Ho, K., and Pehlke, R. D., 1985, ''Metal-Mold Interfacial Heat Transfer,'' Metall. Trans. B, **16B**, pp. 585–594.
[14] Droste, W., Engler, S., and Nishida, Y., 1986, ''The Air Gap Formation Process at the Casting Mold Interface and the Heat Transfer Mechanism Through the Gap,'' Metall. Trans. B, **17B**, pp. 833–844.
[15] Holzhauser, J.-F., Spitzer, K.-H., and Schwerdtfeger, K., 2001, ''Correction on: Laboratory Study of Heat Transfer Through Thin Layers of Casting Slag—Minimization of the Slag/Probe Contact Resistance,'' Steel Res., **72**(7), pp. 281–282.
[16] Stone, D. T., and Thomas, B. G., 1999, ''Measurement and Modeling of Heat Transfer Across Interfacial Mold Flux Layers,'' Can. Metall. Q., **38**(5), pp. 363–375.
[17] Cho, J. W., Emi, T., Shibata, H., and Suzuki, M., 1998, ''Heat Transfer Across Mold Flux Film in Mold During Initial Solidification in Continuous Casting of Steel,'' ISIJ International, **38**(8), pp. 834–842.
[18] Brimacombe, J. K., Muojekwu, C. A., and Samarasekera, I. V., 1995, ''Heat Transfer and Microstructure During Early Stages of Solidification,'' Metall. Mater. Trans. B, **26B**, pp. 361–382.
[19] Ansys, 1999, *Commands Reference Manual*, Version 5.6, Eight Edition, SAS IP Inc.
[20] Gawas, N. L., 2001, ''Numerical Modeling of Solidification Process During Continuous Casting Including the Effects of Interface Heat Flux,'' M.S. thesis, Montana State University, Bozeman, MT.
[21] Siegel, R., 1984, ''Two-Region Analysis of Interface Shape in Continuous Casting With Superheated Liquid,'' ASME J. Heat Transfer, **106**, pp. 506–511.
[22] Wolff, F., and Viskanta, R., 1988, ''Solidification of a Pure Metal at a Vertical Wall in Presence of Liquid Superheat,'' Int. J. Heat Mass Transf., **31**(8), pp. 1735–1744.
[23] Greif, D., 1998, ''Numerical Study of Conjugate Heat Transfer in a Continuously Moving Metal During Solidification,'' M.S. thesis, Montana State University, Bozeman MT.

The Effects of Air Infiltration on a Large Flat Heat Pipe at Horizontal and Vertical Orientations

M. Cerza

B. Boughey

US Naval Academy,
Mechanical Engineering Department,
Annapolis, MD 21402

In the satellite or energy conversion industries flat heat pipes may be utilized to transfer heat to the thermal sink. In this investigation, a large flat heat pipe, 1.22 m×0.305 m ×0.0127 m, fabricated from 50 mil Monel 400 metal sheets and Monel 400 screens was videographed at horizontal and vertical orientations with an infrared video camera. The heat pipe evaporator section consisted of a 0.305 m×0.305 m area (one heated side only) while the side opposite the heated section was insulated. The remaining area of the heat pipe served as the condenser. In the horizontal orientation the heated section was on the bottom. In the vertical orientation the evaporator was aligned below the condenser. The sequence of photographs depicts heat inputs ranging from 200 W to 800 W, and the effect of air infiltration on heat pipe operation for both orientations. For the horizontal orientation, the air is seen to recede towards the small fill pipe as the heat input is increased. For the vertical orientation, the air and water vapor exhibit a buoyant interaction with the result that the air presence inhibits heat transfer by rendering sections of the condenser surface ineffective. The effects depicted in this paper set the stage for future analytical and experimental work in flat heat pipe operation for both normal and variable conductance modes. [DOI: 10.1115/1.1532020]

Keywords: Energy Conversion, Heat Transfer, Heat Pipes, Measurement Techniques, Multi-Phase

Introduction

Figure 1 depicts a conceptual thermophotovoltaic (TPV) energy conversion system utilizing flat heat pipes. Combustion gases from a heat source such as a gas turbine combustor flow through channels on which heat pipes are mounted. These hot side heat pipes serve as emitter surfaces. Across from the hot side heat pipes, TPV cells can be mounted to cold side heat pipes which are heat pipes in contact with the thermal sink. An isothermal emitting surface is needed in TPV energy conversion systems because the voltage outputs of the TPV cells are very sensitive to the wavelength bandwidth of the emitting surface. The emitter's wavelength bandwidth is a function of temperature. On the cold side, the TPV cells could utilize a flat heat pipe, but this is less critical. Flat heat pipes are not new to the industry, several companies have designed them for space or computer applications [1–4].

Flat heat pipes are similar to cylindrical heat pipes. The only real difference between the two is geometrical. While this may seem a minor difference, it presents many challenges from an engineering standpoint. Typically, heat pipes are used to transfer quantities of heat across a distance with only a slight temperature loss from end to end. The cylindrical design works well to serve this purpose. However, when designing an emitter for a TPV energy conversion system, it is advantageous to have a large surface area to volume ratio in order to maximize the power density of the system. A flat heat pipe was conceived for this purpose. Flat heat pipes also have different internal flow and structural design considerations than those of cylindrical heat pipes.

Flow properties in cylinders are different from those in rectangular geometries such as flat plates and/or boxes. The flow of a thin film through a flat wick (such as in the liquid return path of a flat heat pipe) is not the same as the flow of a cylindrical circumferential film. Also, vapor flow through a cylindrical space differs from vapor flow through a rectangular cross section. The flow geometrical differences can alter the steady-state limitations in flat heat pipe design.

The limit most affected in the design of a moderate temperature (100°C) flat heat pipe utilizing water as the working fluid is the capillary limit. The capillary limit involves the ability of the wick to develop the necessary pumping head to overcome the vapor and liquid pressure losses as the working fluid circulates through the heat pipe.

In this investigation, it was desired to qualitatively examine the effects of what would happen if air infiltrated a hermetically sealed flat heat pipe containing only water. In order for a flat heat pipe to withstand pressure differences across its flat surfaces, the flat surface structure needs to be supported. Monel pins were used as support structures in this flat heat pipe design. These pins were welded to the sheet metal surfaces, and the welds, should they crack, would be a source for air infiltration for a heat pipe containing water as the working fluid and operating below 100°C in an atmospheric environment.

It should be pointed out that this flat heat pipe was not designed as a variable conductance or gas loaded heat pipe. There was no noncondensable gas reservoir at the condenser end, however, there was a short 5 cm in length, 18 mm in diameter fill pipe attached to the condenser end. In a gas loaded variable conductance heat pipe (VCHP), Fig. 2, a reservoir which contains an amount of a noncondensable gas is added to the heat pipe condenser end. Marcus [5], and Marcus and Fleischman [6] give an excellent review of a simplified VCHP. A primary goal for a VCHP operating with a constant heat sink temperature is to achieve a steady internal operating temperature at varying heat input conditions. This is accomplished for increasing evaporator heat input by the working fluid vapor compressing the noncondensable gas towards the reservoir, thus, lengthening the active condenser length. The condenser length that contains the gas essentially prohibits heat rejection from that portion of the heat pipe condenser. With proper design, this increase in heat pipe condenser area with increasing

Contributed by the Heat Transfer Division for publication in the JOURNAL OF HEAT TRANSFER. Manuscript received by the Heat Transfer Division July 12, 2001; revision received May 13, 2002. Associate Editor: G. P. Peterson.

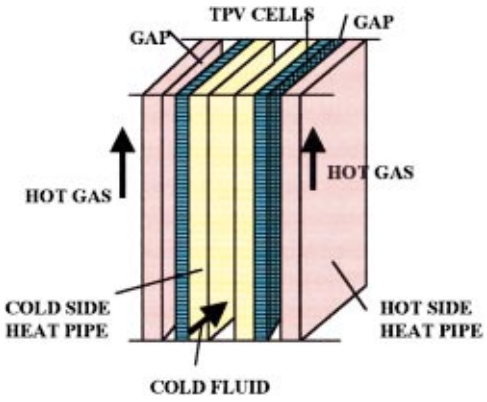

Fig. 1 Schematic of a TPV conversion system

heat input can achieve a nearly isothermal vapor operating condition. Generally, this calls for the gas reservoir volume to be much larger than the condenser volume. In this investigation, the ratio of the fill pipe volume to the condenser volume was 0.002. So if air infiltrates the heat pipe, it will not behave as a traditional VCHP, i.e., for an increasing heat input, a rise in this heat pipe's operating temperature is expected.

Several investigators have examined the effects of noncondensable gas levels on VCHP operation. These have been predominately for cylindrical VCHPs. Kobayashi et al. [7] have conducted an experimental and analytical study to examine the flow field behavior of the vapor/non-condensable gas mixture. They determined that gravity and noncondensable gas level had a strong effect on the location and profile of the gas/vapor interface layer. Peterson and Tien [8] examined the mixed double diffusive convection in gas loaded heat pipes and two-phase thermosyphons. They showed that temperature and concentration gradients can redistribute the gas within the condenser. This redistribution, however, did not greatly alter the overall condenser heat transfer. Peterson et al. [9] also showed that double diffusive convection changes the non-condensable gas flow structure as the Rayleigh number is increased.

The heat pipe employed in this study was a very large flat heat pipe since in the energy conversion industry large surface areas are required to cool large power producing devices. Initially, a small amount of air was loaded into the heat pipe. An attempt was made to compare the performance for this air loaded heat pipe to one without air, but unfortunately, air was believed to have infiltrated the second case. This investigation also presents the use of infrared videography as a diagnostic measurement tool to record the external surface temperatures of the heat pipe's condenser region and to infer what was internally happening between the air and water vapor in the condenser end. The primary focus of this paper is on the qualitative effects of air infiltration in a large, flat heat pipe.

Flat Heat Pipe Fabrication

A flat heat pipe, 1.22 m$\times$0.305 m$\times$0.0127 m, was fabricated from 50 mil Monel R400 metal sheets and Monel R400 screens, [10,11]. The heat pipe was designed to utilize water as the working fluid in an operational temperature range of 25°C to 130°C. Two layers of Monel screens were used, 40 mesh and 120 mesh. The purpose of the two different screen sizes was to design a wick of varying permeability.

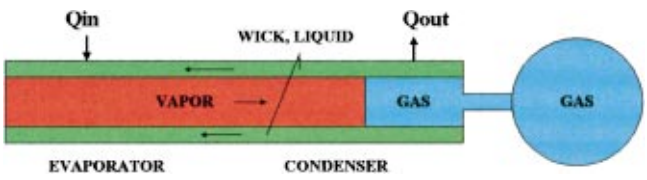

Fig. 2 A variable conductance heat pipe

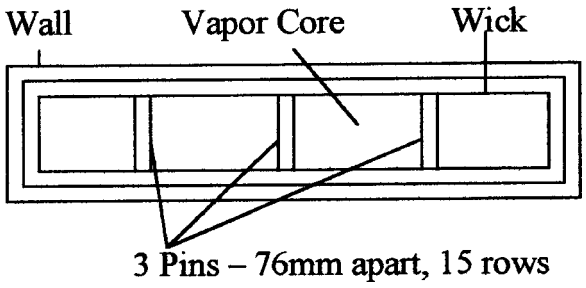

Fig. 3 Heat pipe cross section

Long copper bars with fine radius edges were utilized to facilitate bending the heat pipe to the required dimensions. The two layers of screen were then placed on top of the vessel. The 120 mesh screen was then placed on the top of the 40 mesh screen to aid in the development of the capillary pumping head of this screen wick. The screen was then tack-welded to the vessel wall in regular intervals between the pin spacer locations. The Monel sheets and screens were then punched, making holes in the locations where the support pins were to be TIG welded. The 6.35 mm diameter pins were then cut to the proper length, milled, and deburred to fit into the necessary space. Figure 3 depicts a section of the Monel sheets, screens and pins (Boughey, 1999). The gap size between the Monel sheets was approximately of 0.019 mm. There were 15 rows, three pins per row of Monel pins, TIG welded to the face sheets.

The sides of the two separate halves were welded together, carefully sequencing the welds and using a heat trap to minimize deformation. After this, the ends were welded on and the fill fitting was welded snug to the end. The pins were then placed in their proper spots and TIG welded on both sides of the heat pipe.

Leak-testing and charging consisted in the fabrication of a charging apparatus. A 6.35 mm nipple was fitted to the fill end of the heat pipe (condenser) and mated to an air compressor. The heat pipe was then pressurized for leak testing. To leak test, soapy water was applied to the pressurized heat pipe in order to detect the leaks. Leaks would form bubbles in the soapy water. The heat pipe was allowed to sit pressurized over night and it was discovered that some very small leaks did exist. These were found by injecting a small amount of R134a into the heat pipe and ''sniffing'' it with a Yokogawa refrigerant leak detector. The leaks were then fixed. A bourdon tube pressure gage was mounted on the fill neck.

Charging the heat pipe with working fluid was performed fairly simply. First, the heat pipe and charging assembly were mated to an oil diffusion vacuum pump and evacuated. In the fluid charging column was placed the correct amount of water to charge the heat pipe. These amounts were measured and marked, taking into account the volume that would occupy the fittings as well as the heat pipe. Once evacuation was complete, the valve attached to the vacuum pump and the valve attached to the heat pipe were closed and the vacuum pump was shut off. The valve attached to the fluid column was then opened, and the vacuum inside the fittings drew the water in to fully fill the pipe volume between the fittings. The heat pipe valve was then opened slightly to bleed in the necessary charge (as marked on the column). All valves were then closed and the charging apparatus removed. The heat pipe was charged to 125 percent of the porous volume that the screen wick contained.

Thirty-eight (38), 20 AWG type K thermocouples were mounted on the heat pipe as shown in Fig. 4. The thermocouples were soldered in place. The entire heat pipe was then painted flat black using Krylon paint. The emissivity of the black surface was

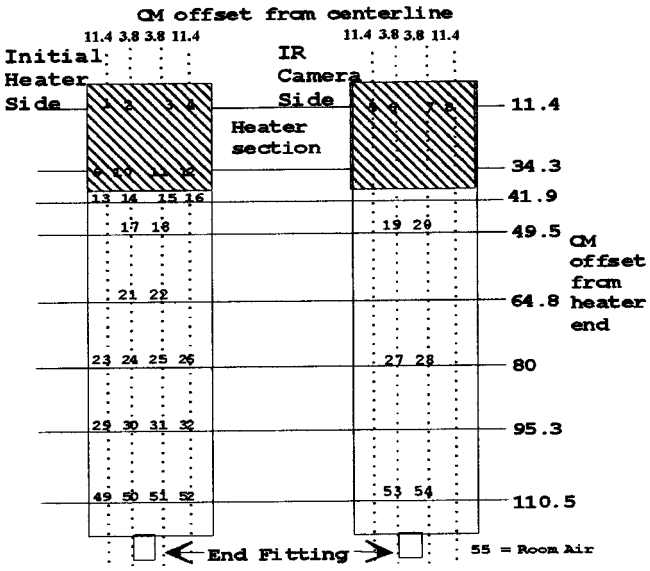

Fig. 4 Thermocouple locations [ii]

measured as 0.94 at 25°C by using thermocouple data on the heat pipe and calibrating the infrared camera with these data. Later, during operational tests, the surface emissivity was measured at 0.95 at 100°C.

A heated plate, 0.304 m×0.304 m, was fabricated from 0.025 m thick aluminum stock. Eight equally spaced holes 15.8 mm in diameter were centered and drilled through the aluminum cross section. Eight 1 KW Watlow firerod cartridge heaters, coated with heat sink compound, were inserted into the holes. The aluminum heater block was coated on one side with the heat sink compound on the side to be in contact with the heat pipe. A 0.304 m ×0.304 m block of wood was then placed on the back side of the aluminum heater block and the wood/aluminum heater assembly was clamped to one side of the evaporator section. The entire heated evaporator section was then covered with thermal insulation. The thermocouples and cartridge heaters were then connected to a data acquisition system. Measurement uncertainty was +/−0.2°C per thermocouple channel and the heater input could be recorded +/−5W. A stand was fabricated so that the heat pipe could be operated at various angles of inclination.

Experimental Investigation

Data was taken for two types of heat pipe orientation and two different non-condensable gas loadings. Two gas loadings were selected in order to discern the effects caused by minor and major air leaks into the heat pipe. The first heat pipe orientation was horizontal. In this orientation the flat side of the heat pipe was parallel to the ground. In addition, the evaporator heater was on the side facing the ground, thus, the evaporator section was heated from below while the top portion of the evaporator section was adiabatic (thermal insulation was wrapped around the entire evaporator section). The second heat pipe orientation was vertical with the evaporator section placed below the condenser section. At 25°C room temperature, the internal pressure of the heat pipe without gas loading would be the saturation pressure of the working fluid at 25°C, or approximately 3.14 kPa for water. Since this pressure represents a partial vacuum, it was very easy to bleed a little air into the heat pipe for the initial gas loading. For the first case, air was bled in until the pressure gage read 33 kPa. Assuming that the air would initially occupy the entire inside volume (0.00472 m^3, approximately) at a partial pressure of 29.86 kPa and temperature of 25°C would mean that the air mass was approximately 0.00165 kg. The water fill was approximately 400 cc.

In addition to the thermocouple measurements for the evaporator and condenser sections, the condenser temperature was also monitored on the side adjacent to the heater by infrared videography. Thus, the entire condenser surface temperature could be monitored and the results would be indicative of what was happening internally with respect to the vapor and gas (air) interfaces. In other words, in a typical heat pipe with no air infiltration, the inside temperature difference between the evaporator and condenser can be very close to an isothermal condition. When a non-condensable gas is introduced, there can be significant temperature differences between where the gas is located in the condenser, and where the vapor is located. These temperature differences would affect the condenser surface temperature distribution and would easily show up on the infrared camera video tape. Hence, one could get a real time thermal image of what was physically happening inside the condenser end of the flat plate heat pipe should air infiltrate the system.

The infrared camera video system was calibrated by using the thermocouple data. The heaters were turned on, and the internal temperature of the heat pipe, before air was added, was set at 100°C (internal pressure conditions equal to atmospheric conditions with water as the working fluid). The emissivity of the infrared camera was then dialed in until the IR camera was depicting a near isothermal condenser region at a temperature of 100°C. This emissivity was 0.95. The IR camera system was now calibrated. Periodically, the emissivity would be checked by comparing thermocouple data to IR data. There was a fluctuation in surface emissivity between 0.93 and 0.95. Care was taken so as not to operate the flat heat pipe above 101 kPa internal conditions in order to prevent any puffing out along the heat pipe flat surfaces which might result in an emissivity calibration error, i.e., partial hemispherical surfaces. It was decided to only report the temperatures in this particular study using the IR camera since the IR camera data was within +/−1°C of the thermocouple data.

With the heat pipe charged with water and air, the apparatus was set in the horizontal orientation and the heat input was set at 200 W. After stabilization of the heat pipe, which took approximately three hours due to the large thermal mass of the heat pipe, temperatures stabilized and IR video data was taken. The heat input was then changed to 400 W and IR data was taken again when the heat pipe temperatures appeared to stabilize. This procedure was followed up to a heat input value of 800 W. The heaters were then shut down and the heat pipe allowed to cool overnight. The next day, it was noticed that the heat pipe temperature was at 24°C, but its internal pressure was at 65 kPa instead of the original 33 kPa, so apparently some leaks had developed. Whether these leaks developed overnight or during the data runs is not clear. The heat pipe was placed in the vertical orientation, and with approximately the same amount of initial air inserted the process was repeated. An effort was made to seal the heat pipe from leaks and attempt a run with no air, but this turned out to be very difficult to achieve with the welded pin fabrication scheme presently employed. However, many of the leaks were sealed and the horizontal and vertical heat pipe results for very little added air show a marked contrast to the ''larger'' added air results. It should also be pointed out that as the internal temperature of the working fluid approached 100°C with increasing heat input, the driving pressure difference from the room (atmospheric) and heat pipe internal pressure became negligible, hence, any air infiltration from the room under these conditions would be very slight. Finally, the materials used in welding the heat pipe might release non-condensable gases when the heat pipe is heated during experimentation.

Experimental Results and Discussion

The flat vapor-air interface profile, VCHP theory without a reservoir of Marcus and Fleischman [6] was used to compare with the horizontal flat heat pipe data. That theory expresses the evaporator heat input as

$$Q = hC(T_v - T_{amb})\left[L_c - \frac{mR_gT_g}{\left[P_0 \exp\left(\frac{h_{fg}}{R_v}\left(\frac{1}{T_0} - \frac{1}{T_v} \right) \right) - P_{vi} \right] A_v} \right]$$

In the above equation, the heat input, Q, is equal to the product of the heat transfer coefficient, h, the condenser perimeter, C, the driving temperature difference, and the condenser length, L_c. The last term on the right hand side represents the estimated inactive condenser length due to the presence of the non-condensable gas. This term is a rearrangement of the perfect gas law. Therefore, L_c minus this length represents the active condenser length.

Figures 5 and 6 show a comparison of the flat vapor-air profile theory by Marcus and Fleischman with the present data for the horizontal cases. As can be seen in Fig. 5, the theory shows that for no gas reservoir, the operating vapor temperature (and corresponding vapor pressure) goes up with increasing heat input. Thus, theory predicts that this heat pipe would not make a good VCHP without a gas reservoir. Moreover, the theory shows that for a moderate quantity of air in the range of 0 to 0.01 kg, there seems to be very little effect on the vapor operating temperature due to the quantity of air. The upper air mass limit of 0.01 kg is actually greater than the mass of air the heat pipe could contain at 100 kPa and 25C (0.0055 kg). The actual data is also presented on Fig. 5. The case of 0.0016 kg of air and the case with very little air, 0.0001 kg, appear to follow the Marcus and Fleischman trend only at a lower operating vapor temperature. This effect could be due to vapor mass diffusion into the air volume and heat pipe axial wall conduction which does not allow the non-active condenser end to completely prohibit heat transfer out of the heat pipe. This would lengthen the active condenser length at a given heat input and result in a lower operating vapor temperature. It is also suspected that the ''insulated'' evaporator section was losing heat to the atmosphere for the larger 0.0016 kg air mass case, hence, the entire prescribed heat input was not going entirely into the heat pipe. This conclusion is supported by observing the $m = 0.0016$ kg of air data on Figure 6. The active condenser length of that presented data appears at low heat inputs to fall very short of the length predicted by the Marcus and Fleischman theory. For the case of little included air, 0.0001 kg, the present data appears to be a much better fit with the Marcus and Fleischman theory.

Infrared (IR) Videographic Results

The following infrared videographic results are shown for the horizontal and vertical orientations. They are also shown in a side by side comparison at a specified heat input for the large (0.0016 kg) and small (0.0001 kg) non-condensable gas loadings.

A. Horizontal Orientation. Figures 7 and 8 depict the large and small flat heat pipe gas loadings at a low heat input of 200 W for the horizontal orientation. It is believed that the presence of air in the heat pipe system would locally inhibit condensation of the water vapor, thus, allowing the local condenser surface temperature (as seen by the IR camera) to drop. As can be seen, the amount of non-condensable gas present in the heat pipe shows remarkable differences in the condenser surface temperature distribution. For the large gas loading, the condenser area is essentially blocked by the air, thus prohibiting effective heat transfer. This region in Fig. 7 shows a temperature very close to the ambient room temperature because the heat pipe is hard to see (an approximate outline has been drawn in). In contrast, Fig. 8 depicts a larger active condenser region that is above the ambient temperature. It is further believed that the heat pipe in Figure 7 has not primed very well. This may be due to the presence of the non-condensable (air), or the heater on the evaporator was not in good thermal conduct. In any event, for a heat input of 200 W, a higher operating temperature in the active condensing region was expected.

Figures 9 and 10 show the large and small gas loading cases at heat inputs of approximately 500 W. These pictures are more typical of the expected results for a water heat pipe with an air loading. In Fig. 9, the gas is compressed towards the end of the condenser region where the fill pipe is located. This is because as the heat input increases, the working fluid operating temperature and pressure for the heat pipe increases and the vapor pushes the air slug back and compresses it. This lengthens the active condenser surface so that the heat input is now rejected through a larger condenser surface area. This increase in active condenser length, however, is not enough to maintain an isothermal vapor temperature as in a well designed VCHP. Thus, the heat pipe's internal temperature and pressure increase. Figure 10 for the small air loading case shows that for approximately the same heat input value, 450 W, the air is compressed almost entirely to the back of the condenser region.

Figures 11 and 12 depict the large and small gas loadings at a heat input of 800 W. In Fig. 11, the surface temperature profile indicates that the air is compressed almost to the end of the condenser section on the right side, but not quite pushed all the way back on the left side, in fact, there is still a small cooler air pocket present in the condenser end. To corroborate the IR data depiction, one could feel, by placing a hand on that area of the condenser surface, that the far left region was indeed cooler than the bulk of the condenser surface. Figure 12 shows the condenser surface temperature to be almost at a uniform 95–100°C. In Fig. 11, the active condenser surface temperature is in the 100–105°C range which is reasonable considering a portion of its condenser surface is cooler due to the presence of air. The horizontal figures show typical behavior for a large flat heat pipe with a large and small amount of air loading. This would be the case if air infiltrated a hermetically sealed heat pipe through cracks in the welds and leaks in the system valves. It should also be pointed out that after the tests of both cases, it was determined that more air appeared to have infiltrated the systems. This was confirmed by taking final pressure readings when the heat pipe cooled down. For the large air case, the initial pressure reading was 33 kPa at 25°C, and the final pressure reading was near 60 kPa at 25°C. For the small air case the initial pressure reading was 3.4 kPa at 25°C (almost free of air), and 10 kPa at 25°C as the final reading, thus some air did infiltrate the small gas case. The reasons for the air infiltration were the Monel pins and welds. There were 45 pins that served as the internal support structure for this heat pipe, hence 90 welds. It was very hard to keep all welds intact, especially during the thermal cycling of the tests, i.e., on/off, etc.

B. Vertical Orientation. The next series of infrared images, Figures 13–18, show the operation of the air infiltrated flat heat pipe in a vertical orientation. For this orientation, the evaporator section was located below the condenser section. The heat input range was again 200–800 W. Figure 13 depicts the large gas loaded case at a heat input of 200 W. As can be seen, the only active portion of the condenser region is in the lower left corner adjacent to the evaporator section (not seen because it was covered with thermal insulation hence the evaporator appears cooler than the condenser on the IR videotape). The heat pipe condenser was operating asymmetrically and the air appears to cover most of the condenser heat transfer area. Figure 14 shows the condenser surface to be more active at 200 W for the small gas loading case. In fact, two thirds of the condenser surface is believed to be actively condensing as indicated by the fairly uniform surface temperature on the order of 33°C. Also seen are some thermocouple wires which are the yellow lines in the picture. The cool spots on both sides of the heat pipe are the PVC clamps.

At a heat input of 400 W for the large gas loading, Fig. 15, the heat pipe condenser is operating in a highly asymmetric fashion. The active condenser region is believed to be the growing ''finger'' on the left. The air which is believed to be depicted by the lower temperature blue 'color' is in the middle and along the right edge. The air inside the condenser section is almost 18°C cooler than the water vapor (white/red). An estimation of the effect of the thermal resistance due to the condensate falling film thickness on

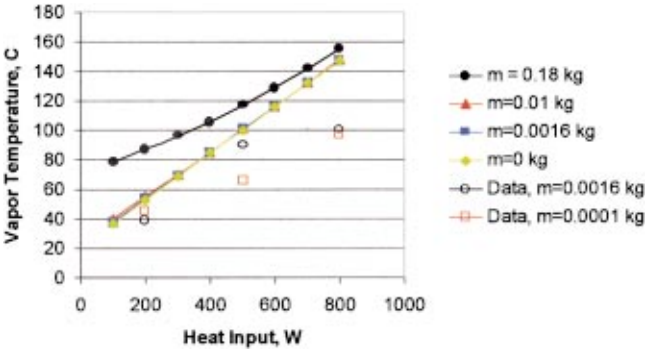

Fig. 5 Comparison of data to flat profile Theory 1

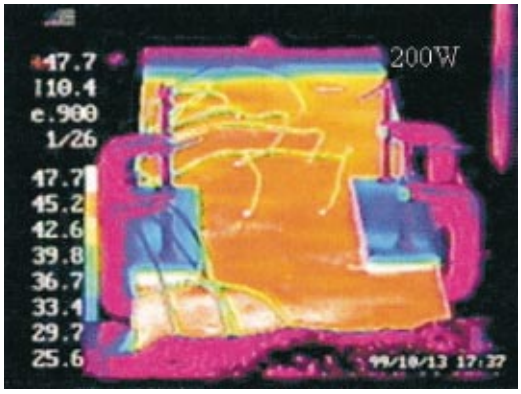

Fig. 8 Horizontal, 200 W, small air

outside surface temperature showed that for a range of condensate film thickness between 0.5 to 2.0 mm, the surface temperature variation should only be about 5°C. What apparently is happening is that as the water vapor gets hotter due to the increase in heat input, it becomes less dense that the cooler air, and since the air has no place to go, a buoyancy driven flow field is believed to be established. The cooler air is more dense than the water vapor and sinks. The asymmetrical flow could have been established by non-uniformities in the evaporator heat flux, which was established by eight cartridge heaters inside an aluminum block, and the entire block coated with heat sink compound on the side in contact with the evaporator. Any gaps in the heater block to the evaporator surface caused by surface warpage could create a non-uniform heating environment. The Monel surface of the heat pipe did exhibit some warpage after the welding processes. The green regions are indicative of a more diffused water-air mixture if one assumes the internal pressure of the heat pipe at any given operating heat input is fairly constant. Due to the relatively large cross sectional area of the vapor core, 0.00387 m^2, the vapor velocities for the present heat input range are very low. Thus, the observed condenser surface temperature distributions are not believed to be caused by differences in pressure due to the vapor velocity from one part of the condenser to another.

The 400 W input small air infiltration case is shown in Fig. 16. The condenser surface temperatures appear to be more symmetrical, but buoyancy effects are still present. As can be seen, the water vapor appears to rise up along both edges of the condenser section. The non-condensable air appears to sink slightly in the central portion. It is interesting to note that in the horizontal ori-

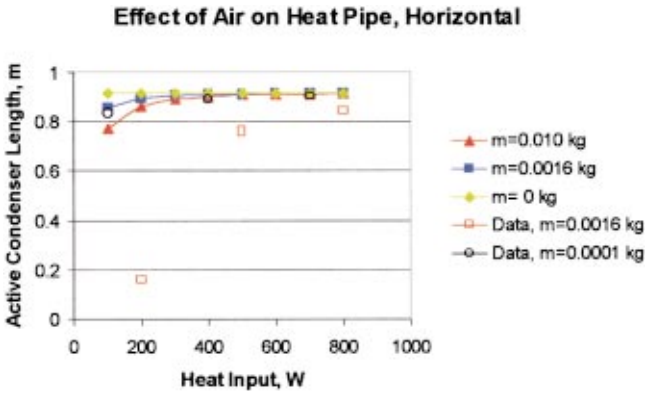

Fig. 6 Comparison of data to flat profile Theory 2

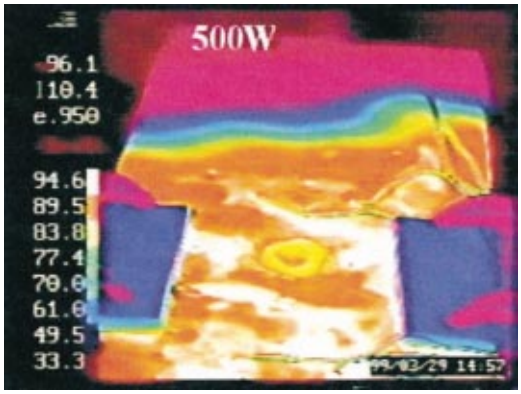

Fig. 9 Horizontal, 500 W, large air

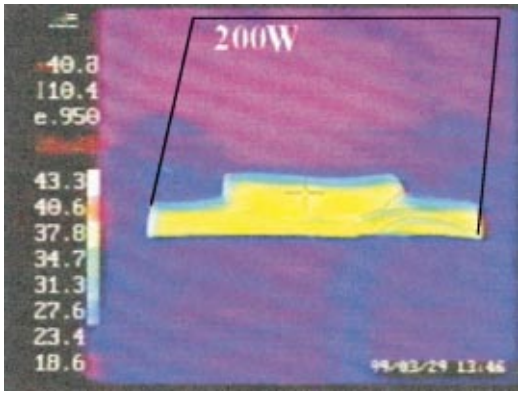

Fig. 7 Horizontal, 200 W, large air

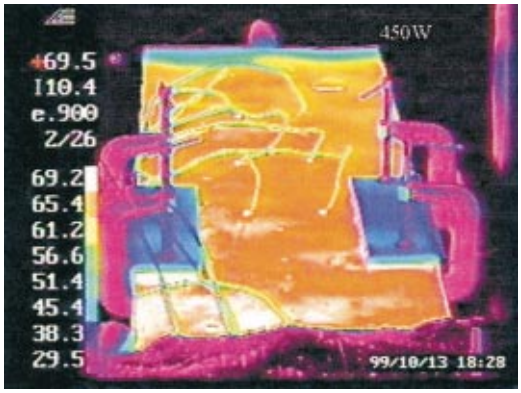

Fig. 10 Horizontal, 450 W, small air

Fig. 11 Horizontal, 800 W, large air

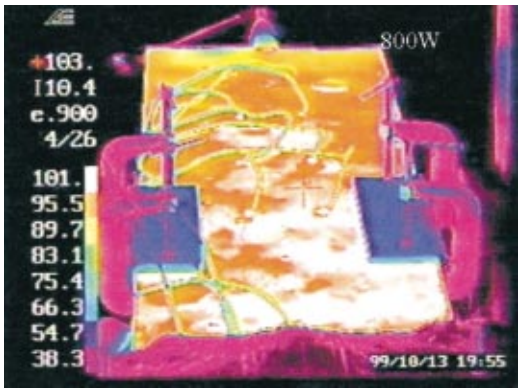

Fig. 12 Horizontal, 800 W, small air

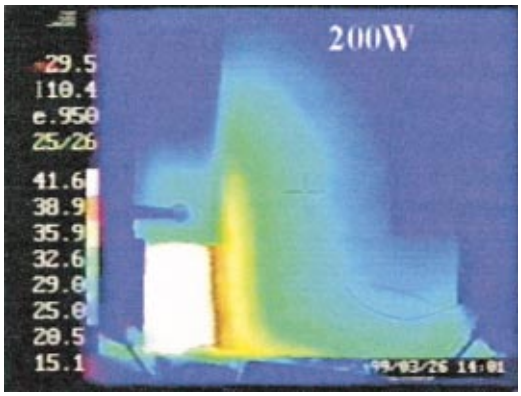

Fig. 13 Vertical, 200 W, large air

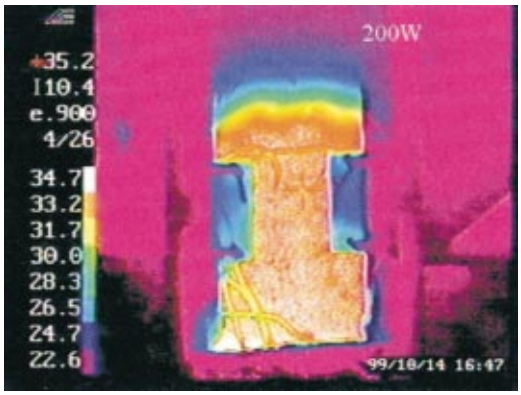

Fig. 14 Vertical, 200 W, small air

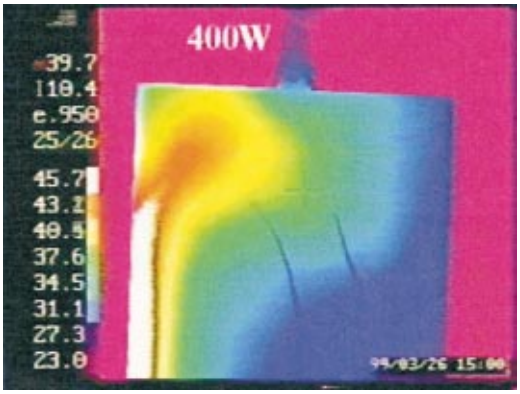

Fig. 15 Vertical, 400 W, large air

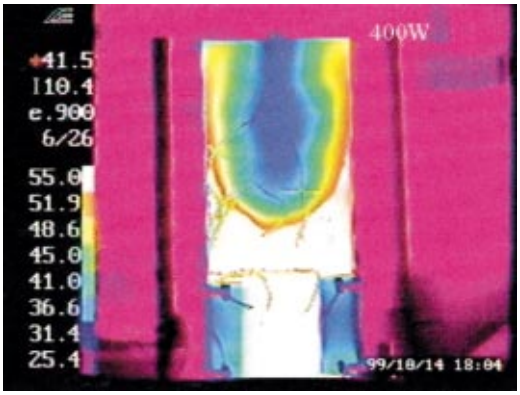

Fig. 16 Vertical, 400 W, small air

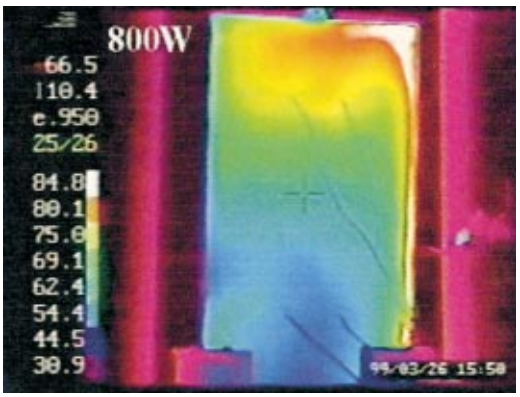

Fig. 17 Vertical, 800 W, large air

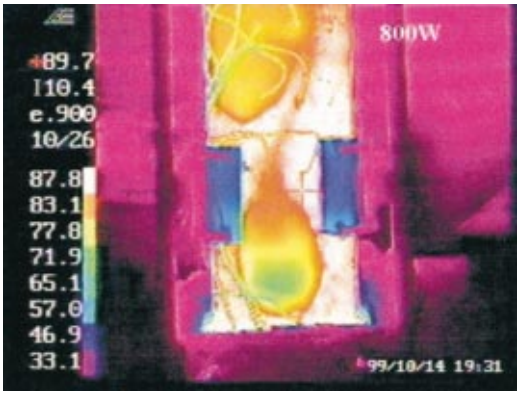

Fig. 18 Vertical, 800 W, small air

entation, the air was more readily compressed towards the fill pipe. Buoyancy effects for the horizontal orientation were minimal. In the vertical orientation, air-water vapor buoyancy effects are more pronounced due to the influence of gravity. It would be interesting to conduct a future study of varying aspect ratios involving the width and depth of the vapor flow channel, with the heat pipe length. Also of interest would be to compare these results to cylindrical gas loaded/air infiltrated heat pipes with varying aspect ratios involving internal vapor flow diameter and heat pipe length.

Figures 17 and 18 depict the 800 W heat input cases for the large and small air infiltrations, respectively. The large air case, Fig. 17 shows the same general trend as Fig. 15. Figure 18 depicts a buoyant effect much like a ''lava'' lamp.

Conclusions

A large, flat heat pipe was fabricated from Monel metal sheets and Monel screens. An attempt was made to add a small amount of non-condensable gas (air) to the heat pipe and observe the effect on its operation. The purpose was to simulate air infiltration of the heat pipe. Two different gas loadings were utilized which were characterized as large, 0.0016 kg of air added, and small, 0.0001 kg of air added. It was not the intent of this investigation to perform a detailed study on the effect of the quantity of air infiltration as it was to determine if a flat, gas loaded heat pipe was a viable candidate for power/energy conversion schemes. The heat input ranged from 200 to 800 W.

The results indicate that the large flat heat pipe could be a viable candidate in energy conversion schemes. Infrared videography was used to capture real time data for the heat pipe condenser section surface temperature distribution. It was shown that these data gave a good indication of what was happening inside the heat pipe and what would happen should air infiltrate the heat pipe core. For the horizontal orientation, the effect of air infiltration caused the heat pipe to operate like a gas loaded heat pipe with no gas reservoir, i.e., for an increase in heat input, an increase in operating temperature and pressure resulted. The air was seen to be compressed to the rear of the condenser section as the heat input increased. In vertical orientation, however, this was not to be the case. The flat heat pipe displayed internal buoyant and diffusive effects between the working fluid vapor and the infiltrating non-condensable gas (air). The air was not readily compressed towards the end of the condenser section, but rather interacted with the water vapor to show appreciable effects believed to be buoyancy driven. These effects were seen for both large and small air infiltration masses.

Acknowledgment

Thanks is expressed to the welders and technicians in the USNA machine shop.

Nomenclature

A_v = vapor core cross sectional area
C = heat pipe perimeter
H = outside heat transfer coefficient
H_{fg} = latent heat of vaporization
L_c = overall condenser length
m = non-condensable mass
P_0 = reference operating pressure
P_{vi} = vapor pressure of fluid in the inactive condenser end
Q = heat input
R_g = gas constant
R_v = gas constant of vapor
T_0 = reference operating temperature
T_{amb} = ambient temperature
T_g = temperature of gas in the inactive condenser region
T_v = temperature of vapor in the active condenser region

References

[1] Tanzer, H. J., 1983, ''*High Capacity Honeycomb Panel Heat Pipes for Space Radiators*,'' AIAA-83-1430, AIAA 18th Thermophysics Conference, Montreal, CN.
[2] Tanzer, H. J., Fleischman, G. L., and Rankin, J. G., 1985, ''*Honeycomb Panel Heat Pipe Development for Space Radiators*,'' AIAA-85-0978, AIAA 20th Thermophysics Conference, Williamsburg, VA.
[3] Rankin, J. G., 1984, ''*Integration and Flight Demonstration of a High-Capacity Monogroove Heat-Pipe Radiator*,'' AIAA-84-1716, AIAA 19th Thermophysics Conference, Snowmass, CO.
[4] Tanzer, H. J., Cerza, M. R., and Hall, J. B., 1986, ''*High Capacity Demonstration of Honeycomb Panel Heat Pipes*,'' 16th Intersociety Conference on Environmental Systems, San Diego, CA.
[5] Marcus, B. D., 1972, ''*Theory and Design of Variable Conductance Heat Pipes*,'' NASA Report NAS 2-5503.
[6] Marcus, B. D., and Fleischman, G. L., 1970, ''*Steady State and Transient Performance of Hot Reservoir Gas-Controlled Heat Pipes*,'' ASME Paper No. NAS2-5503.
[7] Kobayashi, Y., Okumura, A., and Matsue, T., 1991, ''Effect of Gravity and Non-condensable Gas Levels on Condensation in Variable Conductance Heat Pipes,'' J. Thermophys. Heat Transfer, **5**(1), pp. 61–68.
[8] Peterson, P. F., and Tien, C. L., 1990, ''Mixed Double-Diffusive Convection in Gas-Loaded Heat Pipes,'' J. Heat Transfer , **112**(1), pp. 78–83.
[9] Peterson, P. F., Elkouh, N., Lee, K. W., and Tien, C. L., 1989, ''*Flow Instability and Bifurcation in Variable-Conductance Thermosyphons*,'' ASME HTD v115, pp. 1–6.
[10] Boughey, B., Cerza, M., and Lindler, K. W., 1999, ''*Flat Heat Pipe Design, Construction and Analysis*,'' Paper No. 1999-01-2527, 34th Intersociety Energy Conversion Engineering Conference, Vancouver, British Columbia, CANADA.
[11] Boughey, B., 1999, ''*Design, Construction and Analysis of a Flat Heat Pipe*,'' USNA Trident Scholar Report No. 261.

Temperature and Volumetric Fraction Measurements in a Hot Gas Laden With Water Droplets

Paolo Ruffino

Marino di Marzo
e-mail: marino@eng.umd.edu
Department of Mechanical Engineering,
University of Maryland,
College Park, 20742

Two temperatures can be detected in a hot gas laden with water droplets. The lower one is the temperature read by a sensor immersed in the flow. This measurement is affected by significant evaporative cooling resulting in readings much below the real gas temperature. The higher one is the temperature of the gas. The difference between these two temperatures is proportional to the water volumetric fraction in the flow. On this basis, a new technique for the measurement of the water volumetric fraction is proposed. The results are compared with a conventional measurement technique based on optical methods. A novel approach to the gas temperature measurement is also introduced. The sensing device is kept at temperatures exceeding the Leidenfrost transition and therefore it is insensitive to the presence of the water droplets. Independent measurement techniques developed at the Evaporative Cooling Sensor Accuracy Test (ECSAT) facility provide the data to validate the measurements obtained with the Above Leidenfrost Temperature' and Evaporative Cooling (ALTEC) sensor. [DOI: 10.1115/1.1561453]

Keywords: Droplet, Evaporation, Flow, Heat Transfer, Measurement Techniques

Introduction

The evaporative cooling effect produced by minute water droplets carried by a hot gas has several technical applications, such as cooling of engines and electronic components as well as heat transfer enhancement. In fire protection engineering, evaporative cooling has a significant impact on the activation of fire sprinklers. In full-scale tests on warehouse fires it is not uncommon to observe that, upon the activation of a sprinkler (i.e., the primary sprinkler), the adjacent sprinklers respond with large delays or do not activate at all (sprinkler's skipping phenomenon). Further away from the primary sprinkler, as the evaporative cooling effect subsides, sprinklers activate as expected. These observations can be explained by considering the presence of water droplets in the gas plume following the activation of the primary sprinkler. Portion of the spray does not reach the ground and it is entrained by the hot gas ascending plume. Most of these droplets evaporate inside the plume, while a small fraction travels far enough to reach the adjacent sprinklers and impact on their surface.

Several researchers have quantified the evaporative cooling effect associated with water droplets in a hot gas flow. In a fire scenario within an enclosure, a model for estimating the evaporation heat losses due to the water spray introduced by a sprinkler in a smoke layer is reported by Chow [1]. The author points out that the water droplets evaporate while traveling through the hot gas. Therefore, a portion of the water droplets may not be able to reach the burning objects. The model investigates the evaporation of the sprinkler water spray in the hot gas layer near the ceiling of the enclosure.

Grissom and Wierum [2] found that the lowest surface temperature for the existence of spray evaporative cooling could be determined experimentally as a linear function of the impinging water droplets mass flow rate. Evaporative cooling due to a sparse spray is extensively investigated by diMarzo and Tinkler [3]. They derived a model from the results obtained for a single droplet deposited on a low thermal conductivity solid with its surface exposed to radiant heat input from the environment [4]. The model encompasses coupled near and far field close-form solutions. Since the spray is sparse, a simple superposition of the individual droplet cooling effects is adequate to describe the overall spray cooling.

Two temperatures can be measured in a gas laden with water droplets: (a) the lower one includes the evaporative cooling effects described previously; (b) the higher one is independent of the presence of the water droplets and is the actual gas temperature. The Evaporative Cooling Sensor Accuracy Test (ECSAT) facility will provide data relevant to the evaporative cooling phenomenology and we will outline the measurement techniques used to obtain the hot gas temperature and the water volumetric fraction from the experimental data. A newly developed Above Leidenfrost Temperature Evaporative Cooling (ALTEC) sensor provides a direct measurement of the gas temperature. We will introduce the conceptual design of the ALTEC sensor and the theoretical basis for its operation, control and data acquisition. Finally, we will compare the measurements obtained with the ALTEC sensor with the gas temperature and water volumetric faction information from the ECSAT facility and we will draw our conclusions.

ECSAT Facility

The ECSAT facility [5] consists of a square duct (0.61 m $\times$ 0.61 m in cross-section) through which a steady air flow is induced by a fan. Figure 1 provides a depiction of the relevant elements and dimensions of the facility test section. A 70 kW natural gas burner warms up the air at the facility intake. The hot gas proceeds through a tightly packed steel wool region where both the velocities and temperatures are uniformed. Thereafter, the gas enters a plenum and spray nozzles add water in the desired amount and with a prescribed droplet size distribution. The flow is then accelerated through a circular orifice. The orifice cross-sectional area is 0.25 m in diameter and is located 0.5 m downstream of the water spray nozzles. The test section is located downstream the orifice in the vena contracta. Incidentally, within the cross-section, the temperature variation, detected by thermocouples, does not exceed 8°C in both the gas and the gas-water flows. Twenty-eight thermocouples provide a description of the temperature evolution along the 4.7 meters duct downstream of the circular orifice.

Four additional thermocouples (type K, $\pm$2°C) are placed inside the duct, just upstream of the cross section where water drop-

Contributed by the Heat Transfer Division for publication in the JOURNAL OF HEAT TRANSFER. Manuscript received by the Heat Transfer Division March 28, 2001; revision received November 6, 2002. Associate Editor: S. S. Sadhal.

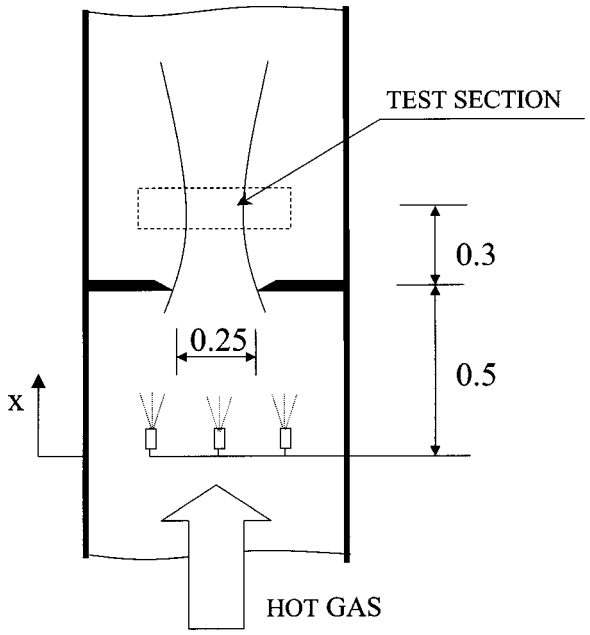

Fig. 1 Sketch of the test section in the ECSAT facility (dimensions in meters)

lets are introduced ($x=0$). Figure 2 shows the typical temperature distribution, for both dry and wet conditions. The first temperature reading for $x=0$ represents the average of the four thermocouple readings at that location. The axial distance along the duct, reported in Fig. 2, is adjusted to reflect the changes in average velocity over the flow cross section due to the orifice restriction. This correction is necessary since we are interested in droplet residence times rather than in the actual physical distance between points. It follows that, in the proximity of the orifice, as the flow velocity increases, the effective distance between thermocouples is appropriately reduced in Fig. 2. A comparison between the two values of the temperature measured at the test section clearly shows the effect of the evaporative cooling in wet conditions. It is worth noting that, due to the heat losses to the external environment, the temperature drops as the flow proceeds downstream the orifice. Note also that the gas temperature upstream the spray nozzle location is equal in both dry and wet conditions. It can be observed that about 1.5 meters downstream the test section, the slope of the temperature distribution for the wet case becomes equal to the slope of the temperature distribution for the dry case.

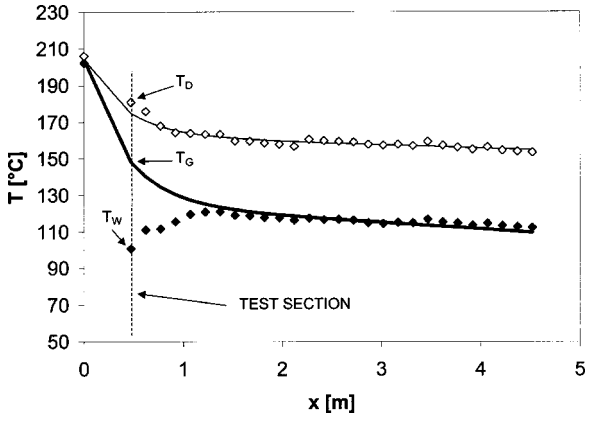

Fig. 2 Temperature distribution downstream the orifice in the ECSAT facility (◇ dry conditions, ♦ wet conditions). The thin line is given by Eq. (6) and the thick line is given by Eq. (5).

This indicates that the water is completely evaporated and the temperature is affected only by the heat losses to the environment. The temperature difference between the two temperature profiles far away from the orifice can be related to the heat required to vaporize the water droplets. Therefore, the thermocouples measure actual gas temperatures at the location just before the sprays nozzles and at the location after the complete evaporation of the water.

Measurement Methods

Temperature of the Hot Gas. To determine the gas temperature between the spray nozzles and the location of the complete evaporation of the water, some information concerning the rate of vaporization of the droplets is needed. Consider the energy balance written for the air flow as:

$$\rho_G \dot{V}_G c_G (T_D - T_G) = \rho_L \dot{V}_G (\beta_0 - \beta)\Lambda \tag{1}$$

The asymptotic temperature difference, ΔT, between the two traces in Fig. 2, that is associated with the sensible heat removed from the air in order to vaporize the droplets, can be expressed in the following form:

$$\Delta T = \frac{\rho_L \dot{V}_G \cdot \beta_0 \cdot \Lambda}{\rho_L \dot{V}_G c_G} \tag{2}$$

With Eq. (2), Eq. (1) can be simplified as:

$$T_D - T_G = \Delta T[1 - f(x)] \tag{3}$$

The function $f(x)$ links the initial volumetric fraction to its evolution along the duct. Note that $f(x)$ must be equal to 1 at the spray nozzles location and it is equal to zero for x greater or equal to x_E, where all the water drops are evaporated. The D^2 law [6] applies to evaporating droplets. Making use of its formulation, a reasonable representation of the data is obtained as:

$$f(x) = \begin{cases} \left(1 - \dfrac{x}{x_E}\right)^{\lambda} & x \leqslant x_E \\ 0 & x > x_E \end{cases} \tag{4}$$

It follows that the interpolation describing the gas temperature between $x=0$ and $x=x_E$ is given by substituting Eq. (4) into Eq. (3) to yield:

$$T_G = T_D - \Delta T\left[1 - \left(1 - \frac{x}{x_E}\right)^{\lambda}\right] \tag{5}$$

The temperature in dry conditions is represented with an exponential fit of the available data in the following form:

$$T_D = (T_0 - M)e^{-Px} + Bx + M \tag{6}$$

The constant B represents the slope of the trace on the right hand side due to the heat transfer losses to the ambient.

It is reasonable to presume that this approach provides a good representation of the hot gas temperature trend. In particular, the intersection of this curve with the vertical dashed line in Fig. 2 provides the hot gas temperature at the test section. As one may notice from the plot, the evaporative cooling reduces the thermocouple reading by some 50°C with respect to the estimated gas temperature.

Gas Velocity. The test section is illuminated by a 600 mW Argon-ion laser sheet. The velocity measurements in the cross-section are obtained with a Particle Tracking Velocimetry (PTV) technique and yield uncertainty in the velocity measurements of 10 percent [7]. Note that the volumetric mean diameter of the droplets is less than 100 μm. This results in a terminal velocity smaller than 0.14 m/s. Since the gas velocities are in excess of 3.5 m/s, the difference between the droplet and gas velocities introduces an error of less than 4 percent in the gas velocity measure-

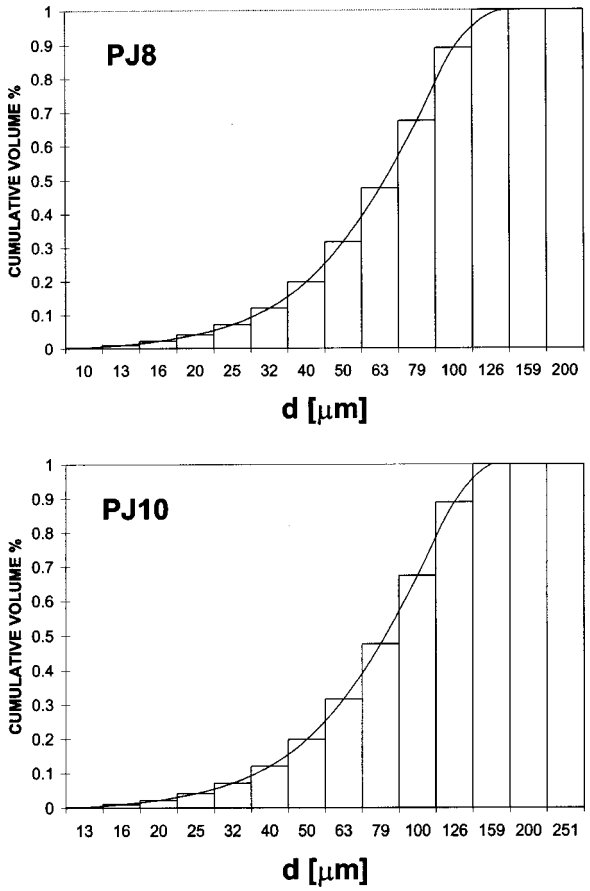

Fig. 3 Droplet Size Distribution for the PJ8 and PJ10 nozzle.

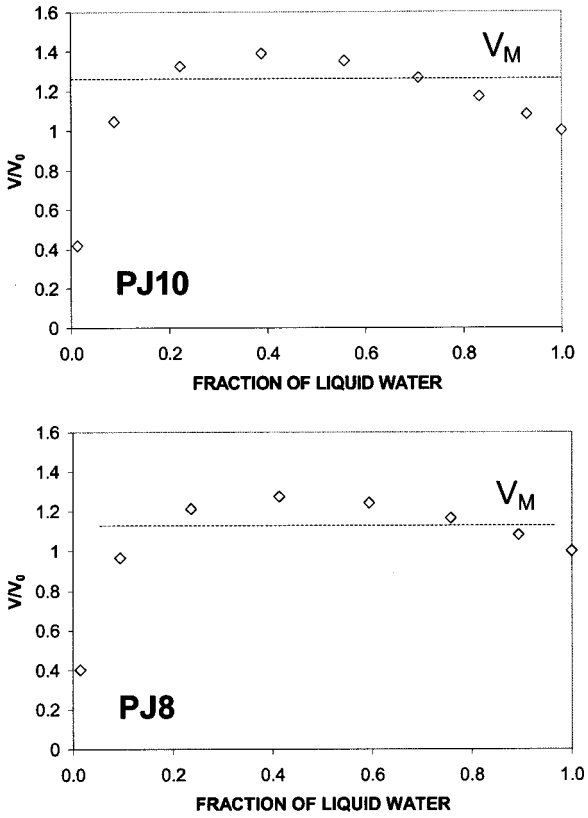

Fig. 4 Residual droplet volume versus the fraction of residual liquid for the PJ8 and PJ10 nozzles

ment. All the streaks are parallel to each other in the test section. Their length is uniform within a 10 percent variation about the average value. This implies that the flow can be considered one-dimensional in the test section.

Volumetric Fraction Via Optical Method. Several techniques are available for measuring the water volumetric fraction. One could resort to shadowgraph imaging [8] or to phase dopler interferometry [9,10]. A simpler approach is used here. The water volumetric fraction is defined as the ratio of the volumetric flow rate of water droplets over the total volumetric flow rate. If the water volume is negligible with respect to the volume of the gas, the volumetric fraction can be expressed as:

$$\beta = \frac{\dot{V}_L}{\dot{V}_G} \tag{7}$$

The droplet size distribution, for the spray nozzles used in the experiments, is shown in Fig. 3. The nozzles are identified as PJ8 and PJ10 respectively [11]. The droplets are grouped by size into N bins, each bin containing n_i droplets of volume V_i. The volumetric flow rate of the water droplets is the volume of the particles flowing through a given cross section in the amount of time while the camera shutter is open (i.e., shutter speed, σ). Therefore we can write:

$$\dot{V}_L = \frac{1}{\sigma}\sum_{i=1}^{N} n_i V_i \tag{8}$$

The minimum particle size optically resolved is 25 μm. This means that no droplets with a diameter less than 25 μm can be observed with the available equipment. Figure 3 shows that, for both nozzle sizes, the contribution of these droplets to the water volume is negligible. Therefore, the limitations of the optical resolution do not introduce a relevant error in the measurements. The mean droplet volume is introduced as:

$$V_M = \frac{\sum_{i=1}^{N} n_i V_i}{\sum_{i=1}^{N} n_i} \tag{9}$$

It is reasonable to assume that the evaporation process is proportional to the droplet surface area. Further, since the water volumetric fraction is in the order of parts per million, it is also reasonable to assume that no coalescence between droplets occurs. Under these circumstances, over a given time interval, each droplet would lose by evaporation a shell of equal thickness. Therefore, the residual water volume and droplets number can be calculated at different times during the evaporation process.

Figure 4 shows that the mean droplet volume remains approximately constant for a large portion of the evaporation process. The mean droplet volume V_M^*, averaged over the liquid fraction from 0.2 to 1, is also reported in Fig. 4 by the dotted lines. The error introduced in the calculations is 7 percent and 10 percent for the PJ8 nozzle and the PJ10 nozzle respectively. With this information, Eq. (8) can be simplified as:

$$\dot{V}_L = \frac{nV_M^*}{\sigma} \tag{10}$$

By substituting Eq. (10) into Eq. (7), the water volumetric fraction β can be expressed as:

$$\beta = \frac{nV_M^*}{\sigma U A^*} \tag{11}$$

$$= \frac{nV_M^*}{A^* L} \tag{12}$$

The cross sectional area A^* is given by the product of the laser sheet thickness times the width of the field of view. The length L is the average length of the droplet streaks and it is equal to the product of the velocity U and the shutter speed σ. At steady state conditions, a set of 30 picture frames of the flow are taken and the number of steaks crossing the area A^* are measured and counted. Once the values of n and L are obtained, Eq. (12) provides an estimate of the water volumetric fraction. The estimated uncertainty on the water volumetric fraction measurement is 40 percent. This is due to the variation associated with the streak number over the 30 picture frames examined in each sample. The average length of the droplet streaks exhibits a variation of about 10 percent about the mean value as noted in the gas velocity section.

Volumetric Fraction Via Evaporative Cooling Effect. Consider the steady-state energy balance written for a cylinder immersed in a hot gas stream laden with water droplets. All the water deposited on the sensor is assumed to evaporate. This is reasonable because the droplets are sparse and the gas temperature high. Therefore, there is little chance for a significant water build-up on the sensor leading to run-off or re-entrainment of the water in the gaseous stream. The collection efficiency κ quantifies the number of droplets that will hit the sensor with respect to the total number of droplets that flow through the sensor cross sectional area, A. Under these premises, the energy balance can be written as:

$$\rho_L A U \beta \kappa \Lambda = Sh(T_G - T_W) \tag{13}$$

Note that the temperature of the wetted sensor (or wet temperature), T_W, can be significantly lower than the hot gas temperature, T_G. Introducing the heat transfer correlation for a cylinder in cross-flow for Reynolds number of the air stream $(U \cdot D/\upsilon_G)$ ranging between 40 and 1000 [12], one obtains:

$$\beta = 0.52\pi \frac{\varepsilon \cdot k_G \mathrm{Pr}^{0.37}}{\kappa \rho_L \upsilon_G^{0.5} \Lambda} \frac{T_G - T_W}{\sqrt{UD}} \tag{14}$$

The parameter ε considers the enhancement of the heat transfer coefficient due to the presence of droplets in the gaseous stream [13]. This parameter is set to 2 for the conditions typical of the applications under consideration. Note that the ratio of the thermal conductivity and the square root of the kinematic viscosity is nearly constant over the range of temperatures of concern [14]. By grouping the numerical values and the physical properties in Eq. (14) into a quantity C, this equation becomes:

$$\beta = \frac{T_G - T_W}{C\sqrt{UD}} \tag{15}$$

The constant C is determined both analytically using Eq. (14) and experimentally using Eq. (15). To determine the value of C analytically, the collection efficiency, κ, is set at 0.96 as it will be discuss later on. Thirteen experiments are conducted for velocities ranging between 3 and 5 m/s, volumetric fraction between 3 and 9 ppm while using the same sensor (i.e., D is kept constant). Figure 5 makes use of Eq. (15) to evaluate the evaporative the constant C. From the data regression shown in the figure, C is set to 85 [K $s^{0.5}$ m^{-1}] when the water volumetric fraction is expressed in parts per million. The two dashed lines identify the uncertainty bounds of ± 10 percent. With this result, the water volumetric fraction can be readily obtained once the wet temperature, the gas temperature, and the gas velocity are measured. The constant C is for water droplets in air over any cylindrical sensing element of diameter D, provided that complete vaporization of the deposited droplets takes place. Incidentally, the value of C deduced from the theory is also shown in Fig. 2. This value, from Eq. (14) is found to be 102 [K $s^{0.5}$ m^{-1}].

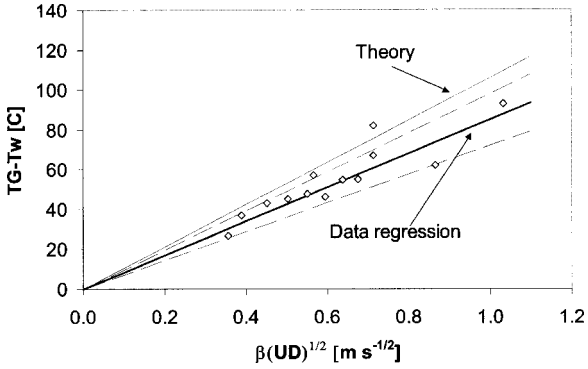

Fig. 5 Evaluation of the constant *C* experimentally using Eq. (15) (Data Regression) and analytically using Eq. (14) (Theory). The dashed lines bound the ±10 percent region about the data regression.

Wet Temperature Sensor

Effect of Sensor Size. Conventional temperature sensors do not measure the temperature of the gas because they are affected by significant evaporative cooling due to the droplets deposited on the sensor surface. Equation (15) shows that for identical flow conditions (U and β constant), the temperature difference is proportional to the square root of the sensor diameter. A brass sensor is exposed to a gas flow laden with water droplets. Without changing the experimental conditions (i.e., the velocity, the gas temperature and the water volumetric fraction) seven brass sleeves of increasing diameter are added to the original sensor. As the sensor diameter is increased the wet temperature detected decreases. Figure 6 shows the results of these experiments in logarithmic scale. The slope of the linear regression through the points (0.48 versus 1/2) confirms the dependency with the square root of the sensor diameter seen in Eq. (15). Therefore, it seems reasonable to have a diameter of the sensor as large as possible in order to achieve a good separation between the two temperatures in the numerator of Eq. (15) and consequently an increased accuracy in the determination of the water volumetric fraction.

Effect of Collection Efficiency. The droplet collection efficiency κ is defined as the ratio between the number of droplets impacting the sensor surface and the number of droplets that would impact the same surface if they had infinite inertia. Aihara and Fu [15] provide an analytical solution for this problem. They determined that the collection efficiency solving the equation of motion for the droplets in the gas flow. The droplet Reynolds

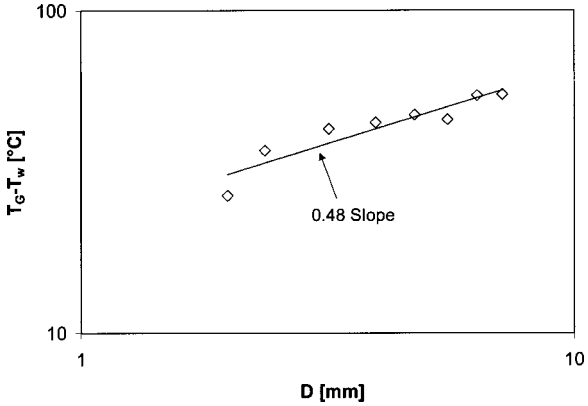

Fig. 6 Difference between the gas temperature and the temperature read by a sensor in a hot gas laden with water droplets as a function of its diameter

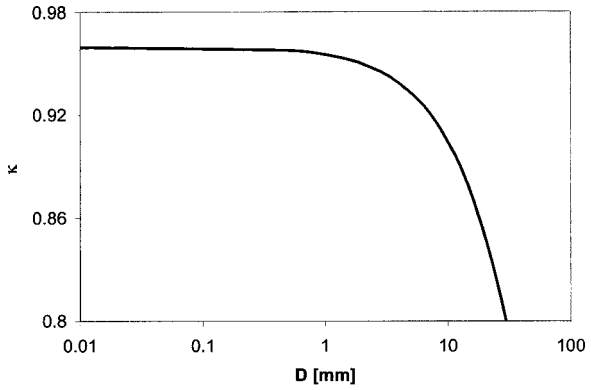

Fig. 7 Collection efficiency as a function of the sensor diameter

number at its terminal velocity in the air is about 0.4. This is consistent with the Stokes flow approximation used in their analysis.

The results of the analysis are shown in Fig. 7. The collection efficiency is plotted versus the diameter of the cylindrical sensor, under conditions typical of a fire scenario that is for velocities of 1–3 m/s and droplet of about 100 μm in diameter. Two observations can be drawn: (a) the collection efficiency approaches an asymptotic value of 0.96 for small sensor diameters; and (b) the collection efficiency decreases if the diameter of the cylindrical sensor increases.

Recall that increasing the sensor size increases the accuracy in the determination of the water volumetric fraction. Therefore, this requirement, in conjunction with the two observations above, suggest that an optimal sensor size must be identified.

Wet Sensor Development. The wet temperature sensor is constituted of a thermocouple inserted in a cylinder. To avoid edge effects, the thermocouple is located at midpoint along the cylinder axis. Aluminum, copper or brass tubes can be used for this purpose. The thermocouple is inserted along the tube axis and the narrow gap between the thermocouple and the internal wall of the tube is filled with conductive paste. The portion of the empty tube, opposite to the thermocouple insertion side, is filled with a solid rod of the same diameter of the thermocouple (i.e., 1.59 mm).

On the basis of the results previously obtained, the optimal diameter of the sensor can be chosen so that the time response is compatible with the time response of the ALTEC sensor and with the restriction to remain in the asymptotic region for the droplet collection efficiency, while achieving the best measurement accuracy possible. The ALTEC sensor time response has been estimated experimentally to be 50 seconds. By using aluminum, we minimize the response time due to its low heat capacity. A 4.76 mm aluminum cylinder yields a time constant of about 30 seconds and a collection efficiency in the asymptotic range. With this arrangement an approximate expression for the water volumetric fraction for gas velocities between 3 and 5 m/s is given as:

$$\beta \approx 0.09(T_G - T_W) \tag{16}$$

This means that the volumetric fraction can be obtained with an uncertainty of ± 1 ppm for a temperature difference uncertainty of ± 10°C.

ALTEC Sensor. Consider a cylindrical heater positioned in cross flow. For temperatures above 300°C, the power required to maintain the heater at a given temperature above the gas temperature both in dry and wet conditions shows similar trends indicating that the evaporative cooling effect is not a factor. For temperatures below 300°C, the heater in wet conditions must supply additional power to evaporate the water deposited on its surface. The reason for this behavior is that, at about 300°C, the Leidenfrost transition occurs and, for temperatures above the transition, the water droplets do not wet the surface. The Leidenfrost phenomena have been the subject of numerous investigations. Emmerson [16] has compared the maximum evaporation time and the Leidenfrost point for discrete droplets of water deposited on smooth surfaces of stainless steel, brass and Monel, for various pressures. The study shows that the Leidenfrost point of water varies with pressure in a way peculiar to the surface material, depending on the 'wettability' of the heating surface. Yao et al. [17] has conducted experiments with water droplets impacting thin steel strips kept at a temperature above the Leidenfrost point. Hatta et al. [18] has performed a study on collision dynamics of water droplets over a rigid surface. In their paper, particular emphasis is given to the above Leidenfrost region, for water particles (300–600 μm) impinging on porous surfaces. Bernardin et al. [19] has used high-speed photographic techniques to record the impact behavior of water droplets over a hot aluminum surface. The main parameters influencing the heat transfer and the impact phenomenon are the injection velocity and the surface temperature. A similar study by Bernardin et al. [20] has shown the influence of the surface roughness on heat transfer regimes induced by water droplets impacting over metallic surfaces.

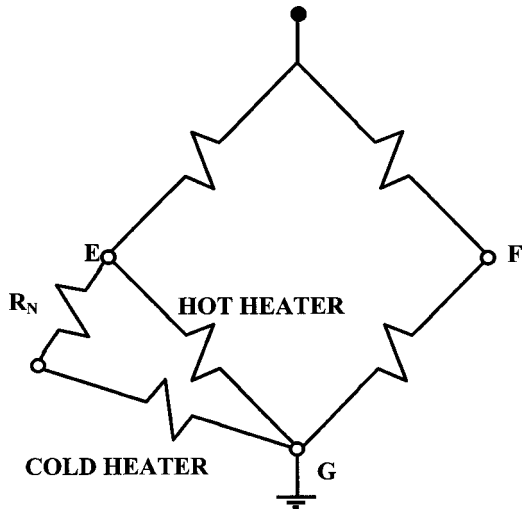

Fig. 8 Controlling circuit for the ALTEC sensor

These observations are at the base of the ALTEC sensor design. Imagine a couple of identical heaters (platinum wires) both kept above the Leidenfrost transition at different temperatures from each other, T_H and T_C. Consider that the heat transfer coefficient between the platinum wires in the ALTEC sensor and the hot gas is inclusive of the radiant heat component. The energy balance for each wire can be written as:

$$\frac{\Delta V^2}{R} = h(T - T_G) \tag{17}$$

The typical arrangement for controlling a single wire heater at a constant temperature is essentially a Wheastone bridge, with an operational amplifier whose output is proportional to the difference of the voltages between the points *E* and *F* shown in Fig. 8. The operational amplifier controls a bipolar gate power transistor so that the ratio of the resistances on the left side of the bridge is constantly equal to the ratio of the resistances on the right side of the bridge. Figure 8 illustrates the adaptation of the original arrangement to include the two heaters of the ALTEC sensor. The resistance between point *E* and point *G* is equivalent to the hot heater in parallel with a circuit containing the cold heater and a resistor *N* in series. By insuring that there is no voltage difference between points *E* and *F*, the controller maintains the overall resis-

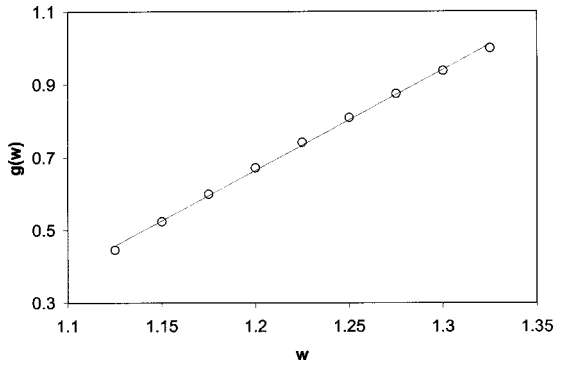

Fig. 9 Function $g(w)$ versus w from Eqs. (22) and (23)

tance of the leg EG equal to the resistance of the resistor N. Introducing the variable w as the ratio of the voltages across the cold heater and the resistor N, one obtains:

$$\frac{R_C}{R_N} = w \tag{18}$$

By recalling that the overall resistance of the leg EG is maintained equal to R_N, one can relate the resistance of the hot wire to w as follows:

$$\frac{R_H}{R_N} = \frac{w+1}{w} \tag{19}$$

By assuming that the heat transfer coefficient is similar for both heaters, Eq. (17), written for both heaters, yields the following ratio:

$$\frac{w^2}{w+1}\frac{\Delta V_H^2}{\Delta V_C^2} = w+1 = \frac{T_H - T_G}{T_C - T_G} \tag{20,21}$$

Note that the electrical resistance of a platinum wire is a linear function of its temperature (i.e., $R = J \cdot T + K$). By combining Eqs. (18), (19), and (21), one can obtain the temperature of the gas as:

$$T_G = \frac{R_N}{J}(w+1-1/w-1/w^2) - \frac{K}{J} = \frac{R_N}{J} g(w) - \frac{K}{J} \tag{22,23}$$

Figure 9 demonstrates that the functional shown in parenthesis is almost linear in the range of interest. Therefore, the gas temperature can be obtained as:

$$T_G = Qw + T^* \tag{24}$$

The principal components of the sensor are the electronic circuit and the measurement sensor. The sensor is constituted of a support frame for the two platinum wires as illustrated in Fig. 10. Three 6.4 mm diameter copper rods have been curved and joined together so that their extremities are equally distant from each other. The clearance is equal to the platinum wires length (30 mm). The wires are attached to the tip of the three rods. A temperature-shrinking Teflon tubing insulates the copper rods from each other. Similarly, a temperature shrinking Teflon tubing cover keeps the overall probe assembly together. In our application, the heating elements are platinum wires of 0.2 mm in diameter.

Results and Discussion

The value of the slope Q in Eq. (24) can be determined experimentally for a variety of conditions. For this reason, about 70 tests are performed both with and without water droplets. The results are plotted in Fig. 11. The gas temperature is read directly with a thermocouple for the dry tests and it is inferred from the ECSAT facility measurements for the wet tests as previously described. The slope Q is consistent for all tests and its numerical value is

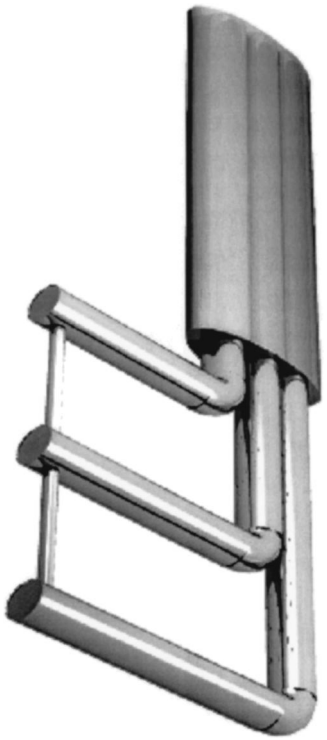

Fig. 10 Sketch of the ALTEC sensor

990 ± 110°C. Figure 11 shows that the data fall in a band ± 110°C about the average value. A single point calibration at ambient temperature is used to determine the parameter T^* in Eq. (24). This test is performed in no flow conditions by exposing the ALTEC sensor to quiescent air. With this information, the calibration is completed to yield:

$$T_G = 990w - 1060 \tag{25}$$

The first set of test is performed in dry conditions and the ALTEC readings are compared with the ones obtained from a K-type thermocouple. Figure 12 illustrates the results. Most of the data fall within a band ± 10°C shown by the dashed lines in the figure. There are some slight discrepancies at temperature less than 130°C. The average error in the range of gas temperature between 100°C and 200°C is 7 percent. At low temperatures, the ECSAT flow velocity is quite high compared to the typical ceiling jet

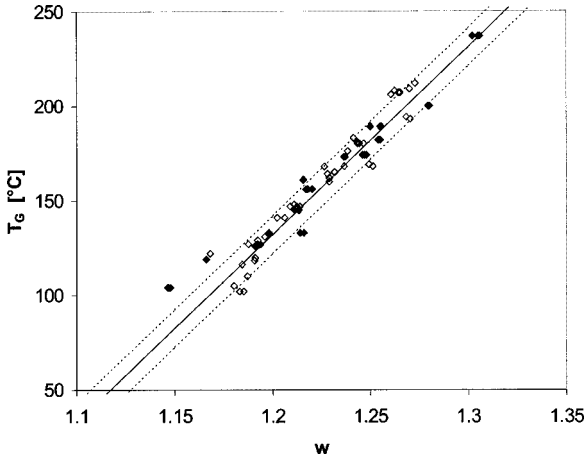

Fig. 11 Calibration curve to determine the slope Q in Eq. (24) (◇ dry conditions, ♦ wet conditions)

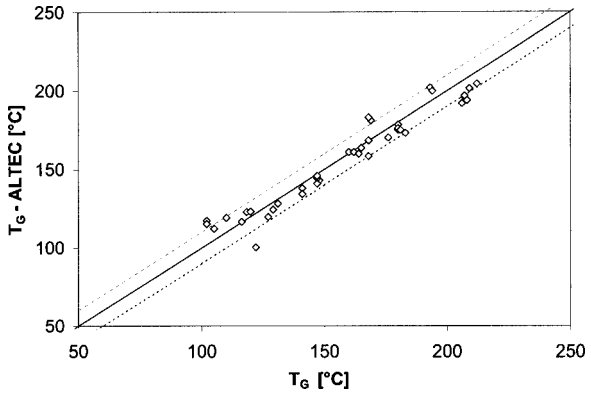

Fig. 12 Comparison between the temperature measured by the ALTEC sensor and the values read by a thermocouple in dry conditions

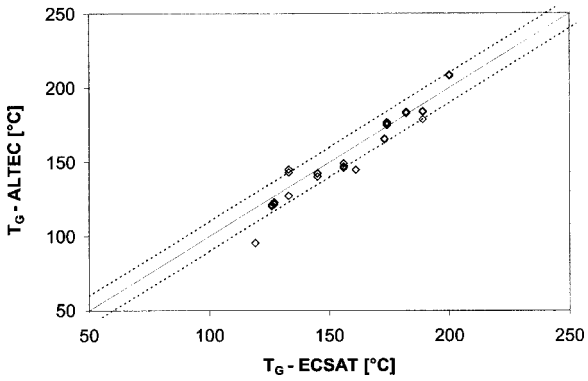

Fig. 14 Comparison between the temperature measured by the ALTEC sensor and the values obtained from the ECSAT facility in wet conditions (the methodology to obtain the ECSAT data is described in the paper)

velocity expected in a fire situation. This is due to the necessity of maintaining an adequate one-dimensionality of the flow downstream the ECSAT orifice. Therefore, in the ECSAT facility, the minimum velocity is about 3.5 m/s. Alpert [21] provides a functional relationship between the ceiling jet velocity and temperature in a fire situation, given a ceiling height and a radial distance from the fire plume impingement point. Figure 13 depicts the velocity-temperature relationship for various ratios H of the ceiling height and the radial distance. Considering a fire sprinkler separation of 3 m, these ratios correspond to ceiling heights ranging form 6 m to 9 m. The ECSAT experimental conditions are also shown in the figure. It is important to consider that in a real scenario it is unlikely to observe velocities of 3 m/s in absence of a hot plume. Therefore, in the ECSAT facility, the ALTEC sensor occasionally performs at unusually high-flow-low-temperature combinations that are not observed in real fire situations. These conditions are off-design and result in inaccuracies for the low values w corresponding to these situations since an unusual high power output is required by the sensor.

A second series of tests has been performed in wet condition. Water droplets are injected through the spray nozzles in the ECSAT facility. The procedure to evaluate the temperature of the gas in presence of water droplets has been explained previously. The gas temperature determined with this approach is identified as the ECSAT temperature. Figure 14 compares the gas temperature deduced from the measurements in the ECSAT facility with the temperature measured with the ALTEC sensor. Also in this case, slight discrepancies are observed for temperatures below 130°C. Most of the data fall within a ±10°C band shown by the dashed lines in the figure. This corresponds to an average error in the range of gas temperature between 100°C and 200°C is 5 percent. The results shown in the figure clearly demonstrate the insensitivity of the ALTEC sensor to the water droplets and the accuracy of the gas temperature readings. The measurement of the gas temperature in presence of water droplets is not documented in the open literature. In fact, the approach presented here is the subject of a patent application.

We can use Eq. (15) with both the gas temperature measured with the ALTEC sensor and the wet temperature measured with the thermocouple inserted in the aluminum cylinder (4.76 mm in diameter) to estimate the local water volumetric fraction.

Figure 15 compares these values of the volumetric fraction with the measurements obtained with the previously described optical method. The appropriate error bars for each measurement are shown in the figure. For the optical technique the error estimates were discussed in previously. For the ALTEC sensor measurements note that the temperatures difference is measured with an uncertainty of ±10°C while the velocity is known with an uncertainty of 10 percent. The constant C introduces an uncertainty of about 10 percent thus resulting in the overall uncertainty for the water volumetric fraction shown in the figure.

Note that while the optical method requires steady state conditions and it is based on the examination of a statistically relevant

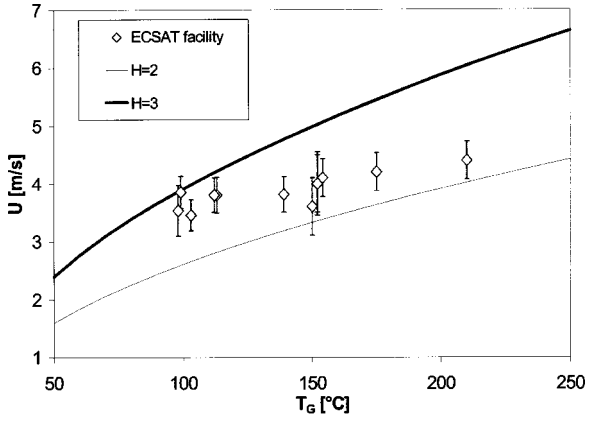

Fig. 13 Velocity-temperature correlations for a natural convection plume versus the ECSAT facility operating conditions. The error bar abound each experimental point represents one standard deviations about the mean value. The solid lines represent the correlation by Alpert [21].

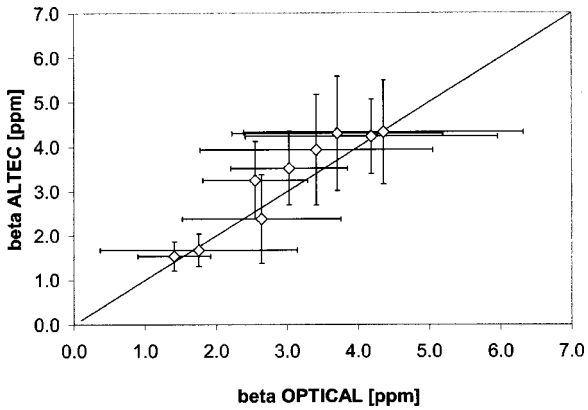

Fig. 15 Water volumetric fraction: values obtained with the ALTEC sensor versus optical measurements. The error bars about each point represent one standard deviation about the mean value.

number of picture frames, the new method proposed here is only limited by the response time of the ALTEC sensor. This methodology is applicable to gas flows where the evaporation rate is substantial. Recall that the droplet impacting the wet sensor must evaporate completely. Therefore, the gas temperature must be reasonably higher than the saturation temperature (about 100°C of temperature difference for water and air) of the liquid and the liquid droplets must be small (about 100 μm in diameter) and sparse (volumetric fractions of about 10 ppm). The available optical techniques [7,8,9] are applicable to far more general conditions. Nonetheless, in several applications (e.g. large fire tests), where optical techniques are impractical to use, a significant number of volumetric fraction and gas temperature measurements can be achieved at a reasonable cost with this approach.

Conclusions

A new measurement technique enables the direct determination of the temperature of a hot gas laden with water droplets. The theoretical approach is presented leading to the design of the ALTEC sensor. The control and data acquisition features are briefly described. A series of tests in dry conditions demonstrate the accuracy of the measurements with respect to a standard thermocouple. Data from the ECSAT facility are used to infer the value of the hot gas temperature in the presence of water droplets. The hot gas temperature is also obtained with the ALTEC sensor. The measurements compare favorably in both cases over the range of conditions typical of fire scenarios. The feasibility and accuracy of the measurements obtained with the newly developed ALTEC sensor are proven and quantified.

A new methodology to measure the evaporative cooling effect due to water droplets in a hot gas flow is presented. Theoretical considerations couple the gas temperature and the wet temperature measurements with the determination of the water volumetric fraction in the gaseous stream. We provide the design details for the wet temperature sensor. The measurements obtained with this novel technique compare favorably with those obtained with a conventional optical method for applications where the droplets evaporation rate is significant.

Acknowledgments

The support of the Building and Fire Research Laboratory of the National Institute of Standards and Technology (NIST) is greatly appreciated. The authors are indebted to Dr. K. Kiger for his insightful comments. The ALTEC sensor is the subject of a patent application (U.S. Patent Pending).

Nomenclature

A = longitudinal cross sectional area of the sensor [m^2]
A^* = laser-sheet cross sectional area [m^2]
B,M,P = parameters in Eq. (6)
C = evaporative cooling constant in Eq. (15) [°C $s^{0.5}$ m^{-1}]
c = specific heat [J kg^{-1} °C^{-1}]
D = sensor diameter [m]
E,F,G = points in Fig. 8
$f(x)$ = function in Eq. (3)
$g(w)$ = function defined in Eq. (23)
H = ratio of the ceiling height and the fire sprinklers separation
h = heat transfer coefficient [W m^{-2} °C^{-1}]
J = platinum wire electrical resistance temperature coefficient [Ω °C^{-1}]
K = platinum wire electrical resistance at 0°C [Ω]
k = thermal conductivity [W m^{-1} °C^{-1}]
L = average length of a droplet streak
N = number of droplet size bins
n = number of droplets through section A^*
n_i = number of droplets in the i-th size bin
Pr = Prandtl number Pr= $\mu_G c_G/\rho_G$
Q = slope in Eq. (24) [°C]
R = electrical resistance [Ohm]
R_N = resistance N (See Fig. 8) [Ohm]
S = sensor heat transfer surface [m^2]
T = temperature [°C]
T^* = intercept in Eq. (24) [°C]
ΔT = temperature difference between the asymptotic temperature distributions in dry and wet conditions [°C]
U = gas velocity [m s^{-1}]
$\dot{V}$ = volumetric flow rate [m^3 s^{-1}]
V_M = mean droplet volume [m^3]
V_M^* = averaged mean droplet volume [m^3]
V_i = volume corresponding to i-th diameter class of the droplet distribution [m^3]
ΔV = voltage difference [Volt]
x = adjusted axial distance along the duct [m]
x_E = distance of complete evaporation of the water droplets from injection [m]
w = resistance ratio as defined in Eq. (18)

Greeks

β = water droplets volumetric fraction
κ = collection efficiency
Λ = latent heat of evaporation [J kg^{-1}]
λ = exponent in Eq. (4)
μ = dynamic viscosity [Pa s]
ε = heat transfer enhancement factor
ρ = density [kg m^{-3}]
σ = video-camera shutter speed [s]
υ = kinematic viscosity [m^2 s^{-1}]

Superscripts/Subscripts

0 = spray nozzle location
C = cold heater
D = dry condition
G = gas
H = hot heater
L = liquid
W = wet condition

References

[1] Chow, W. K., 1989, "On the Effect of a Sprinkler Water Spray," Fire Technol., **25**, pp. 364–373.
[2] Grissom, W. M., and Wierum, F. A., 1981, "Liquid Spray Cooling of a Heated Surface," Int. J. Heat Mass Transf., **24**, pp. 261–271.
[3] diMarzo, M., and Tinker, S., 1996, "Evaporative Cooling Due to a Sparse Spray," Fire Saf. J., **27**, pp. 289–303.
[4] White, G., Tinker, S., and diMarzo, M., 1994, "Modeling of Dropwise Evaporative Cooling on a Semi-Infinite Solid Subjected to Radiant Heat Input," *Int. Proc. IV Int. Symp. on Fire Safety Science*, T. Kashiwagi, ed., International Association of Fire Safety Science, pp. 217–228.
[5] Ruffino, P., and di Marzo, M., 2001, "Measurements of Temperature in a Hot Gas Laden With Water Droplets," NIST-GCR-01-827
[6] Kuo, K. K., 1986, *Principles of Combustion*, Wiley & Sons.
[7] Adrian, R. J., 1991, "Particle-Imaging Techniques for Experimental Fluid Mechanics," Annu. Rev. Fluid Mech., **23**, pp. 261–304.
[8] Crowe, C., Sommerfeld, M., and Tsuji, Y., 1998, *Multiphase Flows With Droplets and Particles*, CRC Press.
[9] Shrakey, P. A., Talley, D. G., Sankar, S. V., and Bachalo, W. D., 2000, "Phase-Doppler Interferometry With Probe-to-Droplet Size Ratios Less Than Unity. II. Application of the Technique," Appl. Opt., **39**(22), pp. 3887–3893.
[10] Widmann, J. F., Presser, C., and Leigh, S. D., 2001, "Improving Phase Doppler Volume Flux Measurements in Low Data Rate Applications," Meas. Sci. Technol., **12**(8), pp. 1180–1190.
[11] Bete Nozzles Inc., private communications.
[12] Zakauskas, A., and Ziugzda, J., 1985, *Heat Transfer of a Cylinder in Cross-Flow*, Hemisphere Publishing Corporation.
[13] Hishida, K., Maeda, M., and Ikai, S., 1980, "Heat Transfer From a Flat Plate in a Two-Component Mist Flow," ASME J. Heat Transfer, **102**, pp. 513–518.
[14] Heskestad, G., and Bill, Jr., R. G., 1988, "Quantification of Thermal Responsiveness of Automatic Sprinkler Including Conduction Effects," Fire Saf. J., **14**, pp. 113–125.
[15] Aihara, T., and Fu, W. S., 1989, "Effect of Droplet-Size Distribution and

Gas-Phase Flow Separation Upon Inertia Collection of Droplets by Bluff-Bodies in a Gas-Liquid Mist Flow,'' Int. J. Heat Mass Transf., **12**, pp. 389–403.
[16] Emmerson, G. S., 1975, ''The Effect of Pressure and Surface Material on the Leidenfrost Point of Discrete Droplets of Water,'' Int. J. Heat Mass Transf., **8**, pp. 381–386.
[17] Yao, S. C., Hochreiter, L. E., and Cai, K. Y., 1988, ''Dynamics of Droplets Impacting on Thin Heated Strips,'' ASME J. Heat Transfer, **110**, pp. 214–220.
[18] Hatta, N., Fujimoto, H., Takuda, H., Kimoshita, K., and Takahashi, O., 1995, ''Collision Dynamics of Water Droplet Impinging on a Rigid Surface Above the Leidenfrost Temperature,'' ISIJ Int., **35**, pp. 50–55.
[19] Bernardin, J. D., Stebbins, C. J., and Mudawar, I., 1997, ''Mapping of Impact and Heat Transfer Regimes of Water Drops Impinging on a Polished Surface,'' Int. J. Heat Mass Transf., **40**(2), pp. 247–267.
[20] Bernardin, J. D., Stebbins, C. J., and Mudawar, I., 1997, ''Effects of Surface Roughness on Water Droplet Impact History and Heat Transfer Regimes,'' Int. J. Heat Mass Transf., **40**(1), pp. 73–88.
[21] Alpert, R. L., 1972, ''Calculation of Response Time of Ceiling-Mounted Fire Detectors,'' Fire Technol., **8**, pp. 181–195.

Marangoni and Variable Viscosity Phenomena in Picoliter Size Solder Droplet Deposition

M. Dietzel

S. Haferl

Y. Ventikos

D. Poulikakos
e-mail: dimos.poulikakos@ethz.ch

Laboratory of Thermodynamics
in Emerging Technologies,
Institute of Energy Technology,
Department of Mechanical
and Process Engineering,
Swiss Federal Institute of Technology,
ETH Center, 8092 Zurich, Switzerland

This paper focuses on the effect that surface tension (Marangoni phenomenon) and viscosity dependence on temperature has on the spreading, transient behavior and final post-solidification shape of a molten Sn63Pb solder droplet deposited on a flat substrate. A Lagrangian finite element formulation of the complete axisymmetric Navier-Stokes equations is utilized for the description of the droplet behavior. Linear temperature dependence for the surface tension and an exponential dependence for the viscosity are assumed. The initial droplet temperature is varied in 50 K steps from 200°C to 500°C, whereas the substrate temperature is kept constant at 25°C. This varies the initial Reynolds number Re_0 from 360 to 716 and the Marangoni number Ma from −9 to −49. The initial Weber number We_0 and initial Prandtl number Pr_0 are for all cases O(1) and $O(10^{-2})$, respectively. The impact velocity and the droplet diameter remain unchanged in all cases examined at 1.5 m/s and 80 microns. A major finding of the work is that, contrary to intuition, the Marangoni effect decreased droplet spreading monotonically. Due to the Marangoni effect, the mechanism that arrested spreading is the surface tension and not the beginning of freezing. Droplet receding during recoiling was aided by the Marangoni effect. On the other hand, the change of viscosity with temperature showed no significant influence on the outcome of the droplet impact. [DOI: 10.1115/1.1532014]

Keywords: Droplet, Heat Transfer, Interface, Microscale, Solidification

1 Introduction

Free surface flows with thermal transport play an important role in a wide range of modern technical applications, such as spray deposition, injection, casting, welding, soldering or extrusion processes, Maronnier and Picasso et al. [1]. In recent years, there has been an increasing interest in micro-scale liquid transport, with many applications ranging from MEMS to the manufacturing of microelectronics. Free surface motion is in many interesting cases complex and influenced by a large number of parameters. The understanding of the underlying physics lends itself to many fundamental investigations.

In this context, the deposition of molten picoliter size solder droplets with diameter O (100 μm) upon a flat conductive substrate is examined, thereby focusing on the effects of a temperature dependence of surface tension (temperature-induced Marangoni effect) and viscosity.

Earlier numerical and experimental investigations have shown that the impact velocity and surface tension are important parameters determining the fluid mechanical behavior of the droplet upon impact within the parametric domain of solder jetting processes, [2,3]. The low impact velocities of O (1 m/s) ensure that no splashing occurs. Considering the importance of surface tension for the problem, a variable surface tension may change the spreading behavior of the droplet markedly.

Numerous literature sources reflect the need for further clarification of both, temperature- and concentration-induced Marangoni effects, especially in small-scale applications. Monti and Savino et al. [4] identified experimentally a reduced wetting of a silicone droplet on a flat substrate caused by Marangoni velocities at the free surface, which entrain surrounding air between the droplet and the substrate. Solutal Marangoni convection is presumed to be of crucial importance in solidification processes leading to phase separation or to local concentration changes in alloys, Cao and Wang et al. [5]. Khodadadi and Zhang [6] observed enhanced melting in molten metal drops due to temperature-induced Marangoni convection with Ma of $O(10^5)$ and Song and Li [7] reported that internal droplet flows are often caused by surface tension forces rather than by buoyancy forces. These authors explicitly stated a significant influence of Marangoni convection on the fluid dynamics of the molten metal, even for rather small Marangoni numbers. Ehrhard and Davis [8] discussed the spreading of droplets on a horizontal plate under the presence of thermocapillary forces, based on the lubrication theory. This work was extended by Braun and Murray et al. [9] to account for solutal Marangoni effects in Pb-Sn alloy droplets with Ma of $O(10^{-1})-O(10^{-2})$. Both investigations reported a reduced spreading if the droplet is heated from the substrate underneath. The accurate prediction of spreading and of the solidified droplet shape is of importance in many applications in microchip manufacturing to ensure the reliability of the process, Waldvogel and Poulikakos [10]. To the best of our knowledge no work on inertia dominated droplet impact flow combined with Marangoni convection has yet been presented in the open literature.

The numerical investigation herein is based on the Lagrangian formulation of the axisymmetric, unsteady Navier-Stokes equations, and the energy equation, which are discretized utilizing the Galerkin finite element method and a deforming, non-adaptive triangulation mesh. The implementation employed extends the methodology of Haferl and Butty et al. [3] to account for the temperature dependence of the surface tension and viscosity.

2 Surface Tension and Viscosity Correlations

Variations in surface tension cause a force acting tangentially to the surface considered. Gradients in surface tension originate from (den Boer [11])

- a temperature gradient, causing a thermocapillary effect
- a concentration gradient, causing a destillocapillary effect
- an electrical potential

Contributed by the Heat Transfer Division for publication in the JOURNAL OF HEAT TRANSFER. Manuscript received by the Heat Transfer Division April 22, 2002; revision received October 11, 2002. Associate Editor: V. Prasad.

Since Sn63Pb is an eutectic alloy, we concentrate in the following on the thermocapillary effect, assuming that neither a marked concentration gradient through a non-eutectic solidification nor an electrical potential is involved in the solder droplet deposition process.

Based on an atomistic approach, Fowler [12] performed a statistical mechanics analysis of the relation between surface tension and intermolecular forces acting at an interface. With r for the distance from the surface, the surface tension coefficient γ can be written as:

$$\gamma = \frac{\pi}{8}\rho_m^2 \int_0^\infty g(r)\partial_r \phi(r) r^4 dr \tag{1}$$

The particle number density ρ_m, the pair correlation function $g(r)$ and the pair potential $\phi(r)$ are depending on temperature, which supports theoretically and from first principles the temperature dependence of surface tension.

Using Eq. (1), it can be shown that Macleod's empirical formula, Eq. (2), for surface tension is supported by the theory of statistical mechanics and thermodynamics, where ρ_{liq} and ρ_{vap} are the densities of the liquid and the vapor phase.

$$\gamma = \mathrm{const}(\rho_{\mathrm{liq}} - \rho_{\mathrm{vap}})^4 \tag{2}$$

In verifying Eq. (2), the approximation is used that the difference in density is proportional to the square root of the difference between the critical and the current temperature of the fluid. Therefore one can write:

$$\gamma = \mathrm{const}(T_C - T)^2 \tag{3}$$

The assumptions made upon deriving Eq. (3) limit the validity to a narrow range close to the critical temperature. More applied expressions replace the square exponent by a parameter α, which was shown to be reasonably close to unity for organic and other compounds by Jasper [13]. This correlation is also commonly used for liquid alloys as solder and sufficiently verified with experiments. Therefore, we relate surface tension linearly with temperature, where the surface tension gradient is noted as $(d_T\gamma)_{\mathrm{ref}}$:

$$\gamma = \gamma_{\mathrm{ref}} + (d_T\gamma)_{\mathrm{ref}}(T - T_{\mathrm{ref}}) \tag{4}$$

Born and Green [14] derived an atomistic expression for viscosity μ based on a generalized hydrodynamic equation describing the mean motion of a cluster of molecules. Using the approaches of Fowler, Born and Green, Egry [15] pointed out that there is a fixed relation between surface tension and viscosity, since they have similar microscopic origins:

$$\mu = \frac{16}{15}\sqrt{\frac{m}{\tilde{k}T}}\gamma \tag{5}$$

In Eq. (5), T is the absolute temperature; $\tilde{k}$ is the Boltzmann constant, and m the atomic mass. Using Eq. (3) in Eq. (5) suggests that viscosity is related to temperature as follows:

$$\mu = \mathrm{const}(T_C \cdot T^{-1/4} - T^{3/4})^2 \tag{6}$$

Equation (6) is again restricted for a narrow range close to the critical point, according to the assumptions made upon deriving Eq. (3). Furthermore, Eq. (5) is derived for pure substances and is not necessarily valid for alloys. Experiments suggest to assume an exponential function for viscosity in the range of a reference point with viscosity μ_{ref} and viscosity coefficient κ, Eq. (7):

$$\mu = \mu_{\mathrm{ref}} \exp[-\kappa(T - T_{\mathrm{ref}})] \tag{7}$$

Koke [16] discussed a more sophisticated approach for viscosity especially for alloys, in particular solder. It is based on the work of Thresh and Crawley [17] and can be cited as follows:

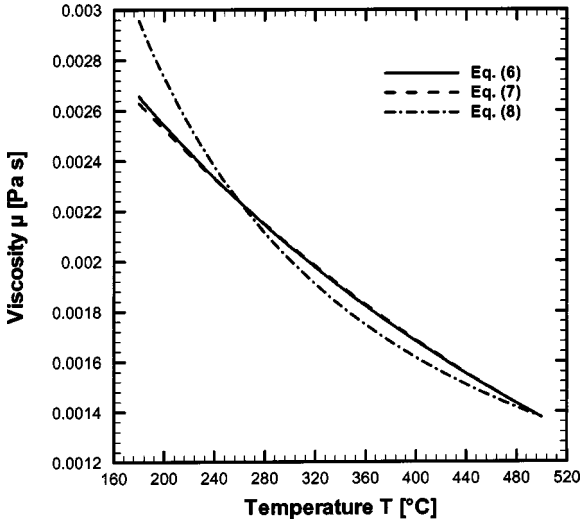

Fig. 1 Comparison of different correlations for viscosity μ

$$\begin{aligned}
\mu_{\mathrm{Solder}} &= \mu_{\mathrm{Pb}} + x_{\mathrm{Sn}}(\mu_{\mathrm{Sn}} - \mu_{\mathrm{Pb}}) \\
\mu_{\mathrm{Sn}} &= 2.75 \cdot 10^{-5}\rho_{\mathrm{Sn}}^{1/3} \exp\left(\frac{0.08849 \cdot \rho_{\mathrm{Sn}}}{T + 273}\right) \\
\mu_{\mathrm{Pb}} &= 2.54 \cdot 10^{-5}\rho_{\mathrm{Pb}}^{1/3} \exp\left(\frac{0.0863 \cdot \rho_{\mathrm{Pb}}}{T + 273}\right) \\
\rho_{\mathrm{Sn}} &= 7.142 \cdot 10^3 - 0.6127 \cdot T \\
\rho_{\mathrm{Pb}} &= 1.109 \cdot 10^4 - 1.3174 \cdot T
\end{aligned} \tag{8}$$

This set of equations provides the viscosity of solder in $[\mathrm{Pa \cdot s}]$ for the case where the temperature T is in [°C]. Figure 1 shows a comparison between Eq. (6), (7), and (8) for solder Sn63Pb and the parametric domain of 180°C to 500°C. Good agreement between the microscopic approach using Fowler's and Born's derivations (Eq. (6)) and the exponential equation for viscosity (Eq. (7)) is found. The more sophisticated approach for mixtures (Eq. (8)) deviates somewhat from the two previous equations, particularly in the temperature range close to the solidification temperature where it emphasizes the increase in viscosity. The general agreement between the microscopic and the macroscopic approach validates the microscopic approach, which leads surface tension and viscosity back to the same intermolecular origin. This justifies the simultaneous consideration of the temperature dependence of surface tension and viscosity in this study. Equation (8) was implemented in the simulations since it provides the most realistic approximation of viscosity progression within the temperature domain considered, especially close to the solidification temperature.

Despite its wide employment in the manufacturing of electronics, it is cumbersome to find complete tables of thermophysical data for solder Sn63Pb. However, the thermophysical properties used in this investigation and provided in Table 1 for a reference temperature of 260°C are carefully chosen and attuned to several literature sources, [18–22].

3 Governing Equations and Solution Procedure

3.1 Set of Equations. The axisymmetric mathematical description of the problem in a dimensionless Lagrangian form of the Navier Stokes equations, Eq. (9)–(12), was discussed in depth by [3]. Here, the equations shall only be repeated briefly for the sake of completeness. Only the necessary extensions to account for the Marangoni and viscosity phenomena are described and discussed with more detail.

Table 1 Thermophysical properties of Sn63Pb @ 260°C

	Density	Viscosity	Surface Tension	Surface Tension Slope	Heat Capacity	Thermal Conductivity	Latent Heat of Fusion	Melting Point
Symbol	ρ	μ_{ref}	γ_{ref}	$d_{T\gamma}$	c_p	K	L	T_m
Unit	[kg/m^3]	[Pa·s]	[mN/m]	[mN/mK]	[J/kgK]	[W/mK]	[J/kg]	[°C]
Liquid	8218	0.002237	498.53	−0.214	238	25	42000	183
Solid	8240	-	-	-	176	48	42000	183

$$D_\tau P+\frac{1}{M^2}\left(\frac{1}{R}\partial_R(RU)+\partial_Z V\right)=0 \quad \text{Continuity} \tag{9}$$

$$D_\tau U-\frac{1}{R}\partial_R(R\overline{\sigma}_{RR})-\partial_Z\overline{\sigma}_{RZ}+\frac{\overline{\sigma}_{\theta\theta}}{R}=0 \quad R\text{-Momentum} \tag{10}$$

$$D_\tau V-\frac{1}{R}\partial_R(R\overline{\sigma}_{RZ})-\partial_Z\overline{\sigma}_{ZZ}-\frac{1}{\mathrm{Fr}}=0 \quad Z\text{-Momentum} \tag{11}$$

$$D_\tau\Theta_i-\frac{2}{\mathrm{Pe}_i}\left[\frac{1}{R}\partial_R(R\partial_R\Theta_i)+\partial_Z^2\Theta_i\right]=0 \quad \text{Energy} \tag{12}$$

$i=1$ Droplet

$i=2$ Substrate

The dimensionless parameters are defined as

$$R=\frac{r}{d_0},\quad Z=\frac{z}{d_0},\quad U=\frac{u}{v_0},\quad \text{Coordinates}$$

$$V=\frac{v}{v_0},\quad \text{Velocities}$$

$$\tau=\frac{t}{d_0/v_0},\quad P=\frac{p-p_{\mathrm{amb}}}{\rho v_0^2},\quad \text{Time, Pressure} \tag{13}$$

$$\overline{\sigma}_{ij}=(\sigma_{ij}+\delta_{ij}p_0)/\rho v_0^2 \quad \text{Stresses}$$

$$\Theta_i=\frac{T_i-\min(T_{1,0},T_{2,0})}{T_{1,0}-T_{2,0}} \quad \text{Temperatures}$$

A sketch of the problem, including the definitions of the coordinates, is shown in Fig. 2. The dimensionless stress components $\overline{\sigma_{ij}}$ in the momentum equations are defined as follows:

$$\overline{\underline{T}}=\begin{bmatrix}\overline{\sigma_{RR}} & \overline{\sigma_{RZ}} & 0\\ \overline{\sigma_{RZ}} & \overline{\sigma_{ZZ}} & 0\\ 0 & 0 & \overline{\sigma_{\theta\theta}}\end{bmatrix}\qquad \begin{aligned}\overline{\sigma}_{RR}&=-P+\frac{2}{\mathrm{Re}}\partial_R U,\quad \overline{\sigma}_{ZZ}=-P+\frac{2}{\mathrm{Re}}\partial_Z V\\ \overline{\sigma}_{\theta\theta}&=-P+\frac{2}{\mathrm{Re}}\frac{U}{R},\quad \overline{\sigma}_{RZ}=\frac{1}{\mathrm{Re}}(\partial_Z U+\partial_R V)\end{aligned} \tag{14}$$

where $\overline{\underline{T}}$ is the dimensionless stress tensor. The characteristic dimensionless numbers of the problem are the initial Reynolds, Froude, Mach, Weber and Peclet number defined as:

$$\mathrm{Re}_0=\frac{\rho\nu_0 d_0}{\mu_0},\quad \mathrm{Fr}=\frac{v_0^2}{d_0 g},\quad M=\frac{\nu_0}{c}$$
$$\mathrm{We}_0=\frac{\rho d_0\nu_0^2}{\gamma_0},\quad \mathrm{Pe}_i=\mathrm{Re}_{0i},\quad \mathrm{Pr}_{0i}=\frac{d_0\nu_0}{\alpha_i} \tag{15}$$

where α_i represents the thermal diffusivities of the different regions ($i=1$ droplet, $i=2$ substrate). The dimensionless initial and boundary conditions have the following form:

$$\tau=0:\quad \begin{cases}U=0,\ V=-1,\ P=\dfrac{4}{\mathrm{We}_0},\\ \Theta_1=0,\ \Theta_2=1\end{cases}$$
$$R=0:\quad U=0,\quad \partial_R V=0,\quad \partial_R\Theta=0 \tag{16}$$
$$Z=0:\quad U=V=0$$

Since the impact velocity of the droplet is small in the solder jetting technology applications we are interested in, splashing is prevented. The initial substrate temperature is equal to the surrounding temperature and both, the free surface of the droplet and the substrate are considered to be adiabatic, which mathematically reads:

$$\nabla\Theta_i\cdot\vec{n}=0 \tag{17}$$

The conservation equation (9)–(12) for mass, momentum and energy are spatially discretized with a Galerkin FEM description. The derivatives of the stress tensor components in space can be avoided and change into a projection of the stress tensor $\overline{\underline{T}}$ onto the outer surface normal. Circumventing these derivatives, a variable viscosity can easily be incorporated by employing a local Reynolds number for each element, no additional term is introduced in the numerical form of the momentum equations. The local Reynolds number is simply defined as:

$$\mathrm{Re}=\frac{\rho\nu_0 d_0}{\mu} \tag{18}$$

where the local viscosity μ is computed with Eq. (8).

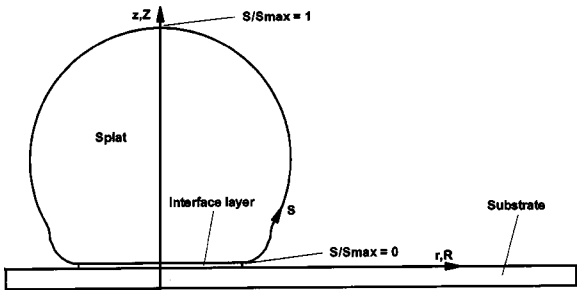

Fig. 2 Sketch of the impingement process

The weak formulation of the momentum equations in this application reads:

$$\int_\Omega \phi_k D_\tau \vec{V} + \underline{\overline{T}} \cdot \nabla \phi_k + \phi_k \cdot \begin{pmatrix} \overline{\sigma}_{\theta\theta}/R \\ 1/\mathrm{Fr} \end{pmatrix} d\Omega = \int_{\partial\Omega} \phi_k \cdot \vec{n} \cdot \underline{\overline{T}} d\Gamma \tag{19}$$

For elements at the free surface, the right hand side of Eq. (19) can be rewritten according to Landau and Lifshitz [23], Chap. VII:

$$\vec{n} \cdot \underline{\overline{T}} = -2 \frac{\overline{H}}{\mathrm{We}} \vec{n} + \frac{\nabla \gamma}{\rho \nu_0^2} \tag{20}$$

This formulation includes a variable surface tension, since a variable Weber number We, and an additional surface tension gradient term is introduced. $\overline{H} = H/d_0$ is the dimensionless curvature, where H is given by:

$$H = \frac{1}{r} \frac{z'}{2 \cdot [(r')^2 + (z')^2]^{1/2}} + \frac{(r'z'' - z'r'')}{2 \cdot [(r')^2 + (z')^2]^{3/2}} \tag{21}$$

The primes in Eq. (21) indicate differentiation of the coordinates r and z with respect to the arc length s of the free surface.

As discussed in section 2, a variable surface tension can be assumed to be a linear function of temperature. Using Eq. (4), Eq. (20) becomes:

$$\vec{n} \cdot \underline{\overline{T}} = -2 \frac{\overline{H}}{\mathrm{We}} \vec{n} + (d_T \gamma)_{\mathrm{ref}} \nabla T / \rho \nu_0^2 \tag{22}$$

Introducing the Marangoni number Ma and using the dimensionless temperature Θ, one further modifies:

$$\vec{n} \cdot \underline{\overline{T}} = -2 \frac{\overline{H}}{\mathrm{We}} \vec{n} + \frac{\mathrm{Ma}}{\mathrm{Re}_0} \nabla \Theta \tag{23}$$

$$\mathrm{Ma} = \frac{\mathrm{Re}_0}{\mathrm{We}_0} \frac{(d_T \gamma)_{\mathrm{ref}} (T_{1,0} - T_{2,0})}{\gamma_0} \tag{24}$$

The Weber number We in Eq. (23) differs from the initial Weber number We_0 expressed in Eq. (17) and has to be defined locally like the local Reynolds number. With Eq. (4) one finds:

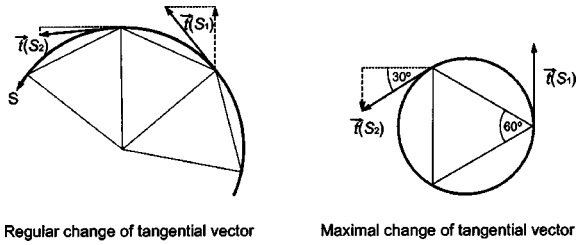

Fig. 3 Maximum change of tangential vector

$$\frac{1}{\mathrm{We}} = \frac{\gamma}{\rho d_0 \nu_0^2} = \frac{\gamma_{\mathrm{ref}} + (d_T \gamma)_{\mathrm{ref}} (T - T_{\mathrm{ref}})}{\rho d_0 \nu_0^2} \Leftrightarrow \frac{1}{\mathrm{We}}$$

$$= \frac{1}{\mathrm{We}_{\mathrm{ref}}} + \frac{\mathrm{Ma}}{\mathrm{Re}_0} (\Theta - \Theta_{\mathrm{ref}}) \tag{25}$$

The maximum values of the two terms on the right hand side of Eq. (23) will be estimated and compared for the case of highest superheat temperature. The first term will be referred to as Laplace term, the second as Marangoni term. Using the first Frenet formula for curvature, one finds for the Laplace term:

$$\frac{1}{\mathrm{We}} |2\overline{H}| = \frac{1}{\mathrm{We}} \left| \frac{t_z}{R} - \vec{t}' \cdot \vec{n} \right| \leqslant \frac{1}{\mathrm{We}} \left(\left| \frac{t_z}{R} \right| + \|\vec{t}'\| \right)$$

$$\leqslant \frac{1}{\mathrm{We}} \left(\frac{1}{R_{\min}} + \|\vec{t}'\|_{\max} \right) \tag{26}$$

where $\vec{t}$ denotes the tangential vector along the surface with arc length s and its z-component t_z. The primes denote again differentiation with respect to the arc length. The minimum radius $R_{\min}$ is equal to the grid size, here equal to $\Delta s_{\min} = 0.02$. For the case $R \to 0$ the z-component of the tangential vector also vanishes due to the symmetry condition. Applying de l'Hôpital's rule:

$$\lim_{t_Z, R \to 0} \left| \frac{t_Z}{R} \right| = \lim_{t_Z, R \to 0} \left| \frac{t_Z'}{R'} \right| = \lim_{t_Z, R \to 0} \left| \frac{t_Z'}{t_R} \right| = |t_Z'| \leqslant \|\vec{t}'\|_{\max} \approx \frac{\sqrt{3}}{\Delta S_{\min}} \tag{27}$$

The last expression in Eq. (27) refers to the fact that the tangential vector can at most change its direction by 120 deg from one element node to the other, Fig. 3. It is assumed that the largest

Table 2 Parameter variations in simulations

Run	$\mu = f(T)$	$T_{1,0}$ [°C]	Θ_{ref} [-]	Θ_m [-]	SHP [-]	$\mathrm{Re}_{\mathrm{ref}}$ [-]	We_{ref} [-]	Ma_{ref} [-]
A1	No	200	1.3429	0.9029	0.09189	360.97	2.8927	0
A2	No	200	1.3429	0.9029	0.09189	360.97	2.8927	−9
A3	Yes	200	1.3429	0.9029	0.09189	360.97	2.8927	−9
B1	No	250	1.0444	0.70222	0.29778	427.65	2.9545	0
B2	No	250	1.0444	0.70222	0.29778	427.65	2.9545	−13
B3	Yes	250	1.0444	0.70222	0.29778	427.65	2.9545	−13
C1	No	300	0.85454	0.57455	0.42545	491.85	3.019	0
C2	No	300	0.85454	0.57455	0.42545	491.85	3.019	−19
C3	Yes	300	0.85454	0.57455	0.42545	491.85	3.019	−19
D1	No	350	0.72308	0.48615	0.51385	552.78	3.0864	0
D2	No	350	0.72308	0.48615	0.51385	552.78	3.0864	−25
D3	Yes	350	0.72308	0.48615	0.51385	552.78	3.0864	−25
E1	No	400	0.6267	0.42133	0.57867	610.25	3.1569	0
E2	No	400	0.6267	0.42133	0.57867	610.25	3.1569	−33
E3	Yes	400	0.6267	0.42133	0.57867	610.25	3.1569	−33
F1	No	450	0.55294	0.37177	0.62824	664.98	3.2307	0
F2	No	450	0.55294	0.37177	0.62824	664.98	3.2307	−40
F3	Yes	450	0.55294	0.37177	0.62824	664.98	3.2307	−40
G1	No	500	0.49474	0.33263	0.66737	716.17	3.308	0
G2	No	500	0.49474	0.33263	0.66737	716.17	3.308	−49
G3	Yes	500	0.49474	0.33263	0.66737	716.17	3.308	−49

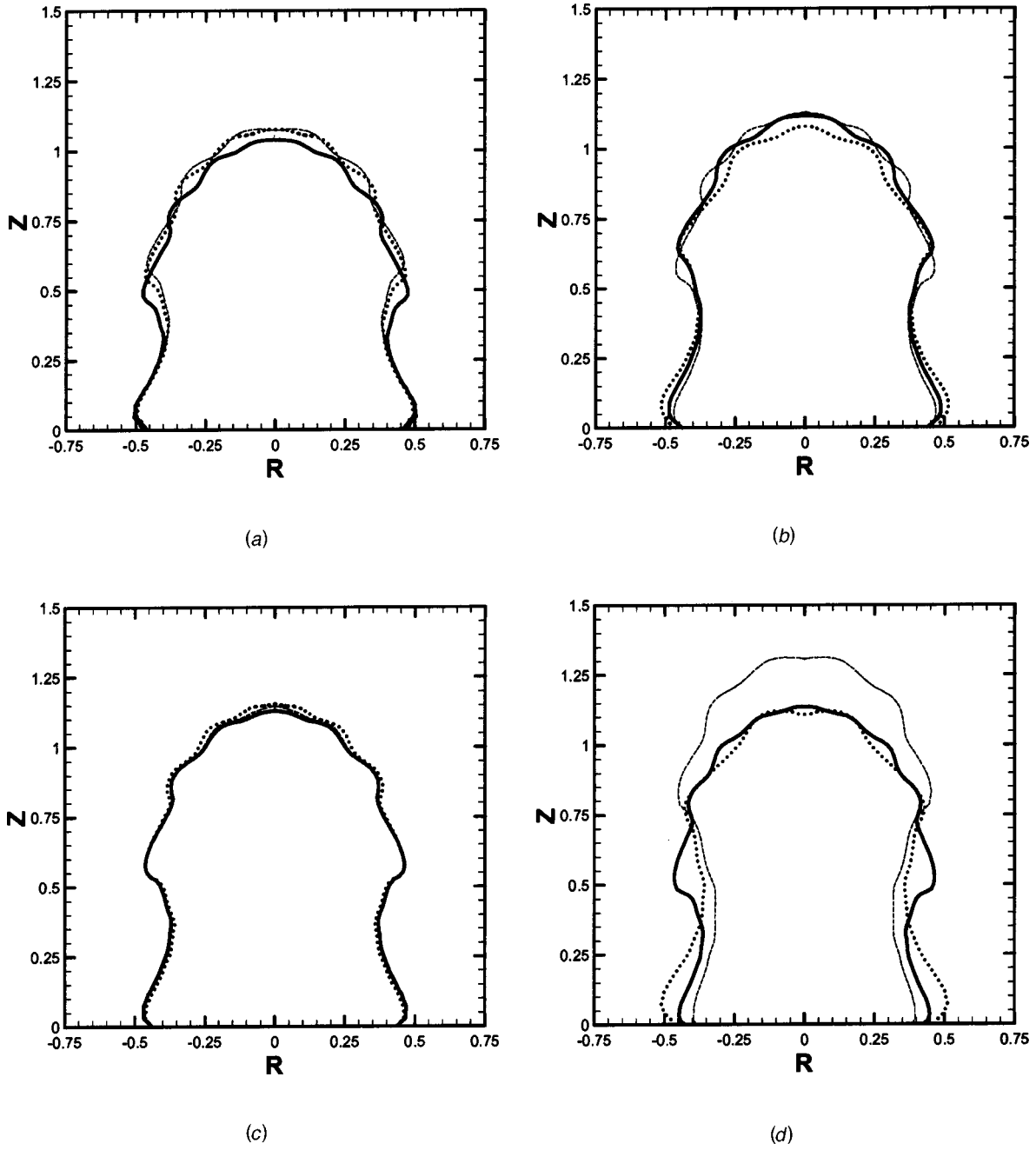

Fig. 4 Change of spreading with increasing droplet superheat (bold dotted line: constant viscosity and surface tension; thin dashed line: constant viscosity and variable surface tension; bold solid line: variable viscosity and surface tension): (*a*) $T_{1,0}$ = 200°C; (*b*) $T_{1,0}$=250°C; (*c*) $T_{1,0}$=300°C; (*d*) $T_{1,0}$=350°C; (*e*) $T_{1,0}$=400°C; (*f*) $T_{1,0}$=450°C; and (*g*) $T_{1,0}$=500°C.

resolvable free surface curvature is the curvature of a circle enclosing one triangular element. However, with this and Eq. (26) one can estimate:

$$\frac{1}{\mathrm{We}}\left|2\overline{H}\right| \leq \frac{1}{\mathrm{We}}\left(2\left\|\vec{t}'\right\|_{\max}\right) \approx \frac{1}{\mathrm{We}}\frac{2\sqrt{3}}{\Delta s_{\min}} \tag{28}$$

The following inequality is valid for the Marangoni term:

$$\left\|\frac{\mathrm{Ma}}{\mathrm{Re}_0}\nabla\Theta\right\| = \left|\frac{\mathrm{Ma}}{\mathrm{Re}_0}\right| \cdot \left\|\nabla\Theta\right\| \leq \frac{\left|\mathrm{Ma}\right|}{\mathrm{Re}_0} 2 \cdot \frac{\Theta_{\max}}{\Delta s_{\min}} \tag{29}$$

The maximum temperature $\Theta_{\max}$ which can occur is equal to 1. With this one finds for the ratio between the Laplace and the Marangoni term:

$$\frac{(\mathrm{Laplace})_{\max}}{(\mathrm{Marangoni})_{\max}} \approx \sqrt{3}\frac{1}{\mathrm{We}}\frac{\mathrm{Re}_0}{\left|\mathrm{Ma}\right|} = 8 \tag{30}$$

Equation (30) indicates that the Laplace term and the Marangoni term are often of the same order of magnitude, especially if the strong overestimation of the Laplace term in Eq. (28) is taken into account. Therefore, incorporating the Marangoni effect in the model is worth pursuing.

To circumvent the problem of singularity caused by enforcing both, the boundary conditions of a moving contact line and a no-slip condition, the Navier-slip condition is introduced at the contact line, Baer and Cairncross et al. [24]:

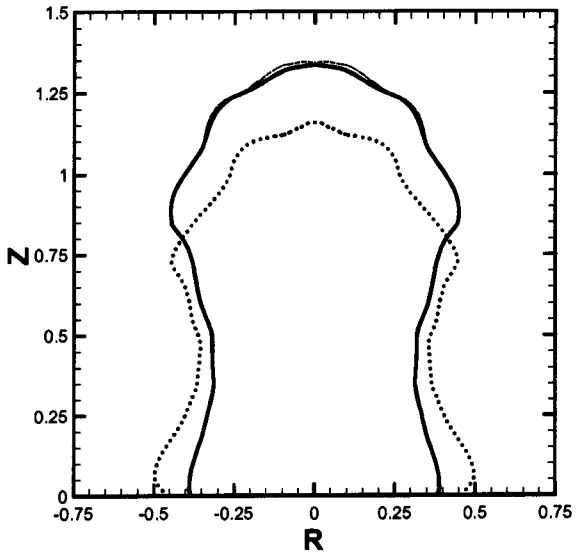

(*e*)

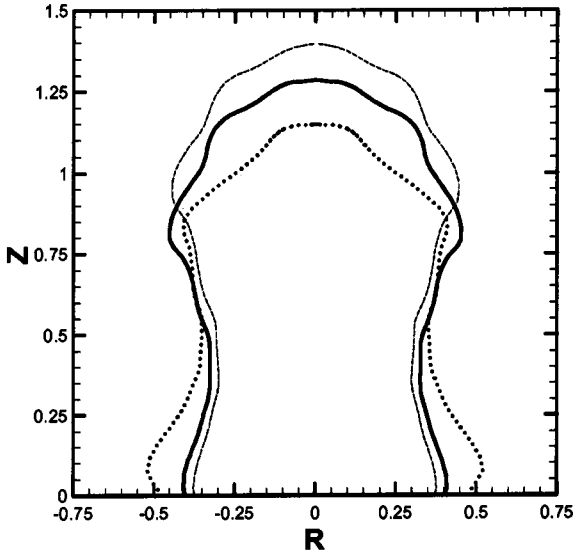

(*f*)

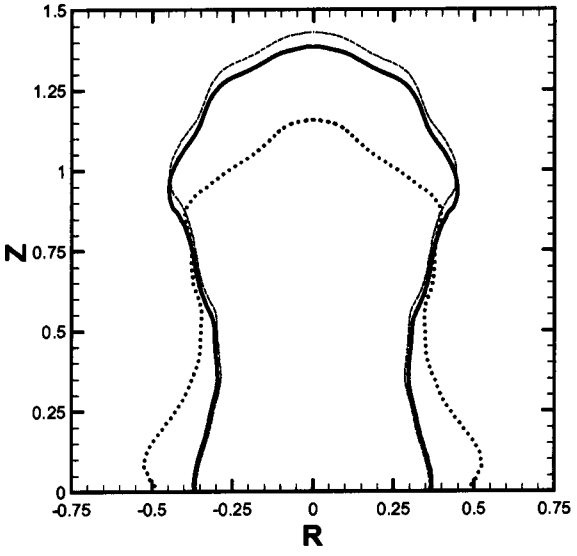

(*g*)

Fig. 4 (***continued***)

$$\vec{n}\cdot\underline{\underline{T}}\cdot\vec{t}=\frac{1}{\varepsilon}\vec{V}\cdot\vec{t} \tag{31}$$

In Eq. (31), $\vec{n}$ and $\vec{t}$ are the normal and tangential unit vectors, respectively. The Navier-slip length ε is assumed to be of the order $O(10^{-3})$ as stated in the same reference. One has to keep in mind that this condition only limits the fluid stresses at the contact line. The temperature dependence of wetting is not taken into account.

The solidification process was numerically modeled by setting the velocities to zero when a grid point reached the solidification temperature. The release of the latent heat of freezing was incorporated utilizing the 'exact specific heat method,' Bushko and Grosse [25]. An inert gas atmosphere was assumed to suppress oxidation of the free surface, as it is indeed the case in solder jetting (free surface oxidation would effect the Marangoni convection as mentioned by Arafune and Sugiura et al. [26]).

3.2 Numerical Solution Procedure. The Navier-Stokes equations in the weak formulation were spatially discretized using triangles and linear shape functions $\phi_k, k=1,2,3$. The commercial meshing tool Hypermesh® created the non-adaptive grid, whereas an automatically initiated remeshing was executed if one of the internal element angles β_i exceeded the range of $15\,\text{deg}<\beta_i<130\,\text{deg}$ through distortion during the transient impact process. The Bach-Hassager iterative scheme was used for solving the fractional time step of Eqs. (9)–(11), describing the fluid dynamical behavior, Bach and Hassager [27]. Convergence was considered as being reached in the fluid mechanical part, when the relative changes of the velocities and pressure values were less than

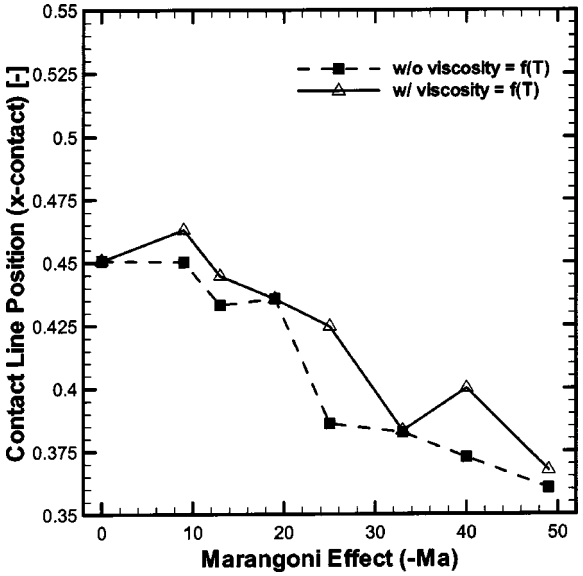

Fig. 5 Spreading versus absolute *Ma*-number

0.1 percent between two iterations. The energy equation (12) was solved as a sub-step, based on the velocities obtained at the end of the fluid-dynamic sub-step, using the Crank-Nicholson scheme. To account for the coupling of momentum and energy equation through the temperature dependence of surface tension and viscosity, the dimensionless maximum time step was chosen with 10^{-4} sufficiently small to avoid unacceptable errors in both, the fluid mechanical solution and the thermal solution. A further reduction of the time step to decrease the maximal possible surface tension and viscosity change within one time step did not show improved results but strongly increased the needed computing time. Moreover, the maximum time step was automatically reduced in sub-iterations if convergence problems occurred.

All simulations were performed using a fine grid of about 6500 elements created with 3500 nodes. The average element length was about 0.02, which is 1/200 of the initial droplet diameter. This high refinement was chosen to resolve even the smallest changes in spreading behavior, since spreading was modeled by connecting a node from the droplet free surface to the substrate. The accuracy of the spreading prediction is therefore in the order of the distance between two neighboring free surface nodes. Each case required a total CPU time of about 28 h (1 GHz, Pentium III) to complete 50,000 time steps. A number of simulations were performed in order to ensure mass and energy conservation. For the mesh density and time step utilized, both mass and energy were conserved within a final error of less than 1 percent compared to the initial values. Furthermore, it was verified that the final droplet shape is sufficiently independent from the mesh size to match the accuracy of those results presented in previous studies [3]. The chosen time step did not show an influence on the final outcome of the solidified droplet.

4 Results and Discussion

4.1 Parameter Variations. In order to investigate the effects which the temperature dependence of surface tension and viscosity has on the spreading, the transient behavior as well as on the end shape of the droplet, simulations were performed utilizing different values of droplet superheat. The initial droplet temperature was changed from 200°C to 500°C in steps of 50 K, causing other parameters to change as well, according to their definition in section 3. The droplet impact velocity was kept constant at 1.5 m/s. The initial droplet diameter also remained unchanged at the typical value for solder jetting of 80 μm. However, due to the change of the initial droplet temperature, the initial Reynolds, Weber and most importantly the Marangoni number changed from case to case. Table 2 summarizes the simulations performed and the corresponding parameter values.

In Table 2, *SHP* is the so-called superheating parameter, which states the degree of superheating of the droplet above its melting temperature of 183°C, Eq. (32).

$$SHP = \frac{T_{1,0} - T_m}{T_{1,0} - T_{2,0}} \tag{32}$$

$\Theta_m = 1 - SHP$ is the dimensionless melting temperature and Θ_{ref} is the dimensionless reference temperature corresponding to the dimensional value of 260°C.

4.2 Influence of Thermal Marangoni Effect. Considering the droplet post-solidification shapes in Fig. 4, every figure com-

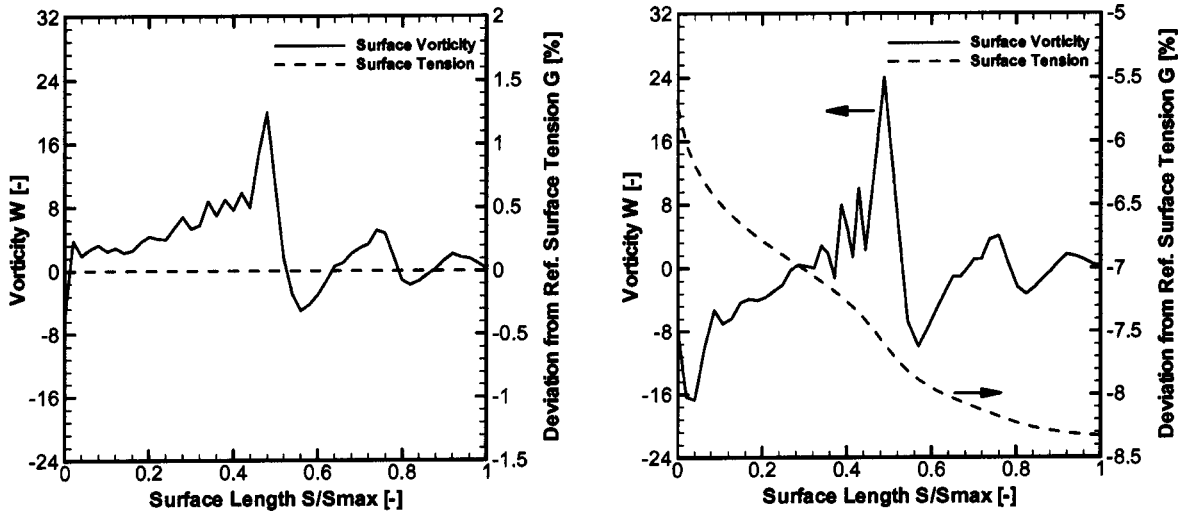

Fig. 6 Vorticity and relative change in surface tension at time $\tau = 0.3$ for: (*a*) invariant; and (*b*) variant thermal properties ($Ma = -49$).

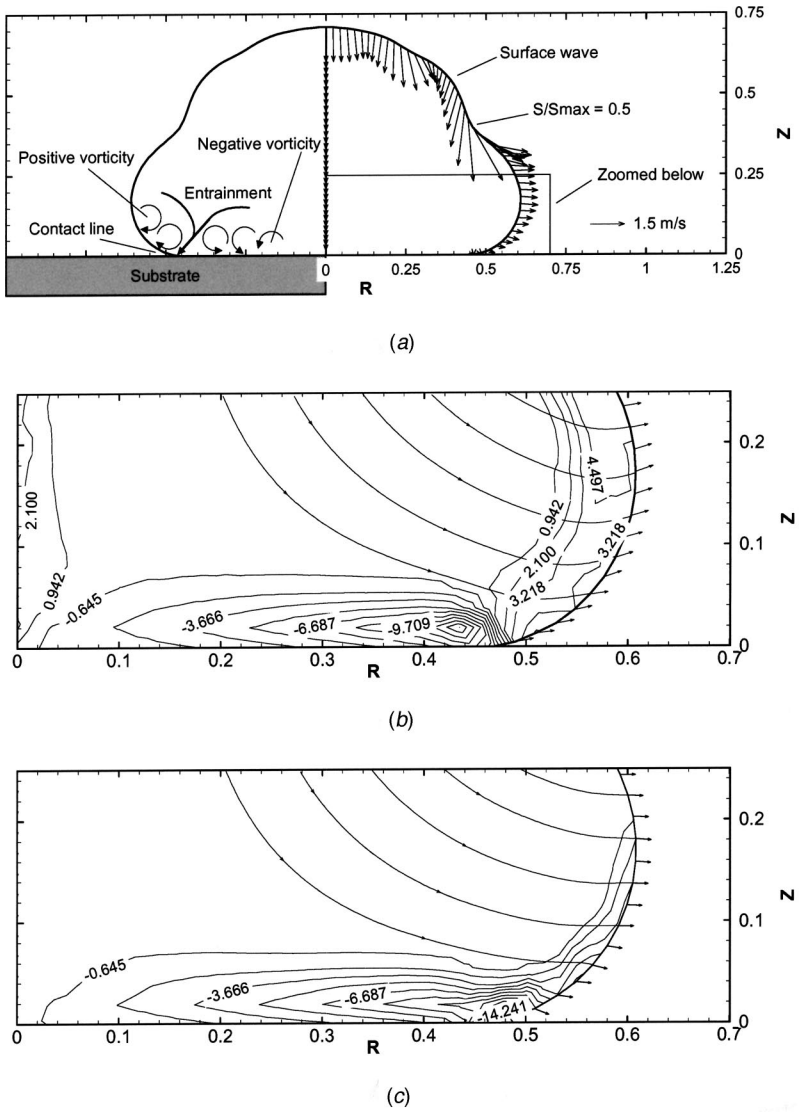

Fig. 7 (*a*) Illustration of spreading mechanism (left) and surface velocity vectors (right) at time $\tau=0.3$; (*b*) vorticity field without Marangoni effect, $\tau=0.3$; and (*c*) vorticity field with Marangoni effect, $Ma=-49$, $\tau=0.3$.

pares the end shapes of three cases: One with constant (independent of temperature) surface tension and viscosity (bold dotted line), one involving only the Marangoni effect (thin dashed line) and the third accounting for both, a change of surface tension and viscosity with temperature (bold solid line). The spreading for the constant property cases increases slightly with droplet superheat but is practically constant. This has to be expected since the increasing wettability with higher temperature is not modeled by the Navier-slip boundary condition as mentioned earlier. On the other hand, the spreading decreases by approximately 20 percent (and with this the contact area by up to 34 percent) between 200°C and 500°C initial droplet temperature if a variation of both properties with temperature is included, Fig. 4. The change of viscosity has a marginal influence on spreading as can be seen comparing the case of a variable surface tension and a constant viscosity and the case with both thermophysical properties as a function of temperature. Plotting the contact line radius *x*-contact versus the absolute Marangoni number, −Ma, shows a monotonic decrease of the spread radius with increasing Marangoni effect, Fig. 5. This clearly indicates that the thermocapillary forces cause the reduced spreading. The small deviations from the main trend in some cases shown in Fig. 5 have the order of the side length of one element, which is within the numerical accuracy of the spreading prediction as outlined prior. The change in spreading also influences the final shape of the droplet: Increased spreading accumulates mass in the outer regions close to the substrate, whereas reduced spreading enhances the recoiling and the final height of the solidified droplet. Following this trend, the end shapes for the constant property cases are wider and flatter, whereas the droplet final shapes for the temperature dependent properties are narrower and taller.

The reduced spreading with increasing absolute Marangoni number is a counter-intuitive result. One can easily verify with Eq. (23) that the direction of the Marangoni force points towards the substrate, since the Marangoni number is negative and the temperature gradient is positive. In other words, the surface temperature is lower closer to the substrate causing a higher surface tension and a pulling force directed to the substrate. One would expect a surface flow in the direction of the contact line, thereby accumulating mass and actually enhancing the spreading. In fact the opposite is observed, spreading is reduced. To further clarify this counter-intuitive result and the influence of the Marangoni effect on the droplet spreading, a detailed investigation of the vorticity evolution ω inside the droplet was performed.

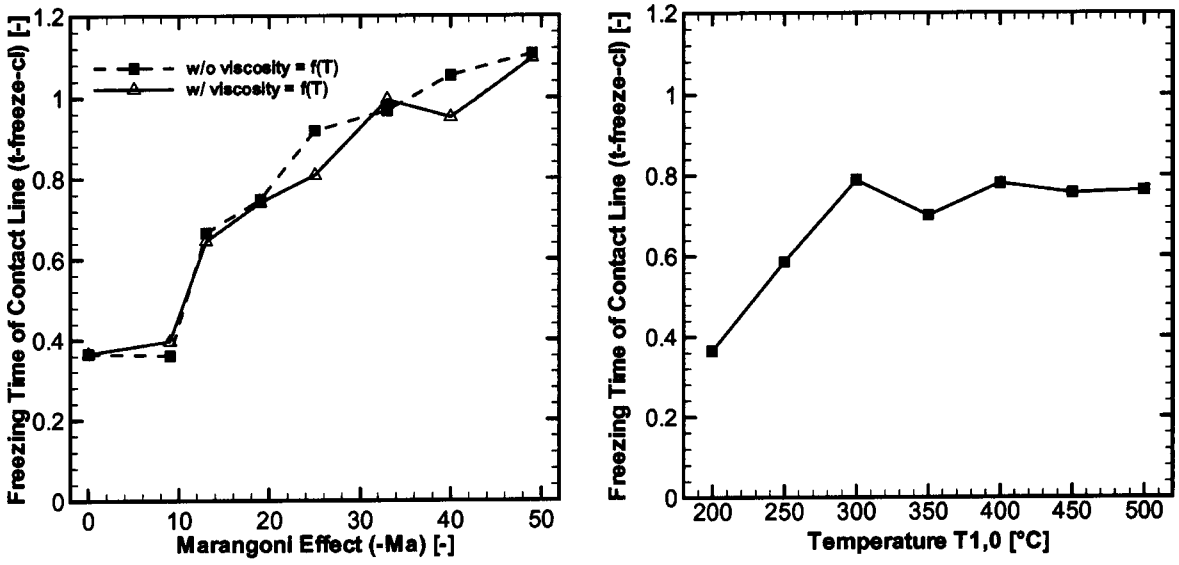

Fig. 8 (*a*) **Contact line freezing time versus absolute value of *Ma*-number; and** (*b*) **contact line freezing time versus superheat temperature.**

The vorticity, Eq. (33), was calculated with a finite element approach and a linear interpolation function for each element, Eq. (34).

$$\omega = \partial_R V - \partial_Z U \tag{33}$$

$$\omega_{elt,i} = \sum_{i=1}^{3} V_i \partial_R \phi_i - \sum_{i=1}^{3} U_i \partial_Z \phi_i \tag{34}$$

The vorticity of a node surrounded by n elements was equated to the area average of the vorticities of the surrounding elements:

$$\omega_{\text{node}} = \sum_{i=1}^{n} \left(\frac{A_i}{\sum_{j=1}^{n} A_j} \right) \omega_{elt,i} \tag{35}$$

Figure 6 shows the vorticity and the relative change of surface tension, G, along the droplet surface for constant, (*a*), and variable, (*b*), surface tension and viscosity, respectively.

$$G = \frac{\gamma - \gamma_{\text{ref}}}{\gamma_{\text{ref}}} \cdot 100 \text{ percent} \tag{36}$$

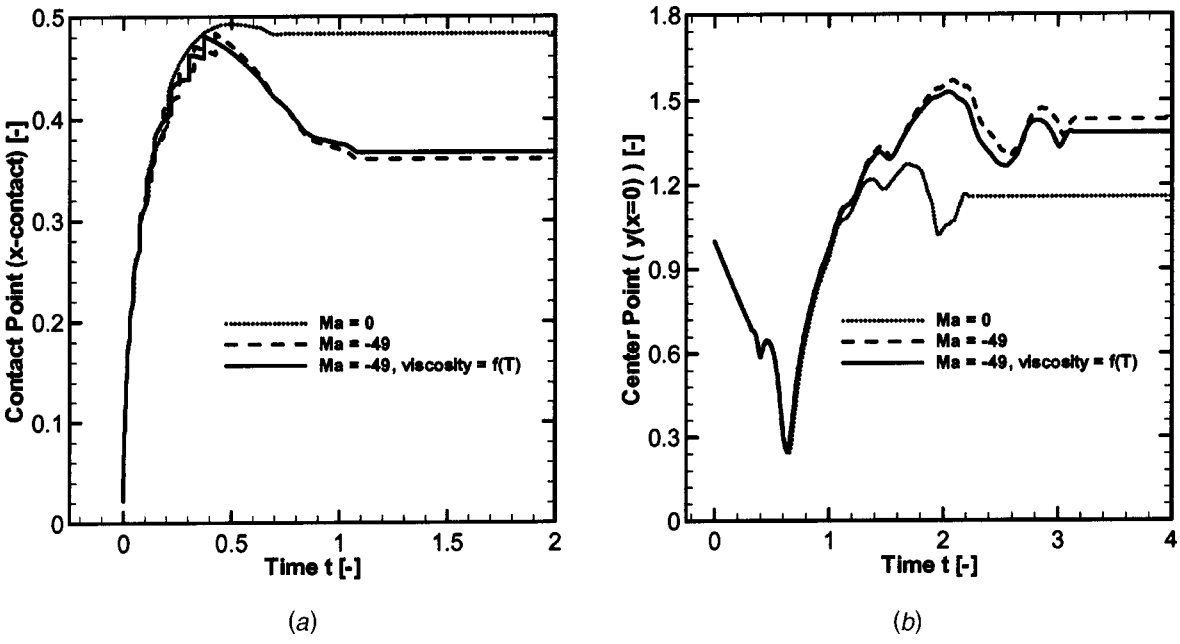

Fig. 9 (*a*) **Droplet spread radius; and** (*b*) **droplet top center of symmetry as a function of time τ.**

Table 3 Reason for contact line arrest upon spreading

Ma	Contact line arrest due to freezing	Contact line arrest due to surface tension
0	●	
−9	●	
−13	●	
−19	(●)	(●)
−25		●
−33		●
−40		●
−49		●

The surface length (arc length) starts from the contact line ($S/S_{max}=0$) and ends at the centerline of the droplet ($S/S_{max}=1$). The case chosen corresponds to maximum superheat at a dimensionless time $\tau=0.3$. The strong correlation between the Marangoni force and vorticity across the surface is clearly observed. The Marangoni effect reduces the vorticity to even negative values at the free surface close to the contact line. This observation enables us to provide an explanation for the reduction of spreading with increasing Marangoni effect: The Marangoni force is surely directed towards the substrate but instead of causing an actual mass flow towards the contact line it only initiates a clockwise fluid rotation close to the free surface. This is understandable since the magnitude of radial flow inertia is large compared to the Marangoni effect, even for large absolute values of the Marangoni number. The peak in vorticity at length $S/S_{max}=0.5$ is caused by a strong change in the curvature of the droplet surface. This is further verified with the right hand side of Fig. 7(*a*), where a depiction of the surface velocity vectors is provided for the same superheat and time step. Fluid above the surface buckling ($S/S_{max}=0.5$) is still moving downward, whereas fluid below this region is already deflected by the impact on the substrate, causing a rapid change of the velocity direction (i.e., a strong vorticity). Examining several frames at different time steps (not shown here for brevity), it was determined that this point of changing curvature also marks the end of a surface wave. This wave travels along the surface towards the centerline. It also explains the slightly deviated velocity vectors on the surface above the point of changing curvature compared to those inside of the fluid, which are still on an undisturbed downward travel in the *Z*-direction. Neither the travel speed nor the amplitude of this wave is affected by the Marangoni effect.

It is actually easier to first focus on the case without Marangoni effect to further understand the mechanism affecting the spreading behavior of the droplet: The vorticity at the free surface is slightly positive for this case, as it can be seen in Fig. 7(*b*), whereas the vorticity of the fluid in the wall region is always negative for all cases, independent whether the Marangoni effect is incorporated or not, since it is initiated by the wall friction. These counter-rotating vorticity regions entrain fluid, which they squeeze and direct towards the contact line region, as it is illustrated on the left hand side of Fig. 7(*a*). On the other hand, the positive vorticity at the free surface cannot be seen in the case accounting for the Marangoni effect: Figure 7(*c*) shows the vorticity field for Ma $=-49$ at the same time step as in Fig. 7(*b*), $\tau=0.3$. Therefore, thermocapillary forces weaken the effect of fluid entrainment to the contact line, since the vorticity at the free surface in the contact area is changed to negative values. The clockwise rotation of the flow in this case acts against the oncoming inertia flow, hence opposing the radial flow. This mechanism causes a reduction in droplet spreading as observed in Fig. 4 and Fig. 5.

Considering the freezing time of the contact line (i.e., the time when the contact line is arrested by freezing) in Fig. 8(*a*), one can see that the contact line is still moving up to three times longer for the highest Marangoni number compared to the lowest Marangoni number. Again, the effect of variable viscosity is not significant. On the other hand, this increase in arrest time of the contact line is less distinct for the cases excluding the Marangoni effect, Fig. 8(*b*). This leads to the assumption that the strong surface vorticity caused by the Marangoni force close to the substrate extends the motion of the contact line to longer times through additional convective heat flux to the contact area, delaying the beginning of freezing. This statement is supported by Fig. 9(*a*), showing the temporal contact line evolution for the highest superheat temperature. The spread radius for cases with and without Marangoni force has an almost identical development until the time $\tau=0.5$. The droplet recoiling starts after this time value, Fig. 9(*b*). It is only for the Marangoni cases that the recoiling leads to a strong receding of the droplet and to a reduction of the spread radius. Hence, the thermocapillary forces seem to promote this droplet receding during recoiling. Table 3 reports the mechanism found

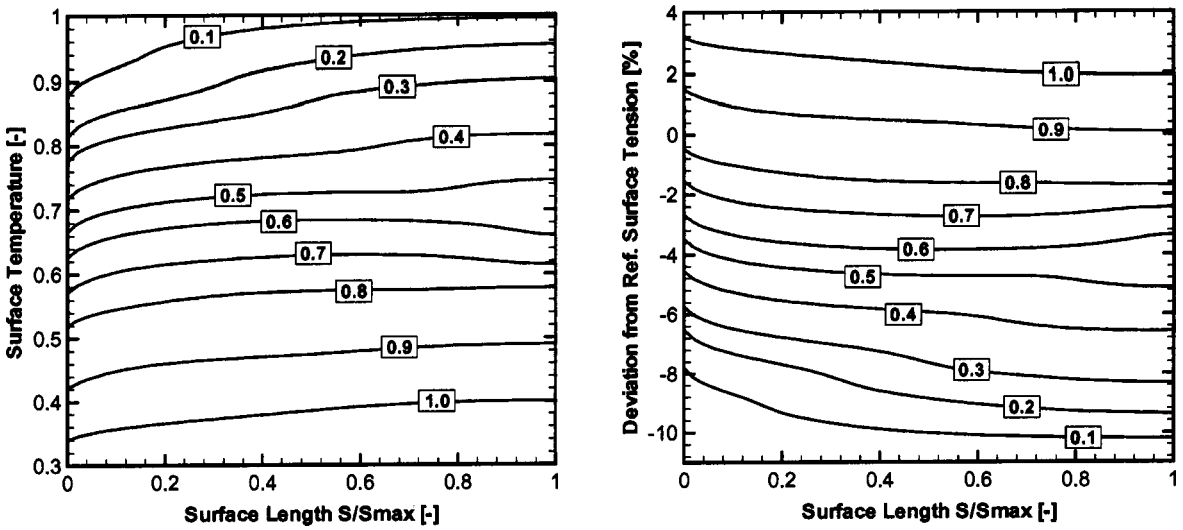

(*a*) (*b*)

Fig. 10 Evolution of surface temperature (*a*) and surface tension in time (*b*)

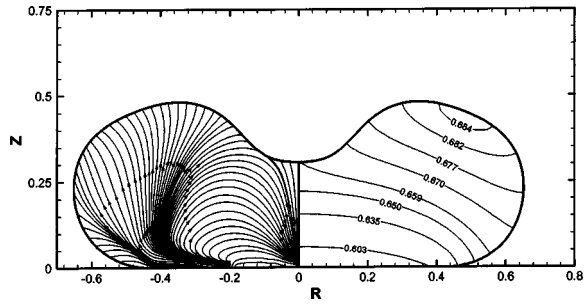

Fig. 11 Streamlines and isotherms in droplet at $\tau=0.6$

for the contact line arrest (end of spreading) for different Marangoni numbers. The onset of freezing stops spreading for the cases with small absolute Marangoni numbers since no significant recoiling occurs. This is the same behavior as for cases without the Marangoni effect and therefore expected to eventuate. In contradiction, the stronger thermocapillary forces for larger absolute Marangoni numbers lead to a strong droplet recoiling after the first spreading and especially before freezing can occur. The mechanism that arrests spreading for larger absolute Marangoni numbers is therefore the surface tension instead of the beginning of freezing.

As outlined in the previous paragraph, the Marangoni effect influences primarily the droplet spreading and the initial recoiling phase, until the dimensionless time is approximately 1.0. Figure 10 shows the time evolution of surface temperature, (*a*), and surface tension, (*b*), from $\tau=0.1$ to $\tau=1$ along the surface length for the case of variable surface tension and viscosity and for the highest superheat temperature. It is demonstrated that a noticeable temperature and surface tension gradient exists primarily only close to the substrate, initially imposed by the boundary conditions. The local droplet temperature and with it the surface tension are approaching uniform values as time increases. This corresponds to a progressively decreasing Marangoni effect.

The surface temperature along the surface length is increasing monotonically with arc length for all times considered except for $\tau=0.6$. In this case, the surface temperature increases within the range $S/S_{\max}=0$ till $S/S_{\max}\approx 0.6$, whereas it decreases again beyond $S/S_{\max}\approx 0.6$. This behavior can be understood when the droplet shape for this time step is considered, Fig. 11. The droplet is at the end of the initial spreading process and starts to recoil. The surface region close to the symmetry axis ($S/S_{\max}\approx 1$) is thereby closer to the colder substrate than the surface at intermediate values of $S/S_{\max}$. Due to the cooling effect of the substrate, the maximum in surface temperature does not occur at the center of symmetry.

5 Conclusion

A numerical investigation was presented studying the effects of thermocapillarity and viscosity variation with temperature for the deposition of picoliter size solder droplets on a flat substrate. Properties of eutectic Sn63Pb were employed in this study because of its wide spread use for electrical joints. Counterintuitively, a reduced spreading with increasing absolute Marangoni number was found (the surface tension maximum occurs in the region of the contact line). This finding was explained through the emergence of strong negative vorticity at the free surface in the contact area instead of the moderate positive vorticity observed when no thermocapillary forces were present. Previous studies of a monotonic droplet spreading without initial inertia showed in principal the opposite behavior. Hence, one should not in general study inertia and thermocapillary effects on droplet spreading separately and then superimpose the solutions. The motion of the contact line in time was shown to be a function of the Marangoni number as well. The initial spreading was limited due to surface tension forces for large absolute Marangoni numbers, whereas the contact line was arrested by the onset of freezing for small absolute Marangoni numbers. Thermocapillary forces support droplet receding after the initial spreading, which also leads to a stronger recoiling phase. The final post-solidified droplet shapes were shown to be narrower and taller for large absolute Marangoni numbers (smaller contact area affecting bonding) compared to the constant surface tension cases. The effect of viscosity variation was found to be minor.

Nomenclature

Latin symbols

c = speed of sound [m/s]
d = droplet diameter [m]
Fr = Froude number [−]
g = gravity [m/s^2]
G = change in surface tension [percent]
H, $\overline{H}$ = curvature [1/m], [−]
k = thermal conductivity [W/mK]
$\tilde{k}$ = Boltzmann constant [J/K]
L = latent heat [J/kg]
M = Mach number [−]
m = mass [kg]
Ma = Marangoni number [−]
$\overline{n}$ = normal vector [−]
p, P = pressure [Pa], [−]
Pe = Peclet number [−]
Pr = Prandtl number [−]
r, R = radial coordinate [m], [−]
Re = Reynolds number [−]
s, S = arc length [m], [−]
Δs = element side length [−]
SHP = superheating parameter [−]
t = time [s]
$\vec{t}$ = tangential vector [−]
T = temperature [K, °C]
u, U = radial velocity [m/s], [−]
v, V = axial velocity [m/s], [−]
We = Weber number [−]
z, Z = axial coordinate [m], [−]

Greek Symbols

α = thermal diffusivity [m^2/s]
δ = Kronecker symbol [−]
ε = Navier-slip coefficient [−]
γ = surface tension [N/m]
κ = viscosity coefficient [1/K]
μ = dynamic viscosity [kg/ms]
ρ = density [kg/m^3]
$\overline{\sigma}$ = shear stress component [−]
τ = time [−]
Θ = temperature [−]

Subscripts

0 = initial
1 = droplet
2 = substrate
amb = ambient
Pb = lead
Sn = tin
z = axial direction
θ = azimuthal direction

Mathematical Operators

D_τ = Lagrangian derivative towards τ
d_T = ordinary derivative towards T
$\partial_{R,Z}$ = partial derivative towards coordinates

References

[1] Maronnier, V., Picasso, M., and Rappaz, J., 1999, ''Numerical Simulation of Free Surface Flows,'' J. Comput. Phys., **155**(2), pp. 439–455.

[2] Attinger, D., Zhao, Z., and Poulikakos, D., 2000, ''An Experimental Study of Molten Microdroplet Surface Deposition and Solidification: Transient Behavior and Wetting Angle Dynamics,'' Journal of Heat Transfer—Transactions of the Asme, **122**(3), pp. 544–556.

[3] Haferl, S., Butty, V., Poulikakos, D., Giannakouros, J., Boomsma, K., Megaridis, C. M., and Nayagam, V., 2001, ''Freezing Dynamics of Molten Solder Droplets Impacting onto Flat Substrates in Reduced Gravity,'' Int. J. Heat Mass Transf., **44**(18), pp. 3513–3528.

[4] Monti, R., Savino, R., and Tempesta, S., 1998, ''Wetting Prevention by Thermal Marangoni Effect. Experimental and Numerical Simulation,'' Eur. J. Mech. B/Fluids, **17**(1), pp. 51–77.

[5] Cao, C. D., Wang, N., Wei, B. B., and de Groh, H. C., 1999, ''Rapid Solidification of Ag-Si Eutectic Alloys in Drop Tube,'' Prog. Nat. Sci., **9**(9), pp. 687–695.

[6] Khodadadi, J. M., and Zhang, Y., 2000, ''Effects of Thermocapillary Convection on Melting within Droplets,'' Numer. Heat Transfer, Part A, **37**(2), pp. 133–153.

[7] Song, S. P., and Li, B. Q., 2000, ''Free Surface Profiles and Thermal Convection in Electrostatically Levitated Droplets,'' Int. J. Heat Mass Transf., **43**(19), pp. 3589–3606.

[8] Ehrhard, P., and Davis, S. H., 1991, ''Nonisothermal Spreading of Liquid-Drops on Horizontal Plates,'' J. Fluid Mech., **229**, pp. 365–388.

[9] Braun, R. J., Murray, B. T., Boettinger, W. J., and McFadden, G. B., 1995, ''Lubrication Theory for Reactive Spreading of a Thin Drop,'' Phys. Fluids, **7**(8), pp. 1797–1810.

[10] Waldvogel, J. M., and Poulikakos, D., 1997, ''Solidification Phenomena in Picoliter Size Solder Droplet Deposition on a Composite Substrate,'' Int. J. Heat Mass Transf., **40**(2), pp. 295–309.

[11] den Boer, A. W. J. P., 1996, ''Marangoni Convection: Numerical Model and Experiments,'' doctoral thesis, Technische Universiteit Eindhoven, Eindhoven.

[12] Fowler, R. H., 1937, ''A Tentative Statistical Theory of Macleod's Equation for Surface Tension, and the Parachor,'' Proc. R. Soc. London, Ser. A, Mathematical Physical and Engineering Sciences, **A159**(896), pp. 229–246.

[13] Jasper, J. J., 1972, ''The Surface Tension of Pure Liquid Compounds,'' J. Phys. Chem. Ref. Data, **1**(4), pp. 841–1009.

[14] Born, M., and Green, H. S., 1947, ''A General Kinetic Theory of Liquids,'' Proc. R. Soc. London, Ser. A, Mathematical Physical and Engineering Sciences, **190**(1020), pp. 455–474.

[15] Egry, I., 1993, ''On the Relation between Surface-Tension and Viscosity for Liquid-Metals,'' Scr. Metall. Mater., **28**(10), pp. 1273–1276.

[16] Koke, J., 2001, ''Rheologie Teilerstarrter Metalllegierunger,'' doctoral thesis, RWTH Aachen, Aachen.

[17] Thresh, H. R., and Crawley, A. F., 1970, ''The Viscosities of Lead, Tin and Pb-Sn Alloys,'' Metall. Trans., **1**, pp. 1531–1535.

[18] Keene, B. J., 1993, ''Review of Data for the Surface-Tension of Pure Metals,'' Int. Mater. Rev., **38**(4), pp. 157–192.

[19] Schwaneke, A. E., Falke, W. L., and Miller, V. R., 1978, ''Surface-Tension and Density of Liquid Tin-Lead Solder Alloys,'' J. Chem. Eng. Data, **23**(4), pp. 298–301.

[20] White, D. W. G., 1971, ''Surface Tensions of Pb, Sn, and Pb-Sn Alloys,'' Metall. Trans., **2**(11), pp. 3067–3071.

[21] NIST, 2001, ''Properties of Solder,'' http://www.boulder.nist.gov/div853/lead%20free/part2.html#%202.2.5.

[22] Carroll, M. A., and Warwick, M. E., 1987, ''Surface-Tension of Some Sn-Pb Alloys.1. Effect of Bi, Sb, P, Ag, and Cu on 60sn-40pb Solder,'' Mater. Sci. Technol., **3**(12), pp. 1040–1045.

[23] Landau, L. D., and Lifshitz, E. M., 1959, *Fluid Mechanics*, Pergamon Press, Oxford; New York, **6**, pp. 238–241.

[24] Baer, T. A., Cairncross, R. A., Schunk, P. R., Rao, R. R., and Sackinger, P. A., 2000, ''A Finite Element Method for Free Surface Flows of Incompressible Fluids in Three Dimensions. Part Ii. Dynamic Wetting Lines,'' Int. J. Numer. Methods Fluids, **33**(3), pp. 405–427.

[25] Bushko, W., and Grosse, I. R., 1991, ''New Finite-Element Method for Multidimensional Phase-Change Heat-Transfer Problems,'' Numer. Heat Transfer, Part B, **19**(1), pp. 31–48.

[26] Arafune, K., Sugiura, M., and Hirata, A., 1999, ''Investigation of Thermal Marangoni Convection in Low and High- Prandtl-Number Fluids,'' J. Chem. Eng. Jpn., **32**(1), pp. 104–109.

[27] Bach, P., and Hassager, O., 1985, ''An Algorithm for the Use of the Lagrangian Specification in Newtonian Fluid-Mechanics and Applications to Free-Surface Flow,'' J. Fluid Mech., **152**, pp. 173–190.

Effectiveness-NTU Relations for Heat Exchangers With Streams Having Significant Kinetic Energy Variation

Gregory F. Nellis
e-mail: gfnellis@engr.wisc.edu
Department of Mechanical Engineering,
University of Wisconsin,
Room 1339 Engineering Research Building,
1500 Engineering Drive,
Madison, WI 53706

Effectiveness-NTU equations are derived for counter and parallel-flow heat exchangers with fluids having high velocities. In this case, the change in the kinetic energy occurring within the heat exchanger will significantly affect the temperature profiles. The effectiveness is found to depend on the usual non-dimensional variables that compare the heat exchanger conductance to the hot- and cold-side capacity rates and on four additional nondimensional quantities that reflect the magnitude and distribution of the kinetic energy on the hot and cold-sides of the heat exchanger. The governing differential equations are derived, nondimensionalized, and solved analytically for the case of an exponentially distributed kinetic energy. Graphical solutions are presented and interpreted for several cases. The solutions are applied to a particular case involving high velocities within a counter-flow heat exchanger used to produce cryogenic temperatures.
[DOI: 10.1115/1.1560154]

Keywords: Analytical, Heat Transfer, Heat Exchangers, Modeling

Introduction

Devices for exchanging heat between flowing streams are typically operated under conditions where the change in the kinetic energy is negligible relative to the change in the thermal energy of the fluids. A well-designed heat exchanger will generally exhibit a small pressure drop and a long residence time for the fluid; both conditions suggest low velocities and small kinetic energy changes. As a result, the ε-NTU relations that are typically used to model heat exchangers are derived based on the assumption of negligible fluid kinetic energy variations in the stream-wise directions. However, there are some energy conversion devices where heat exchange must occur between fluid streams with substantial and varying kinetic energy, sometimes due to velocities in a non-axial direction. Some examples might include the vortex tube, turbine blade cooling, tangentially injected heat exchangers [1,2], nozzles and diffusers [3], and heat transfer problems in high velocity aircraft [4]. A particularly interesting example that has been recently presented in the literature by Kaiser et al. [8] is a novel cryogenic cooling device based on expanding a gas through a nozzle to produce a static temperature drop that can be used to produce low temperature cooling. In order for this refrigerator to operate, the high velocity must be maintained even within the counter-flow heat exchanger that separates the hot and cold ends resulting in a significant interplay between kinetic energy variation and static temperature distribution.

This paper is motivated by the need to understand the behavior of systems in which the heat transfer rate is fundamentally coupled to variations in kinetic energy through the internal temperature profiles. The governing equations within counter- and parallel-flow heat exchangers are derived and the kinetic energy terms are retained. An exponential variation in kinetic energy is assumed and the resulting problem is nondimensionalized and solved. The effectiveness of the heat exchanger in this situation is found to depend on the typical non-dimensional groups, number of transfer units and capacity ratio, and on additional non-dimensional parameters that represent both the magnitude and variation of the kinetic energy. The analytical solution to the problem is presented and shown to limit to the conventional solution as the kinetic energy terms disappear. The analytical solution is used to explore the behavior of a heat exchanger under some conditions of interest. Results are presented graphically for several situations and these figures are interpreted physically. Finally, the solutions are applied to the "Bernoulli" effect cryocooler—a physical device based on producing low temperature refrigeration through the expansion of a gas through a nozzle coupled with a counter-flow heat exchanger. This device relies on the transfer of heat between streams of gas undergoing significant changes in kinetic energy and the coupling between the temperature distribution and kinetic energy variation can conveniently be analyzed using the equations derived in this paper.

Contributed by the Heat Transfer Division for publication in the JOURNAL OF HEAT TRANSFER. Manuscript received by the Heat Transfer Division April 23, 2001; revision received November 6, 2002. Associate Editor: M. K. Jensen.

Analytical Solution

Counter-flow and parallel-flow heat exchangers are illustrated in Figs. 1 and 2. In both cases the cold-side fluid enters (at $x=0$) with a specified mass flow rate ($\dot{m}_c$), static temperature ($T_{c,\text{in}}$) and velocity ($v_{c,\text{in}}$). The hot-side fluid either enters at the other end ($x=L$) in the counter-flow configuration or at the same end ($x=0$) in the parallel-flow configuration. The hot-side fluid has a specified mass flow rate ($\dot{m}_h$), static temperature ($T_{h,\text{in}}$) and velocity ($v_{h,\text{in}}$). If the heat exchanger is well insulated and the cold-side fluid is single-phase then the governing differential equation for the cold-side fluid is:

$$\dot{m}_c \cdot \frac{d}{dx}\left[c_{P,c}\cdot T_c + \frac{v_c^2}{2}\right] = p\cdot U\cdot(T_h - T_c) \tag{1}$$

where c_P is the specific heat at constant pressure, p is the wetted perimeter available for heat transfer, and U is the total conductance that characterizes the heat transfer rate between the two streams. If extended surfaces are present in the heat exchanger then an appropriate surface efficiency must be added, here we are assuming that this effect is included in the calculation of U. Equation (1) implies that the heat exchanger is operating at a steady state. The specific heat is assumed to be constant within the heat exchanger so that the governing differential equation becomes:

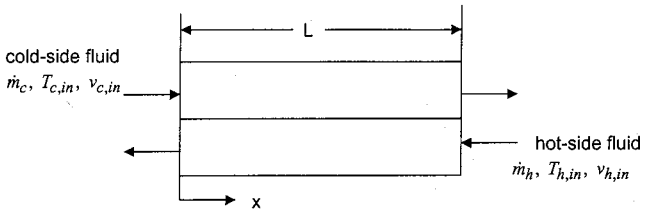

Fig. 1 A counter-flow heat exchanger

$$\frac{dT_c}{dx} = \frac{p \cdot U}{\dot{m}_c \cdot c_{P,c}} \cdot (T_h - T_c) - \frac{1}{c_{P,c}} \cdot \frac{d}{dx}\left(\frac{v_c^2}{2}\right) \tag{2}$$

The governing differential equation for the hot-side fluid depends on the configuration:

$$\frac{dT_h}{dx} = \frac{p \cdot U}{\dot{m}_h \cdot c_{P,h}} \cdot (T_h - T_c) - \frac{1}{c_{P,h}} \cdot \frac{d}{dx}\left(\frac{v_h^2}{2}\right) \quad \text{(counter-flow)} \tag{3a}$$

$$\frac{dT_h}{dx} = -\frac{p \cdot U}{\dot{m}_h \cdot c_{P,h}} \cdot (T_h - T_c) - \frac{1}{c_{P,h}} \cdot \frac{d}{dx}\left(\frac{v_h^2}{2}\right) \quad \text{(parallel-flow)} \tag{3b}$$

In both cases, the fluid is assumed to be single phase with a constant specific heat capacity and total conductance.

The hot and cold-side nondimensional temperatures (Θ_h and Θ_c) and nondimensional axial position (X) [5] are defined to assist in the analysis:

$$\Theta_h \equiv \frac{T_h - T_{c,\text{in}}}{T_{h,\text{in}} - T_{c,\text{in}}} \tag{4a}$$

$$\Theta_c \equiv \frac{T_c - T_{c,\text{in}}}{T_{h,\text{in}} - T_{c,\text{in}}} \tag{4b}$$

$$X = \frac{x}{L} \tag{5}$$

Hot and cold-side number of transfer units (NTU_h and NTU_c) are defined by comparing the heat transfer conductance to the appropriate capacity rate:

$$\text{NTU}_h = \frac{U \cdot p \cdot L}{\dot{m}_h \cdot c_{P,h}} \tag{6a}$$

$$\text{NTU}_c = \frac{U \cdot p \cdot L}{\dot{m}_c \cdot c_{P,c}} \tag{6b}$$

Within the heat exchanger, a local nondimensional kinetic energy (KE) is defined relative to the kinetic energy of the fluid at the inlet:

$$\text{KE}_h = \frac{v_h^2}{v_{h,\text{in}}^2} \tag{7a}$$

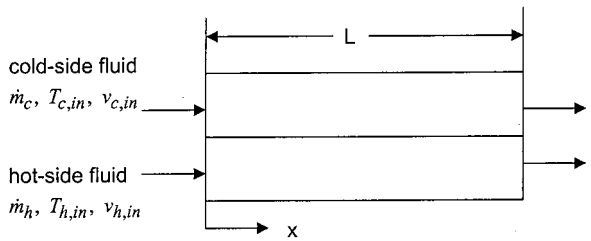

Fig. 2 A parallel-flow heat exchanger

$$\text{KE}_c = \frac{v_c^2}{v_{c,\text{in}}^2} \tag{7b}$$

The kinetic-to-thermal energy ratio (β) is defined as the ratio of the kinetic energy at the inlet to a reference thermal energy change:

$$\beta_h = \frac{v_{h,\text{in}}^2}{2 \cdot c_{P,h} \cdot (T_{h,\text{in}} - T_{c,\text{in}})} \tag{8a}$$

$$\beta_c = \frac{v_{c,\text{in}}^2}{2 \cdot c_{P,c} \cdot (T_{h,\text{in}} - T_{c,\text{in}})} \tag{8b}$$

These definitions lead to a non-dimensional, differential governing equation for the cold-side fluid:

$$\frac{d\Theta_c}{dX} = \text{NTU}_c \cdot (\Theta_h - \Theta_c) - \beta_c \cdot \frac{d}{dX}\text{KE}_c(X) \tag{9}$$

The nondimensional, differential governing equation for the hot-side fluid depends on the configuration:

$$\frac{d\Theta_h}{dX} = \text{NTU}_h \cdot (\Theta_h - \Theta_c) - \beta_h \cdot \frac{d}{dX}\text{KE}_h(X) \quad \text{(counter-flow)} \tag{10a}$$

$$\frac{d\Theta_h}{dX} = -\text{NTU}_h \cdot (\Theta_h - \Theta_c) - \beta_h \cdot \frac{d}{dX}\text{KE}_h(X) \quad \text{(parallel-flow)} \tag{10b}$$

The axial distribution of the kinetic energy must be specified in order to solve these governing equations. The most physically relevant and useful distribution is an exponential decay in the direction of the flow. This situation occurs approximately in swirling flows that are subjected to a viscous torque and has been experimentally measured in several devices such as cyclone separators and vortex tubes [6,7]. The exponential assumed functional form can be used to approximate a large number of actual distributions via appropriate choice of the characteristic length constant and therefore the results will be widely applicable. The length constant that characterizes the kinetic energy decay on each side ($L_{d,h}$ and $L_{d,c}$) is made nondimensional (χ) by comparison with the total length of the heat exchanger. These length constants will be calculated based on the particular application under consideration and may be related to the magnitude of a viscous shear that is degrading the momentum of the fluid (as in a highly swirling flow) or other considerations such as density variations (as in the Bernoulli cryocooler considered in a subsequent section).

$$\chi_h = \frac{L_{d,h}}{L} \tag{11a}$$

$$\chi_c = \frac{L_{d,c}}{L} \tag{11b}$$

The nondimensional kinetic energy distribution in the cold-side fluid is given by:

$$\text{KE}_c(X) = \exp\left(-\frac{X}{\chi_c}\right) \tag{12}$$

The nondimensional kinetic energy distribution in the hot fluid depends on configuration.

$$\text{KE}_h(X) = \exp\left[-\frac{(1-X)}{\chi_h}\right] \quad \text{(counter-flow)} \tag{13a}$$

$$\text{KE}_h(X) = \exp\left(-\frac{X}{\chi_h}\right) \quad \text{(parallel-flow)} \tag{13b}$$

Substitution of these profiles into the non-dimensional, differential governing equations leads to:

$$\frac{d\Theta_c}{dX} = \mathrm{NTU}_c \cdot (\Theta_h - \Theta_c) + \frac{\beta_c}{\chi_c} \cdot \exp\left(-\frac{X}{\chi_c}\right) \tag{14}$$

$$\frac{d\Theta_h}{dX} = \mathrm{NTU}_h \cdot (\Theta_h - \Theta_c) - \frac{\beta_h}{\chi_h} \cdot \exp\left[-\frac{(1-X)}{\chi_h}\right] \quad \text{(counter-flow)} \tag{15a}$$

$$\frac{d\Theta_h}{dX} = -\mathrm{NTU}_h \cdot (\Theta_h - \Theta_c) + \frac{\beta_h}{\chi_h} \cdot \exp\left(-\frac{X}{\chi_h}\right) \quad \text{(parallel-flow)} \tag{15b}$$

These equations can be solved analytically by introducing the appropriate boundary conditions related to the static temperature of the incoming streams:

$$\Theta_c(X=0) = 0 \tag{16}$$

$$\Theta_h(X=1) = 1 \quad \text{(counter-flow)} \tag{17a}$$

$$\Theta_h(X=0) = 1 \quad \text{(parallel-flow)} \tag{17b}$$

The analytical solution is accomplished by introducing a nondimensional temperature difference:

$$\Delta\Theta = \Theta_h - \Theta_c \tag{18}$$

By subtracting Eq. (15*a*) or (15b) from Eq. (14), it is possible to obtain an equation involving only the non-dimensional temperature difference:

$$\frac{d\Delta\Theta}{dX} = (\mathrm{NTU}_h - \mathrm{NTU}_c) \cdot \Delta\Theta - \frac{\beta_h}{\chi_h} \cdot \exp\left[-\frac{(1-X)}{\chi_h}\right] - \frac{\beta_c}{\chi_c} \cdot \exp\left(-\frac{X}{\chi_c}\right) \quad \text{(counter-flow)} \tag{19a}$$

$$\frac{d\Delta\Theta}{dX} = -(\mathrm{NTU}_h + \mathrm{NTU}_c) \cdot \Delta\Theta + \frac{\beta_h}{\chi_h} \cdot \exp\left[-\frac{X}{\chi_h}\right] - \frac{\beta_c}{\chi_c} \cdot \exp\left(-\frac{X}{\chi_c}\right) \quad \text{(parallel-flow)} \tag{19b}$$

The solutions to these equations are:

$$\Delta\Theta = C_1 \cdot \exp[(\mathrm{NTU}_h - \mathrm{NTU}_c) \cdot X] + C_2 \cdot \exp\left[-\frac{1-X}{\chi_h}\right] + C_3 \cdot \exp\left(-\frac{X}{\chi_c}\right) \quad \text{(counter-flow)} \tag{20a}$$

$$C_2 = \frac{-\beta_h}{1-(\mathrm{NTU}_h - \mathrm{NTU}_c)\cdot\chi_h} \quad C_3 = \frac{\beta_c}{1+(\mathrm{NTU}_h - \mathrm{NTU}_c)\cdot\chi_c}$$

$$\Delta\Theta = C_1 \cdot \exp[-(\mathrm{NTU}_h + \mathrm{NTU}_c) \cdot X] + C_2 \cdot \exp\left(-\frac{X}{\chi_h}\right) + C_3 \cdot \exp\left(-\frac{X}{\chi_c}\right) \quad \text{(parallel-flow)} \tag{20b}$$

$$C_2 = \frac{-\beta_h}{1-(\mathrm{NTU}_h + \mathrm{NTU}_c)\cdot\chi_h} \quad C_3 = \frac{\beta_c}{1-(\mathrm{NTU}_h + \mathrm{NTU}_c)\cdot\chi_c}$$

where C_1 is an undetermined constant that will be subsequently set to satisfy the boundary conditions. The nondimensional temperature difference is integrated with respect to axial position using Eq. (14) with Eqs. (20*a*) or (20*b*) in order to obtain the nondimensional cold-side temperature distribution.

$$\Theta_c = \frac{\mathrm{NTU}_c \cdot C_1}{\mathrm{NTU}_h - \mathrm{NTU}_c} \cdot \{\exp[(\mathrm{NTU}_h - \mathrm{NTU}_c)\cdot X] - 1\} + \chi_h \cdot \mathrm{NTU}_c \cdot C_2 \cdot \left[\exp\left(-\frac{1-X}{\chi_h}\right) - \exp\left(-\frac{1}{\chi_h}\right)\right] - (\mathrm{NTU}_c \cdot C_3 \cdot \chi_c + \beta_c) \cdot \left[\exp\left(-\frac{X}{\chi_c}\right) - 1\right] \quad \text{(counter-flow)} \tag{21a}$$

$$\Theta_c = -\frac{C_1 \cdot \mathrm{NTU}_c}{\mathrm{NTU}_h + \mathrm{NTU}_c} \cdot \{\exp[-(\mathrm{NTU}_h + \mathrm{NTU}_c)\cdot X] - 1\} - C_2 \cdot \mathrm{NTU}_c \cdot \chi_h \cdot \left[\exp\left(-\frac{X}{\chi_h}\right) - 1\right] - (\beta_c + \mathrm{NTU}_c \cdot C_3 \cdot \chi_c) \cdot \left[\exp\left(-\frac{X}{\chi_c}\right) - 1\right] \quad \text{(parallel-flow)} \tag{21b}$$

The hot-side fluid nondimensional temperature is the sum of Eqs. (20*a*) and (21*a*) or Eqs. (20*b*) and (21*b*), depending on configuration:

$$\Theta_h = \Theta_c + \Delta\Theta \tag{22}$$

The constant C_1 is obtained by enforcing the hot side inlet temperature boundary condition.

$$C_1 = \frac{1 - \chi_h \cdot \mathrm{NTU}_c \cdot C_2 \cdot \left[1 - \exp\left(-\frac{1}{\chi_h}\right)\right] + (\mathrm{NTU}_c \cdot C_3 \cdot \chi_c + \beta_c) \cdot \left[\exp\left(-\frac{1}{\chi_c}\right) - 1\right] - C_2 - C_3 \cdot \exp\left(-\frac{1}{\chi_c}\right)}{\frac{\mathrm{NTU}_c}{\mathrm{NTU}_h - \mathrm{NTU}_c} \cdot [\exp(\mathrm{NTU}_h - \mathrm{NTU}_c) - 1] + \exp(\mathrm{NTU}_h - \mathrm{NTU}_c)} \quad \text{(counter-flow)} \tag{23a}$$

$$C_1 = 1 - C_2 - C_3 \quad \text{(parallel-flow)} \tag{23b}$$

The effectiveness of a heat exchanger (ε) is typically defined as the ratio of the actual to a theoretical maximum heat transfer rate:

$$\varepsilon = \frac{\dot{Q}}{(\dot{m} \cdot c_P)_{\min} \cdot (T_{h,\mathrm{in}} - T_{c,\mathrm{in}})} \tag{24}$$

After invoking an energy balance on the cold-side fluid, the effectiveness can be written as:

$$\varepsilon = \frac{\mathrm{NTU}_{\max}}{\mathrm{NTU}_c} \cdot \left\{\Theta_c(X=1) + \beta_c \cdot \left[\exp\left(-\frac{1}{\chi_c}\right) - 1\right]\right\} \tag{25}$$

Alternatively, an energy balance on the hot-side fluid yields a different equation for the effectiveness that depends on the configuration:

$$\varepsilon = \frac{\mathrm{NTU}_{\max}}{\mathrm{NTU}_h} \cdot \left\{1 - \Theta_h(X=0) + \beta_h \cdot \left[1 - \exp\left(-\frac{1}{\chi_h}\right)\right]\right\} \quad \text{(counter-flow)} \tag{26a}$$

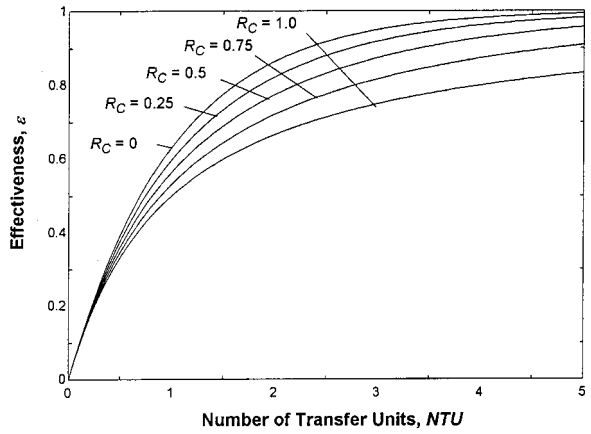

Fig. 3 Effectiveness of a counter-flow heat exchanger predicted by Eq. (25) in the absence of kinetic energy ($\beta=\beta_c=\beta_h=0$)

$$\varepsilon=\frac{\mathrm{NTU}_{\max}}{\mathrm{NTU}_h}\cdot\left\{\Theta_h(X=1)-1+\beta_h\left[\exp\left(-\frac{1}{\chi_h}\right)-1\right]\right\}$$

(parallel-flow) (26*b*)

The effectiveness predictions associated with Eq. (25) and Eqs. (26*a*) or (26*b*), depending on configuration, are consistent when coupled with the analytical solution given by Eqs. (20) through (23), verifying that this solution satisfies energy conservation.

The effectiveness predicted using these equations is a function of six nondimensional variables—the two typical ones that characterize the ratio of heat transfer conductance to capacity rate on each side (NTU_h and NTU_c) as well as four additional groups that characterize both the magnitude of the kinetic energy entering the heat exchanger (β_h and β_c) and the axial distribution of that kinetic energy (χ_h and χ_c) on each side.

$$\varepsilon=\varepsilon(\mathrm{NTU}_h,\mathrm{NTU}_c,\beta_h,\beta_c,\chi_h,\chi_c) \tag{27}$$

In the subsequent section, this analytical solution will be examined and interpreted for a few conditions.

Results

The effectiveness of a heat exchanger is typically given in terms of a number of transfer units (NTU) and a capacity ratio (R_C), defined as:

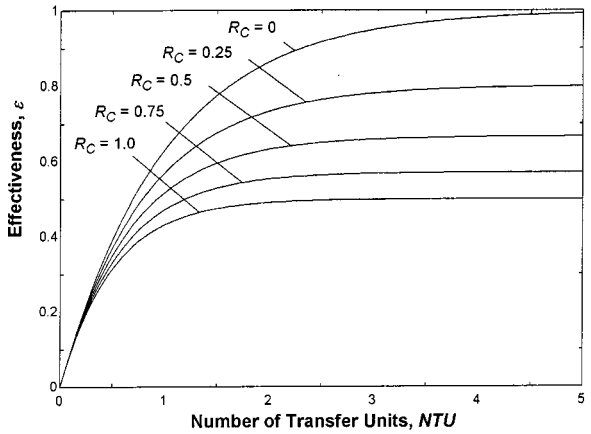

Fig. 4 Effectiveness of a parallel-flow heat exchanger predicted by Eq. (25) in the absence of kinetic energy ($\beta=\beta_c=\beta_h=0$)

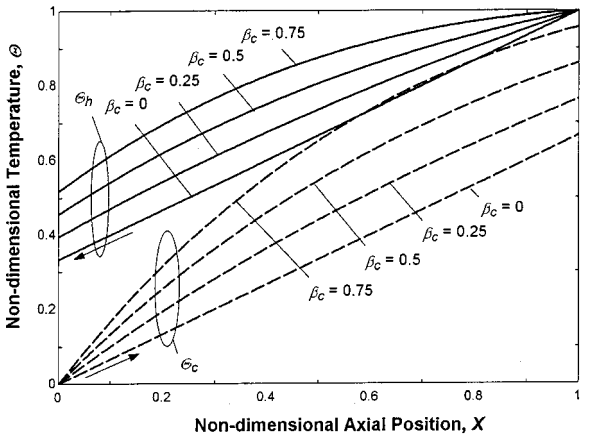

Fig. 5 Nondimensional temperature as a function of *X* for different values of β_c in a balanced, counter-flow heat exchanger ($\mathrm{NTU}_c=\mathrm{NTU}_h=2.0$, $\chi_c=1.0$, $\beta_h=0.0$)

$$\mathrm{NTU}\equiv\frac{p\cdot L\cdot U}{(\dot m\cdot c_P)_{\min}} \tag{28}$$

$$R_C\equiv\frac{(\dot m\cdot c_P)_{\min}}{(\dot m\cdot c_P)_{\max}} \tag{29}$$

Figures 3 and 4 illustrate the effectiveness as a function of the number of transfer units (NTU) for several values of the capacity ratio (R_C) in the counter-flow and parallel-flow configurations, respectively. These figures were developed for the zero-kinetic energy situation ($\beta_c=\beta_h=0$) and in this limit the equations developed earlier faithfully reproduce the results presented in several textbooks on heat exchanger design, for example [5].

As the kinetic energy of the cold-side fluid becomes significant, the effectiveness of the heat exchanger will decrease. This behavior occurs because the reduction in kinetic energy of the cold-side fluid as it moves through the heat exchanger tends to increase its static temperature with a consequent reduction in the temperature difference that drives heat transfer. Figure 5 illustrates how the nondimensional temperature profiles for a balanced (i.e., $R_C=1$) counter-flow heat exchanger are affected when the cold-side kinetic-to-thermal energy ratio is increased. Note that as the dimensionless kinetic energy approaches unity, the velocities will become very large; for example, when $\beta_c=1$ with air at nominally room temperature and a 100°C temperature drop across the

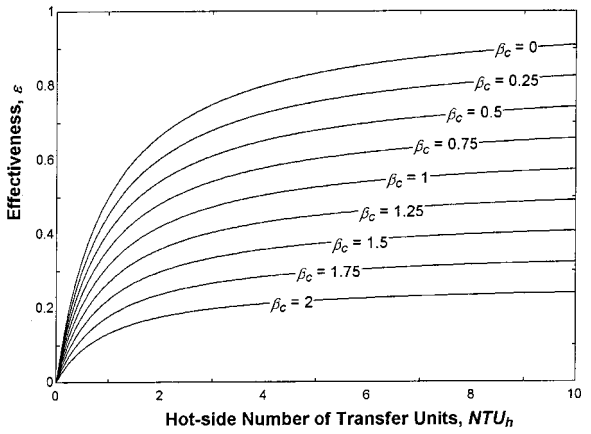

Fig. 6 Effectiveness as a function of NTU_h for different values of β_c in a balanced, counter-flow heat exchanger ($\mathrm{NTU}_c=\mathrm{NTU}_h$, $\chi_c=1.0$, $\beta_h=0.0$)

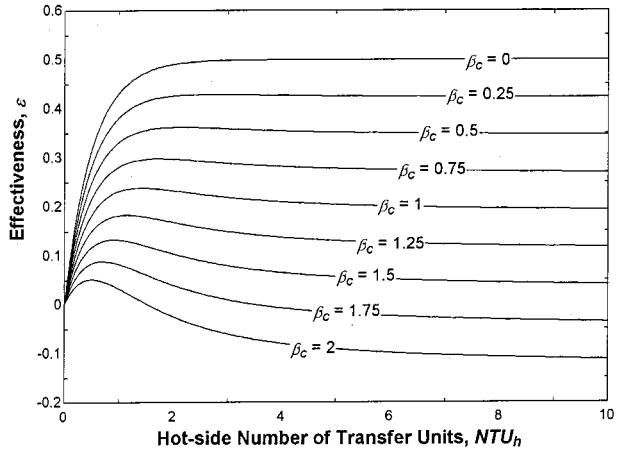

Fig. 7 Effectiveness as a function of NTU_h for different values of β_c in a balanced, parallel-flow heat exchanger ($NTU_c = NTU_h$, $\chi_c = 1.0$, $\beta_h = 0.0$)

heat exchanger the associated Mach number is approximately 1. Figure 6 illustrates the resulting heat exchanger effectiveness as a function of the number of transfer units.

A similar pattern can be observed for the parallel-flow configuration. Figure 7 illustrates the effect of cold-side fluid kinetic energy on the effectiveness of a balanced, parallel-flow heat exchanger as a function of the number of transfer units. Very high levels of kinetic energy in the cold-side fluid may actually result in its static temperature rising above that of the hot-side fluid and locally reversing the direction of heat transfer. This phenomenon explains the peak exhibited by the high kinetic energy curves in Fig. 7 and also the fact that the effectiveness becomes negative at extremely high values of kinetic energy and number of transfer units.

Figures 5 through 7 were generated for the situation where the length constant associated with the kinetic energy decay is comparable to the length of the heat exchanger (i.e., for $\chi_c = 1.0$). Figure 8 illustrates how the cold-side characteristic length of the kinetic energy decay affects the temperature profiles within a balanced, counter-flow heat exchanger. Figure 9 illustrates the resulting heat exchanger effectiveness as a function of the non-dimensional cold-side decay length for various values of the cold-side kinetic-to-thermal energy ratio. If the non-dimensional decay length is very small then the cold-side fluid undergoes a deceleration-related temperature rise almost immediately upon entering the heat exchanger, reducing the temperature difference that drives heat transfer within the heat exchanger and lowering the heat exchanger's effectiveness. In the limit of a vanishingly small decay length ($\chi_c \to 0$) the situation can be adequately modeled using the stagnation temperatures in conjunction with conventional heat exchanger effectiveness correlations. At very large values of the nondimensional decay length ($\chi_c \to \infty$), the velocity

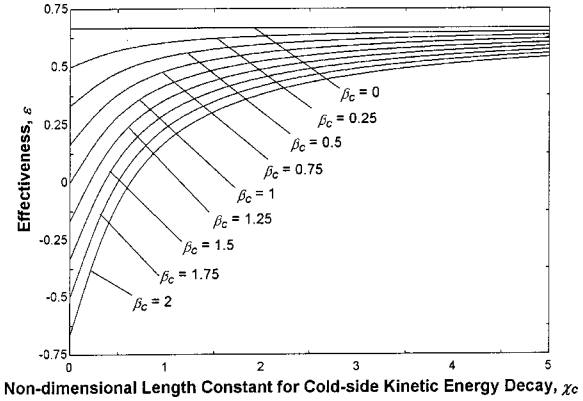

Fig. 9 Effectiveness as a function of χ_c for different values of β_c in a balanced, counter-flow heat exchanger ($NTU_c = NTU_h = 2.0$, $\beta_h = 0.0$)

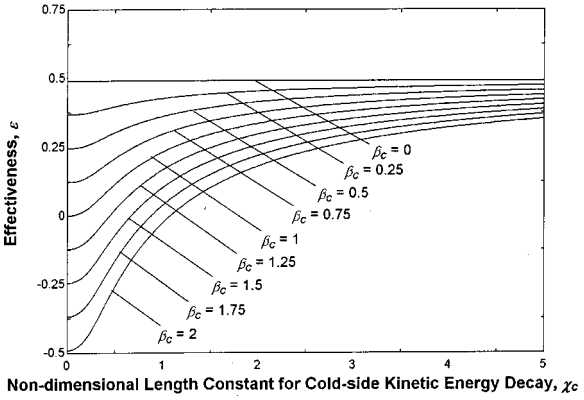

Fig. 10 Effectiveness as a function of χ_c for different values of β_c in a balanced, parallel-flow heat exchanger ($NTU_c = NTU_h = 2.0$, $\beta_h = 0.0$)

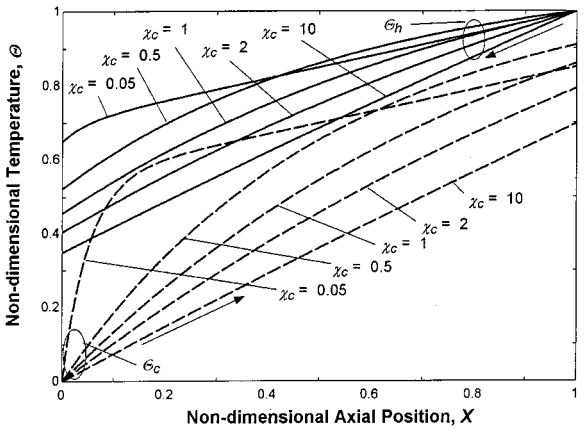

Fig. 8 Nondimensional temperature as a function of X for different values of χ_c in a balanced, counter-flow heat exchanger ($NTU_c = NTU_h = 2$, $\beta_c = 0.5$, $\beta_h = 0.0$)

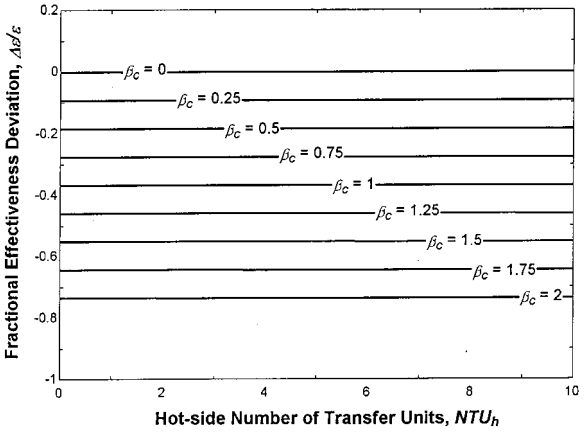

Fig. 11 Fractional deviation in effectiveness as a function of NTU_h for different values of β_c in a balanced, counter-flow heat exchanger ($NTU_c = NTU_h$, $\chi_c = 1.0$, $\beta_h = 0.0$)

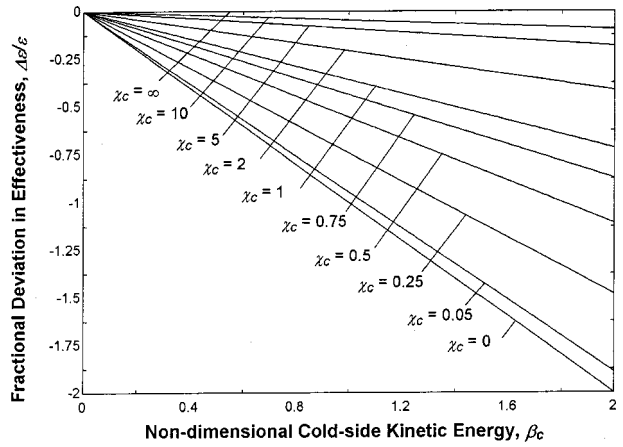

Fig. 12 Fractional deviation in effectiveness as a function of β_c for different values of χ_c in a balanced, counter-flow heat exchanger ($NTU_c = NTU_h$, $\beta_h = 0.0$)

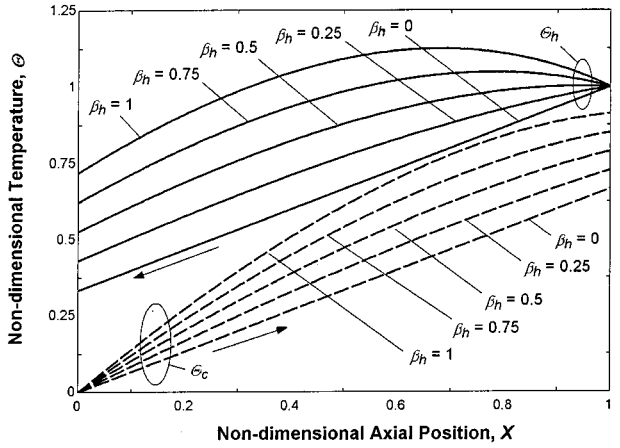

Fig. 13 Nondimensional temperature as a function of X for different values of β_h in a balanced, counter-flow heat exchanger ($NTU_c = NTU_h = 2.0$, $\chi_h = 1.0$, $\beta_c = 0.0$)

change of the fluid within the heat exchanger is insignificant and therefore the kinetic energy, although possibly quite large, has no effect on the internal temperature profiles or the heat exchanger effectiveness. This result is evident by the fact that the effectiveness curves in Fig. 9 approach the zero-kinetic energy solution as χ_c is increased. In this limit, the situation can be adequately modeled using the static temperatures within conventional heat exchanger effectiveness correlations. The equations derived in this paper are needed in the intermediate region, where the decay length and the heat exchanger length are not too different and the inlet kinetic energy is significant. Figure 10 illustrates the effectiveness predicted for the parallel-flow configuration under the same conditions and shows that it behaves in a similar manner.

Figures 8 through 10 were derived for a balanced heat exchanger with a constant number of transfer units ($NTU_h = NTU_c = 2$). Obviously a very large number of similar figures would be required to completely map out all of the possible operating conditions. However under some limiting conditions the effect of kinetic energy can be considered as a perturbation to the more conventional, zero-kinetic energy solutions. The fractional deviation of the effectiveness relative to the zero-kinetic energy solution is defined as:

$$\frac{\Delta\varepsilon}{\varepsilon} = \frac{\varepsilon(\mathrm{NTU}_h, \mathrm{NTU}_c, \beta_h, \beta_c, \chi_h, \chi_c) - \varepsilon(\mathrm{NTU}_h, \mathrm{NTU}_c, \beta_h = 0, \beta_c = 0)}{\varepsilon(\mathrm{NTU}_h, \mathrm{NTU}_c, \beta_h = 0, \beta_c = 0)} \tag{30}$$

Figure 11 illustrates this fractional effectiveness deviation as a function of the number of transfer units for different values of the cold-side kinetic-to-thermal energy ratio. This figure is based on the same information shown in Fig. 6 but reveals that the fractional deviation in effectiveness is essentially independent of the number of transfer units for the balanced, counter-flow configuration. This result is generally true as any of the variables that describe the kinetic energy level or distribution in either the hot- or cold-side fluids are varied. Figure 12 illustrates the fractional deviation in effectiveness as the cold-side kinetic-to-thermal energy ratio is varied for various values of decay length. Figure 12 was developed for a balanced, counter-flow heat exchanger in the limit of infinite number of transfer units, however, Fig. 11 reveals that these results are nearly independent of the number of transfer units and therefore allows this deviation in effectiveness to be applied as a perturbation to the zero-kinetic energy solution.

It is clear that kinetic energy in the cold stream has a negative effect on the heat exchanger's performance. In contrast, kinetic energy in the hot-side fluid will have a positive impact on effectiveness. Figure 13 illustrates how the non-dimensional temperature profiles for a balanced, counter-flow heat exchanger are affected by kinetic energy in the hot-side fluid. The deceleration of the hot-side fluid causes a temperature rise that tends to elevate the temperature difference between the two streams, augment the heat transfer rate, and therefore improve the effectiveness. The effectiveness of a balanced, counter-flow heat exchanger as a function of the number of transfer units is illustrated in Fig. 14 for various values of the hot-side kinetic-to-thermal energy ratio, clearly indicating the positive effect on performance. Figure 15 illustrates the effectiveness of a balanced, parallel-flow heat exchanger as a function of the number of transfer units for various values of the hot-side kinetic-to-thermal energy ratio and shows a

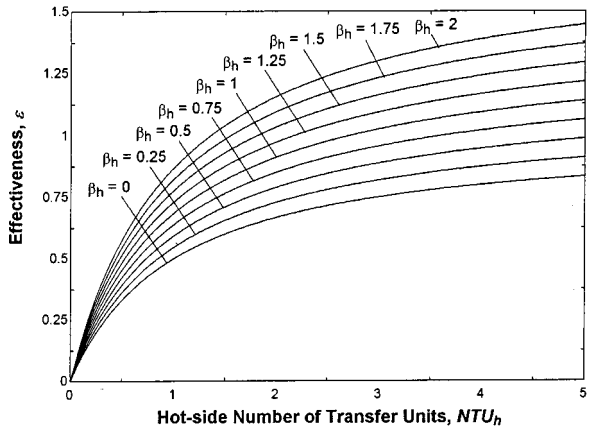

Fig. 14 Effectiveness as a function of NTU_h for different values of β_h in a balanced, counter-flow heat exchanger ($NTU_c = NTU_h$, $\chi_h = 1.0$, $\beta_c = 0.0$)

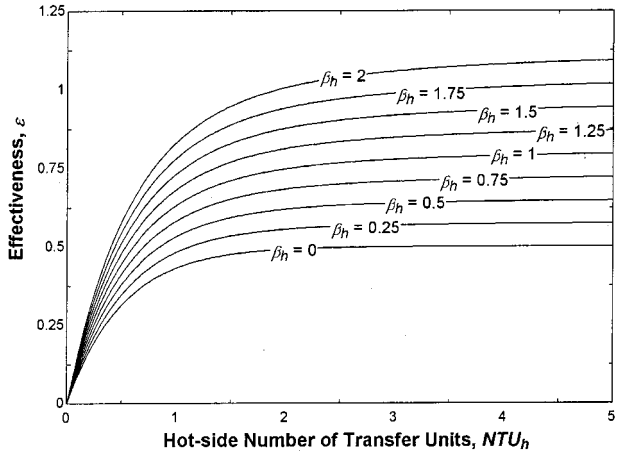

Fig. 15 Effectiveness as a function of NTU_h for different values of β_h in a balanced, parallel-flow heat exchanger ($NTU_c = NTU_h$, $\chi_h = 1.0$, $\beta_c = 0.0$)

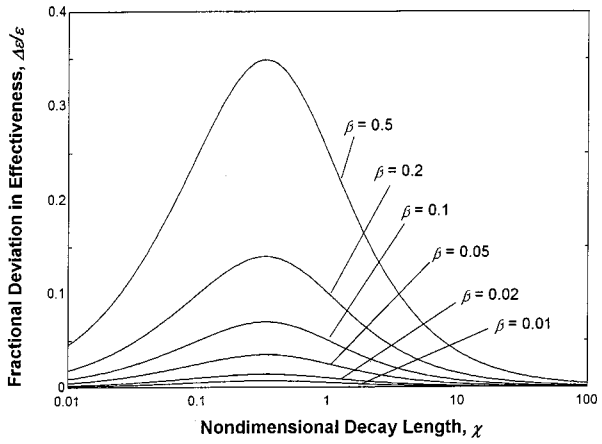

Fig. 17 Fractional deviation in effectiveness as a function of $\chi = \chi_h = \chi_c$ for different values of $\beta = \beta_h = \beta_c$ in a balanced, counter-flow heat exchanger ($NTU_c = NTU_h$)

similar augmentation of the heat transfer rate occurs in this configuration. Figure 16 illustrates the fractional deviation in effectiveness as a function of the kinetic energy in the hot-side fluid as the characteristic length for kinetic energy decay is reduced. This figure was prepared in the limit of infinite number of transfer units but the results are insensitive to the number of transfer units, as with Fig. 12 previously. Notice that the deviation is most pronounced for high levels of kinetic energy and/or short characteristic decay lengths, characteristics that are consistent with our previous observations for cold-side kinetic energy.

Figure 17 illustrates the fractional deviation in effectiveness as a function of the kinetic energy for various values of the decay length when both fluids are characterized by the same conditions ($\beta_h = \beta_c = \beta$ and $\chi_h = \chi_c = \chi$). It is interesting to note that when the decay length is very short, the temperature change produced by kinetic energy occurs immediately upon entering the heat exchanger and, since the level of kinetic energy is assumed to be the same in each stream, the overall effectiveness is unchanged by the presence of kinetic energy. At very large decay length, there is essentially no stream-wise variation of kinetic energy and hence no effect on the effectiveness. At intermediate decay length, the effectiveness is increased by the kinetic energy indicating that the beneficial effect on the hot fluid dominates the negative effect on the cold fluid.

Thus far only balanced heat exchangers have been investigated. Figure 18 illustrates the effectiveness of a counter-flow heat exchanger as a function of the thermal capacity ratio between the cold- and the hot-side fluids as the kinetic energy in the cold-side fluid is varied. In all cases, the number of transfer units based on the side with the minimum capacity rate is held constant. As previously observed for the balanced heat exchanger, the effect of cold-side kinetic energy is to degrade the heat exchanger's performance relative to its zero-kinetic energy counterpart. However, this effect is amplified when the cold-side fluid thermal capacity rate is less than that of the hot-side fluid. Figure 19 illustrates this phenomenon more clearly by showing the fractional deviation in the effectiveness rather than the absolute effectiveness. This trend is true in general for all configurations under all operating conditions. The effect of kinetic energy on one side of the heat exchanger is amplified as the thermal capacity rate on that same side is reduced.

Application of Results to Bernoulli Cryocooler

Figure 20 illustrates a closed-cycle cryocooler, which has been recently proposed by Kaiser et al. [8]. This refrigeration cycle does not rely on either the Joule-Thomson effect or a work-extracting expansion device. It would therefore be free of the

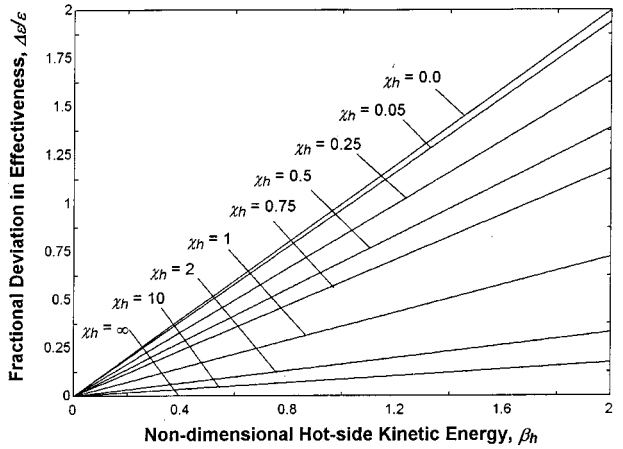

Fig. 16 Fractional deviation in effectiveness as a function of β_h for different values of χ_h in a balanced, counter-flow heat exchanger ($NTU_c = NTU_h$, $\beta_c = 0.0$)

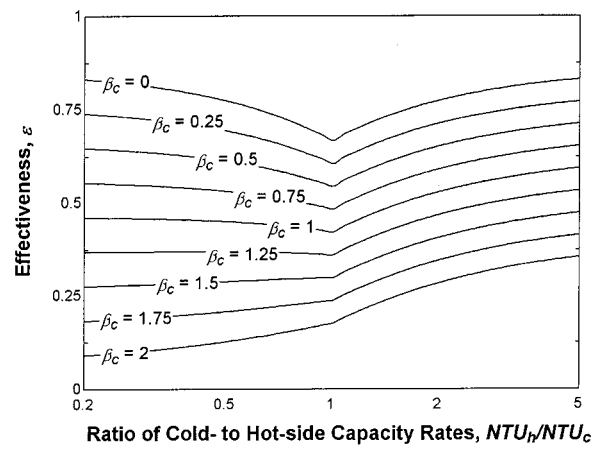

Fig. 18 Effectiveness as a function of cold- to hot-side capacity ratio for various values of β_c in a counter-flow heat exchanger ($NTU_{max} = 2.0$, $\beta_h = 0$, $\chi_c = 1.0$)

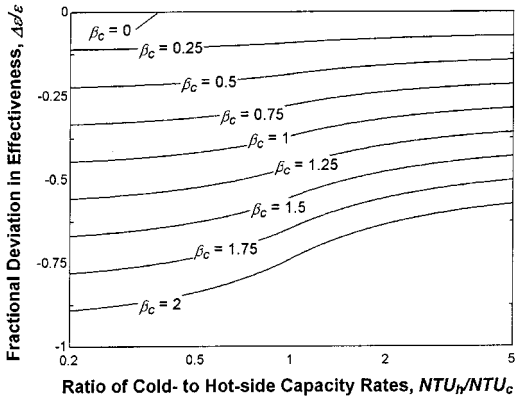

Fig. 19 Fractional deviation in effectiveness as a function of the cold- to hot-side capacity ratio for various values of β_c in a counter-flow heat exchanger ($NTU_{max}=2.0$, $\beta_h=0$, $\chi_c=1.0$)

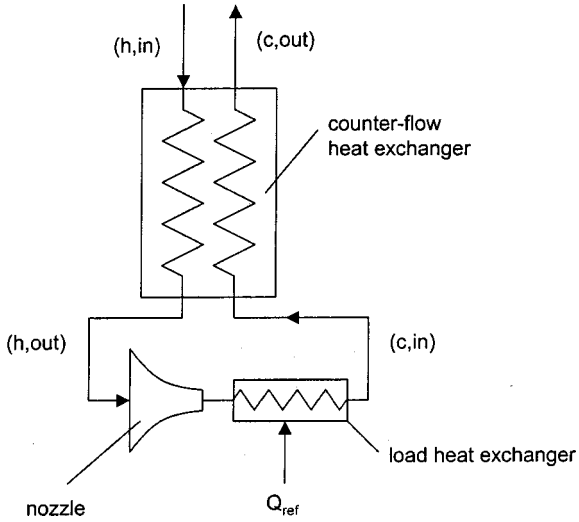

Fig. 20 Schematic of the "Bernoulli" effect cryocooler

constraints related to fluid properties that limit the operating regime of a Joule-Thomson cryocooler and be much less complex then a reverse-Brayton device. Instead, the refrigerator produces cooling through the "Bernoulli" effect. High-pressure gas enters a counter-flow heat exchanger and is cooled to near the load temperature. The gas leaving the counter-flow heat exchanger is expanded through a nozzle to a high velocity, causing a reduction in its static temperature. The fluid is subsequently warmed by accepting the refrigeration heat transfer. The high velocity gas then passes back through the counter-flow heat exchanger where it precools the high-pressure gas. The energy associated with the refrigeration load is carried up the temperature scale by the higher kinetic energy on the low-pressure side of the heat exchanger; it is therefore critical that this high velocity be maintained throughout the heat exchanger. The Bernoulli cryocooler is an ideal application of the previous results as the interplay between heat transfer and kinetic energy is not only significant, it is required in order for the device to operate.

The heat exchanger core geometry envisioned by Kaiser et al. [8] for the Bernoulli effect cryocooler, shown in Fig. 21, is a parallel plate configuration that is conducive to manufacture via micro-machining techniques. The core is composed of a large number of channels (N), each of uniform width (W) and the same length (L). The channels are of uniform thickness, t_h and t_c, on the hot (high-pressure) side and cold (low-pressure) side of the heat exchanger, respectively. Table 1 lists the geometry and operating conditions originally put forward in [8].

We will begin by estimating the velocity distribution in the heat exchanger using the technique outlined by Kaiser et al. [8]. A linear temperature distribution from T_H to T_C is assumed. The flow in the channels is taken to be laminar and fully developed so that the product of the friction factor and Reynolds number is a constant (C), taken to be 64 for consistency with [8]. Finally, the viscosity is assumed to vary as the square root of absolute temperature and the gas is assumed to obey the ideal gas law. Combining these assumptions leads to the following equations for the velocity and pressure distribution on the cold side of the heat exchanger.

$$p_c(X)=p_{c,\text{out}}\sqrt{1+\frac{L\cdot C\cdot\mu_H\cdot v_{c,\text{out}}\cdot TR}{10\cdot t_c^2\cdot p_{c,\text{out}}\cdot(TR-1)}\cdot\left\{1-\left[1-(1-X)\cdot\frac{(TR-1)}{TR}\right]^{5/2}\right\}} \tag{31}$$

$$v_c(X)=\frac{v_{c,\text{out}}\cdot\left[1-(1-X)\cdot\dfrac{(TR-1)}{TR}\right]}{\left(\dfrac{p_c(X)}{p_{c,\text{out}}}\right)} \tag{32}$$

where TR is the temperature ratio spanned by the cooler (T_H/T_C) and μ_H is the viscosity of the gas at the hot inlet temperature. A similar set of equations can be written for the pressure and velocity distributions in the hot channels:

$$p_h(X)=p_{h,\text{out}}\cdot\sqrt{1+\frac{L\cdot C\cdot\mu_H\cdot v_{h,\text{out}}}{10\cdot t_h^2\cdot p_{h,\text{out}}\cdot(TR-1)}\cdot\left\{\left[1-(1-X)\cdot\frac{(TR-1)}{TR}\right]^{5/2}-\left(\frac{1}{TR}\right)^{5/2}\right\}} \tag{33}$$

$$v_h(X)=v_{h,\text{out}}\cdot\frac{[TR-(1-X)\cdot(TR-1)]}{\left(\dfrac{p_h(X)}{p_{h,\text{out}}}\right)} \tag{34}$$

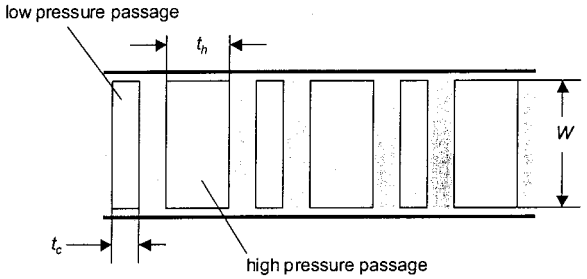

Fig. 21 Heat exchanger core geometry

The hot exit and cold inlet conditions can be connected with a continuity equation and some assumption regarding the efficiency of the nozzle. Here we assume that the nozzle generates no entropy, leading to:

$$v_{c,\text{in}} \cdot p_{c,\text{in}} \cdot t_c = v_{h,\text{out}} \cdot p_{h,\text{out}} \cdot t_h \tag{35}$$

$$v_{c,\text{in}}^2 = v_{h,\text{out}}^2 + 2 \cdot c_p \cdot T_C \cdot \left[1 - \left(\frac{p_{h,\text{out}}}{p_{c,\text{in}}} \right)^{1-\gamma/\gamma} \right] \tag{36}$$

where γ is the ratio of the specific heat capacity at constant pressure to the specific heat capacity at constant volume.

Equations (35) and (36) assume that the cold inlet and hot exit temperatures are not too different and that the flow does not change velocity or lose pressure as it passes through the load heat exchanger. Equations (31) through (36) can be solved simultaneously to yield the pressure and velocity everywhere as a function only of the cold exit conditions. Figure 22 illustrates the velocity and pressure distribution in the hot- and cold-sides of the heat exchanger for the conditions listed in Table 1 with neon gas and a cold exit velocity and pressure of 25 m/s and 500 kPa, respectively. Notice that while the pressure always decreases in the direction of flow, the velocity is governed primarily by density variations caused by temperature and pressure changes. Therefore, the velocity tends to decay in the direction of flow in the hot side and increase in the direction of flow on the cold side.

The analysis described by Kaiser et al. [8] decouples the velocity distribution from the static temperature distribution by separately calculating a pinch-point temperature difference neglecting kinetic energy changes and the heat transfer considering only the kinetic energy changes. Here we will predict the performance of this device more accurately, by considering the coupled effect of kinetic energy variations and temperature distribution using the ε-NTU equations derived in this paper. Figure 23 illustrates the dimensionless kinetic energy variation as a function of axial position for the hot and cold fluids. Also shown in Fig. 23 are the best-fit exponential functions that yield the dimensionless decay lengths (χ_h and χ_c) used in the simulation. This technique is repeated to capture the variation in kinetic energy as the cold exit conditions are varied. The nondimensional kinetic energy in the hot and cold-fluids at the inlets (β_h and β_c) can be calculated from the inlet velocities. The conductance is estimated assuming laminar, fully developed flow so that the Nusselt number (Nu) is a constant, taken to be 7.6. Conduction through the wall separating the two fluids is neglected and the thermal conductivity at the average temperature ($\bar{k}$) is used:

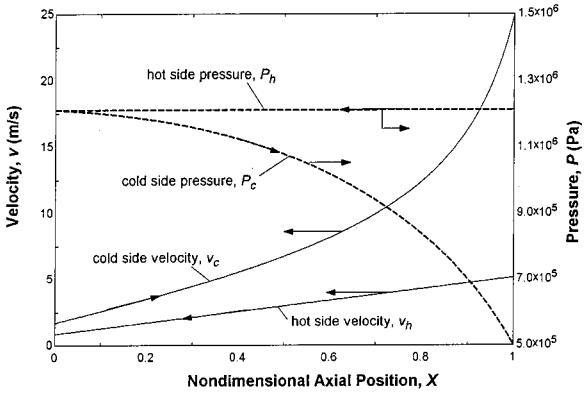

Fig. 22 Velocity and pressure distribution in Bernoulli cryocooler (Neon with $v_{c,\text{out}}=25$ m/s, $P_{c,\text{out}}=100$ kPa, all other conditions as listed in Table 1)

$$U = \frac{\text{Nu} \cdot \bar{k}}{2(t_c + t_h)} \tag{37}$$

The number of transfer units on the hot and cold sides (NTU_h and NTU_c) can be computed according to:

$$\text{NTU}_c = \text{NTU}_h = \frac{2 \cdot U \cdot L \cdot T_{c,\text{in}} \cdot (\gamma - 1)}{t_c \cdot v_{c,\text{out}} \cdot P_{c,\text{out}} \cdot \gamma} \tag{38}$$

The effectiveness of the heat exchanger can be computed using the equations derived in this paper. The effectiveness is used to compute the hot-side exit temperature ($T_{h,\text{out}}$):

$$T_{h,\text{out}} = T_{h,\text{in}} + \frac{(v_{h,\text{in}}^2 - v_{h,\text{out}}^2)}{2 \cdot c_p} - \varepsilon \cdot (T_{h,\text{in}} - T_{c,\text{in}}) \tag{39}$$

The refrigeration load ($\dot{Q}_{ref}$) per mass flow rate can be computed according to:

$$\frac{\dot{Q}_{\text{ref}}}{\dot{m}} = \frac{(v_{c,\text{in}}^2 - v_{h,\text{out}}^2)}{2} - c_P \cdot (T_{h,\text{out}} - T_{c,\text{in}}) \tag{40}$$

The first term in Eq. (40) represents the Bernoulli effect, the refrigeration effect produced by the acceleration of the fluid through the nozzle. The second term represents the loss of refrigeration related to the heat exchanger ineffectiveness. The compressor power ($\dot{W}_c$) per mass flow rate is ideally [8]:

$$\frac{\dot{W}_c}{\dot{m}} = R \cdot T_{h,\text{in}} \cdot \ln\left(\frac{P_{h,\text{in}}}{P_{c,\text{out}}} \right) \tag{41}$$

The coefficient of performance (COP) of the refrigeration cycle, neglecting additional losses such as axial conduction through the heat exchanger and parasitic losses with the environment, is:

$$\text{COP} = \frac{\dot{Q}_L}{\dot{W}_c} \tag{42}$$

Figure 24 illustrates the computed COP for the geometry listed in Table 1 as a function of the cold exit velocity at various values of cold exit pressure. Also illustrated in Table 1 is the COP reported

Table 1 Geometry and operating conditions for Bernoulli effect cryocooler from [8]

Parameter	Symbol	Value	Parameter	Symbol	Value
Cold exit pressure	$p_{c,\text{out}}$	100–500 kPa	Working gas	⋯	Helium or Neon
Hot gas inlet temp.	T_H	300 K	Cold gas inlet temp.	T_C	50 K
Heat exchanger length	L	40 mm	Channel width	W	50 μm
High pressure channel	t_h	50 μm	Low pressure channel	t_c	20 μm
Cold gas exit velocity	$v_{c,\text{out}}$	0–100 m/s	Number of channels	N	200

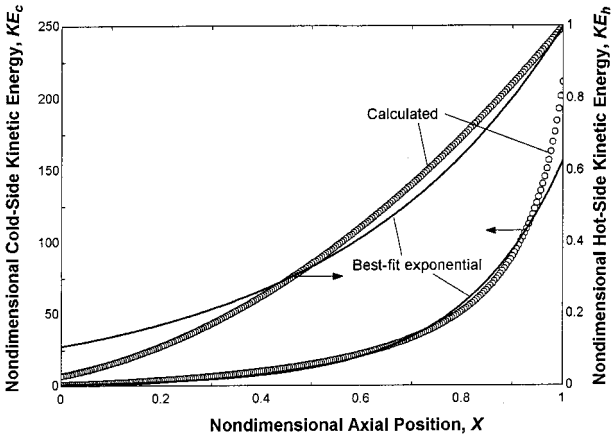

Fig. 23 Calculated kinetic energy distribution and the corresponding best-fit exponential for Bernoulli cryocooler (Neon with $v_{c,out}=25$ m/s, $P_{c,out}=100$ kPa, all other conditions as listed in Table 1)

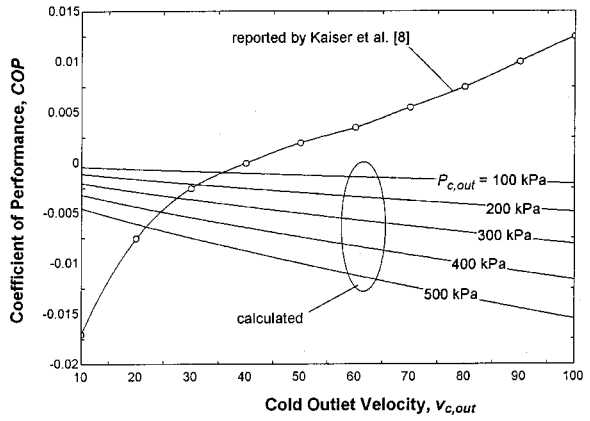

Fig. 24 Coefficient of performance as a function of the cold exit velocity for various cold exit pressures and the results from Kaiser et al. [8] for Bernoulli cryocooler (Neon with all other conditions as listed in Table 1)

by Kaiser et al. for a cold exit pressure of 101.3 kPa. The key difference in the analysis presented here and the original analysis described by Kaiser et al. [8] is the use of a ε-NTU equations that explicitly include the coupling between the kinetic energy variation in the heat exchanger and the temperature profile. This effect appears to be extremely significant for this application, making the cycle non-viable for the proposed geometry under any of the conditions considered here, because the COP is always negative. This analysis is meant only to illustrate an interesting application of the equations derived and presented here and should not be taken as a commentary on the relevance of the Bernoulli effect cryocooler concept.

Conclusions

The governing non-dimensional equations are derived for a counter- and parallel-flow heat exchanger in which the fluid streams are simultaneously experiencing heat transfer and significant changes in their kinetic energy. Analytical solutions to these differential equations are presented for the particular case where the kinetic energy variation is exponential. The effect of kinetic energy on the performance of the heat exchanger is examined in a few interesting cases, allowing the following general conclusions to be drawn:

- Kinetic energy in the cold-side fluid generally degrades the heat exchanger's performance. This degradation becomes less pronounced as the characteristic length for kinetic energy decay becomes larger. This general behavior is true for both the counter-flow and parallel-flow configurations.
- The ratio of the effectiveness with kinetic variation to the zero-kinetic energy effectiveness is essentially independent of the number of transfer units in a balanced, counter-flow heat exchanger. This observation allows the kinetic energy effect to be treated as a perturbation to the more conventional zero-kinetic energy effectiveness solutions.
- Kinetic energy in the hot-side fluid generally improves the heat exchanger's performance. This improvement becomes less pronounced as the characteristic length for kinetic energy decay becomes larger. This general behavior is true for both the counter- and parallel-flow configurations.
- The effect of kinetic energy, positive or negative, is augmented when the capacity rate of the fluid with kinetic energy is decreased.

The ε-NTU solution was also used to analyze a cryogenic refrigeration device that has been proposed which fundamentally relies on the coupling between heat transfer and kinetic energy. The results show that the particular geometry and operating conditions that were initially deemed to be viable will not perform well when the effect of the kinetic energy changes on the static temperature distribution is explicitly considered.

Nomenclature

C = solution constant or the product of friction factor and Reynolds number
COP = coefficient of performance, Eq. (42)
c_p = specific heat capacity at constant pressure, J/kg-K
k = thermal conductivity at mean temperature, W/m-K
KE = nondimensional kinetic energy, Eq. (7)
L = heat exchanger length, m
L_d = length constant characterizing kinetic energy decay, m
$\dot{m}$ = mass flow rate, kg/sec
NTU = number of transfer units, Eq. (6)
Nu = Nusselt number
p = perimeter for heat transfer, m or pressure, N/m^2
$\dot{Q}$ = heat transfer rate, J/sec
R_C = capacity ratio, Eq. (29)
t = channel thickness, m
T = static temperature, K
TR = temperature ratio
U = total conductance for stream-to-stream heat transfer, W/m^2-K
v = velocity, m/sec
W = channel width, m
$\dot{W}$ = power, W
x = axial position, m
X = nondimensional axial position

Greek Symbols

β = nondimensional magnitude of kinetic energy, Eq. (8)
χ = nondimensional length constant for kinetic energy decay, Eq. (11)
$\Delta\varepsilon/\varepsilon$ = fractional deviation relative to the zero-kinetic energy effectiveness, Eq. (30)
$\Delta\Theta$ = non-dimensional temperature difference, Eq. (18)
ε = heat exchanger effectiveness, Eq. (24)
γ = ratio of specific heat capacities
μ = viscosity (N-s/m^2)
Θ = non-dimensional temperature, Eq. (4)

Subscripts

c = cold-side fluid, compressor
h = hot-side fluid

in = inlet
max = maximum
out = outlet
ref = refrigeration

References

[1] Hay, N., and West, J. W., 1975, ''Heat Transfer in Free Swirling Flows in a Pipe,'' ASME J. Heat Transfer, **97**, pp. 411–416.

[2] Chang, F., and Dhir, V. K., 1994, ''Turbulent Flow Field in Tangentially Injected Swirl Flows in Tubes,'' Int. J. Heat Mass Transf., **15**(5), pp. 346–356.

[3] Abdulhadi, M., 1986, ''Dynamics of Compressible Air Flow in Ducts with Heat Exchange,'' Can. Aeronautics Space J., **4**(32), pp. 306–313.

[4] Vargas, J. V. C., and Bejan, A., 2001, ''Thermodynamic Optimization of Finned Crossflow Heat Exchangers for Aircraft Environmental Control Systems,'' Int. J. Heat Mass Transf., **22**, pp. 657–665.

[5] Kays, W. M., and London, A. L., 1998, *Compact Heat Exchangers*, Reprint 3rd ed., Krieger Publishing, Malabar, FL.

[6] Bruun, H. H., 1969, ''Experimental Investigation of the Energy Separation in Vortex Tubes,'' J. Mech. Eng. Sci., **11**(6), pp. 567–582.

[7] Takahama, H., and Yokosawa, H., 1981, ''Energy Separation in Vortex Tubes With a Divergent Chamber,'' ASME J. Heat Transfer, **103**, pp. 196–203.

[8] Kaiser, G., Reisig, L., Thurk, M., and Seidel, P., 1998, ''About a New Type of Closed-Cycle Cryocooler Operating by Use of the Bernoulli Effect,'' Cryogenics, **38**(9), pp. 937–942.